中国石油大学重质油国家重点实验室

工作年报(2006)

地址:北京昌平石油大学

邮编: 102249

电话: 010-89733070

传真: 010-69724721

Email: lab@heavyoil.cn

网址: http://www.heavyoil.cn

目 录

第	[—	部分 年度工作报告	1
	一,	研究工作和水平	1
	Ξ,	队伍建设和人才培养	6
	三、	开放交流与运行管理	7
	四、	实验室大事记	10
	五、	实验室存在的问题,下一年发展思路	13
	六、	依托单位与主管部门的支持	13
第	<u> </u>	部分 2006 年度数据统计	14
	一,	. 人员情况	14
	Ξ,	. 科研项目	17
		1、省部级以上项目	
		2、重要国际合作项目 3、横向协作及技术服务项目	
	=.	3、 傾向	
	`	1、重要期刊论文	
		2、会议论文	
		3、出版专著、教材	52
	四、	专利	52
	五、	. 获奖	54
	六、	学术交流	55
	七、	大型仪器设备	56
	附件	牛 1 代表性论文	57

第一部分 年度工作报告

一、研究工作和水平

1、课题承担情况

2006年,实验室共承担研究课题 89 项,年度经费 1933.3 万元。 新获得 973 项目 1 项,863 项目 3 项,自然科学基金项目 5 项;省部 级项目 14 项,其中教育部重大技术开发项目 1 项。

徐春明教授负责的"重质油化学与开发技术创新引智基地"作为 2007 年度由教育部、国家外国专家局联合实施的"高等学校学科创新引智计划"(又称"111 计划")第二批建设项目得到立项支持,项目总经费 900 万元。该基地项目主要以重质油成因、开采、化学及加工利用为研究内容平台,依托重质油国家重点实验室,吸引了来自加拿大、美国、英国和日本的 12 位知名学者参与,为创新性研究的开展提供优越的国际合作条件。

在国家 863 计划海洋技术领域设置的"天然气水合物勘探开发关键技术"重大项目申报中,通过激烈竞争,实验室陈光进教授领导的研究组赢得了 8 号课题"天然气水合物成藏条件实验模拟技术"(总经费 800 万,国家拨款 400 万,单位配套 400 万)的独立承担权,主要目标是建立天然气水合物成藏过程实验模拟平台;此外陈光进教授还以副课题长身份参加了中海油牵头承担的 9 号课题"天然气水合物开采技术预研究"(总经费 1000 万,国家和中海油分别拨款 500 万),并担任了总重大项目的总体专家。

鲍晓军教授为首席科学家的"973"项目"重油高效转化与优化利用的基础研究"(编号为 2004CB217800)首先以全优的成绩通过中国石油组织的自评估,并顺利通过科技部组织的能源领域项目的中期评估,得到了专家好评。

实验室积极参与的国家自然基金委与中国石油联合资助的重大项目"化工过程中的多尺度时空结构及其效应"取得重要进展,相关研究内容获 2006 年度国家科技进步二等奖。

国际合作方面,徐春明和赵锁奇教授承担的重大国际合作项目"加拿大油砂沥青资源评价及合成原油加工利用的技术研究"通过验收,研究结果已为中国石油投资加拿大油砂沥青的重大决策提供了基础数据。实验室高金森教授为首席科学家的国家科技部国际合作项目"中加实验室合作研究"(2005CB724900)进展顺利。

2、代表性研究水平及实验室最新研究进展

(1)催化裂化汽油辅助反应器改质降烯烃技术

随着环保法规的日益严格,我国石油加工业又面临一个严峻的挑战——清洁油品的生产。由于我国炼油工艺结构绝对地以催化裂化工艺为主,商品汽油中有80%以上来自催化裂化过程。由于催化裂化原料掺炼重油,导致其汽油烯烃含量高达50~60 v%,因此,中国清洁汽油生产的主战场是对催化裂化汽油的改质降烯烃。由于催化裂化汽油90 左右的研究法辛烷值是依靠较高的烯烃含量维持的,如果大幅度地降低烯烃含量,势必造成汽油辛烷值的大幅度降低,使炼油企业无法承受。同时,催化裂化汽油降烯烃反应会带来汽油的损失。因此,

我国清洁汽油生产技术的开发存在着三方面的难度: 烯烃含量大幅度降低, 维持辛烷值不变及尽可能小的汽油损失。

基于大量的石油烃类催化裂化反应机理和规律实验研究发现,重 油催化裂化主反应希望的高温短反应时间,较高的催化剂活性与汽油 降烯烃主要反应,如氢转移、芳构化、异构化等希望的低温长反应时 间和较高的催化剂活性正好相反。因此,为了避免汽油降烯烃反应过 程对主催化裂化反应过程的影响,提出了催化裂化汽油改质降烯烃与 重油催化裂化反应分开在不同的反应器中进行的"异地改质"新思路; 为了实现催化裂化汽油"异地改质"降烯烃的新思路,研制开发了一个 与催化裂化汽油降烯烃反应历程相匹配的输送床与湍动床相组合的 汽油改质用反应器——新型辅助反应器,并将其耦合于现有工业催化 裂化装置中,使催化裂化汽油在该辅助反应器内于优化条件下进行 "异地改质";同时,配套开发设计了一个特殊的分馏塔,单独对改质 油气进行分馏; 通过对催化裂化汽油降烯烃反应历程与动力学等基础 理论研究,获得了催化裂化汽油降烯烃反应的优化条件,结合上述专 门研制开发的装备,形成了成套技术并成功工业化,将催化裂化汽油 的烯烃含量降低至 18v%以下,满足了欧 III 类排放标准。该技术还 能够灵活地通过调整反应操作强度和汽油改质比例增产液化气和丙 烯,实现炼油产品结构的调整,发展石油化工产业。

该技术已在中国石油抚顺石化公司 150 万吨/年、中国石油哈尔 滨石化公司 100 万吨/年、中国石油华北石化公司 100 万吨/年、山东 滨化集团公司 20 万吨/年及中国石油呼和浩特石化公司 90 万吨/年等 5 套重油催化裂化装置上成功工业化。工业应用结果表明,该技术工艺简单,易于实现,由催化裂化装置可直接生产出满足欧 III 标准的清洁汽油。该技术将催化裂化汽油烯烃含量由 50v%左右降至 18v%以下,辛烷值略有增加,改质过程的干气加焦炭损失小于装置总进料的 1.0wt%。实现了重油催化裂化装置重油主提升管反应器和汽油辅助反应器的正常操作运行,解决了汽油烯烃含量超标严重的问题,取得了良好的社会效益和经济效益。从而为我国炼油工业及时为市场提供欧 III 汽油奠定了技术基础,为环境保护事业做出了应有的贡献。到 2005 年 5 月份为止,上述四家炼油企业采用该技术后,新增销售收入总计为 3.47 亿元,新增利润 2.53 亿元。

鉴于该技术对催化裂化汽油改质技术有发展和创新,使用效果良好,获2006年国家科学技术进步二等奖。相关技术内容已获得10项国家发明专利授权。

(2)重油悬浮床加氢第二阶段工业试验取得重要进展

2006年10月至11月底在中国石油抚顺石化分公司石油三厂进行了5万吨重油悬浮床加氢第二阶段工业试验。试验原料为克拉玛依常压渣油。试验目的是在原有第一阶段工业试验打通工艺流程的基础上,进一步进行在中等反应苛刻度下的重油悬浮床加氢工艺试验,考核该工艺反应器的抗焦能力和转化性能。为了保证第二阶段试验成功,在试验前进行了装置改造,主要包括反应器液位计的改造;加热炉负荷的扩能;高压进料泵的改造等。本次试验的主要反应条件为:反应温度425~445℃,氢分压约10MPa,总进料体积空速约为1.0。

试验结果表明,在中等反应苛刻度的条件,轻油(汽、柴油)收率已接近60%,其中以柴油馏份为主。反应后,打开反应器观察表明:整个反应器内部,从反应器内壁至反应器底部以及导流筒的内外壁均完全干净无焦。在整个工业运转过程中,试验装置各主要系统(包括进料系统、催化剂分散系统、反应器系统以及分离系统等)的操作状况十分平稳,未出现任何异常现象。本次试验已达到预期的效果,并取得全套标定数据,试验取得圆满成功。

本工艺开发的下一阶段目标是进一步提高反应苛刻度,以便提高 轻油收率和减少尾油排出量,并实现尾油的合理利用,从而达到较好 的经济效果。

(3) 两段提升管催化系列技术开发取得新进展

两段提升管催化裂化(TSRFCC)技术结合其配套先进装备,可以实现过程的催化作用最大化、反应深度控制的最佳化。技术特点表现为催化剂接力、分段反应、短反应时间和大剂油比。技术效果表现为重油转化率和目的产品收率明显提高,同时柴汽比增加和产品质量显著改善。2002 年工业试验成功后迅速实现工业化推广。目前共有9套装置采用该技术,最大单套装置规模达到 140 万吨/年,总计年加工能力达到700 万吨,年新增经济效益近2亿元,促进了石油炼制技术的重大进展。该技术工业化以后在石油、石化行业引起了强烈反响,科技日报、人民日报海外版、中国石油报、中国石化报、大众日报等多家报纸加以报道。已获发明专利5项,发表论文50多篇。

两段提升管催化裂解多产丙烯(TMP)技术在工艺方面继承了两段提升管催化裂化(TSRFCC)技术分段反应、催化剂接力、短停留时间和大剂油比等技术特点,并赋予其低温大剂油比、组合进料和适宜的停留时间等全新内涵,尽力营造新鲜催化料、回炼油、混合 C4和轻汽油高选择性转化成丙烯的适宜条件。采用配套高 HZSM-5沸石含量、具有适宜重油转化能力的催化剂,可保证重油充分转化的同时,提高丙烯的收率和选择性,兼顾高辛烷值汽油组分,以及柴油组分的生产。该工艺技术已经在大庆炼化分公司建成 12 万吨/年工业试验装置,并进入工业试验阶段。所开发的多产丙烯催化剂或助剂完成工业化生产,并在齐鲁石化、大港石化、玉门炼化等十几家企业获得成功应用。

3、发表论文及授权专利

论文在数量和质量上均有较大突破,在国内外刊物上发表论文 290 篇,其中国外刊物 86 篇,国内刊物 204 篇,SCI 收录 123 篇, EI 收录 146 篇,另有 8 篇会议论文被 ISTP 收录。影响因子 2.0 以上刊物上发表论文 26 篇。

获授权发明专利27项。

二、队伍建设和人才培养

1、实验室队伍基本情况

2006年全室在编固定人员 43 人。其中院士 1 人,教授 27 人; 队伍中具有博士学位的 31 人。

2、队伍建设和人才培养措施与成绩

2006 年,实验室继续注重鼓励支持骨干人员之间团结协作,共同承担重大科研项目,尤其利用教育部优势创新平台建设,通过建成的科研平台和开放课题支持引进人才,在各学科方向形成的同时,也逐渐形成了一支稳定的研究团队。其中非常成功的团队精神就体现在围绕国家 973 项目的协作以及"111 引智计划"平台建设上,形成了一支由鲍晓军、徐春明、高金森、赵锁奇、杨朝合、申宝剑、周亚松、刘晨光、卢春喜、赵震、陈胜利、阎子峰、李春义、孟祥海、时铭显等组成的团队,包括了重油化学、重油催化转化新材料及催化剂、重油轻质化新工艺及配套装备等多个研究方向及多学科的交叉。

3、本年度培养优秀人才情况

2006 年度, 胡玉峰教授获得教育部新世纪人才称号, 孙长宇和刘植昌分别获霍英东教育基金青年教师奖。

在获得的 2006 年度国家科技进步二等奖项目中,实验室高金森教授、徐春明教授和卢春喜教授排在前 3 位。

三、开放交流与运行管理

1. 学术交流

11月12-15日 首届世界重油大会在北京召开。首届世界重油 大会由中国石油天然气集团公司与加拿大阿尔伯达省政府共同发起 和举办,共有40多个国家和地区的600多名代表出席。本实验室协 办了这次大会,其中徐春明教授担任了大会技术论坛中方副主席, Keng H. Chung 教授和赵锁奇教授担任技术论坛分组会主席。赵锁奇教授 的"Kazakstan Residue and Russia Evaluation and Processing Adaptability"和"Characterization and Property Correlations of Athabasca Betumen Derived Synthetic Crude Oil"等学术报告引起与会学者的关注。

2006年8月18-21日由中国颗粒学会主办,重质油国家重点实验室和中国科学院过程工程研究所承办的"中国颗粒学会 2006 年年会暨海峡两岸颗粒技术研讨会"于在北京西郊宾馆举行。实验室主任徐春明教授作了题为"我国石化面临的宏观形势及流态化技术新应用"的大会报告。本次会议一共收到论文与报告 215篇,其中台湾地区论文及报告 44篇。一共有 284名正式代表,另外还有中国石油大学、清华大学、北京化工大学、北京航空航天大学、中国科学院等高校、研究所的 120 多名研究生参加了会议。卢春喜、孙国刚教授还增选为中国颗粒学会第四届理事会理事;卢春喜教授还被推举为中国颗粒学会流态化专业委员会副主任委员。

2. 科研平台建设

四个中心(平台)的建设和运行为实验室重大项目的申请和顺利 开展发挥了重要作用。

公共科研平台运行进入良性发展期,大型仪器设备运行状况良好,材料测试及化学分析主要大型仪器开机率接近最大极限,稳定的技术队伍使实验室对外服务质量得到保障,对外影响不断扩大,对外服务收率也创历年最高值。

3. 运行管理

实验室管理进一步制度化、程序化,管理制度进一步完善。

一些新的规章制度得到较好执行。助理管理员制度的实施为实验室的日常管理提供了制度保障,研究生管理员已经成为实验室日常管理的重要组成部分。经过两年多的摸索与实践,本届助理管理员在数量上有所减少,强化了助理管理员的管理职能,明确分工,注重效率,助理管理员在过去的一年中为实验室日常运行发挥了重要作用。"实验室工作优秀奖"制度经过两年执行取得良好激励效果,在实验室师生中产生较大影响,为促使师生写出高水平研究论文及其它成果起到了积极作用。

实验室高度重视安全管理,在过去的一年中未发生重大事故和重大险情。进一步完善了危险品库房管理办法,实验室危险品出入库专人管理,最大限度减小实验室内部试剂、药品存放量。不仅降低了实验室安全事故风险,同时实验室空间也可以得到更有效利用。实验室废液回收及危险品库房管理办法得到广大的师生的普遍认可,该制度已经被依托单位采纳在更大范围内执行。

强化实验室办公室的服务功能,完善公共办公资源,大大提高了实验室日常办公效率。

实验室网站建设取得较大进展,网站信息量增大,功能增加,外部访问频次和网站影响力综合排名不断上升。投入很大精力对实验室人员、基础设施及研究成果等信息进行了全面整理,经过规范化处理后加入网站数据库中,为下一步功能化网络建设奠定了重要基础。

四、实验室大事记

1、国家科技进步奖取得突破

以高金森教授为负责人,由我室徐春明、卢春喜、刘耀芳、梁咏梅、蓝兴英等人为主要成员完成的"催化裂化汽油辅助反应器改质降烯烃技术的开发和应用"荣获国家科技进步二等奖。

2、加拿大油沙沥青国际合作研究项目通过验收

该项目于2004年10月启动,本实验室和加拿大卡尔加里大学合作,从我国石油资源战略安全和CNPC海外业务发展需要出发,搜集、整理并分析了加拿大油砂沥青资源、开采、集输及加工利用全过程的信息及有关技术经济数据,深入研究了油砂沥青合成原油及其与我国大庆、大港原油混合加工的性能以及油砂沥青的加工技术方案,建立了加拿大油砂沥青及合成原油加工利用数据库,该项目取得的结果可为中国石油天然气集团公司决策投资开发利用加拿大油砂沥青合成原油及油砂沥青资源提供重要技术支撑。11月23-24日 加拿大油沙沥青国际合作研究项目通过验收

- 3、"重油高效转化与优化利用的基础研究""973"项目完成中期评估
- 12月1-2日 "重油高效转化与优化利用的基础研究"项目完成中期评估。

该 973 项目两年来的研究初步确立了"以梯级分离为龙头、以催 化转化为中心、以残渣的高附加值利用相配套"的重油高效转化与优 化利用的技术路线,系统地开展了大港渣油、进口俄罗斯和哈萨克斯 坦渣油的分离研究,提出了渣油梯级分离利用的新判据,初步确立了重油梯级加工利用的必要性和可行性;建立了重油梯级分离中试实验装置,开展了重油残渣分离 - 喷雾造粒的热模实验和残渣输送的冷模流体力学实验,并开始着手相关的工程放大研究;研制出了多种渣油加氢处理催化剂、催化裂化催化剂、多产丙烯的催化剂、催化裂化汽油加氢改质催化剂和非负载型柴油加氢改质催化剂;研制出了可用于燃料电池的碳微球、碳纤维材料以及用于大孔催化材料合成的模板材料

4、重油悬浮床加氢第二阶段工业试验取得成功

2006年10月至11月底在中国石油抚顺石化分公司石油三厂进行了5万吨重油悬浮床加氢第二阶段工业试验。在原有第一阶段工业试验打通工艺流程的基础上,进一步进行在中等反应苛刻度下的重油悬浮床加氢工艺试验,考核该工艺反应器的抗焦能力和转化性能。本次试验已达到预期的效果,并取得全套标定数据,试验取得圆满成功。

- 5、"重质油化学与开发技术创新引智基地"项目立项
- 11月29日 "重质油化学与开发技术创新引智基地"项目立项

由教育部、国家外国专家局联合实施的"高等学校学科创新引智计划"(又称"111计划")第二批建设项目评审工作,我实验室主任徐春明教授负责的"重质油化学与开发技术创新引智基地"作为 2007 年度建设项目予以立项,项目总经费 900 万元。该基地项目涵盖石油勘探、开发、及加工利用,上下游各领域,依托重质油国家重点实验室、石油天然气成藏机理教育部重点实验和石油工程教育部重点实验室

- 室,为创新性研究的开展提供优越条件。
 - 6、组织并参加首届世界重油大会
 - 11月12-15日 首届世界重油大会在北京召开

首届世界重油大会由中国石油天然气集团公司与加拿大阿尔伯 达省政府共同发起和举办,共有 40 多个国家和地区的 600 多名代表 出席。本实验室协办了这次大会,实验室主任徐春明教授担任大会学 术委员会副主席, Keng H. Chung 教授和赵锁奇教授担任技术论坛分 组会主席。

7、"中加科技互补性研究"考察团两度访问我室

"中加科技互补性研究"加方代表团于3月29日和4月28日两度考察我室,就中国和加拿大两国在重质油及油砂利用相关问题进行交流,对我室在能源领域与加方的合作给预高度评价。并对下一步中加科技合作的提出政策建议报告,提交两国政府。

五、实验室存在的问题,下一年发展思路

- 1、在队伍建设上,要进一步采取强化措施,发挥实验室已建成的4个平台的优势,创造宽松环境,采取倾斜政策,进一步改善研究条件以吸引年轻优秀人才;利用已建立的良好国际合作关系,加强国际联合,培养学术骨干,提高创新能力;利用已承担的国家973及国家自然科学基金重大项目,组织团队攻关;在整体提高队伍素质的基础上,着重培养"拔尖的青年优秀骨干",建设"创新群体"。
- 2、不断提高实验室开放水平,充分利用实验室优势研究领域, 在国内国外两个方面进一步加大开放力度并提高开放水平。

六、依托单位与主管部门的支持

依托单位石油大学对实验室发展与建设非常重视,把实验室的发展和建设列为学校工作的最重要任期目标之一,建立了校长负责的"重点实验室工作领导小组"和专题联席会议,能及时讨论并解决实验室发展过程中的有关问题。

主管部门之一的中国石油天然气集团公司每年提供50万元的开发运行经费,保证了实验室的良好运转及对外开放的经费。

第二部分 2006 年度数据统计

一、人员情况

类别	姓名	性别	出生日期	民族	职称	所学专业	最后学位	研究方向	备注
固定人员	鲍晓军	男	1963-04	汉	教授	化学工程	博士	催化新材料研究	
固定人员	陈光进	男	1965-11	汉	教授	化学工程	博士	流体相平衡	
固定人员	陈进富	男	1963-01	汉	副教授	环境工程	硕士	材料、环境工程	
固定人员	陈胜利	男	1962-12	汉	教授	化学工程	博士	催化材料	
固定人员	董智勇	男	1981-07	汉	初级	化学工程	硕士	管理	秘书
固定人员	段爱军	女	1969-07	汉	副研究员	化学工艺	博士	重油催化加工	
固定人员	高金森	男	1964-01	汉	教授	化学工程	博士	清洁燃料生产过程	
固定人员	高伟	男	1959-09	汉	副教授	材料科学	博士	新型陶瓷材料	材料中心副主任
固定人员	郭绍辉	男	1958-09	汉	教授	应用化学	博士	重质油化学	
固定人员	柯明	男	1963-08	汉	副教授	应用化学	博士	清洁燃料生产	
固定人员	蓝兴英	女	1977-11	畲族	讲师	有机化工	博士	数值模拟	
固定人员	李明远	男	1955-03	满族	教授	物理化学	博士	重质油成因及开采化学	
固定人员	李瑞丽	女	1965-05	汉	副教授	石油化工	硕士	重质油组成与加工	
固定人员	梁咏梅	女	1968-05	汉	高工	环境化学	硕士	仪器管理	
固定人员	刘植昌	男	1970-03	汉	副研究员	化学工艺	博士	清洁燃料生产过程	副主任
固定人员	卢春喜	男	1963-02	汉	教授	有机化工	博士	化学工程	
固定人员	毛羽	男	1955-11	汉	教授	化工机械	博士	化学工程	
固定人员	孟祥海	男	1977-10	汉	讲师	化学工艺	博士	化学工艺	

类别	姓名	性别	出生日期	民族	职称	所学专业	最后学位	研究方向	备注
固定人员	申宝剑	男	1964-03	汉	教授	有机化学	博士	催化新材料	材料中心主任
固定人员	时铭显	男	1933-04	汉	教授	化学工程	硕士	轻质化工艺	学术委员会委员
固定人员	史权	男	1972-11	汉	副教授	石油加工	硕士	仪器分析	副主任
固定人员	孙长宇	男	1972-09	汉	教授	化学工艺	博士	流体相平衡	
固定人员	孙学文	男	1965-11	汉	副教授	化学工艺	博士	重质油化学	
固定人员	汪树军	男	1958-03	蒙古族	教授	应用化学	博士	高附加值利用	
固定人员	徐春明	男	1965-02	汉	教授	化学工艺	博士	重质油化学	主任
固定人员	许志明	男	1969-10	汉	副研究员	化学工艺	硕士	重质油化学	
固定人员	张锴	男	1968-08	汉	教授	化学工程	博士	化学工程	
固定人员	赵锁奇	男	1962-04	汉	教授	有机化工	博士	重质油加工过程化学	副主任
固定人员	赵震	男	1964-03	汉	教授	化学工艺、工业催化	博士	石油化工催化	
固定人员	周亚松	男	1964-09	汉	教授	化学工艺	博士	催化材料	
固定人员	郭庆杰	男	1967-03	汉	教授	化学工艺	博士	化学反应工程,流态化工程,颗粒技术	
固定人员	孔瑛	男	1967-01	汉	教授	高分子化学与物理	博士	清洁燃料生产,分离工程	
固定人员	李春义	男	1969-10	汉	教授	工业催化	博士	催化反应工程	
固定人员	刘晨光	男	1962-03	汉	教授	应用化学	博士	清洁燃料生产	学术委员会委员
固定人员	阙国和	男	1938-10	汉	教授	人造石油	学士	重质油转化	学术委员会主任
固定人员	山红红	女	1959-09	汉	教授	化学工艺	博士	石油加工	学术委员会委员
固定人员	王宗贤	男	1958-12	汉	正高	应用化学	博士	重质油加工过程化学	
固定人员	夏道宏	男	1963-01	汉	教授	应用化学	博士	清洁汽油生产过程	
固定人员	阎子峰	男	1965-06	汉	教授	物理化学	博士	重质油转化催化材料与催化剂	
固定人员	杨朝合	男	1964-01	汉	教授	有机化工	博士	石油加工	副主任
固定人员	查庆芳	男	1944-12	汉	教授	燃料化工	大学	新型炭材料	研究中心主任
固定人员	张建芳	男	1939-04	汉	教授	化学工艺	学士	石油加工	

类别	姓名	性别	出生日期	民族	职称	所学专业	最后学位	研究方向 备注
固定人员	郑经堂	男	1955-01	汉	正高	化工,材料	硕士	环保新材料
流动人员	董鹏	男	1940-04	汉	教授	化学工艺	本科	石油焦电流变液,新型大孔材料
流动人员	鄂承林	男	1966-06	汉	讲师	化学工程	博士	化学工程
流动人员	高芒来	男	1965-05	蒙古	教授	应用化学	博士	重质油开采化学与材料
流动人员	郭绪强	男	1963-01	旦	教授	化学工程	博士	高压流体相平衡与物性
流动人员	胡玉峰	男	1968-04	汉	教授	有机化工	博士	液体高压相态
流动人员	柯扬船	男	1964-04	汉	教授	材料	博士	纳米材料
流动人员	李术元	男	1959-09	汉	教授	应用化学	博士	应用化学
流动人员	彭勃	男	1969-12	汉	副教授	应用化学	博士	油水界面物理化学
流动人员	任鲲	男	1971-10	汉	讲师	有机化工	硕士	三次采油聚合物研究
流动人员	王大喜	男	1953-11	汉	教授	应用化学	博士	清洁燃料生产
流动人员	俞英	男	1960-06	汉	教授	应用化学	硕士	清洁燃料生产
流动人员	张民	女	1967-07	汉	讲师	化学工艺	硕士	重质油化学
流动人员	张玉贞	女	1960-07	汉	高工	化学工艺	硕士	石油沥青
流动人员	张文慧	男	1960-05	汉	教授	有机化工	硕士	清洁燃料生产
流动人员	郑晓宇	男	1963-10	汉	副教授	精细化工	博士	强化采油技术

固定人员 43 人,其中院士 1 人,教授 31 人,具有博士学位的 32 人;流动人员 15 人。

二、科研项目

1、省部级以上项目

编号	课题名称	负责人	类别	课题类别	年度 经费	参与人
2004CB217801	重油高效转化与优化利用的化学基础	赵锁奇	主要负责	"973"计划	0	郭绍辉,史权,许志明
2004CB217802	重油催化反应历程的分子模拟和实验研究	王建国	参与	"973"计划	0	高金森
2004CB217803	重油梯级分离的过程工程基础	徐春明	主要负责	"973"计划	0	刘植昌,卢春喜,毛 羽,时铭显,徐春明, 孙学文
2004CB217806	功能化重油催化裂化催化剂的设计与制备	高雄厚, 申宝剑	主要负责	"973"计划	0	申宝剑
2004CB217807	重油加工产品加氢改质催化剂的设计和制备	鲍晓军	主要负责	"973"计划	100	刘晨光,周亚松
2004CB217808	重油残渣高附加值利用新途径的探索	许并社	参与	"973"计划	0	陈胜利
2005CB221205	浆态醇醚燃料合成多相催化剂反应与反应、分离一体化的强化 和控制规律	张锴	主要负责	"973"计划	130	张锴
2005CB221402	合成气制高品质液体燃料	孙予罕	参与	"973"计划	7.5	赵震
2005CB724900	中加实验室合作研究	高金森	主要负责	"973"计划	0	申宝剑,史权,赵锁奇
2010CB209107	气藏气/液/固相互作用热力学理论研究	陈光进	主要负责	"973"计划	0	孙长宇
G2000026409	氢能的规模制备、储运及相关燃料电池的基础研究	汪树军	主要负责	"973"计划	5	汪树军
2006CB932601	纳米粒度标准物质的可控化学合成与量产	陈胜利	主要负责	"973"计划	50	董鹏,袁桂梅

编号	课题名称	负责人	类别	课题类别	年度 经费	参与人
20373043	低碳烷烃选择氧化高分散隔离活性位催化剂的设计及反应机 理研究	赵震	主要负责	国家自然科学基金	7.2	赵震
20376046	一种新型重油催化裂化催化剂孔结构的研究	陈胜利	主要负责	国家自然科学基金	6.6	陈胜利
20376047	催化 C4 烃烷基化离子液体及其催化反应机理分子模拟研究	高金森	主要负责	国家自然科学基金	7.5	高金森
20406012	含 Ti 纳米复合载体及其加氢精制催化剂分子设计研究	段爱军	主要负责	国家自然科学基金	10	段爱军
20473053	同时消除柴油车排放碳颗粒和 NOx 的反应机理和催化剂的研究	赵震	主要负责	国家自然科学基金	8.8	赵震
20476057	一种模拟流化床内时空流体动力学的新方法-多维颗粒床模型	张锴	主要负责	国家自然科学基金	9.2	张锴
20476058	二氧化碳法开发水合物资源的应用基础研究	郭绪强	主要负责	国家自然科学基金	5	郭绪强
20490201	化工过程中的时空多尺度结构研究方法及应用	李静海	参与	国家自然科学基金	79	鲍晓军,卢春喜,徐春 明,张锴
20490202	双气固流态化反应过程直接耦合的多尺度结构分析及放大规 律	徐春明	主要负责	国家自然科学基金	68	卢春喜,徐春明
20490207	气体水合物形成过程中的纳/微尺度强化效应研究	陈光进	主要负责	国家自然科学基金	40	孙长宇
20490209	生产清洁汽油的离子液体烷基化过程中的多尺度结构研究	陈标华	参与	国家自然科学基金	20	刘植昌,赵锁奇
20506016	流动体系中水合物成核与生长动力学及流动特征研究	孙长宇	主要负责	国家自然科学基金	0	孙长宇
20525621	重油梯级分离的化学工程基础研究	徐春明	主要负责	国家自然科学基金	0	徐春明
20576073	柴油耦合深度脱硫新技术及相关基础研究	胡玉峰	主要负责	国家自然科学基金	0	胡玉峰
20576076	提升管进料混合段内气、液、固三相流动特性的研究	鄂承林	主要负责	国家自然科学基金	0	鄂承林

编号	课题名称	负责人	类别	课题类别	年度 经费	参与人
20576078	以复合离子液体为催化剂合成直链烷基苯的研究	刘植昌	主要负责	国家自然科学基金	0	刘植昌
2005AA615030	海底混输系统中水合物浆液阻聚技术	陈光进	主要负责	国家科技重大专项	0	陈光进,孙长宇
040807-06-00	沈阳/大庆减压渣油生产高熔点微晶蜡工艺研究	赵锁奇	主要负责	省部级项目	15	许志明,赵锁奇,孙学 文
04A5050101	非负载型 Ni-Mo-W 加氢催化剂制备新技术研究 省部级项目 瑞玉		省部级项目	0	刘晨光	
04E7024	低级烷烃金属卟啉络合物仿生催化氧化研究	许志明	主要负责	省部级项目	0	许志明,孙学文
04E7025	碳四烷烃催化裂解制丙烯新型催化剂的研究	赵震	主要负责	省部级项目	0	赵震
04E7028	酸性天然气开采及集输过程中的水合物抑制研究	孙长宇	主要负责	省部级项目	0	孙长宇
04E7032	石油焦基双电层电容器制备关键技术	陈进富	主要负责	省部级项目	0	陈进富
04E7035	新型润滑油加氢异构脱蜡催化剂的研究	陈胜利	主要负责	省部级项目	5	陈胜利
050201-01-01	离子液催化碳四烷基化技术研究	刘植昌	主要负责	省部级项目	60	鄂承林,刘植昌
050202-05-00	重油催化裂化与汽油改质双反应器互控技术 DMC 的研究开发	高金森	主要负责	省部级项目	26	高金森
050203-01-04	高硅 NaY 分子筛直接合成技术研究	申宝剑	主要负责	省部级项目	50	申宝剑
050203-01-06	超重力法制备 NAY 分子筛的新技术开发	申宝剑	主要负责	省部级项目	0	申宝剑
050203-03-00	最大限度降低汽油硫含量的催化裂化工艺(MSR)及配套催化剂的研究开发	高金森	主要负责	省部级项目	0	高金森
05E7019	新颖的介孔复合载体制备及柴油深度脱硫催化剂研究	段爱军	主要负责	省部级项目	0	段爱军
05E7025	改性 ZSM-23 分子筛催化裂解制低碳烯烃性能的研究	柯明	主要负责	省部级项目	0	柯明

编号	课题名称	负责人	类别	课题类别	年度 经费	参与人
06A50103	高中油选择性劣质蜡油加氢催化裂化催化剂和工艺研究	周亚松	主要负责	省部级项目	100	周亚松
06B50401	20 万吨/年新型 FCC 汽油加氢改质催化剂现场实验及第二代催化剂研制开发	刘晨光	主要负责	省部级项目	50	刘晨光
104008	FCC 汽油脱硫用分离膜的研究开发	孔瑛	主要负责	省部级项目	20	孔瑛
105045	重油催化装置沉降器结焦机理与抑制技术研究	高金森	主要负责	省部级项目	40	高金森
105083	硫化氢制备氢气和超细粉硫化锌模式放大试验研究	汪树军	主要负责	省部级项目	100	汪树军
105107	地层水合物热力学性质及储气丰度研究	孙长宇	主要负责	省部级项目	0	孙长宇
20040425006	新型燃料电池复合质子膜	陈胜利	主要负责	省部级项目	1.5	陈胜利
200447	地层天然气水合物开采方法研究	孙长宇	主要负责	省部级项目	0	孙长宇
2004527	循环流化床催化剂颗粒磨碎机理研究	郭庆杰	主要负责	省部级项目	2	
2004GG2207015	煤循环流化床大规模制氢集成技术研究	郭庆杰	主要负责	省部级项目	10	
2052010	离子液体氧化脱除轻质油品中的硫化物	孙学文	主要负责	省部级项目	8	孙学文
5020708	利用焦化重蜡油制备优质针状焦研究	王宗贤	主要负责	省部级项目	15	王宗贤
B020411	两段提升管基础理论研究	杨朝合	主要负责	省部级项目	40	杨朝合
B050412A	提高焦化液收改善产品分布新技术及工业化研究	王宗贤	主要负责	省部级项目	40	王宗贤
B050434A	重油悬浮床加氢裂化技术第二阶段试验	阙国和	主要负责	省部级项目	53	阙国和
B050435A	多产丙烯 FCC 催化剂的工业应用	杨朝合	主要负责	省部级项目	23	杨朝合
B060407A	两段催化裂化多产丙稀技术专用催化剂开发	杨朝合	主要负责	省部级项目	135	李春义,杨朝合
B060427A	TMP 技术工业试验	杨朝合	主要负责	省部级项目	30	杨朝合
B060431	用于国IV标准清洁柴油生产的加氢改质催化剂及工艺研究	刘晨光	主要负责	省部级项目	100	刘晨光

编号	课题名称	负责人	类别	课题类别	年度 经费	参与人
B060443A	重油悬浮床加氢工业试验配套技术研究	山红红	主要负责	省部级项目	50	山红红,杨朝合
	具有推力圆锥滚子轴承的储油补偿橡胶密封传动轴开发研究	任琨	主要负责	省部级项目	20	刘植昌
D060441	中海油润滑油馏分分析研究报告	刘晨光	主要负责	省部级项目	24	刘晨光
F050408	甲烷二氧化碳重整反应制合成气技术中试研究	阎子峰	主要负责	省部级项目	10	阎子峰
	新型催化体系用于乙烯聚合制高性能 LLDPE	陈胜利	主要负责	省部级项目	0	陈胜利
	超临界均相条件下丙烯与苯的烷基化反应及催化机理的研究	孙学文	主要负责	省部级项目	10	孙学文
	水合物分离乙烯工艺流程开发和技术经济评价	陈光进	主要负责	省部级项目	40	陈光进
	重油加工催化材料新型孔结构的设计和制备	陈胜利	主要负责	省部级项目	0	陈胜利
	柴油车排放碳黑颗粒催化氧化催化剂的研究	赵震	主要负责	省部级项目	0	赵震
	新型外环流反应器下行管内流体动力学和放大规律研究	张锴	主要负责	省部级项目	0	张锴
NCET-04-0107	计算化学工程在石油化工过程基础研究中的应用	高金森	主要负责	省部级项目	0	高金森
NCET-05-0107	水合物法分离气体混合物技术研究及其产业化中基础科学和 工程问题研究	陈光进	主要负责	省部级项目	10	陈光进
	控制和消除硫化氢大范围空气毒性污染综合技术研究	陈进富	主要负责	省部级项目	8	陈进富
	辽河油田基地生活污水处理示范工程技术研究	陈进富	主要负责	省部级项目	0	陈进富
	催化汽油辅助反应器重催装置专用催化剂的研制及工艺条件 研究	高金森	主要负责	省部级项目	0	高金森

编号	课题名称	负责人	类别	课题类别	年度 经费	参与人
W050508-03-02	高岭土原位晶化复合分子筛催化新材料研究	申宝剑	主要负责	省部级项目	50	申宝剑
W06-03A-01-01- 01-03B	柴油浆态床加氢工艺及其催化剂研究	刘晨光	主要负责	省部级项目	5	刘晨光
W-06-03A-01-01 -02	柴油脱氮吸附剂的研制及吸附脱氮一深度加氢脱硫组合工艺 研究	刘晨光	主要负责	省部级项目	10	刘晨光
W060442A	核壳结构多产丙烯高活性组分的合成	杨朝合	主要负责	省部级项目	5	杨朝合

在研项目80项,年度实到经费1719万元。

2、重要国际合作项目

国别	单位	项目名称	负责人	年度经费	实验室参加人员
加拿大	Calgary 大学	加拿大油砂沥青评价及合成原油加工利用的技术研究	徐春明,赵锁奇	40	李瑞丽,高金森,许志明,孟祥海, 史权,孙学文,董智勇,张民
加拿大	Regina 大学	环境污染修复技术	郭绍辉	240	

年度实到经费 280 万元。

3、横向协作及技术服务项目

项目合同号	项目课题名称	负责人	委托单位	年度经费
H0438	大庆炼化装置建模	卢春喜	大庆炼化分公司	3
H06118	国家储备油料性能评价体系和收储指标研究	李术元	国家物资储备局储备研究所	15
H0569	哈萨克斯坦含硫原油渣油加工技术评价	赵锁奇	中油股份独山子石化分公司	30
	甲苯歧化催化剂的研制与工艺开发	刘晨光	齐鲁石化公司	6
	两段提升管催化裂化技术多产丙烯实验研究	杨朝合	中国石油兰州石化公司	32
	天然气碳质分子筛吸附剂的开发	阎子峰	中国石油庆阳炼化	9
H0664	印尼油砂溶剂抽提技术研究与试验装置	李术元	北京石油化工设计院	120
H0677	中国石油天然气股份有限公司炼油业务绩效分析工作支持系统	董智勇	中国石油规划总院	14
H0682	丁烯歧化生产丙烯催化剂开发	陈胜利	大港石化	20
H0646	新型相变储能材料的研制开发	汪树军	北京立新天华能源科技开发公司	35
H0684	长庆油田特低渗透油藏 MD 膜驱现场试验	高芒来	北京碧能新技术有限公司	30
H0672	氯化物与燃料作用的量子化学研究	王大喜	第二炮兵装备研究院科技部	25
H0628	三2区克上深部调驱工业化实验	郑晓宇	新疆油田公司	104

在研项目 13 项,年度实到经费 443 万元。

三、论文专著

1、重要期刊论文

国外刊物 87 篇,国内刊物 206 篇, SCI 收录 95 篇, EI 收录 123 篇

编号	收录	论文或专著名称	作者	期刊名称	卷期页码
1	SCI	Deep desulfurization of diesel oil and crude oils by a newly isolated Rhodococcus erythropolis strain	于波; 许平; 史权; 马翠卿	APPLIED AND ENVIRONMENTAL MICROBIOLOGY	72(1):54-58
2	SCI,EI	Catalytic pyrolysis of heavy oils: 8-lump kinetic model	孟祥海;徐春明;高金森;李丽	APPLIED CATALYSIS A-GENERAL	301(1):32-38
3	SCI	Synthesis and characterization of turbostratic carbons prepared by catalytic chemical vapour decomposition of acetylene	Li, L; Zhu, ZH; Lu, GQ; 阎子峰; De Marco, R	APPLIED CATALYSIS A-GENERAL	309(2):201-209
4	SCI	Degradation of carbazole and its derivatives by a Pseudomonas sp.	李力; 李庆刚; 李福利; 史 权; 于波; 刘凤瑞; 许平	APPLIED MICROBIOLOGY AND BIOTECHNOLOGY	73(4):941-948
5	EI	Synthesis, characterization, and catalytic performance of a ZSM-5/Y composite	申宝剑; 陈洪林; Guo, JT; 潘 惠芳	BULLETIN OF THE CHEMICAL SOCIETY OF JAPAN	78(12):2238-2244
6	SCI,EI	Secondary cracking of C4 hydrocarbons from heavy oil catalytic pyrolysis	孟祥海;徐春明;高金森	CANADIAN JOURNAL OF CHEMICAL ENGINEERING	84(3):322-327
7	SCI	Effect of valence of copper in La2-xThxCuO4 on NO decomposition reaction	朱君江; 赵震; 肖德海; 李 静; 杨向光; 吴越	CATALYSIS COMMUNICATIONS	7(1):29-32

编号	收录	论文或专著名称	作者	期刊名称	卷期页码
8	SCI,EI	FeHZSM-5 molecular sieves - Highly active catalysts for catalytic cracking of isobutane to produce ethylene and propylene	陆江银; 赵震; 徐春明; 张 匍; 段爱军	CATALYSIS COMMUNICATIONS	7(4):199-203
9	SCI,EI	Nine lumped kinetic models of FCC gasoline under the aromatization reaction conditions	由宏君;徐春明;高金森;刘 植昌;阎平祥	CATALYSIS COMMUNICATIONS	7(8):554-558
10	SCI,EI	CrHZSM-5 zeolites - Highly efficient catalysts for catalytic cracking of isobutane to produce light olefins	陆江银; 赵震; 徐春明; 段爱军; 张匍	CATALYSIS LETTERS	109(2):65-70
11	SCI,EI	Tailoring alumina support with crystalline AlPO4-5 for enhancing hydrodesulfurization activity	申宝剑; 李会峰; 沈师孔	CATALYSIS LETTERS	106(2):55-60
12	SCI	Characterization and activity of Mo supported catalysts for diesel deep hydrodesulphurization	段爱军; 万国赋; 赵震; 徐春明; 郑雁英; 张瑛; 窦涛; 鲍晓军; Chung, Keng	CATALYSIS TODAY	119(4):13-18
13	SCI	Simultaneous removal of NOx and diesel soot particulates over nanometric La2-xKxCuO4 complex oxide catalysts	刘坚; 赵震; 徐春明; 段爱 军; 孟涛; 鲍晓军	CATALYSIS TODAY	119(4):267-272
14	EI	Synthesis of ZSM-5/SAPO-11 composite and its application in FCC gasoline hydro-upgrading catalyst	范煜; 雷多; 石冈; 鲍晓军	Catalysis Today	114(4):388-396
15	SCI,EI	The structures of VOx/MOx and alkali-VOx/MOx catalysts and their catalytic performances for soot combustion	刘坚; 赵震; 徐春明; 段爱 军; 朱玲; 王学忠	CATALYSIS TODAY	118(4):315-322
16	SCI,EI	Fluidization characteristicsof SiO2 nanoparticles in an acoustic fluidized bed	郭庆杰; Li, Y; Wang, MH; Shen, WZ; 杨朝合	CHEMICAL ENGINEERING & TECHNOLOGY	29(1):78-86

编号	收录	论文或专著名称	作者	期刊名称	卷期页码
17	SCI	Influence of sound wave characteristics on fluidization behaviors of ultrafine particles	郭庆杰; Liu, H; Shen, WZ; Yan, XH; Jia, RG	CHEMICAL ENGINEERING JOURNAL	119(1):1-9
18	SCI,EI	Reaction behaviors and mechanisms of catalytic pyrolysis of C4 hydrocarbons	李丽; 高金森; 徐春明; 孟祥海	CHEMICAL ENGINEERING JOURNAL	116(3):155-161
19	SCI,EI	A scale-up strategy for low-temperature methanol synthesis in a circulating slurry bubble reactor	张锴; 赵玉龙	CHEMICAL ENGINEERING SCIENCE	61(5):1459-1469
20	SCI	Computational fluid dynamics (CFD) modeling of spouted bed: Assessment of drag coefficient correlations	杜威; 鲍晓军; 徐健; 魏伟胜	CHEMICAL ENGINEERING SCIENCE	61(5):1401-1420
21	SCI	Computational fluid dynamics (CFD) modeling of spouted bed: Influence of frictional stress, maximum packing limit and coefficient of restitution of particles	杜威; 鲍晓军; 徐健; 魏伟胜	CHEMICAL ENGINEERING SCIENCE	61(14):4558-4570
22	SCI	New class of catalysts for the ammoxidation of propane to acrylonitrile over nickel-molybdenum mixed nitrides	张惠民; 赵震; 徐春明; 段爱 军	CHEMISTRY LETTERS	35(1):36-37
23	SCI,EI	Separation performance of polyimide nanofiltration membranes for concentrating spiramycin extract	史德青; 孔瑛; Yu, JX; 王云 芳; 杨金荣	DESALINATION	191(3):309-317
24	SCI	Separation performance of polyimide nanofiltration membranes for solvent recovery from dewaxed lube oil filtrates	孔瑛; 史德青; 于宏伟; 王云 芳; 杨金荣; Zhang, YY	DESALINATION	191(3):254-261
25	SCI,EI	Colloidal stability variation of petroleum residue during thermal reaction	张龙力;杨国华;阙国和;张 庆轩;杨普江	ENERGY & FUELS	20(5):2008-2012

编号	收录	论文或专著名称	作者	期刊名称	卷期页码
26	SCI,EI	Hydrodesulfurization of resid fluid catalytic cracking diesel oil over TiO2-SiO2 supported catalysts	张振莉;周亚松;张绍金;徐春明	ENERGY & FUELS	20(6):2293-2298
27	SCI	Nanocrystalline zirconia as support for nickel catalyst in methane reforming with CO2	Rezaei, M; Alavi, SM; Sahebdelfar, S; 阎子峰	ENERGY & FUELS	20(3):923-929
28	SCI,EI	Assembly of the presynthesized crystalline AIPO4 structure with alumina and its promotion for aromatic hydrogenation	李会峰; 申宝剑; 王晓华; 沈师孔	Energy and Fuels	20(1);21-25
29	SCI,EI	Preparation and thermal properties of form stable paraffin phase change material encapsulation	刘星; 刘红研; 汪树军; Lu, Z; Hua, C	ENERGY CONVERSION AND MANAGEMENT	47(15-16):2515-25 22
30	SCI	Study of the reaction mechanisms of hydrocarbons with calcium sulfate	岳长涛; 李术元; 丁康乐; 钟宁宁	ENERGY SOURCES PART A-RECOVERY UTILIZATION AND ENVIRONMENTAL EFFECTS	28(15):1377-1385
31	SCI,EI	Preparation of silica-PS composite particles and their application in PET	吴天斌; 柯扬船	EUROPEAN POLYMER JOURNAL	42(2):274-285
32	SCI,EI	Methane hydrate dissociation above O degrees C and below O degrees C 016/j.fluid-2006.01.025	孙长宇; 陈光进	FLUID PHASE EQUILIBRIA	242(2):123-128
33	SCI,EI	The partition coefficients of ethylene between vapor and hydrate phase for methane plus ethylene plus THF plus water systems	张凌伟; 陈光进; 孙长宇; 丁 艳明; 杨兰英	FLUID PHASE EQUILIBRIA	245(2):134-139

编号	收录	论文或专著名称	作者	期刊名称	卷期页码
34	SCI,EI	Effect of the incorporation of ETS-10 into alumina on metal-support interactions and hydrodesulfurization activity	李会峰; 申宝剑; Zhang, Wencheng; Zhao, Ye; 王晓 华; Zhang, Zhihua; 沈师孔	FUEL	85(17-18):2445-24 49
35	SCI,EI	Removal of naphthenic acids from a vacuum fraction oil with an ammonia solution of ethylene glycol	Wang, Yanzhen; Chu, Zhaosheng; Qiu, Bo; 刘晨光; Zhang, Yongning	FUEL	85(17-18):2489-24 93
36	SCI	Thermodynamics and kinetics of reactions between C-1-C-3 hydrocarbons and calcium sulfate in deep carbonate reservoirs	岳长涛; 李术元; 丁康乐; 钟 宁宁	GEOCHEMICAL JOURNAL	40(1):87-94
37	SCI	Fluidization quality improvement for cohesive particles by fine powder coating	Liu, H; Li, Y; 郭庆杰	INDUSTRIAL & ENGINEERING CHEMISTRY RESEARCH	45(5):1805-1810
38	SCI,EI	Computational fluid dynamics (CFD) modeling of fine particle spouting	杜威; 魏伟胜; 徐健; 范煜; 鲍晓军	INTERNATIONAL JOURNAL OF CHEMICAL REACTOR ENGINEERING	4():A27
39	SCI	Micropatterning of polydiacetylene based on a photoinduced chromatic transition and mechanism study	Yuan, Wenfang; 姜桂元, Yanlin; Jiang, Lei	JOURNAL OF APPLIED POLYMER SCIENCE	103(2):942-946
40	SCI	Effect of water content on the solubility of CO2 in the ionic liquid [bmim][PF6]	浮东宝; 孙学文; 蒲劲军; 赵 锁奇	Journal of Chemical and Engineering Data	51(2):371-375
41	SCI,EI	Hydrate formation conditions of methane plus ethylene plus tetrahydrofuran plus water systems	张凌伟; 黄强; 孙长宇; 马庆 兰; 陈光进	JOURNAL OF CHEMICAL AND ENGINEERING DATA	51(2):419-422

编号	收录	论文或专著名称	作者	期刊名称	卷期页码
42	SCI	Mechanistic study of methane reforming with carbon dioxide on a supported nickel catalyst	阎子峰; Qian, Ling; 刘欣梅; Song, Lin-Hua; Song, Chun-Min; Ding, Rong-Gang; Yuan, An; Qiao, Ke	JOURNAL OF CHEMICAL RESEARCH-S	(6):394-400
43	SCI,EI	Interfacial tension of ethylene and aqueous solution of sodium dodecyl sulfate (SDS) in or near hydrate formation region	罗虎; 孙长宇; 黄强; 彭宝 仔; 陈光进	JOURNAL OF COLLOID AND INTERFACE SCIENCE	297(1):266-270
44	SCI,EI	Solubility measurement of methane in aqueous solution of sodium dodecyl sulfate at ambient temperature and near hydrate conditions	彭宝仔; 陈光进; 罗虎; 孙长 宇	JOURNAL OF COLLOID AND INTERFACE SCIENCE	304(2):558-561
45	SCI,EI	Solubility of ethylene in aqueous solution of sodium dodecyl sulfate at ambient temperature and near the hydrate formation region	罗虎; 孙长宇; 彭宝仔; 陈光进	Journal of Colloid and Interface Science	298(2):952-956
46	SCI,EI	Fabrication of SiO2/TiO2 and SiO2/Al2O3 composite inverse opals	周倩; 董鹏; 程丙英	Journal of Crystal Growth	292(2):320-323
47	SCI	Studies on properties of interfacial active fractions from crude and their effect on stability of crude emulsions	李明远; 郭继香; 林梅钦; 吴 肇亮	JOURNAL OF DISPERSION SCIENCE AND TECHNOLOGY	27(5):677-687
48	SCI	The effect of HPAM on crude oil/water interfacial properties and the stability of crude oil emulsions	李明远; Xu, Mingjin; 林梅 钦; 吴肇亮	JOURNAL OF DISPERSION SCIENCE AND TECHNOLOGY	28(1):189-192
49	SCI,EI	Pervaporation performance of crosslinked polyethylene glycol membranes for deep desulfurization of FCC gasoline	Lin, Ligang; 王刚; Qu, Huimin; 杨金荣; 王云芳; 史 德青; 孔瑛	JOURNAL OF MEMBRANE SCIENCE	280(2):651-658

编号	收录	论文或专著名称	作者	期刊名称	卷期页码
50	SCI,EI	Selection and crosslinking modification of membrane material for FCC gasoline desulfurization	Lin, Ligang; 孔瑛; Wang, Gang; Qu, Huimin; Yang, Enrong; 史德青	JOURNAL OF MEMBRANE SCIENCE	285(2):144-151
51	SCI,EI	Characterization and catalytic performances of supported chromia catalysts for C10+ heavy aromatics hydrodealkylation	石德先; 赵震; 徐春明; 段爱 军; 刘坚;窦涛	Journal of Molecular Catalysis A: Chemical	245(1-2):106-113
52	SCI	Influence of cation-adsorption and sonochemical approaches on the preparation of gold catalyst	Xu, XJ; Li, JJ; 刘欣梅; Hao, ZP; Zhao, W	JOURNAL OF NANOSCIENCE AND NANOTECHNOLOGY	6(3):872-874
53	EI	Syngas Production by Methane Reforming with Carbon Dioxide on Noble Metal Catalysts	Rezaei, M.; Alavi, S. M.; Sahebdelfar, S.; 阎子峰	Journal of Natural Gas Chemistry	15(4),327-334
54	EI	Synthesis, Characterization and Thermal Decomposition Mechanism of Cetyltrimethyl Ammonium Tetrathiotungstate	安高军;柳云骐;柴永明;商红岩;刘晨光	Journal of Natural Gas Chemistry	15(2):127-133
55	SCI,EI	The semi-ideal solution theory for mixed ionic solutions at solid-liquid-vapor equilibrium	胡玉峰; 樊栓狮; Liang, DQ	JOURNAL OF PHYSICAL CHEMISTRY A	110(12):4276-4284
56	SCI,EI	Acidity adjustment of HZSM-5 zeolites by dealumination and realumination with steaming and citric acid treatments	范煜; 鲍晓军; 林秀英; 石 冈; 刘海燕	JOURNAL OF PHYSICAL CHEMISTRY B	110(31):15411-154 16
57	SCI,EI	Synthesis and structure characterization of chromium oxide prepared by solid thermal decomposition reaction	Li, L; 阎子峰; Lu, GQ; Zhu, ZH	JOURNAL OF PHYSICAL CHEMISTRY B	110(1):178-183
58	SCI,EI	A novel method to synthesize super-activated carbon for natural gas adsorptive storage	Dai, Xiao-Dong; 刘欣梅; Qian, Ling; 阎子峰; Zhang, Jian	JOURNAL OF POROUS MATERIALS	13(4):399-405

编号	收录	论文或专著名称	作者	期刊名称	卷期页码
59	SCI,EI	Synthesis and characterization of mesostructured tungsten nitride by using tungstic acid as the precursor	白鹏; 刑伟; 阎子峰	JOURNAL OF POROUS MATERIALS	13(2):173-180
60	SCI,EI	Synthesis of mesoporous alumina TUD-1 with high thermostability	Zhang, Zhao-Xia; 白鹏; Xu, Benjing; 阎子峰	JOURNAL OF POROUS MATERIALS	13(4):245-250
61	SCI,EI	Synthesis and characterization of Ni-Mo bimetallic nitride from the mixture of nitrogen and hydrogen	张惠民; 赵震; 徐春明; 段爱 军; Lin, Wenyong; Tian, Hanjing; Wachs, Israel E.	MATERIALS RESEARCH BULLETIN	41(12):2334-2340
62	SCI	Synthesis of mesoporous alumina with highly thermal stability using glucose template in aqueous system	Xu, BJ; 肖天存; 阎子峰; Sun, X; Sloan, J; Gonzalez-Cortes, SL; Alshahrani, F; Green, MLH	MICROPOROUS AND MESOPOROUS MATERIALS	91(3):293-295
63	SCI	Ionic liquid alkylation process produces high-quality gasoline	刘植昌; 张睿; 徐春明; 夏荣 安	OIL & GAS JOURNAL	104(40):52-56
64	SCI,EI	Influence of the aging temperature of catalysts on the aromatization reaction of lanlian FCC gasoline	由宏君;徐春明;高金森; Yan, P.	PETROLEUM CHEMISTRY	46(2):94-98
65	SCI,EI	A new group contribution method for estimating boiling point of heavy oil	赵锁奇; Zhou, YC; 许志明; 徐春明; Chung, KH	PETROLEUM SCIENCE AND TECHNOLOGY	24(4):253-263
66	SCI,EI	Advanced reaction-terminating technique for FCC riser reactor	高金森;徐春明;林世雄	PETROLEUM SCIENCE AND TECHNOLOGY	24(4):367-378
67	SCI	Coke deactivation kinetics of the aromatization reaction	由宏君	PETROLEUM SCIENCE AND TECHNOLOGY	24(7):829-838
68	SCI,EI	Effect of aromatic enrichment on reactivity of FCC slurry	查庆芳; 郭燕生; 吴明铂; Zhang, YZ	PETROLEUM SCIENCE AND TECHNOLOGY	24(4):401-412

编号	收录	论文或专著名称	作者	期刊名称	卷期页码
69	SCI,EI	High-pressure phase behavior and equilibria for Chinese petroleum residua and light hydrocarbon systems. Part I	赵锁奇; 王仁安; 林世雄	PETROLEUM SCIENCE AND TECHNOLOGY	24(4):285-295
70	SCI	High-pressure phase behavior and equilibria for Chinese petroleum residua and light hydrocarbon systems. Part II	赵锁奇; 王仁安; 林世雄	PETROLEUM SCIENCE AND TECHNOLOGY	24(4):297-318
71	SCI,EI	Improving FCC product distribution with two-stage riser technology	山红红; 张建芳; 杨朝合; Ye, ZG	PETROLEUM SCIENCE AND TECHNOLOGY	24(4):379-387
72	SCI,EI	Incipient phase separation behavior and colloidal stability in liquid-phase carbonization of residua	钮根林; Li, SH; 徐春明; 刘 晨光	PETROLEUM SCIENCE AND TECHNOLOGY	24(4):319-326
73	SCI	Influence of aromatization reaction conditions in the presence of HZSM-5 catalyst	由宏君	PETROLEUM SCIENCE AND TECHNOLOGY	24(6):707-716
74	SCI	Methods and applications of molecular simulation in catalyst research	赵亮; 高金森; 徐春明	Petroleum Science and Technology	24(12):1395-1415
75	SCI,EI	Production of light olefins by catalytic pyrolysis of heavy oil	孟祥海;徐春明;高金森	PETROLEUM SCIENCE AND TECHNOLOGY	24(4):413-422
76	SCI,EI	The application of UNIFAC group - Contribution model in vapor-liquid equilibrium of heavy oil	高岱巍; 高金森; 徐春明	PETROLEUM SCIENCE AND TECHNOLOGY	24(5):423-430
77	SCI	The mechanism and kinetics for the alkylation of benzene with ethylene	由宏君; Long, Wenyu; Pan, Yi	PETROLEUM SCIENCE AND TECHNOLOGY	24(9):1079-1088
78	SCI,EI	The absorption and thermal behaviors of PET-SiO2 nanocomposite films	吴天斌; 柯扬船	POLYMER DEGRADATION AND STABILITY	91(9):2205-2212

编号	收录	论文或专著名称	作者	期刊名称	卷期页码
79	SCI,EI	Hydrodynamics of an annulus airlift reactor	孙淑兰; 刘昌见; 魏伟胜; 鲍 晓军	POWDER TECHNOLOGY	162(3):201-207
80	SCI	Tetragonal nanocrystalline zirconia powder with high surface area and mesoporous structure	Rezaei, M.; Alavi, S. M.; Sahebdelfar, S.; 阎子峰	POWDER TECHNOLOGY	168(2):59-63
81	SCI	Adsorptive desulfurization using carbon materials with different surface areas	Xin Sun; Benjing Xu; 肖天 存; 查庆芳; Alshahrani, Farhan M.	PROGRESS IN NATURAL SCIENCE	15():105-110
82	SCI	Computational fluid dynamics for dense gas-solid fluidized beds	张锴; Brandani, Stefano; Bi, Jicheng	PROGRESS IN NATURAL SCIENCE	15():42-51
83	SCI	Deactivation study of CoAPO-11 molecular sieve on skeletal isomerization of 1-hexene	Xu, Benjing; Sun, Xin; 阎子 峰; 肖天存	PROGRESS IN NATURAL SCIENCE	15():52-55
84	SCI	Study of the catalytic combustion of diesel soot over nanometric lanthanum-cobalt mixed oxide catalysts	刘坚; 赵震; 徐春明; 王虹	REACTION KINETICS AND CATALYSIS LETTERS	87(1):107-114
85	SCI	Effects of alkali metal cations on the structures, physico-chemical properties and catalytic behaviors of silica-supported vanadium oxide catalysts for the selective oxidation of ethane and the complete oxidation of diesel soot	赵震; 刘坚; 段爱军; 徐春明; Kobayashi, Tetsuhiko; Wachs, Israel E.	TOPICS IN CATALYSIS	38(4):309-325
86		"节约型社会与防水"系列报道之八——废胶粉改性沥青在 防水材料中的应用前景	孔宪明; 崔海滨;	中国建筑防水	2006(8):14-18
87	SCI,EI	[bmim]Cl/[FeCl3] ionic liquid as catalyst for alkylation of benzene with 1-octadecene	孙学文;赵锁奇;	CHINESE JOURNAL OF CHEMICAL ENGINEERING	14(3):289-293
88	SCI	Effect of petroleum sulphonate on interfacial property and stability of crude oil emulsions	Wang, HY;李明远;吴肇亮;林 梅钦	CHINESE JOURNAL OF CHEMICAL ENGINEERING	13(5):691-695

编号	收录	论文或专著名称	作者	期刊名称	卷期页码
89	SCI,EI	Investigation of N-(hydroxylethyl)pyrrolidone dehydration over REOx-doped nano-ZrO2 catalyst	Zhang, L;刘欣梅;阎子峰	CHINESE JOURNAL OF CHEMICAL ENGINEERING	14(3):309-313
90	EI	Oxidation of Thiophenes over Silica Gel in Hydrogen Peroxide/Formic Acid System	陈兰菊; 郭绍辉; 赵地顺;	Chinese Journal of Chemical Engineering	14(6):835-838
91	SCI,EI	Prediction of activity coefficients for mixed aqueous electrolyte solutions from the data of their binary solutions	刘植昌; 刘艳升; 胡玉峰; Zeng Peng; 樊拴狮; Liang Deqing	CHINESE JOURNAL OF CHEMICAL ENGINEERING	14(4):494-504
92		用于测定介孔的 Kelvin 方程及其修正述评(英文)	张颖; 阎子峰; 胡喜军;	Chinese Journal of Chemical Physics	19(2):102-108
93	SCI	Role of nanosized zirconia on the properties of Cu/Ga2O3/ZrO2 catalysts for methanol synthesis	刘欣梅; 阎子峰; Lu, GQ	CHINESE JOURNAL OF CHEMISTRY	24(2):172-176
94	SCI	Phase transformation of nanosized zirconia	刘欣梅;阎子峰	CHINESE JOURNAL OF STRUCTURAL CHEMISTRY	25(4):424-432
95	SCI,EI	Synthesis of novel ordered carbon nanorods and its application in electrochemical double layer capacitor	邢伟; 刘欣梅; 白鹏; 阎子 峰; Lu Gaoqing	SCIENCE IN CHINA SERIES E-TECHNOLOGICAL SCIENCES	49(4):425-433
96	SCI	含 HF 体系中 SAPO-11 分子筛的合成与表征	张胜振; 陈胜利; 董鹏; 井秀 娟; 姜凯;	催化学报	27(10):868-874
97	SCI	器外预硫化型 MoNiP/γ-Al_2O_3 催化剂的二苯并噻吩加氢 脱硫活性	李彦鹏; 刘大鹏; 刘晓; 柴永明; 刘晨光;	催化学报	27(7):624-630
98	SCI	同位素示踪研究 K_2CO_3/CH_3I 促进的碳酸二甲酯直接 合成反应	蔡振钦;徐春明;赵锁奇;许 志明;孙学文;张民;	催化学报	27(7):615-618
99		双电层电容器的电容特性分析	徐文东; 华贲; 陈进富;	电工电能新技术	25(2):59-63

编号	收录	论文或专著名称	作者	期刊名称	卷期页码
100		反相高效液相色谱法测定离子液体及其中的高沸点有机物	姜晓辉; 孙学文; 赵锁奇; 浮 东宝;	分析测试技术与仪器	12(4):195-198
101		钾修饰 SiO_2 负载超低含量过渡金属催化剂上乙烷选择氧化反应	张哲; 赵震; 徐春明; 段爱 军; 王宏宣;	分子催化	20(1):17-22
102		介孔二氧化锆分子筛的合成机理述评	刘欣梅; 阎子峰;	分子催化	20(1):84-94
103		离子液体催化烷基化反应的研究进展	王鹏; 高金森; 王大喜; 徐春明; 刘植昌;	分子催化	20(3):278-283
104		微孔-介孔复合结构分子筛的合成及表征研究	宋春敏;姜杰;乔柯;孟祥 滨;阎子峰;	分子催化	20(4):294-299
105		在 La 改性 HZSM-5 分子筛上甲醇对噻吩转化反应规律的 影响	罗立文;李俊玲;李虎;于慧征;夏道宏;	分子催化	20(1):11-16
106		烷基吡啶及氯化铝正负离子结构的密度泛函研究	李鸿雁; 王大喜; 窦荣坦; 高金森;	分子科学学报	22(5):306-311
107	SCI,EI	三氯化铝烷基氯化咪唑盐结构和红外光谱的模拟计算	王鹏; 王大喜; 高金森; 董坤; 徐春明; 刘靖疆;	高等学校化学学报	27(8):1505-1508
108	EI	MMT/SiO_2 复合载体制备聚乙烯纳米复合材料的探索研究	孙明卓; 柯扬船; 王皓;	高分子材料科学与工程	22(5):249-253
109		MUF/石蜡的微胶囊制备	刘星; 汪树军; 刘红研;	高分子材料科学与工程	22(2):235-238
110	EI	纳米内核-成核剂复合助剂及与 PP 复合材料的制备和性能	柯扬船; 孙明卓; 宋言新; 杨 光福;	高分子材料科学与工程	22(1):146-150
111		添加剂对多孔陶瓷载体氧化铝涂层的影响	高金良; 刘军霞; 张德权; 李 东风; 张吉瑞;	高校化学工程学报	20(1):142-146

编号	收录	论文或专著名称	作者	期刊名称	卷期页码
112		一种新型气固分离器气相流场实验研究	刘显成; 卢春喜; 时铭显;	高校化学工程学报	20 (6):875-881
113		CO 气源 COS 水解催化剂的工业侧流试验	张文慧; 郭玉峰; 陈光旭; 王 萍; 孔海燕;	工业催化	14(2):49-51
114		SQ105 吸附剂在二氧化碳一步法脱硫工艺中的首次应用	李坚; 王为然; 张文慧; 周广林; 王萍; 陈光旭; 徐春明;	工业催化	14(9):26-28
115		反应温度对催化裂化汽油芳构化的研究	由宏君;徐春明;高金森;	工业催化	14(12):16-20
116		油溶性纳米 MoS_2 加氢催化剂的合成、表征和应用	何杰;安长华;管翠诗;王宗 贤;	工业催化	14(12):11-15
117		氩气自动控制器在 DV_4 光谱仪上的应用	李光科; 查庆芳; 侯宝花;	光谱实验室	23(1):50-52
118		聚苯乙烯胶晶模板法制备三维有序大孔 SiO_2 材料	杨卫亚;郑经堂;谭树成;张 艳姝;赵玉翠;	硅酸盐通报	25(3):181-184
119		表面改性剂在碳酸化法制备白炭黑过程中的作用	何凯; 陈宏刚;	过程工程学报	6(3):402-407
120		不同粒度分布的高硫焦颗粒在强混燃烧器内的流动特性	阮宇军; 卢春喜; 时铭显;	过程工程学报	6(4):517-521
121		石灰窑气碳酸化法制备白炭黑工	何凯; 陈宏刚;	过程工程学报	6(4):554-558
122	EI	单分散胶体颗粒的应用研究进展	陈胜利,董鹏,刘丽霞,周倩,刘 忍肖,祈彦平,袁桂梅	过程工程学报	2006(z2)
123		苯氨基甲酸甲酯精馏残渣中二苯脲的回收方法	张磊; 阙国和; 袁存光;	合成技术及应用	21(3):49-51

编号	收录	论文或专著名称	作者	期刊名称	卷期页码
124		柴油超深度脱硫技术进展	万国赋;段爱军;赵震;马 丽;倪建明;	黑龙江大学自然科学学报	23(5):658-667
125		活性炭催化臭氧氧化法处理奥里油加工废水	曲险峰; 郑经堂;	化工环保	26(3):222-225
126		氧氯化流化床反应器内三级旋风分离器大型冷态对比试验 研究	杨少杰; 陈建义;	化工机械	33(1):1-5
127		FCC 汽油烷基化脱硫技术进展	柯明; 周爱国; 赵振盛; 蒋庆 哲; 宋昭峥;	化工进	25(4):357-361
128		管式裂解炉二维工艺模型研究新进展及应用	张红梅; 贺永殿; 蓝兴英; 徐 春明; 高金森;	化工进展	25(7):791-795
129		胶体晶体模板法制备三维有序排列的大孔 SiO_2 材料	杨卫亚;郑经堂;	化工进展	25(11):1324-1327
130		离子液体对直接合成碳酸二甲酯反应的促进作用及机理分 析	蔡振钦; 赵锁奇; 徐春明; 许 志明; 孙学文;	化工进展	25(5):546-550
131		纳米 TiO_2 光催化剂共掺杂的研究进展	石建稳;郑经堂;胡燕;赵玉翠;	化工进展	25(6):604-607
132		丁硫醚在 Ce-HZSM-5 分子筛上的转化反应研究	李虎; 罗立文; 于慧征; 吕仁 庆; 夏道宏;	化工科技	14(1):5-8
133		甲醇存在时异丁硫醇在 HZSM-5 分子筛上的转化反应研究	于慧征; 罗立文; 李虎; 吕仁 庆; 夏道宏;	化工科技	14(2):16-19
134		乙烯-丙烯酸甲酯共聚物对蜡的作用机理	宋昭睁; 许亚岚; 赵密福;	化工科技	14(2):4-7

编号	收录	论文或专著名称	作者	期刊名称	卷期页码
135	EI	TiO_2-SiO_2 复合氧化物的理化性质及其对柴油加氢精制性能的影响	张绍金; 周亚松; 徐春明;	化工学报	57(4):769-774
136	EI	利用硫化氢制备氢气和硫化锌新方法	王晓明; 汪树军; 刘红研; 厉建祥; 张伟; 王文波; 张琛;	化工学报	57(2):465-469
137	EI	气体水合物形成的热力学与动力学研究进展	孙长宇; 黄强; 陈光进;	化工学报	57(5):1031-1039
138	EI	汽油电化学催化氧化脱硫	王文波; 汪树军; 刘红研; 张 伟; 王义刚;	化工学报	57(12):3033-3039
139	EI	乙烯水合物膜生长动力学	罗虎; 陈光进; 彭宝仔;	化工学报	57(8):1865-1870
140	EI	原位聚合制备三聚氰胺脲醛树脂石蜡微胶囊及性能	刘星; 汪树军; 刘红研;	化工学报	57(12):2991-2996
141		聚乙二醇对碳酸化法白炭黑的表面改性研究	何凯; 陈宏刚;	化学反应工程与工艺	22(2):181-184
142	EI	双组分颗粒声场流态化的实验研究	张建 郭庆杰 刘会娥 陈爽	化学反应工程与工艺	22(5):429-433
143		一种新型气固分离装置结构的优化研究	刘显成; 卢春喜; 严超宇; 时 铭显;	化学反应工程与工艺	22(2):120-124
144		催化加氢热解反应催化剂前躯物四硫代钼酸铵的表征	周建伟; 李术元; 岳长涛; 钟宁宁;	化学试剂	28(2):86-88

编号	收录	论文或专著名称	作者	期刊名称	卷期页码
145		HYPY/SE 提取固体有机质中生物标志化合物的研究	周建伟; 李术元; 岳长涛; 钟 宁宁;	化学通报	2006(5):337-341
146		催化裂化汽油中含硫化合物的分离氧化脱硫研究	陈兰菊; 郭绍辉; 赵地顺;	化学通报	2006(12):945-947
147		反应条件对 FCC 汽油二次芳构化的研究	由宏君;徐春明;高金森	江西科学	24(4):164-169
148	EI	含阴/非双子表面活性剂的金属清洗剂的性能研究	王雨;郑晓宇;马玉华;吴肇亮;	金属热处理	31(9):95-97
149		MD 膜驱剂与阳离子表面活性剂混合体系的胶束性质	杨莉; 高芒来; 刘宏生; 韩翻珍; 郑广;	精细化工	23(12):1233-1237
150		石蜡的聚烯烃定形包覆研究	刘星; 汪树军; 刘红研;	精细化工	23(3):109-114
151		石蜡定形相变材料的包裹及热性能	刘星; 刘红研; 汪树军;	精细化工	23(1):7-11
152		四氯化钛离子液体中辛基酚己二酸酯的 Fries 重排反应	王雨; 郑晓宇; 吴肇亮;	精细化工	23(2):118-120
153		柴油中噻吩类化合物的催化氧化	张玉芬; 周家顺;	精细石油化工进展	7(7):11-16
154		低温 MOCVD 法制备铜纳米棒	张颖; 林粱旭; 阎子峰; 胡喜 军;	科学通报	51(19):2309-2311
155		TSRFCC- I 型两段提升管催化裂化掺炼焦化蜡油研究	杜峰; 张新功; 张建芳; 何长 征;	炼油技术与工程	36(5):11-15

编号	收录	论文或专著名称	作者	期刊名称	卷期页码
156		超稠原油延迟焦化产生弹丸焦的原因及对策	张峰; 陈春茂; 余昌信; 吴 亮; 叶明;	炼油技术与工程	36(12):11-13
157		对重油催化裂化反应历程的若干再认识——"新型多区协 控重油催化裂化技术 MZCC"的提出	高金森;徐春明;卢春喜;毛羽;	炼油技术与工程	36(12):1-6
158		反应-萃取法分离和精制高酸原油中的环烷酸	王延臻; 初照圣; 邱波; 刘晨 光; 张永宁;	炼油技术与工程	36(1):36-38
159		干气用作 FCC 原料雾化介质对反应的影响	张晓松;曹东学;高金森;徐 春明;	炼油技术与工程	36(6):22-26
160		加供氢剂的减压渣油减粘裂化工艺的开发	邓文安; 刘东; 周家顺; 阙国和;	炼油技术与工程	36(12):7-10
161		两段提升管催化裂化多产丙烯催化剂 LTB-2 的应用	孙武; 李晓红; 常增明; 李春 义;	炼油技术与工程	36(9):5-7
162		吸附法催化裂化汽油深度脱硫工艺研究	王治卿	炼油技术与工程	36(5):1-3
163		乙醇柴油的储存稳定性研究	古文英; 史权; 王静媛; 彭 勃; 徐春明;	炼油技术与工程	36(8):51-54
164		重油催化裂化反应历程研究进展	付国庆; 郑俊生; 钮根林; 杜峰; 杨朝合;	炼油技术与工程	36(1):7-11
165		重油催化裂解反应深度函数及裂解产品产率关联模型	李丽; 高金森; 徐春明; 孟祥海;	炼油技术与工程	36(9):8-11
166		复合催化剂上催化裂化汽油催化改质的正交实验研究	闫平祥; 刘植昌; 高金森; 徐 春明;	炼油与化工	2006(1):11-13
167		液固流化床内床层塌落动态过程的数值模拟	陈聪; 李秀春; 高晓根; 张 锴;	煤化工	2006(1):35-38

编号	收录	论文或专著名称	作者	期刊名称	卷期页码
168		车用乙醇汽油金属腐蚀抑制剂的研究	王宗廷; 张云山; 崔新栋;	汽车工艺与材料	2006(10):23-26
169	EI	大港减压渣油超临界萃取萃余残渣结构特征研究	张占纲; 郭绍辉; 赵锁奇; 牟 形;	燃料化学学报	34(4):427-433
170	EI	复合离子液体催化碳四烷基化反应性的研究	刘植昌; 张睿; 刘鹰; 徐春 明;	燃料化学学报	34(3):328-331
171		固体碱对油品中有机硫化物的脱除性能及分析	项玉芝; 夏道宏; 段永锋;	燃料化学学报	34 (5) :633-636
172	EI	固体酸/碱和引发剂促进渣油轻质化的初步研究	石斌; 任振东; 门秀杰; 方日 强; 阙国和;	燃料化学学报	34(4):434-438
173		活性炭的表面化学改性及其对有机硫化物的吸附性能的研究	姚丽群;高利平;托罗别克; 查庆芳;董兆德;	燃料化学学报	34(6):749-752
174		减压渣油供氢剂减黏裂化研究	王治卿; 王宗贤;	燃料化学学报	34(6):745-748
175	EI	纳米 ZrO_2 的合成对负载 Ni 催化剂的 CH_4/CO_2 重整反应的影响	吴萍萍; 刘欣梅; 钱岭; 阎子峰;	燃料化学学报	34(4):444-449
176	EI	石油胶质结构性质的量子化学研究	王大喜;赵玉玲;潘月秋;刘 然冰;高金森;	燃料化学学报	34(6):690-694
177	EI	碳质颗粒添加物对渣油热反应生焦的影响	王继乾; 李明; 李庶峰; 李 传; 阙国和;	燃料化学学报	34(1):36-41
178		新型孔结构渣油催化裂化催化剂	祁彦平; 陈胜利; 董鹏; 徐克 琪; 申宝剑;	燃料化学学报	34(6):685-689
179	EI	液固流化床内床层动态特性的 CFD 模拟	高晓根; 刘文东; 魏耀东; 张 锴;	燃料化学学报	34(4):492-498

编号	收录	论文或专著名称	作者	期刊名称	卷期页码
180	EI	重油催化裂解多产乙烯丙烯催化剂的研究	李成霞; 高永地; 李春义; 山 红红; 杨朝合;	燃料化学学报	34(1):47-50
181		高清净性铜带材冷轧润滑剂研究	蔡振钦;徐春明;赵锁奇;	润滑与密封	2006(5):149-151
182	EI	基于神经网络-遗传算法优化柴油机油台架试验	李为民;徐春明;许志伟;	润滑与密封	2006(4):81-83
183		柴油耦合氧化吸附脱硫的研究	张艳姝;郑经堂;赵玉翠;	山东化工	35(3):13-15
184		减压渣油和沥青生产方案频繁调整的优化操作	逯卫; 李俊玲; 文萍;	山东化工	35(4):21-23
185		Al-MCM-41 介孔分子筛合成及其加氢特性 I.合成及表征	涂永善; 李忠燕; 杨朝合;	石化技术与应用	24(6):437-440
186		塔河常渣在油溶性钼催化剂下的加氢裂化	任振东;石斌;杨江朝;门秀杰;李传;阙国和;	石化技术与应用	24(3):202-204
187		铜醇分散型催化剂在悬浮床加氢过程中的应用	于波; 席思杰; 周家顺;	石化技术与应用	24(5):357-359
188		新型内循环石油焦燃烧器烧焦管内颗粒流动特性	严超宇; 卢春喜; 时铭显; 高 金森;	石化技术与应用	24(6):444-447
189		重油催化裂化反应系统集成技术及应用	卢春喜; 刘为民; 高金森; 徐 春明; 毛羽; 时铭显;	石化技术与应用	24(1):1-4
190	EI	降凝剂对蜡晶晶格参数的影响	蒋庆哲; 宋昭峥; 葛际江; 赵 福麟;	石油大学学报(自然科学版)	30(1):118-122
191	EI	FeCl_3-氯代丁基吡啶离子液体催化苯与丙烯烷基化	孙学文; 赵锁奇;	石油化工	35(9):819-823

编号	收录	论文或专著名称	作者	期刊名称	卷期页码
192	EI	车用燃料油吸附法深度脱硫技术进展	王云芳; 尹风利; 史德清; 杨 金荣; 孔瑛;	石油化工	35(1):94-99
193	EI	离子液体中 K_2CO_3/CH_3I 直接催化合成碳酸二甲酯	蔡振钦; 赵锁奇; 徐春明;	石油化工	35(5);425-428
194	EI	两段提升管催化裂化生产丙烯工艺	李晓红; 陈小博; 李春义; 张建芳; 杨朝合; 山红红;	石油化工	35(8):749-753
195	EI	ZSM-5 沸石和 L 沸石对 FCC 汽油芳构化降烯烃性能比较	柯明; 朱坤磊; 宋昭峥; 刘成 翠; 蒋庆哲;	石油化工高等学校学报	19(1):53-57
196		沸石分子筛选择吸附脱除焦化苯中微量噻吩	李兰; 罗国华; 徐新; 寥容 波; 高金森;	石油化工高等学校学报	19(3):56-59
197		克拉玛依常压渣油悬浮床加氢裂化反应胶体性质	李传; 石斌; 李慎伟; 王继 乾; 阙国和;	石油化工高等学校学报	19(1):34-39
198	EI	空速对催化汽油芳构化的影响	由宏君;徐春明;高金森;	石油化工高等学校学报	19(1):40-43
199		两种道路沥青抗老化性的表征	魏建明; 孙彦; 庞伟伟; 张永和; 张玉贞;	石油化工高等学校学报	19(2):28-40
200	EI	三氯化铁-三异丁基铝-邻菲罗啉催化体系的相态和催化活性	宋昭峥; 柯明; 蒋庆哲;	石油化工高等学校学报	19(1);1-5
201		离心浮选及其研究进展	刘洪敏; 郭绍辉; 闫光绪; 王 嘉麟; 彭鸧威;	石油化工设备	35(6):49-52
202		催化裂化汽提技术的现状与展望	张永民; 时铭显; 卢春喜;	石油化工设备技术	27(2):31-35
203		废胶粉改性沥青性能影响因素研究	崔海滨; 马立强; 孔宪明;	石油沥青	20(3):22-24

编号	收录	论文或专著名称	作者	期刊名称	卷期页码
204		胶粉改性沥青性能正交试验分析	付永然; 王博; 孔宪明;	石油沥青	20(5):69-71
205		阻燃沥青的研究进展与建议	付永然; 林元奎;	石油沥青	20(6):69-71
206		催化裂化与芳构化反应耦合多产优质汽油催化剂的研究	宋春敏; 赵晨曦; 阎子峰;	石油炼制与化工	37(5):7-10
207		减压渣油溶剂脱沥青-焦化总液体收率的研究	李波海; 张玉贞;	石油炼制与化工	37(7):30-33
208		聚丙烯酰胺对喷气燃料中悬浮物形成的影响	南国枝; 范维玉; 孙建章; 赵 升红;	石油炼制与化工	37(1):59-62
209		离子液体催化的苯与丙烯烷基化反应	何绍群; 赵锁奇; 孙学文; 许 志明;	石油炼制与化工	37(3):14-18
210		汽油电化学催化氧化脱硫——酸性电解体系的筛选	汪远昊; 王文波; 刘红研; 王 振新;	石油炼制与化工	37(8):29-33
211		器外预硫化型 MoNiP/γ-Al_2O_3 催化剂的加氢脱硫性能研究	李彦鹏; 刘大鹏; 柴永明; 刘 晨光;	石油炼制与化工	37(5):15-19
212		水溶性分散型加氢催化剂的分离和表征	刘东; 马魁菊; 阙国和;	石油炼制与化工	37(2):38-41
213		橡胶粉的溶解度对改性沥青性质的影响	张小英;徐传杰;张玉贞;	石油炼制与化工	37(3):53-56
214		新型炭复合材料吸附剂脱除汽油中硫化物的研究	王云芳; 尹风利; 史德青; 孔 瑛;	石油炼制与化工	37(6):37-40
215		载体改性对 FCC 汽油选择性加氢脱硫催化剂性能的影响	李宇静; 赵会吉; 安高军; 刘 晨光;	石油炼制与化工	37(8):24-28
216	EI	利用催化加氢热解技术提取沉积有机质中生物标志化合物	周建伟; 李术元; 钟宁宁;	石油学报	27(1):58-63

编号	收录	论文或专著名称	作者	期刊名称	卷期页码
217	EI	MD 膜驱剂的粘土稳定性研究 I.静态试验	林宝辉; 高芒来;	石油学报(石油加工)	22(3):79-84
218	EI	NiW/CTS-n 催化剂的加氢脱芳性能研究	周亚松; 刘全昌; 马海峰;	石油学报(石油加工)	22(3):13-17
219	EI	电解电渗析回收处理汽油碱渣中的氢氧化钠	王延臻; 刘晨光; 李晓燕; 吴冠京;	石油学报(石油加工)	22(6):76-79
220	EI	高演化沉积有机质中共价键结合的生物标志物的提取及分析	周建伟; 李术元; 岳长涛; 钟宁宁;	石油学报(石油加工)	22(4):83-88
221	EI	利用传质助剂提高柴油生物脱硫效率	侯影飞; 孔瑛; 杨金荣; 李海川; 陈嵘;	石油学报(石油加工)	22(4):34-38
222	EI	沥青树脂流变性的研究	侯宝花; 张美荣; 郭燕生; 郭 凡; 查庆芳;	石油学报(石油加工)	22(1):100-104
223	EI	氯化烷基咪唑离子液体分子结构和红外光谱的模拟计算	高金森; 王鹏; 董坤; 王大 喜; 徐春明;	石油学报(石油加工)	22(1);72-76
224		煤与 FCC 油浆共处理重质产物对道路沥青改性作用的评价	薛永兵;杨建丽;刘振宇;张 玉贞;	石油学报(石油加工)	22(1):95-99
225	EI	器外预硫化型 MoNiP/γ-Al_2O_3 催化剂的喹啉加氢脱氮性 能研究	李彦鹏; 刘大鹏; 柴永明; 刘晨光;	石油学报(石油加工)	22(6):1-7
226	EI	室温离子液体催化联苄与十二烯-1 的烷基化反应	王雨; 郑晓宇; 吴肇亮;	石油学报(石油加工)	22(4):39-43
227	EI	水溶性分散型 Fe 催化剂前体在悬浮床加氢过程中的低温 硫化	刘东; 王振波; 孔学; 张宏 玉; 阙国和;	石油学报(石油加工)	22(6):50-55
228	EI	原油减压渣油馏分的油-水界面性质 XI.伊朗轻质减压渣油和大庆减压渣油乳状液的粒度特征	彭勃; 李明远; 赵锁奇; 吴肇 亮; Harald Hoiland;	石油学报(石油加工)	22(1);66-71

编号	收录	论文或专著名称	作者	期刊名称	卷期页码
229	EI	原油减压渣油馏分的油-水界面性质XⅢ.减渣馏分分子参数与其模拟乳状液的稳定性	彭勃; 李明远; Laila Stordrange; Harald Hoiland;	石油学报(石油加工)	22(4):66-71
230	EI	原油减压渣油馏分的油-水界面性质XII.伊朗轻质减渣和大庆减渣乳状液的 Zeta 电位	彭勃; 李明远; 赵锁奇; 吴肇 亮; Harald Hoiland;	石油学报(石油加工)	22(2):103-108
231	EI	圆筒炉内燃烧器出口湍流流动和燃油燃烧的三维数值模拟	周桂娟; 毛羽; 王娟;	石油学报(石油加工)	22(4):49-55
232		渣油悬浮床加氢裂化分散型催化剂的 XANES 研究	王继乾;徐海;阙国和;	石油学报(石油加工)	22(6):24-28
233	EI	渣油悬浮床加氢裂化尾油化学结构及其裂化性能评价	王继乾; 李明; 万道正; 邓文 安; 阙国和;	石油学报(石油加工)	22(5);63-68
234	EI	重油催化裂化沉降器油气相态计算	蓝兴英;徐春明;高岱巍;高金森;	石油学报(石油加工)	22(6):29-32
235	EI	重整生成油选择性加氢脱烯烃 Pd 基催化剂的研究	南军; 柴永明; 李彦鹏; 刘晨 光; 王继锋;	石油学报(石油加工)	22(5):20-25
236		Fenton 试剂处理压裂废液氧化降粘研究	张玉芬; 孙健;	石油与天然气化工	35(6):493-495
237		催化裂化过程中反应温度对硫转化规律的影响	杜峰; 张建芳; 杨朝合;	石油与天然气化工	35(4):280-291
238		离子液体催化合成异丙苯的研究	崔文俊; 何绍群; 赵锁奇; 邹 斌; 马爱青;	石油与天然气化工	35(2):93-95
239		制备条件对重整生成油选择性加氢催化剂性能的影响	南军; 李歧峰; 柴永明; 李彦鹏; 刘晨光;	石油与天然气化工	35(5):371-374

编号	收录	论文或专著名称	作者	期刊名称	卷期页码
240		超(亚)临界丙烷萃取蛋黄卵磷脂-由实验室走向工业化	张民; 胡云翔; 孙学文; 许志明; 赵锁奇;	食品工业科技	2006(1):152-154
241	EI	质子交换膜燃料电池专用碳纸的制备及性能测试	张伟; 汪树军; 刘红研; 潘惠 芳;	太阳能学报	27(2):199-202
242		活性炭纤维负载 TiO_2 光催化剂研究	谭树成; 郑经堂;	炭素	2006(3):15-18
243	EI	轻质油品非加氢脱硫技术研究进展	张艳姝; 郑经堂;	炭素	2006(3):24-28
244		炭/炭复合材料抗氧化研究进展	胡兴华; 吴明铂; 查庆芳;	炭素	2006(3):38-45
245		玉米芯制备多孔炭及其孔结构的表征	郭宁; 吴明铂; 查庆芳; 王晓 惠;	炭素	2006(2):3-8
246		溶胶-凝胶法制备中孔炭材料的研究进展	柳召永; 郑经堂;	炭素技术	25(4):30-34
247		碳包覆纳米金属颗粒的形成及应用	霍俊平; 宋怀河; 陈晓红; 赵 锁奇; 徐春明;	炭素技术	25(3):22-27
248		吸附天然气技术研究进展及发展前景	徐文东;华贲;2陈进富;	天然气工业	26(6):127-130
249		CO 气源脱 COS 水解催化剂的工业侧线试验	周广林; 张文彗; 陈光旭; 王 萍; 孔海燕;	天然气化工(C1 化学与化工)	31(2):56-58
250		吡啶离子液体的热分析研究	何绍群; 赵锁奇; 孙学文; 许 志明; 张民;	天然气化工(C1 化学与化工)	31(1):25-28
251	SCI	二硫代钨酸铵晶体的合成、表征与热分解机理的研究	安高军;柳云骐;柴永明;周同娜;刘晨光;	无机化学学报	22(10):1813-1818

编号	收录	论文或专著名称	作者	期刊名称	卷期页码
252	SCI	颗粒模板法制备大孔 Al_2O_3 材料	王晓冬; 董鹏; 陈胜利;	物理化学学报	22(7):831-835
253	SCI	带电胶体粒子结晶过程的实验研究	刘蕾;徐升华;刘捷;段俐; 孙祉伟;刘忍肖;董鹏;	物理学报	55(11):6168-6174
254	EI	制备高质量聚苯乙烯微球胶粒晶体的蒸发自组装法	王晓冬; 董鹏; 仪桂云;	物理学报	55(4):2092-2098
255	EI	MD 膜驱剂对油藏矿物 ζ 电位的影响	刘宏生; 高芒来;	西安石油大学学报(自然科学 版)	21(5):42-45
256	EI	Sinopec 中低档车用润滑油现状分析与发展探讨	蒋庆哲;潘大新;宋昭峥;柯 明;	西安石油大学学报(自然科学 版)	21(2):52-56
257	EI	晶化时间、模板剂对 Si-MCM-41 结构的影响	蒋庆哲;郑成国;潘胜;宋昭 峥;	西安石油大学学报(自然科学 版)	21(4):86-90
258		不同分子筛上正辛烷反应性能的研究	柯明; 陈彦广; 黄勇; 李可 伟; 宋昭峥; 蒋庆哲;	西南石油学院学报	28(2):75-79
259		乙烯-醋酸乙烯酯的结构与降凝性能的关系	蒋庆哲; 岳国; 宋昭峥; 柯明; 赵密福;	西南石油学院学报	28(2):71-74
260		原油组分与降凝剂相互作用	蒋庆哲; 宋昭峥; 葛际江; 柯明; 赵密福;	西南石油学院学报	28(1):59-64
261		溶胶-凝胶法制备纳米 TiO_2 及其光催化活性研究	石建稳;郑经堂;胡燕;赵玉翠;	稀有金属快报	25(7):22-26
262	EI	钒镧共掺杂 TiO_2 纳米粉体的制备及光催化性能研究	陈姣霞; 郑经堂;	现代化工	26(2):255-257+26 0

编号	收录	论文或专著名称	作者	期刊名称	卷期页码
263	EI	非加氢脱硫技术研究与应用进展	柯明; 周爱国; 周娜; 宋昭 峥; 蒋庆哲;	现代化工	26(s1):62-67
264	EI	碳四烃类催化转化反应规律的研究	闫平祥; 高金森; 徐春明;	现代化工	26(2):320-323+32 7
265	EI	我国含硫渣油加工方法的探讨	徐富贵; 宋昭峥; 罗方敏; 蒋 庆哲; 徐春明; 柯明; 郑成 国;	现代化工	26(10):8-13
266	EI	增产丙烯的技术进展与我国发展对策	张建国; 宋昭峥; 丁宏霞; 徐春明; 蒋庆哲; 柯明; 郑成国;	现代化工	26(2):5-9+11
267	EI	重油催化裂解集总动力学模型研究	李丽; 高金森; 徐春明; 孟祥海;	现代化工	26(2):338-341+34 6
268		汽化法制备不溶性硫黄的研究	袁洪娟; 王延臻; 刘晨光;	橡胶工业	53(9):550-552
269		沥青改性机理研究的新构想	魏建明;李银山;庞伟伟;张 玉贞;	新型建筑材料	2006(1):34-36
270	EI	高附加值石油焦新材料	郑雁军; 崔立山; 崔晓龙; 徐 春明;	新型炭材料	21(1):90-96
271		Ce 掺杂 TiO_2 纳米粒子的制备及其光催化活性研究	胡燕; 郑经堂; 石建稳;	应用化工	35(8):591-593
272		Ce 掺杂 TiO_2 纳米粒子的制备及其光催化活性研究	胡燕; 郑经堂; 石建稳;	应用化工	35(8):591-593

编号	收录	论文或专著名称	作者	期刊名称	卷期页码
273		大港减压渣油超临界萃取物气质联用色谱分析	王艳秋; 王枫; 宗志敏; 孙 琦; 金鑫; 韩丽; 魏贤勇; 赵 锁奇; 鲍晓军;	应用化工	35(11):887-892
274		新型还原法脱除苯并噻吩有机硫	郭秀燕; 李术元; 岳长涛; 倪 贤明;	应用化学	23(9):982-987
275		纳米/亚微米级粒度标准物质的研究	董鹏; 陈胜利; 王晓冬; 袁桂 梅;	中国粉体工业	2006(6):19-22
276	EI	聚乙烯醇包埋石油脱硫菌 UP-2 的研究	张建辉; 孔瑛; 侯影飞; 陈 嵘;	中国环境科学	26(s):92-96
277		新型有序炭纳米棒阵列的合成及在电化学电容器中的应用	邢伟; 刘欣梅; 白鹏; 阎子峰; 逯高清;	中国科学 E 辑	36(7):741-745
278		亚临界丙烷萃取蛋黄粉中蛋黄油的研究	张民; 孙学文; 赵锁奇; 许志明;	中国粮油学报	21(5):117-119
279		CNPC 精细石油化工发展的核心产品筛选模型	任洁梅; 蒋庆哲; 宋昭睁; 罗方敏; 柯明;	中国石油大学学报(自然科学版)	30(6):150-154
280		硅或钛取代 AIPO-11 分子筛的合成及表征	胡松青; 许本静; 阎子峰; 柏晓红; 于静;	中国石油大学学报(自然科学 版)	30(3):113-117
281	EI	硫化氢间接电解制氢电极材料性能研究	邢定峰; 俞英; 黄海燕;	中国石油大学学报(自然科学版)	30(3):126-130
282		络合吸附剂脱除 FCC 汽油中硫化物的研究	王云芳; 尹风利; 张涛; 张坤;	中国石油大学学报(自然科学版)	30(6):125-136
283	EI	汽油在不同碳含量半再生催化剂上的降烯烃规律研究	袁裕霞;杨朝合;山红红;张 建芳;韩忠祥;	中国石油大学学报(自然科学版)	30(3):109-112
284		石油焦燃烧器烧焦管内固体颗粒的停留时间分布实验研究	严超宇; 卢春喜; 高金森; 时 铭显;	中国石油大学学报(自然科学 版)	30(6):102-106

编号	收录	论文或专著名称	作者	期刊名称	卷期页码
285	EI	炭纤维/沥青树脂复合材料的性能研究	郭燕生; 陈丽丽; 查庆芳; 吴 明铂;	中国石油大学学报(自然科学版)	30(5):118-120
286		提升管反应器中催化裂化与热裂化反应的模拟	王刚;高金森;徐春明;冯 钰;曾海;	中国石油大学学报(自然科学 版)	30(2):110-114
287		纤维液膜萃取分离器的流动、传质规律研究	范怡平; 尤明扬; 鄂承林; 李 涛子; 卢春喜; 顾春来; 时铭 显;	中国石油大学学报(自然科学版)	30(6):107-111
288		旋风分离器分离空间流场的理论分析	陈建义; 罗晓兰; 时铭显;	中国石油大学学报(自然科学版)	30(6):84-88
289	EI	用碱处理的 ZSM-5 沸石合成 MCM-41 型结构复合分子筛 的研究	宋春敏; 阎子峰; 王槐平; 姜 杰; 乔柯;	中国石油大学学报(自然科学 版)	30(5):113-117
290	EI	中国石油天然气集团公司清洁燃料生产发展战略和基地优 选模型	蒋庆哲; 岳国; 宋昭峥; 张建 广; 柯明; 罗方敏;	中国石油大学学报(自然科学 版)	30(2):125-132
291	EI	水包稠油乳状液中稠油极性组分与乳化剂的相互作用研究	张铜耀; 范维玉; 南国枝; 李 水平;	中国石油大学学报(自然科学 版)	30(5):101-105
292		大豆油脚浸出油制备生物柴油及性能研究	李为民;徐春明;	中国油脂	31(4):68-71

2、会议论文

国际会议 36 篇, 国内会议 25 篇, ISTP 收录 17 篇

3、出版专著、教材

编号	专著、教材名称	作者	出版单位	书号	出版日期
1	表面活性剂科学与应用	柯明	中国石化出版社	ISBN7-80229-018-X	2006-5
2	石油炼制与化工技术	徐春明、鲍晓军等	石油工业出版社	ISBN7-5021-5683-6	2006-9

四、专利

编号	专利名称	申请日期	授权日期	国别	发明人	是否第一 完成人
ZL01118175.3	固相气体水合物及其制作方法	2001-5-18	2006-6-28	中国	陈光进;阎立军;刘犟	是
ZL03121832.6	利用水合物法分离低沸点气体混合物方法及其系 统	2003-4-14	2006-6-7	中国	陈光进;郭绪强;孙长宇;马庆兰	是
ZL02100334.3	一种天然气脱硫配方	2002-1-11	2006-1-18	中国	刘百军;常靖;鲍晓军;石冈	是
ZL03117055.2	活性组分和助剂纳米级分散的催化剂及一步制备 法	2003-5-21	2006-8-23	中国	单国彬;刘会洲;安振涛;鲍晓军	否
ZL200410030876.7	组合式催化裂化再生工艺方法及设备	2004-4-7	2006-4-26	中国	卢春喜;刘显成;王丽旻;时铭显	是
ZL200310121301.1	一种重油催化裂化沉降器抑制结焦的方法	2003-12-11	2006-7-26	中国	高金森;毛羽;徐春明;曹斌	是

编号	专利名称	申请日期	授权日期	国别	发明人	是否第一 完成人
ZL200410007518.4	一种催化裂化方法以及用于该方法的装置	2004-3-12	2006-7-5	中国	张建芳;马安;山红红;杨朝合;;钮根林;涂 永善;杜峰;孙昱东;;李春义;韩忠祥	是
ZL03148494.8	一种馏分油深度加氢精制的催化剂及其制备方法	2003-7-1	2006-11-8	中国	刘晨光;赵会吉;柳云骐;殷长龙;赵瑞玉	是
ZL03148499.9	用于中间馏分油深度加氢处理的含分子筛催化剂 及其制备方法	2003-7-1	2006-9-13	中国	刘晨光;赵会吉;柳云骐;殷长龙;赵瑞玉	是
ZL03148496.4	一种用于含烯烃石脑油选择性加氢脱硫的催化剂 及其制备方法	2003-7-1	2006-11-8	中国	刘晨光;赵会吉;柳云骐;殷长龙;赵瑞玉	是
ZL03112236.1	原油及馏分油酯化脱酸的方法	2003-6-3	2006-1-4	中国	王延臻;戴林林;马平;刘晨光	是
ZL03148500.6	一种用于含烯烃石脑油馏分加氢改质的催化剂及 其制备方法	2003-7-1	2006-9-13	中国	刘晨光;殷长龙;赵会吉;赵瑞玉;刑金仙	是
ZL200410039453.1	一种固定床加氢用的骨架金属催化剂及其制备方 法	2004-2-3	2006-11-8	中国	刘晨光;赵会吉;白锐;赵瑞玉;殷长龙;邢 金仙;方朝亮;于建宁	是
ZL200410039449.5	一种硫化型加氢催化剂及其制备方法	2004-2-13	2006-1-18	中国	刘晨光;柴永明;赵会吉;赵瑞玉;殷长龙; 邢金仙;方朝亮;于建宁	是
ZL03153101.6	乙醇柴油及其制备方法	2003-8-7	2006-3-29	中国	王学泠;岳国;赵林;王静媛;郭英男;徐春明;史权;杜尚臣;聂勇;邓红波	否
ZL200410039450.8	一种加氢催化剂的现场外预硫化方法	2004-2-13	2006-11-8	中国	刘晨光;柴永明;赵会吉;赵瑞玉;殷长龙; 邢金仙;方朝亮;于建宁	是
ZL200410096436.1	用于轻质油品剂碱抽提-固定床催化氧化脱硫醇的 组合装置	2004-12-1	2006-11-8	中国	夏道宏;项玉芝;郭洪明;张洪滨;张振江; 吴力明	是
ZL02123655.0	催化裂化汽油深度降烯烃增辛烷值的改质方法和 系统	2002-7-5	2006-6-7	中国	高金森;徐春明;白跃华;刘耀芳;卢春喜	是

编号	专利名称	申请日期	授权日期	国别	发明人	是否第一 完成人
ZL02159470.8	双反再系统汽油高品质化与重油催化裂化耦合装 置和方法	2002-12-31	2006-7-26	中国	高金森;徐春明;白跃华	是
ZL01131452.4	离子交换膜燃料电池电极扩散层碳纤维复合纸及 其制备方法 2001-9-11 2006-3-29 中 国 汪树军;张伟;刘红研;赵永丰		是			
ZL200310115456.4	一种有效的 C4 烃类催化转化的工艺方法	2003-12-2	2006-11-1	中国	高金森,徐春明,卢春喜	是
ZL200410024458.7	炼油废碱液处理方法	2004-7-9	2006-2-22	中国	王延臻;刘晨光	是
ZL03153499.6	一种用于渣油悬浮床加氢改质的多功能复合剂	2003-8-15	2006-1-4	中国	阙国和;沐宝权;邓文安;周家顺	是
ZL02117838.0	用于重油悬浮床加氢裂化的残渣油的处理技术	2002-5-23	2006-1-18	中国	沐宝泉;阙国和;李庶峰;邓文安;周家顺	是

五、获奖

编号	项目名称	获奖名称	获奖等级	获奖级别	获奖人员
1	催化裂化汽油辅助反应器改质降烯烃 技术的开发和应用	国家科技进步奖	2	国家级	高金森(1); 徐春明(2); 卢春喜(3); 梁咏 梅(9); 蓝兴英(10)

六、学术交流

姓名	交流类别	地点	开始时间	结束时间	主要内容
徐春明、赵锁奇、 Keng H.Chung	首届世界重油大会	北京	2006-11-12	2006-11-15	徐春明教授任大会技术论坛副主席,赵锁奇教授作学术报告
	The 9th China-Japan Symposium on Fluidization	北京	2006-12	2006-12	学术报告
徐春明、卢春喜、陈 胜利等	中国颗粒学会 2006 年年 会暨海峡两岸颗粒技术 研讨会	北京	2006-8	2006-8	徐春明教授作特邀报告,多名教授作学术报告
徐春明、高金森、赵 震、申宝剑等	The 19 th Canadian Symposiom on catalysis	Saskatoon,Saskat chewan	2006-5-14	2006-5-17	学术报告
穆利·德奥拉	交流访问	实验室	2006-12-18	2006-12-18	印度石油和天然气部部长穆利·德奥拉率代表团访问我室
Vanessa Chang A. Majid Dellah Ri chard Clark	交流访问	实验室	2006-3-29	2006-3-29	加拿大"中加科技互补性研究"项目工作组访问我室,讨论"中加实验室合作研究"国际合作项目
Michael Raymont	交流访问	实验室	2006-3-23	2006-3-23	加拿大 EnergyINet 执行总裁 Michael Raymont 访问我室

(不完全统计)

七、大型仪器设备

设备名称	型号	研究机时	服务机时	设备状况	管理人
AC 模拟蒸馏色谱仪	Agilent6890	500	1250	良好	梁咏梅
AC 预切割汽油烃组成分 析仪	Agilent6890	280	918	良好	梁咏梅
八角度激光光散射分子量 测定仪	DAWN 8	30	30	良好	焦淑静
棒状薄层色谱辅助装置		0	0	良好	刘旭霞
超导核磁共振波谱仪	JNM-LA300	210	500	良好	郭巧霞
恩氏蒸馏实验仪	NDI440	200	90	待修	李瑞丽
高沸点蒸馏装置	860 型	200	310	待修	李瑞丽
高压液相色谱	244 型	0	0	待修	
激光纳米粒度及 Zeta 电位测定仪	Zetasizer Nano ZS	960	960	良好	曾鹏晖
库尔特吸附仪	100CX	0	0	良好	李瑞丽
硫氮分析仪	ANTEK 7000NS	2200	1200	较差	刘旭霞
模拟蒸馏色谱仪	5890- II	0	0	故障	刘旭霞
气体分析仪	HP6890	3126	1000	较好	梁咏梅
全自动比表面积及微孔分 析仪	ASAP2020M	5040	5040	良好	焦淑静
全自动程序升温化学吸附 分析仪	AUTOSORB-1-C/TC D/MS	2160	2160	良好	曾鹏晖
扫描电子显微镜	Cambridge S-360	0	0	很差	焦淑静
色谱质谱联用仪	SSQ710	600	1500	较差	史权
色谱质谱联用仪	Trace-DSQ	1200	2800	良好	史权
数字密度计		200	100	良好	刘旭霞
无汞 PVT 装置	RUSKA2370-601	0	0	改造	许志明
旋转氧弹仪	K70290	0	0	良好	蒋晓明
旋转粘度计	0∼9990Pas	100	200	良好	刘旭霞
元素分析仪	PE2400- II	0	0	停用	刘旭霞
原油实沸点蒸馏仪	10 升蒸馏釜	2010	350	良好	李瑞丽
紫外-可见-近红外光谱仪	U-4100	600	700	良好	赵震
吸附仪	Tristar 3000	1200	1600	正常	阎子峰
吸附议	ASAP 2010	1400	1800	正常	阎子峰
压汞仪	Autopore 9500	200	150	正常	阎子峰
渣油减粘一焦化装置	UPC-1	1000	3000	良好	郭爱军

附件1 代表性论文

编号	收录	论文或专著名称	作者	期刊名称	卷期页码	年报页码
1	SCI,EI	Catalytic pyrolysis of heavy oils: 8-lump kinetic model	孟祥海;徐春明;高金森;李丽	APPLIED CATALYSIS A-GENERAL	301(1):32 ∼38	61
2	SCI,EI	Secondary cracking of C4 hydrocarbons from heavy oil catalytic pyrolysis	孟祥海;徐春明;高金森	CANADIAN JOURNAL OF CHEMICAL ENGINEERING	84(3):322 ~327	68
3	SCI	Effect of valence of copper in La2-xThxCuO4 on NO decomposition reaction	朱君江; 赵震; Xiao, DH; Li, J; Yang, XG; Wu, Y	CATALYSIS COMMUNICATIONS	7(1):29~ 32	74
4	SCI,EI	CrHZSM-5 zeolites - Highly efficient catalysts for catalytic cracking of isobutane to produce light olefins	陆江银;赵震;徐春明;段爱军;张	CATALYSIS LETTERS	109(2):65 ~70	78
5	SCI	Characterization and activity of Mo supported catalysts for diesel deep hydrodesulphurization	段爱军; 万国赋; 赵震; 徐春明; 郑雁英; 张瑛; 窦涛; 鲍晓军; Chung, Keng	CATALYSIS TODAY	119(4):13 ~18	84
6	EI	Synthesis of ZSM-5/SAPO-11 composite and its application in FCC gasoline hydro-upgrading catalyst	范煜; 雷多; 石冈; 鲍晓军	Catalysis Today	114(4):38 8-396	90
7	SCI,EI	A scale-up strategy for low-temperature methanol synthesis in a circulating slurry bubble reactor	张锴; 赵玉龙	CHEMICAL ENGINEERING SCIENCE	61(5):145 9~1469	99

编号	收录	论文或专著名称	作者	期刊名称	卷期页码	年报页码
8	SCI	Computational fluid dynamics (CFD) modeling of spouted bed: Assessment of drag coefficient correlations	杜威; 鲍晓军; 徐健; 魏伟胜	CHEMICAL ENGINEERING SCIENCE	61(5):140 1~1420	110
9	SCI,EI	Colloidal stability variation of petroleum residue during thermal reaction	张龙力;杨国华;阙国和;张庆轩; 杨普江	ENERGY & FUELS	20(5):200 8~2012	130
10	SCI,EI	Hydrodesulfurization of resid fluid catalytic cracking diesel oil over TiO2-SiO2 supported catalysts	张振莉;周亚松;张绍金;徐春明	ENERGY & FUELS	20(6):229 3~2298	135
11	SCI,EI	Preparation of silica-PS composite particles and their application in PET	吴天斌; 柯扬船	EUROPEAN POLYMER JOURNAL	42(2):274 ~285	141
12	SCI,EI	Methane hydrate dissociation above O degrees C and below O degrees C 016/j.fluid-2006.01.025	孙长宇; 陈光进	FLUID PHASE EQUILIBRIA	242(2):12 3~128	153
13	SCI	Fluidization quality improvement for cohesive particles by fine powder coating	Liu, H; Li, Y; 郭庆杰	INDUSTRIAL & ENGINEERING CHEMISTRY RESEARCH	45(5):180 5~1810	159
14	SCI	Effect of water content on the solubility of CO2 in the ionic liquid [bmim][PF6]	浮东宝; 孙学文; 蒲劲军; 赵锁奇	Journal of Chemical and Engineering Data	51(2):371 -375	165
15	SCI	Studies on properties of interfacial active fractions from crude and their effect on stability of crude emulsions	李明远; 郭继香; 林梅钦; 吴肇亮	JOURNAL OF DISPERSION SCIENCE AND TECHNOLOGY	27(5):677 ~687	170
16	SCI,EI	Pervaporation performance of crosslinked polyethylene glycol membranes for deep desulfurization of FCC gasoline	Lin, Ligang; Wang, Gang; Qu, Huimin; 杨金荣; 王云芳; 史德青; 孔瑛	JOURNAL OF MEMBRANE SCIENCE	280(2):65 1~658	181

编号	收录	论文或专著名称	作者	期刊名称	卷期页码	年报页码
17	SCI,EI	The semi-ideal solution theory for mixed ionic solutions at solid-liquid-vapor equilibrium	胡玉峰; 樊栓狮; Liang, DQ	JOURNAL OF PHYSICAL CHEMISTRY A	110(12):4 276~ 4284	189
18	SCI,EI	Synthesis and structure characterization of chromium oxide prepared by solid thermal decomposition reaction	李丽;阎子峰; Lu, GQ; Zhu, ZH	JOURNAL OF PHYSICAL CHEMISTRY B	110(1):17 8~183	198
19	SCI	Ionic liquid alkylation process produces high-quality gasoline	刘植昌; 张睿; 徐春明; 夏荣安	OIL & GAS JOURNAL	104(40):5 2~56	204
20	SCI	含 HF 体系中 SAPO-11 分子筛的合成与表征	张胜振; 陈胜利; 董鹏; 井秀娟; 姜 凯;	催化学报	27(10):86 8~874	209
21	EI	大港减压渣油超临界萃取萃余残渣结构特征研究	张占纲; 郭绍辉; 赵锁奇; 牟彤;	燃料化学学报	34(4):427 -433	216
22	EI	质子交换膜燃料电池专用碳纸的制备及性能测试	张伟; 汪树军; 刘红研; 潘惠芳;	太阳能学报	27(2):199 -202	223
23	SCI	二硫代钨酸铵晶体的合成、表征与热分解机理的研究	安高军;柳云骐;柴永明;周同娜;刘晨光;	无机化学学报	22(10):18 13~1818	227
24	SCI	颗粒模板法制备大孔 Al_2O_3 材料	王晓冬; 董鹏; 陈胜利;	物理化学学报	22(7): 831~835	233
25		纤维液膜萃取分离器的流动、传质规律研究	范怡平; 尤明扬; 鄂承林; 李涛子; 卢春喜; 顾春来; 时铭显;	中国石油大学学报(自然科学 版)	30(6):107 -111	238



Available online at www.sciencedirect.com







Catalytic pyrolysis of heavy oils: 8-lump kinetic model

Xianghai Meng*, Chunming Xu, Jinsen Gao, Li Li

State Key Laboratory of Heavy Oil Processing, China University of Petroleum, Changping, Beijing 102249, China
Received 6 September 2005; received in revised form 4 November 2005; accepted 12 November 2005
Available online 27 December 2005

Abstract

A new 8-lump kinetic model is proposed to describe the heavy oil catalytic pyrolysis process. The kinetic model contains 17 kinetic constants and one for catalyst deactivation. This paper also presents a new catalyst deactivation model, a function of feed properties and operating conditions, in which the deactivation constant doesn't vary with reaction temperature. Kinetic constants and apparent activation energies were determined by the least square regression analysis of the experimental data, obtained in a confined fluidized bed reactor at temperatures of 600, 630, 660 and 700 °C. Most of the apparent activation energies are higher than 100 kJ/mol, between the apparent activation energies for catalytic cracking and those for thermal cracking. The predicted results indicate that catalytic pyrolysis of heavy oils had better be conducted at high temperature and short residence time of oil gas, and heavy oils with the aromaticity higher than 30% had better not be considered as the feeds of catalytic pyrolysis. © 2005 Elsevier B.V. All rights reserved.

Keywords: Kinetic; Model; Lump; Catalytic pyrolysis; Heavy oil

1. Introduction

Heavy oil catalytic pyrolysis is a promising process to convert low value heavy oils into more valuable light olefins. It attracts great interests in recent years [1,2]. The process of heavy oil catalytic pyrolysis involves catalytic reactions and thermal reactions, and the products consist of a mixture of many compounds [3]. One of the most important aspects in understanding heavy oil catalytic pyrolysis is the kinetic study. This is important to design and simulate the reactor, to predict the reaction behaviors and to optimize the operating conditions.

Just like the kinetic studies for fluid catalytic cracking (FCC) [4,5], the complex mixtures in catalytic pyrolysis processes can be described by lumping the large number of chemical compounds into groups of pseudo-components, according to their boiling points and their molecular characteristics. Although many lumping models for catalytic cracking have been developed [6–8], only a few lumping kinetic models for catalytic pyrolysis have been reported.

0926-860X/\$ – see front matter @ 2005 Elsevier B.V. All rights reserved. doi:10.1016/j.apcata.2005.11.010

Some researchers have attempted to study the lumping kinetics for heavy oil catalytic pyrolysis over several catalysts in recent years. Xu [9] presented a 4-lump model, in which dry gas and coke was considered as one lump. Meng et al. [10] proposed a 5-lump model, in which the dry gas plus coke lump was split into dry gas and coke separately. A 16-lump model was recently developed by Wang et al. [11]. In this model, pyrolysis gas was further divided into eight lumps (hydrogen, methane, ethene, ethane, propene, propane, butene and butane), and 70 kinetic parameters plus one catalyst deactivation parameter were used.

This paper presents an 8-lump model for heavy oil catalytic pyrolysis on catalyst CEP-1. The catalyst deactivation model was usually described by an exponential function depending on time-on-stream. In this paper, a novel catalyst deactivation model is introduced. After the estimation of the kinetic parameters, the variation of product yields are predicted with operating conditions and feed properties.

2. Eight-lump kinetic model

2.1. Model description

Generally, the more lumps a model includes, the more kinetic parameters need to be estimated and, consequently, the more experimental data are required. Thus, it is necessary to

^{*} Corresponding author. Tel.: +86 10 8973 3775 (Office); fax: +86 10 6972 4721.

E-mail addresses: mengxh@cup.edu.cn (X. Meng), xcm@cup.edu.cn (C. Xu), jsgao@cup.edu.cn (J. Gao), liliupc@163.com (L. Li).

Nomenclature

C/H atomic ratio of carbon to hydrogen in feeds

 C_i concentration of lump i, mol/g_{gas}

 k_{ij} rate constant for the reaction of lump i to lump j

 M_i molecular weight of lump i, g/mol

 R_{co} catalyst-to-oil weight ratio R_{so} steam-to-oil weight ratio t residence time of oil gas, s t_{c} residence time of catalyst, s T reaction temperature, K

 v_{ij} stoichiometric coefficient for the reaction of

 $\mathrm{lump}\ i\ \mathrm{to}\ \mathrm{lump}\ j$

Greek symbols

 α deactivation constant ϕ deactivation function

establish a simple model that can give the key kinetic information.

To predict the catalytic pyrolysis abilities of various heavy feeds, the feed in the model can be lumped into three groups (paraffinic carbons, naphthenic carbons and aromatic carbons), just as the feed lumps of catalytic cracking models [7,8]. However, the cracking extent of catalytic pyrolysis is more thorough than that of catalytic cracking [3]. During catalytic pyrolysis processes, naphthenic carbons can easily crack into paraffinic carbons, so the feed can be divided into two lumps, non-aromatic carbons and aromatic carbons, in order to simplify the lump model.

Different from catalytic cracking, the aimed products of heavy oil catalytic pyrolysis are light olefins, including ethene, propene and butene. Therefore, ethene and propene plus butene can be considered as two lumps. Gasoline and diesel oil are byproducts of heavy oil catalytic pyrolysis, and their components are similar by group analysis. Consequently, gasoline and diesel oil can be considered as one lump.

The reaction network shown in Fig. 1 can be used to describe the heavy oil catalytic pyrolysis. Aromatic carbons cannot crack into gaseous products, because ring-opening reactions of aromatic carbons are hard to take place in the operating conditions of heavy oil catalytic pyrolysis [11–13]. We investigated the secondary cracking ability of the collected gasoline and diesel oil (high content of aromatic hydrocarbons) from heavy oil catalytic pyrolysis, and analyzed the hydrogen balance and carbon balance. The research results also show that aromatic rings can hardly split. However, dealkylation of aromatic hydrocarbons and cracking of the alkyl groups can occur. This will reduce the boiling points of aromatic carbons to the boiling point range of gasoline and diesel oil, so aromatic carbons can yield gasoline and diesel oil.

An advantage of this model is that it can predict the cracking ability for various heavy feeds. Another advantage is that the proposed model can predict the yields of the aimed products (ethene and propene plus butene) directly. Only 17 kinetic

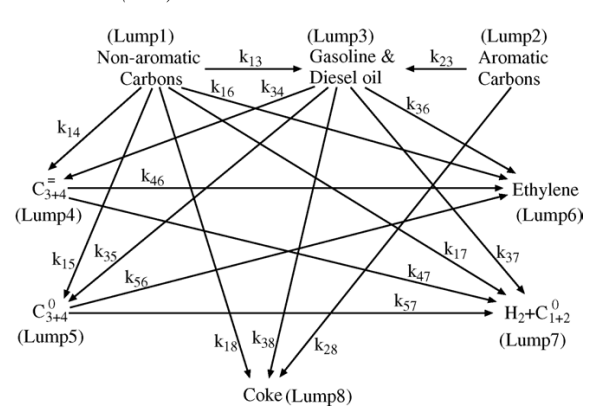


Fig. 1. Reaction network of the 8-lump model.

constants are used to describe the complex catalytic pyrolysis process, and this is also an advantage.

One limitation of the 8-lump model is that the kinetic parameters depend on catalyst properties. One improvement for the model in future is that the feedstocks can be divided into more lumps, in order to better predict the cracking ability for special feeds with a high content of naphthenic or aromatic hydrocarbons.

2.2. Kinetic models

For each reaction, a kinetic expression (r_i) was formulated as a function of lump concentration (C_i) , kinetic constants (k_i) and catalyst deactivation function (ϕ) . If a lump consists of a complex mixture of hydrocarbons, the most reactive molecules disappear first and the remaining molecules have a lower kinetic constant when conversion increases, and the cracking of the lump is usually considered as a second order reaction [5,14].

Non-aromatic carbons, aromatic carbons and gasoline plus diesel oil consist of a complex mixture of hydrocarbons, so their cracking is considered as a second order reaction. The cracking of propene plus butene and propane plus butane is considered as a first order reaction. Based on these assumptions, the reaction rates of the proposed model are:

$$\frac{\mathrm{d}C_1}{\mathrm{d}t} = -(k_{13} + k_{14} + k_{15} + k_{16} + k_{17} + k_{18})C_1^2\phi \tag{1}$$

$$\frac{\mathrm{d}C_2}{\mathrm{d}t} = -(k_{23} + k_{28})C_2^2\phi \tag{2}$$

$$\frac{dC_3}{dt} = \left[v_{13}k_{13}C_1^2 + v_{23}k_{23}C_2^2 - (k_{34} + k_{35} + k_{36} + k_{37} + k_{38})C_3^2 \right] \phi$$
(3)

$$\frac{\mathrm{d}C_4}{\mathrm{d}t} = \left[v_{14}k_{14}C_1^2 + v_{34}k_{34}C_3^2 - (k_{46} + k_{47})C_4\right]\phi\tag{4}$$

$$\frac{\mathrm{d}C_5}{\mathrm{d}t} = \left[v_{15}k_{15}C_1^2 + v_{35}k_{35}C_3^2 - (k_{56} + k_{57})C_5\right]\phi\tag{5}$$

$$\frac{dC_6}{dt} = \left[v_{16}k_{16}C_1^2 + v_{36}k_{36}C_3^2 + v_{46}k_{46}C_4 + v_{56}k_{56}C_5\right]\phi \qquad (6) \qquad \phi = \exp(-\alpha C_c)$$
(11)

$$\frac{\mathrm{d}C_7}{\mathrm{d}t} = \left[v_{17}k_{17}C_1^2 + v_{37}k_{37}C_3^2 + v_{47}k_{47}C_4 + v_{57}k_{57}C_5\right]\phi\tag{7}$$

$$C_{8} = \frac{\left(\frac{1}{1+R_{so}} - C_{1}M_{1} - C_{2}M_{2} - C_{3}M_{3} - C_{4}M_{4} - C_{5}M_{5} - C_{6}M_{6} - C_{7}M_{7}\right)}{M_{8}}$$
(8)

2.3. Catalyst deactivation model

For kinetic studies of lumping models for catalytic cracking/pyrolysis, the catalyst deactivation model (ϕ) is usually described by a function depending on time-on-stream (the residence time of catalyst) or catalyst coke content (the mass fraction of coke on catalyst). Although the catalyst deactivation functions depending on time-on-stream are sometimes used, those depending on the catalyst coke content are much advisable because coke is the main cause of the catalyst deactivation [14,15].

This paper tries to develop a catalyst deactivation function depending on catalyst coke content. During the estimation of the parameters for a catalyst deactivation function, catalyst coke content is an independent variable, but it's not an operating parameter, and its value is unknown at a given operating condition. Therefore, it is important to obtain direct measurement of this deactivation function to avoid introducing new unknown parameters. Here, we obtained a catalyst coke content function by least square regression analysis depending on feed properties and operating conditions, and then use it to develop a catalyst deactivation function.

For catalytic pyrolysis of heavy oils, catalyst coke content (C_c) can be described by a function depending on C/H atomic ratio of the feed, reaction temperature (T), residence time of oil gas (t), catalyst-to-oil weight ratio (R_{co}) , steam-to-oil weight ratio (R_{so}) and residence time of catalyst (t_c) , shown as Eq. (9). The parameters in Eq. (9) are determined by the least square regression analysis of experimental data, and then Eq. (10) is gained. According to the catalyst deactivation function (Eq. (11)) and experimental data, we obtained the catalyst deactivation function used in this paper (Eq. (12)). Unlike the deactivation functions depending on time-on-stream, the deactivation constant in this paper doesn't vary with reaction temperature, because the influence of temperature has already included in the deactivation function.

$$C_{\rm c}(\%) = a \left(\frac{\rm C}{\rm H}\right)^{\rm b} T^{\rm c} t^{\rm d} (1 + R_{\rm co})^{\rm e} (1 + R_{\rm so})^{\rm f} t_{\rm c}^{\rm g} \times 100$$
 (9)

$$C_{c}(\%) = 3.5248 \left(\frac{C}{H}\right)^{4.3889} T^{0.2838} t^{-0.1774} (1 + R_{co})^{-0.4795}$$

$$\times (1 + R_{so})^{-0.3963} t_{c}^{0.2276} \times 100$$
(10)

$$\phi = \exp\left(-2.55 \left(\frac{\text{C}}{\text{H}}\right)^{4.3889} T^{0.2838} t^{-0.1774} (1 + R_{\text{co}})^{-0.4795} \times (1 + R_{\text{so}})^{-0.3963} t_{\text{c}}^{0.2276}\right)$$
(12)

3. Experimental

The experiments of heavy oil catalytic pyrolysis were conducted in a confined fluidized bed reactor. The reactor consists of oil and steam input mechanisms, a reaction zone, temperature control system, and a product separation and collection system. In experiments, various amounts of catalysts were loaded into the reactor, and the catalyst bed was fluidized by steam. The residence times of oil gas and the steam-to-oil weight ratios were varied by changing the flow rates of steam and feeds. The catalyst-to-oil weight ratios were varied by changing the amount of catalysts loaded into the reactor. The residence times of catalyst were varied by changing the feeding time. The experiment has been described in detail by Meng et al. [3].

The experiments were carried out at four temperatures between 600 and 700 °C, with residence time of oil gas, the weight ratios of catalyst-to-oil and steam-to-oil, and the flow rates of feeds and steam varying in 1.5–4.5 s, 6–27, 0.2–1.6, 2–10 g/min and 1.5–6.0 g/min, respectively. The feeds were Chinese Daqing atmospheric residue, Chinese Daqing vacuum gas oil, Chinese Daqing vacuum residue and Chinese Huabei atmospheric residue. The catalyst was CEP-1 (used for Catalytic Pyrolysis Process technology). The properties of the feeds and the catalyst, together with the analysis methods for pyrolysis products, have been introduced in detail in literature [3].

4. Results and discussion

4.1. Kinetic constant determination

A program was compiled in Matlab language for the determination of kinetic constants. The kinetic constants of the 8-lump model were estimated and listed in Table 1. The frequency factors and the apparent activation energies were calculated according to the Arrhenius equation, shown in Table 2.

The kinetic constants of the cracking of the two feed lumps are much higher than those of gasoline plus diesel oil, propene plus butene and propane plus butane. This indicates that it's the cracking reactions of the feeds that primarily take place in the heavy oil catalytic pyrolysis process, and the proportion of the secondary cracking reactions of intermediate products in total cracking reactions is low. The kinetic constant of reaction k_{28} is bigger than that of reaction k_{23} , showing that the aromatic carbons in the feeds are mostly converted into coke.

Table 1 Kinetic constants of the 8-lump model

Reaction	Unit	Reaction temperature, °C				
		600	630	660	700	
k ₁₃	$g \text{ mol}^{-1} \text{ s}^{-1}$	14587	24829	37831	75288	
k_{14}	$g \text{ mol}^{-1} \text{ s}^{-1}$	22705	43019	72028	112815	
k ₁₅	$g \text{ mol}^{-1} \text{ s}^{-1}$	10252	15107	21240	34275	
k ₁₆	$g \text{ mol}^{-1} \text{ s}^{-1}$	5829	12097	22828	42866	
k ₁₇	$g \text{ mol}^{-1} \text{ s}^{-1}$	3327	8062	17965	30667	
k_{18}	$g \text{ mol}^{-1} \text{ s}^{-1}$	4365	7029	9862	15170	
k_{23}	$g \text{ mol}^{-1} \text{ s}^{-1}$	5846	8295	10524	16955	
k_{28}	$g \text{ mol}^{-1} \text{ s}^{-1}$	12591	18045	27605	38996	
k ₃₄	$g \text{ mol}^{-1} \text{ s}^{-1}$	1.4	2.8	5.1	9.9	
k ₃₅	$g \text{ mol}^{-1} \text{ s}^{-1}$	0.6	1.4	2.8	7.2	
k ₃₆	$g \text{ mol}^{-1} \text{ s}^{-1}$	3.1	5.6	10.7	21.1	
k ₃₇	$g \text{ mol}^{-1} \text{ s}^{-1}$	18.7	39.0	85.7	200.0	
k ₃₈	$g \text{ mol}^{-1} \text{ s}^{-1}$	22.5	45.3	80.6	155.1	
k ₄₆	s^{-1}	0.007	0.013	0.023	0.050	
k ₄₇	s^{-1}	0.008	0.018	0.039	0.11	
k ₅₆	s^{-1}	0.020	0.042	0.093	0.25	
k ₅₇	s^{-1}	0.032	0.085	0.21	0.61	

The apparent activation energies of the cracking reactions of the two feed lumps are smaller than those of gasoline plus diesel oil, propene plus butene and propane plus butane. This indicates that the secondary cracking of intermediate products is more sensitive to temperature. It is reported that the apparent activation energies of hydrocarbon catalytic cracking are between 42 and 125 kJ/mol, while those of thermal cracking are between 210 and 293 kJ/mol [16]. Most of the apparent activation energies determined in this paper are higher than 100 kJ/mol, which explains that thermal cracking plays an important role in heavy oil catalytic pyrolysis. This is consistent with the reaction mechanistic pathway of heavy oil catalytic pyrolysis [3].

The apparent activation energies determined in this paper are close to those reported in literature [4,17], but are higher than

 $\begin{tabular}{ll} Table 2 \\ Frequency factors and apparent activation energies of the 8-lump model \\ \end{tabular}$

Reaction	Frequency factor	or	Apparent activation	
	Unit	Value	energy (kJ/mol)	
k ₁₃	$g \text{ mol}^{-1} \text{ s}^{-1}$	1.04×10^{11}	115	
k_{14}	$g \text{ mol}^{-1} \text{ s}^{-1}$	1.48×10^{10}	113	
k ₁₅	$g \text{ mol}^{-1} \text{ s}^{-1}$	1.21×10^{9}	85	
k ₁₆	$g \text{ mol}^{-1} \text{ s}^{-1}$	1.72×10^{12}	141	
k ₁₇	$g \text{ mol}^{-1} \text{ s}^{-1}$	1.15×10^{13}	159	
k ₁₈	$g \text{ mol}^{-1} \text{ s}^{-1}$	7.31×10^{8}	87	
k_{23}	$g \text{ mol}^{-1} \text{ s}^{-1}$	1.49×10^{8}	74	
k_{28}	$g \text{ mol}^{-1} \text{ s}^{-1}$	9.36×10^{8}	81	
k ₃₄	$g \text{ mol}^{-1} \text{ s}^{-1}$	2.66×10^{8}	138	
k ₃₅	$g \text{ mol}^{-1} \text{ s}^{-1}$	1.02×10^{10}	171	
k ₃₆	$g \text{ mol}^{-1} \text{ s}^{-1}$	5.10×10^{8}	137	
k ₃₇	$g \text{ mol}^{-1} \text{ s}^{-1}$	2.33×10^{11}	169	
k ₃₈	$g \text{ mol}^{-1} \text{ s}^{-1}$	3.24×10^{9}	136	
k ₄₆	s^{-1}	1.36×10^{6}	139	
k ₄₇	s^{-1}	5.15×10^{8}	181	
k ₅₆	s^{-1}	1.07×10^{9}	180	
k ₅₇	s^{-1}	8.48×10^{10}	208	

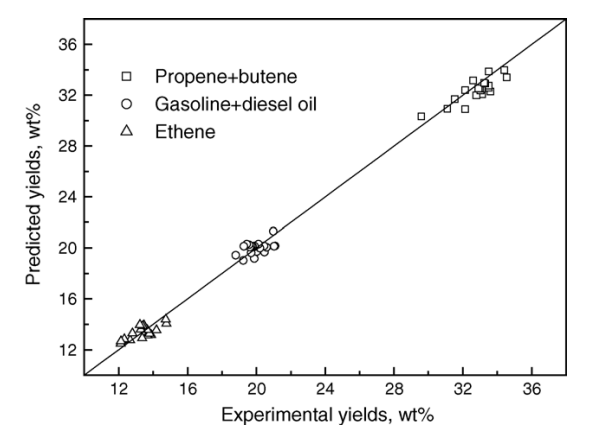


Fig. 2. Experimental yields (plots) vs. predicted ones (line) at 660 $^{\circ}$ C.

those for catalytic cracking reactions at conventional operating conditions [5,18]. This is due to the fact that the reaction temperature of heavy oil catalytic pyrolysis is about 150 $^{\circ}$ C higher than that of conventional catalytic cracking.

For the products of heavy oil catalytic pyrolysis at 660 °C, the experimental yields and the model-predicted ones are shown in Figs. 2 and 3. Figs. 4 and 5 compare the experimental yields with the predicted ones for ethene and propene plus butene at four reaction temperatures. The predicted yields are close to the experimental ones, indicating that the 8-lump kinetic model predicts well the experimental data and the predicted values are reliable.

4.2. Application of the 8-lump model

An important application of the 8-lump model is to predict the product distribution for various heavy feeds at a given operating condition. Some experiments are not necessary thanks to the kinetic model; and consequently, parts of the experimental research expenses can be saved. Some fundamental information can be obtained from the kinetic model, for the design, simulation and optimization of both the reaction

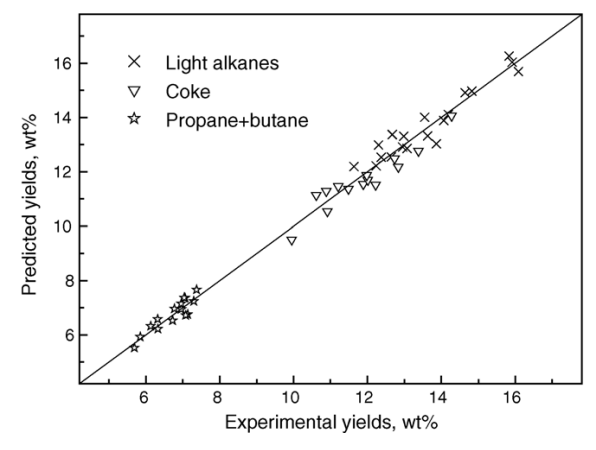


Fig. 3. Experimental yields (plots) vs. predicted ones (line) at 660 °C.

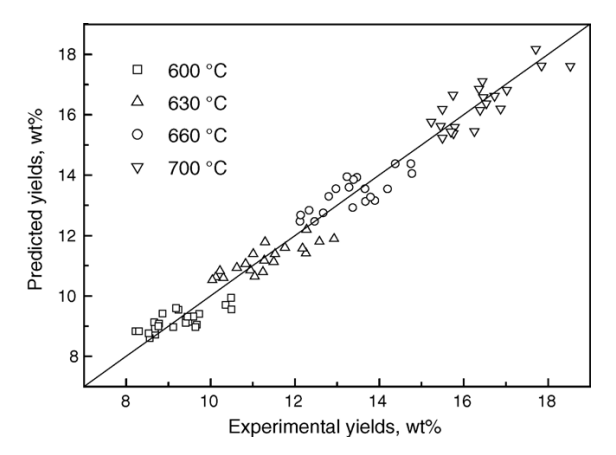


Fig. 4. Experimental yields (plots) vs. predicted ones (line) for ethene.

process and the units related. Two application examples of the 8-lump model are introduced in this paper.

4.2.1. Optimization of operating conditions

For catalytic pyrolysis of various heavy feeds on catalyst CEP-1, the variation of product yields with every operating condition can be predicted by the 8-lump kinetic model, and then the optimal operating conditions can be obtained. In this paper, Chinese Daqing atmospheric residue is used as an example for the optimization of operating conditions.

The variation of product yields with the residence time of oil gas is shown in Fig. 6, keeping reaction temperature, the weight ratios of catalyst-to-oil, steam-to-oil and the residence time of catalyst constant at 660 °C, 16, 0.6 and 30 s, respectively. As the residence time of oil gas prolongs, all product yields increase quickly until a residence time of 0.3 s is reached, and then the yields of ethene, coke and light alkanes go up slowly, while those of gasoline plus diesel oil, propene plus butene and propane plus butane decrease slowly due to secondary reactions.

Fig. 7 shows the effect of the residence time of oil gas on the yields of total light olefins at 600, 630, 660 and 700 °C, keeping

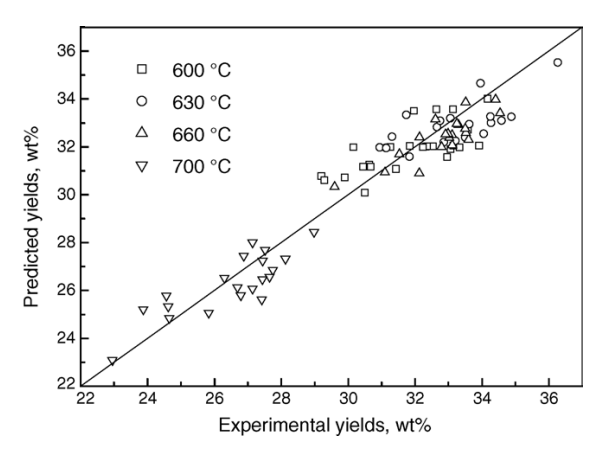


Fig. 5. Experimental yields (plots) vs. predicted ones (line) for propene plus butene.

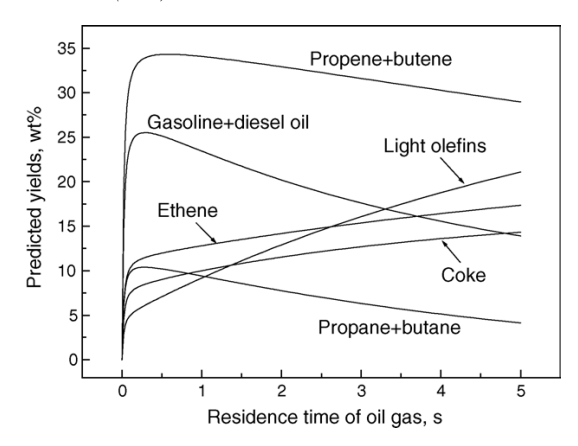


Fig. 6. Variation of predicted product yields with the residence time of oil gas.

the weight ratios of catalyst-to-oil, steam-to-oil and the residence time of catalyst fixed at 16, 0.6 and 30 s, respectively. As the residence time of oil gas prolongs, the yields of total light olefins at 700 and 660 °C pass through maxima at about 0.75 and 2.0 s respectively, while those at 630 and 600 °C increase quickly until a residence time of 0.3 s is reached, and then increase slowly, not reaching maxima until 5.0 s. For the predicted yields of total light olefins, the maximum at 700 °C is 0.3 wt.% higher than that at 660 °C.

The higher the reaction temperature, the bigger the maximum of total light olefins, and the shorter the residence time of oil gas at the maximum of total light olefins. The optimal residence time of oil gas at $700\,^{\circ}\text{C}$ is between 0.5 and 1.5 s, and that at $660\,^{\circ}\text{C}$ is between 1.0 and 3.0 s. The lower the reaction temperature, the longer the optimal residence time of oil gas. This indicates that catalytic pyrolysis of heavy oils should be conducted at high temperature and short residence time of oil gas.

Figs. 8 and 9 show the predicted variation of ethene yields and propene plus butene yields respectively, keeping the weight ratios of catalyst-to-oil, steam-to-oil and the residence time of catalyst constant at 16, 0.6 and 30 s, respectively. The predicted

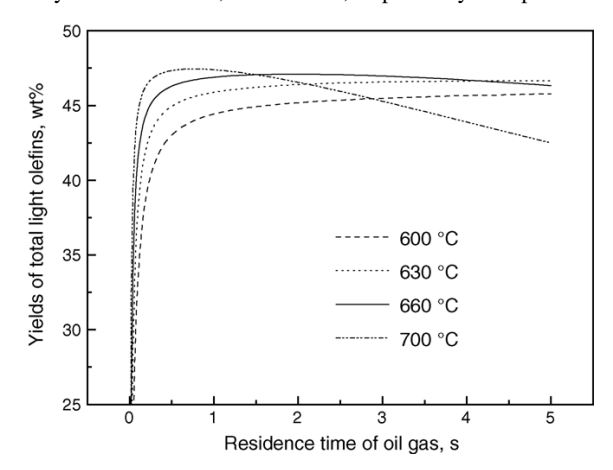


Fig. 7. Variation of the yields of total light olefins with the residence time of oil gas.

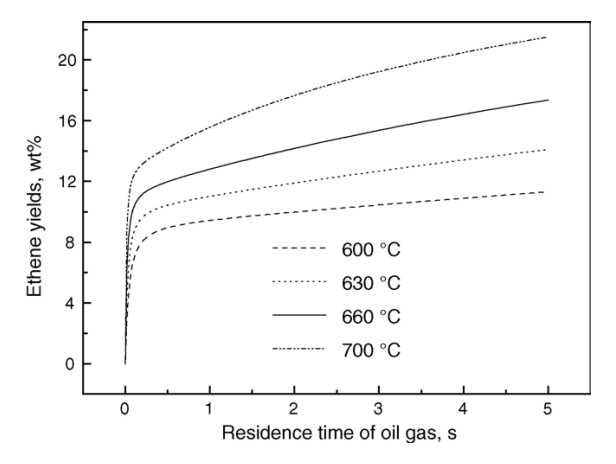


Fig. 8. Variation of predicted ethene yields with the residence time of oil gas.

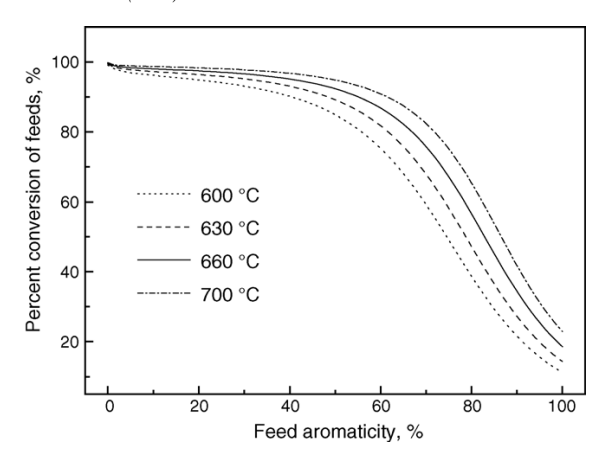


Fig. 10. Variation of the percent conversion of heavy feeds with feed aromaticity.

ethene yields at high temperatures are bigger than those at low temperatures, while the predicted propene plus butene yields at high temperatures are less than those at low temperatures. This explains that the optimal reaction temperature for much ethene production is higher that that for much propene production.

4.2.2. Selection of cracking feeds

For catalytic pyrolysis of heavy oils, the reaction behaviors and product distribution will vary with the feed properties. The 8-lump model can be used to predict the cracking ability of various heavy feeds, to determine whether a heavy feed is suitable for catalytic pyrolysis or not, and to select the better feeds for catalytic pyrolysis.

Figs. 10 and 11 illustrate the influence of feed aromaticity (the content of aromatic carbons in heavy feeds) on the percent conversions of heavy feeds and non-aromatic carbons at various reaction temperatures, keeping the weight ratios of catalyst-to-oil, steam-to-oil and the residence time of catalyst constant at 16, 0.6 and 30 s, respectively. At low feed aromaticity (less than

30%), the percent conversion of heavy feeds and that of non-aromatic carbons are not sensitive to reaction temperature. However, at high feed aromaticity (higher than 30%), these two conversions increase with the enhancement of reaction temperature. The percent conversion of non-aromatic carbons is close to 100% until a feed aromaticity of 30% is reached, and then it decreases as feed aromaticity goes up. The percent conversion of heavy feeds also shows the similar variation with increasing feed aromaticity.

Figs. 12 and 13 show the variation of the predicted yields of ethene and propene plus butene with feed aromaticity, keeping the weight ratios of catalyst-to-oil, steam-to-oil and the residence time of catalyst fixed at 16, 0.6 and 30 s, respectively. The predicted yields of light olefins decrease almost linearly with the increase of feed aromaticity. Considering the percent conversion and the product yields of heavy feeds, together with the economic benefits of catalytic pyrolysis processes, we draw a conclusion that heavy oils with the aromaticity higher than 30% are not suitable for the feeds of catalytic pyrolysis.

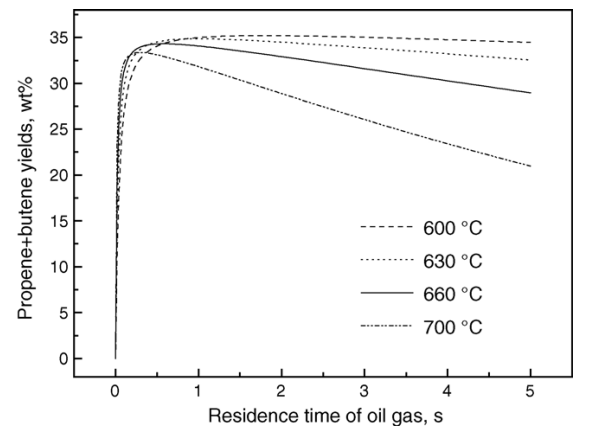


Fig. 9. Variation of predicted propene plus butene yields with the residence time of oil gas.

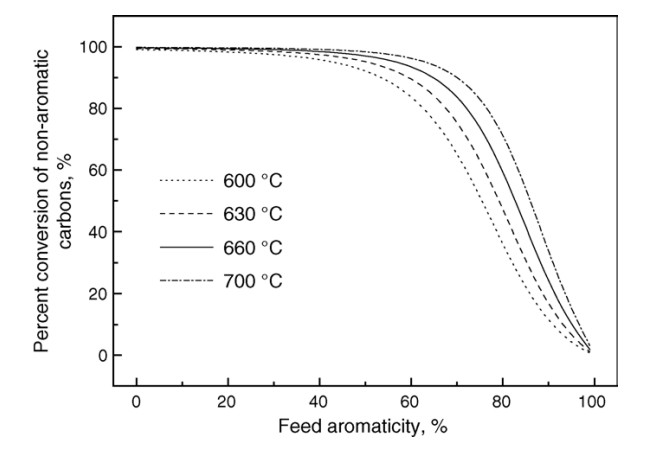


Fig. 11. Variation of the percent conversion of non-aromatic carbons with feed aromaticity.

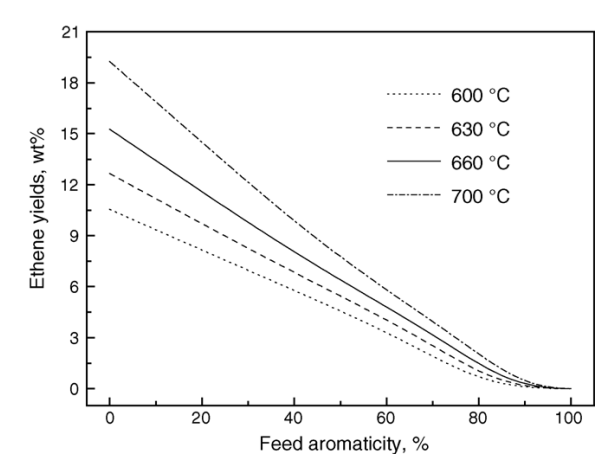


Fig. 12. Variation of predicted ethene yields with feed aromaticity.

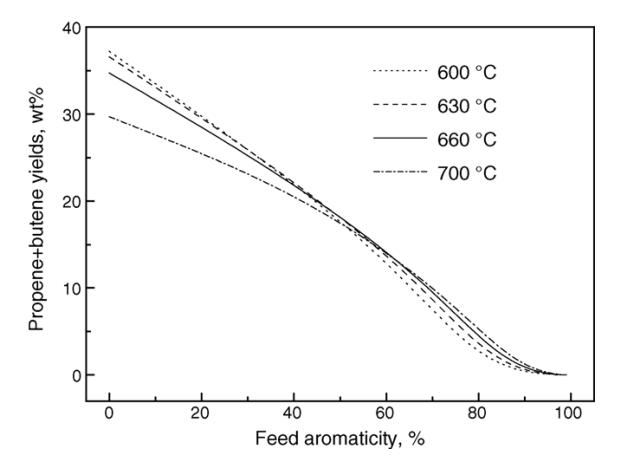


Fig. 13. Variation of predicted propene plus butene yields with feed aromaticity.

5. Conclusions

A new 8-lump kinetic model for heavy oil catalytic pyrolysis is proposed. The model includes non-aromatic carbons, aromatic carbons, gasoline plus diesel oil, propene plus butene, propane plus butane, ethene, light alkanes and coke as lumps, and has 17 kinetic constants and one for catalyst deactivation.

A new catalyst deactivation model is presented. The model is a function of feed properties and operating conditions. The

catalyst deactivation constant was determined by the least square regression analysis of experimental data. This deactivation constant doesn't vary with reaction temperature.

Experimental data obtained in a confined fluidized bed reactor at temperatures of 600, 630, 660 and 700 $^{\circ}$ C were used to estimate kinetic constants and apparent activation energies for each involved reaction. Most of the estimated apparent activation energies are higher than 100 kJ/mol, between the apparent activation energies for catalytic cracking and those for thermal cracking.

Product yields predicted by the 8-lump model show a good agreement with experimental data. The variation of product yields and product distribution with operating conditions and feed properties was predicted. For much production of light olefins, catalytic pyrolysis of heavy oils had better be conducted at high temperature and short residence time of oil gas, and heavy oils with the aromaticity higher than 30% had better not be considered as the feeds of catalytic pyrolysis.

References

- [1] X.M. Li, F.R. Song, Petrochem. Technol. 31 (7) (2002) 569-573.
- [2] X.H. Meng, J.S. Gao, L. Li, et al. Petrol. Sci. Technol. 22 (9/10) (2004) 1327–1341.
- [3] X.H. Meng, C.M. Xu, J.S. Gao, et al. Appl. Catal. A: Gen. 294 (2005) 168–176.
- [4] P. Hagelberg, I. Eilos, J. Hiltunen, et al. Appl. Catal. A: Gen. 223 (2002) 73–84.
- [5] J. Ancheyta-Juárez, F. López-Isunza, E. Aguilar-Rodríguez, Appl. Catal. A: Gen. 177 (1999) 227–235.
- [6] V.W.J. Weekman, Ind. Eng. Chem. Proc. Des. Dev. 7 (1) (1968) 90–95.
- [7] S.M. Jacob, B. Gross, S.E. Voltz, et al. AIChE J. 22 (4) (1976) 701-713.
- [8] X.L. Deng, Y.X. Sha, L.Y. Wang, et al. Petrol. Process. Petrochem. 26 (8) (1994) 35–39.
- [9] Y.H. Xu, Petrol. Process. Petrochem. 32 (11) (2001) 44-47.
- [10] X.H. Meng, C.M. Xu, L. Li, et al. Ind. Eng. Chem. Res. 42 (25) (2003) 6012–6019.
- [11] G.L. Wang, L.Y. Wang, Z.Q. Cui, et al. Petrochem. Technol. 32 (2) (2004)
- [12] X. Dupain, E.D. Gamas, R. Madon, et al. Fuel 82 (2003) 1559-1569.
- [13] V. Cakmma, R. Rausa, J. Anal. Appl. Pyrol. 40–41 (1995) 569–584.
- [14] F.V. Landeghem, D. Nevicato, I. Pitault, et al. Appl. Catal. A: Gen. 138 (1996) 381–405.
- [15] J.W. Chen, H.C. Cao, Catalytic Cracking Technology and Engineering, China Petrochemical Press, Beijing, 1995.
- [16] S.X. Lin, Petroleum Refining Processes, 3rd ed., China Petroleum Industry Press, Beijing, 2004.
- [17] M.A. Abul-Hamayel, Fuel 82 (2003) 1113–1118.
- [18] A. Corma, F.V. Melo, L. Sauvanaud, Appl. Catal. A: Gen. 287 (2005) 34–46

SECONDARY CRACKING OF C4 HYDROCARBONS FROM HEAVY OIL CATALYTIC PYROLYSIS

Xianghai Meng*, Chunming Xu and Jinsen Gao

State Key Laboratory of Heavy Oil Processing, China University of Petroleum, Changping, Beijing, 102249, China

For C4 hydrocarbons from heavy oil catalytic pyrolysis, the cracking behaviours on catalyst CEP-1 and quartz sand were investigated in a confined fluidized bed reactor. C4 hydrocarbons show a good cracking ability on CEP-1, and butene is easier to convert than butane. Only at high reaction temperatures can butane present a good cracking ability. On catalyst CEP-1, C4 hydrocarbons can undergo not only cracking reactions, but also such reactions as hydrogen transfer, polymerization and aromatization. The conversion of C4 hydrocarbons thermal pyrolysis is high, indicating that free radical reactions play an important part in the secondary cracking of C4 hydrocarbons. The product yields of C4 hydrocarbons pyrolysis on quartz sand are usually lower than those on catalyst CEP-1. For both catalytic pyrolysis and thermal pyrolysis of C4 hydrocarbons, the selectivity of propene is higher than that of ethene.

Pour des hydrocarbures en C4 venant de la pyrolyse catalytique d'huiles lourdes, on a étudié les comportements de craquage sur le catalyseur CEP-1 et le sable de quartz dans un réacteur à lit fluidisé confiné. Les hydrocarbures en C4 montrent une bonne capacité de craquage sur le CEP-1, et le butène est plus facile à convertir que le butane. C'est uniquement à des températures de réaction élevées que le butane peut présenter une bonne capacité de craquage. Sur le catalyseur CEP-1, les hydrocarbures en C4 peuvent supporter non seulement des réactions de craquage, mals également des réactions comme le transfert d'hydrogène, la polymérisation et l'aromatisation. La conversion de la pyrolyse thermique des hydrocarbures en C4 est élevée, ce qui indique que les réactions des radicaux libres jouent un rôle important dans le craquage secondaire des hydrocarbures en C4. Les rendements en produits de la pyrolyse des hydrocarbures en C4 sur le sable de quartz sont habituellement plus faibles que ceux sur le catalyseur CEP-1. Tant pour la pyrolyse catalytique que thermique des hydrocarbures en C4, la sélectivité du propène est plus grande que celle de l'éthène.

Keywords: C4 hydrocarbons, secondary cracking, catalytic pyrolysis, thermal pyrolysis, propene, ethene

INTRODUCTION

The studies on converting C4 hydrocarbons into ethene and propene have recently attracted great interest (Lemonidou and Stambouli, 1998; Ji et al., 2005; Jin et al., 2004; Wang et al., 2004; Wang et al., 2002). Butene is relatively easier to convert than butane, and therefore, researchers pay much attention to the cracking behaviours of butane on various catalysts (Lemonidou and Stambouli, 1998; Ji et al., 2005; Wang et al., 2004).

For catalytic pyrolysis of heavy oils, C4 hydrocarbons are significant intermediate products. The produced C4 hydrocarbons can further undergo secondary cracking reactions, yielding ethene, propene and other products. The reaction mechanism of heavy uil catalytic pyrolysis is not well understood and needs further study (Meng et al., 2004; 2005). To the study on C4 hydrocarbons secondary cracking is helpful to the good understanding of the reaction mechanisms of hydrocarbon catalytic pyrolysis.

This paper studies the secondary cracking performance of C4 hydrocarbons from heavy oil catalytic pyrolysis. The influence of

reaction temperature on feed conversion, product yields and liquid components were investigated. Contrast tests of catalytic pyrolysis and thermal pyrolysis of C4 hydrocarbons were conducted, together with the discussion of the experimental results.

EXPERIMENTAL

Feed and Catalyst

According to the distribution of C4 hydrocarbons obtained from catalytic pyrolysis of Chinese Daqling atmospheric residue, a mixture of C4 fractions from four refineries was prepared and used as feed. The components of the feed are given in Table 1. The content of total C4 hydrocarbons in the feed is 92.13 wt%, and that of total C4 alkenes is 65.90 wt%.

THE CANADIAN JOURNAL OF CHEMICAL ENGINEERING

VOLUME 84, JUNE 2006

^{*} Author to whom correspondence may be addressed. E-mail address: mengxh@cup.edu.cn

Component	Value	Component	Value	Component	Value
Methane	0.0225	n-Butane	7.8418	i-Pentane	3.9529
Ethane	0.0098	Propadiene	0.0095	n-Pentane	0.1025
Ethene	0.0431	Acetylene	0.0071	1,3-Butadiene	0.0860
Propane	0.0258	t-2-Butene	14.8256	Propyne	0.2952
Cyclopropane	0.0052	n- Butene-1	13.2622	C5 alkenes	3.0087
Propene	0.1836	i- Butene	27.5001	C6+	0.2046
i-Butane	18.3874	c-2- Butene	10.2263		

The catalyst utilized was CEP-1, and its primary properties are listed in Table 2. CEP-1 is a catalyst for Catalytic Pyrolysis Process (CPP) technology developed by the Research Institute of Petroleum Processing of China, and the U.S. patent (Shi et al., 2001) gives more information of the catalyst.

Item	Value	ftem	Value
Micro-activity Index	70	Particle size distribution, wt%	
Pore volume, cm ³ /g	0.19	0–20µm	1.2
Surface area, m ² /g	80	20 -40 µm	13.4
Packing density, g/cm³	0.97	40-80µm	55.9
Particle density, g/cm ³	1.5	>80µm	29.5

Apparatus

In experiments of catalytic pyrolysis and thermal pyrolysis of C4 hydrocarbons, a confined fluidized bed reactor was used, and the schematic diagram is shown in Figure 1. It is comprised of five sections: oil and steam input mechanisms, a reaction zone, temperature control system, and a product separation and collection system.

The experiments were carried out at various temperatures between 600 and 700°C, with residence times of oil gas, the weight ratios of catalyst-to-oil and steam-to-oil kept constant at 3.0 s, 16.5 and 0.52, respectively. For each experiment, 60 grams of catalyst (or quartz sand for thermal pyrolysis) were loaded into the reactor with an effective volume of about 580 ml. A variable amount of distilled water was pumped into a furnace to form steam, and then mixed with the feed pumped simultaneously by another pump. The mixture was heated to approximately 500°C in a pre-heater, and then entered into the reactor, where C4 feed contacted with fluidized catalysts and reactions took place. The oil gas after reaction was cooled and separated into the liquid product and the gas product, which were collected respectively. The coked catalyst after reaction was drawn out of the reactor by a vacuum pump.

Analytical Methods

Pyrolysis products include pyrolysis gas, pyrolysis liquid and coke. An Agilent 6890 gas chromatograph with Chem Station software was used to measure the volume percentage of the components in pyrolysis gas. The equation of state for ideal gases converts these data to mass percentage. The pyrolysis liquid was analyzed with an AC gasoline component analyzer to get the weight percentage of the components. Coke content on catalysts was measured with a coke analyzer.

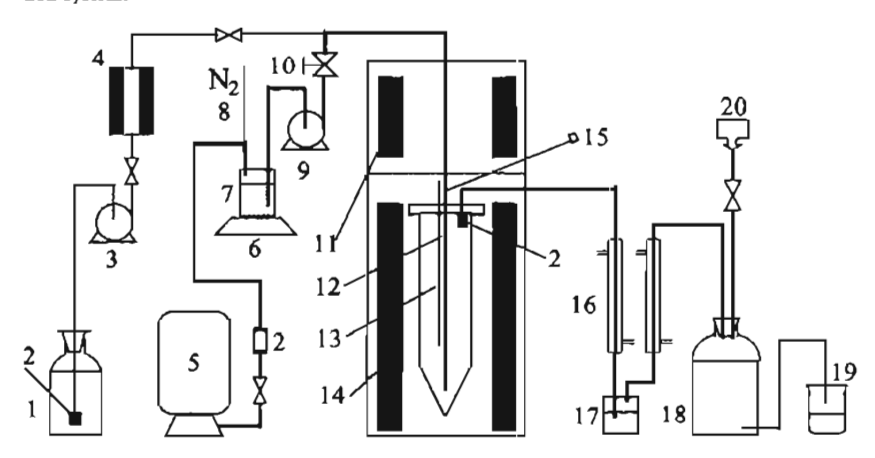


Figure 1. Schematic diagram of the experimental set-up (1 - water tank; 2 - filter; 3 - water pump; 4 - steam furnace; 5 - C4 feed tank; 6 - electronic balance; 7 - C4 buffer tank; 8 - constant-pressure nitrogen; 9 - C4 feed pump; 10 - counterbalance valve; 11 - preheater; 12 - thermocouple; 13 - reactor; 14 - heater; 15 - catalyst inlet and outlet; 16 - condenser; 17 - liquid product sampler; 18 - gas-collection vessel; 19 - beaker; 20 - gas sample bag)

SECONDARY CRACKING OF C4 HYDROCARBONS

Por secondary cracking of C4 hydrocarbons, the influence of reaction temperature on feed conversion, product yields and liquid components was investi-

Effect of Reaction Temperature on Feed Conversion

The variation of conversion with reaction temperature is shown in Figures 2 and 3. The conversion of C4 alkenes is above 80%, much higher than that of C4 alkanes. As reaction temperature goes up, both the conversion of C4 alkenes and that of C4 alkanes increase.

VOLUME 84, JUNE 2006

THE CANADIAN IOURNAL OF CHEMICAL ENGINEERING



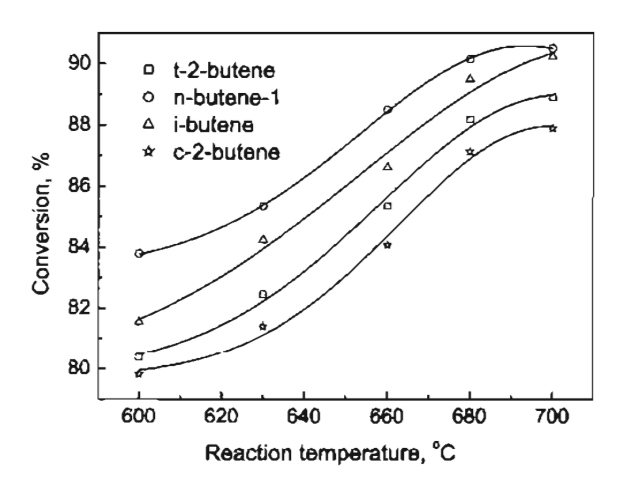


Figure 2. Conversion of C4 alkenes vs. reaction temperature

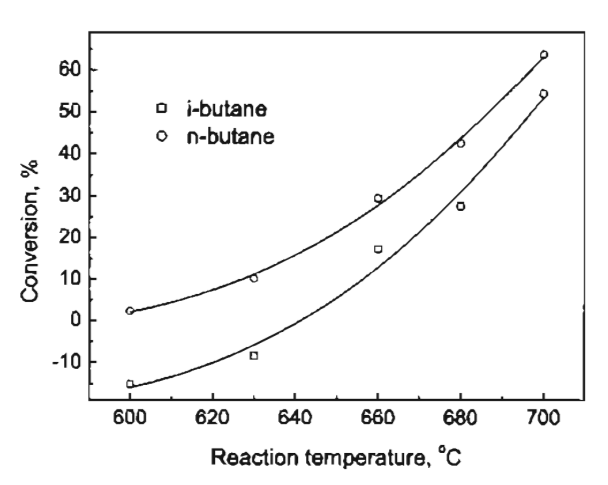


Figure 3. Conversion of C4 alkanes vs. reaction temperature

For C4 alkenes, the conversion of n-butene-1 is the highest, and that of c-2-butene is the lowest. The conversion of n-butane is higher than that of i-butane, and the gap decreases with the enhancement of reaction temperature. When reaction temperature is lower than 640°C, the conversion of i-butane is negative, indicating that I-butane is the product, but not the reactant, from the viewpoint of the whole reaction process.

At acidic centres on catalyst surface, C4 alkenes are easy to form carbonium ions, through which reactions can take place, and consequently, the conversion is high. But for C4 alkanes, the forming rate of carbonium ions is low; in addition, C4 alkenes can convert into C4 alkanes through hydrogen transfer reactions, so the conversion of C4 alkanes at low reaction temperature is low. However, C4 alkanes can undergo free radical reactions at high reaction temperature, so the conversion of C4 alkanes will increase as reaction temperature goes up.

Effect of Reaction Temperature on Product Yields

Figure 4 shows the variation of product yields with reaction temperature. As reaction temperature goes up, the yields of dry

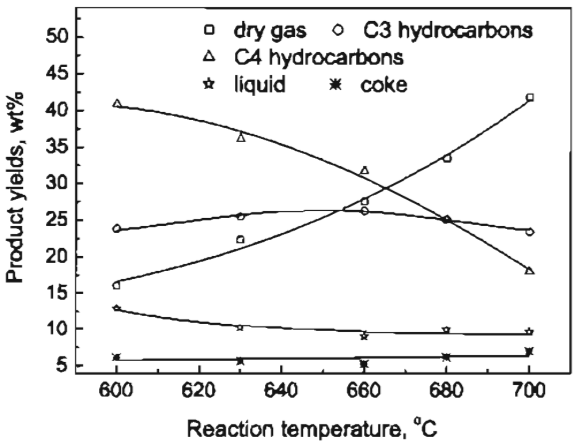


Figure 4. Product yields vs. reaction temperature

gas and coke increase to different extent, and that of C3 hydrocarbons shows a maximum at about 660°C. The yield of liquid products decreases firstly until a reaction temperature of 660°C is reached, and then it remains relatively constant.

In the reaction temperature range of 600 to 700°C, C4 hydrocarbons can not only crack into light hydrocarbons, but also form gasoline and diesel by polymerization, cyclization and aromatization. The formed gasoline and diesel are intermediate products, which can further crack into other products, so the yield of liquid products will decrease with increasing temperature. However, as reaction temperature further increases (over 660°C), the content of chain hydrocarbons (easy to crack) in gasoline and diesel becomes more and more lower, and therefore, the yield of liquid products varies slightly.

As reaction temperature goes up, the variation of light alkenes and light alkanes are shown in Figures 5 and 6, respectively. The yields of ethene and ethene plus propene increase gradually with increasing reaction temperature, while that of propene passes through a maximum at about 660°C. The yields of hydrogen, methane and ethane increase gradually as reaction temperature goes up, and that of propane decreases over 630°C, Indicating that propane further undergoes secondary reactions.

Effect of Reaction Temperature on Liquid Components

For secondary cracking of C4 hydrocarbons, a small quantity of liquid sample was collected, and then the components were measured with an AC gasoline component analyzer. According to the analysis data of the gas sample and the liquid sample, the components in pyrolysis liquid at two reaction temperatures were calculated, listed in Table 3.

The main components in pyrolysis liquid are pentene, pentane, hexene and such aromatics as benzene, toluene, C2 benzene, C3 benzene and heavy aromatics. This shows that such reactions as cracking, polymerization, cyclization and aromatization do take place in the process of C4 hydrocarbons secondary cracking. As reaction temperature goes up, the contents of alkanes, hexene and C3 benzene in pyrolysis liquid decrease, while those of pentene, benzene, toluene and heavy aromatics increase, indicating that the reaction extent becomes more thorough.

THE CANADIAN JOURNAL OF CHEMICAL ENGINEERING

VOLUME 84, JUNE 2006

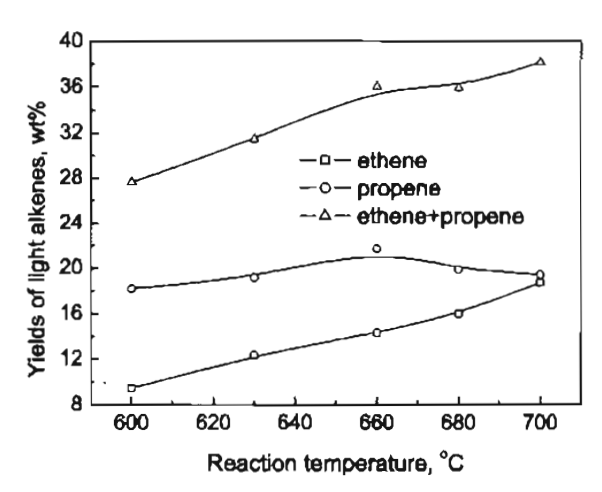


Figure 5. Yields of light alkenes vs. reaction temperature

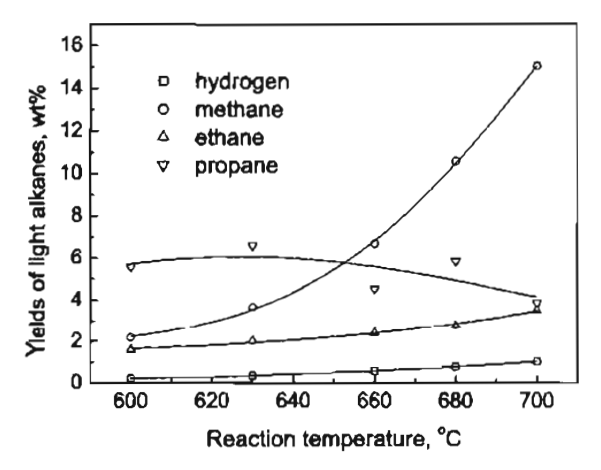


Figure 6. Yields of light alkanes vs. reaction temperature

COMPARISON OF THERMAL PYROLYSIS AND CATALYTIC PYROLYSIS

For the good understanding of the mechanisms of hydrocarbons catalytic pyrolysis, it is necessary to study the behaviours of thermal pyrolysis and compare them with those of catalytic pyrolysis. At high reaction temperature (>600°C), C4 hydrocarbons will certainly undergo free radical reactions, as well as carbonium ion reactions on the active centres of catalyst surface. In order to compare the thermal reactions with the catalytic reactions in the process of C4 hydrocarbons catalytic pyrolysis, we conducted experiments on quart sand and catalyst, respectively.

Comparison of Feed Conversion

The conversion for thermal pyrolysis and catalytic pyrolysis is listed in Table 4. As reaction temperature goes up, both the conversion on quartz sand and that on the catalyst increase, reaching 35.25% and 68.26% respectively at 660°C, and 61.79% and 81.95% respectively at 700°C. The gap of the conversion decreases with increasing reaction temperature, indicating that

Table 3. Co	omponent	contents in	pyrolysis liq	uid, wt%	-
Temp. ℃	Carbon number	Saturates	Olefins	Aromatics	Total
600	5	31.37	34.12	-	65.49
	6	0.36	5.20	0.75	6.31
	7	0.23	0.11	7.31	7.65
	8	0.05	0.02	31.08	11,15
	9	Ö	0	5.14	5.14
	10	0	0	1.06	1.06
	11	0	Ö	0	0
	12+	0	0	3.21	3.21
	Total	32.00	39.45	28.55	100
700	5	12.20	41.44	_	53.64
	6	0.12	3.74	4.37	8.24
	7	0.01	0.01	13.99	14.02
	8	0	0	11.53	11.53
	9	0	0	3.77	3.77
	10	0	0	0.59	0.59
	11	0	0	0	0
	12+	0	0	8.20	8.20
	Total	12.34	45.20	42.46	100

free radical reactions play a more and more important role in the process of C4 hydrocarbons catalytic pyrolysis.

In experimental runs, the conversion of butane on quartz sand is higher than that on the catalyst, but the conversion of butene on quartz sand is lower than that on the catalyst. This shows that the presence of catalyst CEP-1 can promote the conversion of butene. The conversion of butane on catalyst CEP-1 is low, and that of I-butane at reaction temperatures under 630°C is negative. explaining that hydrogen transfer reactions do take place. It is due to the hydrogen transfer reactions that the conversion of butane on the catalyst is lower than that on quartz sand.

For catalytic pyrolysis of C4 hydrocarbons on catalyst CEP-1, the conversion of butene is higher than that of butane, especially at low reaction temperature. This shows that the conversion rate of butene is higher than that of butane. The cracking rate of alkenes is much higher than that of alkanes following the carbonium ion mechanism, therefore, catalytic pyrolysis of C4 hydrocarbons at low temperature mainly follows the carbonium ion mechanism. However, at high reaction temperature (700°C), the conversion of butene is slightly higher than that of butane, showing that the conversion rate of butene is slightly higher than that of butane. The cracking rate of alkenes is similar to that of alkanes following the free radical mechanism, therefore, the free radical mechanism plays a significant role for catalytic pyrolysls of C4 hydrocarbons at high temperature.

Compare of Product Yields

For thermal pyrolysis and catalytic pyrolysis of C4 hydrocarbons, the product yields are listed in Table 5. For thermal pyrolysis of C4 hydrocarbons, the yields of hydrogen, methane, ethane, propane, ethene and propene increase with increasing reaction temperature, and that of liquid plus coke decreases. For catalytic pyrolysis of C4 hydrocarbons, the yields of hydrogen, methane, ethane and ethene increase as reaction temperature goes up, those of propane and propene pass through maxima, and that of liquid plus coke shows a minimum. The yields of ethane and

VOLUME 84, JUNE 2006

THE CANADIAN JOURNAL OF CHEMICAL ENGINEERING

	Thermal pyr	olysis		Catalytic p	yrolysi <u>s</u>			
Temp. °C	600	630	660	700	600	630	660	700
i-Butane	6.84	13.82	28.72	64.40	-15.16	-8 .39	17.31	54.43
n-Butane	6.18	12.59	29.75	66.64	2.32	10.29	29.55	63.65
t-2-Butene	8.73	20.73	49.05	82.39	80.39	85.35	82.46	88.91
1-Butene	31.53	36.05	56.49	84.92	85.79	88.51	85.35	90.52
i-Butene	13.61	12.15	16.12	36.04	81.56	86.62	84.25	90.24
c-2-Butene	11.96	21.92	49.05	82.23	79.82	84.07	81.41	87.90
C4 hydrocarbons	18.87	22.78	35.25	61.79	59.09	63.86	68.26	81.95

	Thermal py	rolysis			Catalytic pyrolysis				
Temp. °C	600	630	660	700	600	630	660	700	
Hydrogen	0.06	0.15	0.41	0.96	0.22	0.36	0.58	1.03	
Methane	0.62	1.96	5.82	16.69	2.20	3.67	6.70	15.06	
Ethane	0.08	0.19	0.48	1.22	1.59	2.03	2.41	3.53	
Propane	0.05	0.06	0.12	0.26	5.58	6.60	4.55	3.89	
Ethene	0.67	1.39	3.84	11.43	9.47	12.82	14.30	18.72	
Propene	3.45	6.13	12.31	19.53	18.18	18.86	21.70	19.44	
CO2+CO	0.44	0.53	0.79	0.97	2.60	3.50	3.55	3.49	
Liquid+coke	12.40	12.31	11.28	10.31	19.16	15.95	14.40	16.66	

	Thermal pyr	rolysis			Catalytic py	rolysis		
Temp. °C	600	630	660	700	600	630	660	700
Hydrogen	0.34	0.65	1.17	1.55	0.38	0.57	0.85	1.26
Methane	3.26	8.60	16.52	27.01	3.72	5.74	9.82	18.38
Ethane	0.43	0.82	1.35	1.97	2.69	3.17	3.54	4.30
Propane	0.29	0.26	0.34	0.42	9.45	10.34	6.66	4.74
Ethene	3.55	6.09	10.90	18.50	16.02	20.07	20.95	22.85
Propene	18.26	26.89	34.92	31.61	30.76	29.54	31.79	23,72
Liquid+coke	65.72	54.04	32.02	16.69	32.42	24.97	21.09	20.33

propane on catalyst are much higher than those on quartz sand, and this also shows that hydrogen transfer reactions play an important role for catalytic pyrolysis of C4 hydrocarbons on catalyst CEP-1.

No matter thermal pyrolysis or catalytic pyrolysis of C4 hydrocarbons, polymerization, cyclization, aromatization and condensation would take place to form liquid products and coke, besides cracking reactions to light products. The yield of liquid plus coke is above 10 wt%, showing that the extent of polymerization, cyclization, aromatization and condensation is not low. As reaction temperature goes up, the yield of liquid plus coke decreases, indicating that the secondary cracking reactions of liquid products take place.

On quartz sand or catalyst CEP-1, C4 hydrocarbons can undergo cracking reactions directly to form light products and aromatization reactions to yield liquid products; or they can polymerize to intermediate liquid products, and then the intermediate products undergo such reactions as cracking, isomerization, aromatization, cyclization and condensation. All of these reactions result in the variation of pyrolysis products.

Comparison of Product Selectivity

In this paper, product selectivity is defined as the product yield when a unit of feeds is converted, that is the ratio of the product yield to the conversion. For thermal pyrolysis and catalytic pyrolysis of C4 hydrocarbons, the product selectivity is given in Table 6.

The product yields of thermal pyrolysis are usually lower than those of catalytic pyrolysis, but the product selectivity of thermal pyrolysis is not always lower than that of catalytic pyrolysis due to the low conversion of thermal pyrolysis.

For the cracking of hydrocarbons, the selectivity of ethene and ethane following the carbonium ion mechanism is generally lower than that following the free radical mechanism. However,

THE CANADIAN JOURNAL OF CHEMICAL ENGINEERING

VOLUME 84, JUNE 2006

the selectivity of ethene and ethane for C4 hydrocarbons catalytic pyrolysis is higher than that for thermal pyrolysis. As for catalytic pyrolysis of C4 hydrocarbons, butene can form isobutyl and tert-butyl carbonium ions that are hard to crack because there are no β C-C bonds in the molecular structure, However, at high reaction temperature (600–700°C), these carbonium ions can absorb the energy about 10 to 25 kJ/mol (Jin. 1986), and change into n-butyl carbonium ions, which can crack at β C-C bonds to form ethene and ethane.

For C4 hydrocarbons thermal pyrolysis, the selectivity of propene is higher than that of ethene. The reactions of C4 hydrocarbons thermal pyrolysis follow the free radical mechanism. According to the mechanism, C4 hydrocarbons will form butyl free radicals, and the ratio of n-butyl primary free radicals to the total butyl free radicals is low. Only n-butyl primary free radicals can yield ethene, while other butyl free radicals tend to yield propene. In addition, since the carbon chain of butyl free radicals is short, butyl free radicals usually undergo primary cracking, and the formed methyl and ethyl free radicals are hard to crack any more. Consequently, the selectivity of ethene is low, while that of propene is high.

CONCLUSIONS

- C4 hydrocarbons have a good cracking ability on catalyst CEP-1, and butene is easier to convert than butane. Reaction temperature does not show a great effect on catalytic pyrolysis of butene, but has a significant influence on that of butane. Only at high reaction temperatures can butane present a good cracking ability.
- On catalyst CEP-1, C4 hydrocarbons can undergo not only cracking reactions, but also such reactions as hydrogen transfer, polymerization and aromatization. The polymerized intermediate products can further undergo cracking, isomerization, cyclization, aromatization and condensation reactions.
- 3. In experimental runs, the conversion of C4 hydrocarbons on quartz sand is high, explaining that free radical reactions play an important role for catalytic pyrolysis of C4 hydrocarbons. The catalyst is of great importance at low reaction temperature, but free radical reactions become more and more important with increasing reaction temperature.
- 4. The product yields on quartz sand are usually lower than those on catalyst CEP-1. The selectivity of ethene and ethane of catalytic pyrolysis is higher than that of thermal pyrolysis. For C4 hydrocarbons thermal pyrolysis, the selectivity of propene is higher than that of ethene.

REFERENCES

- Ji, D., B. Wang, G. Qian, Q. Gao, G. M. Lu, L. Yan and J. S. Suo, "A Highly Efficient Catalytic C4 Alkane Cracking over Zeolite ZSM-23," Catal. Commun. 6, 297-300 (2005).
- Jin, S. T., "Organic Catalysis," Shanghai Scientific and Technical Publisher, Shanghai (1986), 371.
- Jin, W. Q., J. W. Teng, G. L. Zhao, B. Li and Z. K. Xie, "Catalytic Cracking of Mixed C4 Olefins Over PZSM-S Zeolite," Ind. Catal. 12(10), 5-7 (2004).
- Lemonidou, A. A. and A. E. Stambouli, "Catalytic and Non-Catalytic Oxidative Dehydrogenation of n-Butane," Appl. Catal., A General 171, 325-332 (1998).
- Meng, X. H., J. S. Gao, L. Li and C. M. Xu, "Advances in Catalytic Pyrolysis of Hydrocarbons," Pet. Sci. Technol. 22 (9-10), 1327-1341 (2004).

- Meng, X. H., C. M. Xu, J. S. Gao and L. Li, "Studies on Catalytic Pyrolysis of Heavy Oils: Reaction Behaviors and Mechanistic Pathways," Appl. Catal., A General 294, 168-176 (2005).
- Shi, Z. C., F. M. Zhang and S. H. Liu, "Catalyst for Catalytic Pyrolysis Process for the Production of Light Olefins and the Preparation Thereof," US Patent, 6,211,104 (2001).
- Wang, B., Q. Gao, J. D. Gao, D. Ji, X. L. Wang and J. S. Suo, "Synthesis, Characterization and Catalytic C4 Alkene Cracking Properties of Zeolite ZSM-23," Appl. Catal., A General 274, 167-172 (2004).
- Wang, S. Y., X. G. Chen and C. M. Xu, "Study on Catalytic Pyrolysis of C4 Mixture," Pet. Proc. Petrochem. 33(12), 54-57 (2002).

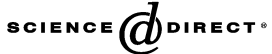
Manuscript received September 20, 2005; revised manuscript received November 11, 2005; accepted for publication January 4, 2006.

VOLUME 84, JUNE 2006

THE CANADIAN JOURNAL OF CHEMICAL ENGINEERING



Available online at www.sciencedirect.com





Catalysis Communications 7 (2006) 29-32

www.elsevier.com/locate/catcom

Effect of valence of copper in La_{2-x}Th_xCuO₄ on NO decomposition reaction

Junjiang Zhu *,a,b, Zhen Zhao c, Dehai Xiao a, Jing Li a, Xiangguang Yang a,*, Yue Wu a

Laboratory of Materials and Devices, Environmental Catalysis Group, Changchun Institute of Applied Chemistry, Chinese Academy of Sciences, 5625 Rennin Street, Changchun, Jilin 130022, PR China
 Graduate Schools of Chinese Academy of Sciences, Beijing 100039, PR China
 State Key Laboratory of Heavy Oil Processing, Beijing University of Petroleum, PR China

Received 1 February 2005; received in revised form 20 July 2005; accepted 12 August 2005 Available online 27 October 2005

Abstract

NO decomposition reaction was investigated over $La_{2-x}Th_xCuO_4$, in which the valence of copper was controlled by Th substitution and was characterized by XPS measurement. A close correlation between the valence of copper and the activity was observed. The activity increased with the decrease of the average oxidation number of copper, and increased with the increase of Cu^+ content, suggesting that the transition metal with low valence (Cu^+) is active for the reaction in the present cases.

Keywords: Perovskite-like oxides; La2-xThxCuO4; XPS; NO decomposition

1. Introduction

 A_2BO_4 , which has the K_2NiF_4 -type structure, consists of alternating layers of perovskite (ABO_3) and rock-salt (AO) and has a well-defined bulk structure so that the composition of cations at both A and B sites can be variously changed [1]. They thus provide an opportunity to control the oxidative state of transition metal(s) and the content of non-stoichiometric oxygen (λ) by partial substitution of the A- and/or B-site cations, without destroying the matrix structure. Therefore, they are suitable materials for the study of correlations between the solid-state chemistry and catalytic properties [2,3].

Catalytic decomposition of NO is the most desirable way of removing NO_x from exhaust gas streams since it does not involve the addition of a supplemental reductant and the products of the reaction (N_2 and O_2) are nontoxic [4,5], and Cu-containing compounds are active catalysts for this reaction [6–10]. Although many schemes have been

1566-7367/\$ - see front matter © 2005 Elsevier B.V. All rights reserved. doi:10.1016/j.catcom.2005.08.008

proposed for the NO decomposition reaction [7,10,11], the conclusion is various and little is known of the factors corresponding for the activity. We previously have reported the structure properties of La_{2-x}Th_xCuO₄ and its activity for NO removal [12,13]. Here, we were interested in investigating the correlation between the valence of copper and the activity of NO decomposition; the catalyst models were selected to be La_{2-x}Th_xCuO₄ (0.0 \leq x \leq 0.4), in which the valence of copper was well controlled by Th substitution.

2. Experimental

The samples, $\text{La}_{2-x}\text{Th}_x\text{CuO}_4$, $0 \le x \le 0.4$, were prepared by citrate method as described elsewhere [14]. Briefly, to an aqueous solution of La^{3+} , Th^{4+} and Cu^{2+} nitrates (Th⁴⁺ was obtained by dissolving ThO₂ in HNO₃ solution) with appropriate stoichiometry, a solution of citric acid 50% in excess of cations was added. The resulting solution was evaporated to dryness, and then the precursors were decomposed in air at 573 K, calcined at 873 K for 1 h and finally pelletized and calcined at 1223 K in air for

^{*} Corresponding author. Tel.: +86 431 5262228; fax: +86 431 5685653. E-mail address: xgyang@ciac.jl.cn (X. Yang).

12 h, the synthesized pellets were pulverized to ca. 40–80-mesh size to be used.

Powder X-ray diffraction (XRD) data were obtained from a X-ray diffractometer (type D/MAX B) over the ranger $20^{\circ} < 2\theta < 80^{\circ}$ at room temperature, operating at 40 KV and 10 mA, using Cu K α radiation combined with nickel filter.

The X-ray photoelectron spectra (XPS) were obtained with an ESCA MARK II instrument employing Mg K α radiation (1253.6 eV) under a high vacuum of 10^{-6} Pa. The binding energies were calibrated by using a C1s peak (284.6 eV) as a background. The surface composition of the catalyst was calculated according to the literature [15].

NO decomposition reaction was carried out in a flow reactor made of quartz with an internal diameter of 6 mm by feeding 1.0 vol.% NO/He at a flow rate of 22.5 ml min⁻¹ over 0.5 g catalyst. The NO decomposition activity was measured at 30 min after the reaction start. The gas composition was analyzed by gas chromatography with molecular sieve 5A (NO, N₂, O₂) and Porapak Q (N₂O) columns. The activity was evaluated in terms of NO conversion as described elsewhere [16].

3. Results and discussion

The crystal structure, surface area, nonstoichiometry, and the average oxidation numbers of copper in the catalysts are summarized in Table 1. The X-ray diffraction patterns showed that the samples were in K2NiF4-type structure although trace of impurities (ThO₂) were detected at x > 0. The structures of all the samples were orthorhombic. According to the tolerance factor t defined for A₂BO₄ oxides: $t = r_{(A-O)}/2^{1/2}r_{(B-O)}$ (where $r_{(A-O)}$ and $r_{(B-O)}$ are distances obtained from ionic radii [17]), the t value relates closely to the structure stability. It has been reported [17] that La₂CuO₄ is in orthorhombic structure because the t value (t = 0.85) is below the threshold of tetragonal structure (0.85 $\leq t \leq$ 1.02). This agrees with the present results. When Th⁴⁺ substituted for La³⁺ in La₂CuO₄, the samples $\text{La}_{2-x}\text{Th }_{x}\text{CuO}_{4} \ (0 \le x \le 0.4)$ maintained the orthorhombic structure, since the introduction of the smaller ionic radii Th^{4+} decreases the t value. Here, we represented the samples as La_{2-x}Th_xCuO₄, although the actual composition is $La_{2-x}Th_xCuO_{4+\lambda}$, or even is $La_{2-x}Th_yCuO_4$ (0 < y < x) due to the appearance of ThO₂.

The average oxidation number of copper in the as-prepared samples decreased obviously from 2.02 for La₂CuO₄ to 1.89 for $La_{1.6}Th_{0.4}CuO_4$, and the composition became more oxygen-rich with Th^{4+} substitution. For example, (based on the principle proposed in [15]), when 40% Th⁴⁺ substituted for La³⁺ in La₂CuO₄ will result in $La_{1.6}Th_{0.4}Cu_{0.88}^{2+}Cu_{0.12}^{+}O_{4.14}$ (see data in Table 1), while La_{1.6}Th_{0.4}Cu²⁺_{0.6}Cu⁺_{0.4}O₄ would represent the composition if the Th⁴⁺ substitution caused only partial reduction of copper $(Cu^{2+} \rightarrow Cu^{+})$. So, the 17.5% increase in positive charge of copper is compensated for the excess oxygen. The average oxidation number of copper was calculated by iodometric titration [18] without treating the as-prepared samples. The stoichiometry was calculated on the assumption that copper was present as either a mixture of Cu²⁺ and Cu³⁺ or a mixture of Cu⁺ and Cu²⁺, and other elements were present as La³⁺, Th⁴⁺, and O²⁻, respectively

In all, the above result showed that the valence of copper could be well controlled by the substitution of Th for La without changing the K₂NiF₄-type structure.

X-ray photoelectron spectra of the Cu2p region were shown in Fig. 1. All the catalysts have intense shake-up satellite peaks on the high binding energy sides of the Cu 2p_{1/} ₂ and Cu 2p_{3/2} peaks. The $I_{\text{sat}}/I_{\text{main}}$ ratio of Cu 2p_{3/2} satellites can be used as a measure of the valence of copper [15], and it is seen that this ratio decreased with the increase of x, indicating the increase of Cu^+ content. This is in agreement with that measured by the iodometric titration method. In addition, by referring the $I_{\text{sat}}/I_{\text{main}}$ ratio of CuO ($I_{\text{sat}}/I_{\text{main}} = 0.53$ [19]), we also assumed that the $I_{\text{sat}}/I_{\text{main}} = 0.53$ I_{main} ratio is 0.53 for Cu²⁺ and the intensity ratio is proportional to the fraction of Cu²⁺ [15]. Then, from the observed ratio listed in Fig. 1, we can obtain the oxidation state of copper to be 1.98, 1.91, 1.89, 1.85 and 1.79 for x = 0-0.4, respectively. These values were in generally agreement with those listed in Table 1.

The surface and the bulk composition of the metallic elements are summarized in Table 2, they were calculated from the XPS peaks and the quantities of the starting materials, respectively. The Cu content on the surface decreased with the increase of x and was always lower than that in the

Table 1 Physical properties and catalytic activity of $La_{2-x}Th_xCuO_4$ (0.0 $\le x \le 0.4$)

Catalysts	Structure	Surface area (m ² /g)	Ox. no. of Cu ^a	Content of Cu ⁺ (%)	$\lambda^{\mathbf{b}}$
La ₂ CuO ₄	K ₂ NiF ₄ (O ^c)	2.5	2.02	0	+0.01
La _{1.9} Th _{0.1} CuO ₄	$K_2NiF_4(O) + ThO_2 (tr.^d)$	2.8	1.98	2	+0.05
La _{1.8} Th _{0.2} CuO ₄	$K_2NiF_4(O) + ThO_2$	2.7	1.95	5	+0.07
La _{1.7} Th _{0.3} CuO ₄	$K_2NiF_4(O) + ThO_2$	2.4	1.91	9	+0.11
La _{1.6} Th _{0.4} CuO ₄	$K_2NiF_4(O) + ThO_2$	2.2	1.89	11	+0.14

^a Average oxidation number of copper.

 $^{^{}b}\ \lambda\ in\ La_{2-x}Th_{x}CuO_{4+\lambda}.$

^c O, orthorhombic.

d tr., trace.

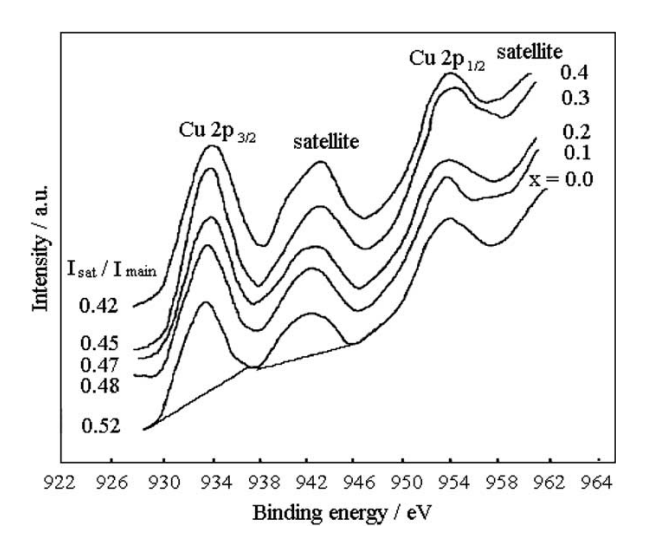


Fig. 1. XPS spectra of $Cu 2p_{3/2}$ in $La_{2-x}Th_xCuO_4$ (0.0 $\leq x \leq$ 0.4).

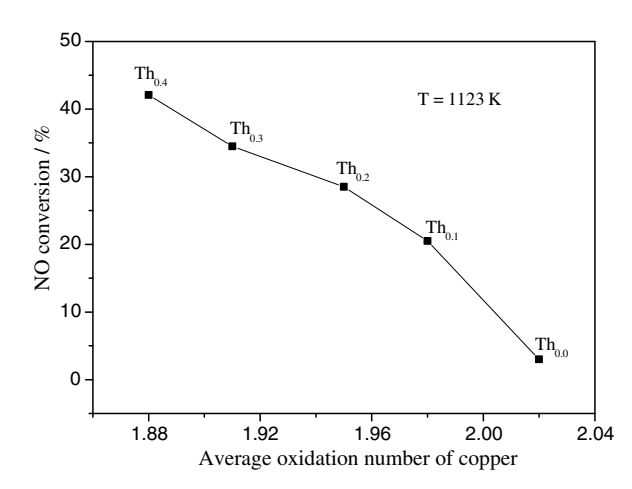


Fig. 2. Correlation between NO conversion and average oxidation number of copper without pretreatment of the catalyst. $Th_{0.4}$, $Th_{0.3}$, $Th_{0.2}$, $Th_{0.1}$ and $Th_{0.0}$ represent the NO conversion of $La_{1.6}Th_{0.4}CuO_4$, $La_{1.7}Th_{0.3}CuO_4$, $La_{1.8}Th_{0.2}CuO_4$, $La_{1.9}Th_{0.1}CuO_4$ and La_2CuO_4 , respectively.

Table 2 Surface and bulk composition of $La_{2-x}Th_xCuO_4$ (0.0 $\leqslant x \leqslant$ 0.4)

Catalysts	Surface comp	Surface composition (%)			Bulk composition (%) ^a			
	La	Th	Cu	La	Th	Cu		
La ₂ CuO ₄	84.89	0.00	15.11	66.67	0.00	33.33		
La _{1.9} Th _{0.1} CuO ₄	66.21	18.33	15.46	63.33	3.33	33.33		
La _{1.8} Th _{0.2} CuO ₄	56.14	29.51	14.35	60.00	6.67	33.33		
La _{1.7} Th _{0.3} CuO ₄	49.34	38.13	12.53	56.67	10.00	33.33		
La _{1.6} Th _{0.4} CuO ₄	45.32	42.24	12.44	53.33	13.33	33.33		

^a These values were calculated from the quantity of the starting material.

bulk, due to the enrichment of La and/or Th on the surface. With the Th substitution, the surface Th content increased significantly and was far higher than that in the bulk, suggesting that the enrichment of Th on the surface is strong. This might be one of the reasons that ThO_2 was formed in the system.

The activity of NO decomposition at 1123 K over the catalysts was shown in Fig. 2 (Note: ThO₂ showed no activity for NO decomposition in the experiment, and hence its influence was neglected). By correlating the average oxidation number of copper with the activity, it is obvious that the activity decreased with the increase of the average oxidation number of copper, indicating that the low valence copper (Cu⁺ ions, as shown in Table 1) accounts for the reaction, or is the active site of NO decomposition (Cu⁺ \rightarrow Cu²⁺).

The reason why the activity decreases with the increase of average oxidation number of copper is not obvious at present although many works in this field have done [20]. It could possibly be due to the easier oxidation of Cu^+ in the redox cycle of $Cu^+ \leftrightarrow Cu^{2+}$, resulting in the active adsorption of NO, i.e., $Cu^+ + V_o + NO \rightarrow [Cu^{2+} - V_o - NO^-] \rightarrow Cu^{2+} + 1/2N_2 + O^-$ (V_o : oxygen vacancy),

since the adsorption of NO on the active site is difficult at high temperatures (T = 1123 K) [16]. The presence of Cu^+ is possible because of the introduction of the high valence ions Th^{4+} .

4. Conclusion

We investigated the NO decomposition reaction over well-characterized $La_{2-x}Th_xCuO_4$ catalyst, in which the valence of copper was controlled by Th substitution. The valence of copper decreased with the increase of Th content. A close correlation between the activity of NO decomposition and the valence of copper was observed. The low valence Cu^+ is active for the reaction due to the easier oxidation of Cu^+ in the redox cycle of $Cu^+ \leftrightarrow Cu^{2+}$, resulting in the active adsorption of NO.

Acknowledgments

Financial support from the Ministry of Science and Technology of China (2004CB 719500) and the Natural Science Foundation of China (20177022) is gratefully acknowledged.

References

- R.J.H. Voorhoeve, Advanced Materials in Catalysis, Academic Press, New York, 1977.
- [2] T. Nitadori, S. Kurihara, M. Misono, J. Catal. 98 (1986) 221.
- [3] T. Nitadori, M. Misono, J. Catal. 93 (1985) 459.
- [4] O. Kubaschewski, C.B. Alckock, P.J. Spencer, Materials Thermochemistry, sixth ed., Pergamon Press, Oxford, 1993.
- [5] Y. Teraoka, H. Fukada, S. Kagawa, Chem. Lett. (1990) 1.
- [6] M. Iwamoto, H. Hamada, Catal. Today 10 (1991) 57.
- [7] H. Yasuda, M. Misono, et al., J. Chem. Soc., Chem. Commun. (1990) 1094.
- [8] Z. Zhao, X.G. Yang, Y. Wu, Environ. Chem. 14 (1995) 402 (Chinese).
- [9] C. Tofan, D. Klvana, J. Kirchnerova, Appl. Catal. A Gen 223 (2002) 275.

- [10] B. Moden, P.D. Costa, B. Fonfe, D.K. Lee, E. Iglesia, J. Catal. 209 (2002) 75.
- [11] J.W. London, A.T. Bell, J. Catal. 31 (1973) 96.
- [12] Z. Zhao, X.G. Yang, Y. Wu, J. Rare Earth. 14 (1996) 241.
- [13] Y. Wu, Z. Zhao, Y. Liu, X.G. Yang, J. Mol. Catal. A 155 (2000)
- [14] Z.L. Yu, L.Z. Gao, S.Y. Yuan, Y. Wu, J. Chem. Soc. Faraday Trans. 88 (1992) 3245.
- [15] N. Mizuno, M. Yamato, M. Tanaka, M. Misono, Chem. Mater. 1 (1989) 232.
- [16] Z. Zhao, X. Yang, Y. Wu, Appl. Catal. B: Environ. 8 (1996) 281.
- [17] P. Ganguly, C.N.R. Rao, J. Solid State Chem. 53 (1984) 193.
- [18] D.C. Harris, T.A. Hewton, J. Solid State Chem. 69 (1989) 182.
- [19] D.C. Frost, A. Ishitani, C.A. Mcdowell, Mol. Phys. 24 (1972) 861.
- [20] H. Shimada, S. Miyama, H. Kuroda, Chem. Lett. (1988) 1797.

CrHZSM-5 zeolites – Highly efficient catalysts for catalytic cracking of isobutane to produce light olefins

Jiangyin Lu, Zhen Zhao,* Chunming Xu, Aijun Duan, and Pu Zhang

Faculty of Chemical Science and Engineering, State Key Laboratory of Heavy Oil Processing, China University of Petroleum, 18#, Fuxue Road, Chang Ping District, Beijing 102249, China

Received 26 January 2006; accepted 2 February 2006

The CrHZSM-5 catalysts with trace amount of Cr were firstly used for catalytic cracking of isobutane, and the effect of Cr-loading on the catalytic performances of CrHZSM-5 catalysts for the cracking of isobutane was also studied. The results suggested that when the loading of Cr in the CrHZSM-5 catalysts was less than 0.038 mmol/g Cr, especially at Cr loading of 0.004 mmol/g, both the reactivity of isobutane cracking and the selectivity to light olefins of CrHZSM-5 samples were greatly enhanced compared with the unpromoted HZSM-5, and very high yields of olefins($C_2 + C_3$) and ethylene were obtained. For instance, the yield of olefins($C_2 + C_3$) and ethylene reached 56.1% and 30.8%, respectively, at 625 °C when 0.004 mmol/g Cr was loaded on HZSM-5 sample.

KEY WORDS: CrHZSM-5 zeolite; catalytic cracking; isobutane; light olefins.

1. Introduction

At present, ethylene is primarily produced by steam cracking, and propylene is the main byproduct in this process, accounting for over 90% of total propylene output. The method of steam cracking for producing ethylene and propylene cannot satisfy a fast growing demand for them today. The new methods to produce propylene including the catalytic cracking of C4 olefins [1–2] or C4 alkanes feedstocks [3–6], Oxidative dehydrogenation of propane, and catalytic cracking of heavy oil are indispensable and significant to be studied and developed.

Nowadays, the turnout of C_4 fraction is about 150–200 million tons every year in the world. It is predicted that the C_4 fraction will be another valuable petrochemical material that could be well utilized after ethylene and propylene. C_4 fraction is mainly produced from catalytic cracking and steam pyrolysis. The utilization of C4 in chemical industry was mainly olefins, and C4 alkanes were primarily used as fuel. Isobutane was one of the main components of C4 alkanes which is often used for alkylation reaction to produce high octane number gasoline[7,8], and dehydrogenation to produce isobutene [9–11].

ZSM-5 zeolite has been extensively studied as the active catalyst for a variety of reactions owing to its reactivity and special pore structure [12–14]. Alfons *et al.* [3,4] reported the kinetic and product distribution pattern of isobutane pyrolysis. Ararwal *et al.* [15]

*To whom correspondence should be addressed. E-mail: zhenzhao@cup.edu.cn investigated the catalytic cracking of isobutane and methylcyclohextane over USY zeolite, and discriminated reaction steps with kinetic significance, introduced model parameter, and undertook interrelated kinetic calculation. Sun *et al.* [16] reported the isobutane catalytic cracking over HZSM-5 under low pressure and dehydrogenation kinetics.

In this paper, isobutane was used as feedstock to investigate its catalytic cracking property over CrHZSM-5 to produce light olefins. Very high reactivity and selectivity for catalytic cracking of isobutane was obtained over CrHZSM-5 catalysts with trace amount of Cr. For example, the yields of olefins($C_2 + C_3$) and ethylene reached 56.1% and 30.8%, respectively, at 625 °C.

2. Experimental

The HZSM-5 zeolite was manufactured by Qi Lu Petrochemical Corporation Catalysts factory (Si:Al mole rate = 32). The zeolite was impregnated by certain concentration $Cr(NO_3)_3$ · $9H_2O$ solution with an incipient-wetness impregnation method. The loading amounts of Cr were 0.00, 0.004, 0.010, 0.019, 0.038, 0.077, 0.154 and 0.231 mmol/g, respectively. The impregnation period lasted for half an hour at the temperature range of 30–40°C and then dried at 120 °C and finally calcined at 700 °C in air atmosphere for 4 h. After finishing the preparation of this series of catalysts, they were marked as 0#, 1#, 2#, 3#, 4#, 5#, 6# and 7# according to the different concentrations of Cr correspondingly.

1011-372X/06/0600-0065/0 © 2006 Springer Science+Business Media, Inc.

In a fixed-bed flow reactor the catalytic reaction was carried out by passing a gaseous isobutane (2 mL min $^{-1}$, 99.9%) in a N₂ flow at a total flow rate 40 mL min $^{-1}$ over 200 mg catalyst (total pressure: 1 atm). The products were analyzed on-line using a gas chromatograph (SP3420) equipped with a 50 m PONA capillary column and FID detector [5].

Acidic amounts of the zeolite were measured by NH₃-TPD (Temperature-programmed desorption of ammonia) method. 0.2 g samples with the sizes of 40-80 mesh were pretreated at 500 °C for 2 h, cooled to 120 °C and adsorbed NH₃ for 30 min, then temperature-programmed desorption started at a rate of 15 °C/ min from 120 to 800 °C. The signal was monitored with a TCD detector. In order to obtain the total acid amount, the desorbed ammonia was absorbed by HCl solution (0.01 mol/L) and then titrated by NaOH solution (0.01 mol/L), finally the acidic amount and density of the zeolite were calculated. According to the temperature of the desorption peak and the relative intensity of acid sites of the samples was analyzed, and the acid amount of the acid sites with different intensities by peak areas were calculated.

UV-Vis absorption spectra of the samples were measured with a spectrophotometer (Hitachi U-4100) equipped with the integration sphere diffuse reflectance attachment.

3. Results and discussion

The effect of loading amount of Cr(III) on the reactivity and selectivity of CrHZSM-5 catalysts for the cracking of isobutane are shown in table 1.

The results in table 1 indicate that the reactivity of the catalysts for catalytic cracking changed obviously with the loading amount of Cr(III). For the CrHZSM-5 samples with the loading amount of Cr (III) below 0.038 mmol/g Cr, the reactivities of CrHZSM-5 samples were higher than that of 0#, HZSM-5 sample. The highest catalytic cracking reactivity was obtained over 1# sample, and the reactivity of catalytic cracking slowly decreased with the further increasing of Cr-loading amount. In the same temperature range, the loading amount of Cr had also large effect on the selectivity of the product. The selectivity to aromatic hydrocarbon and butene smoothly increased with rising the loading amount of Cr(III), while the selectivity to methane, ethylene, propane and olefins $(C_2 + C_3)$ slowly decreased with the increasing loading amount of Cr(III).

The product yields of ethylene, proylene and olefins($C_2 + C_3$) in the catalytic cracking isobutane over CrHZSM-5 catalysts are shown in figure 1.

It can be seen from figure 1 that the yields of ethylene and olefins ($C_2 + C_3$) over $1\# \sim 4\# CrHZSM-5$ samples were apparently higher than those of 0#, the unmodified HZSM-5 sample, which were all more than 24.9% and 51.8% at 625 °C, respectively. Especially at 625 °C, over 1# CrHZSM-5 samples, the yields of olefins ($C_2 + C_3$) and ethylene could reach 56.1%, 30.8%, respectively, which were much higher than those of 0#, HZSM-5 sample.

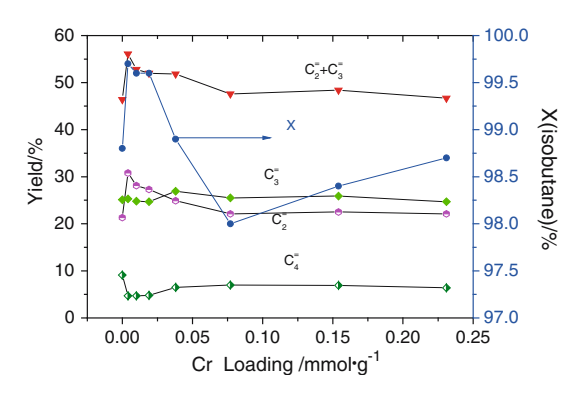
Compared with unmodified HZSM-5 zeolite, the olefins of propylene and ethylene of $1\#\sim4\#$ could keep high yields at the temperatures of 600 and 625 °C, and the yield of butene obviously decreased. These results demonstrate that a small amount of Cr played an important role of modification, not only did it enhance

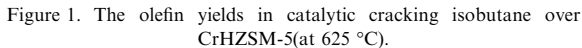
Table 1

The reactivity and the selectivity (%) of CrHZSM-5 for the cracking of isobutane to produce light olefins

Catalysts	Temperature	Conversion				Selec	ctivity (%)			
	(°C)	(%)	Methane	Ethane	Propane	Ethylene	Propylene	Butene	Arene	Olefins $(C_2 + C_3)$
0#	600	93.4	13.4	0.4	2.7	19.5	30.6	12.7	10.1	50.1
White	625	98.8	12.8	0.4	2.2	21.6	25.4	9.2	14.7	47.0
1#	600	97.0	15.0	0.8	3.5	27.1	29.3	7.6	14.3	56.4
White	625	99.7	15.4	1.0	2.9	30.9	25.4	4.7	19.2	56.3
2#	600	96.5	14.5	0.9	3.3	25.0	28.5	7.7	14.0	53.5
White	625	99.6	15.2	1.1	2.5	28.2	24.9	4.7	20.0	53.1
3#	600	96.5	14.0	1.0	3.2	24.3	28.6	8.1	16.8	52.9
Lightyellow	625	99.6	14.7	1.3	2.4	27.4	24.8	4.8	21.6	52.2
4#	600	94.0	13.4	1.1	2.8	22.1	30.3	9.7	15.1	52.4
Light green	625	98.9	14.1	1.4	2.3	25.2	27.2	6.6	20.3	52.4
5#	600	92.4	13.7	1.4	2.5	20.4	29.3	10.4	18.4	49.7
Light green	625	98.0	14.2	1.7	2.2	22.6	26.0	7.1	23.4	48.6
6#	600	93.3	14.0	1.3	2.3	20.3	29.1	10.2	18.1	49.4
Green	625	98.4	14.7	1.5	1.8	22.9	26.3	7.0	23.1	49.2
7#	600	94.3	13.1	1.1	2.3	19.7	27.6	9.6	17.3	47.3
Green	625	98.7	13.6	1.3	1.8	22.4	25.0	6.5	24.5	47.4

Note: The butene was mainly i-butene, 2-butene (including *trans*-butene and *sis*-butene), the arene included benzene and toluene, the selectivity of olefins included ethylene and propylene without butene and dibutene.





the reactivity for the catalytic cracking of isobutane, but also increased the selectivity of olefins, especially the selectivities to ethylene.

In order to study the nature of catalytic cracking of isobutane over CrHZSM-5 zeolite samples and exclude the effect of pyrolysis of isobutane, a comparative study of isobutane pyrolysis was also made. The product yield of isobutane pyrolysis as a function of reaction temperature is showed in figure 2.

It can be seen from figure 2 that isobutane did not undertake pyrolysis below 575 °C. When the temperature was at 625 °C, the conversion of isobutane was about 2%. It demonstrates that although obvious pyrolysis could occur at 625 °C, the catalytic cracking is still major reaction. Besides ethylene, propylene, butene, dibutene and a small amount of ethane, methane are the main products of the pyrolysis reaction. At 850 °C (conversion nearly 100%), the yield of methane could reach 30.2%.

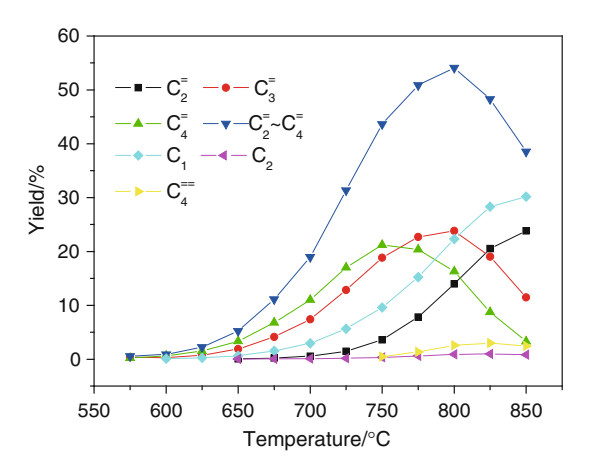


Figure 2. Product yield of isobutane pyrolysis as a function of reaction temperature.

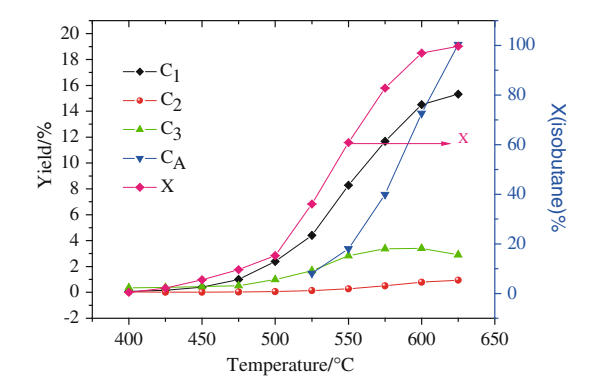


Figure 3. The yields of alkanes and aromatic hydrocarbon over 1#CrHZSM-5 catalyst as a function of reaction temperature.

In addition, a small amount of alkyne, complex olefin, coke and carbon deposition could be formed, these products were all the results of dehydrogenation and cracking of isobutene at high temperatures.

As 1#CrHZSM-5 sample gave good reactivity and high light olefins yields, it was chosen to investigate the effect of reaction temperature on the catalytic performance for catalytic cracking of isobutane.

The reaction started from 400 °C and followed temperature-programmed heating at a rate of 3 °C/min to study the isobutane catalytic cracking reaction over CrHZSM-5 molecular sieve. The effects of reaction temperature on the yields of alkanes including aromatic hydrocarbon and olefins are shown in figures 3 and 4.

From figure 3 the yields of methane and aromatic hydrocarbon dramatically increased when temperature rose from 500 to 550 °C, while the yield of propane increased slowly and that of ethane remained very low. At 625 °C, the yield of aromatic hydrocarbon was 19.2%, methane was 15.3%, propane and ethane were 2.9% and 1.0%, respectively.

It can be seen from figure 4 that the yields of olefins($C_2 + C_3$), and propylene rapidly increased with the increasing of reaction temperature. They reached the maximum value of 56.1% at 625 °C and 28.4% at 600 °C, respectively. The yield of ethylene was 30.8% at 625 °C and the maximum value of the yield of butene was 8.8% at 575 °C.

The isobutane mainly undertook catalytic cracking rather than pyrolysis (see figure 2) when the reaction temperatures were lower than 575 °C. Therefore, the cracking of isobutane over 1# CrHZSM-5 catalyst at the temperature below 575 °C could be classified into catalytic cracking reaction. When the reaction temperatures were higher than 575 °C, the catalytic cracking and pyrolysis reactions coexist, and the higher the temperature is, the higher extent of pyrolysis is. It can also be observed that the yields of methane, ethylene and aromatic hydrocarbon increased with the rising of reaction temperature, while the yields of propane, propylene and

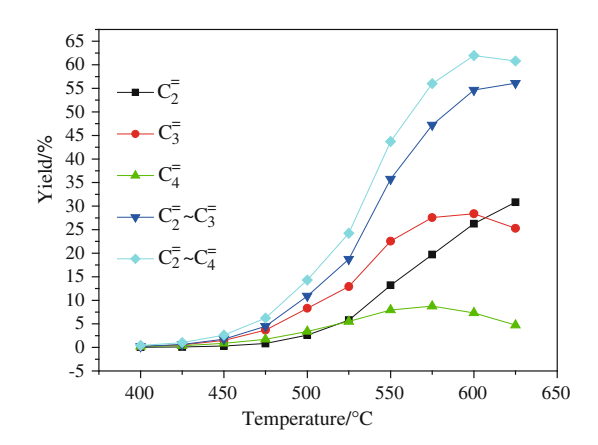


Figure 4. The yields of olefins over 1#CrHZSM-5 catalyst as a function of reaction temperature.

butene increased at first and then decreased, and they reached the maximum value at about 600 °C.

It is well known that the acidity of the catalysts plays an important role in the catalytic cracking of hydrocarbon. The effect of Cr addition on the acidity of HZSM-5 catalysts was evaluated by means of NH₃–TPD (Table 2). The results, as shown in figure 5, indicate that the acidic amount of the catalysts firstly increased quickly and then slowly increased with increasing of loading amount of Cr(III). In the meantime, the strength of strong acid of $1\#\sim 4\#$ CrHZSM-5 samples obviously reduced. The weak acidic amount of $1\#\sim 4\#$ CrHZSM-5 samples are evidently increased compared with that of 0#, which maybe related to its high reactivity and high selectivity. It is obvious that suitable acidic amount and density are favorable high reactivity and high yield of CrHZSM-5 samples.

Figure 6. show UV–Vis spectra of calcined CrHZSM-5 catalysts. It was found previously [17–19] that there may be three species inside calcined CrHZSM-5 catalysts: framework Cr(III), extraframework Cr(III), and extraframework Cr(VI).

The spectra of calcined CrHZSM-5 catalysts are dominated by two intense bands around 259 and 350 nm. These bands are usually assigned as $O^{2-} \rightarrow Cr(VI)$ charge transfers of a monochromate species [18–20]. This kind of loaded Cr(VI) dispersed on the HZSM-5 zeolite surface. The molecular structure of the anchored Cr(VI) from monochromate to dichromate or to polychromate have been proposed. Chromium(VI) oxide compounds prefer tetrahedral coordination both in aqueous solution and in a crystalline lattice [21]. A band around 450 nm which is the characteristic of Cr(VI) polychromate is not obvserved [20] for the samples with Cr loading of 0.004 mmol/g. These results indicate that Cr(VI) monochromate(CrO₄²⁻) predominates on the HZSM-5 samples with trace amount of Cr.

With the increasing of Cr loading on the HZSM-5 zeolites, besides the two absorption bands at 259 and 350 nm, a shoulder absorption band at around 460 nm appeared [22], and its intensity increased with the further increasing in Cr loading and a complete absorption band at 460 nm was observed when Cr-loading is equal to or greater that 0.154 mmol/g. There results indicate that polymeric chromate formed in the samples with high-loading of Cr. At same time, a very weak absorption band centered at around 600 nm, which has been assigned to d-d transitions of Cr(III) [20] was observed when Cr-loading is equal to 0.019 mmol/g, and its intensity increased with the further rising of Cr-loading. These results suggest that some amounts of Cr(III) existed on the samples in which the Cr-loading amount is equal to or greater than 0.019 mmol/g. Moreover, with the increasing of Cr-loading amount, absorption edge from 450 to 550 nm and 600 to 800 nm shifted to longer wavelength demonstrating that the domain size of CrHZSM-5 catalysts become longer with the increasing of Cr-loadings.

We conclude that Cr(VI) always predominates in calcined CrHZSM-5 catalysts. Comparing with high Cr(III) concentration loaded, low concentration of Cr(III) is almost oxidized to Cr(VI) after calcinations, which is impossible to obtain Cr(VI) by calcinations of common

Table 2 NH₃-TPD results of CrHZSM-5 catalysts with different Cr(III) loadings

Catalyst	BET	Peak1		Pea	k 2	Acid	Acid	
	(m^2/g)	Temperature (°C)	Weak acid amount	Temperature (°C)	Strong acid amount	amount (mmol/g)	density $(\mu \text{ mol/m}^2)$	
0#	318.0	277.8	0.113	519.7	0.362	0.475	1.494	
1#	331.1	276.8	0.163	517.6	0.382	0.545	1.646	
2#	327.6	282.6	0.172	506.1	0.419	0.591	1.804	
3#	306.4	283.1	0.169	509.3	0.428	0.597	1.948	
4#	291.0	284.8	0.196	512.0	0.443	0.639	2.196	
5#	316.8	278.6	0.225	516.1	0.462	0.687	2.169	
6#	297.4	302.4	0.216	531.8	0.429	0.645	2.169	
7#	295.2	296.6	0.201	509.6	0.414	0.615	2.083	

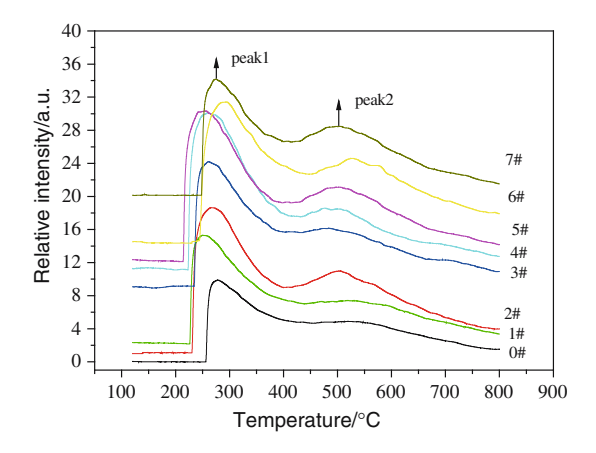


Figure 5. NH₃-TPD profile of CrHZSM-5 catalysts.

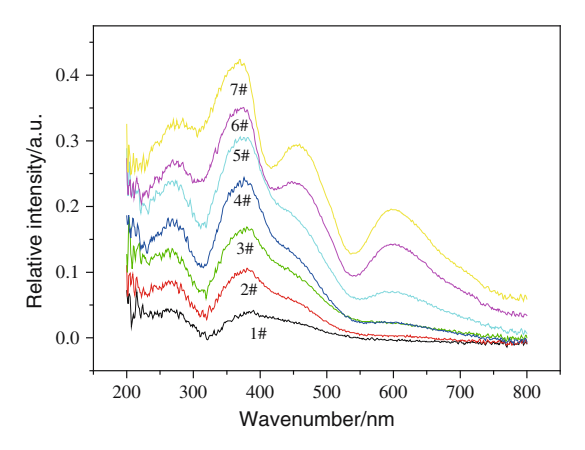


Figure 6. UV-Vis spectra of CrHZSM-5 catalysts.

chromium(III) salts [23]. It is postulated that Cr is uniform, isolated and well dispersed in calcined CrHZSM-5 catalysts. In $1\#\sim 4\#$ and, especially, $1\#\sim 2\#$ samples, the majority species of Cr in catalysts were uniform, isolated and well dispersed, and almost oxidized to Cr(VI) after calcinations.

One conceivable function of a trace amount of Cr is the changing of the acidity of the HZSM-5 catalysts because the suitable strength and amounts of acidity of the catalysts are favorable for getting high selectivity to the light olefins in the catalytic cracking of isobutene. Another reason is that the presence of a small amount of Cr may be favorable for the dehydrogenation of isobutane to isobutene which are easily to be further cracked to light olefins. Therefore, the conversion of isobutane over CrHZSM-5 was enhanced compared with that of unpromoted one, HZSM-5. When the loading amount of Cr was more than 0.038 mmol/g, the reactivity of catalytic cracking of CrHZSM-5 catalysts

decreased, which might be due to the existence of a marjory of Cr(III), and Cr(III) with large domain size, which can cover the outer surface of the zeolite catalysts, or combined with acid sites. The further studies are needed to deduce the exact functions of trace amount of Cr for isobutane catalytic cracking.

4. Conclusions

Compared with unmodified HZSM-5 catalysts, the CrHZSM-5 catalyst with trace amount (0.004–0.038 mmol/g) of Cr played an important role in promoting the catalytic performance for cracking of is obutane. Not only did it enhance the reactivity of isobutane catalytic cracking, for instane, 1#CrHZSM-5 catalyst could lower down the cracking temperature of is obutane by 200 °C compared with pyrolysis, but also increased the selectivities to ole fins and ethylene. At 625 °C, the very high yield of ole fins (C₂ + C₃) and the high yields of ethylene were 56.1% and 30.8%, respectively.

One reason is that a trace amount of Cr alters the acidity of the HZSM-5 catalysts. The suitable strength and amounts of acidity of the catalysts are favorable for obtaining high selectivity to the light olefins in the catalytic cracking of isobutene. Another reason is that the presence of a little amount of Cr maybe favorable for the dehydrogenation of isobutane to isobutene which are easier than isobutane to be cracked to light olefins.

Acknowledgments

The research was supported from the National Basic Research Program of China (grant No. 2004CB 217806 and 2005CB221402), the National Natural Science Foundation of China (Grant NO. 20373043), and the Scientific Research Key Foundation for the Returned Overseas Chinese Scholars of State Education Ministry.

References

- G.L. Zhao, J.W. Teng, W.Q. Jin, W.M. Yang, Z.K. Xie and Q.L. Chen, Chin. J. Catal. 25 (2004) 3.
- [2] G.L. Zhao, J.W. Teng, W.Q. Jin, W.M. Yang, Z.K. Xie and Q.L. Chen, Chin. J. Catal. 24 (2003) 119.
- [3] B. Alfons, G. Buekens and G.F. Froment, Ind. Eng. Chem. Process. Des. Develop. 10 (1971) 309.
- [4] K.M. Sundaram and G.F. Froment, Ind. Eng. Chem. Fundam. 17 (1978) 174.
- [5] J.Y. Lu, Z. Zhao, C.M. Xu and P. Zhang, Petro. Sci. 1 (2005) 52.
- [6] D. Ji, B. Wang, G. Qian, Q. Gao, G. Lu, L. Yan and J.S. Suo, Catal. Comm. 6 (2005) 297.
- [7] T. Rorvik, H.B. Mostad, A. Karlsson and O.H. Ellestad, Appl. Catal. A Gen. 156 (1997) 267.
- [8] A. Feller, I. Zuazo, A. Guzman, J.O. Barth and J.A. Lercher, J. Catal. 216 (2003) 313.
- [9] R.D. Cortright and J.A. Dumesic, J Catal. 157 (1995) 576.
- [10] H. Shimada, T. Akazawa, N. Ikenaga and T. Suzuki, Appl. Catal. A General 168 (1998) 243.

- [11] S.M. Al-Zanhrani, N.O. Elbashir, A.E. Abasaeed and M. Abdulwashed, Ind. Eng. Chem. Res. 40 (2001) 781.
- [12] N.Y. Chen and W.E. Garwood, Catal. Rev. Sci. Eng. 28 (1986) 185.
- [13] M. Gabriele and A.L. Johannes, J. Catal. 139 (1993) 24.
- [14] N.R. Meshram, S.G. Hegde and S.B. Kulkarni, Zeolites 6 (1986) 434.
- [15] N. Ararwal, A. Marco, S. Castillo, R.D. Cortright, R.J. Madon and J.A. Dumesic, Ind. Eng. Chem. Res. 41 (2002) 4016.
- [16] Y.P. Sun and T.C. Brown, J Catal. 194 (2000) 301.
- [17] L. Davydov, E. P. Reddy, P. France and P. G. Smirniotis, J. Catal. 203 (2001) 157.
- [18] N. Ulagappan and C.N.R. Rao, Chem. Commun. 9 (1996) 1047.
- [19] Z.D. Zhu, Z.X. Chang and L. Kevan, J. Phys. Chem. B 103 (1999) 2680.
- [20] B.M. Weckhuysen, I.E. Wachs and R. Schoonheydt, Chem. Rev. 96 (1996) 3327.
- [21] M.A. Vuurman and I.E. Wachs, J. Phy.Chem. 96 (1992) 5008.
- [22] P. McCarthy, J. Lauffenburger, P. Skonezny and D. Rohrer, Inorg. Chem. 20 (1981) 1566.
- [23] M. Maciejewski, K. Köhler, H. Schneider and A. Baiker, J. Solid State Chem. 119 (1995) 13.





Catalysis Today 119 (2007) 13-18



Characterization and activity of Mo supported catalysts for diesel deep hydrodesulphurization

Aijun Duan ^{a,*}, Guofu Wan ^a, Zhen Zhao ^a, Chunming Xu ^a, Yanying Zheng ^b, Ying Zhang ^b, Tao Dou ^b, Xiaojun Bao ^b, Keng Chung ^c

^a State Key Laboratory of Heavy Oil Processing, China University of Petroleum, Beijing 102249, PR China

^b Key Laboratory of Catalysis, China University of Petroleum, Beijing 102249, PR China

^c Syncrude Canada Ltd., 9421-17 Avenue, Edmonton, Alberta T6N 1H4, Canada

Available online 8 September 2006

Abstract

Various highly dispersed Mo supported catalysts with various carriers were prepared for deep hydrodesulphurization of diesel. The carriers included a high surface area and large pore volume γ -Al₂O₃, two types of meso-microporous composite molecular sieves prepared by incipient-wetness impregnation method. A new mesoporous MoSiO_x catalyst synthesized with in situ composite method was also studied. The hydrodesulphurization experiments were carried out in a micro-reactor over different catalysts including Mo supported series and a commercial catalyst. Spectroscopic techniques (FT-IR and UV-vis DRS) were utilized to determine the structure of MoO_x species. The catalyst characterizations of BET, XRD, FT-IR, UV-vis DRS and FTIR pyridine adsorption indicated that the existences of metal active component of Mo in the catalysts were highly dispersed nano MoO₃ clusters and the Mo series catalysts had high surface areas and plenty of large pores which were propitious to the diffusions of reactant and product molecules. Cat_{NiMo} exhibited the highest *B/L* acidity ratio and higher total concentration of Brønsted acid sites and Lewis acid sites, and its HDS activity also gave the highest in this study to produce a sulphur-free diesel, which was verified by the sulphur content in products analyzed by GC-MS methods.

© 2006 Elsevier B.V. All rights reserved.

Keywords: Hydrodesulphurization; Molybdenum and nickel catalyst; Ultra low sulphur diesel; Mesoporous materials

1. Introduction

Recently the stringent environmental regulations established high quality transportation fuel specification to reduce automobile emissions and to minimize the environmental pollution, e.g. the sulphur content in diesel is required to be lowered to or less than 50 ppm in America, in European countries the sulphur in diesel less than 10 ppm S has been implemented since 2005. To meet this assignment, it has been paid more attentions in product upgrading via deep or ultra deep hydrodesulphurization (HDS) of diesel [1,2].

It is well known that alkyl substituted dibenzothiophenes (DBT) are the most refractory sulphur compounds in light oil for HDS. Transitional metal sulphides (TMS) hydroprocessing catalysts have been widely used for 70 years. Metal sulphides

0920-5861/\$ – see front matter \odot 2006 Elsevier B.V. All rights reserved. doi:10.1016/j.cattod.2006.08.049

from group VI (Mo, W) promoted by sulphides of group VIII (Co, Ni), generally supported on alumina, are the most economical TMS which have high activity, selectivity and stability for heteroatom removal and product refining [3,4]. The active phase on these hydroprocessing catalysts has a Ni(Co)Mo(W)S-like structure, and active sites are located at edge surfaces of the $Mo(W)S_2$ [5,6].

One of the important factors that affect the efficiency of a hydrodesulphurization catalyst is the interaction between the active phases and the support. Metal–support interactions influence not only the dispersion of the active components, but also their reducibility and sulphidability, e.g. modification of the morphology of the sulphide active phase, interactions of chemical environment of acid sites. The development of new supports for hydrotreatment catalysts have been very active urged by the stringent regulations concerning the restricted level of sulphur admitted in fuels. Some results have been summarized in reviews and open literatures concerning hydrotreatment catalyst and deep hydrodesulphurization

^{*} Corresponding author. Fax: +86 10 89731586. E-mail address: duanaijun@cup.edu.cn (A. Duan).

[7–10]. The typical specific surface area of such tranditional oxide supports before 1991 remained below 100 m²/g (after calcination at 773 K), and the porosity were also not adapted for hydrotreating applications. Many improvements of new type support preparation, resulted in higher specific surface area and larger pore diameters, were obtained in the past decade.

Many supports were used in hydrotreating catalyst as carbon, simple oxides (TiO₂, ZrO₂), binary oxides, acidic materials and clays [11]. For instance, mixed oxide supports include TiO₂–ZnO, TiO₂–SiO₂ and TiO₂–Al₂O₃ composites [12]; acidic supports involve silica–alumina or different kinds of zeolite and mesoporous materials [13]. Since TiO₂ supports have no pore system, their specific surface areas are very small compared to that of alumina, furthermore, the active anatase structure possesses only low thermal stability, which made TiO₂ support alone unsuitable for industrial applications [14]. But the TiO₂-Al₂O₃ oxide composites that were often composed of a heterogeneous mixture of the two oxides provided much higher specific surface areas and revealed a positive effect on tetralin conversion [15].

Acidic supports are not only to provide acidity but also to offer an ordered pore structure that facilitates high activity. Due to the high surface area of these mesoporous materials, high active phase loading is easy to be achieved [16]. The applications of mesoporous supports like MCM-41 and SBA-15 might conduce to improve the selectivity as their parallel pores might act as microreactors, in which the reactant and the intermediary products will be in the prolonged contact with the active phase [17].

In this paper, various Mo supported catalysts over γ -Al₂O₃ and two type mesoporous sieve supports and a mesoporous composite MoSiO_x were prepared for diesel hydrotreating and were compared with a commercial catalyst.

2. Experimental

2.1. Feed properties

The feedstock was a 320 ppm sulphur diesel which was a blend of two commercial available diesels: a partially hydrotreated diesel from Fushun refinery and a catalytic cracking diesel from Shengli refinery in China. The properties of the diesel feedstock are shown in Table 1.

Table 1 Diesel feedstock properties

Properties	
Density at 20 °C (g/cm ³)	0.8195
Sulphur (ppm)	319.82
Distillation (°C)	
IBP	154
10%	218
30%	258.2
50%	290
70%	316.1
95%	365
FBP	450.8

2.2. Catalyst preparation

The $\gamma\text{-}Al_2O_3$ used in this study had a high surface area and large pore volume. Catalyst samples were prepared by impregnation of the $\gamma\text{-}Al_2O_3$ supports with aqueous solutions of ammonium heptamolybdate and/or nickel nitrate separately through incipient-wetness impregnation method, and the precursors were dispersed in an ultra-sonic unit for 30 min. The catalyst samples were dried in air for 8 h at 120 °C and calcined for 5 h at 550 °C. The active metal loadings of MoO_3 vary from 1 to 24 wt.%. These samples are labeled as: Cat 1–7 for MoO_3 content of 1, 4, 8, 12, 16, 20 and 24 wt.%. The bimetallic catalyst Cat_NiMo contains 16 wt.% MoO_3 and 3.5 wt.% of NiO. The catalysts were presulphided in a 2 wt.% CS_2 in cyclohexane stream for 4 h at 300 °C.

A mesoporous composite $MoSiO_x$ was prepared by the solgel process according to the following proportions of chemicals: 1 tetraethyl orthosilicate (TEOS):1 Mo:2.16 NaOH:0.13 cetyltrimethyl-ammonium bromide (CTMAB):107 H₂O:3.56 Acac. The sequence of preparation procedure were adding 1 mol/L NaOH solution, (NH₄)₆Mo₇O₂₄·4H₂O, Acac, CTMAB and TEOS. The mixture was agitated for 3 h and aged for 7 days, then washed, filtered and calcined at 550 °C for 5 h. The MoO₃ content in the mesoporous material prepared by in situ synthesis in the strong caustic media reached 5 wt.%.

Two types of mesoporous sieves, MEM-1 and MEM-2 with different acidity were prepared by adding the grains of 5 g silica gel, 1 g sodium aluminate and 0.5 g sodium hydroxide into 2.23 g TEAOH solution at controlled pH value and mixed with 3.25 g PEG400 at 140 °C for 28 h. The resulting carriers were obtained after drying at 100 °C for 12 h and calcination at 550 °C for 5h. These carriers were supported with 3 wt.% NiO and 12 wt.% MoO₃.

2.3. Catalyst characterization

The specific surface area of catalyst samples was determined by the BET method. X-ray powder diffraction (XRD) profiles were recorded in an XRD-6000 X-ray diffractometer using Cu $K\alpha$ radiation under 40 kV, 30 mA, scan range from 5 to 75° at a rate of 4° min⁻¹ The IR spectra were taken within the range of 6000-400 cm⁻¹ on an FTS-3000 spectrophotometer using 2 mg of the sample mixed with 200 mg of KBr, which was pressed into a transparent disc. The UV-vis diffuse reflectance spectra (DRS) experiments were performed on a Hitachi U-4100 UV-vis spectrophotometer with the integration sphere diffuse reflectance attachment. The powder samples were loaded in a transparent quartz cell and were measured in the region of 200-800 nm under ambient conditions. The standard support reflectance was used as the baseline for the corresponding catalyst measurement. FTIR spectra of adsorbed pyridine were recorded in order to evaluate the acidity of samples in BIO-RAD FTS3000 spectrophotometer with resolution of 4 cm⁻¹. The catalyst samples were made in the form of a self-supporting thin wafer, placed at the center of the cell vertical to the IR beam. Samples were pretreated in the infrared cell and fitted with greaseless stopcocks and KBr

windows, then the spectrum was scanned with an infrared spectrometer at speed of 20 scans/spectrum.

2.4. Catalytic activity

Catalyst activity test were performed in a JQ-II fixed-bed high-pressure micro-hydrotreating apparatus. Catalyst were presulphided at 350 °C for 4 h with a continuous stream of 3 wt.% CS₂/hexane solutions. After that, the diesel feedstock was fed continuously to the reactor. The experimental conditions are: total pressure, 5 MPa; reaction temperature, 350 °C; liquid hourly space velocity (LHSV), 1 h⁻¹ and hydrogen-to-hydrocarbon ratio, 600 mL/mL. Reaction products were collected to determine the catalyst activities after 12 h feed on-stream.

The contents of sulphur in feed and products were measured with a PFPD detector in an ANTEK7000NS system, according to the ASTM 5463 method. The distribution of sulphur species was determined by GC–MS.

3. Results and discussion

3.1. Catalyst characterization

The textural properties and pore size distributions of catalysts are typically shown in Table 2 and Fig. 1, respectively. The catalysts include a commercial NiMo/ γ -alumina catalyst (Com) with 2.7 wt.% NiO and 26.5 wt.% MoO₃, and a series of Mo supported catalysts (which have been labeled above).

Comparison with the pore size distributions of alumina-supported molybdenum (Mo) series catalysts and commercial alumina-supported NiMo catalyst in Table 2, the mesoporous γ -Al₂O₃ support exhibits higher surface area of 280 m²/g and wider pore size of 12.3 nm, which result in high surface area and large pore size over Mo series catalysts, e.g. the surface area and the average pore size of Cat 6 are 239 m²/g and 11.9 nm, but those of commercial catalyst are 155 m²/g and 7.9 nm. As one of the Mo supported series catalysts, Cat 4 and Cat 7 also have the similar average pore sizes, but have different surface areas for different MoO₃ loading over γ -Al₂O₃ support (the Mo contents of Cat 4, Cat 6 and Cat 7 are 12, 20 and 24 wt.%), which indicate that the Mo Cat series catalysts and Cat_{NiMo} catalyst, supported on γ -Al₂O₃, have high surface area and large average pore size. It is well known that high

Table 2 Catalyst textural properties

Catalysts	$A_{\rm BET}~({\rm m}^2/{\rm g})$	A _{micro} (m ² /g)	V _{BJH} (cm ³ /g)	Average pore diameter (nm)
Cat 4	264	9	0.71	12.0
Cat 6	239	7	0.71	11.9
Cat 7	223	8	0.68	11.7
Com	155	0	0.30	7.9
$MoSiO_x$	$\sim \! 1000$	0	1.50	3.7
MEM-1	189	128	0.19	4.0
MEM-2	236	163	0.21	3.6
γ -Al ₂ O ₃	280	22	0.75	12.3

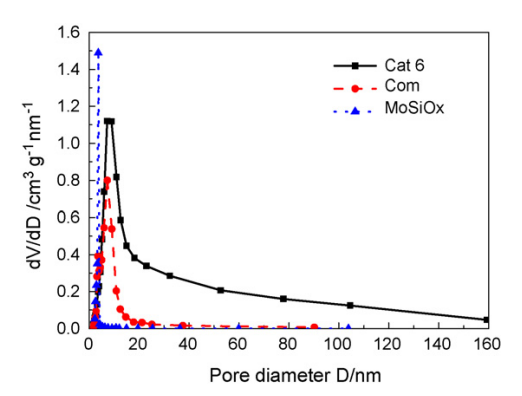


Fig. 1. Pore size distribution.

surface area is adequate for dispersing metal to form active sites, while large pore diameter reduces the diffusion hindrance and promotes the contacts of reactant molecules with active sites on the catalyst surface.

The typical pore size distributions of several catalysts in Fig. 1 show that Cat 6 catalyst, as a representative of Mo Cat series, possesses plenty of pores with different pore-sizes even as large as 100 nm that provide unblocked channels for reactant molecules with various sizes. The commercial catalyst has a symmetrical distribution around 7.9 nm in pore size and the mesoporous $MoSiO_x$ catalyst reveals a relatively uniform pore size of 3.7 nm, which maybe induces internal diffusion limitation of large size molecules.

Fig. 2 presents XRD patterns of Mo Cat series catalysts, indicating no apparent signals of MoO₃ crystal. This suggests that the dispersion of MoO₃ on catalyst was either relatively high or the crystallite size of MoO₃ was very small. Fig. 3 shows the low-angle XRD pattern (Fig. 3a) and wide-angle XRD pattern (Fig. 3b) of mesoporous MoSiO_x. In Fig. 3a, the very intense reflection peak at 1.96° (2θ) and the reflection line in the range of $3-3.75^{\circ}$ (2θ) are characteristic of the mesoporous MoSiO_x structure. The XRD pattern in Fig. 3b shows the spectrum of wider angle corresponding to 2θ from 5 to 75°, indicating no peak corresponding to ordered crystal. This suggests that the MoO_x was highly dispersed with particle size less than 40 Å which was beyond XRD detection limitation. The finely dispersed nanocrystalline MoO_x particles are believed to

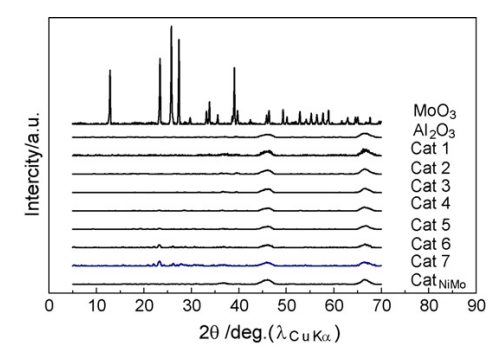


Fig. 2. XRD patterns of Mo Cat series catalysts.

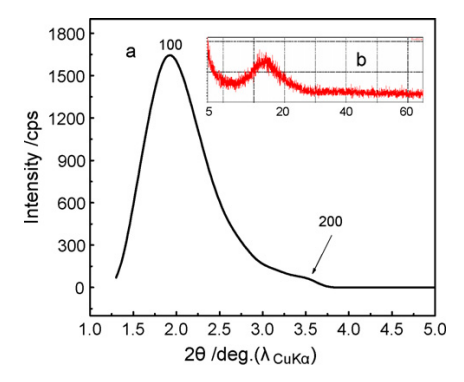


Fig. 3. (a) The low-angle and (b) wide-angle XRD patterns of MoSiO_x.

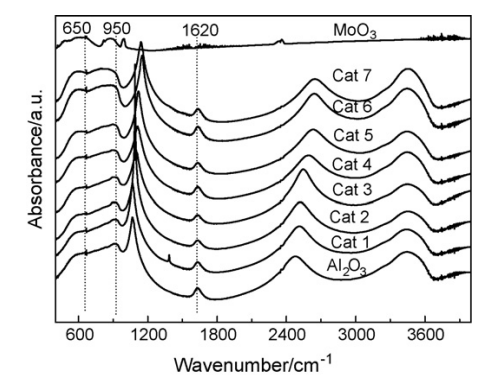


Fig. 4. FT-IR spectra of catalysts.

improve the catalyst activity, since the higher active surface with smaller size of active phase provides more effective contacts with the reactants [18–20].

FT-IR spectroscopy in Fig. 4 shows the surface compositions and structures of the Mo Cat series catalysts. The band at 950 cm⁻¹ characterizes the stretching mode of terminal Mo=O bonds in molybdenum octahedral in polymeric molybdenum compounds (iso- and heteropolymolybdates). The band at $650 \, \mathrm{cm}^{-1}$ ascribes to the characteristic bridged Mo-O-Mo bonds. The increased trend of band intensities between $600 \, \mathrm{and} \, 950 \, \mathrm{cm}^{-1}$ corresponds to an increase in Mo loading, suggesting the polymer formation of molybdenum-oxygen (MoO_x) species (clusters). The bands at $1620 \, \mathrm{and} \, 3500 \, \mathrm{cm}^{-1}$ indicate the deformation and stretch vibration of the O-H bonds. The high-

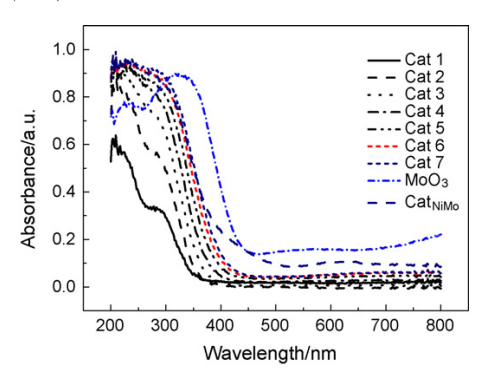


Fig. 5. UV-vis DR spectra of catalysts.

intensity band at 1100 cm⁻¹ is likely ascribed to the deformation vibration of the Al–OH bond [21,22].

The UV-vis DRS was applied to determine the structures of supported Mo catalysts in the 200-800 nm region. The DR spectra in Fig. 5 show that there is no typical signal of MoO₃ crystal existing in the catalyst surface which is consistent with the XRD analysis. When Mo loading is low, the Mo surface species are mostly Mo⁶⁺ over alumina support; with Mo loading increasing a few of low valence Mo species appear. The bands at 220-250 nm are commonly attributed to the tetrahedral molybdate, whereas the band at 320 nm is assigned to the Mo-O-Mo bridge bond of the octahedral coordination [23,24]. The band at 280 nm is assigned to monomer, dimer or polymerized molybdate species, but the assignment is not clear yet [25]. The broad band at 280-400 nm in Fig. 5 indicates that both the tetrahedral and octahedral molybdates can be present on the support. There were more tetrahedral species at low Mo loadings and more octahedral species at high Mo loadings. The red shift of the lowest energy transition absorption of molybdate indicates that the molybdate species formed larger clusters as Mo loading increased [26,27], but the active phase is still in high dispersion and there is no large size MoO₃ crystal over catalyst surface.

The IR spectra of the pyridine adsorbed on the various samples in the region 1700–1400 cm⁻¹ are shown in Fig. 6. The bands at 1540 and 1450 cm⁻¹ are related to the adsorption of the pyridine molecule on Brønsted acid sites and Lewis acid sites. Table 3 is the acid strength distributions of samples quantitatively calculated from IR results of pyridine adsorption at 200 and 350 °C, respectively, which recompile the

Table 3 Acidity of different catalysts

Sample	Concentratio	Concentration of acid sites (mmol/g _{cat})											
	Brønsted		Lewis	Lewis			B/L						
	250 °C	350 °C	250 °C	350 °C	250 °C	350 °C	250 °C	350 °C					
Com	1.8	0.7	17.7	5.4	19.5	6.1	0.10	0.13					
Cat 6	2.3	1.3	20.1	8.6	23.4	9.9	0.11	0.15					
Cat _{NiMo}	4.2	3.4	24.7	13.8	28.9	17.2	0.17	0.25					
MEM-1	5.4	1.0	30.9	14.6	36.3	15.6	0.17	0.07					
MEM-2	3.7	1.0	20.7	10.2	24.4	11.2	0.18	0.10					

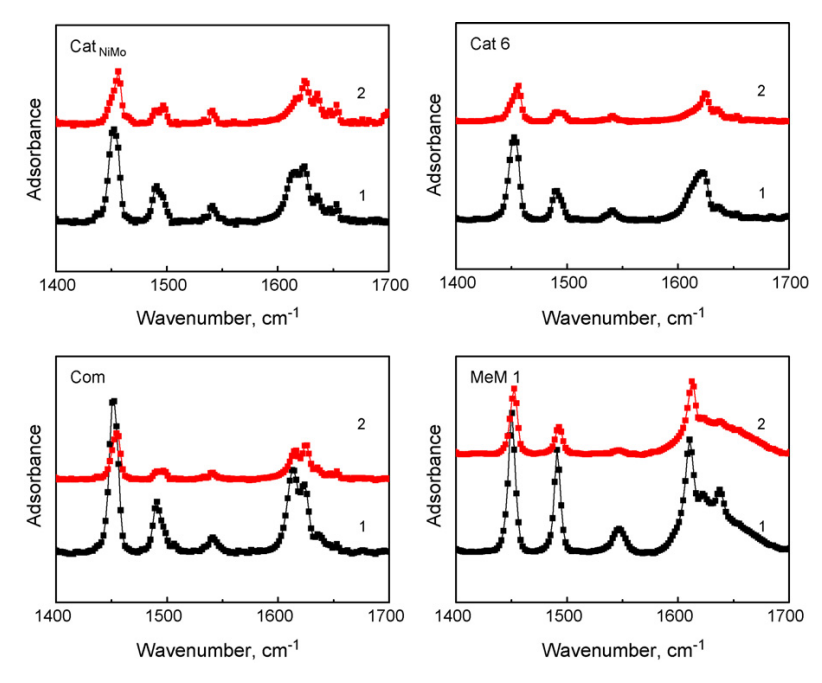


Fig. 6. IR spectra of the pyridine adsorbed on various catalysts at different temperatures: (1) 200 °C and (2) 350 °C.

concentrations of total acid sites, Brønsted, Lewis and *B/L* ratios of all catalysts.

From these data the B/L ratio follows the order: $Cat_{NiMo} > MEM-2 > Cat 6 > MEM-1 > Com$; the total acidity follows: $MEM-1 > Cat_{NiMo} > MEM-2 > Cat 6 > Com$. It is clear that Cat_{NiMo} exhibits the highest B/L ratio and the concentrations of Brønsted and Lewis acid sites keep relatively high level at these two thermal desorption temperature. The MEM-1 and MEM-2 catalysts give also high concentration of Brønsted acid sites and Lewis acid sites at low temperature, but the concentration of medium and strong Brønsted acid sites decline sharply. Compared with the commercial catalyst, catalysts Cat 6 and Cat_{NiMo} produce more Brønsted and Lewis acid sites, which should be of significance for hydrotreating applications.

3.2. Catalytic activity

Table 4 shows the HDS activities over various catalysts. The HDS efficiency data of the Mo supported series catalysts indicate that in the low Mo loading range, HDS activity of Mo Cat series catalysts increases with Mo loading, which may be enhanced not only by the increased dispersion of Mo but also by

higher Brønsted acid sites concentration, until the Mo loading is as high as 20–24 wt.% of MoO_3 . When MoO_3 loading is greater than 20 wt.%, the HDS efficiencys are above 95%, which are comparable to that of commercial catalyst. For the bimetallic Cat_{NiMo} catalyst, the sulphur content in the product is so low that it is below the detection limit of PFPD and GC–MS analyses, thus its HDS activity is near to 100% which is superior to that of commercial catalyst.

Since the total Mo content was only 5 wt.% incorporated into the framework of mesoporous $MoSiO_x$ catalyst, the HDS activity was as low as 80.6%. So the amounts of MoO_3 over the catalyst surface should be kept on a relatively high level for the future preparation.

Even though the meso-microporous composite molecular sieves carrier catalysts, MEM-1 and MEM-2 show high acidities as shown in Table 3, their HDS activities are much lower than that of other catalysts. That maybe due to the mesoporous material and molecular sieves having uniform pore distribution less than 4 nm (see Table 2 and Fig. 1), which restrict the internal diffusivity of reactant molecules in the pores of molecular sieves.

Table 5 compares the sulphur compounds in the feedstock and reaction products over various catalysts. Since the

Table 4 HDS efficiency over various catalysts at 350 $^{\circ}\text{C},$ 5 MPa, 1 h^{-1} and 600 mL H_2/mL oil

Catalysts	Cat 1	Cat 3	Cat 4	Cat 6	Cat 7	Cat _{NiMo}	$MoSiO_x$	Com	MEM-1	MEM-2
MoO ₃ (wt.%)	1	8	12	20	24	16	5	26	12	12
NiO (wt.%)						3.5		2.7	3	3
Sulphur in product (ppm)	124.9	25.1	26.4	16.0	15.5	_	61.9	17.5	36.7	71.0
HDS Conv. (%)	61.0	92.2	91.7	95.1	95.2	~ 100	80.6	94.5	88.5	77.8

Table 5 Comparison of product sulphur compounds with various catalysts at 350 °C, 5 MPa, 1 h⁻¹ and 600 mL H_2/mL oil

	Sulphu	Sulphur contents (by GC-MS, ppm)						
	Feed	Cat 1	Cat 3	Cat 4	Cat 6	Cat 7	Cat _{NiMo}	
BT	3.9	0	0	0	0	0		
C1-BT	34.6	2.4	0	0	0	0		
C2-BT	59.9	11.8	0.3	0	0	0	0	
C3-BT	34.4	11.7	0.7	0.3	0	0	0	
≥C4-BT	33.4	5.6	0	0	0	0	0	
DBT	6.7	3.8	0	0	0	0	0	
C1-DBT	23.3	15.9	5.8	0.7	0	0	0	
C2-DBT	38.0	20.9	5.3	0.7	0.3	0.3	0	
≥C3-DBT	39.0	25.5	6.2	0.8	0.7	0.3	0	
Total	273.2	97.6	18.2	2.5	1.0	0.6	0	

BT, benzothiophene; Ci-BT, alkyl-benzothiophene; DBT, dibenzothiophene; Ci-DBT, alkyl-dibenzothiophene.

feedstock was a blend of partially hydrotreated diesels from the commercial refineries, the sulphur compounds in the feedstock were primarily alkyl-benzothiophenes (alkyl-BT) and alkyldibenzothiophenes (alkyl-DBT). These refractory sulphur compounds needed to be decomposed in hydrotreating process. The percentages of alkyl-BT and alkyl-DBT over total sulphur content in feedstock are 51.9 and 33.4 wt.%, respectively. From the data in Table 5, the amounts of alkyl-BT and alkyl-DBT in the diesel products over the Mo series catalysts decreased greatly with increasing Mo loadings, e.g. for Cat 6 and Cat 7 the total sulphur are even near to trace amounts, which verify their good hydrogenation abilities in HDS reaction. As for the Cat_{NiMo} catalyst, no sulphur compounds is detected by PFPD and GC-MS methods, and it shows very high activity towards >C₃ DBT, which is consistent to the high surface area and large pore diameters of its γ-Al₂O₃ support. Therefore, comparing catalyst activities, Cat_{NiMo} catalyst is capable of producing ultra low sulphur diesel in order to meet the stringent fuel specifications.

4. Conclusions

The catalyst characterizations of BET, XRD, FT-IR, UV-vis DRS and FTIR pyridine adsorption shows that the existences of metal active component Mo in the supported catalysts are highly dispersed nano MoO₃ clusters which favors the HDS activity, and the Mo series catalysts have high surface areas and plenty of large pores propitious to the diffusions of reactant and product molecules.

HDS activity of Mo Cat series catalysts increases with Mo loading, which is enhanced not only by the increased dispersion of Mo but also by higher Brønsted acid sites concentration, until the Mo loading is as high as 20–24 wt.% of MoO₃. Cat_{NiMo} exhibits the highest *B/L* ratio and higher total concentrations of Brønsted acid sites and Lewis acid sites, and its HDS activity is superior to that of commercial catalyst (HDS efficiency for

Com catalyst is 95 wt.%). As concerning the HDS of sulphur compounds it is found that synthesized Cat_{NiMo} catalyst shows very high activity towards $\geq C_3$ DBT, which is capable of producing a sulphur-free diesel.

The mesoporous $MoSiO_x$ catalyst shows a relatively low HDS activity as the MoO_3 loading is only 5 wt.%. The mesomicroporous composite molecular sieves carrier catalysts, MEM-1 and MEM-2 show that the former has the highest total acidity, but their HDS activities are much lower than that of Mo Cat series for their typical pore diameter less than 4 nm.

Acknowledgements

This work was supported by NSFC project (No. 20406012), CNPC project (04A5050102 and 05E7019), the National Basic Research Program of China (No. 2004CB217806), and SKLHOP open project 2004–06 of China University of Petroleum (Beijing).

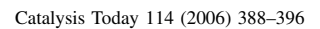
References

- [1] D.D. Whitehurst, H. Farag, T. Nagamatsu, Catal. Today 45 (1998) 299.
- [2] J.J. Lee, H. Kim, S.H. Moon, Appl. Catal. B 41 (2003) 171.
- [3] J.W. Ward, in: G. Poncelet (Ed.), Preparation of Catalysts, Elsevier Science, Amsterdam, 1983, p. 212.
- [4] J.V. Lauritsen, S. Helveg, E. Lagsgaard, J. Catal. 197 (2001) 1.
- [5] D.R.M. Perez, T. Samuel, B. Gilles, C. Alejandra, Y.M. Jose, et al. J. Catal. 225 (2004) 288.
- [6] H. Shimada, Catal. Today 86 (2003) 17.
- [7] H. Topsøe, B.S. Clausen, F.E. Massoth, in: J.R. Anderson, M. Boudart (Eds.), Hydrotreating Catalysts, Catal. Science Technol., vol. 11, Springer, Berlin, 1996.
- [8] P.T. Vasudevan, J.L.G. Fierro, Catal. Rev. Sci. Eng. 38 (1996) 161.
- [9] D.D. Withehurst, T. Isoda, I. Mochida, Adv. Catal. 42 (1998) 345.
- [10] C. Song, Catal. Today 86 (2003) 211.
- [11] G. Murali Dhar, B.N. Srinivas, M.S. Rana, et al. Catal. Today 86 (2003) 45–60.
- [12] S.K. Maity, J. Ancheyta, L. Soberanis, et al. Appl. Catal. A 244 (2003) 141.
- [13] T. Klimova, E. Rodriguez, M. Martinez, et al. Microporous Mesoporous Mater. 44-45 (2001) 357.
- [14] S. Yoshinaka, K. Segawa, Catal. Today 45 (1998) 293.
- [15] M. Breysse, P. Afanasiev, C. Geantet, et al. Catal. Today 86 (2003) 5.
- $[16]\ C.\ Song,\ K.M.\ Reddy,\ Appl.\ Catal.\ A\ 176\ (1999)\ 1.$
- [17] S. Dzwigaj, C. Louis, M. Breysse, et al. Appl. Catal. B 41 (2003) 181.
- [18] H. Topsoe, B.S. Clausen, N. Topsoe, in: D.L. Trimm, S. Akashah, M. Absi Halabi (Eds.), Catalysts in Petroleum Refining, Stud. Surf. Sci. Catal., vol. 53, Elsevier, Amsterdam, 1990, p. 77.
- [19] S.M.A.M. Bouwens, R. Prins, V.H.J. de Beer, J. Phys. Chem. 95 (1991) 123.
- [20] R. Prins, in: G. Ertl, H. Knozinger, J. Weitkam (Eds.), Handbook of Heterogeneous Catalysis, VCH, Weinheim, 1908.
- [21] R.G.V. Rama, S. Venkadesan, V. Saraswati, J. Mater. Sci. 111 (1989) 103.
- [22] F.E. Massoth, Adv. Catal. 27, 283.
- [23] T. Klimova, M. Calderón, J. Ramırez, Appl. Catal. A 240 (2003) 29.
- [24] M. Cheng, F. Kumata, T. Saito, T. Komatsu, Appl. Catal. A 183 (1999) 100
- [25] Y. Iwasawa, M. Yamagishi, J. Catal. 82 (1983) 373.
- [26] G. Xiong, C. Li, Z. Feng, J. Catal. 186 (1999) 234.
- [27] G. Xiong, Z. Feng, J. Li, et al. J. Phys. Chem. 104 (2000) 3581.



Available online at www.sciencedirect.com







Synthesis of ZSM-5/SAPO-11 composite and its application in FCC gasoline hydro-upgrading catalyst

Yu Fan a,b, Duo Lei b, Gang Shi b, Xiaojun Bao a,b,*

^a State Key Laboratory of Heavy Oil Processing, China University of Petroleum, Beijing 102249, PR China ^b The Key Laboratory of Catalysis, China National Petroleum Co., China University of Petroleum, Beijing 102249, PR China

Available online 3 April 2006

Abstract

This article describes the synthesis, characterization and application of a novel aluminosilicate/silicoaluminophosphate composite zeolite ZSM-5/SAPO-11. The composite was synthesized by the in situ overgrowth of SAPO-11 on ZSM-5 and was characterized by means of X-ray diffraction (XRD), scanning electron microscopy (SEM), Fourier transformed infrared (FT-IR) spectrometry, N₂ adsorption and infrared spectroscopy of adsorbed pyridine. The results were compared with those of the mechanical mixture composed of individual ZSM-5 and SAPO-11. In the mechanical mixture, the ZSM-5 phase was morphologically separate from the SAPO-11 phase, while the ZSM-5/SAPO-11 composite existed in a form of a core-shell structure, with the ZSM-5 phase as the core and the SAPO-11 phase as the shell. Compared with the mechanical mixture, the composite had more mesopores and moderate acidity distribution, which could accelerate the diffusion of substances and enhance the synergetic effect between Brönsted and Lewis acids. The comparison of the catalytic performances of the mechanical mixture and the composite-based Ni–Mo catalysts for FCC gasoline hydro-upgrading showed that, due to the above advantages of the composite, the corresponding catalyst yielded improved gasoline research octane number, high liquid yield, good desulfurization activity and lower coke amount and thus could be considered as a potential catalyst system for hydro-upgrading FCC gasoline.

© 2006 Elsevier B.V. All rights reserved.

Keywords: ZSM-5/SAPO-11 composite; Synthesis; Characterization; FCC gasoline hydro-upgrading

1. Introduction

Air pollution in urban regions caused by exhaust emissions from gasoline-powered motor vehicles has become a serious issue in both developed and developing countries due to the high content of sulfur compounds and olefins in most gasoline. In air, unburned olefins can easily react with NO_x to form photo-chemical smog, and sulfur compounds can degrade the effectiveness of automobile catalytic converters for NO_x , CO, and hydrocarbon emissions control by poisoning three-way catalysts. Thus, most of the countries over the world have tightened their regulations on gasoline compositions, especially on the contents of sulfur compounds and olefins. It has been reported that more than 90% of sulfur compounds and about 90% of olefins in typical refinery gasoline pools come from FCC gasoline [1], so this stream is obviously a focal point in

producing clean gasoline. In China, approximately 80% of the gasoline pool comes from FCC gasoline, resulting in higher sulfur and olefin contents in the commercial gasoline. Various measures (such as optimization of the FCC process, use of new FCC catalysts [2], or selective hydrogenation [3,4]) have been taken, but none of them enables satisfactory sulfur and olefin control without loss in the gasoline research octane number (RON). Therefore, it is still a great challenge for the refineries in China to produce the clean gasoline that meets the more stringent specification of clean fuels.

In order to reduce the contents of sulfur compounds and olefins of FCC gasoline as well as preserve its RON, researchers have proposed various hydro-upgrading processes that combine hydrodesulfurization (HDS) with hydrocracking and hydroisomerization [5–7], but most of them involve a high operating cost because of lower gasoline yield. In previous papers [8–10], we found that reducing the olefin content in FCC gasoline by only hydroisomerization was unable to preserve gasoline RON. Because the arene content in FCC gasoline produced in China is usually in the range of 12–18 vol.%, much lower than 35 vol.%

0920-5861/\$ – see front matter @ 2006 Elsevier B.V. All rights reserved. doi:10.1016/j.cattod.2006.02.050

^{*} Corresponding author. Fax: +86 10 8973 4979. E-mail address: baoxj@cup.edu.cn (X. Bao).

as regulated by Category 3 Unleaded Gasoline of the World-Wide Fuel Charter, there is some leeway to preserve gasoline RON by converting olefins (especially C5-C7 olefins) in FCC gasoline into i-paraffins and arenes that have higher RON. Thus, from the point of view of olefin and sulfur content reduction as well as gasoline RON preservation, a novel catalyst system with balanced desulfurization, olefin hydroisomerization and olefin aromatization abilities need to be developed. Intuitively, it is expected that this kind of catalyst system can be obtained by combining or compositing different zeolites with desired properties. It has been widely recognized that zeolite ZSM-5 has excellent activity for both HDS [11,12] and light alkane and alkene aromatization [13-15]. Moreover, silicoaluminophosphate zeolite SAPO-11 has been widely applied to the isomerization of C₄-C₇ hydrocarbons for producing gasoline with high RON [16-19] and to the dewaxing process for making high quality diesel and lube oil basestocks via isomerization of long-chain alkanes [20,21] due to its superior hydroisomerization activity. Naturally, it is reasonable to conceive that a catalyst system based on a ZSM-5/SAPO-11 composite with suitable composition should provide a balanced desulfurization, hydroisomerization and aromatization performance and thereby benefit the upgrading of FCC gasoline. While reports on the synthesis and applications of aluminosilicate/aluminosilicate composite zeolites are abundant in literatures, as extensively reviewed by Smirniotis and Davydov [22], only limited information is available on the preparation and application of aluminosilicate/silicoaluminophosphate composite zeolites [23,24]. In addition, most of the composite zeolites reported in the literatures consisted of two or more individual zeolites mixed mechanically; few of them were made by synthesis. The mechanical mixing may inhibit the intimate contacts of different zeolites and thereby downgrade their synergism. For this purpose, a series of aluminosilicate/silicoaluminophosphate ZSM-5/SAPO-11 composites were synthesized by a two-step crystallization method in the present investigation. They were characterized by means of X-ray diffraction (XRD), scanning electron microscopy (SEM), N2 adsorption, Fourier transformed infrared spectroscopy (FT-IR) and infrared spectroscopy of adsorbed pyridine. In addition to this, composite-supported Ni-Mo catalysts were made and their catalytic performance for upgrading FCC gasoline was assessed.

2. Experimental

2.1. Synthesis of SAPO-11 and ZSM-5

SAPO-11 was synthesized according to the method reported by Lok et al. [25]. The detailed procedure was described elsewhere [9].

ZSM-5 was synthesized as follows: firstly, aluminum sulfate (Beijing Chemical Co., PR China) was dissolved in distilled water, followed by the addition of sulfuric acid (98 wt.%; Beijing Chemical Co., PR China) to form solution A; secondly, tetraethylammonium hydroxide (TEAOH) (20 wt.%; Beijing Chemical Co., PR China), distilled water and sodium silicate (26.3 wt.% SiO₂, 8.2 wt.% Na₂O; Beijing Aviation Materials

Institute, PR China) were mixed in proper proportions to form solution B; thirdly, solution A was slowly added to solution B under agitation. The resulting mixture with the molar composition of 9.7 Na₂O:1 Al₂O₃:40 SiO₂:10 (TEA)₂O:1800 H₂O was further stirred vigorously for 1 h to get a homogenous gel. Fourthly, the gel was then moved to a 150 ml stainless steel autoclave and heated at 448 K for 72 h; finally, the resulting solid was filtrated, washed with deionized water, dried overnight at 383 K, and calcined in air at 823 K for 4 h to remove the organic template.

2.2. Synthesis of ZSM-5/SAPO-11 composite

The synthesis of ZSM-5/SAPO-11 composite is schematically depicted in Fig. 1.

In the first step, zeolite ZSM-5 was synthesized by the method mentioned above, except that its crystallization time was shortened to 48 h and post-treatments (such as filtration, washing, drying and calcination) were omitted.

In the second step, ZSM-5/SAPO-11 composite was synthesized by the following procedure: firstly, a diluted solution of phosphoric acid (85 wt.%; Beijing Jinxing Chemical Plant, PR China) in distilled water was prepared; secondly, pseudoboehmite (73 wt.% Al₂O₃; Tianjin Hengmeilin Chemical Co., PR China) and silica sol (25 wt.% SiO2; Beijing Changhong Chemical Plant, PR China) were slowly added to the phosphoric acid solution and the resulting mixture was vigorously stirred for 2.5 h; thirdly, the uniform mixture obtained and di-n-propylamine (DPA) (99 wt.%; Beijing Jinxing Chemical Plant, PR China) were subsequently added drop by drop into the above crystallization product of ZSM-5 to allow at least 2 h stirring before they were completely added. The molar composition of the resulting homogenous gel was 1 DPA:1 Al₂O₃:1 P₂O₅:0.3 SiO₂:50 H₂O. Fourthly, the gel was moved into stainless steel autoclaves (150 ml) and heated at 458 K for 24 h. Fifthly, the solid product recovered by centrifugation was washed with deionized water and dried at 383 K for 12 h. Finally, to remove amine the solid product was calcined at 823 K for 8 h at a heating rate of 2 K/min, with two stops at 553 and 663 K for 1 h each, before the final calcination temperature was reached.

2.3. Catalyst preparation

The bifunctional catalysts investigated in this work are composed of H-form zeolites as the acid part, Ni–Mo as the metal part, and a binder (pseudoboehmite). The catalyst preparation procedure consists of three main steps: preparation of H-type zeolites, incorporation of metallic function, and activation of the metal part. Firstly, in order to obtain H-form zeolites, ion exchange was carried out three times (each time for 3 h) with 1 M NH₄NO₃ solution at 353 K, followed by calcination in air at 823 K for 4 h; then, the supported catalysts were prepared by impregnating H-form zeolites with (NH₄)₆Mo₇O₂₄ (Beijing Chemical Co., PR China) and Ni(NO₃)₂ (Beijing Chemical Co., PR China) using the fractional step method. Finally, the impregnated solids were extruded using pseudoboehmite as binder and then calcined at 773 K for 4 h.

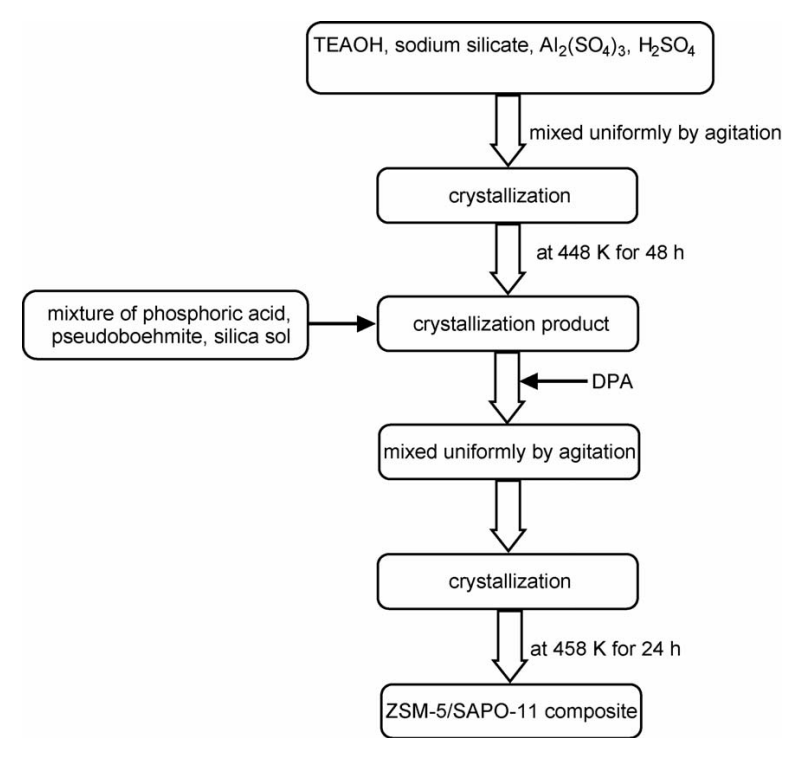


Fig. 1. Schematic for synthesizing ZSM-5/SAPO-11 composite.

2.4. Characterization

The phase structures of the calcined samples were characterized by XRD (Shimadzu 6000, Japan) using Cu K α radiation. The instrument was operated at 40 kV and 30 mA with 2θ scanning speed at 4°/min; diffraction lines of 2θ between 5° and 35° were obtained. The mass fraction of SAPO-11 in ZSM-5/SAPO-11 composites was calculated from the integral intensity of the diffraction peak at $2\theta = 21.1^{\circ}$ where there was no diffraction peak of ZSM-5. Similarly, the mass fraction of ZSM-5 in the composites was calculated at $2\theta = 7.8^{\circ}$. The working curves were obtained by plotting the intensity of the diffraction peak at $2\theta = 21.1^{\circ}$ versus the mass fraction of SAPO-11 and the intensity of the diffraction peak at $2\theta = 7.8^{\circ}$ versus the mass fraction of ZSM-5, respectively, by measuring a series of mechanical mixtures prepared with known mass fractions of SAPO-11 and ZSM-5 in them.

The crystal size, the morphology and the elemental composition of the samples were determined by SEM (435VP, LEO, UK) equipped with an energy-dispersive X-ray spectrometer (EDS, Link-ISIS-300, Oxford, UK).

 N_2 adsorption and desorption isotherms were obtained at 77 K using a volumetric adsorption apparatus (ASAP 2405N, Micromeritics, USA). The pore structures were estimated according to the Brunauer–Emmett–Teller (BET) method and the static volumetry. The samples were degassed at 573 K for 24 h under vacuum prior to the analysis.

The IR spectra were measured on a MAGNA-IR 560 FTIR instrument (Nicolet Co., USA) with a resolution of 1 cm⁻¹. The

samples, each 15 mg, were extruded into the self-supported circular wafers 12 mm in diameter. The wafers were evacuated in situ in an IR cell at 623 K for 4 h, and after the temperature was decreased to room temperature, IR spectra were recorded. Subsequently, the samples were dehydrated at 773 K for 5 h under a vacuum of 1.33×10^{-3} Pa, followed by the adsorption of purified pyridine vapor at room temperature for 20 min. Finally, the system was evacuated at different temperatures and pyridine-adsorbed IR spectra were recorded.

2.5. Catalytic performance assessment

The catalytic performance assessment experiments were carried out in a flowing-type apparatus designed for continuous operation. This apparatus consists of a gas-feeding system controlled by a mass flowmeter and a syringe pump liquid feeding system. The reactor, with an internal diameter of 10 mm, was filled with the catalyst sample (ca. 6 g). There were three heating zones in the reactor, with the top one as the preheater. The temperature of each zone was independently controlled within ± 1 K by thermostats. The temperature of the catalytic bed was measured by a thermocouple placed inside the reactor and was kept constant (± 1 K). The reaction products were analyzed by an Agilent 1790 gas chromatograph to which a flame ionization detector and a HP-PONA capillary column $(50 \text{ m} \times 0.2 \text{ mm})$ were attached. The coke deposited on the catalysts after the reaction was quantified by an automatic carbon analyzer (HV-4B, Wuxi Analysis Instruments Inc., PR

Table 1 Properties of FCC gasoline

Density (20 °C, g cm ⁻³)	$^{\circ}$ S (μ g g ⁻¹) Benzene (vol.%)			Lumped composition (vol.%)				
				n-Paraffins	i-Paraffins	Olefins	Naphthenes	Arenes
0.714	300	0.68	91.7	6.3	28.3	41.1	7.0	17.4

In all runs, the catalysts to be tested were brought to the identical reaction conditions. The presulfurization of the catalysts was firstly carried out at 503, 563 and 593 K for 6 h, respectively, by flowing a stream containing 3 wt.% CS_2 in octane over the catalysts; then, pure hydrogen gas and FCC gasoline were fed into the reactor at a predetermined flow rate after the temperature was increased to the reaction temperature; finally, the reaction was carried out under the conditions of temperature 643 K, FCC gasoline liquid hourly space velocity (LHSV) $2 h^{-1}$, total pressure 2.0 MPa, and volumetric ratio of H_2 to oil 200. The properties of FCC gasoline used are listed in Table 1.

3. Results and discussion

3.1. XRD

The XRD patterns of the samples are shown in Fig. 2. The typical characteristic peak at $2\theta = 7.8^{\circ}$ attributed to ZSM-5 and that at $2\theta = 21.1^{\circ}$ attributed to SAPO-11 can be clearly visualized in the diffraction pattern of the ZSM-5/SAPO-11 composite, despite the fact that some characteristic peaks attributed to individual ZSM-5 and SAPO-11 phases overlap with each other, demonstrating that both ZSM-5 and SAPO-11 phases are present in the composite obtained.

3.2. SEM

The SEM images of the samples are presented in Fig. 3. As shown in Figs. 3a and b, the single SAPO-11 phase is present in the form of pseudo-spherical aggregates of the size ranging from 7 to 8 μ m consisting of uniform cubic plate monocrystals

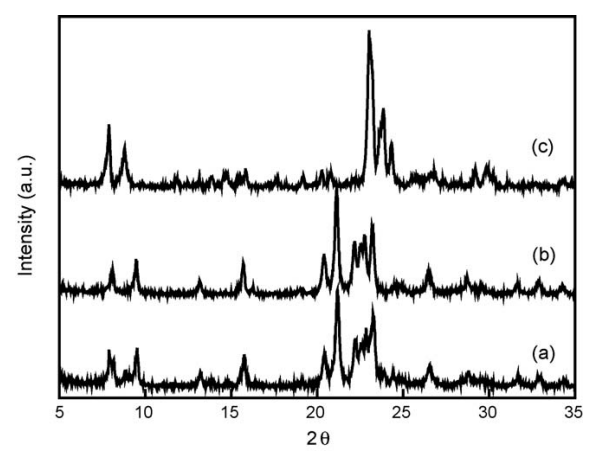


Fig. 2. XRD patterns of (a) the composite, (b) SAPO-11 and (c) ZSM-5.

ca. $0.5~\mu m$ in size (Fig. 3a), and the ZSM-5 phase alone is present in the form of spherical aggregates of the size ranging from 3 to $5~\mu m$ consisting of nonuniform columnar monocrystals ca. $1~\mu m$ long (Fig. 3b). For the mechanical mixture of ZSM-5 and SAPO-11, Fig. 3c clearly shows that the large pseudo-spherical particles assigned to SAPO-11 are separate from the small spherical ones assigned to ZSM-5. For the SAPO-11/ZSM-5 composite obtained by the overgrowth of SAPO-11 on ZSM-5, however, the ZSM-5 phase in the composite is covered by a film of SAPO-11 (Fig. 3d and e), showing a completely different morphological structure from that of the mechanical mixture.

Comparing Fig. 3d with e, one can see that the morphologies of ZSM-5 as the core of the composite are disparate in the two figures. This can be explained as follows: after the spherical ZSM-5 particles were put in the synthesis environment of SAPO-11, the different crystallization time leads to the difference in environmental variables (such as pH value, concentrations of DPA and the precursors of silicon, aluminum and phosphorus species) around the ZSM-5 particles. Some conditions around the spherical ZSM-5 particles may restrain their growth, but promote the overgrowth of the SAPO-11 phase on their surface, resulting in the morphology that the ZSM-5 phase is enveloped by the SAPO-11 phase (Fig. 3d), similar to the growth of epitaxial FAU-on-EMT zeolite [26]. Some conditions are favorable for the dissociation of the spherical aggregate into the monocrystals and thus beneficial to their growth. A faster growth rate of the monocrystals along the axes a and c than that along the axis b will lead to the emergence of the rhombohedral ZSM-5 phase (Fig. 4), in accordance with the growth of the ZSM-5 monocrystal in the presence of F [27]. Moreover, if the growth rate of the ZSM-5 phase is fast enough to surpass that of the SAPO-11 phase, the former will protrude out of the latter, as shown in Fig. 3e.

To further confirm the existence of both ZSM-5 and SAPO-11 phases in the composite, we used SEM-EDS analysis; the results are given in Table 2. Combining Fig. 3e and Table 2, one can conclude that the rhombohedral section as the core of the composite and the pseudo-spherical aggregate as the shell of the composite correspond to the ZSM-5 phase and the SAPO-11 phase, respectively, because their compositions in the composite are consistent with those of the corresponding single phases.

3.3. FT-IR

The FT-IR spectra of the ZSM-5/SAPO-11 composite and the mechanical mixture with the same composition are shown in Fig. 5. In the mechanical mixture, the peaks at 1104, 709 and 469 cm⁻¹ can be assigned to the asymmetric stretching

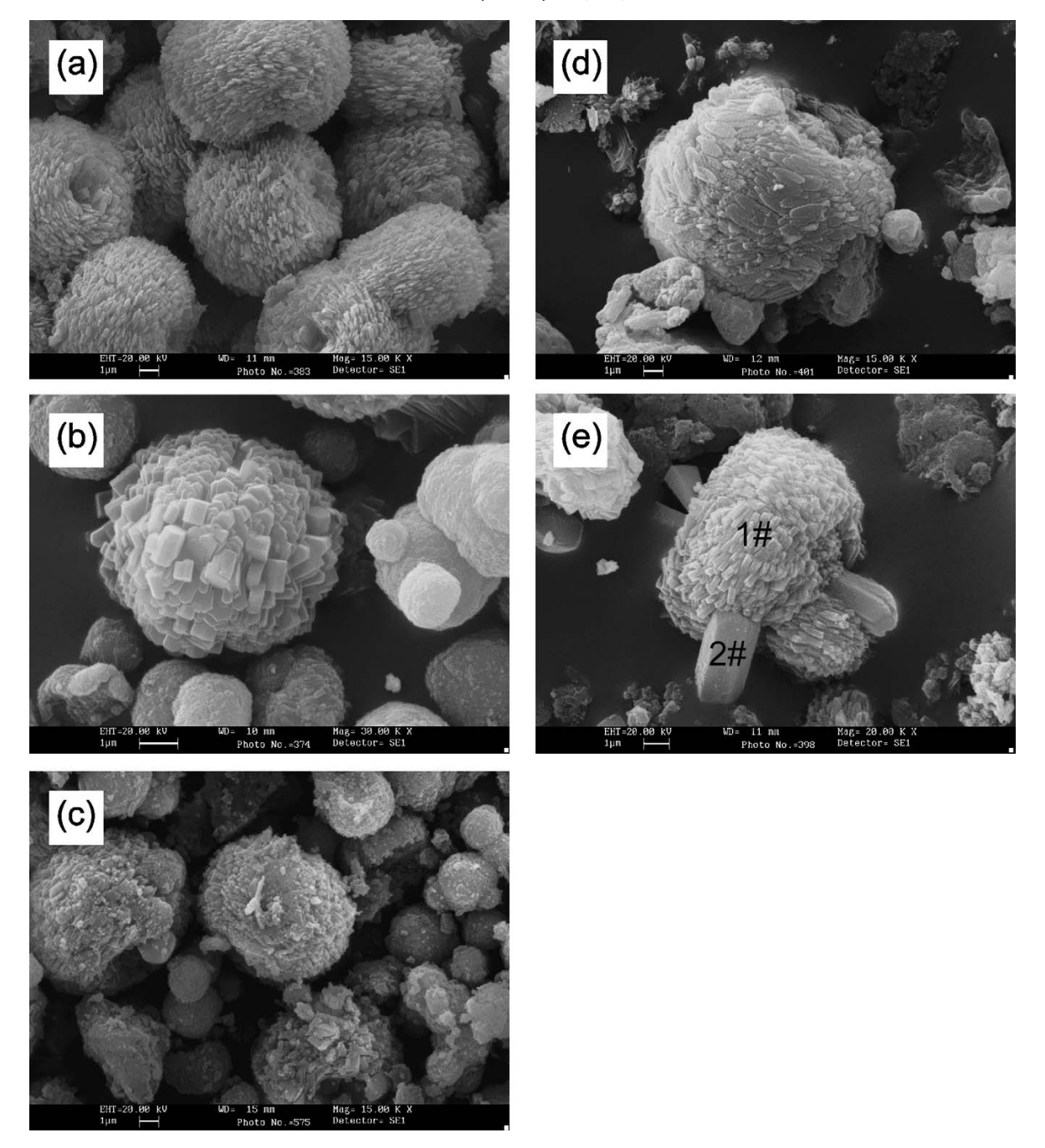


Fig. 3. SEM images of the as-synthesized samples (a) SAPO-11, (b) ZSM-5, (c) mechanical mixture, (d) composite crystallized for 24 h, and (e) composite crystallized for 42 h.

vibration, symmetric stretching vibration and bending vibration of inner tetrahedra, respectively [28]. The peak at 544 cm⁻¹ can be ascribed to the asymmetric stretching vibration of five-membered rings in ZSM-5 [29] and the deformation vibration of six-membered rings in SAPO-11 [30]. Fig. 5 shows that the wavenumbers of the above peaks originally at 709, 544 and 469 cm⁻¹ for the mechanical mixture now shift to 713, 548 and

472 cm⁻¹ for the composite, respectively, due to the interfacial interactions between the two phases in the composite, as reported by Karlsson et al. [31] for a MFI/MCM-41 system. Meanwhile, one should also notice that the peak at 626 cm⁻¹ in the mechanical mixture, standing for the deformation vibration of tetrahedron outer links of four-membered rings in SAPO-11, disappears in the composite. Because the vibration of

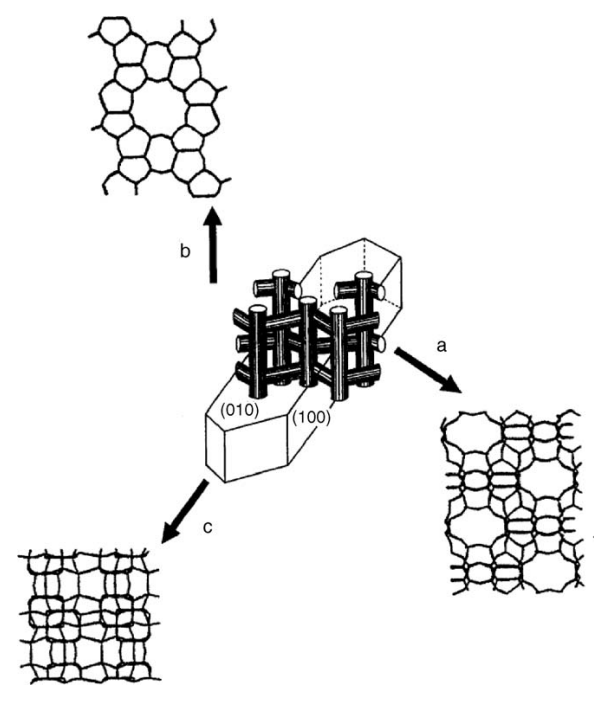


Fig. 4. General sketch of monocrystal and pore structure of ZSM-5.

tetrahedron outer links is sensitive to any change in zeolite structure, we believe that the disappearance of the peak at 626 cm⁻¹ can be attributed to a particular conjunction form of tetrahedrons and a special skeleton structure at the interface in the composite that do not exist in the mechanical mixture. The results introduced here are similar to those observed by Liu et al. [32] in synthesizing kaolin/NaY/MCM-41 composites.

3.4. Pore structure

The N_2 adsorption–desorption isotherms of the ZSM-5/SAPO-11 composite and the mechanical mixture are presented in Fig. 6. The large hysteresis loops in the two isotherms appear with the relative pressure P/P_0 ranging from 0.45 to 1.0, which can be attributed to the mesoporous structure. Obviously, the hysteresis loop of the composite is larger than that of the mechanical mixture, suggesting that, when one composites the two zeolites, more mesopores are formed due to the increscent interspaces among the different crystals.

The pore structure parameters of the samples are summarized in Table 3. Compared with SAPO-11 with a one-dimensional pore system consisting of non-intersecting elli-

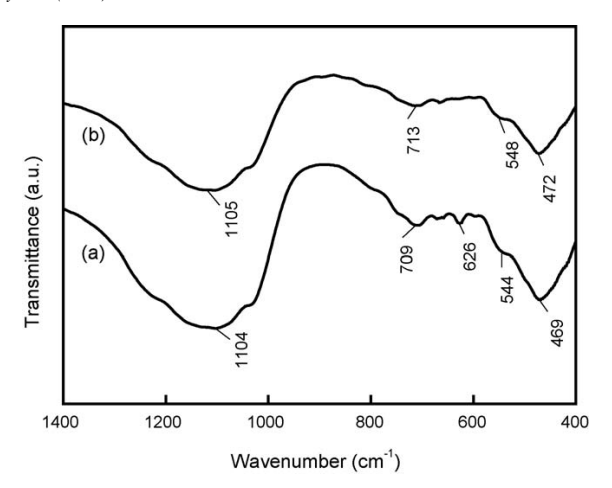


Fig. 5. IR spectra of (a) the mechanical mixture and (b) the composite in the framework vibration region.

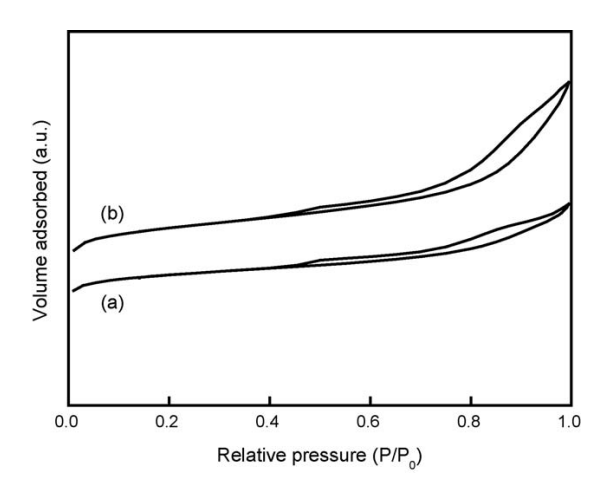


Fig. 6. N_2 adsorption–desorption isotherms of (a) the mechanical mixture and (b) the composite.

ptical 10-membered ring pores of 0.39 nm \times 0.63 nm [33], ZSM-5 has more open structure owing to its two perpendicularly intersecting channel systems with the nearly circular pore openings of 0.54 nm \times 0.56 nm and the elliptical pore of 0.51 nm \times 0.54 nm [34]. From Table 3, it can be seen that the composite has more mesopores and fewer micropores than the mechanical mixture, so the former is superior in minimizing the side reactions by accelerating the diffusion of reactants, intermediates and products.

Table 2
Results of SEM-EDS analysis of the different samples

	SAPO-11	ZSM-5	SAPO-11 phase in composite (1#)	ZSM-5 phase in composite (2#)
SiO ₂ /Al ₂ O ₃ (mol/mol)	0.43	35.8	0.54	37.6
P_2O_5/Al_2O_3 (mol/mol)	0.85	-	1.33	0.14

Table 3
Pore structure parameters of the samples

Samples	Surface area (m ² /g)			Pore volume (ml/g)		
	Micropore	Mesopore	Total	Micropore	Mesopore	Total
ZSM-5	284	82	366	0.13	0.14	0.27
SAPO-11	186	67	253	0.087	0.13	0.22
Mechanical mixture	205	70	275	0.089	0.13	0.22
Composite	178	125	303	0.082	0.25	0.33

3.5. FT-IR of adsorbed pyridine

The FT-IR spectra of adsorbed pyridine on the H-form samples in the region of 1600–1400 cm⁻¹ are shown in Figs. 7–10. The bands at 1545 and 1455 cm⁻¹ correspond to those specific to the pyridine molecules chemisorbed on Brönsted and Lewis acid sites, respectively [35,36], and that at 1490 cm⁻¹ is ascribed to a combination of adsorbate on both Brönsted and Lewis sites.

The quantitative determination of Brönsted and Lewis acidity by FT-IR analysis is based on the integrated Lambert-Beer law:

$$A_{\rm I} = C_{\rm s} \varepsilon_{\rm I} \tag{1}$$

where $A_{\rm I}$ (cm⁻¹) is the integrated absorbance, $C_{\rm s}$ (μ mol/cm²) is the concentration of surface acid sites, and $\varepsilon_{\rm I}$ (cm/ μ mol) is the integrated molar extinction coefficient.

Consequently, the concentrations of Brönsted and Lewis acid sites in reference to a unit weight of dry sample $\{C_{sw} (\mu mol/g)\}$ can be determined by

$$C_{\rm sw} = A_{\rm I} \pi R^2 / w \varepsilon_{\rm I} \tag{2}$$

where R (cm) is the radius of the sample wafer and w (g) is the weight of the dry sample.

The values of $C_{\rm sw}$ are determined via Eq. (2) from the values of $A_{\rm I}$, on the basis of the spectra of the different samples shown

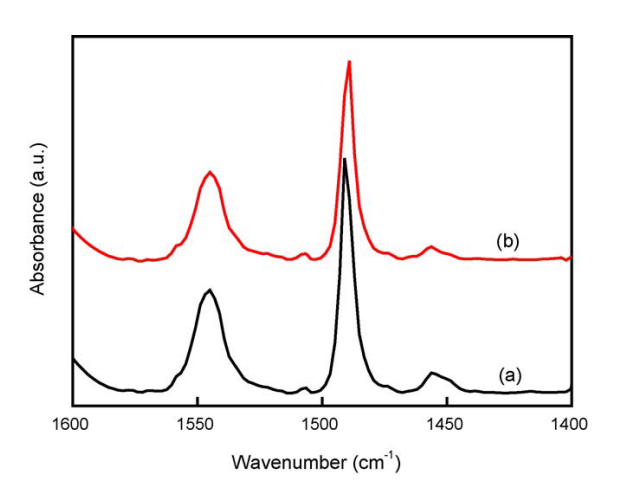


Fig. 7. IR spectra of the pyridine adsorbed on H-form ZSM-5 at (a) 473 K and (b) 623 K.

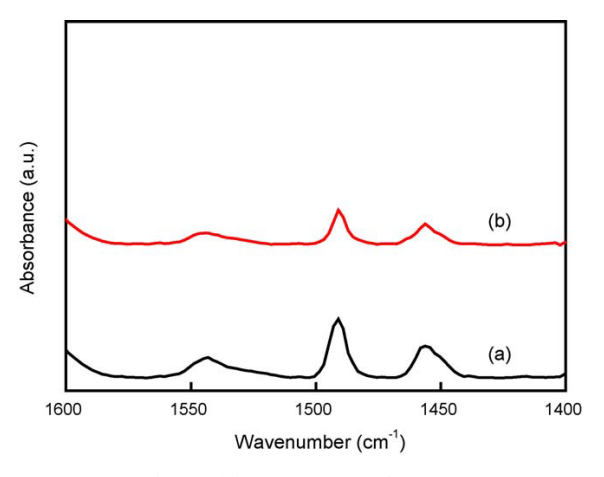


Fig. 8. IR spectra of the pyridine adsorbed on H-form SAPO-11 at (a) 473 K and (b) 623 K.

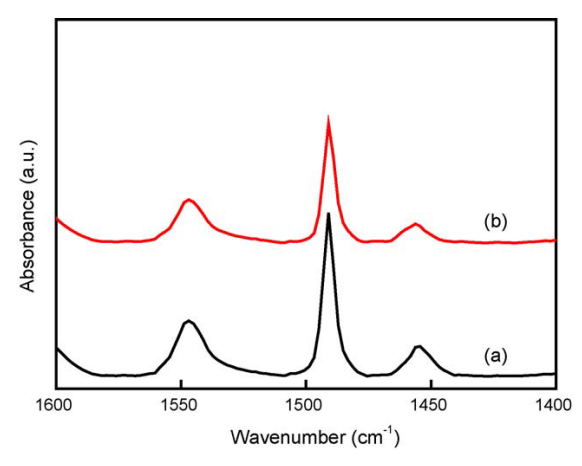


Fig. 9. IR spectra of the pyridine adsorbed on the H-form mechanical mixture at (a) 473 K and (b) 623 K.

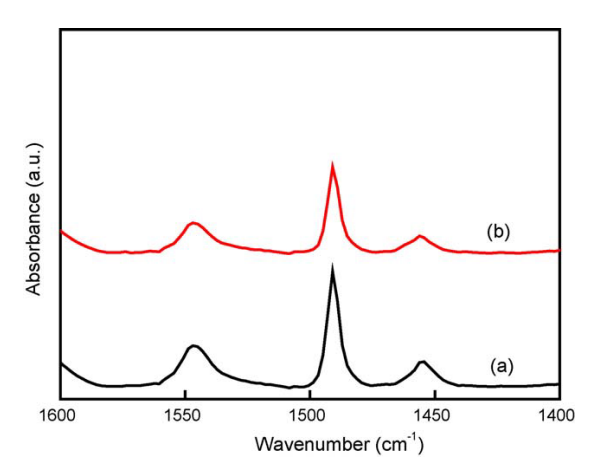


Fig. 10. IR spectra of the pyridine adsorbed on the H-form composite at (a) 473 K and (b) 623 K.

Table 4 Acidity of the samples

Samples	Acidity (µmol/g)							
	Weak acid		Medium and strong acid		Total			
	Lewis	Brönsted	Lewis	Brönsted				
ZSM-5	21.4	79.7	33.3	347.5	481.9			
SAPO-11	45.2	69.5	58.3	18.6	191.6			
Mechanical mixture	24.3	75.4	31.6	137.1	268.4			
Composite	33.8	64.7	44.6	96.1	239.2			

in Figs. 7–10 and those of ε_I relative to Brönsted and Lewis acid sites calculated according to Emeis [37]. Thus, the total Brönsted and Lewis acidity can be calculated from the IR results of pyridine adsorption at 473 K, and the medium and strong Brönsted and Lewis acidity can be obtained according to the IR spectra of pyridine adsorption at 623 K.

Table 4 gives some quantitative information about the acidic properties of the H-form samples. Among the above four samples, the total acidity is in the order of ZSM-5 \gg mechanical mixture > composite > SAPO-11; the total Lewis acidity is in the sequence of SAPO-11 > composite > mechanical mixture ≈ ZSM-5, and the total Brönsted acidity is in the order of ZSM-5 ≫ mechanical mixture > composite > SAPO-11, indicating that SAPO-11 has the most Lewis acid sites and ZSM-5 has the most Brönsted acid sites among them. As shown in Table 4, the medium and strong Brönsted acidity in ZSM-5 can be as high as up to 347.5 µmol/g, much more than the others, so the medium and strong Brönsted acidity in the mechanical mixture of ZSM-5 and SAPO-11 promptly increases from 18.6 µmol/g of SAPO-11 to 137.1 µmol/g, resulting in the great increase in the acid strength of the mechanical mixture. Compared with the mechanical mixture, the composite has moderate acid strength and an acid-type distribution that are expected to be able to enhance the synergism effect between Brönsted and Lewis acids and thus to improve the catalytic activity of the compositederived catalyst. The appropriate acidity distribution of the composite is attributed to the conversion of some Brönsted acid sites in the ZSM-5 phase into the Lewis acid sites because of the hydrothermal effect in the subsequent synthesis of SAPO-11, as explained in the literature [38]. The acidity characteristic of the composite can be also explained as follows: as shown in Fig. 3, the ZSM-5 phase is covered in part by the SAPO-11 phase in the composite, so the surface of the composite presents an acidity distribution similar to that of the SAPO-11, which leads to the large reduction in the Brönsted acidity of the composite compared with the ZSM-5 and the mechanical mixture.

3.6. Catalytic performance

By impregnating the above four H-form samples with $(NH_4)_6Mo_7O_{24}$ and $Ni(NO_3)_2$ by the fractional step method, extruding each of them with pseudoboehmite as binder, and calcining them at 773 K for 4 h, we made the four Ni–Mo catalysts supported on ZSM-5, SAPO-11, the mechanical

Table 5 Hydro-upgrading results of FCC gasoline over the four catalysts^a

	Catalyst					
	A	В	С	D		
Lumped composition of	the liquid pro	oduct (vol.%)				
n-Paraffins	11.3	12.3	11.5	9.2		
i-Paraffins	36.3	48.7	40.2	45.3		
Olefins	26.5	11.1	13.9	10.4		
Naphthenes	8.3	8.7	12.0	7.5		
Arenes	17.6	19.1	22.4	27.6		
Benzene (vol.%)	0.45	0.51	0.53	0.47		
HDS (%)	92.0	94.3	92.7	93.3		
RON	86.9	87.9	89.2	91.8		
Liquid yield (wt.%)	94	100	99	99		
Coke (mg)	41.2	3.1	16.3	5.1		

HDS: defined as the percentage conversion of total sulfur compounds in FCC gasoline. Coke: defined as the coke amount deposited on per gram catalyst.

^a Time on stream = 24 h.

mixture and the composite, respectively; they are denoted as Catalyst A, B, C and D.

The reaction performances of the four catalysts for upgrading FCC gasoline are presented in Table 5. All the four catalysts have good HDS performance (with a HDS ratio > 90%), so the emphasis of the discussion below is placed on the hydroisomerization and aromatization activities of the catalysts.

As shown in Table 5, it is evident that, after a 24 h run, the catalyst with ZSM-5 as supporter (Catalyst A) becomes inactive in aromatization and gives the lowest i-paraffins content, product RON and liquid yield among the four catalysts, due to the fact that too much medium and strong Brönsted acid sites in ZSM-5 zeolite lead to the poor stability of the catalyst [15]. The catalyst with SAPO-11 as supporter (Catalyst B) shows excellent hydroisomerization activity (giving an increment of 20.4 vol.% in the i-paraffins content compared with that of the feedstock) and the highest liquid yield (100 wt.%) because of the weaker acid strength and the more Lewis acid sites in SAPO-11 (Table 4), but suffers a product RON loss by 3.8, fully demonstrating the inability of hydroisomerization alone in preserving gasoline RON. Compared with the two catalysts above, the catalyst with the mechanical mixture as supporter (Catalyst C) provides the product with an improved product RON, but still lower than that of the feedstock; moreover, the high coke deposition may also restrict its application. The catalyst with the ZSM-5/SAPO-11 composite as supporter (Catalyst D) displays the best aromatization activity (giving an increment of 10.2 vol.% in the arenes content compared with that in the feedstock) and HDS performance (93.3%), excellent hydroisomerization activity, and superior RON preservability, illustrating the importance of aromatization in maintaining gasoline RON. In addition to the above-mentioned advantages, Catalyst D also offers higher liquid yield and lower coke deposition, presenting itself as a potential catalyst system for further commercial development, in which the long-term stability is crucial.

The superior reaction performance of Catalyst D is closely related to the specific acidity and pore structure of the composite. As shown in the above SEM images, the ZSM-5 phase is completely separate from the SAPO-11 phase in the mechanical mixture, while the two phases in the composite are intimately bonded by the interfacial effect, and thus their synergism in acidity and pore structure is enhanced. This feature of the ZSM-5/SAPO-11 composite cannot be obtained simply by mixing the same single zeolites, as proven by Guo et al. with *n*-heptane cracking as an example reaction for a Beta/MCM-41 system [39]. Therefore, there is no doubt that the ZSM-5/SAPO-11 composite is more effective for hydroupgrading FCC gasoline than the mechanical mixture.

4. Conclusions

ZSM-5/SAPO-11 composites were synthesized through in situ crystallization of SAPO-11 on ZSM-5 and applied to hydro-upgrading FCC gasoline. The SEM analysis results showed that the composites had the morphology with ZSM-5 as the core and SAPO-11 as the shell. Compared with the mechanical mixture consisting of individual ZSM-5 and SAPO-11, the composite had more mesopores favorable for the diffusion of substances and suitable acidity distribution advantageous to enhancing the synergism effect between Brönsted and Lewis acids. These two effects markedly improved the reaction performance of the composite-derived FCC gasoline hydro-upgrading catalyst. They thus provided a catalyst with balanced HDS, hydroisomerization and aromatization activities that contributed to RON preservation, high liquid yield and good stability in the case of the olefin and sulfur reduction. Such results mean that the ZSM-5/SAPO-11 composite-supported Ni-Mo catalyst could be taken as a potential catalyst system for hydro-upgrading FCC gasoline.

Acknowledgement

The authors acknowledge the financial support from the Ministry of Science and Technology of China through the National Basic Research Program (No. 2004CB217807).

References

- S. Brunet, D. Mey, G. Pérot, C. Bouchy, F. Diehl, Appl. Catal. A: Gen. 278 (2005) 143.
- [2] J. Balko, D. Podratz, J. Olesen, NPRA Annual Meeting, AM-00-14, 2000.
- [3] J.P. Greeley, NPRA Annual Meeting, AM-00-11, 2000.
- [4] J.L. Nocca, J. Cosyns, Q. Debuisschert, B. Didillon, NPRA Annual Meeting, AM-00-61, 2000.

- [5] N.P. Martinez, J.A. Salazar, G.J. Antos, M. Anand, NPRA Annual Meeting, AM-00-52, 2000.
- [6] S.S. Shih, P.J. Owens, S. Palit, D.A. Tryjankowski, NPRA Annual Meeting, AM-99-30, 1999.
- [7] D.D. Li, Y.L. Shi, Y.J. Hu, Y.B. Xi, M.F. Li, Y.H. Shi, CN Patent 1,465,666 (2002).
- [8] Y. Fan, X.J. Bao, G. Shi, W.S. Wei, J. Xu, Appl. Catal. A: Gen. 275 (2004) 61.
- [9] Y. Fan, X.J. Bao, D. Lei, G. Shi, W.S. Wei, J. Xu, Fuel 84 (2005) 435.
- [10] Y. Fan, X.J. Bao, G. Shi, W.S. Wei, J. Xu, Acta Petrol. Sin. 21 (2005) 1.
- [11] M. Sugioka, F. Sado, T. Kurosaka, X. Wang, Catal. Today 45 (1998) 327.
- [12] D. Li, H.F. Xu, G.D. Guthrie, J. Catal. 189 (2000) 281.
- [13] T. Komatsu, M. Mesuda, T. Yashima, Appl. Catal. A: Gen. 194/195 (2000) 333.
- [14] V.R. Choudhary, K. Mantri, C. Sivadinarayana, Micropor. Mesopor. Mater. 37 (2000) 1.
- [15] S.K. Sahoo, N. Viswanadham, N. Ray, J.K. Gupta, I.D. Singh, Appl. Catal. A: Gen. 205 (2001) 1.
- [16] V. Nieminen, N. Kumar, T. Heikkilä, E. Laine, J. Villegas, T. Salmi, D.Y. Murzin, Appl. Catal. A: Gen. 259 (2004) 227.
- [17] F.J. Machado, C.M. López, Y. Campos, A. Bolívar, S. Yunes, Appl. Catal. A: Gen. 226 (2002) 241.
- [18] I. Eswaramoorthi, N. Lingappan, Appl. Catal. A: Gen. 245 (2003) 119.
- [19] M. Höchtl, A. Jentys, H. Vinek, J. Catal. 190 (2000) 419.
- [20] J. Walendziewski, B. Pniak, Appl. Catal. A: Gen. 250 (2003) 39.
- [21] X.D. Huang, L.J. Wang, L.D. Kong, Q.Z. Li, Appl. Catal. A: Gen. 253 (2003) 461.
- [22] P.G. Smirniotis, L. Davydov, Catal. Rev.-Sci. Eng. 41 (1999) 43.
- [23] R.J. Pellet, P.K. Coughlin, A.R. Springer, R.T. Gajek, US Patent 4,861,739 (1989).
- [24] C.H.M. Tsang, P.S.E. Dai, R.H. Petty, US Patent 5,888,921 (1999).
- [25] B.M. Lok, C.A. Messina, R.L. Patton, R.T. Gajek, T.R. Cannan, E.M. Flanigen, US Patent 4,440,871 (1984).
- [26] A.M. Goossens, B.H. Wouters, P.J. Grobet, V. Buschmann, L. Fiermans, J.A. Martens, Eur. J. Inorg. Chem. 5 (2001) 1167.
- [27] W. Fan, R. Li, J. Ma, B. Fan, J. Cao, Micropor. Mater. 4 (1985) 301.
- [28] P.A. Jacobs, J.A. Martens, Stud. Surf. Sci. Catal. 33 (1987) 26.
- [29] O.G. Somani, A.L. Choudhari, B.S. Rao, S.P. Mirajkar, Mater. Chem. Phys. 82 (2003) 538.
- [30] M. Alfonzo, J. Goldwasser, C.M. López, F.J. Machado, M. Matjushin, B. Méndez, M.M. Ramírez de Agudelo, J. Mol. Catal. A: Chem. 98 (1995) 35
- [31] A. Karlsson, M. Stöcker, R. Schmidt, Micropor. Mesopor. Mater. 27 (1999) 181.
- [32] H.T. Liu, X.J. Bao, W.S. Wei, G. Shi, Micropor. Mesopor. Mater. 66 (2003) 117.
- [33] J.M. Campelo, F. Lafont, J.M. Marinas, Appl. Catal. A: Gen. 152 (1997) 53.
- [34] G.T. Kokotailo, S.L. Lawton, D.H. Olson, W.M. Meier, Nature 272 (1978) 437.
- [35] G. Busca, Catal. Today 41 (1998) 191.
- [36] J.A.Z. Pieterse, S. Veefkind-Reyes, K. Seshan, L. Domokos, J.A. Lercher, J. Catal. 187 (1999) 518.
- [37] C.A. Emeis, J. Catal. 141 (1993) 347.
- [38] S.M. Campbell, D.M. Bibby, J.M. Coddington, R.F. Howe, R.H. Meinhold, J. Catal. 161 (1996) 338.
- [39] W.P. Guo, L.M. Huang, P. Deng, Z.Y. Xue, Q.Z. Li, Micropor. Mesopor. Mater. 44/45 (2001) 427.



Chemical Engineering Science 61 (2006) 1459-1469

Chemical Engineering Science

www.elsevier.com/locate/ces

A scale-up strategy for low-temperature methanol synthesis in a circulating slurry bubble reactor

Kai Zhang^{a, b,*}, Yulong Zhao^b

^aState Key Laboratory of Heavy Oil Processing, University of Petroleum, Beijing, 102249, China ^bInstitute of Coal Chemistry, Chinese Academy of Sciences, Taiyuan, 030001, China

Received 5 January 2005; received in revised form 23 August 2005; accepted 26 August 2005 Available online 20 October 2005

Abstract

Slurry bubble column reactors are being increasingly utilized in the large-scale conversion of coal or natural gas to liquid hydrocarbons and alcohols. A new suite of tools for developing low-temperature methanol synthesis in circulating slurry bubble reactors is explored in this study. The scale-up strategy consisting of hydrodynamics in cold flow units, catalyst performance evaluation in an autoclave, and process investigation in a pilot-scaled circulating slurry bubble reactor is presented. This methodology should be helpful for designing and scaling-up the low-temperature methanol synthesis and other related processes in slurry bubble column reactors, which will enhance and speed them towards commercial application.

© 2005 Elsevier Ltd. All rights reserved.

Keywords: Low-temperature methanol synthesis; Circulating slurry bubble reactor; Scale-up strategy; Hydrodynamics; Catalytic reaction

1. Introduction

Methanol (MeOH) synthesis on a large scale is of interest, as a means of conversion of fossil fuel (coal and natural gas) to primary chemicals, vehicle fuel and fuel cell. Furthermore, MeOH can be transferred into liquid transportation fuels, such as Mobil's methanol-to-gasoline process. Commercial processes from syngas (CO + H₂) are still under high temperature. A typical process designed by ICI operates at 490-540 K. It is well known that the efficiency of MeOH synthesis is severely limited by thermodynamics because it is an extremely exothermic reaction (Wender, 1996; Tijm et al., 2001). For example, at 573 K and 50 bar, the theoretical maximum of a one-pass CO conversion process is around 20% (Reubroycharoen et al., 2003). Therefore, developing a low-temperature process for MeOH synthesis will greatly reduce the production cost by utilizing the intrinsic thermodynamic advantage at low temperature (Zheng et al., 2002; Zhang et al., 2003a).

0009-2509/\$ - see front matter © 2005 Elsevier Ltd. All rights reserved. doi:10.1016/j.ces.2005.08.040

An alternative method via methyl formate (MeF) at low-temperature of around 373 K in a liquid phase has been proposed by Christiansen in 1919, and has achieved great success in recent years (Sapienza et al., 1986; Liu et al., 1989, 1998; Marchionna et al., 1997, 1998; Zhao et al., 1998, 1999, 2001, 2005a,b; Lee and Aika, 1999; Li and Jiang, 1999; Linghu et al., 1999; Ohyama, 1999; Tsubaki et al., 2001; Zheng et al., 2002; Zhang et al., 2003a). This process consists of two-steps - MeOH carbonylation to MeF followed by hydrogenolysis of MeF to two MeOH molecules as shown below:

$$\begin{split} CH_3OH+CO&=HCOOCH_3,\\ HCOOCH_3+2H_2&=2CH_3OH,\\ Net \quad 2H_2+CO&=CH_3OH. \end{split}$$

The reactions can be carried out either concurrently in a single reactor or in two separate reactors (Linghu et al., 1999).

Slurry bubble columns provide many advantages over fixed bed reactors, such as simple construction and absence of moving parts, high heat and mass transfer rates, isothermal condition, and on-line catalyst addition and withdrawal (Fan, 1989; Dudukovic et al., 1999; Joshi, 2001; Zhang, 2002), which is a potential reactor for the commercial process of low temperature

^{*} Corresponding author. State Key Laboratory of Heavy Oil Processing, University of Petroleum, Beijing, 102249, China. Tel.: +86 10 89733939. *E-mail address*: kaizhang@bjpeu.edu.cn (K. Zhang).

methanol synthesis (LTMS) (Zhang et al., 2003a; Zhao et al. 2005a,b). However, a major problem to restrict its commercial application is due to the difficulty in scaling-up the results from small laboratory batch equipment, such as stirred tank, to large continuous industrial unit. Often results from small-scale test units predict reactant conversion and space-time yield, which cannot be achieved when the equipment size is increased. Fischer-Tropsch synthesis plant in Brownsville, Texas, was a representative case, which conversion was only 50% or so that obtained in laboratory units (Safoniuk et al., 1999). This is a common problem for multiphase reactors, including gas-liquid bubble column and gas-solid fluidized bed too. Some promising scale-up strategies have been provided by Horio et al. (1986), and Glickman et al. (1994) for gas-solid fluidized beds, and by Krishna et al. (1996) and Safoniuk et al. (1999) for gas-liquid-solid fluidized beds and/or slurry bubble columns. But all of the methods aforementioned were based on the hydrodynamic analogies under ambient condition without taking actual chemical reaction process into consideration. As Joshi (2001) concluded, the present design practice for multiphase systems is still closer to an art than science after more than half century of research. We believe that a sophisticated integration of the fluid dynamics in multiphase reactors together with the heterogeneous catalytic reaction behaviour is a practicable solution to this problem.

A generally used scale-up strategy for multiphase reactors makes a separation between the more chemistry oriented "Process research" and the more physics/mechanics oriented "Engineering research" (Krishna et al., 1996). Up to now, the majority of the literature concerning LTMS has been carried out in autoclaves (e.g. Sapienza et al., 1986; Liu et al., 1989; Marchionna et al., 1997, 1998; Zhao et al., 1998, 1999, 2001; Lee and Aika, 1999; Li and Jiang, 1999; Ohyama, 1999; Tsubaki et al., 2001). Accordingly, a scale-up strategy of LTMS technology in the slurry bubble reactor is provided for the future commercial process in this study, which is composed of (1) hydrodynamics in cold flow units with different column structures using different three-phase systems, (2) catalyst preparation and performance evaluation in an autoclave, and (3) process exploration in a continuous slurry bubble reactor with a capacity of two ton per year.

2. Hydrodynamics in cold flow units

To be robust and reliable, any new multi-phase reactor needs to be based on a thorough understanding of the underlying fundamentals of hydrodynamics. As MeOH synthesis is a gas volumetric contraction process, gas flow rate decreases from the bottom to the top in slurry bubble reactors. To meet this feature, experiments were designed to investigate the hydrodynamic analogies in cylindrical columns with inner diameters and heights of 0.042 m/1.5 m (CSBC1), 0.05 m/2.0 m (CSBC2) and 0.1 m/4.75 m (CSBC3), and to explore gas volumetric contraction reaction in a tapered column (TSBC), respectively. The TSBC included a conical section and a cylindrical section. The conical section was inner diameter increased from

0.10 m at the bottom to 0.20 m at the top with a height of 3.00 m. The cylindrical section located above the conical section with an inner diameter of 0.20 m and a height of 1.20 m. CSBC1 was made of glass and the others were made of Plexiglas. In the CSBC3, eight sampling tubes at 0.05, 0.20, 0.40, 0.80, 1.20, 1.60, 2.00 and 2.80 m, but seven pressure tappings at 0.05, 0.40, 0.80, 1.20, 1.60, 2.00 and 2.80 m above the distributor, respectively. In the TSBC, however, eight sampling tubes and eight pressure tappings were placed at 0.05, 0.40, 0.80, 1.20, 1.60, 2.00, 2.40 and 2.80 m above the distributor at each side of the column. The investigated systems include gas-liquid phase (air-water, nitrogen-actual liquid medium) and gas-liquid-solid phase (air-water-quartz sand, nitrogenactual liquid medium-Cu-based catalyst powder). The actual liquid medium was a mixture of sodium methoxide (CH₃ONa) solution, xylene and OP-10. Here, OP is short for polyethylene oxide alkyl phenol. A relatively detailed investigation was performed using air-water and air-water-quartz systems in CSBC3 and TSBC (Section 2.1), whilst some preliminary experiments were explored using air-water-quartz sand and nitrogen-actual liquid medium-Cu-based catalyst powder systems in CSBC1 and CSBC2 (Section 2.2).

2.1. Flow regime and three holdups using air-water/air-water-quartz system

In this section, flow regime and three holdups were investigated in detail in CSBC3 and TSBC. Axial solid concentration profile measured by the sample withdrawal method was explained in a previous paper (Zhang, 2002). Local gas holdup was obtained by pressure drop technique, whilst overall gas holdup was obtained in two ways. One method was called the weighed average method based on the data of local gas holdups. The other one was called the bed expansion technique. They appear to be in close agreement with a maximum error of $\pm 10\%$ (Zhang et al., 2003b). A perforated plate with orifice diameter of 8×10^{-4} m and open area of 0.4% was employed. It should be mentioned here that the superficial gas velocity in the TSBC is based on the cross-sectional area of the bottom of the column.

2.1.1. Flow regime and overall gas holdup

Hydrodynamics, transport and mixing properties depend strongly on the prevailing flow regime in bubble columns. Three regimes (bubbly flow, transitional flow, and turbulent flow regimes) occur in succession with increasing superficial gas velocity according to the upward movement of the bubble swarms in bubble columns. The transitional velocity decreases at the presence of solid particles and it further decreases with the increase of solid concentration. These are consistent with results in the CSBC (Fan, 1989).

Fig. 1 shows that overall gas holdup within the TSBC is smaller than that within the CSBC since the superficial gas velocity decreases progressively along the axial direction in the TSBC. In our experimental range, the effect of static height on overall gas holdup can be neglected in the CSBC. However, overall gas holdup decreases monotonically with the increase

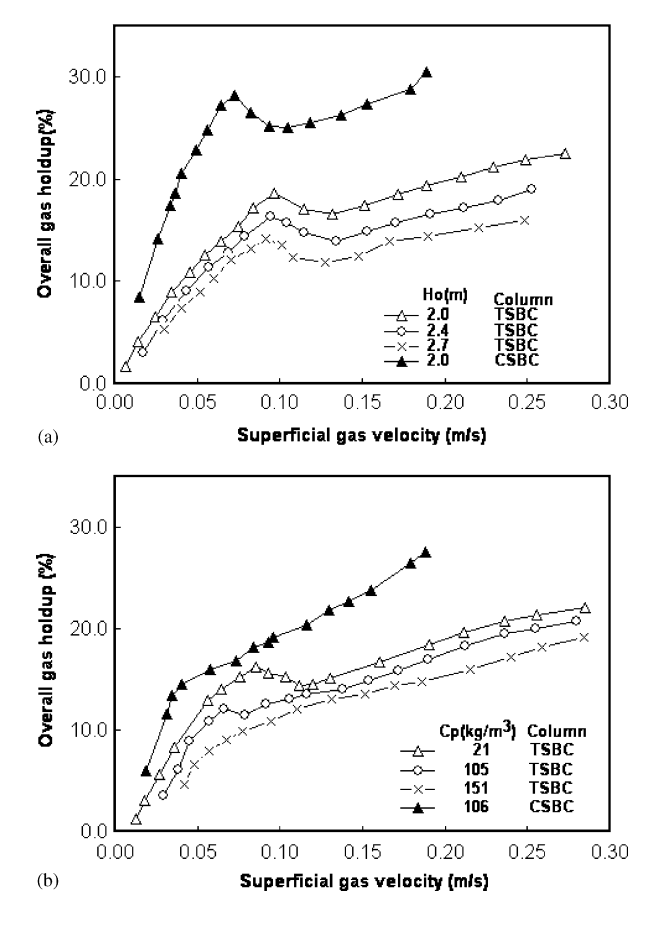


Fig. 1. Comparison of overall gas holdup in TSBC and CSBC: (a) Gas-liquid system and (b) gas-liquid-solid system.

of static height in the TSBC (see Fig. 1a). This is also attributed to gas velocity decreasing progressively in the axial direction. The overall gas holdup is reduced with the presence of solid particles and further reduces with the increase of solid concentration (see Fig. 1b). The most plausible explanation is apparent slurry viscosity increases with increasing solid concentration. The resulting bubble is of a coalescing nature, which in turn increases the size of the bubble as well as the rising velocity of the bubble.

2.1.2. Axial solid concentration profile

The sedimentation—dispersion model has been used to describe the axial profile of solid concentration in the cylindrical column since 1966 (such as by Cova, 1966). Later, Zhang (1992, 2002) extended this model to the tapered column. A more uniform concentration distribution in either CSBC or TRBC results from both an increase of solid dispersion coefficient and a decrease of solid settling velocity with increasing superficial gas velocity. The smaller the particle size, the more uniform the axial solid concentration profile (see Fig. 2a). Although the size distribution of the catalyst particles occurs in the com-

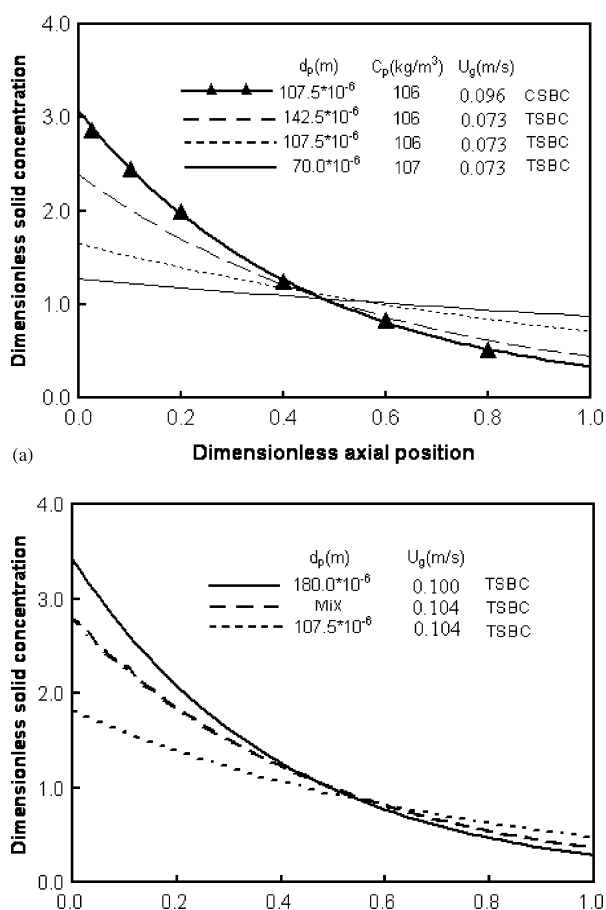


Fig. 2. Effect of particle diameter on axial solid concentration profile: (a) Mono-dispersed particle system $(H_0=1.61\,\mathrm{m})$, (b) comparison of mono-dispersed and binary particles $(H_0=2.01\,\mathrm{m},\,C_p=158\,\mathrm{kg/m}^3)$.

Dimensionless axial position

mercial reactor for LTMS process, great insight into their general behaviour can be found from investigating binary mixture. As shown in Fig. 2b, the concentration of larger particles are higher than that of smaller particles at the bottom, while the concentration of smaller particles are higher than that of larger particles at the top.

The effect of static slurry height on axial solid concentration profile in the TSBC is different from that in the CSBC. In the CSBC, the influence of the dimensionless static slurry height on axial solid concentration is too slight to be considered in our experimental range. However, as shown in Fig. 3 the gradient of axial solid concentration profile becomes steep when static slurry becomes high in the TSBC. The most probable reason is that the superficial gas velocity decreases from the bottom to the top in the TSBC.

It is clear that the TSBC can provide more uniform profile of axial solid concentration than the CSBC when their diameters

(b)

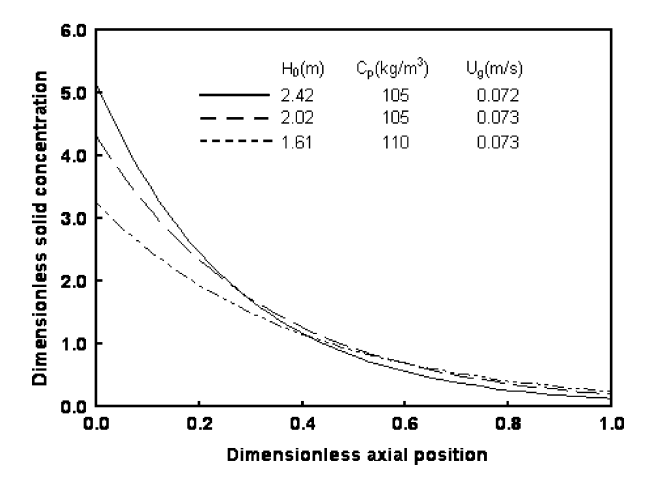


Fig. 3. Effect of static slurry height on axial solid concentration profile in the TSBC: $(d_p=180\times 10^{-6}\,\mathrm{m}).$

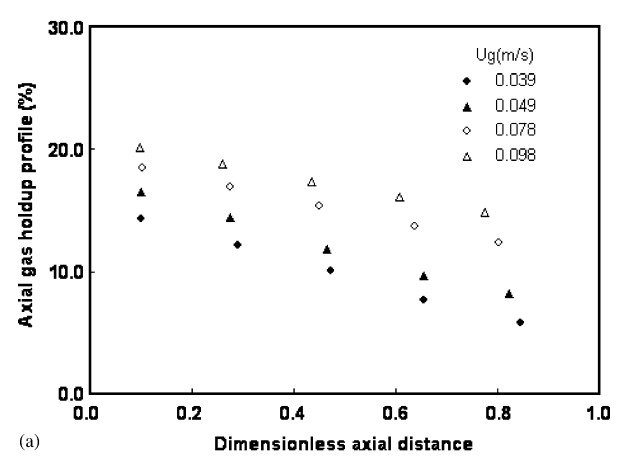
of the bottom are equal (see Fig. 2a). This fact reveals that the actual axial solid concentration distribution is more uniform than the data obtained from the conventional cylindrical column for the gas volumetric contraction reaction.

2.1.3. Axial gas holdup profile

Any system property that affects the bubble size or the bubble rising velocity will affect gas holdup because gas holdup depends on the bubble size and the bubble rising velocity. The effects of gas velocity, static slurry (liquid) height, solid concentration, and particle diameter on axial profile of gas holdup are explained below.

Similar to overall gas holdup, local gas holdup depends heavily on the prevailing flow regime. As shown in Fig. 4a, an increase in gas velocity leads to the increase of local gas holdup at any axial position and local gas holdups progressively decrease with an increase of axial height due to the reduction of gas velocity from the bottom to the top in the TSBC. The rational explanation is that bubbles rise vertically without remarkable interaction and their sizes depend on the distributor design and on the physical property of liquid in the bubbly regime while bubbles tend to coalesce or break up in the transitional or turbulent regime.

The sedimentation—dispersion model can be used to describe axial solid holdup profile in both CSBC and TSBC as mentioned above, which means that solid holdups decrease exponentially in the axial direction. As expected, gas holdups increase following an exponential curve at low gas velocity, while becoming more uniform at high gas velocity within the cylindrical column. The axial profile of gas holdups decreases with an increase of the axial position within the tapered column (see Fig. 4b). This indicates that in tapered columns the superficial gas velocity has a greater influence on the axial profile of gas holdups than solid concentration.



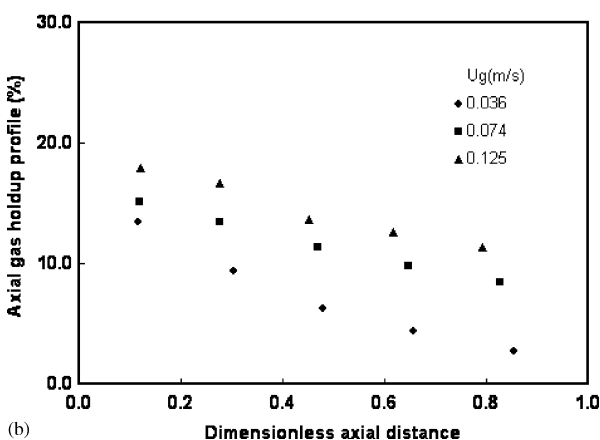


Fig. 4. Dependence of local gas holdup on the dimensionless column height in TSBC: (a) Gas-liquid system and (b) gas-liquid-solid system $(Cp=106\,\mathrm{kg/m^3})~(H_0=2.0\,\mathrm{m}).$

2.2. Preliminary fluid dynamics using air—water-quartz sand/N₂-actual liquid medium-Cu-based catalyst powder systems

Following the above section, some preliminary experiments were explored using air–water-quartz sand and N_2 -actual liquid medium-Cu-based catalyst powder systems in CSBC1 and CSBC2. Two distributors were employed, i.e., a sintered plate in CSBC1 for N_2 -actual liquid medium-Cu-based catalyst powder system and a perforated plate in CSBC2 for air–water-quartz sand system. The fluid dynamics, including the gas velocity for complete solid suspension, flow regime, phase mixing, and bubble movement behaviour, are obtained by naked eyes observation as follows:

- 1. The critical gas velocity for complete catalyst suspension in the slurry of mixture of xylene and MeONa solution was approximately 0.2 cm/s in CSBC1 (Zhao et al., 2005a), which is lower than the critical gas velocity for quartz sand in tap water.
- 2. Bubbly flow, turbulent flow, and slugging regimes occur in the order of increasing superficial gas velocity according to the upward movement of bubble swarms in the column.

- 3. At low gas velocity, bubbles are small and uniform in size. They rise vertically without remarkable interaction. Gas holdup depends mainly on superficial gas velocity and slurry concentration at the same flow regime. Generally, overall gas holdup increases with increasing superficial gas velocity and decreasing slurry concentration.
- 4. Axial solid concentration profile becomes more uniform with an increase in superficial gas velocity.
- 5. For N₂-actual liquid medium-CuCr catalyst powder system, reasonable superficial gas velocity ranged from 0.2 to 8.0 cm/s (Zhao et al., 2005a).

3. Catalyst preparation and performance evaluation in an autoclave

To grasp chemical reaction process is necessary for developing a catalytic reactor. MeOH carbonylation is a homogeneously catalyzed reaction using alkali metal methoxides as catalyst in the liquid phase, while hydrogenolysis of MeF is carried out in both gas and liquid phases using a heterogeneous copper-based catalyst. Commercial CH₃ONa was employed as carbonylation catalyst, but the Cu-based catalyst for hydrogenation was developed by our group (Zhao et al., 1998, 2001).

The solid CuCr oxide catalyst was prepared by coprecipitation with Cu(NO₃)₂, CrO₃ and aqueous ammonia under a temperature of 30 °C. Main physical properties of the solid catalyst are particle diameter (less than 44 µm), bulk density (1005 kg/m³), pore volume (0.15 mL/g), and specific surface area by BET method (56.4 m²/g). Experiments were conducted in a 1-L magnetically stirred autoclave as shown in Fig. 5. Syngas with H₂/CO ratio of 2 or so was continuous phase whilst a mixture of liquid CH₃ONa solution and solid CuCr powders was batch phase. The Cu-based catalyst was first pretreated in situ with feed syngas when the reactor was heated to the required temperature. After the autoclave was cleaned and dried, the desired amount of slurry was charged. The autoclave was then vacuumed, flushed with syngas, and pressurized to the required value at ambient temperature. The syngas from high-pressure cylinder was controlled and metered by an on-line mass flow controller and was fed into the autoclave.

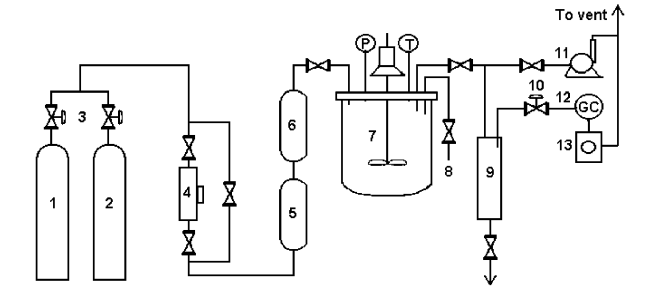


Fig. 5. A sketch of the autoclave: 1. Syngas cylinder, 2. N₂ cylinder, 3. pressure reducing regulator, 4. mass flow meter, 5. water removal 6. CO₂ removal, 7. stirred reactor, 8. liquid sampling tube, 9. chilled condenser, 10. back pressure regulator, 11. vacuum pump, 12. gas chromatograph, and 13. wet-test meter.

Table 1 GC analysis condition

	For gas composition	For liquid composition
Column dimension	3 mm(diameter) × 3000	0 mm(length)
Detector	TCD	FID
Separation column	Molecular sieve 5A	PEC, 20000/SH-101 silanized white support
Column temperature	Ambient	130 °C
Carrier gas	Ar	N_2

Table 2 Physical properties of liquid medium and their effects on CO conversion

Liquid medium	Xylene	Methanol
Density (25 °C), g/ml	0.878	0.787
Boiling point, °C	137-144	64-65
Dielectric constant	2.270-2.568	32.63
M.W.	106	32
Time on stream/h	CO conversion/%	
1	93.78	78.13
2	96.70	76.06
3	96.80	76.73
4	97.27	73.28
5	97.92	71.22

A back-pressure regulator was used to maintain the pressure inside the stirred tank. Effluent gas was withdrawn from the top of the autoclave and cooled in a high-pressure condenser, while non-condensable effluent gas was depressurized and then measured with a wet-test meter before it was vented. The composition of feed gas, tail gas, and liquid samples was determined using the same gas chromatograph but the analysis condition was different (see Table 1).

3.1. Determination of stirring speed and repetition of Cu-based catalyst preparation

The CO conversion increases with an increase of stirring speed from 600 to 1000 rpm because the contact area between gas and slurry phases increases with decreasing the size of bubble when stirring speed becomes high. Therefore, the effect of extend diffusion can be neglected when the stirring speed is greater than 1000 rpm.

The repetition of preparation is a key role for any commercially catalytic reaction process. In this section the stability of No. 202-03 solid CuCr catalyst was tested. The average error for the catalyst calcined is 3.0% with maximum error of 5.74%, and the average error of space time yield (STY) for three times experiments is within 5%, which indicates that this kind of preparation method is reliable and stable.

3.2. Effects of liquid phase medium, temperature and pressure

The reaction performance of LTMS depends upon the polarity of liquid phase reported by Onsager (1986). Two kinds of liquid media (xylene and MeOH) were employed in this study. Table 2 lists their physical properties and the effects on

Table 3 Effect of pressure on the product distribution of catalyst system, Reaction conditions: CuCr catalyst 30 g/l, MeONa $0.8\,$ mol/l, xylene $20.93\,$ NL/h $(120\,^{\circ}\text{C})$

Pressure (MPa)	CO conversion (%)	Liquid produc	t
		MeF (%)	MeOH (%)
3.5	94.99	2.01	97.99
4.7	99.13	1.99	98.01

reaction performance. It can be seen that CO conversion in xylene medium is higher than that in MeOH medium. The dielectric constant of xylene is much lower than that of MeOH. This result may be explained by solvent effects in carbonylation of methanol (Nguyen and Sridhar, 1996). Therefore, xylene was selected as liquid medium.

Temperature affects reaction rate, syngas solubility, and solution vapour pressure. According to thermodynamic theory, a decrease of temperature shifts the equilibrium composition towards the formation of MeF for MeOH carbonylation reaction. However, the rate of MeF hydrogenation is too slow at low temperature. From the viewpoint of kinetics, an increase of temperature favours the rate of a chemical reaction. As it is known that hydrogenolysis process is the essential rate-control step for LTMS, which indicates that the CO conversion increases with an increase of temperature in the range of 100–140 °C. For a commercial technology, the catalyst stability has to be taken into consideration. Accordingly, a reasonable temperature is lower than 120 °C for the actual slurry bubble reactor.

The reactive activity of the catalyst increases regularly with the increase of pressure (see Table 3). As expected, an increase of pressure is advantageous to a reaction of volume contraction such as LTMS. However, the composition of liquid products varies slightly with a change of pressure, which indicates that the almost same influence of pressure on both carbonylation and hydrogenation reaction rates.

4. Process development for LTMS in a circulating slurry bubble reactor

Once some insight into the hydrodynamics in cold flow units and the chemical reaction behaviours in an autoclave is established, next step is to design a slurry bubble column reactor under suitable operating conditions. Based on the fluid dynamics in Section 2, we have learnt that MeOH and xylene are soluble but CH₃ONa solution and xylene are insoluble in bubble columns. In this case, another medium would be required to make xylene, MeOH and CH₃ONa mix uniformly in the bubble column. OP-10 was chosen after theory analysis and experimental exploration. This phenomenon guides a mixture containing CH₃ONa solution, xylene, and OP-10 should be a relatively satisfactory liquid medium for LTMS process in slurry bubble columns. Accordingly, three phases consist of syngas with H₂/CO ratio of about 2 as the gas phase, a mixture of CH₃ONa solution, xylene and OP-10 as the liquid phase, and CuCr catalyst powders as the solid phase.

4.1. Explorative investigation in a slurry-batch bubble reactor

In order to develop a novel LTMS process in continuous slurry bubble reactors, preliminary experiments were first carried out in a slurry-batch bubble reactor of 50 mm × 5 mm diameter and 4500 mm height as schematically illustrated in Fig. 6. A sintered plate was employed as the gas distributor. Liquid and solid phases were added into the reactor before the operation, but gas phase was introduced continuously in the bottom of the reactor through the distributor during experimental process. The CuCr catalyst was thoroughly mixed with CH₃ONa solution before they were added in the middle of the column, then a part of OP-10 was introduced at the same position. Finally, xylene mixed with the left OP-10 was added at the top of the column. When the reactor was heated to the required temperature, the syngas from high-pressure cylinders was controlled and metered by an on-line mass flow meter. It was fed into the reactor after oxygen, water and CO2 were absorbed on molecular seizes 13X and 5A. The system was pressurized at the required temperature. Two pressure regulators were installed before the syngas entered the reactor and after the tail gas left the product receiver, respectively, which can control the pressure inside the bubble column reactor. The effluent gas from the top of the reactor was cooled by water. Condensed liquid product was collected into the product receiver. After being depressurized, the non-condensable gas from the top of the product receiver was metered by an on-line wet-test meter. The majority of the non-condensable was vented whilst the other was collected into a gas holder for gas analysis (Zhao et al., 2005a). The compositions of feed gas, tail gas and liquid product were analyzed by gas chromatography as depicted in Section 3.

As a case study, Fig. 7 shows syngas conversion varies with time on stream. The trend of syngas conversion decreases with increasing reaction time, and the syngas conversion is lower than 40% after 8 hours of the beginning operation. Average CO conversion is about 78% within 9h. Liquid compositions in the upper part of the reactor and in the product receiver are

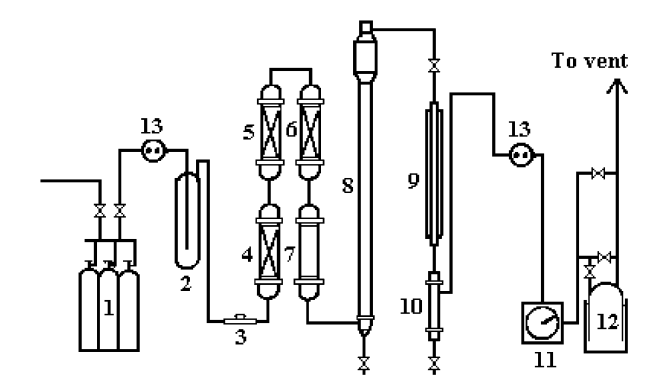


Fig. 6. A sketch of the slurry-batch bubble column reactor: 1. Syngas cylinders, 2. pressure buffer tank, 3. mass flow meter, 4. oxygen removal, 5. water removal, 6. CO₂ removal, 7. preheater, 8. slurry bubble reactor, 9. water condenser, 10. product receiver, 11. wet-test meter, 12. gas holder, and 13. pressure regulators.

listed in Table 4. The ratio of MeOH to MeF is much higher in the product receiver than that in the upper section of the reactor. According to the chemical equilibrium of two-step MeOH synthesis, there exists a synergy of the process coupling carbonylation and hydrogenolysis reactions. It is necessary for the two-step LTMS technology to have optimum MeOH and MeF concentrations or a suitable concentration ratio of MeOH to MeF. Accordingly, MeOH and MeF should be partly removed from the reactor during operation. Furthermore, it is engineering requirement that liquid product have to be separated from the slurry in the reactor. These two issues suggest that an integrated process of reaction and separation is a potential technology for a commercial LTMS process. A circulating slurry bubble reactor system, consisting of bubble column reactor, separator and slurry recycle unit, is a relatively reasonable method for the synergy of coupling two-step MeOH synthesis.

4.2. Process development of LTMS in a continuous slurry bubble reactor

Based on the hydrodynamic experiments in different slurry bubble columns under ambient condition (Section 2), heterogeneous catalytic reaction behaviour of two-step LTMS in an autoclave (Section 3) and an explorative investigation in a slurrybatch bubble reactor (Section 4.1), a continuous circulating

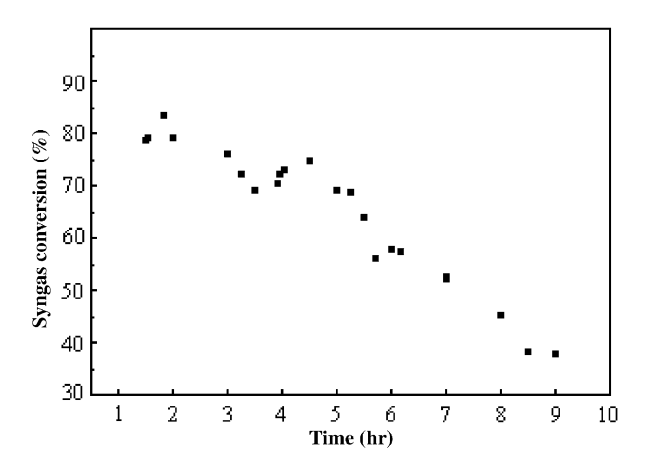


Fig. 7. Variation of syngas conversion with time on stream. Reaction conditions: CuCatE cat $120\,\mathrm{g}$, CH₃ONa $685\,\mathrm{mL}$ (5.25 N), OP-10 $400\,\mathrm{mL}$, Xylene $3400\,\mathrm{mL}$; $90\,^\circ\mathrm{C}$, $4.8\,\mathrm{MPa}$, $\mathrm{SV}100^{-1}$, $\mathrm{H}_2/\mathrm{CO} = 2$, flow rate $0.5\,\mathrm{m}^3/\mathrm{h}$.

Table 4
Liquid compositions in the upper section of the reactor and in the product receiver

	Xylene (%)	МеОН (%)	MeF (%)	Ratio of MeOH to MeF
In the upper of the reactor	59.74	26.16	7.39	1:0.28
In the product receiver		61.36	2.76	1:0.045

slurry bubble reactor with a capacity to 2 tons per year, made of stainless steel, is conceptually illustrated in Fig. 8. Table 5 lists their main geometry. A detailed explanation can be found in a previous paper (Zhang et al., 2003a). Gas—liquid—solid system was syngas/liquid-phase medium/Cu-based catalyst powders. The syngas with an approximate stoichiometric ratio for methanol synthesis ($H_2/CO \approx 2$) was used as the gaseous reactant. The liquid medium used was a mixture containing sodium methoxide, xylene, and OP-10.

Before the run, the trapped air in the system was purged with N₂ or syngas and vented to desired purity. Then both liquidphase medium and Cu-based catalyst were added into the system. The syngas with $H_2O < 380 \,\mathrm{mg/m^3}$ and $CO_2 < 100 \,\mathrm{ppm}$ from high-pressure cylinders was controlled and metered by an on-line mass flow meter. It was fed into the bottom of the bubble reactor after water and CO₂ were respectively removed less than 5 and 10 ppm by sample analysis technique. We managed the feed flow rate from 0.52 to 0.56 Nm³/hr. The system was pressurized at ambient temperature. Two back-pressure regulators were installed to maintain the pressure in both the bubble reactor and the separator. Then the slurry pump was started at the recycle flow rate of 0.05 m³/h with a fluctuation of less than 10%. Reactant gas, recycle slurry, and the reaction section in the bubble reactor were heated to the required temperatures by two preheaters and three electric heating coils. When the reaction section reached the desired temperature, it was taken as the start time of the operation. The main temperatures and pressures in the system are listed in Table 5. The effluent gas from the top of the separator was defoamed by a filter, cooled by water, and further cooled by ice, while the effluent gas from the top of the bubble reactor was only cooled by water. The condensed liquid was separated in the expansion vessels and was collected into product receivers. After being depressurized, the non-condensable gas from the expansion vessels was metered by an on-line wet-test meter and vented. The compositions of feed gas, tail gas and liquid product were analyzed by gas chromatography as depicted in Section 3. Two continuous 100-h runs were accomplished in this investigation. The compositions of gas, liquid medium and solid catalyst are listed in Table 6.

4.2.1. Per-pass conversion

The per-pass conversions of CO can be estimated by the following method:

$$X_{\text{CO}} = \frac{V_0 C_0 - V_1 C_1 - V_2 C_2}{V_0 C_0} \times 100\%,$$

where, X_{CO} , V and C are the conversion of CO, the volumetric flow rate, and the volumetric concentration of CO, respectively. Subscript 0 stands for the feed gas, 1 for the effluent gas from the top of the bubble reactor and 2 for the effluent gas from the top of the separator.

In order to control a suitable range of slurry heights in the reactor and separator, the flow rates of recycle slurry and effluent gases had to be adjusted according to operating conditions. In addition, some unexpected troubles, such as valve failure, line blockage, and the slurry pump pause, were met

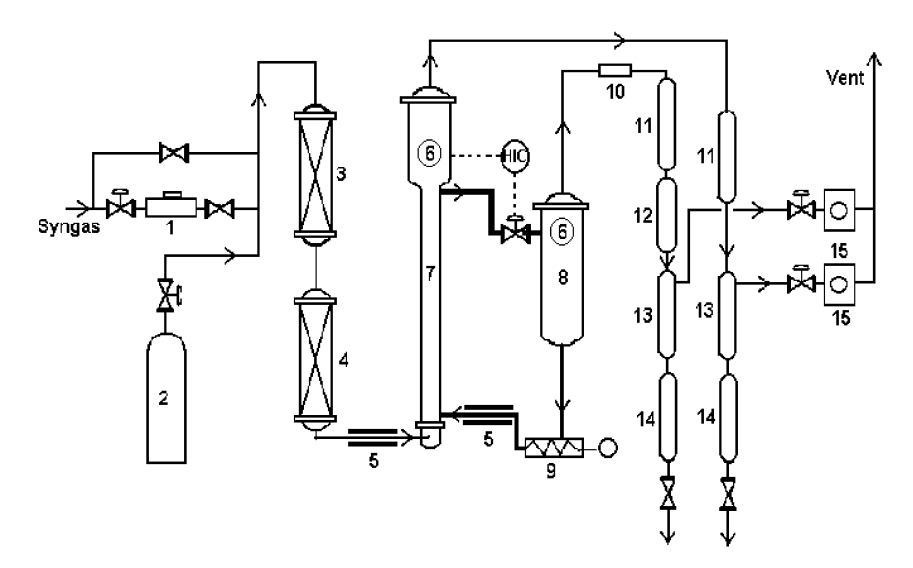


Fig. 8. A sketch of the circulating slurry reactor: 1. Mass flow meter, 2. N₂ cylinder, 3. water removal, 4. CO₂ removal, 5. preheaters, 6. magnetic liquid level indicators, 7. bubble reactor, 8. separator, 9. slurry recycle pump, 10. filter, 11. water condensers, 12. chilled condenser, 13. expansion vessels, 14. product receivers and 15. wet-test meters.

Table 5
Main geometry and operating conditions

	Geometry	Geometry		Pressure (MPa)	
	Diameter (mm)	Height (m)			
Cylindrical section of	f the bubble reactor				
•	45×3	4.8	80-120	4.2-4.6	
Enlarged section of the	he bubble reactor				
· ·	159 × 6	1.2	80–100	4.2-4.6	
Separator	159×6	1.64	70–90	0.3-0.5	

Table 6 Composition of feeds

Run no.	The composition of slurry	The composition of slurry						
	CH ₃ ONa solution* (L)	Xylene (L)	Op-10 (L)	Total liquid (L)	Cu-based Cat			
1	3.50	14.02	2.48	20.00	600			
2	4.08	15.58	2.51	22.17	700			
	The mean composition of syngas (vol%)							
	H_2	CO	CH_4					
No. 1	68.81	30.14	1.05					
No. 2	68.94	30.64	0.42					

^{*}Note: Solvent, methanol; CH₃ONa concentration, 26.1%; NaOH concentration, 0.4%.

during two 100-h operations. These situations would cause sharp fluctuations of per pass conversions. A five-point median filter that the central point is replaced by the median value of five consecutive data points (Harris et al., 2003) is used to process the original experimental data in this study. As an example, Fig. 9 plots the per-pass conversions of CO and $\rm H_2$ during Run No. 2. CO conversion keeps almost constant for

50 h or so, and then it decreases gradually with increasing reaction time. It is clear that the stability of the catalyst system is poor although its initial activity is quite high. However, the circulating slurry bubble reactor has an advantage over a slurry-batch bubble reactor, seen by comparing Fig. 7 with Fig. 9, which indicates that the circulating slurry bubble system, consisting of reactor, separator and slurry recycle pump,

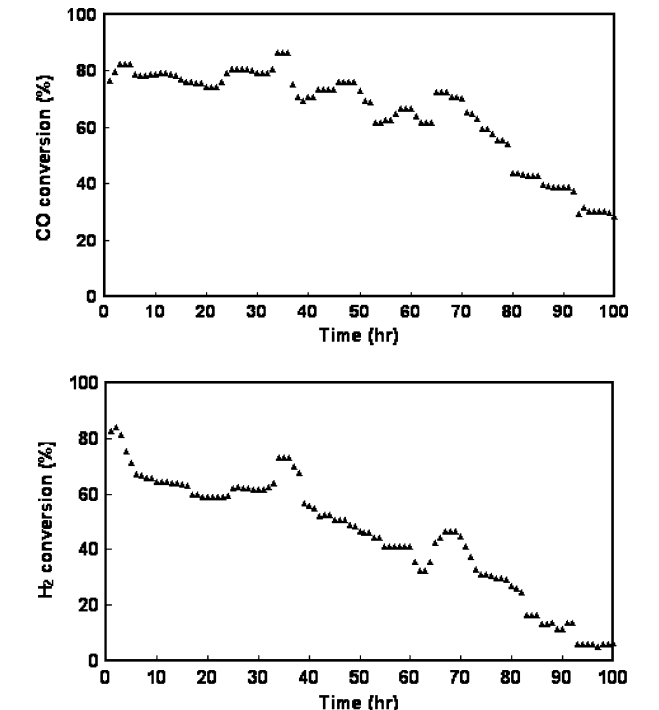


Fig. 9. CO and H₂ per-pass conversions (Run no. 2).

is a potentially commercial LTMS process to deal with a synergy of MeOH carbonylation and MeF hydrogenolysis reactions as well as liquid product separation from the slurry in the reactor.

4.2.2. Effects of operating conditions and axial concentration profile

The effects of temperature and pressure on per-pass conversion were tested during the steady operation. It was the same as in the autoclave and slurry-batch bubble reactor, conversion of CO, $\rm H_2$ or syngas increased with increasing pressure and temperature in the slurry-continuous bubble reactor.

Solid concentration decreases exponentially from the bottom to the top in bubble columns based upon the sedimentation-dispersion model in Section 2.1.2. Three samples were obtained from the different axial position in the cylindrical section of the bubble reactor just before shutdown and catalyst concentrations presented nearly uniform profile. This result comes from the small diameter of catalyst, a high ratio of liquid density to solid density, and high slurry circulating velocity. The relatively uniform catalyst concentration in the slurry bubble reactor is helpful to remove the reaction heat, especially for strong exothermal reaction.

4.2.3. Compositions of liquid product and slurry remaining

After the shutdown, the condensed liquid product and the slurry remaining in the circulating slurry bubble reactor were analyzed using the gas chromatograph aforementioned. As listed in Table 7, the composition of liquid product consisted

Table 7
Composition of the condensed liquid product (wt%)

Run no.	МеОН	MeF	DME	Ratio of MeOH to MeF
No. 1	79.52	19.25	1.23	1:0.24
No. 2	82.16	17.04	0.80	1:0.21

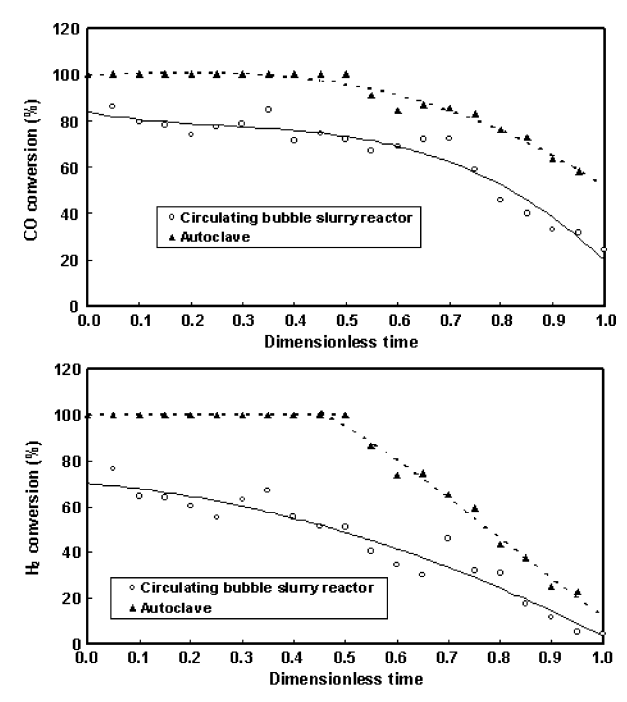


Fig. 10. Comparison of per-pass conversion in different reactors.

of MeOH, MeF, and DME (dimethyl ether). The selectivity of product, including MeOH and MeF, was greater than 98% and the ratio of MeOH to MeF in the product receiver was close to that in the upper section in the slurry-batch column reactor as listed in Table 4, which also shows a circulating slurry bubble reactor has advantage over a slurry-batch bubble reactor. Moreover, about 5% (wt%) MeF was found in the slurry remains. This value was less than in the liquid product.

4.3. Evaluation in a stirred reactor

In order to evaluate the feasibility of the circulating slurry reactor for LTMS process, parallel experiments were conducted in a 1-L magnetically stirred autoclave. The experimental set-up used the same as that in Section 3, but the operating condition was the same as in Section 4.2.

Fig. 10 compares per-pass syngas conversions for Run 2 in the circulating bubble reactor to the autoclave. It was surprising that there was no effluent gas from the autoclave at the beginning of the reaction period. The reason was that the initial activity of catalyst was so high that the system pressure decreased sharply and was lower than the designed

back pressure value. It was found that the effluent gas from the separator was strongly affected by the recycle flow rate of slurry. The unreacted syngas was dissolved into the bulk slurry in the bubble reactor under high pressure and then degassed, together with the gaseous products, from the slurry in the separator under low pressure. The scale-up efficiency of the circulating slurry bubble reactor was about 80% of that achieved in the autoclave although the recycle flow rate used in this circulating bubble reactor was about 10 times higher than the design parameter of a commercial process because of the limitation of the slurry pump. Furthermore, OP-10 was added in the circulating bubble column reactor, but it was absent in the autoclave. Zhao et al. (2005b) reported that OP-10 influences the reaction behaviour of LTSM. This influence needs to be further investigated in future work.

5. Conclusion

A scale-up strategy for LTMS in bubble column reactors is provided, which separates the more physics/mechanics oriented "Engineering research" and the more chemistry oriented "Process research". The roadmap is illustrated as below:

- hydrodynamics in cold-model slurry bubble columns (Engineering Research),
- catalyst performance in an autoclave (Process Research),
- probing the operating conditions in a slurry-batch pilot installation.
- 2 continuous 100-h runs in a 2 T/a circulating slurry bubble reactor based on the fundamental investigation in the above three aspects (Engineering Research + Process Research) and.
- evaluating in a stirred reactor.

We have shown that an advanced scale-up method for slurry bubble column reactors is very promising to support LTMS technology towards commercialization process, although the catalysts were deactivated in a short period in both the slurry bubble reactors and autoclave. This requires that catalyst system with stable activity be developed in the near future.

Looking ahead, it is clear that the intensification of R&D for LTMS in slurry bubble column reactors will continue, under the ever-increasing pressure from the market to increase the speed of innovation and to reduce the cost of technology commercialization. The pressure will further enhance the already strong role of the scale-up strategy in the work process, leading to more directed experimentation, more efficient data sampling technique, more fundamentally oriented calculational method, and more all-encompassing optimization tool.

Notation

C volumetric concentration of CO

 C_p average solid concentration in the slurry, mass per

volume, kg (solid)/m³(slurry)

 d_p particle diameter, m

 H_0 static liquid (slurry) height based on the distributor,

m

 U_g superficial gas velocity, m/s V volumetric flow rate, NL/h

 $X_{\rm CO}$ CO conversion

Subscripts

) feed gas

1 effluent gas from the top of the bubble reactor

effluent gas from the top of the separator

Acknowledgements

Financial support from Major State Basic Research Development Program of China (973 Program, 2005CB221205), Scientific Research Foundation for the Returned Overseas Chinese Scholars, State Education Ministry (2004-527), Chinese Academy of Sciences, and National Natural Science Foundation of China (No. 29136015) is gratefully acknowledged. Kai Zhang is a former student of Professor Bijiang Zhang and has received excellent guidance during his studies. Kai has enjoyed many formal and informal discussions on the application of multiphase reactors into the arena of chemical, energy and environmental engineering. Kai would also like to acknowledge the kind hospitality of Professors Rex Thorpe and John Davidson whilst he wrote part of this paper at the Department of Chemical Engineering, University of Cambridge supported by Royal Society Royal Fellowship.

References

Cova, D.R., 1966. Catalyst suspension in gas-agitated tubular reactors. I & EC Process Design and Development 5 (1), 20–32.

Dudukovic, M.P., Larachi, F., Mills, P.L., 1999. Multiphase reactors revisited. Chemical Engineering Science 54 (13–14), 1975–1995.

Fan, L.S., 1989. Gas-Liquid-Solid Fluidization Engineering. Butterworth, Stoneham, MA.

Glickman, L.R., Hyre, M.R., Farell, P.A., 1994. Dynamic similarity in fluidization. International Journal of Multiphase Flow 20S, 331–386.

Harris, A.T., Davidson, J.F., Thorpe, R.B., 2003. The influence of the riser exit on the particle residence time distribution in a circulating fluidised bed riser. Chemical Engineering Science 58 (16), 3669-3680.

Horio, M., Nonaka, A., Sawa, Y., Muchi, I., 1986. A new similarity rule for fluidised bed scale-up. A.I.Ch.E. Journal 32, 1466-1482.

Joshi, J.B., 2001. Computational flow modelling and design of bubble column reactors. Chemical Engineering Science 56, 5893–5933.

Krishna, R., Ellenberger, J., Sie, S.T., 1996. Reactor development for conversion of natural gas to liquid fuels: a scale-up strategy relying on hydrodynamic analogies. Chemical Engineering Science 51 (10), 2041–2050.

Lee, E.S., Aika, K., 1999. Low-temperature methanol synthesis in liquid-phase with a Raney Nickel-alkoxide system: effect of Raney Nickel pretreatment and reaction conditions. Journal of Molecular Catalysis A 141 (1–3), 241–248

Li, K., Jiang, D., 1999. Methanol synthesis from syngas in the homogeneous system. Journal of Molecular Catalysis 147 (1-2), 125-130.

Linghu, W., Liu, Z., Zhu, Z., Yang, J., Zhong, B., 1999. Methanol synthesis in an integrated two-stage reactor. Chemical Engineering Science 54 (15–16), 3671–3675.

- Liu, X., Wu, Y., Chen, W., Yu, Z., 1998. Concurrent synthesis of methanol and methyl formate catalyzed by copper-based catalysts in a slurry phase. Studies in Surface Science and Catalysis 119, 557-560.
- Liu, Z., Tierney, J.W., Shah, Y.T., Wender, I., 1989. Methanol synthesis via methyl formate in a slurry reactor. Fuel Processing Technology 23, 149–167.
- Marchionna, M., Lami, M., Galletti, A.M.R., 1997. Synthesizing methanol at lower temperatures. Chemical Technology 27 (4), 27–31.
- Marchionna, M., Girolamo, M.D., Tagliabue, L., Spangler, M.J., Fleisch, T.H., 1998. A review of low temperature methanol synthesis. Studies in Surface Science and Catalysis 119, 539–544.
- Nguyen, D.A., Sridhar, T., 1996. Solvent effects in the carbonylation of methanol. Industrial Engineering Chemistry Research 35, 3044–3054.
- Ohyama, S., 1999. Low-temperature methanol synthesis in catalytic systems composed of nickel compounds and alkali alkoxides in liquid phases. Applied Catalysis A: General 180 (1–2), 217–225.
- Onsager, T.O., 1986. Process for the preparation of methanol in liquid phase, WO 8603190.1986-06-05.
- Reubroycharoen, P., Yamagami, T., Vitidsant, T., et al., 2003. Continuous low-temperature methanol synthesis from syngas using alcohol promoters. Energy & Fuels 17, 817–821.
- Safoniuk, M., Grace, J.R., Hackman, L., McKnight, C.A., 1999. Use of dimensional similitude for scale-up of hydrodynamics in three-phase fluidised beds. Chemical Engineering Science 54, 4961–4966.
- Sapienza, R.S., Slegeir, W.A., O'Hare, T.E., Mahajan, D., 1986. US Patent 4614749.
- Tijm, P.J.A., Waller, F.J., Brown, D.M., 2001. Methanol technology developments for the new millennium. Applied Catalysis A: General 221, 275–282.
- Tsubaki, N., Ito, M., Fujimoto, K., 2001. A new method of low-temperature methanol synthesis. Journal of Catalysis 197 (1), 224–227.

- Wender, I., 1996. Reactions of synthesis gas. Fuel Processing Technology 48, 189–297
- Zhang, K., 1992. Investigation on fluid dynamics in bubble slurry columns, M. Engineering Thesis, Institute of Coal Chemistry, Chinese Academy of Sciences, China (in Chinese).
- Zhang, K., 2002. Axial solid concentration distribution in tapered and cylindrical bubble columns. Chemical Engineering Journal 86, 299–307.
- Zhang, K., Song, H.S., Sun, D.K., et al., 2003a. Low-temperature methanol synthesis in a circulating slurry bubble Reactor. Fuel 82 (2), 233–239.
- Zhang, K., Zhao, Y., Zhang, B., 2003b. Gas holdup characteristics in a tapered bubble column. International Journal of Chemical Reactor Engineering 1, S3.
- Zhao, Y., Bai, L., Hu, Y., Zhong, B., Peng, S., 1998. Performance of CuCr/CH3ONa catalyst system for low temperature methanol synthesis in slurry phase. Journal of Fuel Chemistry & Technology 26 (6), 497–500 (in Chinese).
- Zhao, Y., Bai, L., Hu, Y., Zhong, B., Peng, S., 1999. Catalytic performance of CuCr/CH3ONa used for low temperature methanol synthesis in slurry phase. Journal of Nature Gas Chemistry 8 (3), 181–187.
- Zhao, Y., Bai, L., Hu, Y., Su, X., 2001. Comparison of performance of CuCr/CH3ONa catalytic systems for low temperature methanol synthesis in slurry phase. Journal of Fuel Chemistry & Technology 29 (4), 360–362 (in Chinese).
- Zhao, Y., Huang, Z., Wu, Y., 2005a. Exploration of low temperature methanol synthesis in bubble column slurry reactors. Journal of Fuel Chemistry & Technology 33(6), accepted for publication (inChinese).
- Zhao, Y., Huang, Z., Zhang, K., Li, S., 2005b. Investigation of low temperature methanol synthesis in a bubble column slurry reactor with a flash column. Fuel Process Technology, accepted for publication.
- Zheng, J., Tsubaki, N., Fujimoto, K., 2002. The promoting effect of alcohols in a new process of low-temperature synthesis of methanol from CO/CO2/H2. Fuel 81 (1), 125–127.



Chemical Engineering Science 61 (2006) 1401-1420

Chemical Engineering Science

www.elsevier.com/locate/ces

Computational fluid dynamics (CFD) modeling of spouted bed: Assessment of drag coefficient correlations

Wei Du^a, Xiaojun Bao^{a, b, *}, Jian Xu^b, Weisheng Wei^b

^aState Key Laboratory of Heavy Oil Processing, China University of Petroleum, Beijing 102249, PR China ^bThe Key Laboratory of Catalysis, China National Petroleum Co., China University of Petroleum, Beijing 102249, PR China

Received 3 March 2005; received in revised form 5 July 2005; accepted 6 August 2005 Available online 11 October 2005

Abstract

In the computational fluid dynamics (CFD) modeling of gas-solids two-phase flows, drag force is the only accelerating force acting on particles and thus plays an important role in coupling two phases. To understand the influence of drag models on the CFD modeling of spouted beds, several widely used drag models available in literature were reviewed and the resulting hydrodynamics by incorporating some of them into the CFD simulations of spouted beds were compared. The results obtained by the different drag models were verified using experimental data of He et al. [He, Y.L., Lim, C.J., Grace, J.R., Zhu, J.X., Qin, S.Z., 1994a. Measurements of voidage profiles in spouted beds. Canadian Journal of Chemical Engineering 72 (4), 229–234; He, Y.L., Qin, S.Z., Lim, C.J., Grace, J.R., 1994b. Particle velocity profiles and solid flow patterns in spouted beds. Canadian Journal of Chemical Engineering 72 (8), 561–568.] The quantitative analyses showed that the different drag models led to significant differences in dense phase simulations. Among the different drag models discussed, the Gidaspow (1994. Multiphase Flow and Fluidization, Academic Press, San Diego.) model gave the best agreement with experimental observation both qualitatively and quantitatively. The present investigation showed that drag models had critical and subtle impacts on the CFD predictions of dense gas-solids two-phase systems such as encountered in spouted beds.

Keywords: Drag force; CFD modeling; Spouted beds; Gas-solids two-phase flow

1. Introduction

Spouted beds, originally invented in Canada by Mathur and Gishler (1955) as an alternative to fluidized beds for handling coarse particles, are now widely applied in various physical operations such as drying, coating and granulation. The distinctive advantages of spouted beds as reactors for various chemical processes are also well recognized in recent years. In addition to their ability to handle coarse particles, spouted beds also possess certain structural and flow characteristics that are very desirable in some chemical reaction systems. For example, the toroidal nature of particle motion in spouted beds makes it possible to

E-mail address: baoxj@cup.edu.cn (X. Bao).

0009-2509/\$ - see front matter © 2005 Elsevier Ltd. All rights reserved. doi:10.1016/j.ces.2005.08.013

recirculate heat in an organized manner, thus leading to extended ranges of flammability, enhanced reaction rates, and super-adiabatic temperatures, considerably higher than the adiabatic flame limit of premixed reactants for a given preheat temperature (Weinberg et al., 1988). Consequently, increasing attention has been paid to the application of spouted beds as chemical reactors, including as combustion reactors (Arbib and Levy, 1982; Khoshnoodi and Weinberg, 1978; Konduri et al., 1995, 1999; Lim et al., 1988; Vuthaluru and Zhang, 2001a,b; Weinberg et al., 1988), coal gasification reactors (Arnold et al., 1992; Song and Watkinson, 2000; Sue-A-Quan et al., 1995; Tsuji and Uemaki, 1994), catalytic partial oxidation reactors (Marnasidou et al., 1999; Wei et al., 2003), catalytic oxidative coupling reactors (Do et al., 1995; Mleczko and Marschall, 1997), catalytic polymerization reactors (Olazar et al., 1997), and pyrolysis reactors (Aguado et al., 2000; Olazar et al., 2000; Uemura et al., 1999a,b). While promising results have been reported in

^{*}Corresponding author. The Key Laboratory of Catalysis, China National Petroleum Co., China University of Petroleum, Beijing 102249, PR China. Tel.: +8610 89734836; fax: +8610 89734979.

bench- and pilot-scale spouted bed reactors, the information on the development of spouted beds as chemical reactors is inadequate. One such inadequacy is that abundant results now available in literature are derived from experiments under ambient conditions, whereas most of the spouted beds as chemical reactors should be operated at elevated temperature and pressure, such as in coal gasification and methane partial oxidation.

In addition to the experimental works as summarized by Mathur and Epstein (1974) and Epstein and Grace (1997), now there is a growing interest to use computational fluid dynamics (CFD) methods to explore the possibility of spouted beds as chemical reactors (Huilin et al., 2001; Kawaguchi et al., 2000; Krzywanski et al., 1992). The two most commonly used methods for modeling gas-solids two-phase systems are the discrete element method (DEM) and the twofluid model (TFM). In the DEM approach, the gas phase is described by a locally averaged Navier-Stokes equation, the motion of individual particles is traced, and the two phases are coupled by interphase forces. For the TFM approach, the different phases are mathematically treated as interpenetrating continua, and the conservation equation for each of the two phases is derived to obtain a set of equations that have similar structure for each phase. Both of the two approaches are adopted in spouted bed modeling. Krzywanski et al. (1992) developed a multi-dimensional model to describe the gas and particle dynamic behavior in a spouted bed. Kawaguchi et al. (2000) proposed an Eulerian-Lagrangian approach, the three-dimensional motion of solids was discretely traced by solving Newton's equation of motion using the DEM. Huilin et al. (2001) presented a two-fluid gas-solids flow model for spouted beds, viewing spout and annulus as two interconnected regions. Huilin et al. (2004) also incorporated a kinetic-frictional constitutive model for dense assemblies of solids in the simulation of spouted beds. The model treated the kinetic and frictional stresses of particles additively.

From the point of view of computation, the TFM approach is much more feasible for practical applications to complex multiphase flows, therefore extensive attention has been given to improving its accuracy. The success of the TFM depends on the proper description of the solid stress and the interfacial forces. By introducing the concepts of solid "pressure" and "viscosity", the well-known granular kinetic theory has been well established and now has being widely employed for the solid stress calculation. However, less effort was made to the study of the interfacial forces in the past.

The interfacial forces include drag force, lift force and virtual mass force, etc. In coupling the equations of the two phases, due to the large difference in their densities, those forces other than drag force are less significant, and thus can be usually neglected. Consequently, in most reports, whenever the interfacial forces were dealt with, only drag force was considered. Some authors had noticed that the choice of drag models played a critical role in simulat-

ing gas-solids two-phase flows. Yasuna et al. (1995) showed that the solution of their model was sensitive to the values of drag coefficients. O'Brien and Syamlal (1993) suggested that the drag force correlations for fine particles should be corrected to account for the formation of clusters. Enwald et al. (1996) found that the predictions based on different drag models were in good agreements with each other for the dilute region, but obviously different for the dense region. van Wachem et al. (2001) noticed that flow predictions were not sensitive to the use of different solid stress models or radial distribution functions, as the different approaches were very similar in dense flow regimes, but the application of different drag models significantly impacted the flow of the solid phase. More or less, these results signify that an improper choice of drag models may yield inaccurate results or even lead to incorrect descriptions of gas-solids two-phase flows. Unfortunately, by digging out in literature, we found that a detailed examination to the effect of drag models on CFD modeling seems unavailable.

In spouted bed systems, the volume fraction of particles can vary from almost zero to the maximum packing limit, leading to much more complex behavior of drag forces than that in normal fluidization systems. By incorporating various drag models into the two-fluid model, the present study is conducted with the aim of fully understanding the influence of the choice of drag models on simulation and thereby laying a basis for the CFD modeling of spouted beds.

2. Model equations

It is well known that the gas-solids flow in a spouted bed can be divided into three zones: the spout zone in the bed center, where the spouting gas and particles rise at high velocity and the particle concentration is low; the annulus zone between the spout and the wall, where particles move slowly downwards; and the fountain zone where the particles rise to their highest position and then rain back to the surface of the annulus. Thus, a cyclic pattern of solids movement is established.

In the present investigation, the TFM approach is adopted to model the complex gas—solids flow in a spouted bed. By the TFM approach, the two-phase in spouted beds is treated as interpenetrating continua by incorporating the concept of phase volume fractions. The volume fractions represent the space occupied by each phase, and the laws of mass and momentum conservation are satisfied by each phase individually.

2.1. Conservation equations of mass and momentum

The volume fraction balance equation is (q = g, s):

$$\sum_{q=1}^{n} \alpha_q = 1. \tag{2.1}$$

The mass conservative equation for phase q (q = g, s) is

$$\frac{\partial}{\partial t}(\alpha_q \rho_q) + \nabla \cdot (\alpha_q \rho_q \overrightarrow{v}_q) = 0. \tag{2.2}$$

The momentum conservative equation for phase q (q = g, s) is

$$\begin{split} &\frac{\partial}{\partial t} (\alpha_{q} \rho_{q} \overrightarrow{v}_{q}) + \nabla \cdot (\alpha_{q} \rho_{q} \overrightarrow{v}_{q} \overrightarrow{v}_{q}) \\ &= -\alpha_{q} \nabla P + \nabla \cdot \overline{\overline{\tau}}_{q} + \sum_{p=1}^{n} \overrightarrow{R}_{pq} + \alpha_{q} \rho_{q} \\ &\times (\overrightarrow{F}_{q} + \overrightarrow{F}_{\text{lift},q} + \overrightarrow{F}_{vm,q}), \end{split} \tag{2.3}$$

where \overrightarrow{F}_q is the external body force, $\overrightarrow{F}_{\text{lift},q}$ is the lift force, $\overrightarrow{F}_{vm,q}$ is the virtual mass force, and \overrightarrow{R}_{pq} is the interaction force between the two phases. In this investigation, only drag force and gravity are considered with the lift force and virtual mass force neglected.

2.2. Kinetic theory of granular flow equations

Closure of the solid phase momentum equation requires a description of the solid phase stress. The granular kinetic theory derived by Lun et al. (1984) is adopted in this study.

Analogous to the thermodynamic temperature for gases, the granular temperature Θ_s can be introduced as a measure of the particle velocity fluctuations, i.e.,

$$\Theta_s = \frac{1}{3}(v_s^2). \tag{2.4}$$

The solid phase stress depends on the magnitude of the particle velocity fluctuations. The granular temperature conservative equation is

$$\frac{3}{2} \left[\frac{\partial}{\partial t} (\rho_s \alpha_s \Theta_s) + \nabla \cdot (\rho_s \alpha_s \overrightarrow{v}_s \Theta_s) \right] \\
= (-p_s \overline{\overline{I}} + \overline{\overline{\tau}}_s) : \nabla \overrightarrow{v}_s - \nabla (k_{\Theta_s} \nabla \Theta_s) \\
- \gamma \Theta_s + \phi_{is}, \tag{2.5}$$

where $(-p_s\overline{1}+\overline{\tau}_s):\nabla\overrightarrow{v}_s$ is the generation of energy by the solid stress tensor, $k_{\Theta_s}\nabla\Theta_s$ is the diffusion of energy (k_{Θ_s}) is the diffusion coefficient), $\gamma\Theta_s$ is the collisional dissipation of energy, $\gamma\Theta_s=((12(1-e_{ss}^2)g_{0,ss})/d_p\sqrt{\pi})\rho_s\alpha_s^2\Theta_s^{3/2}$, and $\phi_{gs}=-3\beta_{gs}\Theta_s$ is the energy exchange between fluid and solid phase.

The solid pressure is given by (Lun et al., 1984)

$$P_s = \alpha_s \rho_s \Theta_s + 2\rho_s (1 + e_{ss}) \alpha_s^2 g_{0,ss} \Theta_s, \tag{2.6}$$

where $g_{0,ss}$ is the radial distribution function expressed by

$$g_{0,ss} = \left[1 - \left(\frac{\alpha_s}{\alpha_{s,\text{max}}}\right)^{1/3}\right]^{-1}.$$
 (2.7)

The solid bulk viscosity is given as (Lun et al., 1984)

$$\lambda_{s} = \frac{4}{3} \alpha_{s}^{2} \rho_{s} d_{p} g_{0,ss} (1 + e_{ss}) \sqrt{\frac{\Theta_{s}}{\pi}}.$$
 (2.8)

The solid shear viscosity is given by Ding and Gidaspow (1990) as follows:

$$\begin{split} \mu_{s} &= \frac{4}{5} \alpha_{s}^{2} \rho_{s} d_{p} g_{0,ss} (1 + e_{ss}) \sqrt{\frac{\Theta_{s}}{\pi}} \\ &+ \frac{10 \rho_{s} d_{p} \sqrt{\pi \Theta_{s}}}{96 (1 + e_{ss}) g_{0,ss}} \left[1 + \frac{4}{5} g_{0,ss} \alpha_{s} (1 + e_{ss}) \right]^{2}. \end{split} \tag{2.9}$$

2.3. Turbulence model

Turbulence predictions for the continuous phase are obtained using the standard k– ε model supplemented with extra terms dealing with the interphase turbulent momentum transfer.

The Reynolds stress tensor for the continuous phase is

$$\overline{\overline{\tau}}_{q}^{"} = -\frac{2}{3} (\rho_{g} k_{g} + \rho_{g} \mu_{t,g} \nabla \cdot \overrightarrow{U}_{g}) \overline{\overline{I}}
+ \rho_{g} \mu_{t,g} (\nabla \cdot \overrightarrow{U}_{g} + \nabla \cdot \overrightarrow{U}_{g}^{T}),$$
(2.10)

where $\mu_{t,q}$ is the turbulent viscosity.

Turbulence predictions of the continuous phase are obtained from the modified k– ε model expressed by Eqs. (2.11) and (2.12).

$$\begin{split} &\frac{\partial}{\partial t} (\alpha_g \rho_g k_g) + \nabla \cdot (\alpha_g \rho_g \overrightarrow{U}_g k_g) \\ &= \nabla \cdot \left(\alpha_g \frac{\mu_{t,g}}{\sigma_k} k_g \right) + \alpha_g G_{k,g} - \alpha_g \rho_g \varepsilon_g \\ &+ \alpha_g \rho_g \Pi_{k,g} \end{split} \tag{2.11}$$

$$\frac{\partial}{\partial t} (\alpha_{g} \rho_{g} \varepsilon_{g}) + \nabla \cdot (\alpha_{g} \rho_{g} \overrightarrow{U}_{g} \varepsilon_{g})$$

$$= \nabla \cdot \left(\alpha_{g} \frac{\mu_{t,g}}{\sigma_{z}} \varepsilon_{g} \right) + \alpha_{q} \frac{\varepsilon_{q}}{k_{q}} (C_{1} G_{k,q} - C_{2} \rho_{g} \varepsilon_{g})$$

$$+ \alpha_{v} \rho_{g} \Pi_{\tau,g}, \tag{2.12}$$

where $\Pi_{k,g}$ and $\Pi_{z,g}$ represent the influence of the dispersed phase on the continuous phase.

Predictions for the turbulence quantities of the dispersed phase are obtained using the Tchen theory of dispersion of discrete particles by homogeneous turbulence (Hinze, 1975). These turbulence quantities include

$$k_s = k_g \left(\frac{b^2 + \eta_{sg}}{1 + \eta_{sg}} \right), \tag{2.13}$$

$$k_{sg} = 2k_g \left(\frac{b + \eta_{sg}}{1 + \eta_{sg}}\right),\tag{2.14}$$

$$D_{t,sg} = \frac{1}{3} k_{sg} \tau_{t,sg}, \tag{2.15}$$

$$D_s = D_{t,sg} + (\frac{2}{3}k_s - b\frac{1}{3}k_{sg})\tau_{F,sg}, \tag{2.16}$$

$$b = (1 + C_V) \left(\frac{\rho_s}{\rho_g} + C_V \right)^{-1}, \tag{2.17}$$

where C_V in Eq. (2.17) is the added-mass coefficient, equal to 0.5. And $\tau_{F,sg}$ in Eq. (2.16) is the characteristic particle relaxation time connected with inertial effects acting on a dispersed phase. $\tau_{t,sg}$ in Eq. (2.15) is the Lagrangian integral time scale calculated along particle trajectories.

2.4. Drag models

Generally, the drag force acting on a particle in fluid–solids systems can be represented by the product of a momentum transfer coefficient β and the slip velocity $(\overline{v} - u)$ between the two phases:

$$f_{\text{drag}} = \frac{3}{4} C_D \frac{\alpha_s \rho_g}{d_p} |\overline{v} - u| f(\alpha_g)(\overline{v} - u) = \beta(\overline{v} - u). \quad (2.18)$$

The correlations of β are usually obtained from pressure drop measurements in fixed, fluidized, or settling beds. For the motion of particle swarms, however, it has been found that the volume fraction of the particle phase has a complex and subtle influence on drag force.

An earlier drag model was proposed by Richardson and Zaki (1954)

$$\beta = \frac{\rho_s \alpha_g g}{u_t \alpha_e^{n-1}},\tag{2.19}$$

where the exponent n depends on the Reynolds number based on the terminal velocity of an isolated particle. Garside (1977) gave

$$\frac{5.1 - n}{n - 2.7} = 0.1 \, Re_t^{0.9}. \tag{2.20}$$

This expression is still widely used by many researchers (Burger et al., 2000; Ocone et al., 1993; Sinclair and Jackson, 1989)

By extending the work of Richardson and Zaki (1954), Wen and Yu (1966) presented a correlation for high void fraction ($\alpha_s \ge 0.8$):

$$\beta = \frac{3}{4} C_D \frac{\alpha_s \rho_g}{d_p} |\bar{v} - u| \alpha_g^{-2.65}, \tag{2.21}$$

Gidaspow et al. (e.g., Ding and Gidaspow, 1990) employed the Ergun (1952) equation for dense phase calculation and the Wen–Yu (1966) equation for dilute phase calculation:

$$\begin{split} \beta_{\text{Ergun}} &= 150 \frac{\alpha_s^2 \mu_g}{\alpha_g d_p^2} + 1.75 \frac{\alpha_s \rho_g}{d_p} |\overline{v} - u|, \quad \alpha_g < 0.8, \\ \beta_{\text{Wen-Yu}} &= \frac{3}{4} C_D \frac{\alpha_s \rho_g}{d_p} |\overline{v} - u| \alpha_g^{-2.65}, \quad \alpha_g \geqslant 0.8, \end{split} \tag{2.22}$$

where drag coefficient C_D was expressed by

$$C_D = \begin{cases} \frac{24}{\alpha_g Re_p} [1 + 0.15(\alpha_g Re_p)^{0.687}], & Re_p < 1000\\ 0.44, & Re_p \ge 1000 \end{cases}$$
(2.23)

$$Re_p = \frac{\rho_g |\overline{v} - u| d_p}{\mu_g}.$$
 (2.24)

This kind of treatment has been widely adopted in the CFD modeling of gas-solids fluidized beds (Hoomans et al., 1996; Kawaguchi et al., 1998; Mikami et al., 1998; Pita and Sundaresan, 1991, 1993). To avoid the discontinuity of the two equations, Gidaspow (1994) introduced a switch function that gave a rapid transition from one regime to the other

$$\varphi_{gs} = \frac{\arctan[150 \times 1.75(0.2 - \alpha_s)]}{\pi} + 0.5. \tag{2.25}$$

Thus, the momentum transfer coefficient can be expre-

$$\beta = (1 - \varphi_{gs})\beta_{\text{Ergun}} + \varphi_{gs}\beta_{\text{Wen-Yu}}.$$
 (2.26)

According to Eq. (2.26), the momentum transfer coefficient β can be rewritten as

$$\beta = \frac{3}{4} C_D \frac{\alpha_s \rho_g}{d_p} |\overline{v} - u| f(\alpha_s). \tag{2.27}$$

Di Felice (1994) gave a newer form of the factor $f(\alpha_s)$

$$f(\alpha_s) = \alpha_g^{-x},\tag{2.28}$$

where x is an empirical coefficient depending on the particle Reynolds number (Re_P)

$$x = 3.7 - 0.65 \exp[-\frac{1}{2}(1.5 - \log_{10} Re_p)^2],$$
 (2.29)

$$C_D = \left(0.63 + 4.8/\sqrt{Re_P}\right)^2. \tag{2.30}$$

Syamlal and O'Brien (1988) proposed a model of the two-phase drag coefficient based on measurements of the terminal velocities of particles in fluidized or settling beds in the form

$$\beta = \frac{3}{4} \frac{C_D}{f^2} \frac{\rho_g |\overline{v} - u|}{d_p} \alpha_g \alpha_s, \tag{2.31}$$

$$C_D = \left(0.63 + 4.8\sqrt{f/Re_t}\right)^2,$$
 (2.32)

where f is the ratio of the falling velocity of a suspension (superficial) to the terminal velocity of a single particle. Here, the expression due to Garside and Al-Dibouni (1977) was used.

$$f = 0.5 \left(A - 0.06 Re + \sqrt{(0.06 Re)^2 + 0.12 Re(2B - A) + A^2} \right), \quad (2.33)$$

$$A = \alpha_{g}^{4.14}$$
.

$$B = \begin{cases} \alpha_g^{2.65}, & \alpha_s < 0.15, \\ 0.8\alpha_g^{1.28}, & \alpha_s \ge 0.15. \end{cases}$$
 (2.34)

This expression is also widely adopted by researchers (van Wachem et al., 1998, 1999).

Arastoopour et al. (1990) proposed a gas-solids drag coefficient model that gave continuous values over all ranges of solid volume fractions, Enwald et al. (1996) used this model in their work

$$\beta = \left[\frac{17.3}{Re_p} + 0.336 \right] \frac{\rho_g}{d_p} |\overline{v} - u| \alpha_s \alpha_g^{-2.8}, \tag{2.35}$$

$$Re_p = \frac{d_p |\overline{v} - u| \rho_g}{\mu_g}.$$
 (2.36)

In addition to these correlations, many other correlations are also available in literature, such as

(1) Louge et al. (1991) model:

$$\beta = \frac{3}{4} C_D \frac{\rho_g |\overline{v} - u|}{d_p} \alpha_s, \tag{2.37}$$

$$C_D = \frac{24}{Re_p} (1 + 0.15 Re_p^{0.687}), \quad 0 < Re_p < 800.$$
 (2.38)

(2) Gibilaro et al. (1985) model:

$$\beta = \left[\frac{17.3}{Re_P} + 0.336\right] \frac{\rho_g}{d_P} |\overline{v} - u| \alpha_s \alpha_g^{-1.8}, \tag{2.39}$$

where

$$Re_{P} = \frac{d_{P}\alpha_{g}|\overline{v} - u|\rho_{g}}{2\mu_{g}}.$$
 (2.40)

(3) Nieuwland et al. (1994) model:

$$\beta = \frac{3}{4} C_D \frac{\alpha_s \rho_g}{d_p} |\overline{v} - u| f(\alpha_s), \tag{2.41}$$

$$f(\alpha_s) = \begin{cases} \frac{1}{0.997 + 442.35\alpha_s - 1733.42\alpha_s^2}, & \alpha_s < 0.1276, \\ \frac{1}{29.22}, & \alpha_s \geqslant 0.1276. \end{cases}$$
(2.42)

(4) Andrews and O'Rourke (1996) model:

$$\beta = C_D \frac{3}{8} \frac{\rho_g}{\rho_s} \frac{|\overline{v} - u|}{R_P},\tag{2.43}$$

$$C_D = \frac{24}{Re} \left(\alpha_g^{-2.65} + \frac{Re^{2/3}}{6} \alpha_g^{-1.78} \right), \tag{2.44}$$

$$Re = \frac{2\rho_g|\overline{v} - u|R_p}{\mu_g},\tag{2.45}$$

$$R_P = \left(\frac{3V_p}{4\pi}\right)^{1/3}. (2.46)$$

(5) Zhang and Reese (2003) model:

$$\beta = \begin{cases} 150 \frac{\alpha_s^2 \mu_g}{\alpha_g d_p^2} + 1.75 \frac{\alpha_s \rho_g}{d_p} U_r, & \alpha_s < 0.8, \\ \frac{3}{4} C_D \frac{\alpha_s \rho_g}{d_p} U_r \alpha_g^{-2.65}, & \alpha_s \geqslant 0.8. \end{cases}$$
 (2.47)

$$U_r = \left[(\overline{v} - u)^2 + \frac{8T}{\pi} \right]^{1/2}, \tag{2.48}$$

$$C_D = \left(0.28 + \frac{6}{\sqrt{Re_P}} + \frac{21}{Re_P}\right). \tag{2.49}$$

One of the difficulties encountered in the simulation of circulating fluidized beds (CFBs) is the prediction of the clustering effect. The terminal velocity of a cluster usually exceeds the terminal velocity of a single particle. By introducing a correction factor *Rt*, O'Brien and Syamlal (1993) obtained a correlation that took into account the clustering effect:

$$f_{\text{clus}} = Rt \left\{ 1 + C Re_p \,\alpha_g \, \exp[-0.005(Re_p - 5)]^2 -90(Re_p - 0.92)^2 \right\}. \tag{2.50}$$

Yang et al. (2003) proved that the drag coefficient of particles was reduced if they were grouped in aggregates by using the EMMS (energy-minimization multi-scale) model. They proposed a new approach to calculate drag coefficient. To embed the approach into the TFM, they derived a new correlation according to the EMMS model.

$$\omega = \begin{cases} -0.5760 + \frac{0.0214}{4(\alpha_g - 0.7463)^2 + 0.0044}, & (0.74 \leqslant \alpha_g \leqslant 0.82), \\ -0.0101 + \frac{0.0038}{4(\alpha_g - 0.7789)^2 + 0.0040}, & (0.82 \leqslant \alpha_g \leqslant 0.97), \\ -31.8295 + 32.8295\alpha_g, & (\alpha_g \geqslant 0.97), \end{cases}$$

$$(2.51)$$

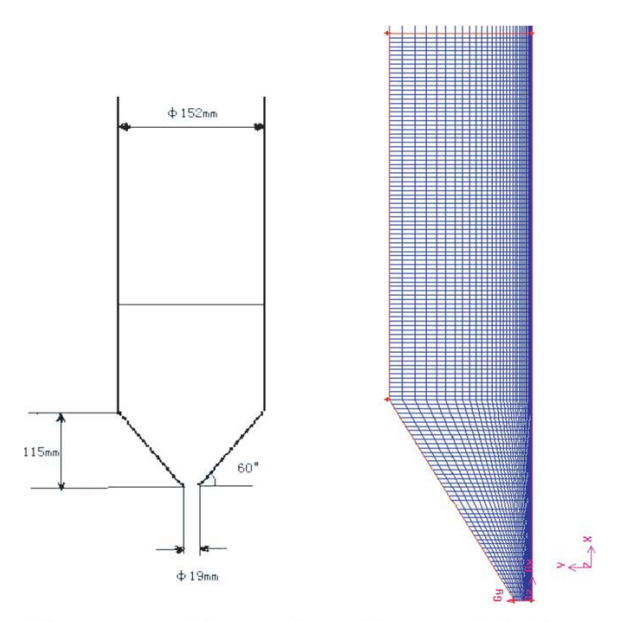
where ω is the correction factor of drag coefficients. Then, the drag model can be rewritten as

$$\beta = \begin{cases} 150 \frac{\alpha_s^2 \mu_g}{\alpha_g d_p^2} + 1.75 \frac{\alpha_s \rho_g}{d_p} | \overline{v} - u|, & \alpha_s < 0.74, \\ \frac{3}{4} \frac{\alpha_s \alpha_g}{d_p} \rho_g | \overline{v} - u | C_D \omega, & \alpha_s \geqslant 0.74. \end{cases}$$

$$(2.52)$$

The model was said to be capable of reflecting the real mechanisms of gas-solids interactions.

In this study, the most commonly used Richardson and Zaki (1954), Gidaspow (1994), Syamlal and O'Brien (1988), Di Felice (1994) and Arastoopour et al. (1990) models are selected to examine their influence on CFD modeling.



The geometry of the vessel

The numerical grids

Fig. 1. Geometry of the spouted bed (He et al. 1994a,b) and numerical grids used.

Table 1
The experimental conditions used by He et al. (1994a,b)

Parameter	Description	Spouted bed used by He et al. (1994a,b)
$\rho_s (\text{kg/m}^3)$	Solid density	2500
$\rho_g (\text{kg/m}^3)$	Gas density	1.225
μ_g (Pas)	Gas viscosity	1.7894E-05
d_P° (mm)	Particle diameter	1.41
e_{ss}	Particle restitution coefficient	0.9
$\alpha_{s, \max}$	Maximum solid packing volume fraction	0.59
H_m (mm)	Packing bed height	325
D_c (mm)	Column diameter	152
D_i (mm)	Orifice diameter	19

3. Model solution procedure

In the present investigation, the experimental results obtained by He et al. (1994a,b) in a spouted bed (Fig. 1) with the geometry described in Table 1 are adopted to validate the model predictions. Using optical fiber probe systems, He et al. (1994a,b) measured the voidage profiles and the vertical particle velocity profiles in the spout, annulus and the fountain regions of the spouted bed. The gas they used was air and the solids were glass beads. The corresponding experimental conditions are also listed in Table 1.

The commercial CFD simulation package FLUENT 6.1 is used to simulate the hydrodynamics of the spouted bed.

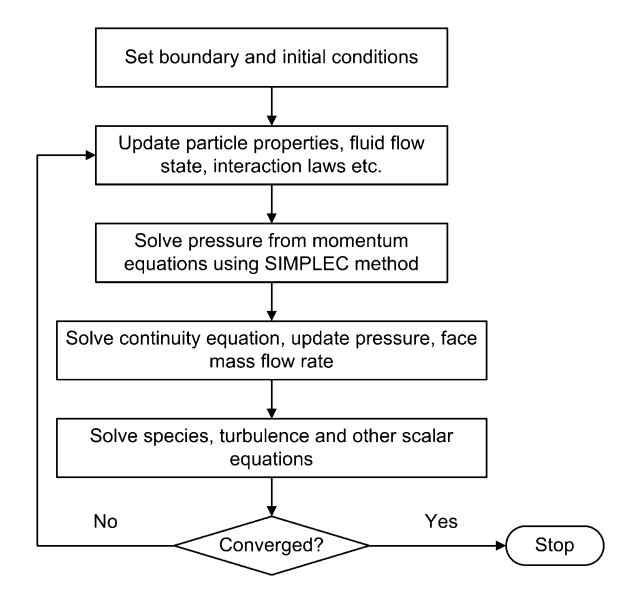


Fig. 2. Flow sheet of the simulation algorithm.

The set of governing equations are solved by a finite control volume technique. The pressure–velocity coupling is obtained using SIMPLEC algorithm. The two-dimensional axial symmetry is assumed. The grid in the computation domain is showed in Fig. 1. The computation needs 8 s real time for the spouted bed to reach at its steady-state, and the time intervals used in the first 2000 steps are $1\times 10^{-3}\,\mathrm{s}$, and in the remaining 3000 steps $2\times 10^{-3}\,\mathrm{s}$. The simplified flow sheet of the simulation algorithm is shown in Fig. 2.

The boundary conditions are as follows:

- (1) at the entrance, the gas injects only in the axial direction, so the inlet gas velocity condition is: $u_{x,0} = 64$ U and $u_{y0} = 0$;
- (2) at the outlet, an outflow boundary condition is given, the velocity gradient is zero, i.e., $\partial u_x/\partial x = 0$;
- (3) on the wall, a no slip boundary condition is assumed.

4. Results and discussion

4.1. Quantitative analysis of the drag models

The drag functions as a function of solids volume fraction based on the different drag models are calculated and plotted in Fig. 3. The calculations are made with the relative interstitial velocity at 10.0 m/s (which is typical in the spout region) and the particle diameter and Reynolds number 1.41 mm and 953, respectively. Fig. 3 shows that in dilute region (solids volume fraction < 0.2), all drag models except for the Richardson and Zaki (1954) model give nearly identical results. When the solids volume fraction is increased

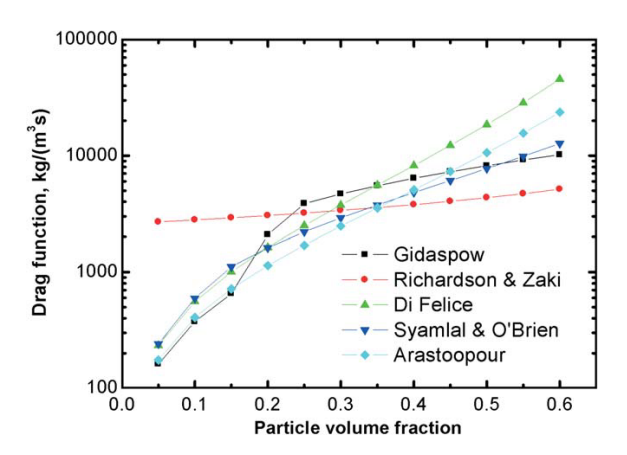


Fig. 3. Comparison of drag models.

up to 0.2, their differences emerge: (1) the drag function based on the Richardson and Zaki (1954) model is insensitive to solids volume fraction; (2) that based on the Di Felice (1994) model rapidly increases with increasing solids volume fraction, a similar tendency exists for the Arastoopour et al. (1990) model when solids volume fraction is higher than 0.45; (3) those based on the Gidaspow (1994) model and the Syamlal and O'Brien (1988) model are very close and show a smoothly increasing tendency with the increasing solids volume fraction. It is also observed that the drag functions obtained by the Gidaspow (1994) model and by the Syamlal and O'Brien (1988) model intersect each other with solids volume fraction at ca. 0.18 and 0.52, respectively, within this range the drag function curve by the Syamlal and O'Brien (1988) model is below that by the Gidaspow (1994) model. These results reflect that the differences in drag functions are mainly caused by the different varying trends of α_g with increasing solids fraction. It is also noted that when the particle volume fraction is between 0.18–0.35, the Gidaspow (1994) model gives the highest estimation of the drag function. As mentioned before, the solids volume fraction in spouted beds can vary from almost zero to the maximum packing limit, so the choice of drag models may have a profound influence on the CFD simulation of spouted beds.

Obviously, the differences among the drag models mainly occur when the solids volume fraction is higher than 0.2 which is the typical solids volume fraction in spouted beds except in the region near the orifice, signifying that the accuracy of the prediction in dense region accounts for the simulation differences. Enwald et al. (1996) made a similar comparison for a system of 0.7 mm particles operating at a relative interstitial velocity of 1.0 m/s, and their results also showed that differences emerged in dense region. However, Yasuna et al. (1995) found that this trend was not so obvious for Geldart B particles unless the solids volume fraction was close to the maximum packing limit.

4.2. Effect of the choice of drag models on simulated flow patterns

With the inlet gas jetting velocities at 0.594, 0.648, and $0.702\,\text{m/s}$, respectively, the flow patterns simulated using different drag coefficient correlations at the time 8 s after the gas is introduced to the spouted bed are presented in Figs. 4-8.

Figs. 4 and 7 show that by the Richardson and Zaki (1954) model and Di Felice (1994) model, the fountain is formed at low gas spouting velocity, but the inner void center is unstable, presenting itself more or less like a bubble/slug flow. By the Gidaspow (1994) model, as shown in Fig. 5, the spout, annulus and fountain can be clearly visualized and the spouting is stably established. By Syamlal and O'Brien (1988) model, as shown in Fig. 6, and by Arastoopour et al. (1990) model, as shown in Fig. 8, the spouting onsets at a gas velocity of 0.704 and 0.594 m/s, respectively. By comparing to the experimental minimum spouting velocity 0.54 m/s reported by He et al. (1994a,b), it can be seen that the two drag coefficient models underestimate the gas-solids drag of the spouted bed system. It can be observed that at a little higher gas velocity than the experimental value a good recirculation of particles is established, and the three flow regions can be clearly observed.

The results stated above reveal that the choice of drag models can significantly affect the simulated flow patterns. It seems that both under- and over-estimations of drag coefficients in the dense phase bring about the deviation of the flow pattern from stable spouting operation, resulting in a bubble/slug flow pattern. For dense phase systems, van Wachem et al. (2001) showed that the Syamlal and O'Brien (1988) model led to lower predictions of pressure drop and bed expansion, in good agreement with our results.

The gas-solids two-phase contacting operations can be classified to several kinds of flow regimes, such as fixed bed, bubbling fluidization, slugging fluidization, fast fluidization and turbulent fluidization, etc., each of the regimes occurs over a definite range of gas velocities and gas and solid properties. Grace (1986) gave a phase diagram by plotting dimensionless gas velocity vs. dimensionless particle diameter. The phase diagram showed that the spouted bed regime occurred only in a very limited region. Many other researchers obtained their phase diagrams by plotting bed depth vs. gas velocity (Becker, 1961; Mathur and Epstein, 1974; Pallai and Nemeth, 1969) to represent the flow transitions to the spouted bed regime. These studies showed that there exist a minimum spouting velocity and a maximum spouting velocity only between which stable spouting takes place. Beyond this region, the stable spouting may be replaced by poor quality fluidization or directly transforms from the quiescent to the aggregative fluidization state. As discussed above, the use of the different drag models in the CFD modeling of the spouted bed can bring about significantly different predictions of drag force acting on particles, similar to that arisen by increasing gas velocity, i.e., gas

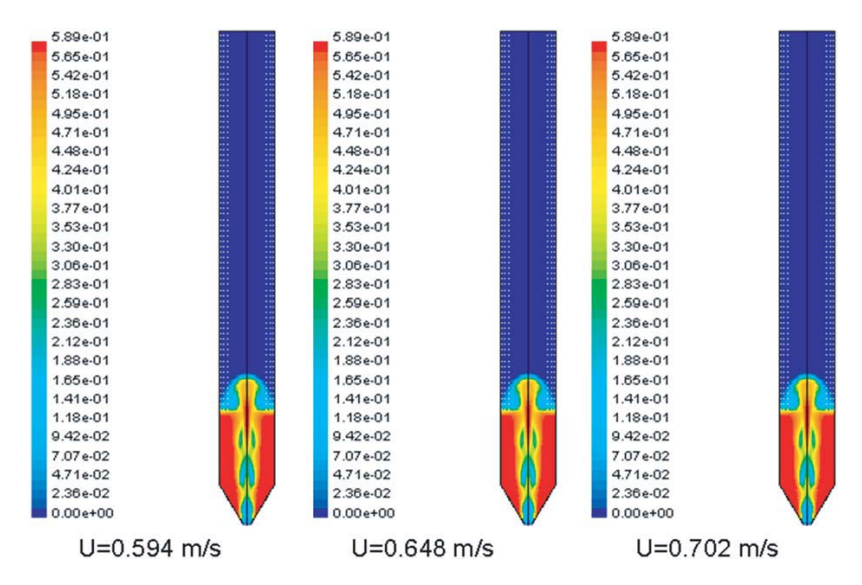


Fig. 4. Instantaneous particles concentration distributions at $t = 8 \,\mathrm{s}$ (Richardson and Zaki (1954) model).

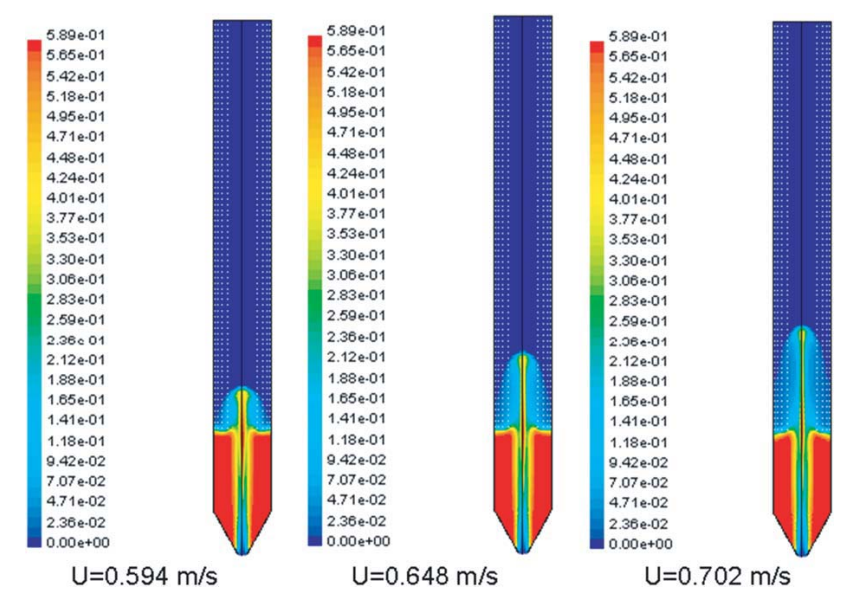


Fig. 5. Instantaneous particles concentration distribution at t = 8 s (Gidaspow (1994) model).

momentum, which naturally leads to the transition of the flow regime in the spouted bed.

4.3. Voidage profiles

Figs. 9–11 show the experimental and simulated voidage distributions at different injecting gas velocities. In these figures, z denotes the height from the bottom of the vessel. Based on the previous discussion, only the results by the Gidaspow (1994) model, the Arastoopour et al. (1990) model

and the Syamlal and O'Brien (1988) model are chosen for further discussion.

All the simulated voidage profiles show that in the spout, the voidage decreases with the increasing bed height, illustrating a qualitative agreement with the experimental tendency except in the higher part of the column, where the maximum voidage does not appear at the axis. Both the experimental and simulated results reveal that there is a denser particle concentration zone near the axis and a particle core forms at the top of fountain. The quantitative comparisons

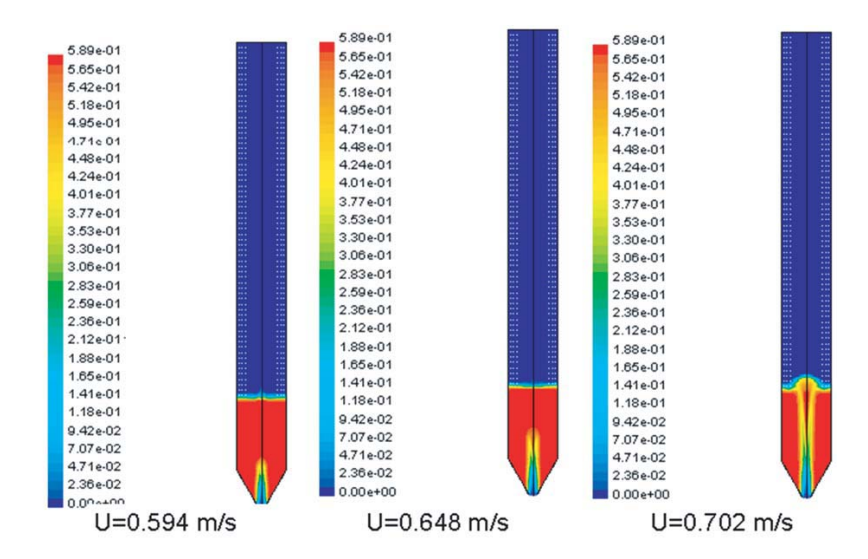


Fig. 6. Instantaneous particles concentration distributions at t = 8 s (Syamlal and O'Brien (1988) model).

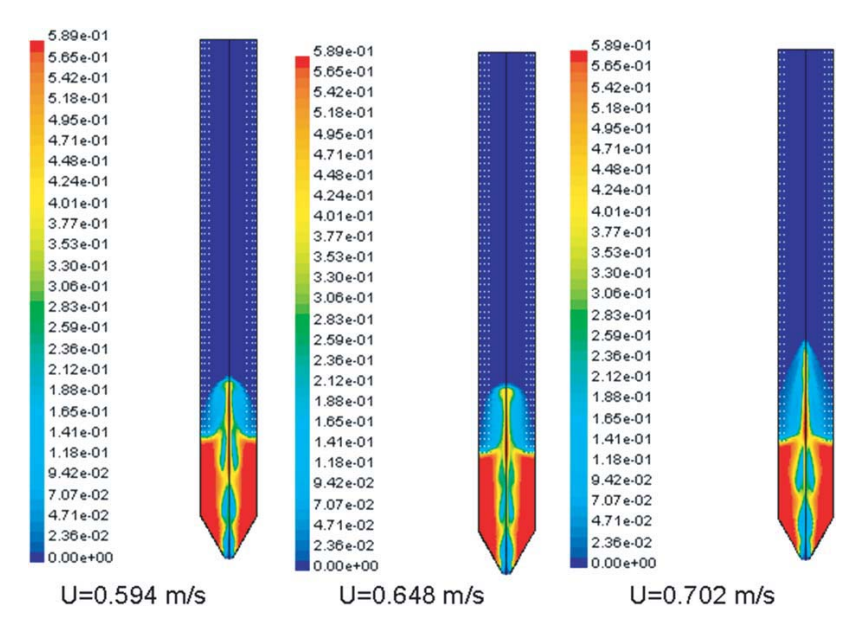


Fig. 7. Instantaneous particles concentration distributions at t = 8 s (Di Felice (1994) model).

further confirm that as long as spouting is established, all drag models yield the predictions that are fairly in agreement with experimental results except in the upper part of the column. It is also found that the value of the voidage in the annulus is a little bit higher than that of a loosely packed bed, in agreement with those observed by He et al. (1994a,b), but contrary to those experimentally witnessed by the authors of the present investigation (Wang et al., 2000).

Because the momentum gained by the particles is equal to that lost by the gas, the particles must obtain a certain velocity (terminal settling velocity) to reach up to the top of the spouted bed. Lim and Mathur (1978) related n_z , the particle number at a given height in the spout, to solids volume fraction by

$$n_z = D_s^2 (1 - \alpha_s) / d_p^2. (4.1)$$

From the experimental voidage profiles at $U = 0.594 \, \text{m/s}$, the integration-averaged porosity of the bed is about 0.69, or the average solids fraction is about 0.31. At the initial spouting point, the average solids fraction must be larger than

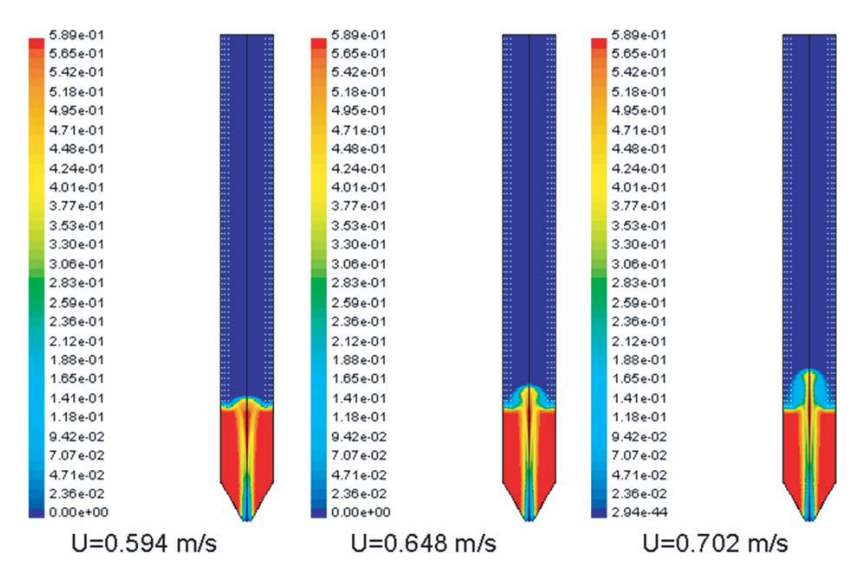


Fig. 8. Instantaneous particles concentration distributions at t = 8 s (Arastoopour (1990) model).

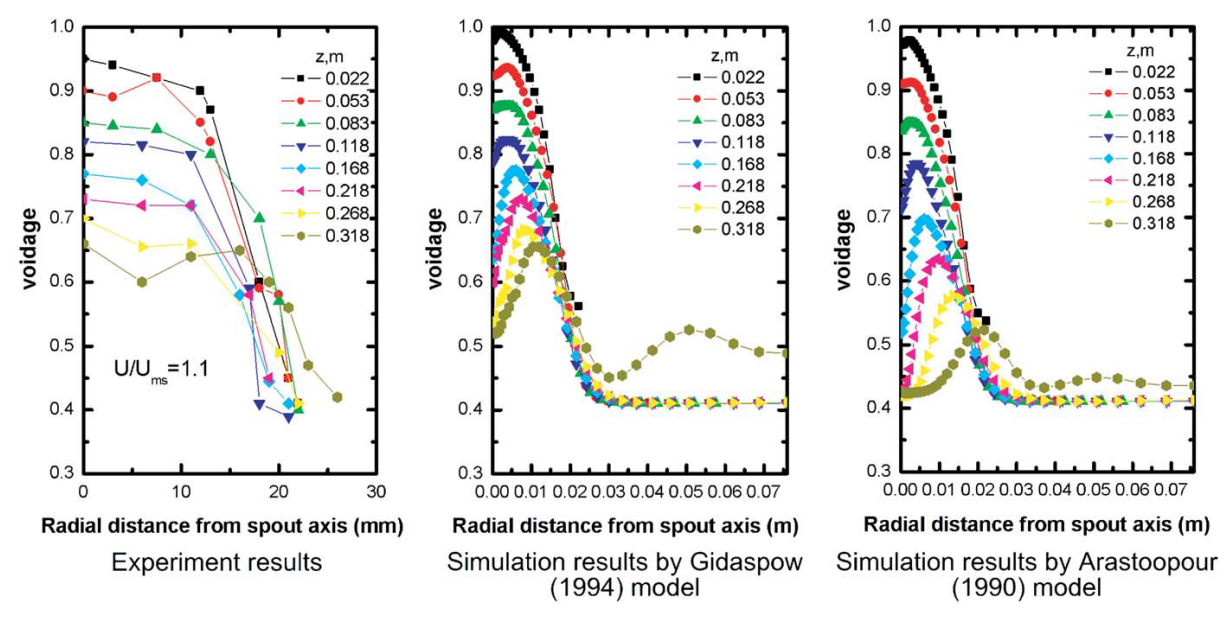


Fig. 9. Voidage profiles $(U = 0.594 \,\mathrm{m/s})$.

0.31, thus the drag coefficients calculated by the different models with the solids volume fraction ranging from about 0.3 to 0.35 would mainly account for the differences of the minimum spouting velocities calculated, i.e., the higher the drag coefficients are, the lower minimum spouting velocities are, which is in good agreement with the previous discussion on the quantitative analysis of drag models. As illustrated in Fig. 2, when the solids fraction is in the range of 0.3 to 0.35, the Gidaspow (1994) model gives the highest drag coefficient and the Syamlal and O'Brien (1988) model gives

the lowest, exactly reverse to the tendency of the minimum spouting velocity calculated.

Lefroy and Davidson (1969) analyzed the particle momentum balance, and wrote the fluid-particle interaction coefficient as

$$\beta u^2/\alpha_s = (\rho_s - \rho_g)(1 - \alpha_s)g. \tag{4.2}$$

Based on the above equation and the previous quantitative analyses, it can be deduced that a higher interaction coefficient could result in a higher voidage (lower solids volume

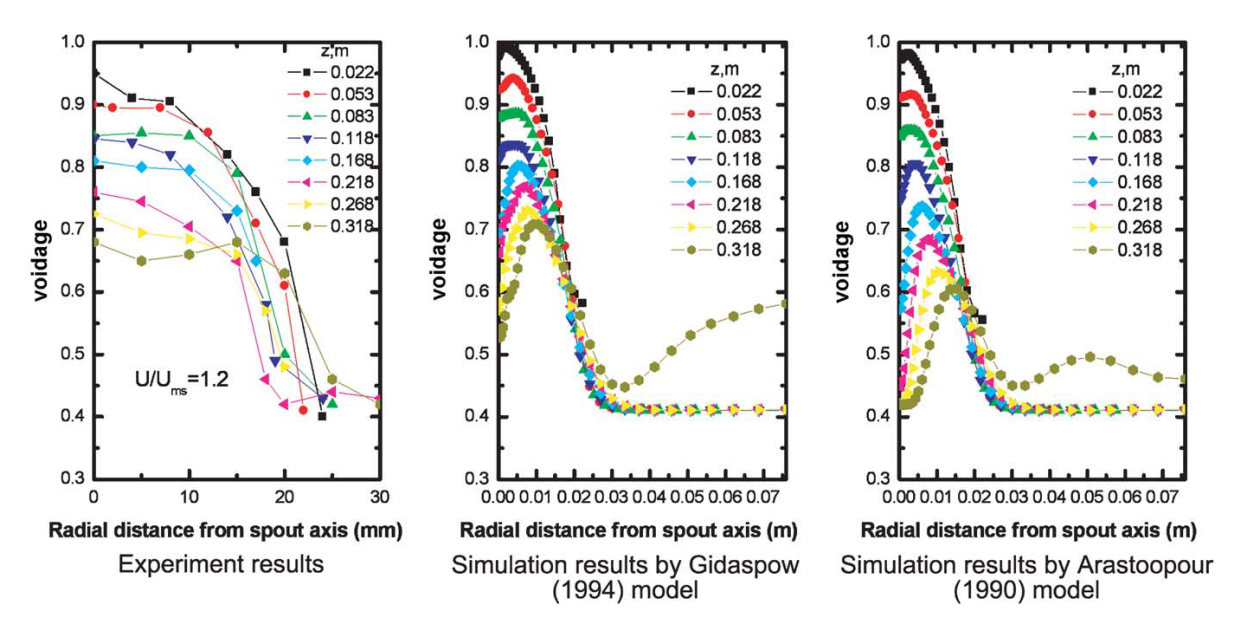


Fig. 10. Voidage profiles (U = 0.648 m/s).

fraction) and vice versa, which means that drag models affect the prediction of voidage profiles through their effect on interaction coefficient.

Another difference between the simulated and the experimental results is that the experimentally observed high particle concentration zone, or the so-called spout wall occurring near the interface between the spout and the annulus, cannot be predicted by the simulation. This is because the solids concentration in the spout wall is higher than the maximum packing limit and thus cannot be simulated, as reported by Huilin et al. (2004).

4.4. Particle velocity along the bed axis

As shown in Fig. 12, the simulated particle velocity profiles along the bed axis indicate that the particles are rapidly accelerated to their maximum velocity at a height of about 0.06–0.07 m, slightly higher than the experimental results which are about 0.05 m. At the higher height, at the first the particles are gradually decelerated, and then their velocity is sharply decreased to zero after they reach at the fountain region. Quantitatively, the simulated velocities are lower than the experimental results when the voidage is approaching to 1, although they qualitatively follow the same tendency. The Gidaspow (1994) model gives the closest results to the experimental data among all models.

He et al. (1994b) measured the particle velocities in the fountain only at $U/U_{\rm ms}=1.3$ and found that the height for the particle velocity to decrease to zero was about 0.7 m. By the Gidaspow (1994) model, this height is about 0.6 m; and by the Arastoopour et al. (1990) and Syamlal and O'Brien (1988) models, this height is lower than 0.45 m. Because

the latter two models overestimate the minimum spouting velocity, thus at the gas velocity of 0.702 m/s they predict less excess of the spouting state over the initial spouting state than the Gidaspow (1994) model.

4.5. Particle velocity in the spout

Figs. 13-15 are the radial distributions of particle velocities. In the spout, there exists a particle accelerating region near the inlet of the bed and a decelerating region in the upper part of the bed. As shown in Figs. 13-15, the particle velocities have their maxima at the bed axis and decrease to zero at the spout-annulus interface. Near the boundary between the spout and the annulus, the measured particle velocities vary in a complex way which is maybe caused by the measurement error. Qualitatively speaking, the simulated particle velocity distributions are in good agreement with those experimentally measured in spite of some quantitative differences. Although the Gidaspow (1994) model gives the closest results to the experimental data among all models, it is obvious that the differences between them are large, unlike the quantitative agreement in computing the minimum spouting velocity and the voidage profile.

From the point of view of the force balance, drag force is the only accelerating force and the gravity is the main decelerating force, therefore the drag models accounts for the differences of the results. The Gidaspow (1994) model gives the predictions of the lowest minimum spouting velocity, highest voidage fraction, and the highest particle velocity, which is thought to be reasonable from their coherence. Thorley et al. (1959) made an analysis based on the particle force balance in the spout. For the n_z particles defined

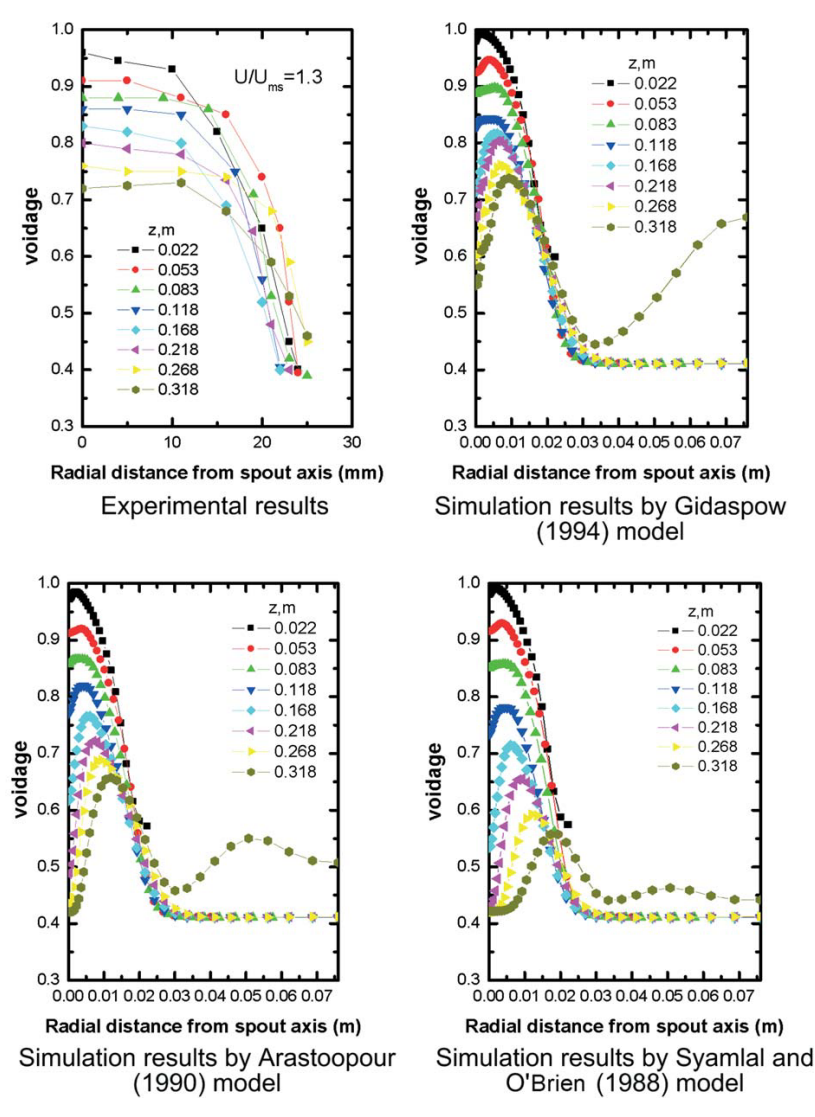


Fig. 11. Voidage profiles $(U = 0.702 \,\mathrm{m/s})$.

by Eq. (4.1) at a given bed height, the force balance can be expressed as (Thorley et al., 1959)

$$\frac{1}{6}\pi d_p^3 \rho_s \frac{\mathrm{d}(n_z v)}{\mathrm{d}t} = \left[n_z \frac{1}{2} \rho_f (u - v)^2 \frac{1}{4} \pi d_p^2 C_D \right] - \left[n_z \frac{1}{6} \pi d_p^3 (\rho_s - \rho_g) g \right].$$
(4.3)

After rearrangement, Eq. (4.3) can be reduced to

$$\frac{-v^2 d\alpha_s}{(1-\alpha_s) dz} + \frac{v^2 dD_s^2}{D_s^2 dz} + \frac{v dv}{dz}
= \frac{3C_D}{4d_p} \frac{\rho_s (u-v)^2}{\rho_p} - \frac{(1-\alpha_s)(\rho_s - \rho_g)g}{\rho_s}.$$
(4.4)

The spout can be considered as three successive zones, corresponding to the regions of the initial particle acceleration (Zone I), the subsequent particle deceleration within bed (Zone II), and the final deceleration in the fountain (Zone III). Combined with the boundary conditions for each region, the equation can be simplified into

$$\begin{split} \frac{v}{\mathrm{d}z} &= \frac{3C_D}{4d_p} \frac{\rho_s (u-v)^2}{\rho_p} - \frac{(1-\alpha_s)(\rho_s-\rho_g)g}{\rho_s}, \quad \text{(Zone I)}, \\ \frac{v^2}{2z} \frac{\mathrm{d}v^2}{\mathrm{d}z} &+ \frac{(1-\alpha_s)(\rho_s-\rho_g)g}{\rho_s} = 0, \quad \text{(Zone II)}, \\ \frac{v}{\mathrm{d}z} &= -\frac{(1-\alpha_s)(\rho_s-\rho_g)g}{\rho_s}, \quad \text{(Zone III)}. \end{split}$$

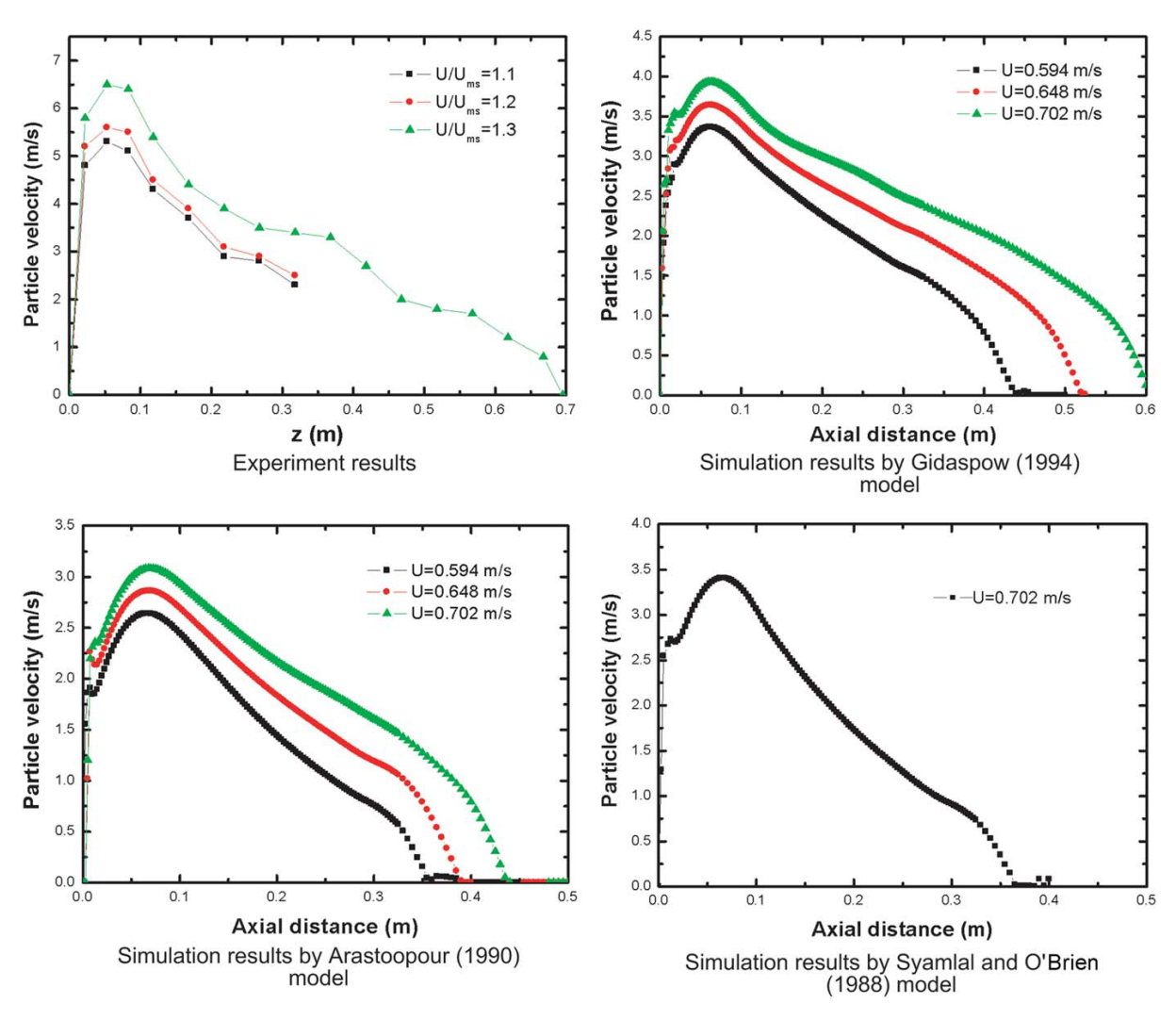


Fig. 12. Particle velocity along the axis.

In Zone I, the increasing drag coefficient results in increasing particle velocity. In Zones II and III, the drag term can be neglected as an approximation, the particle velocity is related to that which is already increased in the end of Zone I.

4.6. Particle velocity in the annulus

The experimental and simulated particle velocity profiles in the annulus are given in Figs. 16–18. Before discussion, it should be pointed out that in these figures the downward (negative) velocities in the annulus are plotted as positive values for convenience. The experimental particle velocities in the annulus have a nearly flat distribution in the cylindri-

cal part of the column, obviously different from the simulated particle velocities that increase to their maximum at first and then decrease to zero at the wall. The particle velocities in the annulus increase with the decreasing bed height, consistent with the experimental results. He et al. (1994,b) thought that this was due to the solids cross-flow from the annulus to the spout. Just like the computation of the particle velocity in the spout, here the Gidaspow (1994) model also gives the higher predictions that are closer to the experimental results. At the height $z = 0.318 \,\mathrm{m}$ (Figs. 17 and 18), the particle velocity measured is different from that predicted by the Gidaspow (1994) model because the particles are in the fountain region, as the simulation results indicate.

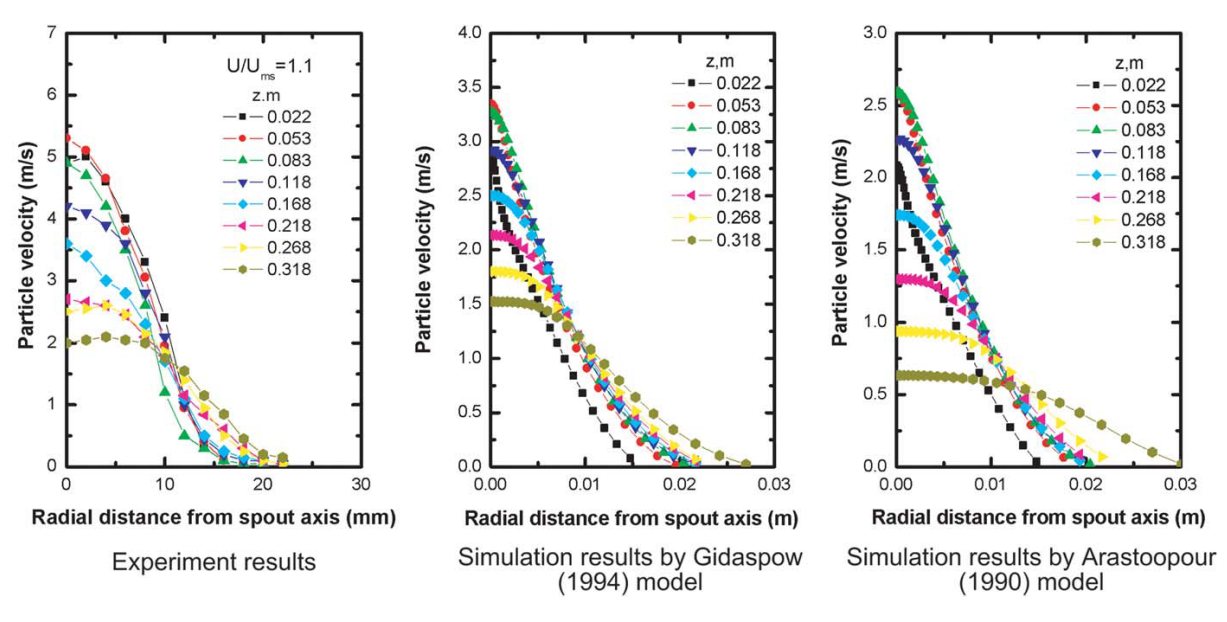


Fig. 13. Particle velocity in the spout ($U = 0.594 \,\mathrm{m/s}$).

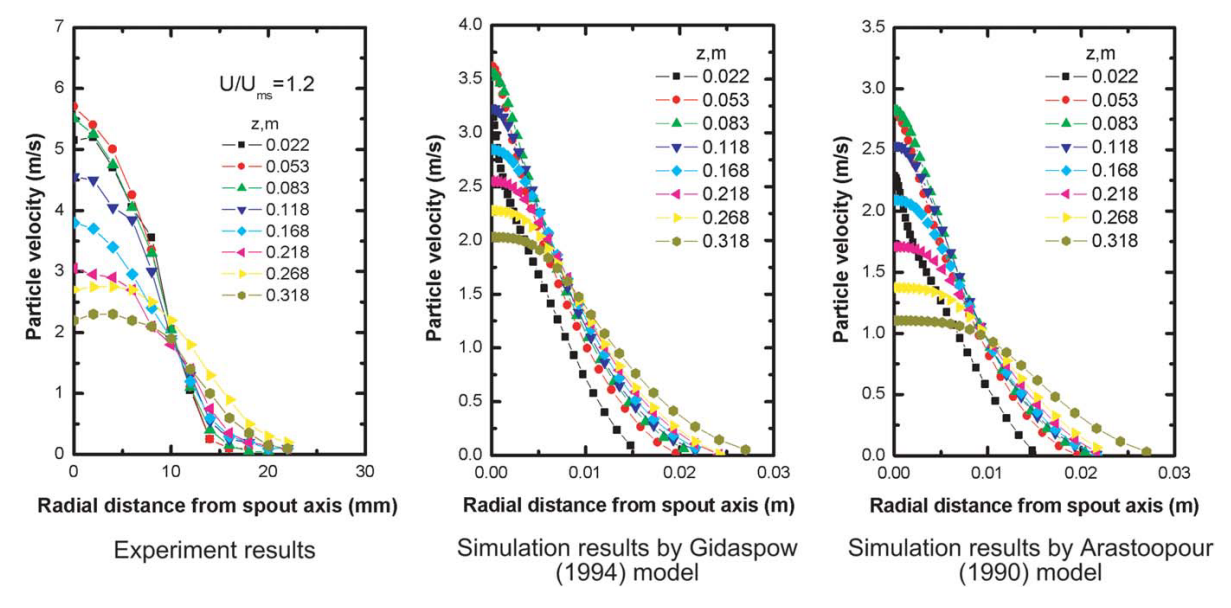


Fig. 14. Particle velocity in the spout $(U = 0.648 \,\mathrm{m/s})$.

The simulated particle velocities in both the spout and the annulus are lower than those measured. Huilin et al. (2004) showed the particle velocities in the spout were in good agreement with the experimental data, but they did not give the particle velocities in the annulus. By the DEM

simulation, Kawaguchi et al. (2000) reported that the particle velocities in the spout agreed well with the experimental results, but those in the annulus were much higher than the experimental data. Limited by the computational capacity, they employed larger particles to decrease the number of

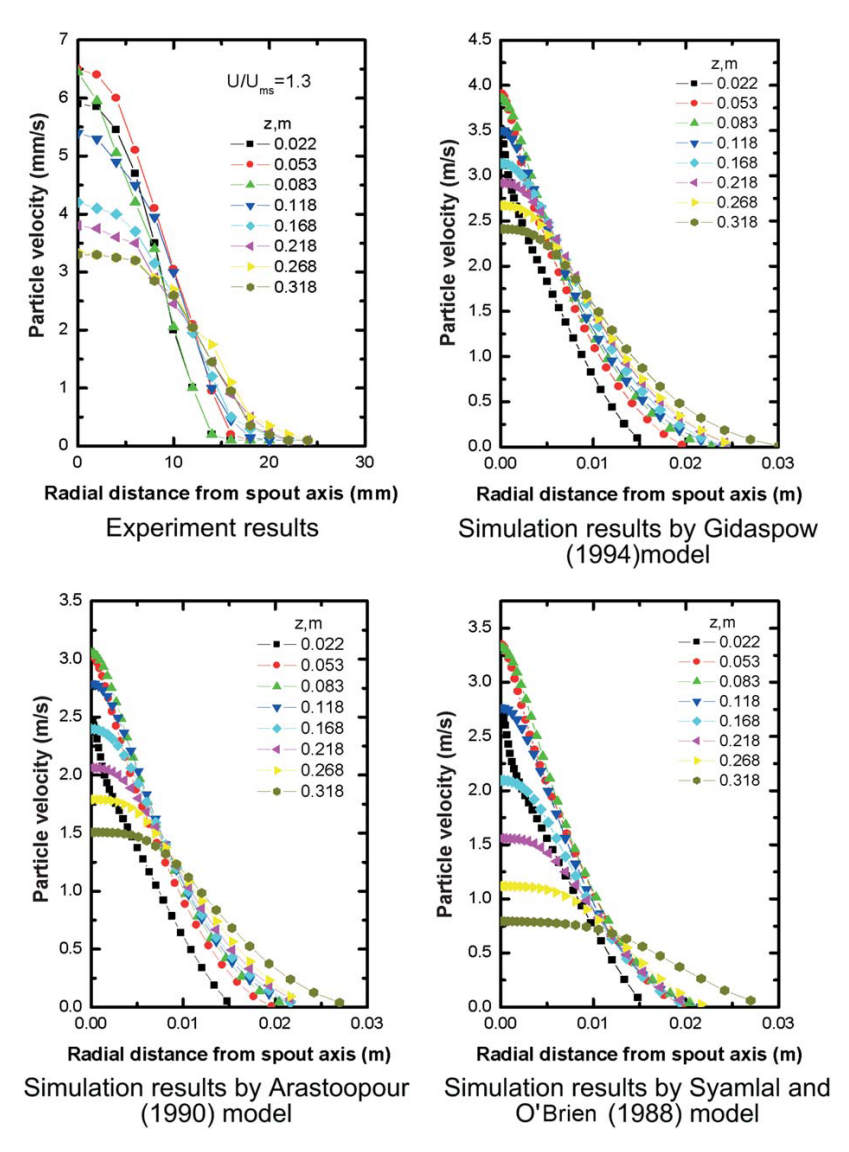


Fig. 15. Particle velocity in the spout $(U = 0.702 \,\mathrm{m/s})$.

particles involved, but by the principle of similarity (Glicksman, 1984), the similarity between the simulation and the experimental systems could be no longer satisfied.

Just like the influence of operating conditions on the spouting behavior, the choice of drag models may greatly alter the magnitude of the only-accelerating force drag and thus can significantly affect the simulated flow patterns and the distributions of local bed porosity and particle velocity. As shown by Grace (1986) for gas—solids fluidization beds and by Mathur and Epstein (1974) for spouted beds, the spouting is a so restricted phenomenon that even a

slight change in operating conditions can result in flow pattern transition, therefore careful attention should been paid to the selection of drag models in simulating spouted beds.

5. Conclusion

By incorporating several widely used drag models, including Gidaspow (1994) model, the Syamlal and O'Brien (1988) model, the Richardson and Zaki (1954) model, the Di Felice (1994) model and the Arastoopour et al. (1990)

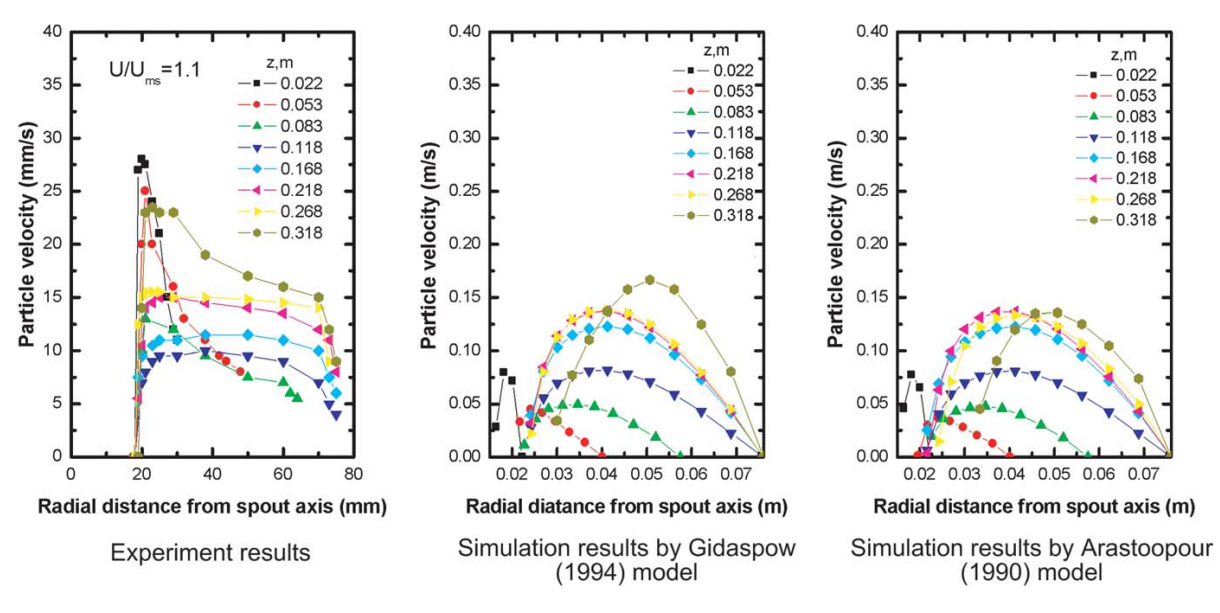


Fig. 16. Particle velocity in the annulus $(U = 0.594 \,\mathrm{m/s})$.

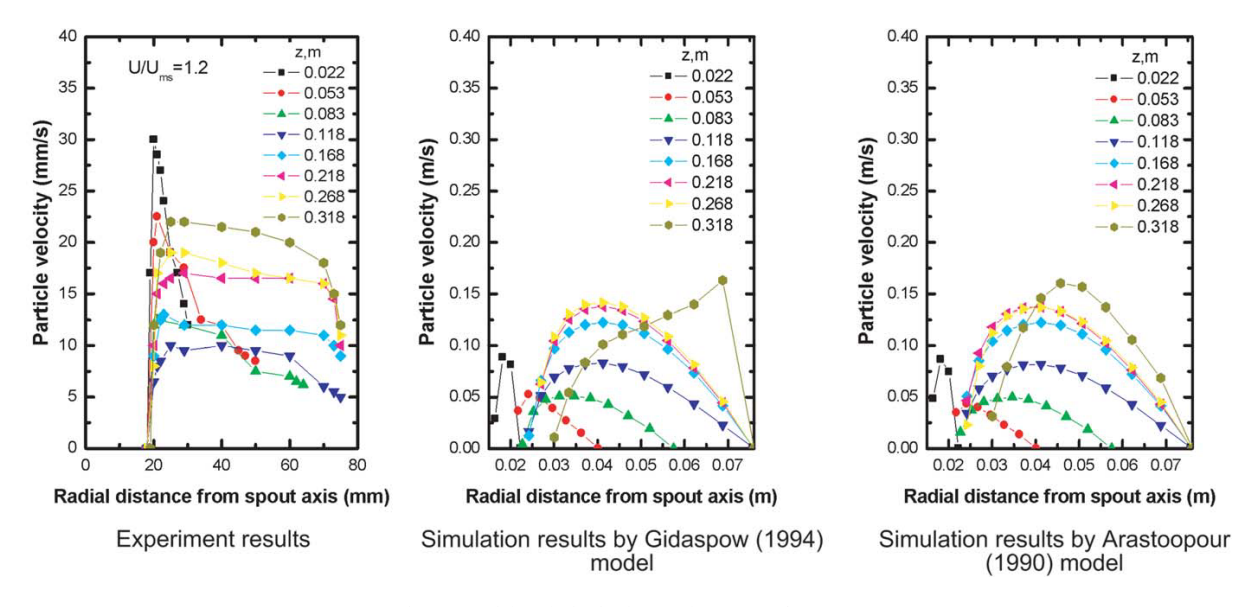


Fig. 17. Particle velocity in the annulus ($U = 0.648 \, \mathrm{m/s}$).

model, into the two-fluid model, their influences on the CFD simulation of spouted beds are assessed. The resulting hydrodynamic properties are compared to the experimental results of He et al. (1994a,b). The simulation results by the five different drag models show that the Gidaspow model (1994), the Syamlal and O'Brien (1988) model, and the Arastoopour et al. (1990) model can qualitatively predict the flow pattern, voidage profiles, particle velocity profiles inside the spouted

bed, with the Gidaspow (1994) model giving the best fits to the experimental data. Since the drag force is the only accelerating force acting on particles, thus the selection of drag models make difference in the CFD simulation of the spouted beds. The expressions of the exponent term α_g in the model equations cause the difference among them, especially in dense phase region that is most commonly encountered in spouted bed systems.

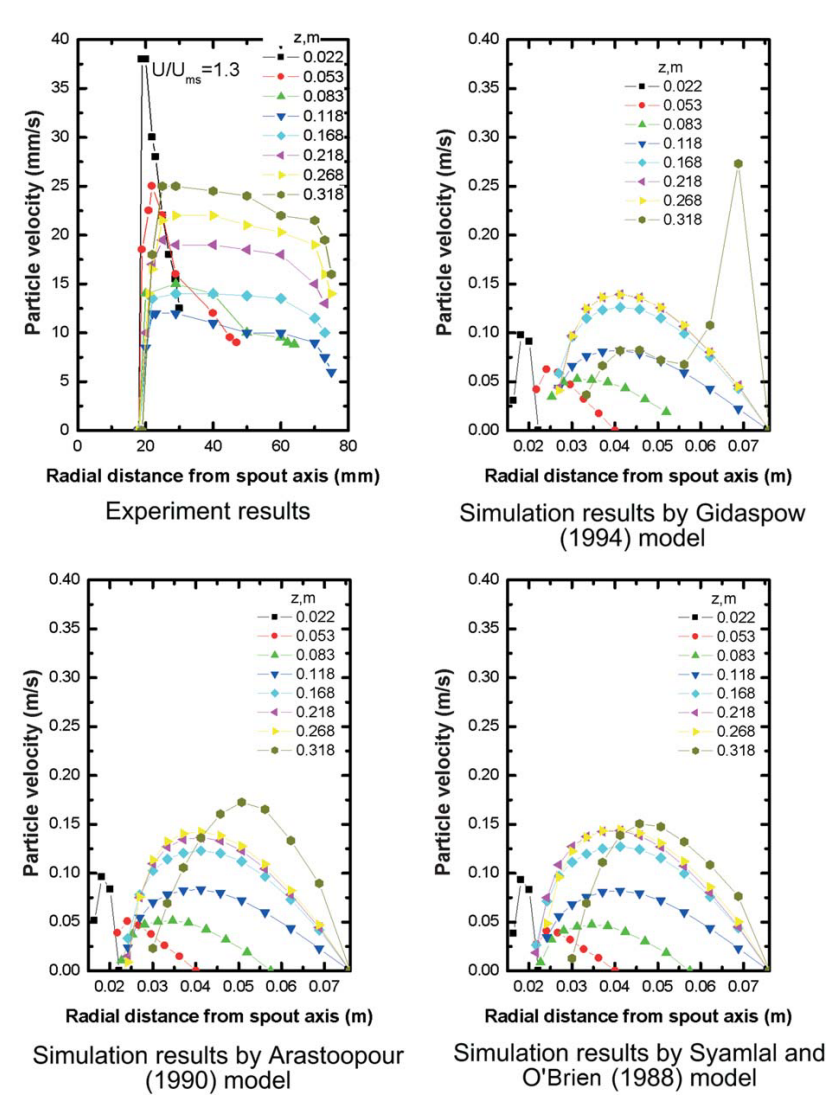


Fig. 18. Particle velocity in the annulus ($U = 0.702 \,\mathrm{m/s}$).

Notation		f	ratio of the falling velocity of a suspension to the terminal velocity of a single
A, B	coefficient in the Syamlal and O'Brien		particle
	model	$F_{{ m lift},q}$	lift force, N
C	experimental constant in the Syamlal	F_q	external body force, N
	equation	$F_{vm,q}$	virtual mass force, N
C_D	drag coefficient	g	gravitational constant, 9.81 m/s ²
C_{μ} , C_3 , C_V , C_{β}	coefficients in turbulence model	$g_{0,ss}$	radial distribution function
d_p	particle diameter, m	H_m	packing bed height, m
$\dot{D_c}$	column diameter, m	k	turbulence quantities
D_i	orifice diameter, m	k_g	turbulence quantities of gas phase
D_s	spout diameter, m	k_s	turbulence quantities of solid phase
e_{ss}	the coefficient of restitution of particles	$k_{oldsymbol{arTheta}_{s}}$	diffusion coefficient, J kg ⁻¹

n	exponent in the Richardson and Zaki	$ au_{\scriptscriptstyle S}$	solid stre
	model	$ au_{t,g}$	character
n_z	particle number at a given height in the		bulent ed
	spout	$ au_{t,sg}$	Lagrangia
P	fluid pressure, N/m ²	$\overline{\overline{ au}}_q^{\prime\prime}$	Reynolds
$P_{\scriptscriptstyle S}$	solid pressure, N/m ²	φ_{gs}^q	switch fu
Re	Reynolds number	$\Pi_{k,g}^{r,gs},\Pi_{z,g}$	influence
Re_p	particle Reynolds number	k,g, 2,g	tinuous p
Re_t	Reynolds number based on particle ter-	Φ_{gs}	energy ex
	minal velocity	- 83	phase, J
R_p	coefficient in the Gibilaro model and	ω	correction
•	the Andrews and O'Rourke model		
R_{pq}	interaction force between phases, N	Subscripts	
Rt	velocity ratio correction factors for	1	
	clustering effects	g	gas
t	time, s	max	maximun
и	gas velocity, m/s	p	particle
u_t	terminal velocity of a particle,m/s	q	phase
u_x	gas velocity in x (axial) direction, m/s	S	solid
u_y	gas velocity in y (radial) direction, m/s	t	terminal
U	superficial gas velocity, m/s	x	axial dire
v	particle velocity, m/s	y	radial dir
v_q	phase q velocity, m/s	,	
$v_{\scriptscriptstyle S}$	particle velocity fluctuation, m/s		
V_p	particle volume, m ³	Acknowledgem	ients
X	empirical coefficient in the Di Felice		

Greek letters

α_g	gas volume fraction
α_q	volume fraction of phase q
$\alpha_{\scriptscriptstyle S}$	solids volume fraction
$\alpha_{s, \max}$	the maximum of solids volume fraction
β	fluid-particle interaction coefficient,
	$kg/m^3 s$
$\beta_{ m Ergun}$	fluid-particle interaction coefficient of
8	the Ergun equation, kg/m ³ s
$\beta_{ m Wen-Yu}$	fluid-particle interaction coefficient of
. ,,,,,,	the Wen–Yu equation, kg/m ³ s
3	turbulence dissipation rate, m ² /s ³
ε_g	turbulence dissipation rate of gas
	phase, m^2/s^3
$\mathcal{E}_{\mathcal{S}}$	turbulence dissipation rate of solid
	phase, m^2/s^3
Θ_{s}	granular temperature, m ² /s ²
λ_s	the solid bulk viscosity, Pas
μ_g	gas viscosity, Pas
μ_s	solid shear viscosity, Pas
$\mu_{t,q}$	turbulent viscosity, Pas
ρ_g	gas density, kg/m ³
ρ_q	density if phase q , kg/m^3
ρ_s	particle density, kg/m ³
$ au_{F,sg}$	characteristic particle relaxation time
	connected with inertial effects, s

model

$ au_s$	solid stress tensor, N/m ²
$\tau_{t,g}$	characteristic time of the energetic tur-
-76	bulent eddies, s
$ au_{t,sg}$	Lagrangian integral time scale, s
$ar{\overline{ au}}_{q}^{\prime\prime}$	Reynolds stress tensor, N/m ²
ϕ_{gs}	switch function in the Gidaspow model
$\Pi_{k,g}^{s},\Pi_{z,g}$	influence of dispersed phases on con-
70 -70	tinuous phase
Φ_{gs}	energy exchange between fluid or solid
Ü	phase, J
ω	correction factor of drag coefficient

g	gas
max	maximum
p	particle
q	phase
S	solid
t	terminal velocity
X	axial direction
y	radial direction

The authors acknowledge the support (in part) by the National Natural Science Foundation of China through the program "Time and Spatial Multi-scale Interactions in Chemical Engineering and Their Effects" (Grant No. 20490200).

References

Aguado, R., Olazar, M., Barona, A., Bilbao, J., 2000. Char-formation kinetics in the pyrolysis of sawdust in a conical spouted bed reactor. Journal of Chemical Technology and Biotechnology 75 (7), 583-588.

Andrews, M.J., O'Rourke, P.J., 1996. The multiphase particle-in-cell (MP-PIC) method for dense particulate flows. International Journal of Multiphase Flow 22 (2), 379-402.

Arastoopour, H., Pakdel, P., Adewumi, M., 1990. Hydrodynamic analysis of dilute gas-solids flow in a vertical pipe. Powder Technology 62 (2),

Arbib, H.A., Levy, A., 1982. Combustion of low heating value fuels and wastes in the spouted bed. Canadian Journal of Chemical Engineering 60 (3), 528-531.

Arnold, M.S., Gale, J.J., Laughlin, M.K., 1992. British coal spouted fluidised bed gasification process. Canadian Journal of Chemical Engineering 70 (5), 991-997.

Becker, H.A., 1961. An investigation of laws governing the spouting of coarse particles. Chemical Engineering Science 13 (4), 245-262.

Burger, R., Concha, F., Fjelde, K.K., Karlsen, K.H., 2000. Numerical simulation of the settling of polydisperse suspensions of spheres. Powder Technology 113 (1), 30-54.

Di Felice, R., 1994. The voidage functions for fluid-particle interaction system. International Journal of Multiphase Flow 20 (1), 153-159.

Ding, J., Gidaspow, D., 1990. A bubbling fluidization model using kinetic theory of granular flow. A.I.Ch.E. Journal 36 (4), 523-538.

Do, K.T., Edwards, J.H., Tyler, R.J., 1995. Catalytic oxidative coupling of methane: I. comparison of experimental performance data from various

- types of reactor. Canadian Journal of Chemical Engineering 73 (3), 327-336.
- Enwald, H., Peirano, E., Almstedt, A.E., 1996. Eulerian two-phase flow theory applied to fluidization. International Journal of Multiphase Flow 22 (1), 21–66.
- Epstein, N., Grace, J.R., 1997. Spouting of particulate solids. In: Fayed, M.E., Otten, L. (Eds.), Handbook of Powder Science and Technology, second ed. Chapman & Hall, New York (Chapter 10).
- Ergun, S., 1952. Fluid flow through packed columns. Chemical Engineering Progress 48 (2), 89–94.
- Garside, J., Al-Dibouni, M.R., 1977. Velocity-voidage relationship for fluidization and sedimentation. Industrial Engineering Chemistry Process Design Development 16 (2), 206–214.
- Gibilaro, L.G., Di Felice, R., Waldram, S.P., 1985. Generalized friction factor and drag coefficient correlations for fluid-particle interactions. Chemical Engineering Science 40 (10), 1817–1823.
- Gidaspow, D., 1994. Multiphase Flow and Fluidization. Academic Press, San Diego.
- Glicksman, L.R., 1984. Scaling relationships for fluidized beds. Chemical Engineering Science 39 (9), 1373–1379.
- Grace, J.R., 1986. Contacting models and behavior classification of gas-solid and other two-phase suspensions. Canadian Journal of Chemical Engineering 64 (6), 353–363.
- He, Y.L., Lim, C.J., Grace, J.R., Zhu, J.X., Qin, S.Z., 1994a. Measurements of voidage profiles in spouted beds. Canadian Journal of Chemical Engineering 72 (4), 229–234.
- He, Y.L., Qin, S.Z., Lim, C.J., Grace, J.R., 1994b. Particle velocity profiles and solid flow patterns in spouted beds. Canadian Journal of Chemical Engineering 72 (8), 561–568.
- Hinze, J.O., 1975. Turbulence. McGraw-Hill Publishing Co., New York.
 Hoomans, B.P.B., Kuipers, J.A.M., Briels, W.J., Van Swaaij, W.P.M.,
 1996. Discrete particle simulation of bubble and slug formation in a two-dimensional gas-fluidised bed: a hard-sphere approach. Chemical Engineering Science 51 (1), 99–118.
- Huilin, L., Yongli, S., Yang, L., Yurong, H., Bouillard, J., 2001. Numerical simulations of hydrodynamic behavior in spouted beds. Chemical Engineering Research and Design 79 (5), 593–599.
- Huilin, L., Yurong, H., Wentie, L., Jianmin, D., Gidaspow, D., Bouillard, J., 2004. Computer simulations of gas–solid flow in spouted beds using kinetic-frictional stress model of granular flow. Chemical Engineering Science 59 (4), 865–878.
- Kawaguchi, T., Tanaka, T., Tsuji, Y., 1998. Numerical simulation of two-dimensional fluidized beds using the discrete element method (comparison between the two- and three-dimensional models). Powder Technology 96 (2), 129–138.
- Kawaguchi, T., Sakamoto, M., Tanaka, T., Tsuji, Y., 2000. Quasi-threedimensional numerical simulation of spouted beds in cylinder. Powder Technology 109 (1), 3–12.
- Khoshnoodi, M., Weinberg, F.J., 1978. Combustion in spouted beds. Combustion and Flame 33 (1), 11–21.
- Konduri, R.K., Altwicker, E.R., Morgan III, M.H., 1995. Atmospheric spouted bed combustion: the role of hydrodynamics in emissions generation and control. Canadian Journal of Chemical Engineering 73 (5), 744–754.
- Konduri, R.K., Altwicker, E.R., Morgan III, M.H., 1999. Design and scale-up of a spouted-bed combustor. Chemical Engineering Science 54 (2), 185–204.
- Krzywanski, R.S., Epstein, N., Bowen, B.D., 1992. Multi-dimensional model of a spouted bed. Canadian Journal of Chemical Engineering 70 (5), 858–872.
- Lefroy, G.A., Davidson, J.F., 1969. The mechanics of spouted beds. Transactions of Institute of Chemical Engineers 47, T120–T128.
- Lim, C.J., Mathur, K.B., 1978. Modeling of particle movement in spouted beds. In: Davidson, J.F., Keairns, D.L. (Eds.), Fluidization. Cambridge University Press, Cambridge, pp. 104–109.
- Lim, C.J., Watkinson, A.P., Khoe, G.K., Low, S., Epstein, N., Grace, J.R., 1988. Spouted, fluidized and spout-fluid bed combustion of bituminous coals. Fuel 67 (10), 1211–1217.

- Louge, M.Y., Mastorakos, E., Jenkins, J.K., 1991. The role of particle collisions in pneumatic transport. Journal of Fluid Mechanics 231, 345–359
- Lun, C.K.K., Savage, S.B., Jeffrey, D.J., 1984. Kinetic theories for granular flow: inelastic particles in Couette flow and slightly inelastic particles in general flow field. Journal of Fluid Mechanics 140, 223–256.
- Marnasidou, K.G., Voutetakis, S.S., Tjatjopoulos, G.J., Vasalos, I.A., 1999. Catalytic partial oxidation of methane to synthesis gas in a pilot-plant-scale spouted-bed reactor. Chemical Engineering Science 54 (15), 3691–3699.
- Mathur, K.B., Epstein, N., 1974. Spouted Bed. Academic Press, New York.Mathur, K.B., Gishler, P.E., 1955. A technique for contacting gases with coarse solid particles. A.I.Ch.E. Journal 1 (1), 157–164.
- Mikami, T., Kamiya, H., Horio, M., 1998. Numerical simulation of cohesive powder behavior in a fluidized bed. Chemical Engineering Science 53 (10), 1927–2940.
- Mleczko, L., Marschall, K.J., 1997. Performance of an internally circulating fluidized-bed reactor for the catalytic oxidative coupling of methane. Canadian Journal of Chemical Engineering 75 (3), 610–619.
- Nieuwland, J.J., Huizenga, P., Kuipers, J.A.M., van Swaaij, W.P.M., 1994. Hydrodynamic modeling of circulating fluidised beds. Chemical Engineering Science 49 (24B), 5803–5811.
- O'Brien, T.J., Syamlal, M., 1993. Particle cluster effects in the numerical simulation of a circulating fluidized bed. In: Avidan, A. (Ed.), Circulating Fluidized Bed Technology IV, Proceedings of the Fourth International Conference on Circulating Fluidized Beds. Somerset, PA, August 1–5.
- Ocone, R., Sundaresan, S., Jackson, R., 1993. Gas-particle flow in a duct of arbitrary inclination with particle–particle interactions. A.I.Ch.E. Journal 39 (8), 1261–1271.
- Olazar, M., Arandes-Jose, M., Zabala, G., Aguayo, A.T., Bilbao, J., 1997. Design and operation of a catalytic polymerization reactor in a dilute spouted bed regime. Industrial and Engineering Chemistry Research 36 (5), 1637–1643.
- Olazar, M., Aguado, R., Bilbao, J., Barona, A., 2000. Pyrolysis of sawdust in a conical spouted-bed reactor with a HZSM-5 catalyst. A.I.Ch.E. Journal 46 (5), 1025–1033.
- Pallai, I., Nemeth, J., 1969. Analysis of flow forms in a spouted bed apparatus by the so-called phase diagram. International Congress of Chemical Engineers (CHISA). Third, Prague, September, Paper No. C2.4. Czechoslovak Society for Industrial Chemistry.
- Pita, J.A., Sundaresan, S., 1991. Gas-particle flow in vertical pipes. A.I.Ch.E. Journal 37 (7), 1009–1018.
- Pita, J.A., Sundaresan, S., 1993. Developing flow of a gas-particle mixture in a vertical riser. A.I.Ch.E. Journal 39 (4), 541–552.
- Richardson, J.R., Zaki, W.N., 1954. Sedimentation and fluidization: part I. Transactions of Institute of Chemical Engineering 32 (1), 35–53.
- Sinclair, J.L., Jackson, R., 1989. Gas-particle flow in a vertical pipe with particle–particle interactions. A.I.Ch.E. Journal 35 (9), 1473–1486.
- Song, B.H., Watkinson, A.P., 2000. Three-stage well-mixed reactor model for a pressurized coal gasifier. Canadian Journal of Chemical Engineering 78 (1), 143–155.
- Sue-A-Quan, T.A., Cheng, G., Watkinson, A.P., 1995. Coal gasification in a pressurized spouted bed. Fuel 74 (2), 159–164.
- Syamlal, M., O'Brien, T.J., 1988. Simulation of granular layer inversion in liquid fluidized beds. International Journal of Multiphase Flow 14 (4), 473–481.
- Thorley, B., Saunby, J.B., Mathur, K.B., Osberg, G.L., 1959. An analysis of air and solid flow in a spouted wheat bed. Canadian Journal of Chemical Engineering 37 (2), 184–192.
- Tsuji, T., Uemaki, O., 1994. Coal gasification in a jet-spouted bed. Canadian Journal of Chemical Engineering 72 (3), 504–510.
- Uemura, Y., Azeura, M., Ohzuno, Y., Hatate, Y., 1999a. Products from flash pyrolysis of plastics. Proceedings of the International Conference on Solid Waste Technology and Management. Widener University, School of Engineering, Chester, PA, USA, 91–96.

- Uemura, Y., Ohe, H., Ohzuno, Y., Hatate, Y., 1999b. Carbon and hydrogen from hydrocarbon pyrolysis. Proceedings of the International Conference on Solid Waste Technology and Management. Widener University, School of Engineering, Chester, PA, USA, 622–627.
- van Wachem, B.G.M., Schouten, J.C., Krishna, R., van den Bleek, C.M., 1998. Eulerian simulations of bubbling behaviour in gas-solid fluidized beds. Computers and Chemical Engineering 22 (suppl.), 299–306.
- van Wachem, B.G.M., Schouten, J.C., Krishna, R., van den Bleek, C.M., 1999. Validation of the Eulerian simulated dynamic behavior of gas-solid fluidized beds. Chemical Engineering Science 54 (13–14), 2141–2149
- van Wachem, B.G.M., Schouten, J.C., van den Bleek, C.M., Krishna, R., Sinclair, J.L., 2001. Comparative analysis of CFD models of dense gas-solid systems. A.I.Ch.E. Journal 47 (5), 1035–1051.
- Vuthaluru, H.B., Zhang, D.K., 2001a. Effect of coal blending on particle agglomeration and defluidisation during spouted-bed combustion of low-rank coals. Fuel Processing Technology 70 (1), 41–51.
- Vuthaluru, H.B., Zhang, D.K., 2001b. Effect of Ca- and Mg- bearing minerals on particle agglomeration defluidization during fluidized-bed combustion of a south Australian lignite. Fuel Processing Technology 69 (1) 13–27

- Wang, S.N., Xu, J., Wei, W.S., Shi, G., Bao, X.J., Bi, H.T., 2000. Gas spouting hydrodynamics of fine particles. Canadian Journal of Chemical Engineering 78 (1), 156–160.
- Wei, W.S., Xu, J., Fang, D.W., Bao, X.J., 2003. Catalytic partial oxidation of methane with air to syngas in a pilot-plant-scale spouted bed reactor. Chinese Journal of Chemical Engineering 11 (6), 643–648.
- Weinberg, F.J., Bartleet, T.G., Carleton, F.B., Rimboti, P., Brophy, J.H., Manning, R.P., 1988. Partial oxidation of fuel-rich mixtures in a spouted bed combustor. Combustion and Flame 72 (3), 235–239.
- Wen, C.Y., Yu, Y.H., 1966. Mechanics of fluidization. Chemical Engineering Progress Symposium Series 62 (2), 100–111.
- Yang, N., Wang, W., Ge, W., Li, J., 2003. CFD simulation of concurrentup gas-solid flow in circulating fluidized beds with structure-dependent drag coefficient. Chemical Engineering Journal 96 (1-3), 71-80.
- Yasuna, J.A., Moyer, H.R., Elliott, S., Sinclair, J.L., 1995. Quantitative predictions of gas-particle flow in a vertical pipe with particle-particle interactions. Powder Technology 84 (1), 23–34.
- Zhang, Y., Reese, J.M., 2003. The drag force in two fluid models of gas-solid flows. Chemical Engineering Science 58 (8), 1641–1644.

Colloidal Stability Variation of Petroleum Residue during Thermal Reaction

Longli Zhang,* Guohua Yang, Guohe Que, Qingxuan Zhang, and Pujiang Yang

State Key Laboratory of Heavy Oil Processing, College of Chemistry and Chemical Engineering, China University of Petroleum (East China), Dongying, Shandong Province 257061, P.R.China

Received November 15, 2005. Revised Manuscript Received April 6, 2006

The linkages between coking characteristics, colloidal stability, and molecular characteristics of petroleum residue during thermal reaction were studied. First, the results reveal that the colloidal stability decreases sharply during the coke-induction period and changes little after that. This observation proves that the colloidal stability variation determines the coking characteristics of residue. Second, the asphaltene concentration increases as reaction time progresses, reaches its maximum at the end of the coke-induction period, and then declines thereafter. This result reveals that asphaltene aggregation happens when the colloidal stability of the residue decreases to its limit and that the aggregated asphaltenes will transform into coke to abate the worsening of the colloidal stability. Furthermore, the variation in fraction composition shows that the saturated solubility of asphaltenes in residue decreases as the reaction goes on after the coke-induction period. Moreover, both the VPO molecular-weight value and the mean dipole-moment value of asphaltenes show maxima at the end of the coke-induction period, which reveals that asphaltenes with larger MW values and more polarity prefer to aggregate and transform into coke.

1. Introduction

Petroleum residues are found to be colloidal systems, and asphaltenes are considered to be the cores of them. 1-6 The colloidal stability of petroleum residue plays an important role in its coking characteristics during thermal reaction. Many researchers pointed out that a decline in the colloidal stability of the residue during thermal reaction would cause asphaltene to aggregate and ultimately transform into coke. 7,8 Wiehe⁷ made a detailed analysis about the asphaltene aggregation in residue. Moreover, Rahimi at al.8 had observed an asphaltene aggregating phase in petroleum residue during thermal reaction just before coking, which was a direct proof of this mechanism. Because the colloidal stability of the residue is difficult to describe quantitatively, there was no systematic report about the colloidal stability variation in petroleum residue during thermal reaction. There are few reports about the relationship between the colloidal stability variation and coking characteristics. Particularly, a report about the linkage between molecular characteristics and the colloidal stability of the residue is absent. This paper will focus on the two relationships.

P. Fotland^{9,10} investigated asphaltene precipitation in crude oil by the mass fraction normalized conductivity method and

- * To whom correspondence should be addressed. E-mail: lizhang@ hdpu.edu.cn.
 - (1) Dickie, J. P.; Yen, T. F. Anal. Chem. 1967, 39 (14), 1847–1852.

- (2) Yen, T. F. Fuel Sci. Technol. Int. 1992, 10 (4-6), 723-733. (3) Sheu, E. Y. Energy Fuels 2002, 16 (1), 74-82. (4) Storm, D. A.; Sheu, E. Y.; DeTar, M. M. Fuel 1993, 72 (7), 977-
- (5) Storm, D. A.; Sheu, E. Y. Fuel 1995, 74 (8), 1140-1145.(6) Li, S.; Liu, C.; Que, G.; et al. Fuel 1996, 75 (8), 1025-1029.
- (7) Wiehe, I. A. Ind. Eng. Chem. Res. 1993, 32 (11), 2447-2454.
- (8) Rahimi, P. M.; Gentzis, T.; Chung, K.; et al. *Prepr. Am. Chem. Soc.*, *Div. Fuel Chem.* **1997**, *42*(1), 146–152...
- (9) Fotland, P.; Anfindsen, H.; Fadnes, F. H. Fluid Phase Equilib. 1993,
- (10) Fotland, P.; Anfindsen, H. Fuel Sci. Technol. Int. 1996, 14 (1-2),

validated that the maximum of mass fraction normalized conductivity when adding normal alkanes to crude oil is the starting point of asphaltene precipitation.

If experimental conditions are fixed, the amount of normal alkane needed to cause asphaltenes to aggregate is larger when the residue sample is more stable. So the ratio of added normal alkane to residue sample can be taken as the colloidal stability parameter of the residue sample. This method was used to study the variation in the colloidal stability of the residue during thermal reaction, and the relationship between colloidal stability and coking characteristics was studied as well.

The polarity of asphaltene molecules plays an important role in the colloidal characteristics of the residue. Although petroleum residue contains polar molecules, which is accepted by most researchers, there have been few reports about the dipole moment values of petroleum residue molecules.11-14 In this study, residue samples are fractioned by liquid chromatography, the mean dipole moment values of asphaltene were measured, and the linkage between molecular characteristics and the colloidal stability of the residue is discussed.

The relationship between colloidal stability and coking characteristics of petroleum residue during thermal reaction were studied. Furthermore, the fraction composition and the mean dipole moment of asphaltenes were measured to reveal their effect on the colloidal stability of the residue.

2. Experimental Section

Five kinds of atmosphere residues were studied, the boiling points of which were more than 350 °C. The samples were

⁽¹¹⁾ Carnahan, N. F.; Louis, J.; Antón, R.; et al. Energy Fuels 1999, 13, 3(2), 309–314. (12) Murgich, J.; Abanero, J. A.; Strausz, O. P. *Energy Fuels* **1999**, *13*,

^{3 (1), 278-286.}

⁽¹³⁾ Maruska, H. P.; Rao, B. M. L. Fuel Sci. Technol. Int. 1987, 5 (2),

⁽¹⁴⁾ Kellomäki, A. Fuel 1991, 70, 1103-1104.

Table 1. Properties of DGAR, MEAR, and THAR

properties (m%)	DGAR	KLAR	MEAR	LHAR	THAR
С	86.44	86.40	84.48	87.0	84.56
H	12.47	12.46	11.32	11.4	10.63
S	0.25	0.13	3.8	0.37	3.25
N	0.62	0.41	0.2	0.92	0.55
ash	0.014	0.085	0.018	0.049	0.050
oxygen	0.21	0.52	0.18	0.26	0.96
	SA	RA Compo	sition		
saturate	52.6	50.4	37.2	29.2	28.1
aromatics	25.0	22.2	46.0	28.7	37.6
resin	21.8	27.2	14.2	40.3	17.4
C ₇ -asphaltene	0.6	0.2	2.6	1.8	16.9

DaGang AR (DGAR), Kalamayi AR (KAR), Middle East AR (MEAR), LiaoHe AR (LHAR), and TaHe AR (THAR). Their properties are shown in Table 1.

Thermal reactions were performed under nitrogen, and the initial pressure was 1.0 MPa at 25 °C. During thermal reaction, samples were collected at various times by immerging on-line sampling equipment in the liquid. Through this sample collection method, samples from the same autoclave reaction can be compared. Because the critical temperature of light components was lower than the reaction temperature, the components were in the gaseous state under the reaction conditions and the boiling points of the samples were higher than 250 °C. To study the colloidal stability variation in samples collected at different thermal reaction time, we studied the samples directly without distillation, which included leaving the coke in them.

Separation Scheme. Every sample collected from the thermal reaction was stirred to ensure equality and then divided into three parts. The samples were separated in order to measure the coke characteristics and colloidal stability parameters. The coke content is defined as the mass percentage of tolueneinsoluble material.

The asphaltene was isolated by the addition of a 30:1 excess of *n*-pentane to the residuum at room temperature. The suspension was heated to boil and filtered after cooling down. The precipitate was extracted by n-pentane until the filtrate was colorless. The n-pentane was removed from the maltene by distillation; the maltene was then fractioned into five fractions by liquid chromatography, which included saturates in addition to light aromatics, heavy aromatics, light resins, middle resins, and heavy resins.15

The colloidal stability parameters were characterized through the mass fraction normalized conductivity method. 9,10,16 The stability of the residue samples decreased with the addition of n-heptane, and the colloidal stability of the residue then decreased and collapsed. So the ratio of added n-heptane to residue sample can be taken as the colloidal stability parameter of the residue sample. A Hewlett-Packard impedance analyzer (HP4194A impedance/gain/phase analyzer) was used to measure the conductivity of residue solutions. The employed frequency was 1 kHz. The mass fraction normalized conductivity can then be calculated from the dilution ratio and the conductivity of residue solution

The conductivity is measured at 35 \pm 0.1 °C. The conductivity of the residuum solution is measured after the addition of approximately 3 mL of *n*-heptane and mixing for about 5 min. The mass fraction normalized conductivity of the residue can be calculated from the conductivity and dilution ratio of the residue solution by formulas 1 and 2.

$$\Lambda = \kappa(1 + x\rho) \tag{1}$$

$$x = V\rho/M \tag{2}$$

where Λ is the mass fraction normalized conductivity of residuum (S/m), κ the measured conductivity of residuum (S/ m), x the ratio of solvent to the weight of residuum (g/g), ρ the density of solvent (0.685 g/cm³ for *n*-heptane), V the volume of n-heptane added (cm 3), and M the mass of the residue sample

Because the viscosity of the solution decreases as a result of the dilution, the mass fraction normalized conductivity of the residue sample does not decrease except when asphaltene aggregation happens. The maximum of the mass fraction normalized conductivity of the residue sample is a sign of asphaltene aggregation. So the ratio of added n-heptane to residue sample when asphaltene aggregation happens can be taken as the colloidal stability parameter of the residue sample, which is shown as formula 3.

$$P = M_{\rm h}/M_{\rm r} \tag{3}$$

where P is the colloidal stability parameter of the residue sample (g/g), M_h the mass of added *n*-heptane to cause asphaltene aggregation (g), and M_r the mass of the residue sample (g).

The molecular weights of separated fractions from residue or thermal samples were measured by a Knauer vapor pressure osmometer at 45 °C, using benzene as the solvent.

In addition, the mean dipole moments of asphaltenes were calculated by the method developed by Guggenheim and Smith.^{17,18} They developed a method for gaining the apparent polarization and dipole moment of a polar solute in a nonpolar solvent by measuring the dielectric constant and refractive index of the solutions. The formulas are as follows

$$P_{2\mu} = 3M_2 v_1 \left(\frac{\alpha}{(\epsilon_1 + 2)^2} - \frac{v}{(n_1^2 + 2)^2} \right)$$
 (4)

$$\alpha = \frac{\partial \epsilon_{12}}{\partial w_2} \tag{5}$$

$$\alpha = \frac{\partial \epsilon_{12}}{\partial w_2}$$
 (5)
$$v = \frac{\partial n_{12}^2}{\partial w_2}$$
 (6)

where w_2 is the weight fraction of solute, ϵ_{12} the dielectric permittivity of solution, n_{12} the refractive index of solution, M_2 the molecular weight of the solute, and v_1 the specific volume of the solvent.

The fractions were diluted separately by benzene, which is a nonpolar solvent. The dielectric permittivities and refractive indexes of these solutions were measured. The dielectric permittivity of the solutions was measured by using a HP4194A analyzer. The refractive index of solutions was measured by using a refractive meter. The mean dipole moment of fractions could then be computed.

The relationship between coking characteristics and colloidal stability variation of all five residua during thermal reaction were studied, and three residua were selected to study the linkage between molecular characteristics and the colloidal stability.

3. Results and Discussions

3.1. Relationship between Colloidal Stability Parameters (CSP) Variation and Coking Characteristics. First, the relationship between colloidal stability parameters (CSP) and

⁽¹⁵⁾ Liu, C. G.; et al. *Acta Pet. Sin.* **1987**, *3*(1), 90–98. (16) Zhang, L. L.; Yang, G. H.; Huanget, Q. S.; et al. *Prepr. Am. Chem. Soc., Div. Pet. Chem.* **2002**, *47*(1), 26–28.

⁽¹⁷⁾ Guggenheim, A. *Trans. Faraday Soc.* **1949**, *45*, 714–720. (18) Smith, J. W. *Trans. Faraday Soc.* **1950**, *46*, 394–399.

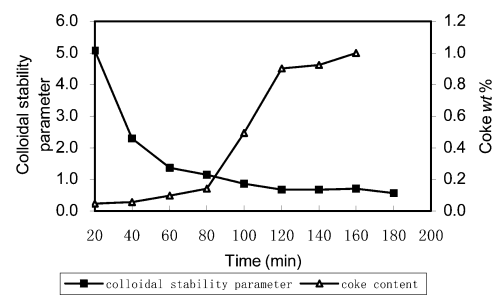


Figure 1. Variation in CSP and coking characteristics of DGAR during thermal reaction at 405 °C.

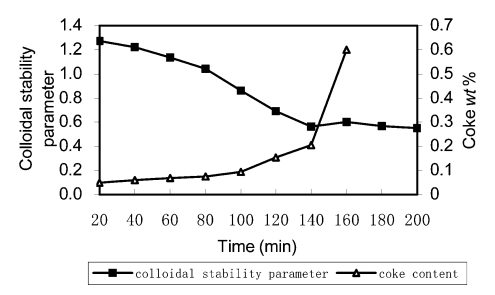


Figure 2. Variation in CSP and coking characteristics of MEAR during thermal reaction at 400 °C.

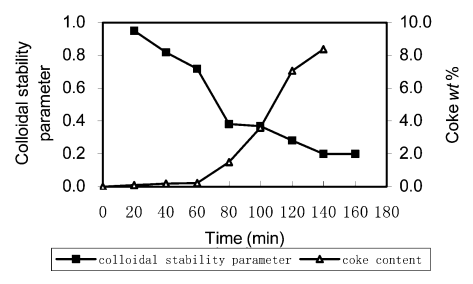


Figure 3. Variation in CSP and coking characteristics of THAR during thermal reaction at 400 $^{\circ}\mathrm{C}.$

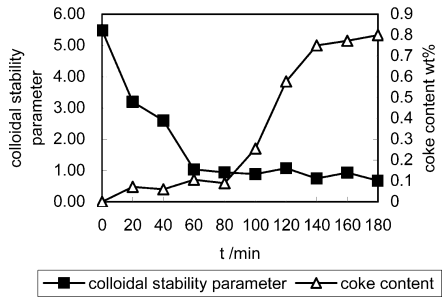


Figure 4. Variation in CSP and coking characteristics of LHAR during thermal reaction at 400 $^{\circ}\mathrm{C}.$

coking characteristics during thermal reaction of DGAR, KAR, MEAR, LHAR, and THAR were studied.

It can be seen in Figures 1–5 that there exists a cokeinduction period for all residue samples studied. For example, they are 80 min for DGAR, 120 min for MEAR, and 80 min for THAR. During this period, no coke formation is observed. However, coke forms rapidly after that. On the contrary, for all residue samples studied, the colloidal stability of the residue samples decreases upon increasing thermal reaction time but shows little dependence on it after the coke-induction period is reached. This phenomenon reveals that the coking characteristics

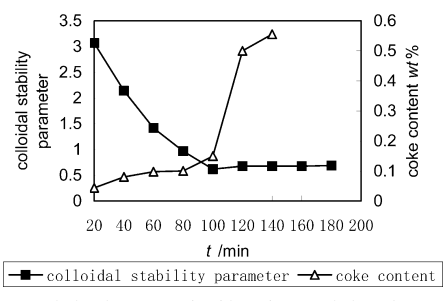


Figure 5. Variation in CSP and coking characteristics of KLAR during thermal reaction at 400 $^{\circ}\text{C}.$

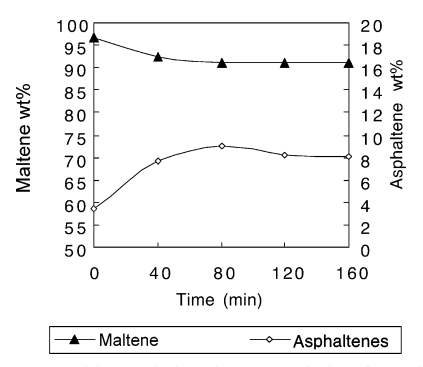


Figure 6. Composition variations in DGAR during thermal reaction.

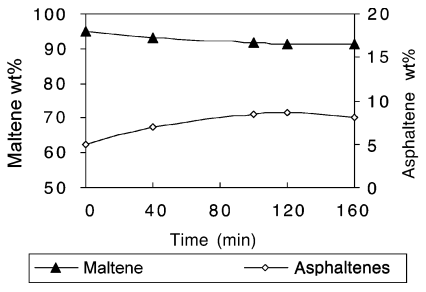


Figure 7. Composition variations in MEAR during thermal reaction.

of a residue are determined by its colloidal stability. As thermal reaction progresses, the colloidal stability of the residue declines to its utmost, and asphaltene solubility reaches the saturation state. It could be inferred that the asphaltene aggregation happens, and aggregated asphaltenes would ultimately transform into coke.

3.2. Fraction Composition Variation of Residue during Thermal Reaction. The colloidal stability variation of residue came from the shift in fraction composition and the molecular characteristics of every fraction. Wiehe⁷ analyzed the SARA (saturates, aromatics, resins, and asphaltenes) composition of fractions during thermal reaction and found that the fraction composition played an important role in the coking characteristics of a residue. In this study, the toluene-soluble parts of reacted residue samples were separated into *n*-pentane asphaltenes and *n*-pentane soluble maltenes. The composition variations with thermal reaction time are shown in Figures 6–8.

It can be seen from Figures 6–8 that asphaltene concentration in residue increases quickly during the coke-induction period, reaches a maximum at the end of the coke-induction period, and then decreases slowly during coke production. This phenomenon proves that asphaltenes aggregate and transform into coke at the end of the coke-induction period.

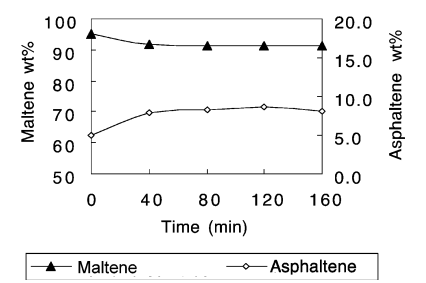


Figure 8. Composition variations in THAR during thermal reaction.

Table 2. Molecular Weights of Fractions of DGAR during Thermal

reaction time (min)	F1	F2	F3	F4	F5	C ₅ -asp		
DGAR	660	1020	1560	1680	1300	4740		
40	470	1030	1110	940	1100	4800		
80	440	750	920	650	780	5250		
120	360	670	870	570	680	6580		
160	350	600	930	1310	610	5050		

Table 3. Molecular Weights of Fractions of MEAR during Thermal Reaction

r	eaction time (min)	F1	F2	F3	F4	F5	C5-asp
	MEAR	290	510	930	610	600	4610
	40	290	470	580	570	570	4670
	80	270	320	540	580	530	4170
	100	270	320	450	480	540	3540
	160	250	340	490	420	510	2050

Table 4. Molecular Weights of Fractions of THAR during Thermal Reaction

1100011011						
reaction time (min)	F1	F2	F3	F4	F5	C ₅ -asp
THAR	400	510	960	570	1890	7700
40	450	330	590	460	580	16130
80	380	400	610	380	490	8930
120	350	380	470	380	490	6820
160	520	360	660	580	740	3520

The proportion of maltene decreases sharply during the cokeinduction period and decreases slowly after that. The enhancement of asphaltenes and abatement of the maltene portion deteriorate the colloidal stability of the residue samples. So the colloidal stability of the residue decreases sharply during the coke-induction period and changes little thereafter.

It can be concluded that the variation in asphaltenes and the maltene proportion has an intrinsic relationship to the colloidal stability variation. During the coke-induction period, the increase in asphaltene content and decrease in maltene content caused the colloidal stability to deteriorate and resulted in the saturation of asphaltene. In other words, asphaltenes stay in the saturated state after the coke-induction period. The excess of asphaltene would aggregate and transform into coke. The decrease in asphaltene content can ameliorate the colloidal stability of the residue, so the colloidal stability parameter does not decrease after the coke-induction period.

3.3. Molecular-Weight Variation in Fractions during Thermal Reaction. During thermal reaction, the colloidal stability variations come from the composition of the fractions and their characteristics. The molecular-weight values are important parameters for the characteristics of residue fractions. The molecular-weight values of every fraction were measured by the VPO method. The MW data of fractions at different reaction times are shown in Tables 2–4.

First, for almost all the samples, the MW values of the fractions of maltenes decrease as the reaction goes on. This phenomenon comes from the thermolysis of residue molecules

Table 5. Mean Dipole Moments of Residue Samples during
Thermal Reaction

		1	reaction t	ime (min)	
	0	40	80	100	120	160
DGAR μ (Debye)	11.7	15.6	15.3		16.3	10.8
MEAR μ (Debye)	14.3	16.4	12.9	12.4		9.7
THAR μ (Debye)	17.6	27.7	22.0		22.9	9.8

and the transformation of components. The downtrend of saturate will pick up with the colloidal stability deterioration as the thermal reaction progresses.

Second, the MW values of the asphaltenes increase at first, reach a maximum at the end of the coke-induction period, and then decrease as the reaction advances. During the coke-induction period, the condensation and aggregation reactions tend to increase the measured MW value of them. At the end of the coke-induction period, the large molecules prefer to aggregate and transform into coke, accompanied by a decrease in the asphaltene MW value. The result is consistent with the conclusion that asphaltenes having a larger conglomerating tendency prefer to transform into coke.

Third, the variation in the MW values of the fractions is consistent with the colloidal stability change. The fraction of resin has an important protective ability to the asphaltene fraction, and the protection ability is more prominent when the difference between them is less. During the coke-induction period, the uptrend of asphaltene MW and the downtrend of resin MW would weaken the protection ability of resins, which is consistent with the rapid deterioration of colloidal stability. Furthermore, the downtrend of asphaltene MW and resin MW is consistent with the slow deterioration of colloidal stability after the coke-induction period.

3.4. Dipole Moment Variations of Fractions during Thermal Reaction. The polarity of asphaltenes is closely related to the colloidal stability of the residue samples. The mean dipole moments of the asphaltenes were measured. The dipole moments of asphaltenes are shown in Table 5.

Table 5 shows the variation in the mean dipole moments of the asphaltenes during thermal reaction. For the three residues studied, the mean dipole moments of the asphaltenes kept increasing as the thermal reaction advanced; the dipole moments then reached their maximum and decreased thereafter. The time to gain the maximum is approximately equal to that of the coke-induction period. This result reveals that the asphaltenes with more polarity tend to aggregate and transform into coke, which made the polarity of the asphaltenes kept in the residue decrease after the coke-induction period.

As the polarity of the asphaltenes decreases, their solubility should increase if the peptization ability of maltene was unchanged. But the data in this research showed that the content of asphaltenes decreased after the coke-induction period, which illuminated that the peptization ability of maltene decreased or that the compatibility between asphaltenes and maltenes declined after the coke-induction period was reached.

4. Conclusions

The relationship between the colloidal stability variation and the coking characteristics of petroleum during thermal reaction was studied. The linkage between asphaltene molecular characteristics and the colloidal stability of the residue was discussed. The conclusions are as follows.

The colloidal stability of the residues decreases sharply during the coke-induction period and changes little thereafter. This phenomenon reveals that the colloidal stability of the residue has an intrinsic relationship to its coking characteristics.

Asphaltene concentration in the residue increased quickly during the coke-induction period and reached a maximum at the end of the coke-induction period. It can be concluded that the variation in the asphaltene and maltene proportion has an intrinsic relationship to the colloidal stability variation and that the deterioration of colloidal stability will cause asphaltenes to aggregate and transform into coke.

The MW values of asphaltenes reached their maximum at the end of the coke-induction period, but MW values of resins decreased as the thermal reaction continued. This phenomenon revealed that the characteristics of residue influenced the colloidal stability of the residue very much.

The mean dipole moments of asphaltenes reach their maximum at the end of the coke-induction period, which reveals that the asphaltenes with more polarity preferentially aggregate and transform into coke.

Generally, the linkage between molecular characteristics, the colloidal stability variation, and the coking characteristics of petroleum during thermal reaction can be described as follows. As the thermal reaction occurs, the asphaltene concentration increases and the maltene concentration decreases, which causes the colloidal stability of the residue to deteriorate. At the same time, the polarity of the asphaltene molecules increases, which signifies a decrease in the colloidal stability of the residue. As the colloidal stability of the residue decreases, the asphaltene

concentration can be dispersed. When the colloidal stability of the residue decreases to a critical value, the asphaltene solubility limit will be exceeded. The excessive asphaltenes then aggregate to form a second liquid phase and transform into coke thereafter. This triggers the formation of coke at the end of the coke-induction period and causes a decrease in the asphaltene concentration from its maximum value. Because the asphaltene molecules with more polarity prefer to aggregate and transform into coke, the dipole moment of asphaltenes in the residue decreases from its maximum value. Moreover, the colloidal stability of the residue changes little thereafter, because the concentration and polarity of the asphaltene molecules decrease after the coke-induction period.

Acknowledgment. This work was partially supported by the National Science Fund committee of China (20506017), the open fund from the State Key Laboratory of Heavy Oil Processing of China (2004HD-04), and the doctor's fund of China University of Petroleum (Y030427). The authors thank the Petrophysics Laboratory of Well Logging Company of ShengLi Petroleum Bureau for supplying the HP 4194A and senior engineer Bingkai Liu for enthusiastic help. The authors are grateful to Shengchuang Yang and Liping Huang, who did many measurements. The authors are grateful to Professor E. Y. Sheu of Vanton Research Laboratory for critical review of this paper.

EF050378O

Hydrodesulfurization of Resid Fluid Catalytic Cracking Diesel Oil over TiO₂-SiO₂ Supported Catalysts

Zhenli Zhang,* Yasong Zhou, Shaojin Zhang, and Chunming Xu

State Key Laboratory of Heavy Oil Processing, China University of Petroleum, Beijing 102249, China

Received April 30, 2006. Revised Manuscript Received August 29, 2006

New catalysts for deep hydrodesulfurization (HDS) of diesel oil were prepared by loading the active metal components on the TiO2-SiO2 composite supports, which were synthesized by a sol-gel and supercritical fluid drying method. The HDS performance of the prepared catalysts for RFCC (resid fluid catalytic cracking) diesel oils was evaluated in a fixed-bed reactor under different conditions. The major sulfur compounds in the RFCC diesel oils are alkyl substituent benzothiophenes (BTs), dibenzothiophene (DBT), and alkyl substituent dibenzothiophenes (DBTs), in which the alkyl DBTs with alkyl groups at the 4 and/or 6 positions, such as 4,6-DMDBT and 4-MDBT, are the refractory compounds. The effects of the catalyst properties on the HDS performance for different sulfur compounds, especially the refractory compounds, in the diesel oils were studied. It was found that the catalysts supported on TiO2-SiO2 composites with higher ratios of Lewis acid sites and with Ni-W active components presented better HDS performance for the alkyl DBTs. The HDS performance of the catalysts for removing of alkyl DBTs can be further improved through increasing the concentration and intensity of Lewis acid by adding F and P into the catalysts.

1. Introduction

Deep hydrodesulfurization (HDS) of diesel oil has attracted much attention recently as the tolerated sulfur content in diesel fuel will be gradually lowered, e.g., to 50 or 30 μ g/g this year in the U.S. and the European Union, and even to lower levels in the near future according to more stringent environmental legislation.1-4 Such a low sulfur level is difficult to achieve because of the alkyl benzothiophenes (DBTs), especially those with one or two alkyl groups at the 4 and or 6 positions of DBT, such as 4-MDBT and 4,6-DMDBT, which have been considered to be the most refractory compounds and are hard to remove due to the steric hindrance of the alkyl groups against the interaction between the sulfur atom and the active sites on the catalyst.5-11 So, the reaction mechanism and kinetics of different kinds of sulfides have been studied in the past decades by using thiophenic compounds as model compounds, through which it is expected that some hints for developing more

* Corresponding author. Tel.: +86-10-89733501. Fax: +86-10-69724721. E-mail address: zhzhl0204415@163.com.

(1) Vargas-Villamil, F. D.; Marroquín, J. O.; de la Paz, C.; Rodríguez, E. *Chem. Eng. Process.* **2004**, *43*, 1309–1316. (2) Kagami, N.; Iwamoto, R.; Tani, T. *Fuel* **2005**, *84*, 279–285.

- (3) Fujikawa, T.; Kimura, H.; Kiriyama, K.; Hagiwara, K. Catal. Today **2006**, 111, 188-193.
- (4) Xue, M.; Chitrakar, R.; Sakane, K.; Hirotsu, T.; Ooi, K.; Yoshimura, Y.; Tola, M.; Feng, Q. *J. Colloid Interface Sci.* **2006**, *298*, 535–542. (5) Corma, A.; Martinez, A.; Martinez-Soria, V. *J. Catal.* **2001**, *200*,
- (6) Ma, X. L.; Sun, L.; Song, C. S. Catal. Today 2002, 77, 107-116. (7) Atanasova, P.; Tabakova, T.; Vladov, Ch.; Halachev, T.; Lopez Agudo, A. *Appl. Catal. A* **1997**, *161*, 105–119.
- (8) Kwak, C.; Lee, J. J.; Bae, J. S. *Appl. Catal. A* **2000**, *200*, 233–242. (9) Yumoto, M.; Usui, K.; Watanabe, K. *Catal. Today* **1997**, *35*, 45–
- (10) Ma, X. L.; Sakanishi, K.; Mochida, I. Hydrodesulfurization Reactivites of Various Sulfur Compounds in Vacuum Gas Oil. *Ind. Eng. Chem.* Res. 1996, 35, 2487-2494;
- (11) Ma, X. L.; Sakanishi, K.; Mochida, I. Hydrodesulfurization Reactivities of Various Sulfur Compounds in Diesel Fuel. *Ind. Eng. Chem. Res.* **1994**, *33*, 218–222.

efficient HDS catalysts and optimizing the processing conditions in deep HDS will be given. 12-17 Many approaches have been conducted to enhance the catalyst activity for deep HDS, and some interesting results have been reported. 18-22 In the previous work, TiO2, SiO2, NH3-Y-zeolite, and some synthesized composites, such as ZrO₂-SiO₂, ZrO₂-Y₂O₃, and TiO₂-Al₂O₃, have been applied as supports for HDS catalysts instead of the Al₂O₃ support used in the commercial catalysts, such as Co-Mo/Al₂O₃ and Ni-Mo/Al₂O₃. ^{4,23-26} These studies offer some guidance for developing the HDS catalysts, but it is difficult to reflect directly the HDS performance of the developed catalysts for real diesel fuel as they used the model, where the sulfur compounds and coexisting compounds are quite different from those in the real fuel. $^{27-30}$

```
(12) Kabe, T.; Aoyama, Y.; Danhong, W. Appl. Catal. A 2001, 209, 237-
```

(13) Brian, M. M. Oil Gas J. 2000, 98, 72-74.

(14) Marin, C.; Escobar, J. Fuel Process. Technol. 2004, 86, 391–405.
(15) Vradman, L.; Landau, M. V. Fuel 2003, 82, 633–639.
(16) Yoshimura, Y.; Yasuda, H. Appl. Catal. A 2001, 207, 303–307.
(17) Le Bihan, L.; Yoshimura, Y. Fuel 2002, 81, 491–494.
(18) Sets. V. Lucco, V. Mill. V. Chimalan, V. Fuel 2002, 81, 491–494.

(18) Sato, K.; Iwata, Y.; Miki, Y.; Shimada, H. J. Catal. 1999, 186,

(19) Takaaki, I.; Shinichi, N.; Ma, X.; Yozo, K.; Isao, M. Appl. Catal. A 1997, 150, 1–11. (20) Kraus, H.; Prins, R. J. Catal. 1997, 170, 20–28.

(21) Vradman, L.; Landau, M. V. Catal. Lett. **2001**, *77*, 47–54. (22) Isao, M.; Kinya, S.; Ma, X.; Nagao, S.; Takaaki, I. Catal. Today

1996. 29. 185-189.

(23) Inoue, S.; Muto, A.; Kudou, H.; Ono, T. Appl. Catal. A 2004, 269,

(24) Mohan, S. R.; Maity, S. K.; Ancheyta, J.; Murali Dhar, G.; Prasada Rao, T. S. R. Appl. Catal. A 2004, 268, 89–97.
 (25) Fujikawa, T.; Kimura, H.; Kiriyama, K.; Hagiwara, K. Catal. Today

2006, 111, 188-193 (26) Ramirez, J.; Gutierrez-Alejandre, A. *Catal. Today* **1998**, *43*, 123–133.

(27) Miller, J. B.; Ko, E. I. J. Catal. 1996, 159, 58-68.

(28) Liu, Z.; Tabora, J.; Davis, R. J. J. Catal. 1994, 149, 117–126.
(29) Atanasova, P.; Halachev, T. Appl. Catal. A 1994, 108, 123–139.
(30) Kraus, H.; Prins, R. J. Phys. Chem. 1995, 99, 16080–16086.

10.1021/ef0601925 CCC: \$33.50 © 2006 American Chemical Society Published on Web 09/23/2006

Table 1. Metal Contents in Catalysts

catalysts	NiW/TS-1	NiW/TS-4	CoMo/TS-1	CoMo/TS-4	NiW/Al ₂ O ₃
	Сс	ntent of Met	tal Component	t (wt %)	
NiO	2.71	2.16	-		2.16
WO_3	25.73	19.75			19.75
CoO			1.27	3.02	
MoO_3			12.38	14.21	

In recent years' investigations of the preparation and application of the nanometer TiO₂—SiO₂ composites, the present authors found that the catalysts supported on these oxides showed better performance for the HDS of petroleum fractions.³¹ In the present study, the authors examined further the effects of the physicochemical properties of these catalysts and the reaction conditions on removal of different sulfur compounds in real diesel oils from resid fluid catalytic cracking (RFCC). Since real diesel oils were used as the feedstock, the experimental results can directly reflect the HDS performance of the developed catalysts for the real feedstock and the provided information is better for guiding the development of deep HDS catalysts and for optimizing the processing conditions.

2. Experimental

2.1. Preparation of the Catalysts. Certain amounts of metal Ni and W or Co and Mo were loaded by impregnation on the two $\text{TiO}_2-\text{SiO}_2$ composite supports, in which the atomic Ti/Si ratio was 1 and 4, respectively, denoted as TS-1 and TS-4. After drying at 120 °C for 4 h and calcining at 500 °C for 3 h, the catalysts, NiW/TS-1, NiW/TS-4, CoMo/TS-1, and CoMo/TS-4, were obtained. A traditional catalyst NiW/Al₂O₃ provided by China National Petroleum Corporation (CNPC) was chosen as a reference to compare with the developed catalysts. The detailed metal contents of the catalysts are listed in Table 1. The catalysts were presulfided with 2 wt % CS₂ in cyclohexane at 300 °C and 4 MPa for 4 h before test.

2.2. Catalysts Characterization. After deaerating at 1.3 KPa and 200 °C for 4 h, the specific surface area and pore volume of the catalysts were measured by using the American Micromeritics ASAP-2400 instrument. The different types of acid sites (Brönsted acid and Lewis acid) on the catalysts were analyzed by pyridine adsorption using the Nicolet Magana 560 E.S.P Fourier transfrom infrared (FTIR) instrument. The acid concentration and distribution were evaluated by the NH₃-TPD (temperature programmed desorption) method using a TP-5000 instrument.

2.3. Evaluation of HDS Performance of Various Catalysts for Real Diesel Oil. The evaluation of the various catalysts for the HDS of real diesel oils was conducted in a continuous-flow microreactor, which was made of steel alloy with a diameter of 8 mm and a catalyst bed volume of 2 mL. The feedstocks were Daqing RFCC diesel oil and Jinxi RFCC diesel oil, provided by China National Petroleum Corporation (CNPC). The major properties and composition of the diesel oils are listed in Table 2. The HDS reaction was carried out at a temperature of 320–360 °C, a total pressure of 4–6 MPa, a liquid hour space velocity (LHSV) of 1–2 h⁻¹, and a hydrogen/oil ratio of 600 mL/mL. The hydrodesulfurized oil was sampled periodically for analysis.

2.4. Analysis of the Concentration of Different Sulfur Compounds in the Diesel Oils and Treated Diesel Oils. The total sulfur content was analyzed by using an ANTEK7000NS instrument. A gas chromatograph with a plus flame photometric detector (GC-PFPD) was used to analyze the concentration of different types of sulfur compounds, grouped as C₂-BT, C₃-BT, DBT, C₁-DBT, C₂-DBT, and C₃-DBT. The instrument was the SP3420 gas chromatogram with an HP5 elastic quartz capillary column (30 m × 0.25 mm × 0.25 mm). The detector temperature was 280 °C, and the column temperature was programmed at 40 °C for 2 min, 4 °C/

Table 2. Properties of Jinxi RFCC Diesel Oil and Daqing RFCC Diesel Oil

properties	Jinxi RFCC	Daging RFCC
density (20 °C) (g/cm ³)	0.8776	0.8716
viscosity (mm ² /s)	4.1907	3.1707
solidifying point (°C)	-4	-20
distillation (°C)		
initial boiling point	180	170
10%	215	198
30%	245	228
50%	279	258
70%	322	298
90%	360	354
95%	>365	>365
sulfur (μg/g)	1377	831
nitrogen (µg/g)	1805	559
cetane number	33.0	26.5
aromatics (wt %)	53.1	59.7
monocyclic aromatics (wt %)	24.6	25.6
dicyclic aromatics (wt %)	23.9	28.2
tricyclic aromatics (wt %)	4.32	5.47
saturated hydrocarbons (wt %)	45.8	39.9
paraffin (wt %)	25.9	28.3
naphthene (wt %)	19.5	9.1
resin (wt %)	1.58	1.06

Table 3. Physicochemical Properties of Supports and Catalysts

samples	$\mathrm{B/L}^a$	surface area (m²/g)	pore volume (mL/g)
NiW/TS-1	1.2	166	0.35
NiW/TS-4	0.7	201.5	0.41
CoMo/TS-1	0.5	126.3	0.23
CoMo/TS-4	0.3	120.5	0.21
TS-1	0.5	437.4	1.39
TS-4	0.3	309.5	0.55

^a The ratio of Brönsted acid sites to Lewis acid sites on the basis of FTIR analysis.

min to 270 °C, and 270 °C for 5 min. In the sulfur quantitative analysis by GC-PFPD, the nonlinear response of the PFPD was considered, but the quenching effect was ignored.³²

3. Results and Discussion

3.1. Type and Strength of Acid Sites on Catalysts. Table 3 lists the physicochemical properties and the ratios of Brönsted acid sites to Lewis acid sites of the four HDS catalysts supported on TS-1 and TS-4. As expected, the loading of metals reduced the surface area of the catalysts. It is clear that the ratios of Brönsted acid sites to Lewis acid sites on the catalysts supported on TS-1 are higher than those on TS-4, regardless of the metal components, which is consistent with the acidity character of the supports. Table 4 lists the acid site concentration and distribution on the supports and catalysts, which were obtained by the NH3-TPD method. It was found that the total acid site concentration of the support TS-1 (0.463 mmol/g) is larger than that (0.395 mmol/g) of the support TS-4, which may be attributed to the higher specific surface area of TS-1 than TS-4, as shown in Table 3. Most of the acid sites on TS-1 and TS-4 are medium in strength; this accounts for 61.2 and 75.9% of the sites, respectively. After loading of Ni and W metals, the acid distribution for catalyst NiW/TS-1 changed less, while the concentration of the strong acid sites on NiW/TS-4 increased obviously, from 0.011 mmol/g for TS-4 up to 0.183 mmol/g for NiW/TS-4, indicating that the loading of Ni and W on TS-4 increases the concentration of the strong acid sites significantly.

3.2. Sulfur Compounds in the RFCC Diesel Oils. The GC-PFPD chromatograms of Jinxi RFCC diesel oil and Daqing

⁽³¹⁾ Zhou, Y.-S.; Fan, X.-H. Chem. J. Chin. Univ. 2003, 24, 1266-

⁽³²⁾ Ma, X. L.; Velu, S.; Kim, J. H.; Song, C. S. Appl. Catal. B 2005, 56, 137-147.

Table 4. Acidity Intensity and Distribution of Supports and Catalysts

total acid size			acid (mmol/g)		distribution of acid sites (%)		
samples	(mmol/g)	weak	medium	strong	weak	medium	strong
NiW/TS-1	0.3436	0.13673	0.2068		39.81	60.19	
NiW/TS-4	0.2666	0.0378	0.0461	0.1826	14.18	17.3	68.52
TS-1	0.4629	0.1797	0.2831		38.83	61.17	
TS-4	0.3950	0.0844	0.2999	0.0106	21.37	75.94	2.69

Table 5. Sulfur Content for Each Group of Sulfur Compounds in Jinxi and Daqing RFCC Diesel Oils

S	рт	СРТ	Срт	Срт	DDT	C DDT	C ₂ -DBT	C DDT
$(\mu g/g)$	DΙ	C _l -D _l	C ₂ -D ₁	C3-D1	ומע	C ₁ -DB1	C ₂ -DB1	C3-DB1
Jinxi	20	85	183	112	309	145	202	133
Daging	16	63	138	112	45	114	171	50

RFCC diesel oil are shown in Figure 1 and 2, respectively. Table 5 lists the sulfur concentration of different groups of the sulfur compounds in the two oils according to the calculation on the basis of the GC-PFPD chromatograms. It shows that the sulfur compounds in Jinxi RFCC diesel oil and Daqing RFCC diesel oil are similar. These sulfur compounds are BT, DBT, and their alkyl-substituted derivatives, which can be grouped as C₁-BT, C₂-BT, C₃-BT, DBT, C₁-DBT, C₂-DBT, and C₃-DBT. Jinxi RFCC diesel oil has a relatively higher concentration of the C₃-DBTs than Daqing RFCC diesel oil, because the former is heavier than the latter, as shown in Table 2.

3.3. HDS Reactivity of Different Groups of Sulfur Compounds in Diesel Oils. Table 6 lists the HDS conversion of different groups of sulfur compounds in Jinxi RFCC diesel oil over the different catalysts. The HDS was conducted at 360 °C

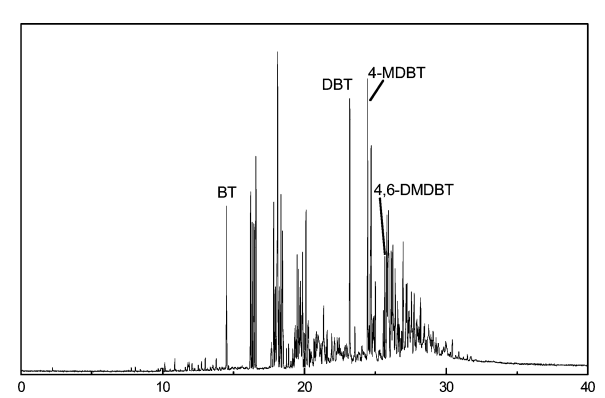


Figure 1. GC-PFPD chromatogram of Jinxi RFCC diesel oil

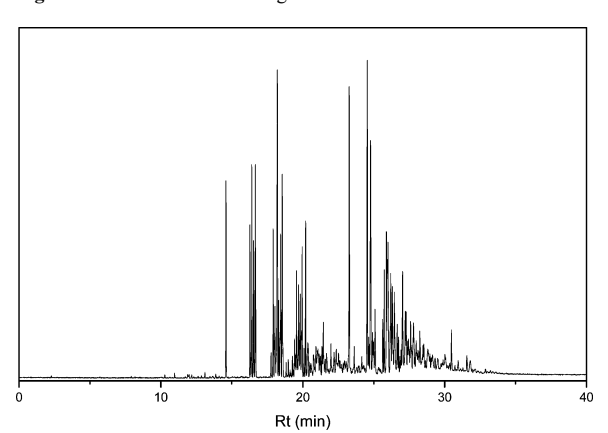


Figure 2. GC-PFPD chromatogram of Daqing RFCC diesel oil

Table 6. HDS Conversion of Each Group of Sulfur Compounds in Jinxi RFCC Diesel Oil^a

		HDS (%)					
S compnd	CoMo/TS-1	CoMo/TS-4	NiW/TS-1	NiW/TS-4	NiW/ Al ₂ O ₃		
C ₂ -BT	95.8	90.7	98.0	92.4	89.6		
C_3 -BT	95.6	91.4	97.6	92.3	90.4		
DBT	98.5	97.6	99.1	98.5	95.7		
C_1 -DBT	82.8	83.4	86.2	87.6	81.1		
C_2 -DBT	70.3	79.2	77.2	85.2	78.5		
C ₃ -DBT	63.9	75.9	71.4	83.5	73.4		

 $^a\, \rm HDS$ conditions: 360 °C, 4.0 MPa, LHSV 2.0 1/h, and hydrogen/oil ratio 600 mL/mL.

and 4.0 MPa with an LHSV of 2.0 1/h and a hydrogen/oil ratio of 600 mL/mL. In a comparison of the reactivity of various sulfur compound groups, it was found that C2-BT and C3-BT groups exhibited similar reactivity, regardless the type of the catalysts, indicating that the length and position of the alkyl groups at benzothiophenes (BTs) have little influence on their HDS reactivity. However, the alkyl DBTs showed quite different conversion over the catalysts, changing from 64% for C₃-DBT to 98% for DBT over CoMo/TS-1, as listed in Table 6. This implies that the number and the position of alkyl groups in DBTs have a strong effect on their HDS reactivity, as reported in the literature. 10,11 In a comparison of the HDS conversion of alkyl BTs and alkyl DBTs, the conversion of alkyl DBT is dramatically lower than that of DBT and C_n-BT. By comparing the GC-PFPD chromatograms of the initial fuel and the treated fuel, as shown in Figures 1 and 3, the above results can be explained by the reasoning that the presence of alkyl groups at the 4 and/ or 6 positions of DBTs, such as 4-MDBT and 4,6-DMDBT, has a tremendous restriction to the adsorption of the sulfur atom on the active sites of the catalysts. The removal of such alkyl DBTs becomes the bottleneck for production of ultra-low-sulfur diesel oil. Therefore, the key to realize deep HDS of diesel oil is to improve the HDS performance of the catalysts for such alkyl DBTs.

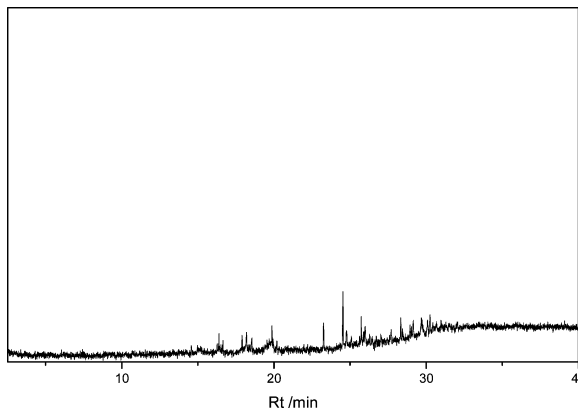


Figure 3. GC-PFPD chromatogram of the hydrodesulfurized Jinxi RFCC diesel oil over NiW/TS-4. HDS conditions: 360 °C, 4.0 MPa, LHSV 2.0 1/h, and hydrogen/oil ratio 600 mL/mL.

Table 7. HDS Conversion of Each Group of Sulfur Compounds
Over Catalysts Modified by Adding F^a

		•				
		HDS (%)				
sulfur compound	NiW/TS-4	NiW/2F-TS-4	NiW/3F-TS-4	NiW/4F-TS-4		
C ₂ -BT	97.1	95.1	96.9	98.4		
C_3 -BT	97.1	96.9	97.3	98.2		
DBT	98.9	99.3	99.4	99.7		
C_1 -DBT	81.4	88.3	88.3	89.7		
C_2 -DBT	65.4	79.2	78.7	81.7		
C ₃ -DBT	51.1	63.9	65.4	69.9		

^a HDS conditions: 360 °C, 4.0 MPa, LHSV 2.0 1/h, and hydrogen/oil ratio 600 mL/mL

3.4. Effect of the Active Metal Component and Support on HDS of Different Sulfur Compounds. In a comparison of the loaded metals, as listed in Table 6, it was found that NiW was more active than CoMo, regardless of the support, especially for removal of the alkyl DBTs (C₁-DBT, C₂-DBT, and C₃-DBT). This may be ascribed to the fact that NiW/TS-1 and NiW/TS-4 have higher surface areas than CoMo/TS-1 and CoMo/TS-4 and/ or the fact that NiW has higher hydrogenation activity than CoMo. In a comparison of the support, it was interesting that for the alkyl BTs and DBT the activity of the catalysts with different supports increased in the order Al₂O₃ < TS-4 < TS-1. However, for the alkyl DBTs, the catalysts with a TS-4 support (NiW/TS-4 and CoMo/TS-4) had significantly higher activity than others. This indicates that the catalysts supported on TS materials show better HDS performance in comparison with the traditional catalyst NiW/Al₂O₃ and that TS-4 support improves significantly the HDS performance of the catalysts for the refractory sulfur compounds. Such results might be explained by the different acidity features of the supports and catalysts. As shown in Tables 3 and 4, NiW/TS-4 has a relatively lower ratio of Brönsted acid sites to Lewis acid sites and has more strong acid sites than NiW/TS-1, although the total acid sites on the former is less than that of the latter. This indicates that more Lewis acid sites and more strong acid sites may favor the HDS of the alkyl DBTs, while more Brönsted acid sites and more weak and medium acid sites may benefit the HDS of the alkyl BTs.

In order to remove alkyl DBTs with steric hindrance, the aromatic cycle in these molecules must be hydrogenated to form torsional naphthene or rotary paraffin, which will decreases the steric hindrance toward the interaction between the sulfur atoms and the active sites on the catalysts. The catalysts supported on TS-4 have relatively large amounts of strong Lewis acid sites, which may be a benefit for such hydrogenation, resulting in better HDS performance. Thus, it is clear that removal of the substituent DBTs is the key for producing the ultra-low-sulfur diesel oil. The influence of the metal composition and acidity of supports on the catalyst performance should be considered in the design and development of the catalysts.

3.5. Effect of F and P Modification on the HDS of Different Sulfur Compounds. Adding acidic components, such as

Table 8. Acid Characteristics of Catalysts Modified by Adding F and P

		acid (µmol/g)				
	I	3]	L		
sample	200 °C	350 °C	200 °C	350 °C		
TS-4	25.4	0.0	77.4	13.1		
2F-TS-4	45.8	0.0	192.9	42.9		
3F-TS-4	25.4	0.0	151.2	23.8		
4F-TS-4	27.1	0.0	152.4	28.6		
2P-TS-4	42.4	0.0	185.7	34.5		
3P-TS-4	22.0	0.0	145.2	21.4		
4P-TS-4	22.0	0.0	147.6	22.6		
5P-TS-4	25.4	0.0	164.3	27.4		

the elements F or P, into the catalysts is a simple way to increase the Lewis acid concentration of catalysts. In the present study, modification of the HDS catalyst by adding F and P was conducted. The modified catalysts were labeled as NiW/nX-TS-4, where X was the element F or P and n was the weight percentage of F or P in the support. Table 7 lists the HDS results of Jinxi RFCC diesel oil over the catalysts modified by adding different percentages of F. The HDS was performed at 320 °C and 4.0 MPa with an LHSV of 2.0 1/h. The hydrogen/oil ratio was 600 mL/mL. The results showed that the catalysts modified by F had significantly better HDS performance for C_n-DBTs than the unmodified catalysts. The concentration of strong Lewis acid sites on the catalysts modified by adding F was enhanced significantly, as shown in Table 8. These results explain why the NiW/nF-TS-4 showed better HDS performance than NiW/ TS-4, which is in agreement with the foregoing discussion about the relationship between the acidity type and HDS performance of the catalysts.

Table 9 lists the HDS results of Jinxi RFCC diesel oil over the catalysts modified by adding P. The HDS was conducted at 320 °C and 4.0 MPa with an LHSV of 2.0 1/h and a hydrogen/oil ratio of 600 mL/mL. The results also show that modification by adding P plays an important role in improving the performance of the catalysts for converting C_n-DBTs. The results further prove that the increase in Lewis acid concentration on catalysts favors the HDS of alkyl DBTs.

The HDS conversions for Jinxi RFCC diesel oil over the catalysts modified by F and P, respectively, as a function of the reaction time are shown in Figures 4 and 5. These show that the activity of the catalysts decreased obviously with increasing reaction time. This phenomenon may be contributed to (1) the loss of F and P in the catalyst within the reaction process, resulting in the decrease of HDS catalytic activity and (2) the polymerization and carbonization of some active compounds, such as olefin and/or polycyclic aromatics, coexisting in the RFCC diesel oil in the presence of the strong acid sites, which deactivate the catalyst. In order to find which factor is more responsible for the deactivation of the catalyst, the HDS of BT in n-heptane with $1000 \mu g/g$ sulfur content was performed under the same reaction conditions. The results are shown in Figure 6. If the deactivation of the catalyst was due to the loss

Table 9. HDS Conversion of Each Group of Sulfur Compounds Over Catalysts Modified by Adding Pa

		•	HDS (%)	,	,
			прз (%)		
sulfur compound	NiW/TS-4	NiW/2P-TS-4	NiW/3P-TS-4	NiW/4P-TS-4	NiW/5P-TS-4
C ₂ -BT	97.1	97.7	95.6	96.6	98.2
C ₃ -BT	97.1	97.7	96.1	96.9	98.7
DBT	98.9	99.4	99.3	99.3	99.6
C_1 -DBT	81.4	86.2	85.8	85.8	91.0
C_2 -DBT	65.4	72.3	75.2	76.2	84.2
C ₃ -DBT	51.1	59.4	66.2	69.9	77.4

^a HDS conditions: 360 °C, 4.0 MPa, LHSV 2.0 1/h, and hydrogen/oil ratio 600 mL/mL.

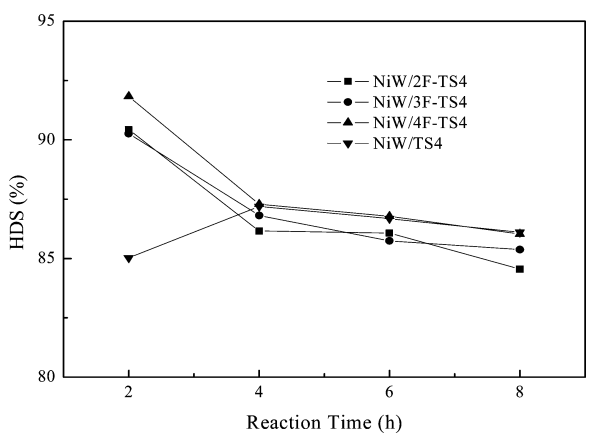


Figure 4. HDS conversion of Jinxi RFCC diesel oil over the catalysts modified by adding F as a function of reaction time. HDS conditions: 360 °C, 4.0 MPa, LHSV 2.0 1/h, and hydrogen/oil ratio 600 mL/mL.

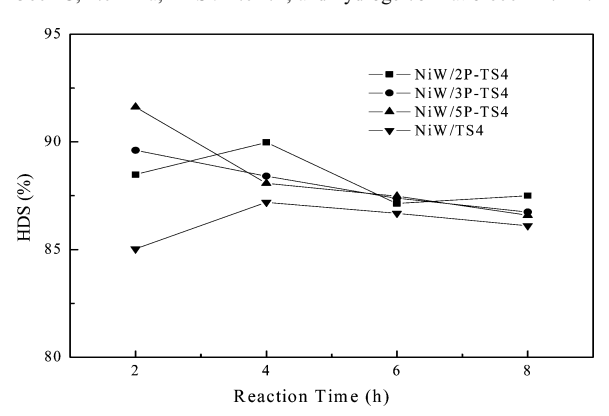


Figure 5. HDS conversion of Jinxi RFCC diesel oil over the catalysts modified by adding P as a function of reaction time. HDS conditions: 360 °C, 4.0 MPa, LHSV 2.0 1/h, and hydrogen/oil ratio 600 mL/mL.

of F and P within the reaction process, the same result should be found for the HDS of BT in n-heptane. However, the figure shows that the activity of the catalyst for the HDS of BT in n-heptane was stable with increasing reaction time. This indicates that the main reason for the deactivation of the catalyst was not due to the loss of F and P in the catalyst but, more likely, to the polymerization and/or carbonization of the coexisting olefin and polycyclic aromatics at the strong acid sites of the catalyst surface.

3.6. Effect of Reaction Conditions on the HDS of Different Sulfur Compounds. The reaction conditions have different effects on various reactions such as desulfurization, hydrogenation, and cracking, which occur in the RFCC HDS process. As the HDS reaction is exothermal, the equilibrium conversion of the sulfur compounds decreases with increasing reaction temperature on the basis of the thermodynamic principle, but the reaction rate is accelerated at higher temperatures according to the kinetic theory. The effect of the reaction conditions, including temperature, pressure, and LHSV, on the HDS of real RFCC diesel oil was also examined in the present study.

Table 10 shows the sulfur content for different groups of sulfur compounds in Jinxi RFCC diesel oil hydrodesulfurised over NiW/TS-4 at a pressure of 4.0 MPa, an LHSV of 2.0 1/h, a hydrogen/oil ratio of 600 mL/mL, and temperatures of 320 and 360 °C, respectively. The results show that the higher reaction temperature favors the conversion of the alkyl DBTs,

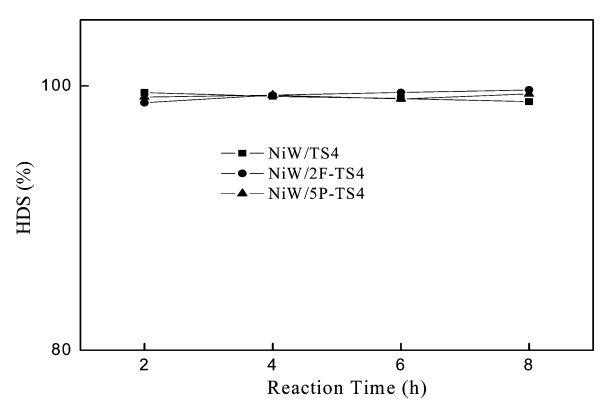


Figure 6. HDS conversion of BT in n-heptane over the modified catalysts as a function of reaction time. HDS conditions: 360 °C, 4.0 MPa, LHSV 2.0 1/h, and hydrogen/oil ratio 600 mL/mL

Table 10. Effect of Temperature on the HDS of Different Groups of Sulfur Compoundsa

	content $(\mu g/g)$				
sulfur compounds	feedstock	320 °C	360 °C		
C2-BT	183	7.5	9.9		
C3-BT	112	4.4	6.9		
DBT	309	2.7	3.6		
C1-DBT	145	16	14		
C2-DBT	202	36	25		
C3-DBT	133	34	15		

^a HDS conditions: 4.0 MPa, LHSV 2.0 1/h, and hydrogen/oil ratio 600 mL/mL

while the alkyl BTs and DBT are easily converted even at lower reaction temperatures. This result can be explained by the following two aspects: (1) There is a big difference in the reactivity and activation energy of the sulfur compounds. 10,11,33,34 The conversion of the refractory sulfur compounds can be increased more significantly by increasing the temperature, as they have a higher activation energy. (2) The acidity properties of catalysts are also influenced by temperature. The Brönsted acid sites of TiO₂-SiO₂ composite oxides originate from the surface hydroxyl, which are reduced by dehydroxylation under higher temperature. Thus, the high temperature causes a decrease of the total number of Brönsted acid sites on the catalyst, resulting in poorer performance for removal of alkyl BTs and DBT. Consequently, the increase in temperature leads to a significant increase of HDS conversion of the alkyl DBTs and a slight decrease in the HDS conversion of the alkyl BTs.

In order to improve the approachability of the sulfur atoms to the active sites on catalysts in the HDS of alkyl DBTs, the key is to weaken the steric hindrance of the alkyl groups at the 4 and/or 6 positions. One of the ways is to increase the saturation degree of the aromatic ring through hydrogenation. On the basis of both the kinetic theory and thermodynamics, the increase in pressure favors the hydrogenation reaction. Thus, the increase in the pressure should result in an increase of HDS conversion, especially for the alkyl DBTs. Table 11 lists the concentrations of the different groups of sulfur compounds in the treated Jinxi RFCC diesel oil on NiW/TS-4 at different pressures. The reaction was conducted at 320 °C with an LHSV of 2.0 1/h and a hydrogen /oil ratio of 600 mL/mL. As expected, the increase in the pressure reduced the alkyl DBTs significantly.

⁽³³⁾ Bataille, F.; Lemberton, J.-L.; Michaud, P.; Perot, G.; Vrinat, M.; Lemaire, M.; Schulz, E.; Breysse, M.; Kasztelank, S. *J. Catal.* **2000**, *191*,

⁽³⁴⁾ Orozco, E. O.; Vrinat, M. Appl. Catal. A 1998, 170, 195-206.

Table 11. Effect of Pressure on the HDS of Different Groups of Sulfur Compounds^a

		content (µg/g)	
sulfur compounds	feedstock	4.0 MPa	6.0 MPa
C2-BT	183	5.2	7.5
C3-BT	112	3.2	4.4
DBT	309	3.5	2.7
C1-DBT	145	27	16
C2-DBT	202	70	36
C3-DBT	133	65	34

^a HDS conditions: 360 °C, LHSV 2.0 1/h, and hydrogen/oil ratio 600 mJ/mJ

Table 12. Effect of LHSV on the HDS of Different Groups of Sulfur Compounds^a

	content (µg/g)				
sulfur compounds	feedstock	2.0 1/h	1.0 1/h		
C2-BT	183	5.2	10		
C3-BT	112	3.2	6.1		
DBT	309	3.5	4.5		
C1-DBT	145	27	18		
C2-DBT	202	70	31		
C3-DBT	133	65	19		

^a Reaction conditions: pressure 4.0 MPa, temperature 320 °C, and H₂/ oil ratio 600 mL/mL.

Table 13. Hydrodesulfurization of Different Sulfur Compounds in Daqing RFCC Diesel^a

		NiW/TS-4		NiW/TS-1	
sulfur content ($\mu g/g$)	feedstock	360 °C	320 °C	360 °C	320 °C
C ₂ -BT	138		1.0		1.4
C ₃ -BT	112	2.2	1.0	2.9	1.7
DBT	45	1.0	1.4	1.1	2.5
C_1 -DBT	114	3.1	5.5	3.8	9.9
C_2 -DBT	171	6.1	14	7.8	19
C_3 -DBT	50	2.4	7.4	3.4	14

^a Reaction conditions: pressure 6.0 MPa, LHSV 1.0 1/h, and H₂/oil ratio 600 mL/mL.

The effect of LHSV on the HDS of different sulfur compounds was also examined at 320 °C and 4.0 MPa with a hydrogen/oil ratio of 600 mL/mL. Table 12 lists the changes in the sulfur concentration for different sulfur compounds in the treated Jinxi RFCC diesel oil on NiW/TS-4 at LHSVs of 2.0 and 1.0 1/h, respectively. The results show that a lower LHSV increases the conversion of the alkyl DBTs.

3.7. Effect of the Composition of Diesel Oils on the HDS Performance. The sulfur content and distribution in the two RFCC diesel oils are different, as shown in Table 5, which may influence the HDS performances of the catalysts. Table 13 shows the sulfur content for different sulfur compounds in the hydrodesulfurised Daqing RFCC diesel oil. By a comparison of Tables 10 and 13, it is found that the concentrations of the

remaining sulfur compounds, especially alkyl DBTs, in the treated Daqing RFCC diesel oil are much less than those in the treated Jinxi RFCC diesel oil. One of the major reasons may be that Daqing RFCC diesel oil contains less sulfur compounds, especially the less heavy sulfur compounds, such as C₃-DBTs, than Jinxi RFCC diesel oil.

The experimental results in Table 13 also show that the catalyst supported on TS-4 has better HDS performance for the HDS of the alkyl DBTs than the catalyst supported on TS-1, which is in agreement with the results for the HDS of Jinxi RFCC diesel oil (see Table 6).

4. Conclusions

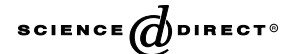
- (1) The major sulfur compounds in RFCC diesel oils are the BT, DBT, and alkyl-substituted derivatives. There are some differences in the distribution of sulfur compounds in diesel oils from different sources, which may result in the different HDS reactivity.
- (2) Among the sulfur compounds in RFCC diesel oils, DBT and alkyl BTs are easily removed, while alkyl DBTs, especially those with one or two alkyl groups at the 4 and/or 6 positions, are more different to remove from diesel oil, which becomes the main barrier in the deep HDS of diesel oil.
- (3) The developed catalysts with Ni and W active metals on TiO_2-SiO_2 have better HDS performance than those with Co and Mo active metals on the same support. The catalysts supported on TS-1 with relatively larger amounts of Brönsted acid sites and with more weak and medium acid sites have better HDS performances for alkyl BTs and DBT, while the catalysts supported on TS-4 with relatively larger amounts of Lewis acid sites and with more strong acid sites show better HDS performance for alkyl DBTs.
- (4) The HDS performance of the catalysts for alkyl DBTs can be enhanced through increasing the concentration and intensity of Lewis acid sites by adding F or P into the catalysts. However, the stability of such catalysts is reduced in the HDS process of RFCC diesel oil due to the presence of the strong acid sites on the catalyst surface, which accelerate polymerization and carbon deposition on the catalyst surface, resulting in deactivation of the catalysts.
- (5) Under the studied reaction conditions, the HDS conversion of alkyl DBTs in the RFCC diesel oil over NiW/TS-4 can be increased through increasing the temperature, raising the pressure, and/or reducing the LHSV.

Acknowledgment. This work was supported financially by the National Natural Science Foundation of China (No. 20276040), the National Basic Research Program of China (No. 2004CB217807), and the CNPC Innovation Foundation (03E7015).

EF0601925



Available online at www.sciencedirect.com



European Polymer Journal 42 (2006) 274-285



www.elsevier.com/locate/europoli

Preparation of silica-PS composite particles and their application in PET

Wu Tianbin, Ke Yangchuan *

State Key Laboratory of Heavy Oil Processing, Faculty of Chemical Engineering, China University of Petroleum, 18 Fuxue Road, Changping, 102249 Beijing, PR China

> Received 5 June 2005; received in revised form 29 July 2005; accepted 3 August 2005 Available online 12 September 2005

Abstract

To investigate how the superfine particles disperse in the polymers, the paper presented the preparation of monodisperse silica particles by Stöber method, and then grafted by γ -methacrylic propyl trimethoxysilane (MPS) as a coupling agent. Using these modified particles, the more stable silica-PS superfine composite particles with higher monodispersity than these of previous reports are prepared and reported through dispersion polymerization (DP) method, whose morphology is investigated with transmission electron microscope (TEM). Their high stability is provided from the bonding of C=C groups of MPS to the silanol groups on the surface of silica particles from FTIR.

Using this DP process, the influence of different size grafted silica particles on the morphology, polystyrene (PS) encapsulation behavior and the distribution in these composite particles have been investigated. When the grafted silica size is in nanoscale or less than 54 nm, the spherical shape of neither silica particles nor their composite particles is regular, but they can homogeneously disperse in polystyrene. As the size (d_n) of grafted silica particles increase to submicrometer (or 100 nm $< d_n < 1000$ nm), their coefficient variance of size distribution (C_v) ranges from only 9.0% to 1.5%. These obtained particles are completely encapsulated by PS with more regular shape, and have their C_v below 7%. When the size of silica particles reaches 380 nm, their C_v obviously reduces to 2.5%, and specially, the number of grafted silica particles approaches to one in each of the composite particles. But, when the silica size reaches 602 nm, PS can hardly encapsulate grafted silica particles and free silica particles appear in reactive system.

Furthermore, using the silica particles of 380 nm, a series of core-shell structured superfine composite particles of 640–1100 nm with C_v lower than 11% are obtained. Under the set conditions, the preparing factors on these composite particles using 380 nm grafted silica particles is discussed, and the best reaction condition for the well-dispersed and regular periphery silica-PS composite particles is optimized as, the additions amounts of PVP, styrene, AIBN, grafted SiO_2 and H_2O are 0.23 mmol L^{-1} , 0.60 mol L^{-1} , 6.10 mmol L^{-1} , 0.10 mol L^{-1} and 5.50 mL, respectively. Under this case, the composite particles can be prepared with $C_{\rm v}$ below 8%.

At last, these composite particles are mixed with poly(ethylene terephthalate) (PET) to investigate their nucleation effect. Results show that all different size particles can promote PET's crystallization and enhance the crystallization rate, and PET's crystallization temperature (Tmc) is obviously enhanced from 193 to 205 °C through differential scanning calorimetry (DSC). It is strongly suggested that different silica size level all play nucleation role in PET, and thus explain the nucleation effect of multiscale inorganic particles.

© 2005 Elsevier Ltd. All rights reserved.

0014-3057/\$ - see front matter © 2005 Elsevier Ltd. All rights reserved. doi:10.1016/j.eurpolymj.2005.08.002

Corresponding author. Tel.: +86 10 89733270; fax: +86 10 69724721. E-mail addresses: wtianbin@sohu.com (Wu Tianbin), kyc01@sohu.com (Ke Yangchuan).

1. Introduction

Superfine inorganic particles now have been applied to petroleum engineering for stabilizing the emulsion, and petrochemical polymer materials for creating the high performance composite materials [1-10]. In these applications, the dispersion behavior of the particles greatly affect the properties of inorganic-polymer composite materials due to their high surface energy and easy agglomeration, bad compatibility with polymer matrix and inhomogeneous dispersibility in them. Thus, the key factors preparing the inorganic-polymer composite materials lies in solving the disperse problem of inorganic phase in polymer matrix. Several methods have been used to prevent inorganic particles of nanoscale from agglomerating [1-8], in which the most popular way is to treat the inorganic phase through organic molecules such as surfactant. However, directly mixing the treated inorganic nanoscale particles with polymer still leads to significant agglomeration. Thus, the layered silicates are suggested as the precursor preparing the polymer based nanocomposites through a new way called intercalation polymerization technology (IPT) [1,2]. Generally, the layer gallery [11] of 1 nm in this layered silicate is provided as a space for monomers intercalating. Finally, the monomers will polymerize in the space once initiated under polymerization condition. Meanwhile, the original micronmeter-sized particles of the layered silicate is delaminated or exfoliated into nanoscale layers and in situ dispersed in the polymer matrix. This dispersing method thus has attracted much attention [12]. By the IPT method, the polyester-layered silicate nanocomposites (NPET) are successfully prepared with the exfoliated layers of homogeneous dispersion [1,2], and higher crystallization behavior, e.g., more enhanced heat distortion temperature than their pure counterpart.

While, these effects introduced from layered silicates are related to multiple scale effect of exfoliated layers and/or polymer's double melting behavior [13]. So far, the relationship between the multiscale effects of layers and multiple melting crystallization behavior for a polymer is not established because of its high difficulty. Therefore, using the single scale or monodisperse silica particles as the nucleation or crystallization centers of polymers should provide a proper way to get insight of these behavior.

As for the monodisperse particles, they have many applications to fields such as, separating the mixtures in the chromatographical column as the solid fillers, standard calibration, photonic crystals, biomedical examinations, etc. [14–16]. Their composite particles

through encapsulating the inorganic particles with polymers offer good dispersibility of inorganic particles in organic media, enhancing the stability of its final product [17–19], facilitating their storage or transport behavior [20,21], and providing many potential applications in adhesives, textiles, optics and electronics [22,23].

The monodisperse composite particles are prepared by the most traditional method of an emulsion polymerization (EP) in the presence of inorganic particles [24,25]. Ding et al. prepared monodisperse silica-PS composite particles with core-shell structure by in situ EP of styrene on the surface of silica nanoparticles grafted with the oleic acid [24]. In the produced coating, the C=C bonds of oleic acid are covalently attached to silanol groups at the surface of nanosized silica, the coating layer thickness can be altered by the amount of styrene and the diameters of composite particles be controlled by the amount of grafted silica. Zhang et al. have successfully prepared different size monodispersed silica-PS core-shell microspheres with different cores by EP and found their monodispersity and diameters depend on the concentration of emulsifier and the size of silica nanoparticles grafted with MPS [25]. On the other hand, Gu et al. have synthesized silica-PS core-shell particles with micron sizes through soap-free emulsion polymerization of styrene initiated with the ionic initiator KPS, the methacryloxypropyltrimethoxysilane as a coupling reagent and NaSS as the stabilizer [26]. They demonstrated that the shell thickness of composite particles changed as styrene concentration and the size of silica particles in submicron and micron scale. Although the EP can conveniently prepare the monodisperse core shell silica-PS composite particles, the emulsion system easily bring about polluting environment due to the existence of emulsifier. Therefore, more attention was paid to dispersion polymerization (DP) preparing fine particles.

So far, the preparation of the core–shell inorganic-polymer composite particles through DP has a few reports [5–8,27,28]. In this DP process, the monomer, stabilizer and initiator are dissolved in reaction medium forming homogeneous mixture prior to reaction. Then, polymeric particles will deposit from reaction medium by means of stabilizer when the polymeric chain exceed the critical chain length [29,30]. More recently, DP method is mainly used to prepare micron-sized particles or monodisperse microspheres [31], and prepare inorganics-polymer composite particles [5–8,27,28,32]. Lascelles et al. described the influence of synthesis parameters on the formation of silica–polypyrrole nanocomposites [32]. Bourgeat-Lami et al. reported the preparation of silica–PS composite particles in an ethanol–water

medium in the presence of grafted silica nanoparticles [6–8]. They both demonstrated that if silica particles are only modified with MPS, PS can successfully encapsulate silica particles, and concluded that these composite particles contain a great number of silica particles with their diameter less than 120 nm. Under the same polymerization conditions, only a small number of silica particles encapsulated in each composite particle, or close to one in some cases can be obtained when the silica particle size is up to 450 nm. This size may determine the shape and dispersion behavior of the composite particles. Nevertheless, their obtained composite particles have still high coefficient variance of $C_{\rm v}$.

This paper prepared the silica-PS composite particles by DP method in an ethanol-water medium at the presence of grafted silica particles. Monodisperse silica particles are modified with a coupling agent of MPS. It dealt with how reactive conditions including the size and concentration of silica, and the amount of styrene, initiator, stabilizer and water, affect the monodisperse and morphology of silica-PS composite particles. The optimized conditions for silica-PS composite particles with regularly shaped periphery are presented. Thus, the paper first found that the critical size of silica for well-dispersed silica-PS composite particles with regularly shaped periphery is 380 nm, while nanosilica particles such as 32 or 54 nm cannot obtain the monodisperse composite particles under the same reaction conditions as above.

Finally, the paper reported a new composite material of these monodisperse composite particles with PET, which showed an interesting and practical nucleation effect.

2. Experiment and characterization

2.1. Materials

Absolute ethanol (99.5%) and ammonia (NH₃, 25% aqueous solution) were purchased from Beijing YILI Fine Chemical Co., Ltd and used as received. Tetraethyl orthosilicate (Si(OC2H5)4, TEOS) was obtained from Beijing Bei Hua Fine Chemical Co., Ltd and distilled ahead of preparation of silica. The coupling agent, γ-methacrylic propyl trimethoxysilane (MPS) was purchased from Beijing Shenda Fine Chemical Co., Ltd and used as received. The initiator, 2,2'-azobis (isobutyronitrile) (AIBN) was purchased from Shanghai No. 4 Reagent & H.V. Chemical Co., Ltd and recrystallized from ethanol. The monomer, styrene (St), and the stabilizer, poly(N-vinyl pyrrolidone) (PVP) were purchased from Beijing chemical reagents company. Styrene was distilled under reduced pressure prior to DP and PVP was use without further purification. PET was obtained from Liaoyang Petrochemical Company, China, and the intrinsic viscosity of PET in phenol-o-dichlorobenzene mixture (60:40) at 25 °C is 0.650 dL/g.

2.2. Preparation

2.2.1. Preparation of silica particles

Silica particles in the present of aqueous alcohol were prepared according to the Stöber method [33] that the mixture of water, ammonia and ethanol was mixed with the solution of TEOS in a 500 mL Erlenmeyer flask, then the reaction mixture was stirred at ambient temperature for several hours. Consequently, monodisperse silica particles with size from 32 to 602 nm are presented for the further experiment.

2.2.2. Preparation of grafted silica particles and silica-PS composite particles

In this experiment, grafted silica particles and silica-PS composite particles were prepared by two-step methods. Firstly, silica particles were added into an ethanol-water medium in a 250 mL four-necked flask equipped with a condenser. MPS was introduced and ammonia was added a few drops. Here, a typical molar ratio of MPS and silica particles is 1:18. The reaction went on in a nitrogen atmosphere under stirring for 12 h at 50 °C. At the end of modification reaction, some of grafted silica particles were taken out for characterization of TEM and FTIR. Secondly, poly(N-vinyl pyrrolidone) (PVP) and the styrene containing the initiator (AIBN) were introduced into the flask. The reaction carried out in a nitrogen atmosphere under stirring for 12 h at 75 °C. The resulting particles were centrifuged two times in ethanol, and composite particles were obtained.

2.2.3. The melting mixture of silica-PS composite particles with PET

After silica–PS composite particles were washed with toluene to remove free PS and dried, they were sufficiently mixed with PET powder by ball mill to obtain the new composite materials (SNPET). SNPET were pressed into films with 0.1 mm thickness by tablet machine at 275 °C and quenched in the ice-water mixture to form amorphous samples. Films quenched were dried under vacuum at room temperature for 24 h before DSC scanning.

2.3. Characterization

The diameter and morphology of the silica particles and silica–PS composite particles were investigated by transmission electron microscopy (TEM). TEM was carried out with H-800 operated at 150 kV. The samples of the grafted silica and un-grafted silica particles for measurements were prepared through washing with ethanol and drying, finally examined with FT-IR (Magan-ar560) through compressing with KBr powder. The analysis of DSC (NETZSCH DSC 204 F1 Phoenix) was carried out

in the temperature range from 25 to 300 °C. The composite material was heated from 25 to 300 °C with a rate of 10.0 °C min $^{-1}$ and then held at 300 °C for 2 min to remove thermal history, followed by cooling to 50 °C with a rate of 10.0 °C min $^{-1}$. Crystallization temperature ($T_{\rm mc}$) and melt temperature ($T_{\rm mc}$) were obtained from the DSC thermogram.

3. Result and discussion

3.1. Characterization and morphology of silica particles

Several reaction conditions preparing silica particles by referring to Stöber method are given in Table 1. It is seen that the average diameters of prepared silica particles range from 32 to 602 nm and the size of silica particles increases with the increase of NH_3 molar concentrations. The diameter and morphology of these silica particles were investigated by transmission electron microscopy (TEM) at an accelerator voltage of 150 kV

The monodisperse particles are characterized with some defined concepts of d_n and C_v . d_n is the average size of silica particles, defined as $d_n = (\sum n_i d_i / \sum n_i)$, or number average particle size [34]. C_v is the coefficient of variance of particle size distribution, $C_v = \frac{(\sum (d_i - d_n)^2 / \sum n_i)^{1/2}}{d_n} \times 100$. When the size of particles is more than 150 nm, C_v is less than 5% (sample D–F in Table 1) in accordance with previous literature [35]. In the C_v formula, n_i is the number of silica particles with the size of d_i .

Fig. 1 shows TEM morphology of silica particles with different size (sample A–F in Table 1). It is seen that the morphology of silica particles is irregular when the size of silica is 32 nm shown in Fig. 1a. However, it is quite clear that the surface of silica particles is becoming more spherical and regular in shape with increasing the size of silica particles. At the same time, the monodisperse of silica particles becomes better and better with the increase of the size of silica according to the $C_{\rm v}$ in

Table 1. Consequently, the monodisperse and morphology of silica will be improved with the increase of silica diameter.

3.2. Characterization of un-grafted and grafted silica particles

In order to obtain a functionalized group on the surface of these silica particles, it is quite necessary that the silica particles are modified by MPS as a coupling agent. Fig. 2a shows the infrared spectra of un-grafted and grafted silica. The obvious difference is that the grafted silica particles with a stable modified surface have a strong absorption peak at 1721 cm⁻¹, which indicates that MPS is bonded to the silanol groups on the surface of silica.

Fig. 2b shows TEM image of grafted silica with an average diameter of 253 nm and the $C_{\rm v}$ of 3.5%. It was found by calculating the diameter from TEM images that the size difference between un-grafted and grafted silica is not obvious. Consequently, the monodisperse silica particles with different size modified by MPS are obtained. A typical mass ratio of silica and MPS equals about 5 through TGA method. These modified particles are then used to prepare composite particle through DP process.

3.3. Effect factors on preparation silica—PS composite particles

3.3.1. Comparison of un-grafted and grafted silica

Fig. 3 shows TEM images of silica–PS composite particles in the presence of un-grafted and grafted silica particles through DP. In the presence of un-grafted silica, PS can almost not encapsulate silica particles (Fig. 3a), therefore, most of silica particles still stay free during dispersion polymerization. However, in the presence of grafted silica, silica particles are completely encapsulated with polystyrene (Fig. 3b), and then free silica can nearly not be observed in dispersion medium. It can be concluded that PS can successfully encapsulate grafted silica once silica particles are modified by MPS.

Table 1
Reaction conditions in the preparation of silica particles by Stöber and the size of silica

Sample	TEOS ($mol L^{-1}$)	$NH_3 \text{ (mol } L^{-1})$	$H_2O \ (mol \ L^{-1})$	d_n^{a} (nm)	$C_{\mathrm{v}}^{\mathrm{b}}$ (%)
A	0.20	0.14	2.80	32	13.5
В	0.20	0.14	4.80	54	11.5
C	0.20	0.40	6.80	110	8.7
D	0.20	0.60	6.80	250	2.7
E	0.20	0.60	16.0	380	2.5
F	0.20	2.00	6.00	602	1.5

 $^{^{\}rm a}$ $d_{\rm n}$ is the average size of silica particles.

 $^{^{\}rm b}$ $C_{\rm v}$ is the coefficient of variance of particle size distribution.

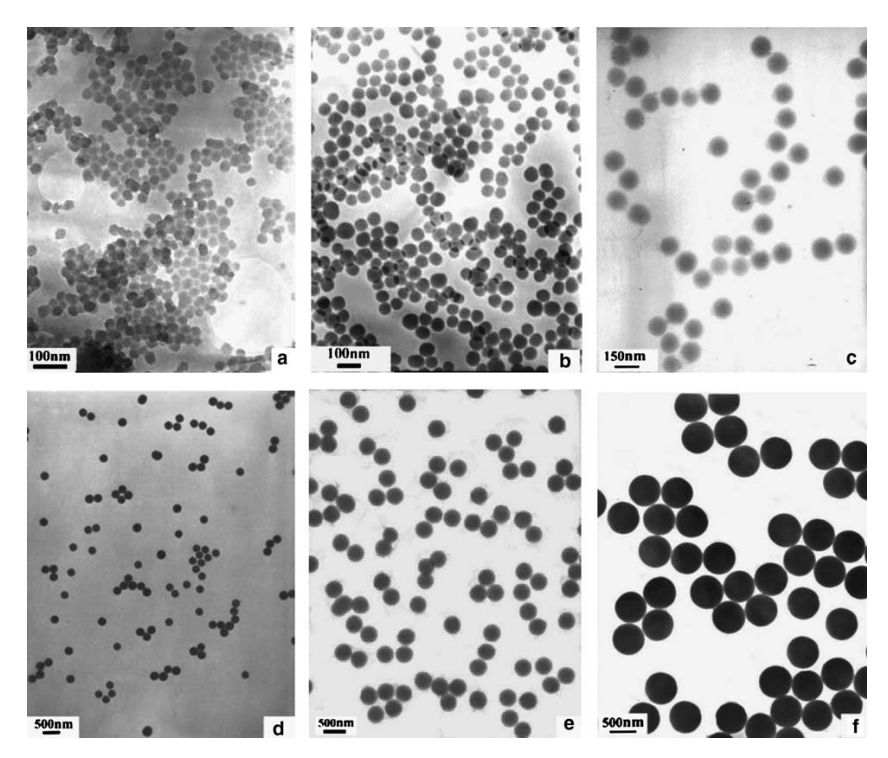


Fig. 1. TEM image of silica particles with the different size of 32 nm (a), 54 nm (b), 110 nm (c), 250 nm (d), 380 nm (e) and 602 nm (f).

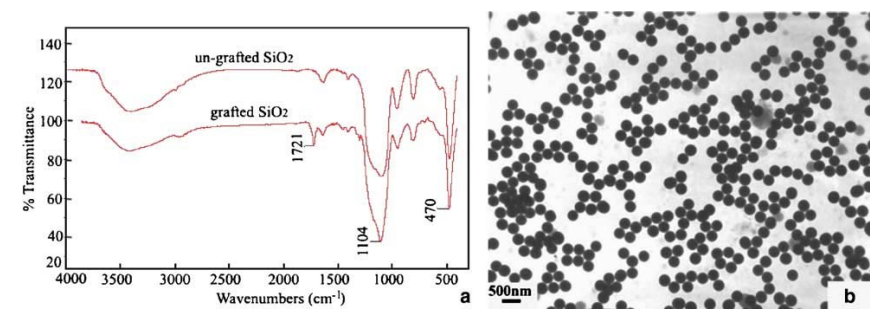


Fig. 2. The infrared spectra (a) and TEM image of grafted silica particles (b).

This is resulted from that, the unsaturated C=C groups on the surface of grafted silica react with styrene strongly improving the silica dispersity in PS, and greatly promoting growth of silica-PS composite particles in a more and homogeneous way.

3.3.2. Influence of different average size of grafted silica particles on the composite particles

The grafted silica particles with different size from nanometer to submicrometer apply to reveal how this silica affects the monodisperse and morphology of silica–PS composite particles. The reaction conditions for preparing silica–PS composite particles with the grafted silica particles through DP process are listed in Table 2.

TEM micrographs of composite particles prepared at the different size of grafted silica particles are shown in Fig. 4, where all the reactive conditions are the same as shown in Table 2. All images except Fig. 4f shows that grafted silica particles are situated in the polystyrene and no free silica particles are found. However,

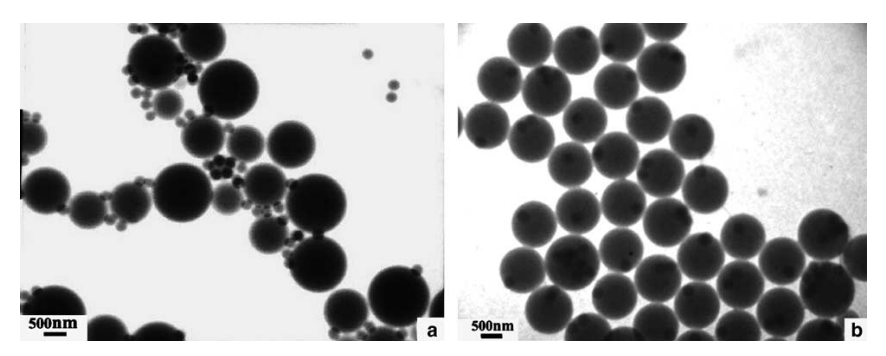


Fig. 3. TEM images of silica–PS composite particles in the presence of un-grafted silica (a) and grafted silica (b). Reaction conditions: un-grafted silica or grafted silica, 0.10 mol L^{-1} ; St, 0.60 mol L^{-1} ; AIBN, 6.10 mmol L^{-1} ; PVP, 0.23 mmol L^{-1} ; CH₃CH₂OH, 94.5 mL; H₂O, 5.5 mL.

Table 2 The size and $C_{\rm v}$ of silica–PS composite particles prepared with the different size of grafted silica particles

Sample	d_n^{a} (nm)	D_n^{b} (nm)	C _v c (%)	
A-0	32	=	=	
B-0	54	88	20.0	
C-0	110	874	6.8	
D-0	250	1030	4.5	
E-0	380	1020	5.3	
F-0 [5]	410	860	12.0	
G-0	602	_	_	

Reaction conditions: grafted silica, 0.10 mol L^{-1} ; St, 0.60 mol L^{-1} ; AIBN, 6.10 mmol L^{-1} ; PVP, 0.23 mmol L^{-1} ; CH₃CH₂aOH, 94.5 mL; H₂O, 5.5 mL.

- ^a d_n is the average size of silica particles.
- ^b D_n is the average size of silica-PS composite particles.
- $^{\rm c}$ $\, {\rm C_{v}}$ is the coefficient of variance of particle size distribution.

the morphology and average size of composite particles, as well as the number of grafted silica particles in each composite particle will greatly change with varying the size of grafted silica particles from nanoscale (d_n < 100 nm) to submicrometer (100 nm $\leq d_n \leq$ 1000 nm). When the size of grafted silica is 32 and 54 nm respectively (samples A-0 and B-0 in Table 2), the composite particles containing grafted silica is not spherical but the grafted silica particles (dark) are interconnected with polystyrene (light) (Fig. 4a and b). It is probable that the silica nanoparticles ($d_n < 100 \text{ nm}$) with higher surface energy have more cross-linking interaction with polystyrene main chains than the micron-sized ones, which cause composite particles to stack together. It is obviously seen from Fig. 4a and b that the morphology of core-shell silica-PS composite particles is quite different from that of Bourgreat-Lami [7,8]. As the silica size increases to submicrometer, the monodispersity of silica-PS composite particles is greatly improved. When the grafted silica size reaches 110 nm, each composite particle is almost spherical and contains two or more than two grafted silica particles (Fig. 4c). With continuously increasing silica size from 250 nm to 380 nm (Fig. 4d and e), the monodisperse of composite particles become better and the number of grafted silica in each composite particle gradually decreases to one when silica size approaches to 380 nm (Fig. 4e). Simultaneously, it is seen from Fig. 4c-e that many cores in the composite particles are not located in the center of the particles, which may be resulted from the gravity effect during dispersion polymerization. In dispersion solution, the force of composite particles in the direction of perpendicularity is inhomogeneous, leading to the deviation of silica from the center of the composite particles. In addition, during polymerization, the inhomogeneous nucleation of silica in styrene solution may cause the deviation of silica from the center. However, polystyrene can hardly encapsulate grafted silica when its size is over 602 nm (samples G-0 in Table 2) and free silica particles are observed in reactive system (Fig. 4f). Consequently, grafted silica particles with different size significantly influence on the morphology of composite particles and the distribution of silica in composite particles.

3.3.3. Determining the best size of grafted silica particles for the composite particles

Fig. 5 shows how silica size affects on C_v of both silica and silica-PS composite. As the size of silica increases, C_v of silica reduces slowly, but C_v of silica-PS composite decreases quickly and later increases.

It is seen from Fig. 5 that the change of silica size can severely affect on the monodisperse of composite particles. When silica size is 250 and 380 nm, C_v of the corresponding composite particles is 4.5%, 5.3%, respectively, which is lower than that of the other composite particles with the silica size of 54, 110 and 410 nm. However, the number of silica in each composite particle is almost one when silica size is at 380 nm (Fig. 4e) and one or more

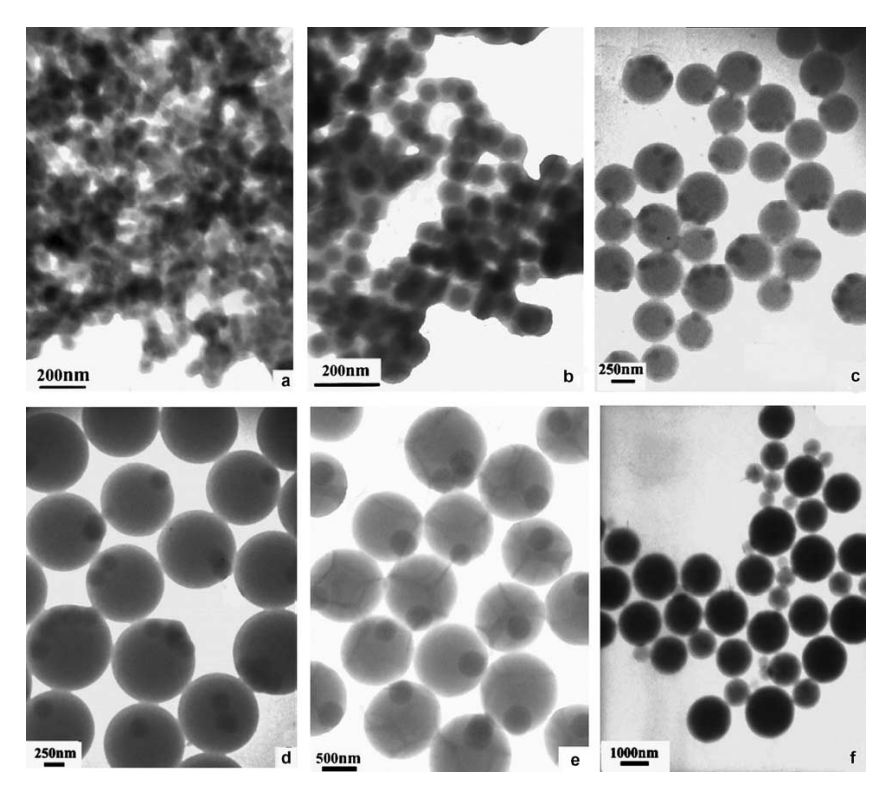


Fig. 4. TEM images of silica–PS composite particles at the different size of grafted silica particles: (a) sample A-0 in Table 2; (b) sample B-0 in Table 2; (c) sample C-0 in Table 2; (d) sample D-0 in Table 2; (e) sample E-0 in Table 2; (f) sample F-0 in Table 2.

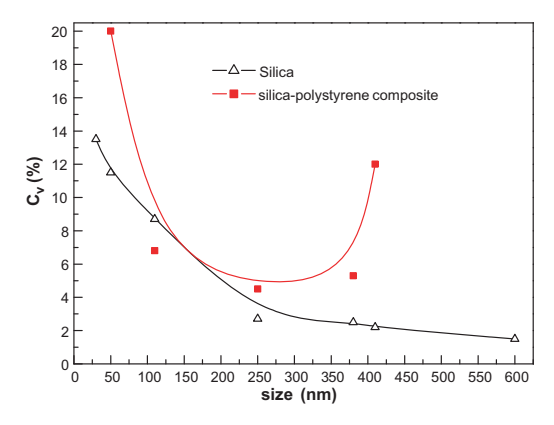


Fig. 5. Plot of the effect of silica size on C_v of both silica and silica-PS composite.

than one when silica size is at 250 nm (Fig. 4d). Thus, the size with 380 nm is a critical size of silica for the best monodispersity and encapsulation in preparing the composite particles. These grafted silica particles with

380 nm are further used to investigate the factors of reaction conditions.

3.3.4. The effect of reaction conditions on the best size of grafted silica particles and the composite particles

The grafted silica particles with the size of 380 nm are selected to be the critical scale to investigate the effect of different reaction conditions on the morphology and monodisperse of final silica–PS composite particles.

TEM morphology of silica for 380 nm size is seen in Fig. 1e. The reaction conditions for preparing silica-PS composite particles through DP process in the presence of 380 nm grafted silica particles are shown in Table 3.

TEM images of sample E-1 and E-2 in Table 3 are shown in Fig. 6, in which all conditions except PVP concentration are the same. PVP as a stabilizer plays an important role on the surface of PS. When PVP concentration is lower, silica–PS composite particles are easily conglutinated together (Fig. 6a). As PVP concentration increase, the size of composite particles will slightly reduce from 800 to 760 nm, but composite particles become more spherical and regular in shape (Fig. 6b). Therefore, enhancing PVP in a proper amount can

Table 3
The different reaction conditions for preparing silica—PS composite particles through DP

Sample	$\begin{array}{c} St\\ (mol\ L^{-1}) \end{array}$	$\begin{array}{c} AIBN \\ (mmol \ L^{-1}) \end{array}$	$\begin{array}{c} PVP \\ (mmol \ L^{-1}) \end{array}$	Grafted silica (mol L ⁻¹)	EtOH (mL)	H ₂ O (mL)	d_n^{a} (nm)	C _v ^b (%)
E-1	0.40	4.30	0.10	0.10	94.5	5.5	800	6.2
E-2	0.40	4.30	0.23	0.10	94.5	5.5	760	5.9
E-3	0.40	3.00	0.23	0.10	94.5	5.5	_	_
E-4	0.40	6.10	0.23	0.10	94.5	5.5	670	7.7
E-5	0.40	6.10	0.23	0.10	94.5	9.5	_	_
E-6	0.40	6.10	0.30	0.10	94.5	5.5	640	11.3
E-7	0.60	6.10	0.30	0.10	94.5	5.5	993	5.1
E-8	0.60	6.10	0.30	0.05	94.5	5.5	1094	6.1
E-9	0.60	6.10	0.30	0.23	94.5	5.5	_	_
E-0	0.60	6.10	0.23	0.10	94.5	5.5	1020	5.3

 $^{^{}a}$ d_{n} is the average size of silica-polystyrene composite particles.

 $^{^{\}rm b}$ $C_{\rm v}$ is the coefficient of variance of particle size distribution.

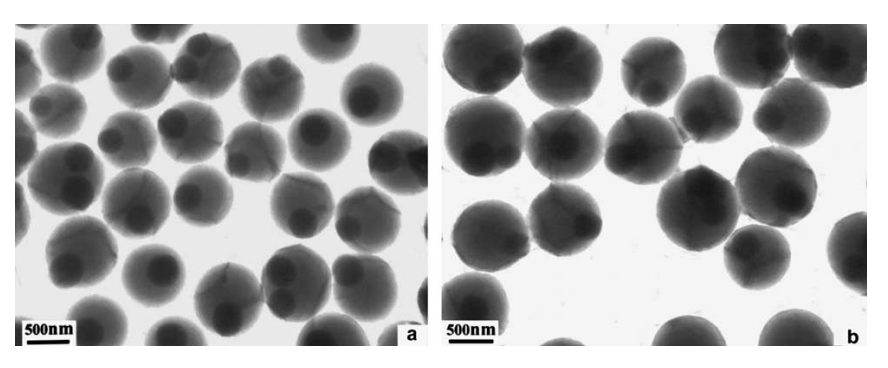


Fig. 6. TEM images of silica—PS composite particles under the condition of changing PVP concentration: (a) sample E-1 in Table 3; (b) sample E-3 in Table 3.

effectively prevent composite particles from conglutinating each other and improve the morphology and monodisperse of silica–PS composite particles.

AIBN as an initiator has a significant influence on preparing silica–PS composite particles. At a low AIBN concentration of 3.00 mmol L^{-1} (sample E-3 in Table 3), grafted silica cannot be entirely encapsulated by polystyrene and silica particles enable both polystyrene particles linked together (Fig. 7a). That is, if the lower AIBN concentration is, the worse effectively polystyrene particles encapsulate grafted silica. As AIBN concentration increases to 6.10 mmol L^{-1} (sample E-4 in Table 3), all the silica particles are placed inside polystyrene particles (Fig. 7b).

Simultaneously, silica-PS composite particles in samples E-4 become smoother than that of sample E-3. Because the unsaturated C=C groups on the surface of grafted silica react with styrene in the presence of AIBN, increasing the amount of AIBN will obtain more primary free radical particles which can quickly induce grafted silica and styrene to form the large size and

monodisperse of silica–PS composite particles. Thus, addition of a suitable amount of AIBN leads to synthesize regularly spherical and well-monodisperse silica–PS composite particles.

Fig. 8 shows two TEM typical images about silica-PS composite particles when varying the amount of water in ethanol-water medium (seen in Table 3). The addition of water can adjust the polarity of reaction medium. The less the amount of water is added, the lower the polarity of disperse system is, and vice verse. When addition of the amount of water is 5.50 mL (sample E-4 in Table 3), grafted silica particles are nearly located inside polystyrene (Fig. 8a). However, with increasing the amount of water of 9.50 mL (sample E-5 in Table 3), some free silica particles can be seen in reaction system (Fig. 8b). Because the hydrophobicity of the surface of grafted silica modified by MPS cannot be compatible with water, some grafted silica particles are free in reaction system and the monodisperse of silica-PS composite particles will decline with the increase of the amount of water during DP.

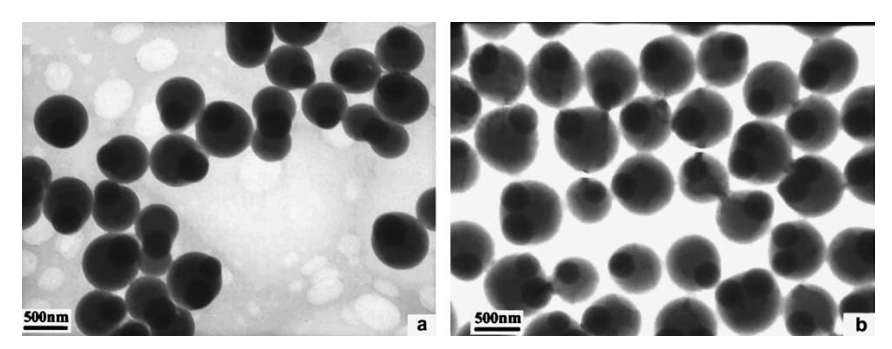


Fig. 7. TEM images of silica-PS composite particles under the condition of changing AIBN concentration: (a) sample E-3 in Table 3; (b) sample E-4 in Table 3.

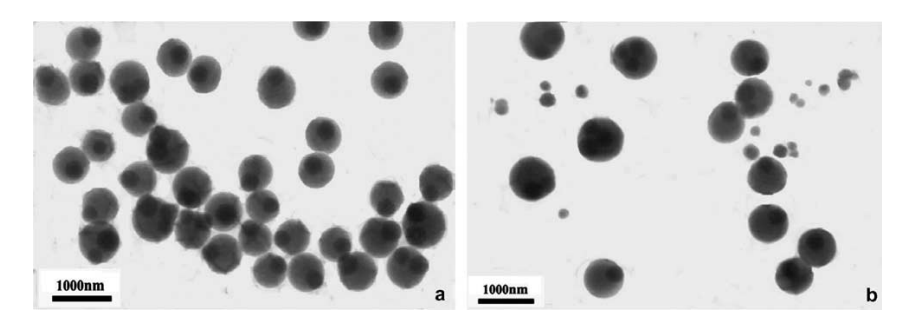


Fig. 8. TEM images of silica–PS composite particles under the condition of changing H_2O concentration: (a) sample E-4 in Table 3; (b) sample E-5 in Table 3.

Although the average size of polystyrene particles increases with the increase of the amount of styrene, the morphology and size of composite particles are still seriously affected by the grafted silica. TEM images of sample E-6 and E-7 in Table 3 are for styrene monomer concentration of 0.40 and 0.60 mol $\rm L^{-1}$ under the same other conditions shown in Fig. 9. At a low styrene concentra-

tion of 0.40 mol L^{-1} (sample E-6 in Table 3), the surface of silica–PS composite particles is obviously not smooth and some of grafted silica particles are partially protruded from the surface of polystyrene (Fig. 9a). However, increasing the amount of styrene of 0.60 mol L^{-1} (sample E-7 in Table 3), the surface of silica–PS composite particles become smoother. Moreover, the average size and

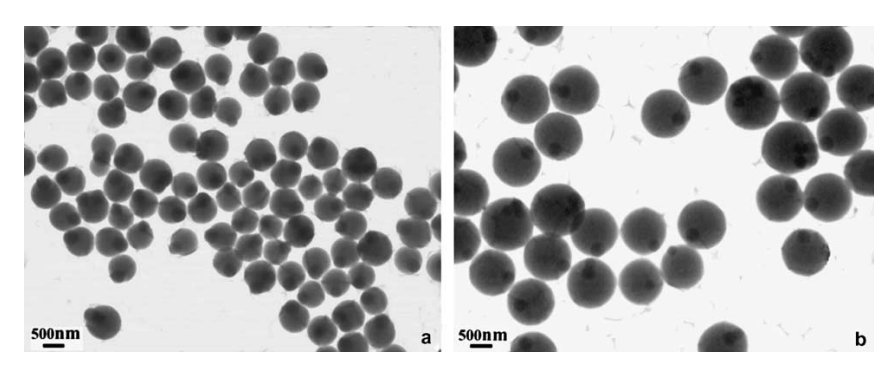


Fig. 9. TEM images of silica–PS composite particles under the condition of changing St concentration: (a) sample E-6 in Table 3; (b) sample E-7 in Table 3.

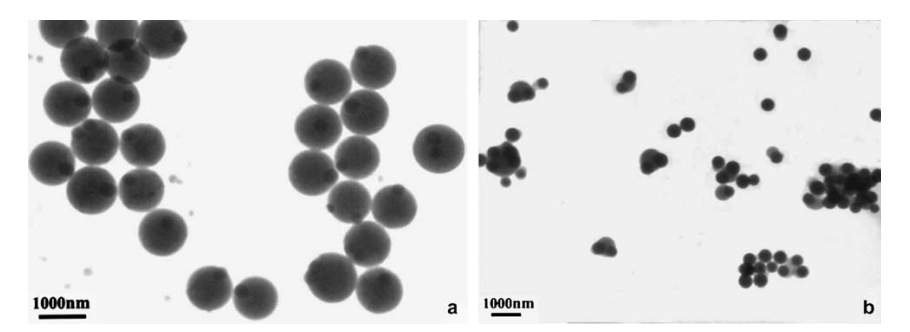


Fig. 10. TEM images of silica-PS composite particles under the condition of changing grafted silica concentration: (a) sample E-8 in Table 3; (b) sample E-9 in Table 3.

monodisperse of composite particles get larger and better (Fig. 9b). Thus, increasing the amount of styrene will quicken the reactive rate of DP and promote grafted silica particles contact with styrene, polystyrene particles easily encapsulate silica to form the well-shaped silica—PS composite particles.

The addition amount of grafted silica is one of the most important factors on the morphology of silica-PS composite particles. At a low amount of grafted silica of $0.05 \text{ mol } L^{-1}$ (sample E-8 in Table 3), the number of silica particles placed inside each composite particle is almost one and the surface of composite particles becomes smooth (seen TEM in Fig. 10a). With increasing the amount of silica to $0.10\,\mathrm{mol}\,L^{-1}$ (sample E-7 in Table 3), there are two or more than two silica particles in each composite particle and the monodisperse of composite particles becomes better (Fig. 9b). When the silica concentration continuously increases to 0.23 mol L (sample E-9 in Table 3), most of silica particles are not inside composite particles during polymerization (Fig. 10b). Keeping the constant amount of styrene, the styrene adsorbing on the surface of silica particles gradually decreases with the increase of silica concentration. Therefore, grafted silica particles cannot obtain

enough styrene monomer, and some free grafted silica particles appear in reaction system.

Therefore, according to the above discussion, for the size of grafted silica particles of 380 nm, the best reaction condition that can obtain the well-dispersed silica–PS composite particles with regularly shaped periphery (seen in Fig. 4e) is that the addition amounts of PVP, styrene, AIBN, grafted SiO₂ and H₂O are 0.23 mmol L⁻¹, 0.60 mol L⁻¹, 6.10 mmol L⁻¹, 0.10 mol L⁻¹ and 5.50 mL, respectively.

3.3.5. The nucleation effect of grafted silica particles in PET

The most important for silica–PS core–shell composite particles is that they can further disperse in polymer melt. They are mixed with PET to prepare the new composite materials (SNPET). As shown in Table 4, $T_{\rm mc}$ of SNPET is higher than that of pure PET, that is to say, silica particles can become nucleation centers of PET in which can accelerate the crystallization. Under the condition of the same silica content, the dispersion in PET and the size of silica particles can seriously affect the crystallization rate of SNPET. The higher $T_{\rm mc}$ of SNPET is, the quicker the rate of crystallization of

Table 4
The comparison of thermal and crystallization behavior for PET and SNPET

Sample	PET/SiO ₂ /PS (g/g/g) ^a	$D_{SiO_2} (nm)^b$	$T_{\rm m}^{\ \ c} (^{\circ}{\rm C})$	$T_{\mathrm{mc}}^{}}$ (°C)	$\Delta T_{\mathrm{mc}}^{}}(^{\circ}\mathrm{C})$
PET	100/0/0	-	249.9	193.4	56.5
SNPET-1	100/2/0.2	54	251.5	205.0	46.5
SNPET-2	100/2/0.2	110	251.2	200.0	51.2
SNPET-3	100/2/0.2	250	250.9	197.6	53.3
SNPET-4	100/2/0.2	380	252.7	204.0	48.7
SNPET-5	100/2/0.2	50-300	253.0	204.5	48.5

^a Mass ratio of (PET, SiO₂ and PS).

^b The size of silica particles.

^c Melt temperature.

^d Crystallization temperature from melt.

 $^{^{\}mathrm{e}}$ The difference between temperature T_{m} and T_{mc} .

composite materials is. When the silica size is 54 nm and 380 nm, $T_{\rm mc}$ of SNPET is 205.0 and 204.0 °C, respectively, which is higher than that of other composite materials. The reason for this is suggested that silica particles encapsulated with PS (Fig. 4b and e) homogeneously disperse in PET forming many nucleation centers and quickening the SNPET crystallization rate. Similarly, at the silica size of 110 nm and 250 nm, their disperse behavior of composite particles in PET also show nucleation effect, but their $T_{\rm mc}$ is lower than that at 380 nm due to more silica particles agglomerated in each PS particle (Fig. 4c and d). All these results are reasonably used to explain the nucleation effect of the multiscale silica particles with 50-300 nm in PET (seen sample SPET-5, Table 4), it is strongly suggested that different silica size level all play nucleation role in PET (further data will be published elsewhere).

4. Conclusion

Preparation of silica–PS composite particles with silica particle size from 32 to 602 nm in DP process is reported and their morphology is characterized with TEM. Grafted silica particles with MPS as a coupling agent can obviously enhance the stability, dispersion and encapsulation behavior of monodisperse silica–PS composite particles, which is resulted from that the unsaturated C=C groups are bonded to the silanol groups of silica surface investigated from FTIR.

Via DP process, the core-shell composite particles are prepared, in which grafted silica particles are used, the ethanol-water acts as medium, PVP as a stabilizer and AIBN as an initiator. The results show that modified silica particles can be successfully encapsulated with PS while the un-modified silica particles can almost not be encapsulated with it. The grafted silica particles and their sizes from nanometer to submicrometer are factors on the silica morphology and distribution of composite particles. With increase of the grafted silica size, the morphology of silica-PS composite particles becomes more and more regular. The number of grafted silica particles in each composite particle is more than two with silica size less than 380 nm while approaches to one with silica size is over 380 nm. However, when the grafted silica particle size increases to 602 nm, PS can hardly encapsulate them.

Using the grafted silica particle size of 380 nm, the best reaction conditions obtaining the well-dispersed silica–PS composite particles with regularly shaped periphery are presented as, the addition amounts of PVP, styrene, AIBN, grafted SiO_2 and H_2O are 0.23 mmol L^{-1} , 0.60 mol L^{-1} , 6.10 mmol L^{-1} , 0.10 mol L^{-1} and 5.50 mL, respectively.

The encapsulation of silica particles with polystyrene by DP process effectively improves the dispersion of

inorganic particles in PET. They act as nucleation centers in PET, improve its crystallization behavior and primarily explain the nucleation effect of different size level of multiple scale particles (further data will be published elsewhere).

Acknowledgements

Some of this work supported by China National Petroleum Corporation (CNPC) innovation funds and CNPC key project (2002–2004) are very appreciated.

References

- [1] Ke YC, Long CF, Qi ZN. J Appl Polym Sci 1999;71:1139.
- [2] Ke YC, Zhu CF, Yang ZB. J Appl Polym Sci 2002;85:2677.
- [3] Hasegawa H, Araik SS. J Polym Sci Part A: Polym Chem Ed 1987;25:3117.
- [4] Haga Y, Watanabe T, Yosomiya R. Angew Makromol Chem 1991;189:23.
- [5] Wu TB, Ke YC, Wang YH, Dong P. Acta Polymerica Sinica 2005;2:289.
- [6] Bourgeat-Lami E, Lang J. Macromol Symp 2000;151:377.
- [7] Bourgeat-Lami E, Lang J. J Colloid Interf Sci 1998;197: 293
- [8] Bourgeat-Lami E, Lang J. J Colloid Interf Sci 1999;210: 281.
- [9] Ke YC, Wu TB, Wang Y. Petro Sci 2005;2:70.
- [10] Iribarne JV, Anthony EJ, Iribarne A. Fuel Process Technol 2003;82:27.
- [11] Tyan HL, Leu CM, Wei KH. Chem Mater 2001;13:222.
- [12] Fu X, Qutubuddin S. Polymer 2001;42:807.
- [13] Holdsworth PJ, Turner-Jones A. Polymer 1971;12:195.
- [14] John S. Phys Rev Lett 1987;58:2486.
- [15] Yamada K, Morita H, Shinya A, Notomi M. Opt Commun 2001;198:395.
- [16] Ugelstad J, Berge A, Ellingsen T, Schmid R, Nilsen TN, Mork PC, et al. Prog Polym Sci 1992;17:87.
- [17] Zeng CC, Lee LJ. Macromolecules 2001;34:4098.
- [18] Fan X, Xia C, Advincula RC. Langmuir 2003;19:4381.
- [19] Weimer MW, Chen H, Giannelis EP, Sogah DY. J Am Chem Soc 1999;121:1615.
- [20] Kuno M, Oku T, Suganuma K. Scripta Mater 2001;44: 1583.
- [21] Jain TK, Roy I, De TK, Maitra A. J Am Chem Soc 1998; 120:11092.
- [22] Mayvile FC, Partch RE, Matijevic E. J Colloid Interf Sci 1987;120:135.
- [23] Mi KK, Chul AK, Seong DA, Seung RK, Kyung SS. Synthetic Met 2004;146:197.
- [24] Ding XF, Zhao JZ, Liu YH, Zhang HB, Wang ZC. Mater Lett 2004;58:3126.
- [25] Zhang K, Chen HT, Chen X, Chen ZM, Cui ZC, Yang B. Macromol Mater Eng 2003;288:380.
- [26] Gu SC, Kondo T, Konno M. J Colloid Interf Sci 2004;272:
- [27] Stejskal J, Kratochvil P, Armes SP, Lascelles SF, Riede A, Helmstedt M, et al. Macromolecules 1996;29:6814.

- [28] Flitton R, Johal J, Maeda S, Armes SP. J Colloid Interf Sci 1995;173:135.
- [29] Tseng CM, Lu YY. J Polym Sci Part A: Polym Chem Ed 1986;24:2995.
- [30] Lu YY. J Polym Sci Part B: Polym Phys 1988;26:1187.
- [31] Cao TY, Dai B, Dai JY. Acta Polymerica Sinica 1997;2:
- [32] Lascelles SF, McCarthy GP, Butterworth MD, Armes SP.
- Colloid Polym Sci 1998;276:893.

 [33] Stöber W, Fink A, Bohn E. J Colloid Interf Sci 1968;26: 62.
- [34] Gu SC, Takeshi M, Mikio K. J Colloid Interf Sci 1998; 207:113.
- [35] Dong P. Prog Nat Sci 2000;10:575.



Available online at www.sciencedirect.com





Fluid Phase Equilibria 242 (2006) 123-128

www.elsevier.com/locate/fluid

Methane hydrate dissociation above 0 °C and below 0 °C

Chang-Yu Sun*, Guang-Jin Chen

State Key Laboratory of Heavy Oil Processing, China University of Petroleum, Beijing 102249, PR China Received 22 January 2005; received in revised form 23 January 2006; accepted 23 January 2006

Abstract

The kinetic data of methane hydrate dissociation at various temperatures and pressures were measured in a sapphire cell apparatus by depressurizing method. When the temperature was higher than 0° C, the experimental results showed that the hydrate dissociation rate was controlled by intrinsic dissociation reaction. When the temperature was lower than 0° C, water generated from the hydrate dissociation would transform into ice rapidly at the surface of hydrate crystal. The released gas diffused from the hydrate and ice mixture to the bulk of gas phase. With the hydrate continuous dissociation, the boundary of ice—hydrate moved toward water/ice phase. The hydrate dissociation was controlled by gas diffusion, and the hydrate dissociation process was treated as a moving boundary problem. Corresponding kinetic models for hydrate dissociation were established and good agreements with experimental data were achieved.

© 2006 Elsevier B.V. All rights reserved.

Keywords: Methane: Hydrate: Dissociation: Kinetics: Diffusion

1. Introduction

Substantial amounts of hydrates have been determined to be at the ocean bottom and in permafrost regions of the earth. These solid hydrate fields can become a future hydrocarbon resource. It was estimated that the methane gas potential of in situ hydrate resources is around 20 million trillion cubic meters in the world [1], several times the known reserves of conventional natural gas [2]. This huge energy source holds at least twice the amount of combustible carbon present in all other fossil fuels on the earth [3].

How to exploit the natural gas from these fields safely and economically requires knowledge of the thermodynamics and kinetics of hydrate formation and dissociation. All known methods of hydrate decomposition are based on shifting the thermodynamic equilibrium in a three-phase system (water-hydrate-gas), which can be achieved by [4]:

- increasing the system temperature above the temperature of hydrate formation at a specified pressure;
- decreasing the system pressure below the pressure of hydrate formation at a specified temperature;

0378-3812/\$ – see front matter © 2006 Elsevier B.V. All rights reserved. doi:10.1016/j.fluid.2006.01.025

injecting inhibitors to shift the pressure–temperature equilibrium.

Gas production by heating hydrates was shown to be thermodynamically possible [5]. Kamath et al. [6] have studied three-phase interfacial heat transfer during the dissociation of propane hydrates. Ullerich et al. [7] described the decomposition of a synthetic core of methane hydrate as a moving boundary heat transfer problem. Jamaluddin et al. [8] combined heat transfer with intrinsic kinetics to simulate the decomposition of a core of methane hydrate. Selim and Sloan [9] considered the convective–conductive heat transfer in their one-dimensional model

But for the heat stimulating method, the large amount of energy required to dissociate hydrates makes the thermal recovery of gas from the in situ hydrates unfeasible [10,11]. On the other hand, hydrate dissociation by depressurization was shown to be a viable option. Kim et al. [12] developed a model for the intrinsic rate of gas hydrate decomposition and determined the rate constant from experimental data for methane. Their experimental work was maintained at a constant temperature and pressure in a semi-batch stirred-tank reactor during the hydrate decomposition. Yousif et al. [13] used a Kim's model [12] to describe a dissociation process of methane hydrate in porous media by depressurization. Ohgaki et al. [14]

^{*} Corresponding author. Tel.: +86 1089 733252; fax: +86 1089 733252. E-mail address: changyusun@263.net (C.-Y. Sun).

evaluated the decomposition of carbon dioxide, methane and carbon dioxide-methane mixed gas hydrates under isothermal isobaric conditions. Stern et al. [15] and Shirota et al. [16] performed methane hydrate decomposition experiments below the ice point. In Tsypkin's multiphase one-dimensional model [17], movement of water and gas in the reservoir was described and heat and mass balance at the dissociation front were included. Goel et al. [18] developed a model to predict the performance of the hydrate dissociation in porous media, incorporating decomposition kinetics into the radial diffusivity equation. Clarke and Bishnoi [19-21] determined the intrinsic rate of ethane, methane, and mixtures of methane and ethane hydrate decomposition in a semi-batch stirred-tank reactor. Ji et al. [22] and Ahmadia et al. [23] described a one-dimensional model for natural gas production from the dissociation of methane hydrate in a confined reservoir by a depressurizing well. The approach accounted for the heat released by hydrate dissociation and convection-conduction heat transfer in the gas and hydrate zone.

Many factors, such as temperature, pressure, and the surface area of hydrate particle, will influence on the hydrate dissociation rate. The mechanism of hydrate dissociation when the temperature is above $0\,^{\circ}\text{C}$ and below $0\,^{\circ}\text{C}$ will be different. In this study, the kinetic data of dissociation using depressurizing method at specified temperatures were obtained for methane hydrate in a transparent sapphire cell. The experiments were conducted in two temperature regions, above $0\,^{\circ}\text{C}$ and below $0\,^{\circ}\text{C}$, to examine the different mechanism of hydrate dissociation. Kinetic models were also formulated to describe the dissociation data above $0\,^{\circ}\text{C}$ and below $0\,^{\circ}\text{C}$, respectively.

2. Experimental

2.1. Experimental setup

The experimental apparatus used in this work has been described in detail in the previous papers published by this laboratory [24,25]. It has also been used to studied the effect of surfactant on the formation and dissociation kinetic behavior of methane hydrate [26]. Fig. 1 is the schematic diagram of the experimental apparatus. It consists of a cylindrical transparent sapphire cell (2.54 cm in diameter, the maximum workspace of the cell $78~\text{cm}^3$) installed in a constant temperature bath and equipped with a magnetic stirrer for accelerating the equilibration process. The formation/dissociation of the hydrate crystals in the solution can be observed directly through the transparent cell wall. To collect the dissociation gas, an aerometer is used which has a volume of 2~L (accurate to 0.1~mL). The accuracy of temperature and pressure measurement is $\pm 0.1~\text{K}$ and $\pm 0.025~\text{MPa}$, respectively.

2.2. Experimental procedure

De-ionized water with a volume of about 30 mL was injected into the vacuumed high pressure sapphire cell. Then methane gas was introduced to the cell until the desired pressure was attained, which was above the three-phase equilibrium pressure. When both pressure and temperature conditions became

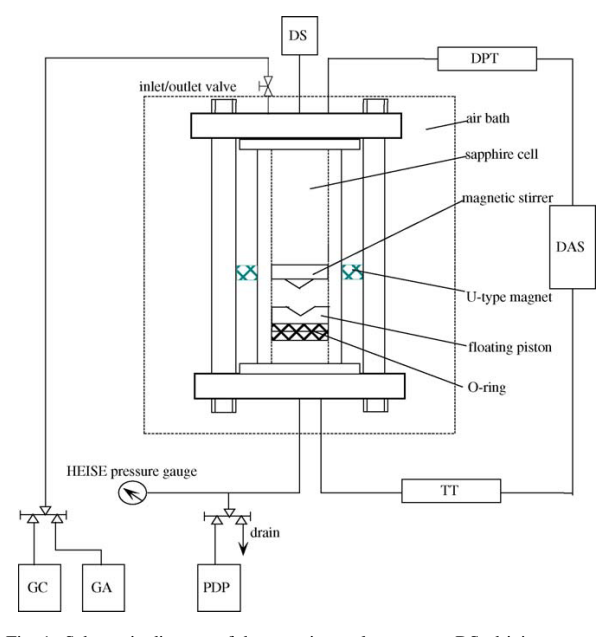


Fig. 1. Schematic diagram of the experimental apparatus. DS: driving system; DPT: differential pressure transducer; DAS: data acquistion system; PDP: positive displacement pump; GC: gas cylinder; GA: gas aerometer; TT: temperature transmitter.

stable, stirring was started and hydrate will form with the continuous gas consumption. After about majority of the water was converted into the hydrate, the cell was depressurized to a pressure about 0.05 MPa above the equilibrium pressure which was accomplished by releasing the gas to the atmosphere. When the system was stable, the cell was further depressurized to the dissociation pressure. Then it maintained this pressure by use of the movement of piston. Gas hydrate started to decompose and the temperature of the cell was maintained by the air bath. The volume of gas flowing out of the cell was collected in an aerometer and the dissociation time was also counted.

If the target temperature was lower than 0 °C, the hydrate was first cooled down to the desired temperature which was the dissociation reaction condition and kept for about 4 h. Then the vent was opened slowly and the system pressure decreased gradually until it reached somewhat above the equilibrium formation pressure of methane hydrate at present temperature. After that, the system was depressurized rapidly to atmospheric pressure. The reason for depressurizing the system in such two stages was stated by Shirota et al. [16]. Soon after the system pressure decreased to 0.1 MPa, the vent was closed and the system was connected to the aerometer to recover the gas evolved during dissociation.

Using above procedure, the experiments of methane hydrate dissociation were conducted at the temperatures of $0.6\,^{\circ}\text{C}$, $2.6\,^{\circ}\text{C}$, $4.6\,^{\circ}\text{C}$, and $5.8\,^{\circ}\text{C}$, pressure from $1.0\,\text{MPa}$ to $3.0\,\text{MPa}$. Methane hydrate dissociation data were measured at the atmospheric pressure when the temperatures were $-2.5\,^{\circ}\text{C}$, $-4.4\,^{\circ}\text{C}$, $-6.2\,^{\circ}\text{C}$ and $-9.2\,^{\circ}\text{C}$. In these experiments, the influence of heat transfer was eliminated by immersing the transparent sapphire cell in a constant temperature bath.

3. Development of the kinetic model

Water is released from the destruction of clathrate host lattice at the surface of a hydrate particle and desorption of the methane molecule from the surface of hydrate particle [12]. When the temperature is higher than $0\,^{\circ}\text{C}$, the generated water flows down to the bottom of the cell. The released methane gas can easily transfer the clearance between the hydrate particles and the destructed clathrate lattice. Therefore, the mass transfer resistance can be eliminated. But when the temperature is lower than $0\,^{\circ}\text{C}$, the water generated from the hydrate dissociation will transform into ice rapidly at the surface of hydrate crystal. Under the circumstances, the released gas will then diffuse from the hydrate and ice mixture to the bulk of gas phase and the influence of mass transfer should be considered. So the kinetic model of dissociation should be built in two cases.

3.1. When $T > 0^{\circ}C$

The sapphire cell was immersed in a constant temperature bath to maintain the experimental temperature. We know that the dissociation of solid hydrates is an endothermic process. When the temperature was above $0\,^{\circ}\text{C}$, the decomposition of hydrate was rapid. But the amount of hydrate formation in the sapphire cell in this work was no more than $30\,\text{cm}^3$. And the specified experimental pressure when T was above $0\,^{\circ}\text{C}$ is close to the equilibrium pressure to decrease the dissociation driving force and the rate of hydrate dissociation, so as to attain thermal equilibrium between the decomposing hydrate with constant temperature bath. Therefore, during the development of the kinetics model when the temperature is higher than $0\,^{\circ}\text{C}$, the hydrate dissociation was assumed under isothermal conditions and the heat transfer effect was ignored. The similar assumption was also made by the previous researchers [12–14].

The methane gas from hydrate dissociation is generated at the solid surface and then enters the bulk gas phase. And the total moles of methane gas $n^{\rm H}$ contained in the hydrate particles will decrease with the dissociation of hydrate. The molar rate at which methane is released from the hydrate surface is $(-dn^{\rm H}/dt)$.

When the temperature is higher than 0 °C, the hydrate dissociation process occurs at the solid surface and the mass transfer resistance of the released gas can be ignored. It may be assumed that the fugacity of methane at the solid surface is equal to the fugacity of methane in the bulk gas phase. The hydrate dissociation is then recognized as an intrinsic reaction, thus the rate of hydrate dissociation is written as

$$-\frac{\mathrm{d}n^{\mathrm{H}}}{\mathrm{d}t} = k'n^{\mathrm{H}} \tag{1}$$

When t is equal to zero, $n^{\rm H} = n_0^{\rm H}$. Here $n_0^{\rm H}$ is the total moles of gas contained in the hydrate particles initially, and k' is the apparent dissociation rate constant. Integrating Eq. (1) and substituting the initial condition that when t = 0, gives

$$\frac{n^{\mathrm{H}}}{n_0^{\mathrm{H}}} = \exp(-k't) \tag{2}$$

The rate of hydrate dissociation is assumed to be proportional to a driving force, the difference between methane fugacity at the three-phase equilibrium pressure and at the experimental condition. Therefore the hydrate dissociation when the temperature is higher than $0\,^{\circ}\text{C}$ can be treated as a first-order reaction under the conditions of three-phase coexistence.

3.2. When $T < 0^{\circ}C$

Ershov and Yakushev [27] found out that between $-1\,^{\circ}\mathrm{C}$ and $-18\,^{\circ}\mathrm{C}$, natural gas hydrate remained stable. In this work, the experimental temperature was $-2.5\,^{\circ}\mathrm{C}$, $-4.4\,^{\circ}\mathrm{C}$, $-6.2\,^{\circ}\mathrm{C}$, and $-9.2\,^{\circ}\mathrm{C}$, respectively, and the dissociation rate was much slow compared with that when $T>0\,^{\circ}\mathrm{C}$. Although the dissociation of hydrates at the atmospheric pressure was an endothermic process, the hydrate decomposed percentages was small and absorbed low quantity of heat compared with that when $T>0\,^{\circ}\mathrm{C}$ at the same dissociation time. In addition, the whole dissociation time was also long enough to attain thermal equilibrium between constant temperature bath and the hydrate mixtures. Therefore the temperature fluctuation was small and the system could also be assumed to be under isothermal condition when T was below $0\,^{\circ}\mathrm{C}$.

The dissociation process can be described based on the ice-shielding mechanism [28]. The dissociation water is usually considered to be blown away from the surface immediately by the methane gas arised from the solid particle. But when the temperature is lower than 0 °C, the dissociation water will transform into ice rapidly at the particle surface. The released gas has to diffuse from the ice and hydrate mixture to the bulk methane phase. And the thickness of ice layer will increase with the continuous dissociation of hydrate. At the same time the thickness of hydrate layer will be lessened. The intrinsic dissociation rate is rapid compared with the diffusion rate and the dissociation of hydrate is controlled by the diffusion process. Based on the mass balance on the hydrate surface, the hydrate dissociation rate can be connected with the increasing of the thickness of ice layer or the decreasing of the thickness of hydrate layer.

$$-\frac{\mathrm{d}n}{\mathrm{d}t} = -A_{\mathrm{geo}}\rho \frac{\mathrm{d}S}{\mathrm{d}t} \tag{3}$$

where $A_{\rm geo}$ is the geometrical surface area of hydrate, S the thickness of ice layer, ρ moles of methane per unit volume of hydrate, and n is moles of gas component. The molar volume for ice phase is assumed to be equal to that of hydrate phase.

Fig. 2 shows the schematic diagram of hydrate dissociation when T < 0 °C. Initially when t = 0, the hydrate layer separates the gas phase and water/ice phase. The gas phase pressure is constant, and the gas concentration of the hydrate–gas interface (1–3), C^0 , remains constant. The gas concentration of the hydrate–water/ice interface (3–4), C^* , is equal to the three-phase equilibrium concentration, C_{eq} , at the bulk water temperature.

After starting the hydrate dissociation process (t>0), the generated water will change into ice rapidly at the particle surface. However part of hydrate on the surface is not decomposed, resulting in that there exists clearance between hydrate and ice or among hydrate particles. The dissociation gas must

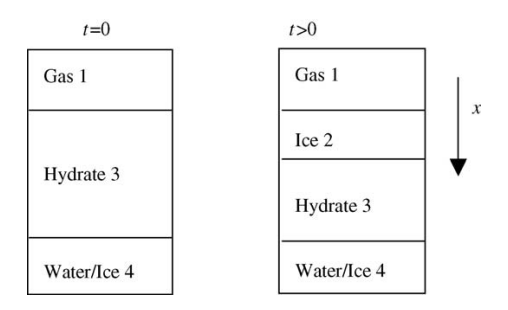


Fig. 2. Schematic diagram of hydrate dissociation when T < 0 °C.

diffuse across the clearance to the bulk gas phase. The thickness of ice layer will increase with the continuous dissociation of hydrate. Whereas the thickness of hydrate layer will reduce. The ice-hydrate boundary (2–3) will move toward the water/ice phase (4). Since the generated water will transform into ice rapidly and the density of ice is similar to that of hydrate, the gas-ice interface (1–2) may be assumed to keep immovable during the hydrate dissociation process. The hydrate dissociation when $T < 0\,^{\circ}\mathrm{C}$ could then be described as a moving boundary (ice-hydrate interface) phenomenon.

The one-dimensional gas concentration distribution in the ice zone (2) is governed by the Fick's second law of diffusion. The governing differential equation and the relevant initial and boundary conditions for the ice zone are given below:

Diffusivity equation:

$$-\frac{\partial C}{\partial t} = D \frac{\partial^2 C}{\partial x^2} \tag{4}$$

Here x refers to the spatial displacement of the moving boundary. The sign '-' in Eq. (4) shows that the diffusion direction is opposed to x.

Initial condition:

$$C(x, t = 0) = C_{\text{eq}} \tag{5}$$

Boundary conditions:

$$C(0,t) = C^0 \tag{6}$$

$$C[S(t), t] = C^* \tag{7}$$

From the mass balance at the ice-hydrate interface (2-3), yields:

$$-DA\frac{\partial C}{\partial x} = \rho A \frac{dS}{dt}, \quad x = S(t), \quad t > 0$$
 (8)

where D is the diffusion coefficient of gas through the ice layer, and C is gas concentration.

When the hydrate dissociation is controlled by gas diffusion, the gas concentration of the hydrate–water/ice interface (3–4), C^* , is equal to the three-phase equilibrium concentration, $C_{\rm eq}$. Then from Eq. (4), yields:

$$-\frac{C - C_{\text{eq}}}{C^0 - C_{\text{eq}}} = \text{erf}\left(\frac{x}{\sqrt{4Dt}}\right) \tag{9}$$

Introducing C from Eq. (9) into Eqs. (8) and (3), the value of diffusion coefficient of gas through the ice layer can be obtained.

At the beginning period of the hydrate dissociation, the transformed ice covers on the surface of hydrate softly. The generated gas diffuses through the clearance between hydrate and ice or among hydrate particles, which is governed by Fick's second law of diffusion. Since the continuous dissociation of hydrate increases the thickness of ice layer, the ice layer becomes compact. Thus Fick's law of diffusion cannot be preserved and the diffusion coefficient should be revised according to the dimension of clearance. However, the fraction of clearance cannot be determined experimentally. As it is noted, the clearance among ice, hydrate, and ice—hydrate mixture minishes with the increasing of the thickness of ice layer. Then the effective diffusion coefficient of gas can be expressed with the square ratio of the thickness of ice layer:

$$D_{\text{eff}} = D \frac{S_0^2}{S_t^2} \tag{10}$$

where S_0 is a referenced thickness and S_t is the thickness at t. In this paper the thickness of ice layer when t = 1 min is chosen as the referenced thickness which is determined from the experimental data.

4. Result and discussion

4.1. When $T > 0^{\circ}C$

When the temperature is higher than $0\,^{\circ}$ C, methane hydrate dissociation is governed by the intrinsic reaction. The apparent rate constant k' in Eq. (2) at different temperatures and pressures could be obtained according to the experimental data. The results of methane hydrate dissociation at four experimental conditions were shown in Fig. 3. The driving force Δf during the dissociation process was the difference between methane fugacity at the equilibrium pressure and at the experimental pressure. The three-phase equilibrium pressure was calculated by Chen–Guo

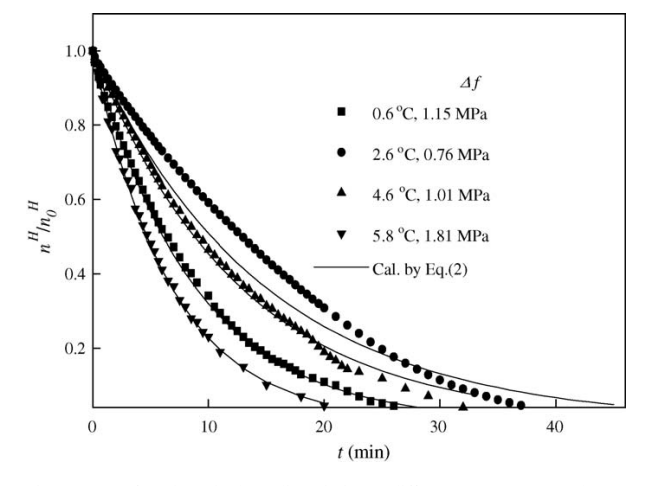


Fig. 3. Rate of methane hydrate dissociation at different temperature and pressure.

hydrate model [29], and the fugacity coefficient was calculated using the Peng–Robinson equation of state [30]. From Fig. 3 it could be seen that the kinetic model of Eq. (2) could fit the experimental data although the deviation at 2.6 °C was a little large. The average calculated error of the fraction of methane contained in the hydrate $(n^{\rm H}/n_0^{\rm H})$ at different conditions was 4.8%.

What was measured in the laboratory is the global rate of reaction, which was the rate associated with the bulk temperature and pressure. By eliminating the heat transfer effects, it was possible to isolate the intrinsic kinetics of gas hydrate dissociation from the experimental data. We could also use the same experimental method to study the influence of additive, porous medium, and gas composition, to obtain the general law of hydrate dissociation.

4.2. When $T < 0 \,^{\circ}C$

If only taking the intrinsic reaction into account as the kinetic model when T>0 °C, the apparent rate constant and the calculated error when T < 0 °C were listed in Table 1. The value of k' in Eq. (2) was determined from the experimental data during the whole dissociation process. It could be seen that the average deviation of the fraction of methane contained in the hydrate $(n^{\rm H}/n_0^{\rm H})$ was large (the error was much larger when expressing with the generated methane volume deviation). The results showed that the whole hydrate dissociation process at T < 0 °C was not controlled by the intrinsic reaction. At the initial stage of hydrate dissociation when the temperature was below 0°C, only a thin ice layer covered over the hydrate and the influence of intrinsic reaction was significant. For example, the first 20 min of methane hydrate dissociation at -2.5 °C could be described as an intrinsic reaction process and the corresponding apparent rate constant was $0.0158 \,\mathrm{min}^{-1}$.

On the other hand, the gas diffusion and ice–hydrate moving boundary theory could be successfully applied to hydrate dissociation kinetics when $T < 0\,^{\circ}\text{C}$. The diffusion coefficient obtained from Eqs. (3)–(10) and the calculated error for the generated methane were also listed in Table 1. Fig. 4 showed the time evaluation of the experimental and calculated volume of dissociated methane gas when $T < 0\,^{\circ}\text{C}$. The results revealed that the calculated precision could be significantly improved using the gas diffusion and ice–hydrate moving boundary theory.

Table 1 The apparent rate constant, diffusion coefficient, and the calculated error

<i>T</i> (°C)	$k' (\min^{-1})^a$	$D (cm^2/s)^b$	ADD (%) ^c	ADD (%)d
-9.2	0.000226	0.00274	13.6	4.5
-6.2	0.000712	0.00794	9.19	3.8
-4.4	0.000953	0.0270	13.1	6.1
-2.5	0.00276	0.0351	12.6	6.2

- ^a Regressed from the experimental data (based on intrinsic reaction).
- ^b Regressed from the experimental data (based on diffusion theory).
- ^c The average calculated deviation of (n^H/n_0^H) based on intrinsic reaction.
- ^d The average calculated deviation of decomposed gas volume based on diffusion theory.

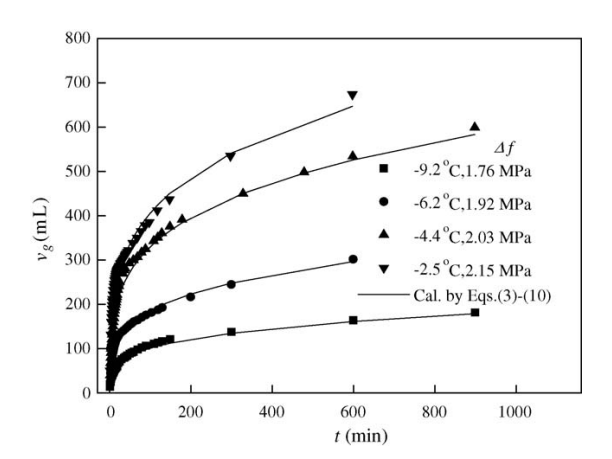


Fig. 4. Methane volume of dissociation at different time when T < 0 °C.

According to the ice-shielding mechanism [28], the kinetic process of the hydrate decomposition in a static system below 0 °C could be assumed as following two sequential steps:

- Destruction of clathrate host lattice at the surface of a hydrate particle and desorption of the methane molecule from the surface of hydrate particle, which could be described by Eq. (2).
- (2) Diffusion of methane molecule through ice layer and being released to gas phase, which could be described by Eqs. (3)–(10).

So the kinetic model of hydrate dissociation includes two parameters: apparent rate constant k' and diffusion coefficient D. Since the influence of intrinsic reaction is only significant at the initial stage and the influence time cannot be determined, only the gas diffusion and ice—hydrate moving boundary theory was used in this paper, which is much suitable for the total hydrate dissociation process at T < 0 °C.

Fig. 5 listed the calculated results based on the model from Eqs. (3)–(9) and that from Eqs. (3)–(10), respectively. It can be seen that at earlier dissociation stage (t<100 min), model from

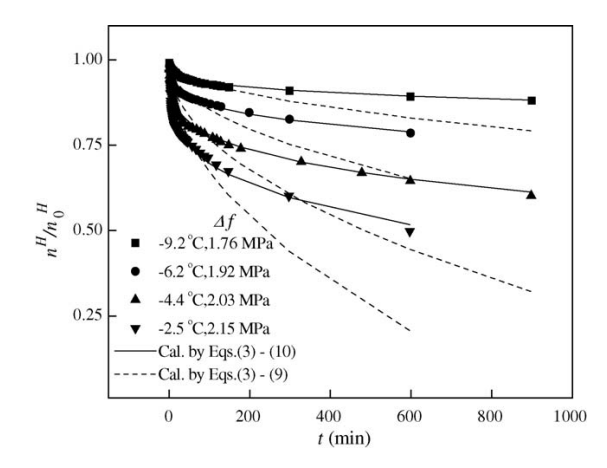


Fig. 5. The influence of the revised diffusion coefficient.

Eqs. (3)–(9) can also describe the experimental behavior successfully, without introducing the effective diffusion coefficient of gas in Eq. (10). It can be because that there existed clearance between hydrate and ice. At the initial period, the decomposed gas diffused through the clearance which was governed by Fick's second law of diffusion. But with the prolonging of dissociation time, the ice layer became thicker and more compact. Fick's diffusion law was no longer suitable for the dissociation process at this higher diffusion resistance. The calculated value from Eqs. (3)–(9) gradually deviated the experimental data with the increasing of dissociation time. The solid line curves in Fig. 5 were the calculated results after introducing the concept of the effective diffusion coefficient of gas. It should be noted that the calculated values from Eqs. (3)–(10) were significantly close to the experimental data.

5. Conclusion

The kinetics of methane hydrate dissociation was studied experimentally in a sapphire cell in two temperature regions, above 0 °C and below 0 °C. It was revealed that the hydrate dissociation when the temperature is above 0 °C can be treated as a first-order reaction. The hydrate dissociation model based on intrinsic dissociation reaction was built and the average calculated error of the fraction of methane contained in the hydrate at different conditions was 4.8%.

When the system temperature was lower than 0 °C, because of the formation of ice, the hydrate dissociation was controlled by gas diffusion, and the hydrate dissociation process was then treated as a moving boundary problem. The kinetic model for hydrate dissociation considering mass transfer was established and good agreements with experimental data were achieved.

Acknowledgement

Financial support received from the National Natural Science Foundation of China (Grant numbers: 20490207 and 20506016), the Key Project of Chinese Ministry of Education (No. 105107), and a Foundation for the Author of National Excellent Doctoral Dissertation of PR China (No. 200447) is gratefully acknowledged.

References

- [1] T.S. Collett, V.A. Kuuskraa, Oil Gas J. 11 (May) (1998) 90-95.
- [2] Y.F. Makogon, Hydrates of Hydrocarbons, Penn Well, Tulsa, OK, 1997.
- [3] M.D. Max, A. Lowrie, J. Pet. Geol. 19 (1996) 41-56.
- [4] E.D. Sloan, Clathrate Hydrates of Natural Gases, second ed., Marcel Dekker Inc., NY, 1998.
- [5] G.D. Holder, P.F. Angert, V.T. John, S. Yen, J. Pet. Technol. (May) (1982) 1127–1132.
- [6] V.A. Kamath, G.D. Holder, P.F. Angert, Chem. Eng. Sci. 39 (1984) 1435–1442.
- [7] J.W. Ullerich, M.S. Selim, E.D. Sloan, AIChE J. 33 (1987) 747-752.
- [8] A.K.M. Jamalludin, N. Kalogerakis, P.R. Bishnoi, Can. J. Chem. Eng. 67 (1989) 948–955.
- [9] M.S. Selim, E.D. Sloan, AIChE J. 35 (1989) 1049-1052.
- [10] P.L. McGuire, Paper SPE 10832 Presented at the 1982 Unconventional Gas Recovery Symposium, Pittsburgh, May, 1982, pp. 16–18.
- [11] V.A. Kamath, S.P. Godbole, J. Pet. Technol. (November) (1987) 1379–1388.
- [12] H.C. Kim, P.R. Bishnoi, R.A. Heidemann, S.S.H. Rizvi, Chem. Eng. Sci. 42 (1987) 1645–1653.
- [13] M.H. Yousif, H.H. Abass, M.S. Selim, E.D. Sloan, SPE Reserv. Eng. (February) (1991) 69–76.
- [14] K. Ohgaki, S. Nakano, T. Matsubara, S. Yamanaka, J. Chem. Eng. Jpn. 30 (1997) 310–314.
- [15] L.A. Stern, S. Circone, S.H. Kirby, J. Phys. Chem. B 105 (2001)
- [16] H. Shirota, I. Aya, S. Namie, P. Bollavaram, D. Turner, E.D. Sloan, Proceedings of the Fourth International Conference on Gas Hydrates, Yokohama, Japan, 2002, pp. 972–977.
- [17] G. Tsypkin, in: G.D. Holder, P.R. Bishnoi (Eds.), Gas Hydrates: Challenges for the Future, vol. 912, New York Academy of Sciences, New York, 2000, pp. 428–436.
- [18] N. Goel, M. Wiggins, S. Shah, J. Petrol. Sci. Eng. 29 (2001) 115-127.
- [19] M.A. Clarke, P.R. Bishnoi, Chem. Eng. Sci. 55 (2000) 4869–4883.
- [20] M.A. Clarke, P.R. Bishnoi, Can. J. Chem. Eng. 79 (2001) 143-147.
- [21] M.A. Clarke, P.R. Bishnoi, Chem. Eng. Sci. 56 (2001) 4715–4724.
 [22] C. Ji, G. Ahmadia, D.H. Smith, Chem. Eng. Sci. 56 (2001) 5801–5814.
- [23] G. Ahmadia, C. Ji, D.H. Smith, J. Petrol. Sci. Eng. 41 (2004) 269–285.
- [24] C.F. Ma, G.J. Chen, F. Wang, C.Y. Sun, T.M. Guo, Fluid Phase Equilib. 191 (2001) 41–47.
- [25] C.Y. Sun, G.J. Chen, W. Lin, T.M. Guo, J. Chem. Eng. Data 48 (2003) 600–602.
- [26] W. Lin, G.J. Chen, C.Y. Sun, X.Q. Guo, Z.K. Wu, M.Y. Liang, L.T. Chen, L.Y. Yang, Chem. Eng. Sci. 59 (2004) 4449–4455.
- [27] E.D. Ershov, V.S. Yakushev, Cold Regions Sci. Tech. 20 (1992) 147–156.
- [28] S. Takeya, W. Shimada, Y. Kamata, T. Ebinuma, T. Uchida, J. Nagao, H. Narita, J. Phys. Chem. A 105 (2001) 9756–9759.
- [29] G.J. Chen, T.M. Guo, Fluid Phase Equilib. 122 (1996) 43-65.
- [30] D.Y. Peng, D.B. Robinson, Ind. Eng. Chem. Fundam. 15 (1976) 59-64.

Fluidization Quality Improvement for Cohesive Particles by Fine Powder Coating

Huie Liu, Yan Li, and Qingjie Guo*

State Key Laboratory of Heavy Oil Processing, College of Chemistry and Chemical Engineering, China University of Petroleum, Dongying 257061, Shandong, P. R. China

A dry coating method via fine powder is used to improve the fluidization quality for cornstarch particles, belonging to the Geldart C group, which cannot fluidize normally. Two kinds of SiO₂ fine powder are used to coat cornstarch particles. Both a conventional fluidized bed and a magnetic fluidized bed (MFB) are employed for the coating of cornstarch particles. The coating time ranges from 10 to 15 min in this study. The coated particles are observed via the scanning electron microscope (SEM) images. Furthermore, the fluidization behaviors of the coated particles are investigated. The results show that coating with fine SiO₂ powder is an effective method to improve the fluidization quality of cohesive cornstarch particles. However, no significant difference in fluidization quality is observed between particles coated in a conventional fluidized bed and those coated in a MFB.

1. Introduction

Cohesive particles, most belonging to the Geldart C group, are difficult to fluidize under normal conditions.¹ Slugs, channels, and agglomerates are marked characteristics of their fluidization behavior.² These characteristics bring the problem of weak contact between gas and solids and limit the processing of cohesive particles in fluidized reactors. Many researchers have developed methods to solve the above problems, all of which can be classified into two groups:² external method and intrinsic method.

The external method employs external forces to overcome the adhesion force between particles. For example, Chirone et al., 3.4 Nowak et al., 5 Levy et al., 6 and Herrera et al. 7 introduced an acoustic field into the bed. With the presence of an acoustic field, the size of agglomerates, the minimum fluidization velocity, and the entrainment of fine powder decreased. Mori et al., 8 Dutaa et al., 9 Jaraiz et al., 10 Tang et al., 11 and Nam et al. 12 found that a vibrating field promoted the fluidization of fine powder. Also, a magnetic field can significantly influence the fluidization behavior of particles. 13,14 Recently, magnetic particles and a magnetic field were also applied to improve fluidization quality of Geldart C powder. 15,16

The intrinsic method is altering the intrinsic properties of particles. Kusakabe et al. 17 used nitrogen as the fluid and found that fine particles could be fluidized stably at reduced pressure. A lot of experiments have demonstrated that the fluidization quality of fine powder can improve significantly as another kind of particle is added into the bed. $^{2,9,18-21}$ A great advantage of this method is that no additional device is needed; thus, the investment for equipment is low. Wang 19 investigated the fluidization behavior of four kinds of Geldart C powders, CaCO3, Ni, $\alpha\text{-FeO(OH)}$, and $\gamma\text{-Fe}_2\text{O}_3$, when adding group A, B, C, and D particles, respectively. It is shown that each kind of fine powder has an optimal match particle and an optimal proportion for additive particles.

Cornstarch particle, a kind of Geldart C cohesive particle, is employed in this investigation. It can be seen from the following work that this kind of particle is difficult to fluidize. Nevertheless, the fluidization of cornstarch particles is of important significance for the pharmacy industry. In the present study, a dry coating method via fine powder is developed to improve the fluidization quality for cornstarch particle. Two different kinds of coating methods were explored. One is coating in a conventional fluidized bed, and the other is coating in a magnetic fluidized bed (MFB). Moreover, the proportion of the fine powder is changed to investigate the best matching.

2. Experiment

The experimental setup is shown in Figure 1. The fluidized bed is made of glass with a height of 1.6 m and an inner diameter of 0.056 m. A porous steel plate is used as a gas distributor. A U-manometer is installed at the bed bottom to measure the pressure drop across the bed. The fluidization gas, air, is supplied with a compressor, and the gas flowrate is measured with a rotameter. A 0.61 m high coil encircling the bed is used to generate an axial magnetic filed through the bed. The coil has an inner diameter of 0.14 m and an outer diameter of 0.16 m. A HT102 type gaussmeter is used to measure the magnetic flux density. Four kinds of particles are used in this work. The physical properties of the materials used in the experiment are listed in Table 1. Two kinds of particle size for the cornstarch and SiO_2 are listed in the table, in which d_{p1} is obtained from a Coulter LS-230 laser diffraction particle size analyzer and d_{p2} is obtained by measuring from scanning electron microscope (SEM) images. The particle sizes obtained from the SEM images are given here because they will be used for comparison with the coated particles in the following parts. The particle size of magnetic particle is obtained through screening. Figure 2 shows the particle size distributions of cornstarch and the two kinds of SiO2.

The fluidization behaviors of pure cornstarch particles are first investigated. The total weight of cornstarch particles used is 140 g. In theory, the pressure drop can be calculated from the weight of the particles above the manometer, i.e., Mg/A, equaling 462.55 Pa. Under the same conditions, two curves of pressure drop versus increasing gas velocity (exps 1 and 2) are drawn, as shown in Figure 3. The line of theoretical pressure drop is also shown in the figure. As expected, the pressure drop first undergoes a sharp increase, to a highest value even much higher than the theoretical pressure drop, and then a quick

10.1021/ie050083y CCC: \$33.50 © 2006 American Chemical Society Published on Web 02/03/2006

^{*} To whom correspondence should be addressed. Mailing address: College of Chemistry and Chemical Engineering, China University of Petroleum, Beier Road 271#, Dongying 257061, Shandong, P. R. China. Tel.: 86-546-8396753. Fax: 86-546-8391971. E-mail: qjguo@mail.hdpu.edu.cn.

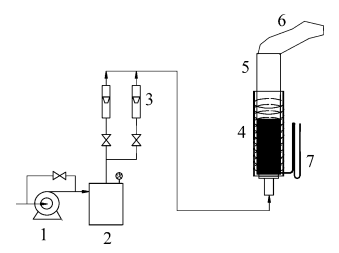


Figure 1. Schematic diagram of the experimental apparatus: (1) compressor; (2) surge tank and desiccator; (3) rotameter; (4) coil; (5) fluidized bed; (6) filter bag; (7) manometer.

Table 1. Physical Properties of the Experimental Materials

material	$d_{\rm pl}, \mu {\rm m}$	d_{p2} , μm	$\rho_{\rm b}$, kg·m ⁻³	$\rho_{\rm t}$, kg·m ⁻³
cornstarch	13.47	10.7	444	564
1# SiO ₂	2.97	2.5	500	625
2# SiO ₂	8.56	10.0		
Fe_3O_4		752.26	2000	2000

decline, to a lowest value near zero where an open valley forms. Finally, the pressure drop continues to increase and becomes relatively stable, and it is observed that the particles suffer plugs, channels, and full fluidization states in turn. Moreover, the two fluidization curves differ greatly in their configurations. These are typical characteristics of cohesive particles.

To improve the fluidization quality, a dry particle coating method, i.e., coating the cohesive cornstarch particles with another kind of fine powder (SiO₂), is used in this work. It is expected that the surface property of the cohesive particles can be modified when coated by fine powder, and thus, the fluidization quality can be improved. The coating is performed in a conventional bubbling fluidized bed and a preliminary study for coating in a magnetic fluidized bed is also carried out. All the work is aimed at improving the coating effect, thereby enhancing the fluidization behavior of the cohesive particles.

3. Results and Discussion

3.1. Coating Cornstarch Particles with 1# SiO2 Powders and Fluidization of the Coated Particles. 3.1.1. Selection of Coating Time. Cornstarch particles, mixed with the 1# SiO₂ powder $(d_{p1} = 2.97 \, \mu \text{m})$ in the proportion of 0.95:0.05 (wt), are fed into the fluidized bed and fluidized for a certain period of time to coat the cornstarch particles with the SiO₂ powder. The gas velocity used in the coating process is 0.18 m·s⁻¹. A 140 g portion of coated particles discharged from the bed is used to observe the fluidization behaviors in a conventional fluidized bed. Cornstarch particles coated for 5, 10, and 15 min are investigated, respectively, and curves of the pressure drop across the bed with increasing gas velocity are presented in Figure 4. It is shown that, with the increase of gas velocity, the fluctuation of the pressure drop for the coated particles is much less than that of pure cornstarch particles, which indicates that the coated particles can fluidize more smoothly. As expected, the longer coating time used, the better the fluidization behavior of the coated particles. However, no marked difference can be observed when the coating time is longer than 10 min. Accordingly, a coating time of 10-15 min is used in the following experiments.

3.1.2. Coating in a Conventional Fluidized Bed and Fluidization of the Coated Particles. Different proportions of $1\# SiO_2$ powders $(d_{p1} = 2.97\mu m)$, 1% (wt), 2% (wt), 3% (wt), 5% (wt), 8% (wt), 10% (wt), and 15% (wt) are used to blend with the cornstarch particles. The coating is carried out in a conventional fluidized bed without any magnetic particles and

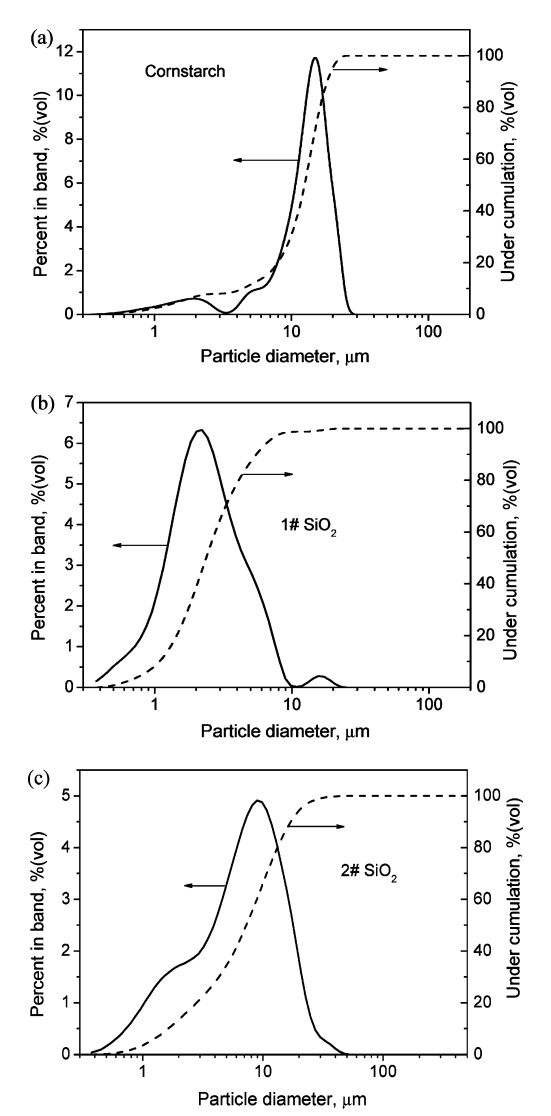


Figure 2. Particle size distributions from Coulter LS-230 laser diffraction particle size analyzer: (a) cornstarch; (b) 1# SiO₂; (c) 2# SiO₂.

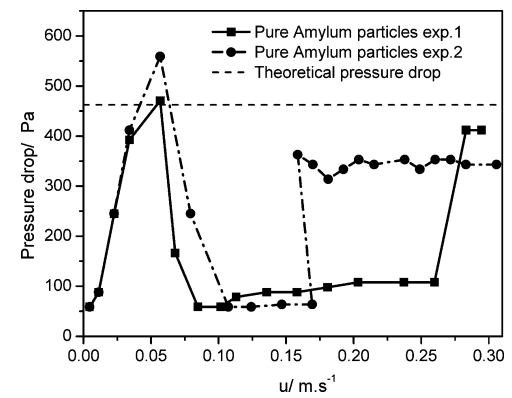


Figure 3. Fluidization curves of pure cornstarch particles.

magnetic field, with the gas velocity being $0.18~\text{m}\cdot\text{s}^{-1}$ and the coating time being 15 min. A 140 g portion of coated particles is used to investigate the fluidization behaviors. The curves of pressure drop versus increasing superficial gas velocity for the

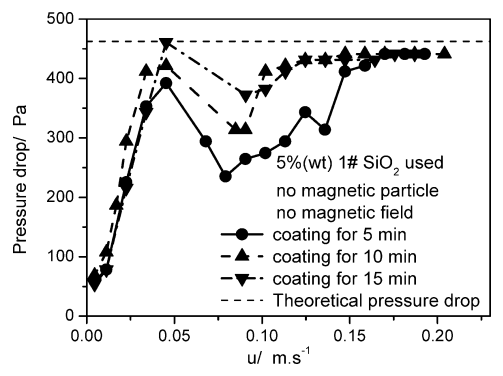


Figure 4. Influence of coating time on fluidization behavior of coated cornstarch particles.

seven groups of coated cornstarch particles are shown in Figure 5. The theoretical pressure drops are also illustrated in dashed lines in Figure 5. The pressure drops go through an increase and a decline and eventually arrive at a plateau. The plateau values of the pressure drops are somewhat smaller than the theoretical values. Probably, some elutriation of very fine particles took place, and there were some errors in the pressure drop measurement. It is obvious that the pressure drop curves exhibit smaller fluctuation for the coated cornstarch particles compared with that of the pure ones (as shown in Figure 3) when the proportion of SiO2 is higher than 1% (wt). The fluidization behavior of cornstarch particles coated with 1% (wt) SiO₂ is somewhat like that of pure ones, and the pressure drop curve undergoes a sharp increase, a quick decline to a lowest value near zero where an open valley forms, and finally a plateau. This indicates that 1% (wt) is too low a proportion for SiO₂ to improve the fluidization quality of cornstarch particles. Under the conditions of 2-15% (wt) SiO_2 used for coating, no significant slugs and channels are observed, suggesting that the coating method does improve the fluidization quality for the cornstarch particles. In this study, a superficial minimum fluidization velocity, $U_{
m mf, super}$, is defined as the lowest superficial gas velocity at which the pressure drop across the bed reaches a plateau. The values of $U_{
m mf,super}$ for the seven groups of particles

Table 2. Superficial Minimum Fluidization Velocity for Figure 5

plot	a	b	c	d	e	f	g
proportion of SiO ₂ , % (wt)	1	2	3	5	8	10	15
$U_{\rm mf, super}, { m m} \cdot { m s}^{-1}$	0.210	0.125	0.125	0.136	0.147	0.147	0.170

are measured in this study, as shown in Table 2, which reveals that the $U_{
m mf, super}$ has a lowest value. The pressure drop curves tend to fluctuate sharply when the content of SiO₂ powder is too low (such as 1% (wt)) or too high (such as 15% (wt)), which means that the fluidization behavior of the cohesive particles is undesirable when too little or too much fine powder exists. It is anticipated that the state of the cornstarch particles changes little when too little fine powder is blended and that the strong adhesion force among the fine SiO₂ particles becomes dominant when too much SiO₂ exists in the particle mixtures. With respect to this study, 2% (wt) SiO₂ fine powder is an appropriate proportion to coat the cohesive particles for approaching stable fluidization.

To depict the coating effect, samples of pure cornstarch particles and some coated ones (2% (wt), 5% (wt), 10% (wt), and 15% (wt) SiO₂ powder is used, respectively) were observed by a scanning electron microscope (SEM), and the images are shown in Figures 6 and 7. It is clearly seen from Figure 7 that some fine particles adhere to the surfaces of cornstarch particles, and these fine particles should be SiO₂. However, it also can be seen that some SiO₂ powder exists among the cornstarch particles, instead of adhering to the surfaces of cornstarch particles. The more SiO₂ powder used, the more of it fails to coat the surfaces of cornstarch particles. The average diameters of the coated particles in Figure 7a-d are obtained by measuring the particle size in the SEM images, being 11.6, 11.6, 11.4, and 10.4 μ m, respectively. The particle sizes in Figure 7a-c are larger than the average diameter of pure cornstarch particles (i.e., $10.7 \mu m$ from the SEM image). This indicates that some SiO₂ powder does coat on the cornstarch particles, whereas, for the size increase that is much smaller than 5 μ m (i.e., double $d_{\rm p2}$ of SiO₂), most of the SiO₂ powder coating on the cornstarch particles should be very fine, which indicates that a finer SiO₂ powder may give a good coating effect. Thus, further research

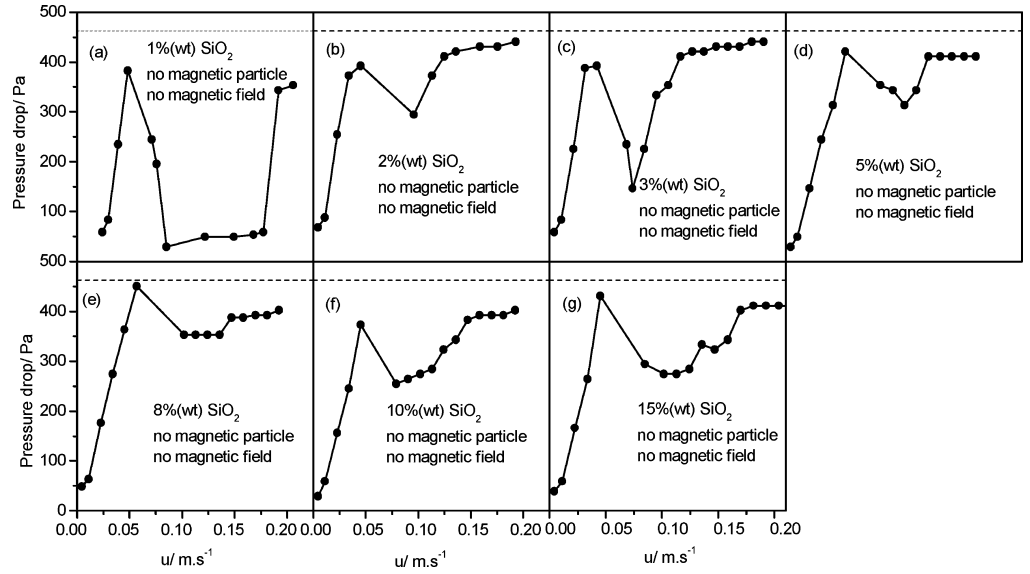


Figure 5. Fluidization curves of cornstarch particles coated with different proportions of 1# SiO2, without magnetic particles and a magnetic field: (a) 2% (wt) 1# SiO₂; (b) 3% (wt) 1# SiO₂; (c) 5% (wt) 1# SiO₂; (d) 8% (wt) 1# SiO₂; (e) 10% (wt) 1# SiO₂; (f) 15% (wt) 1# SiO₂.



Figure 6. SEM image for pure cornstarch particles.

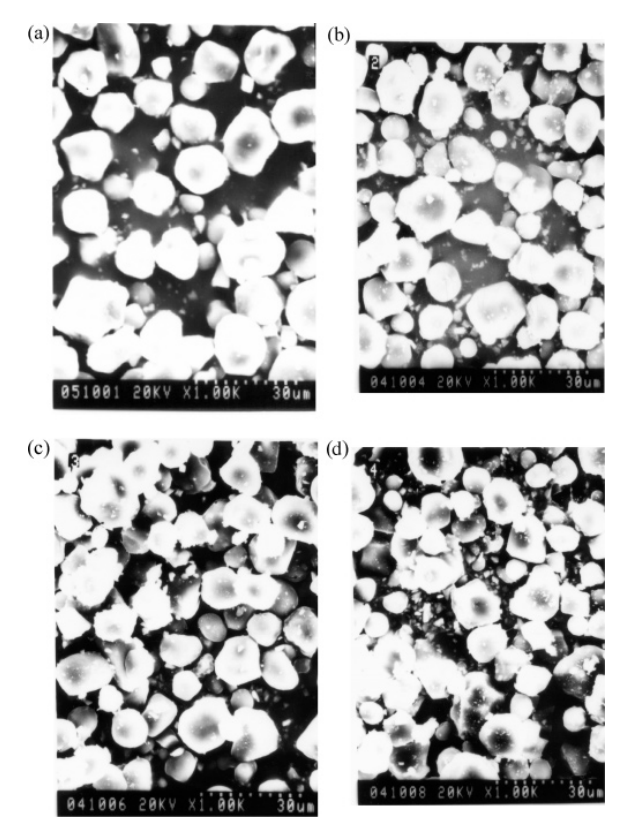


Figure 7. SEM images for cornstarch particles coated in a conventional fluidized bed: (a) with 2% (wt) 1# SiO₂ powder; (b) with 5% (wt) 1# SiO₂ powder; (c) with 10% (wt) 1# SiO₂ powder; (d) with 15% (wt) 1# SiO₂ powder.

in this regard is needed. In Figure 7d, the average particle size is slightly smaller than that of pure cornstarch particles. It is expected that when 15% (wt) SiO_2 powder is used, much of it fails to coat the surfaces of cornstarch particles. However, it is difficult to distinguish the cornstarch particles and the small SiO_2 particles in our measurement. The average particle size we obtained is that of the particle mixture. Thus, the average particle size decreases slightly.

3.1.3. Coating in a Magnetic Field and Fluidization of the Coated Particles. Much work has been done on magnetic fluidization of Geldart C particles. ^{15,16} It was reported that magnetic particles form a chain structure in a magnetic field,

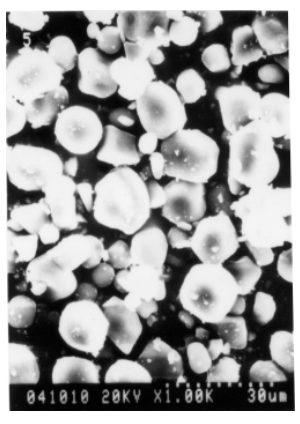


Figure 8. SEM image for cornstarch particles coated with 5% (wt) $1 \# SiO_2$ powder in a magnetic fluidized bed (B = 12.27 mT).

which splits the bubbles and eliminates the channels effectively. Accordingly, a magnetic field improves the fluidization quality. In the following work, magnetic particles and a magnetic field are used to improve the fluidization quality of the particle mixture of cornstarch and SiO₂ and thereby to improve the coating effect.

The cornstarch particles mixed with various proportions of 1# SiO₂ powder (3%, 5%, 8%, 10%, and 15% (wt), respectively), together with 10% (wt) magnetic particles, Fe₃O₄, are fluidized in an axial uniform magnetic field for about 15 min, thereby to coat the SiO₂ powder on the surfaces of cornstarch particles. The magnetic flux density in the bed, measured by a guassmeter, is 12.27 mT, and the gas velocity is 0.18 m·s⁻¹. The particle mixture is discharged afterward, separating the magnetic particles from the coated cornstarch particles using a magnet. A SEM image for a sample of the coated particles (with 5% (wt) SiO₂) was shown in Figure 8. As has been pointed out, Figure 7b gives the SEM image for cornstarch particles coated in a conventional fluidized bed with the same mass fraction of SiO₂. It can be seen that more very fine SiO₂ particles exist among those large cornstarch particles in Figure 7b when compared with Figure 8. This may indicate that more SiO₂ particles coat on the cornstarch particles in Figure 8, because the proportion of SiO₂ used is the same in these two figures.

The fluidization behaviors of these coated cornstarch particles are also investigated. The curves for pressure drop across the bed versus increasing gas velocity are presented in Figure 9, with theoretical pressure drop curves in dashed lines. The $U_{\rm mf,super}$ values are summarized in Table 3. A comparison of $U_{\rm mf,super}$ values in Tables 2 and 3 reveals that the $U_{\rm mf,super}$ values are very close under the same mass fraction of SiO₂ no matter if the magnetic fields exist or not. This indicates that the fluidization behavior of the cornstarch particles coated in a magnetic fluidized bed is similar to that of those coated in a conventional fluidized bed. Maybe, the size of the magnetic particles used in the present work is not the appropriate one. This calls for further efforts to investigate the fit size of magnetic particles.

3.2. Adding 2# SiO₂ Powder and Fluidization of the Particle Mixture. To clarify the advantage of the coating method on improvement of fluidization quality for Geldart C particles, $2\# SiO_2$ powder ($d_{p1} = 8.56 \mu m$) is also used in this study. It is expected that $2\# SiO_2$ powder may not coat cornstarch particles for its size is too large and it may just act as a kind of additive particle. Particle mixtures of cornstarch and $2\# SiO_2$ are first blended in a conventional fluidized bed

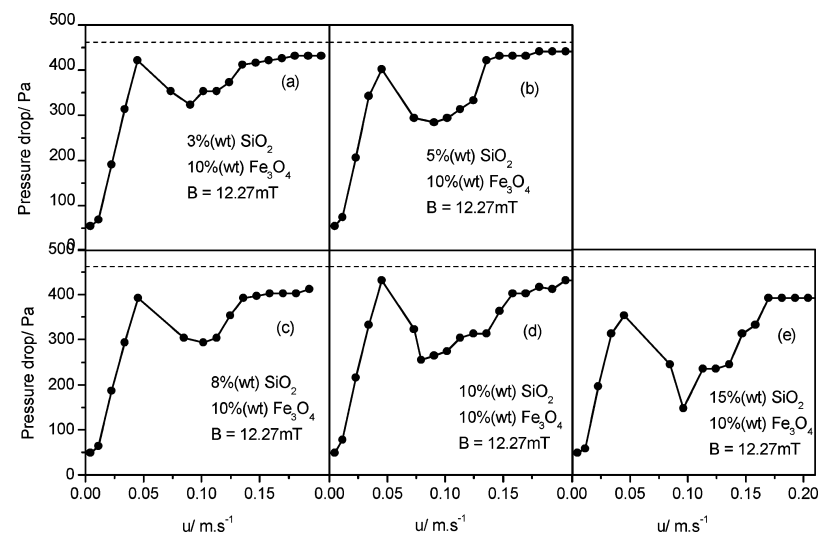


Figure 9. Fluidization curves of cornstarch particles coated with different proportions of 1# SiO2, with 10% (wt) magnetic particles and the magnetic flux density being 12.27 mT.

Table 3. Superficial Minimum Fluidization Velocity for Figure 9

plot	a	b	c	d	e
proportion of SiO2, % (wt)	3	5	8	10	15
$U_{\rm mf.\ super},{ m m\cdot s^{-1}}$	0.136	0.136	0.136	0.159	0.170

or in a magnetic fluidized bed to realize full mixing. Two kinds of mass fractions of 2# SiO2, 3% (wt) and 5% (wt), are investigated in this study. The fluidization behaviors of the mixed particles are studied, and the curves of pressure drop across the bed versus gas velocity are shown in Figure 10, in which the theoretical pressure drops are also marked in dashed lines. The mixed particles can fluidize more stably than the pure cornstarch particles, as shown in Figure 3. No significant channeling was observed, and the mixed particles could eventually fluidize smoothly. These results show that adding 2# SiO₂ powder can improve the fluidization behavior for cornstarch particles. However, with an increase of the gas velocity, the pressure drops across the bed first increase sharply to a maximum value much higher than the theoretical one, as shown in Figure 10. This phenomenon, corresponding to an obvious plug state, is similar to that of the pure cornstarch particles. Thus, the fluidization quality for cornstarch particles mixed with 2# SiO₂ powder is not as good as that for those coated with 1# SiO₂ particles. The above evidence confirms that coating cornstarch particles with 1# SiO2 powder is more effective for fluidization quality improvement than adding the larger one, 2# SiO₂ powder.

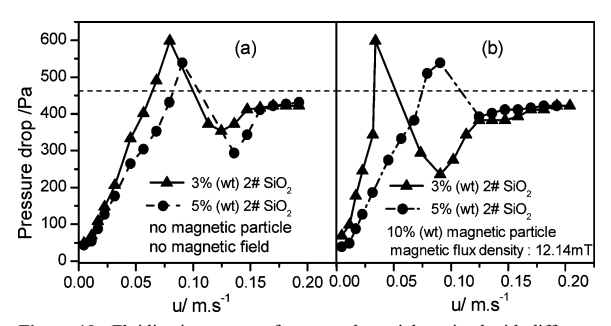


Figure 10. Fluidization curves of cornstarch particles mixed with different proportions of 2# SiO₂: (a) without magnetic particles and a magnetic field; (b) with the presence of 10% (wt) Fe $_3$ O $_4$ magnetic particles and the magnetic flux density being 12.14 mT.

4. Conclusions

The cornstarch particle used in this study is a typical Geldart C cohesive particle, which cannot fluidize normally. Coating with fine SiO₂ powder is an effective method to improve the fluidization quality of the cohesive cornstarch particles. In the present study, the following conclusions can be drawn: (1) The longer coating time used, the better the fluidization quality for the coated particles. However, no marked difference can be observed when the coating time is longer than 10 min. (2) When coating is carried out in a conventional fluidized bed, 2% (wt) 1# SiO₂ powder ($d_{p1} = 2.97 \mu m$) gives the best results for fluidization quality improvement of cornstarch particles. (3) No significant difference exists between the fluidization behavior of particles coated in a magnetic fluidized bed and that of those coated in a conventional fluidized bed. (4) Coating cornstarch particles with 1# SiO₂ ($d_{\rm pl} = 2.97 \,\mu{\rm m}$) powder is more effective for fluidization quality improvement than adding 2# SiO₂ (d_{p1} = $8.56 \mu m$) particles.

Acknowledgment

This research is supported by the Natural Science Foundation of Shandong Province under Contract No. Z2003B01 and by Project, sponsored by SRF for ROCS and SEM, 2004527.

Nomenclature

A =cross sectional area of the fluidized bed, m²

B = magnetic flux density, T

 $d_{\rm pl}$ = average particle diameter obtained from Coulter LS-230 laser diffraction particle size analyzer, μm

 $d_{\rm p2}$ = average particle diameter measured from SEM images,

 $g = \text{acceleration of gravity, } 9.81 \text{ m} \cdot \text{s}^{-2}$

M = the total particle weight above the manometer in smooth fluidization, kg

 $U_{
m mf, \ super} = {
m superficial \ minimum \ fluidization \ velocity, \ m\cdot s^{-1}}$

 $\rho_{\rm b} = \text{bulk density of particle, kg} \cdot \text{m}^{-3}$

 $\rho_{\rm t} = {\rm tap\ density\ of\ particle,\ kg\cdot m^{-3}}$

Literature Cited

(1) Geldart, D. Types of gas fluidization. Powder Technol. 1973, 7, 285-292

- (2) Wang, Z.; Kwauk, M.; Li, H. Fluidization of fine particles. *Chem. Eng. Sci.* **1998**, *53* (3), 377–395.
- (3) Chirone, R.; Massimilla, L.; Russo, S. Bubbling fluidization of a cohesive powder in an acoustic field. In *Fluidization VII*; Potter, O. E., Nicklin, D. J., Eds.; New York, 1992; pp 545–553.
- (4) Chirone, R.; Massimilla, L.; Russo, S. Bubble-free fluidization of a cohesive powder in an acoustic field. *Chem. Eng. Sci.* **1993**, *48* (1), 41–52.
- (5) Nowak, W.; Hasatani, M.; Derczynski, M. Fluidization and heat transfer of fine particles in an acoustic field. *AIChE Symp. Ser.* **1993**, *89* (296), 137–149.
- (6) Levy, E. K.; Shnitzer, I.; Masaki, T.; et al. Effect of an acoustic field on bubbling in a gas in a gas fluidized bed. *Powder Technol.* **1997**, 90, 53–57.
- (7) Herrera, C. A.; Levy, E. K. Bubbling characteristics of sound-assisted fluidized beds. *Powder Technol.* **2001**, *119*, 229–240.
- fluidized beds. *Powder Technol.* **2001**, *119*, 229–240.

 (8) Mori, S.; Yamamoto, A.; Haruta, T.; Yamada, T.; Mizutani, E. Vibrofluidization of very fine particles. In *Fluidization '88-Science and Technology*; Kwauk, M., Kunii, D., Eds.; Academic Press: Beijing, 1988; pp 75–81
- (9) Dutta, A.; Dullea, L. V. Effects of external vibration and the addition of fibers on the fluidization of a fine powder. *AIChE Symp. Ser.* **1991**, 87 (281), 38–46.
- (10) Jaraiz, E.; Kimura, S.; Levenspiel, O. Vibrating beds of fine particles: estimation of interparticle forces from expansion and pressure drop experiments. *Powder Technol.* **1991**, *72*, 23–30.
- (11) Tang, H.; Zhao, J. The agglomerating behavior of fine particles in a Vibro-fluidized bed. *Chem. Ind. Eng.* (Tianjin, China) **1996**, *13* (3), 6–20.
- (12) Nam, C. H.; Pfeffer, R.; Dave, R. N.; Sundaresan, S. Aerated vibrofluidization of silica Nanoparticles. *AIChE J.* **2004**, *50* (8), 1776–1785.

- (13) Rosensweig, R. E. Fluidization: Hydrodynamic stabilization with a magnetic field. *Science*. **1979**, *204*, 57–60.
- (14) Jaraiz, E.; Levenspiel, O.; Fitzgerald, T. J. The use of magnetic fields in the processing of solids. *Chem. Eng. Sci.* **1983**, *38* (1), 107–114.
- (15) Zhu Q.; Li H. Study on magnetic fluidization of group C powders, *Powder Technol.* **1996**, *86*, 179–185.
- (16) Lu, X.; Li, H. Fluidization of CaCO₃ and Fe₂O₃ particle mixtures in a transverse rotating magnetic field. *Powder Technol.* **2000**, *107*, 66–78
- (17) Kusakabe, K.; Kuriyama, T.; Morooka, S. Fluidization of fine particles at reduced pressure. *Powder Technol.* **1989**, *58*, 125–130.
- (18) Liu, Y.; Kimura, S. Fluidization and entrainment of difficult-to-fluidize fine powder mixed with easy-to-fluidize large particles. *Powder Technol.* **1993**, *75*, 189–196.
- (19) Wang, Z. Fluidization of Fine particles and effects of additive particles. Ph.D. Dissertation, Institute of Chemical Metallurgy, Academia Sinica, Beijing, 1995 (in Chinese).
- (20) Zhou, T.; Li, H. Effect of adding different size particles on fluidization of cohesive particles. *Powder Technol.* **1999**, *102*, 215–220.
- (21) Zhou, T.; Ye, H.; Dave, R.; Pfeffer, R. Behavior of cohesive particles coated with nanoparticles in a fluidized bed. *Chin. J. Process Eng.* **2004**, *4* (Suppl.), 567–572.

Received for review January 20, 2005 Revised manuscript received October 16, 2005 Accepted January 9, 2006

IE050083Y

Effect of Water Content on the Solubility of CO₂ in the Ionic Liquid [bmim][PF₆]

Dongbao Fu, Xuewen Sun, Jinjun Pu, and Suoqi Zhao*

State Key Laboratory of Heavy Oil, China University of Petroleum, Beijing, 102249, China

The solubility of CO_2 in the ionic liquid 1-butyl-3-methylimidazolium hexafluorophosphate ([bmim][PF₆]) and the liquid-phase molar volume were determined, in a precision high-pressure PVT apparatus, for water mass fraction of [bmim][PF₆] ranging from 0.0067 % to 1.6 % and over temperature and pressure ranges of (40 to 60) °C and (1 to 25) MPa. The deviation in solubility, at the same temperature and pressure, with different water mass fractions was not more than 15 %, and the average is 6.7 %. Solubility pressures were correlated with an average relative uncertainty of about 1 % by means of the extended Henry's law for all water mass fractions investigated at less than 6 MPa.

Introduction

Ionic liquids (IL), holding great potential as replacements for traditional organic solvents, have attracted more and more attention due to their lack of volatility and other unique characteristics. 1-5 However, separation and recovery of IL is one of the major challenges in future industry applications. Distillation, liquid-liquid extraction, and supercritical fluid extraction are known feasible separation methods. Distillation, a reasonable option owing to no appreciable vapor pressure of IL, would not be prudent for thermally labile or low-volatility products. Cross-contamination between the phases presents a problem for liquid-liquid extraction.^{6,7} Comparatively, supercritical fluid extraction with CO2 can be used to separate both volatile and relatively nonvolatile organic compounds from ionic liquids without any IL contamination.^{8,9} Knowledge of the phase behavior of the CO₂ + IL systems, which is a crucial aspect of this methodology, has been the focus of much research in recent years.10-24

Several research groups studied the effect of water content on the solubility of CO2 in some IL. Blanchard et al. 10 reported solubility data of CO₂ in [bmim][PF₆] with two different water mass fractions (0.15 % and 2.3 %). Those data were measured at 40 °C and less than 10 MPa. They concluded that drying of IL samples prior to use was crucial as a small amount of water in the IL had a dramatic effect on the phase behavior with CO₂. Aki et al.22 reported solubility data of CO2 in 1-butyl-3methylimidazolium bis(trifluoromethylsulfonylimide) ([bmim]-[Tf₂N]) with two different water mass fractions (0.045 % and 1.35 %). Those solubilities were measured at 25 °C and less than 7 MPa. They concluded that the presence of water had essentially no effect on the solubility of CO₂ in [bmim][Tf₂N]. Baltus et al.²³ studied the solubility of CO₂ in several ionic liquids at 25 °C with pressures at or less than 0.1 MPa. The data, which were measured with a quartz crystal microbalance, indicated that humidity had a small effect on the solubility of CO₂ in [bmim][Tf₂N] and 1-octyl-3-methylimidazolium bis-(trifluoromethylsulfonylimide) ([C₈mim][Tf₂N]). Scovazzo et al.²⁴ measured the Henry's constants of CO₂ + [bmim][PF₆] and CO₂ + 1-ethyl-3-methylimidazolium bis(trifluoromethylsulfonylimide) ([emim][Tf2N]) for both dry and water-saturated

* Corresponding author. E-mail: sqzhao@cup.edu.cn. Tel: +86-10-89733743. Fax: +86-10-69724721.

ionic liquids at 30 °C and less than 0.1 MPa. The results indicated that moisture had a small effect on the solubilities. To sum up, there are different conclusions about the effect of water content on the solubility of CO_2 in ionic liquids, and no systematical exploration has been carried out.

It is almost inevitable for ionic liquid [bmim][PF₆] to absorb moisture in industrial processes due to its hydroscopic property. The question arises as how the water content affects the phase behavior. In this work, phase behavior data are reported for the system of CO_2 + [bmim][PF₆] within water mass fraction of [bmim][PF₆], temperature and pressure ranges of (0.0067 to 1.6) %, (40 to 60) °C, and (1–25) MPa, respectively.

Experimental Section

Materials. CO₂ with a purity of 99.995 % was supplied by Beijing Analytical Instrument Factory. 1-Methylimidazole (99 % purity) and potassium hexafluorophosphate (98 % purity) were used as received from Fluka. 1-Bromobutane was analysis reagent grade and produced by Beijing Chemical Reagent Factory. [bmim][PF₆] was synthesized and characterized following procedures reported elsewhere.^{25,26} Five samples of [bmim][PF₆] with different water mass fractions were prepared by different pretreatment. [bmim][PF₆] with water mass fraction of 0.0067 % was obtained by contacting the sample with water mass fraction 0.15 % with 3 Å molecular sieve, 0.15 % by vacuum-drying at 80 °C for 48 h, 0.89 % by injection of quantitative water into the sample with water mass fraction 0.15 %, 1.6 % by centrifugal separation between wet IL and water at ambient temperature 16 °C, and 2.2 % by separatory funnel separation between wet IL and water at ambient temperature 24 °C. It is noteworthy to mention that sample with water mass fraction of 2.2 % is not a true solution and, therefore, was not included as a part of this study. Water mass fraction of this sample declined to 1.1 % after 40 min and 2000 revolution/ min centrifugal separation at ambient temperature 24 °C. All the water concentrations were measured by Karl Fischer analysis. Sample density measurements were performed at 40 °C, and ambient pressure with AP PAAR density meter DMA 48. The results were shown in Table 1.

Apparatus and Procedure. The main apparatus is a Ruska PVT 2730-601 device, which is shown schematically in Figure 1. The model 2730 PVT system is a high precision instrument

10.1021/je0502501 CCC: \$33.50 © 2006 American Chemical Society Published on Web 02/16/2006

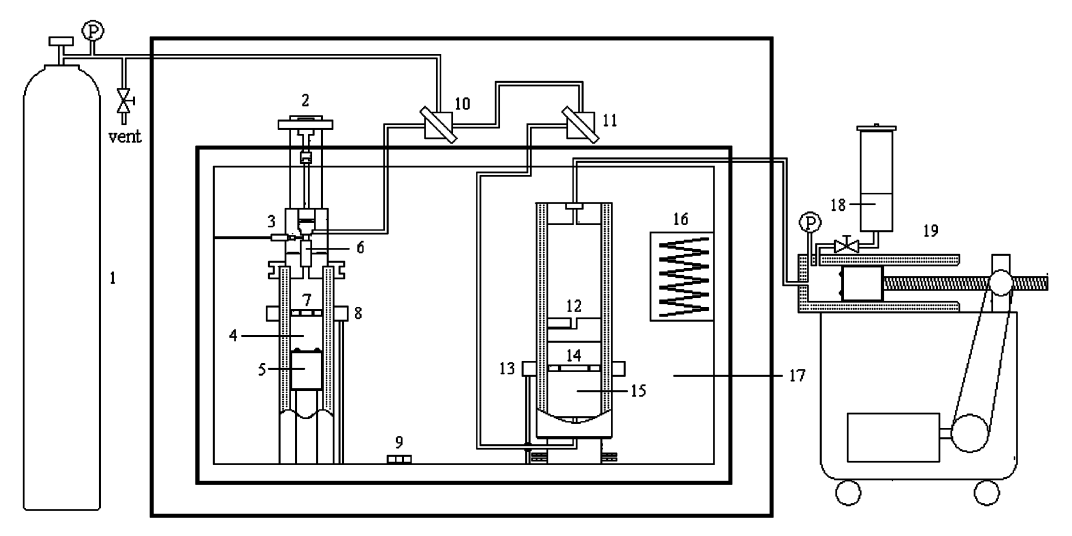


Figure 1. Schematic diagram of Ruska PVT 2730-601: 1, CO2 reservoir; 2, pump cell shutoff valve; 3, temperature and pressure transducer; 4, pump cell; 5, pump piston; 6, sapphire tube; 7 and 14, stirring magnet; 8 and 13, stirring collar; 9, oven RTD; 10, charging valve; 11, floating piston cell shutoff valve; 12, floating piston; 15, floating piston cell; 16, heater; 17, thermostat; 18, hydraulic oil; 19, digital positive placement pump.

Table 1. Densities of [bmim][PF₆] (1) with Different Water (2) Mass Fractions w2 at 40 °C and Ambient Pressure

pretreatment	w_2	$\rho/(g \cdot cm^{-3})$
3 Å molecular sieve	0.0067 %	1.3587
vacuum-drying	0.15 %	1.3576
water injection	0.89 %	1.3473
centrifugal separation	1.6 %	1.3355

used to perform volumetric and phase behavior studies. The system is based on a unique dual-cell arrangement where the main cell volume is varied by the vertical movement of a dynamically sealed piston driven by a computer-controlled stepping motor. The second cell contains a floating piston operated by an external pump. The cells are connected by smallbore tubing through a sapphire sight glass at the top of the main cell and placed in a constant-temperature bath. This configuration allows phase volume measurements to be made by positioning the phase boundary at a reference point in the sight glass. The computer then automatically calculates the volumes above and below the reference point. The maximum pressure accessible with this apparatus is 68.9 MPa. The resolutions of pressure, volume, and temperature in the system are 0.007 MPa, 0.01 mL, and 0.1 °C, respectively.

A static method, one of the commonly used techniques, 8,10,20,22 was used to determine the solubility of CO₂ in [bmim][PF₆] with different water concentrations. In a typical experiment, known amounts of CO2 and [bmim][PF6] were metered into the main cell while the sample within was vigorously stirred to ensure equilibrium. Up and down stirring mode of the PVT apparatus was helpful to reach equilibrium quickly. The criterion of reaching phase equilibrium was invariable whole volume over 40 min in the constant pressure mode. Subsequently, the liquidphase volume was determined at constant pressure. The composition of the IL-rich liquid phase was calculated on the basis of material balance, along with the assumption of a pure CO₂ vapor phase. This assumption was verified by experiments done by many researchers.^{8-11,14} In addition, water in [bmim]-[PF₆] can hardly enter CO₂-rich phase due to strong hygroscopicity of [bmim][PF₆] and very low solubility of water in CO₂, even at high pressures.²⁷ For example, the water mass fraction of sample was merely reduced to 1.5 % from 1.6 % after experiments at 60 °C and (1 to 9) MPa. The estimated

uncertainties in the calculated liquid-phase mole fractions and liquid molar volumes are \pm 0.001 and \pm 0.1 mL/mol, respectively, based on propagation of random errors in the measurements of the pressures, volumes, and temperatures.

Results and Discussion

The phase behavior of $CO_2 + [bmim][PF_6]$ systems with different water contents was determined by the static method. The results are presented in Table 2, which give a systematical knowledge about how pressure, temperature, and water content affect the solubility of CO2 in [bmim][PF6] as well as the liquid molar volume.

The solubility of CO₂ in [bmim][PF₆] with water mass fraction of 0.15 % is illustrated in Figure 2 where the mole fraction of CO₂ in the IL-rich phase is plotted as a function of pressure. As can be seen from Figure 2, the solubility increased dramatically with increasing pressure at pressure < 10 MPa, increased slowly and then more at > 10 MPa, and increased very little at > 15 MPa. As expected, the solubility decreased with an increase in temperature, but the temperature dependence is quite small over the temperature and pressure range studied.

Figure 3 shows the P-x diagram of $CO_2 + [bmim][PF_6]$ systems with different water contents at 50 °C, from which can be seen that the mole fraction of CO2 decreased regularly with an increase in water mass fraction at the same temperature and pressure. Also, this figure indicates that influence of water content on the solubility is not so significant throughout the temperature and pressure range investigated, which can be clearer for mole fraction CO2 calculated on a basis of water free (i.e., the formula $x_{\rm CO_2} = n_{\rm CO_2}/(n_{\rm CO_2} + n_{\rm IL} + n_{\rm H_2O})$ turned into $x_{\rm CO_2} = n_{\rm CO_2}/(n_{\rm CO_2} + n_{\rm IL})$). The deviation in solubility, at the same temperature and pressure, with different water mass fraction investigated was not more than 15 %, and the average is 6.7 %. On the water free basis, the average deviation reduced to 3.9 %. Figure 4 was provided for contrast, in which mole fraction CO2 was calculated with the latter formula.

The solubility pressures were correlated by means of the extended Henry's law²⁰ for all water mass fractions investigated at pressures less than 6 MPa. It should be noticed that solubility must be on the molality scale for better linearity. Henry's constants resulting from the correlations were given in Table

Table 2. Mole Fraction Solubility of CO₂ (2) x_2 in [bmim][PF₆] (1) with Different Water (3) Mass Fractions w_3 and Liquid Molar Volumes $V_{\rm m}$ at (40, 50, and 60) °C

		t =	= 40 °C	t =	= 50 °C	t =	= 60 °C
	P		V_{m}		V_{m}		$V_{ m m}$
w_3	MPa	x_2	mL·mol ⁻¹	x_2	mL·mol ⁻¹	x_2	mL·mol ⁻¹
0.0067 %	1	0.129	187.2	0.112	192.7	0.099	195.3
	2	0.215	169.7	0.200	176.2	0.179	178.8
	3	0.288	156.3	0.271	162.7	0.243	168.3
	4	0.356	144.7	0.331	151.1	0.301	157.7
	5	0.412	136.8	0.383	141.9	0.350	148.5
	6	0.456	129.9	0.425	135.9	0.391	140.8
	7	0.490	124.3	0.465	128.3	0.426	135.0
	8	0.510	121.4	0.492	123.6	0.454	130.3
	9	0.529	117.2	0.514	120.3	0.478	125.8
0.15 %	1	0.131	183.0	0.110	183.6	0.094	196.5
	2	0.232	165.2	0.197	168.4	0.171	183.1
	3	0.312	151.4	0.268	157.9	0.235	171.0
	4	0.376	139.8	0.324	150.3	0.290	161.2
	5	0.427	131.0	0.374	141.9	0.335	153.2
	6	0.469	123.8	0.416	134.7	0.375	146.0
	7	0.503	118.2	0.451	128.4	0.408	139.9
	8	0.525	115.3	0.479	123.5	0.436	135.1
	9	0.554	109.1	0.499	120.3	0.460	131.3
	10	0.571	105.4	0.519	117.5	0.481	127.7
	12	0.626	92.3	0.553	110.3	0.510	121.8
	15	0.641	90.2	0.570	107.1	0.541	115.7
	20	0.648	88.2	0.590	103.2	0.564	111.1
	25	0.658	86.2	0.606	99.9	0.580	107.7
0.89 %	1	0.116	169.6	0.096	171.5	0.082	179.2
	2	0.205	156.4	0.174	159.5	0.152	167.9
	3	0.278	145.1	0.240	149.4	0.211	158.4
	4	0.339	135.6	0.296	140.9	0.262	150.5
	5	0.390	127.9	0.345	133.5	0.307	143.4
	6	0.432	121.5	0.386	127.2	0.346	137.2
	7	0.466	116.5	0.421	122.0	0.379	132.1
	8	0.492	112.4	0.448	117.7	0.407	127.9
1.60/	9	0.504	110.8	0.467	114.8	0.429	124.6
1.6 %	1	0.126	151.8	0.108	155.1	0.083	161.5
	2	0.215	139.0	0.183	144.9	0.161	149.3
	3	0.280	130.3	0.246	136.5	0.220	140.7
	4	0.338	122.7	0.297	129.5	0.274	133.1
	5	0.386	116.6	0.343	123.4	0.320	126.8
	6	0.426	112.4	0.380	118.5	0.358	121.5
	7	0.455	108.3	0.410	114.9	0.390	117.3
	8	0.467	107.5	0.429	112.9	0.417	113.5
	9	0.473	107.5	0.452	109.9	0.441	110.5

 ax_2 , mole fraction CO₂ in the liquid phase; $x_2 = n_2/(n_1 + n_2 + n_3)$. w_3 , water mass fraction of the [bmim][PF₆] + water mixture; $w_3 = m_3/(m_1 + m_3)$. $V_{\rm m}$, liquid molar volumes; $V_{\rm m} = V_{\rm liquid}/(n_1 + n_2 + n_3)$.

3. From Table 3, one can concluded that the Henry's constant increased with an increase in temperature. However, there was no obvious regularity about the influence of water content on Henry's constant.

The solubility of CO_2 in [bmim][PF₆] has been reported by several research groups. 10,20,22,28 The results obtained at 40 °C in this work are compared with those reported by various research groups in Figure 5. Our results agree well with the values reported by Kamps et al. 20 over all the pressure range. From Figure 5, one can also conclude that the solubility results for CO_2 in [bmim][PF₆] from various research groups are not in good agreement. The discrepancy in the solubility measurements may be related to the instability of [PF₆] anion, 22 different experimental techniques, uncertainties, impurities, and so on.

Another value measured in this work was the molar volume of the liquid phase, which can reflect liquid expansion. The volume of normal organic liquids will increase significantly by addition of CO₂. For example, a liquid composition of 0.74 mole fraction CO₂, for toluene + CO₂ system at 40 °C and 7 MPa, will give a 134 % increase in the volume of liquid phase. But

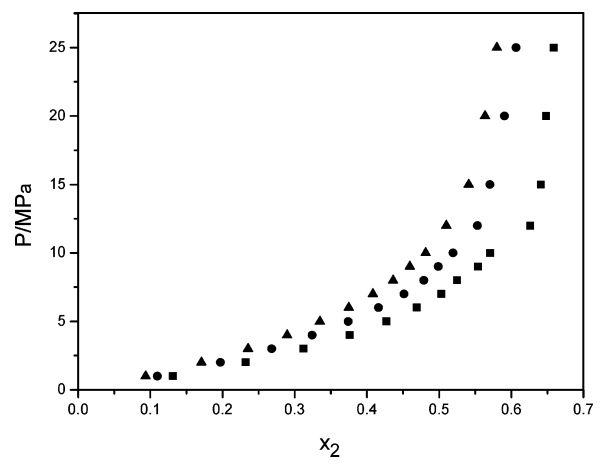


Figure 2. Solubility of CO₂ (2) in [bmim][PF₆] (1) with water mass fraction 0.15 %: ■, t = 40 °C; •, t = 50 °C; •, t = 60 °C.

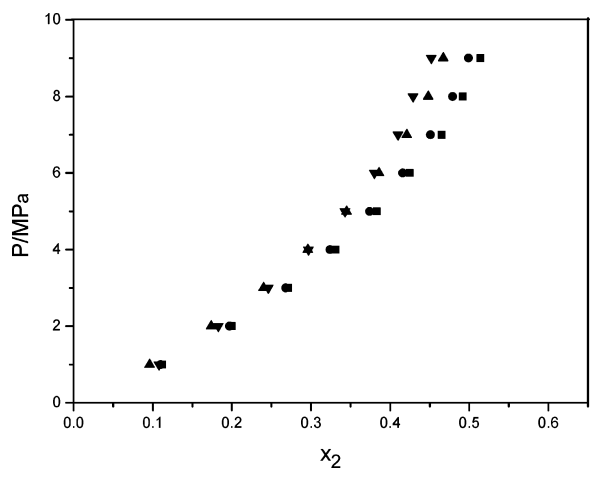


Figure 3. Solubility of CO₂ (2) in [bmim][PF₆] (1), calculated by the formula $x_{\rm CO_2} = n_{\rm CO}/(n_{\rm CO_2} + n_{\rm IL} + n_{\rm HyO})$, with different water mass fractions at 50 °C: ■, 0.0067 %; ●, 0.15 %; ▲, 0.89 %; ▼, 1.6 %.

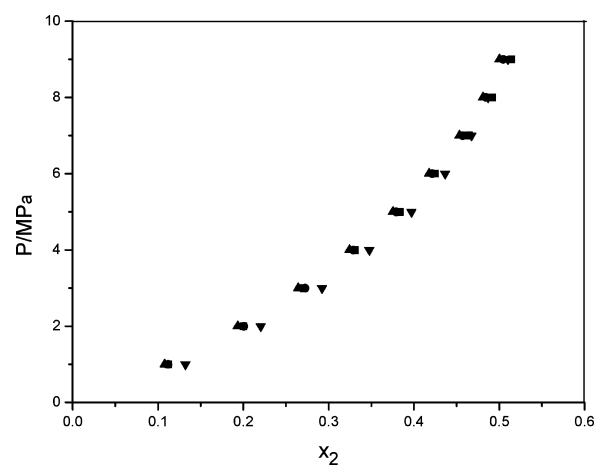


Figure 4. Solubility of CO₂ (2) in [bmim][PF₆] (1), calculated by the formula $x_{\text{CO}_2} = n_{\text{CO}_2}/(n_{\text{CO}_2} + n_{\text{IL}})$, with different water mass fractions at 50 °C: ■, 0.0067 %; ●, 0.15 %; ▲, 0.89 %; ▼, 1.6 %.

lack of significant expansion of the liquid was found for $\rm CO_2$ dissolved in [bmim][PF $_6$]. Simultaneously, molar volumes of the liquid phase decrease dramatically with increasing $\rm CO_2$

Table 3. Henry's Constants of CO_2 (2) in [bmim][PF₆] (1) with Different Water (3) Mass Fractions w_3 at (40, 50, and 60) °C and Pressures Less than 6 MPa^a

	Henry's constant/MPa•kg•mol ^{−1}						
w_3	<i>t</i> = 40 °C	$t = 50 ^{\circ}\text{C}$	<i>t</i> = 60 °C				
0.0067 %	2.05 ± 0.02	2.33 ± 0.02	2.71 ± 0.02				
0.15 %	1.91 ± 0.02	2.36 ± 0.02	2.77 ± 0.02				
0.89 %	1.96 ± 0.01	2.39 ± 0.01	2.84 ± 0.02				
1.6 %	1.83 ± 0.03	2.21 ± 0.04	2.44 ± 0.03				

^a On the molality scale.

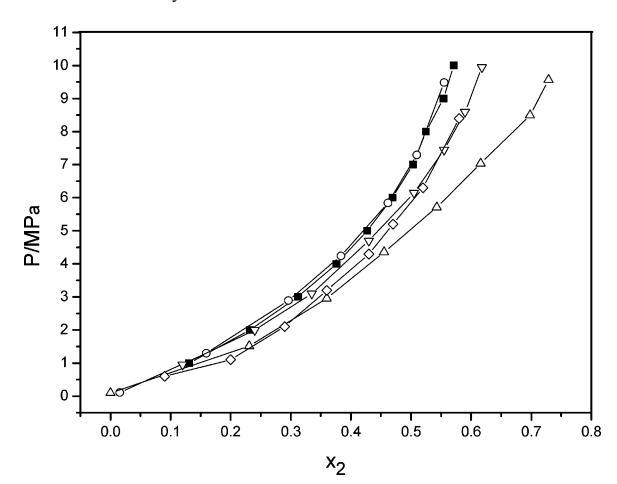


Figure 5. Comparison of the solubility of CO_2 (2) in [bmim][PF₆] (1) at 40 °C with literature data (water mass fraction = 0.15 %): \blacksquare , this work; \bigcirc , Kamps et al.;²⁰ \triangle , Blanchard et al.;¹⁰ ∇ , Liu et al.;²⁸ \diamondsuit , Aki et al.²²

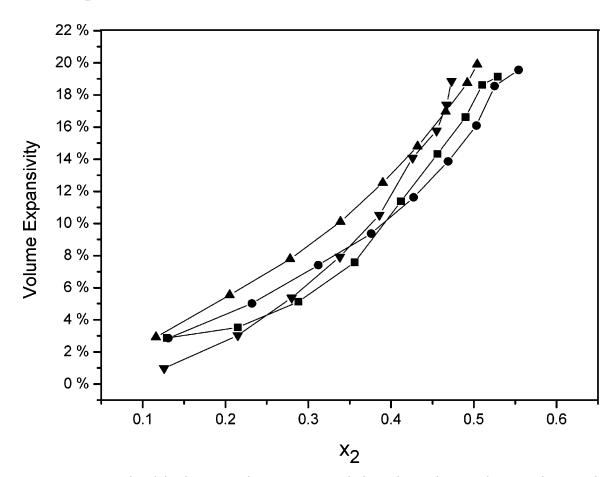


Figure 6. Liquid-phase volume expansivity, based on change in total volume as defined by eq 1, of the system $CO_2(2) + [bmim][PF_6](1)$ with different water mass fractions at 40 °C: ■, 0.0067 %; ●, 0.15 %; ▲, 0.89 %; ▼, 1.6 %.

solubility, as can be seen from Table 2. The effect of water content on the volume expansion can be seen from Figure 6 and Figure 7. There are two definitions of liquid-phase volume expansion.²² One definition is based on the change in absolute volume of the liquid:

$$\frac{\Delta V}{V} = \frac{V_{\rm L}(T, P, x_1) - V_2(T, P_0)}{V_2(T, P_0)} \tag{1}$$

where V_L is the total volume of the liquid mixture at a given temperature and pressure and V_2 is the volume of the liquid at

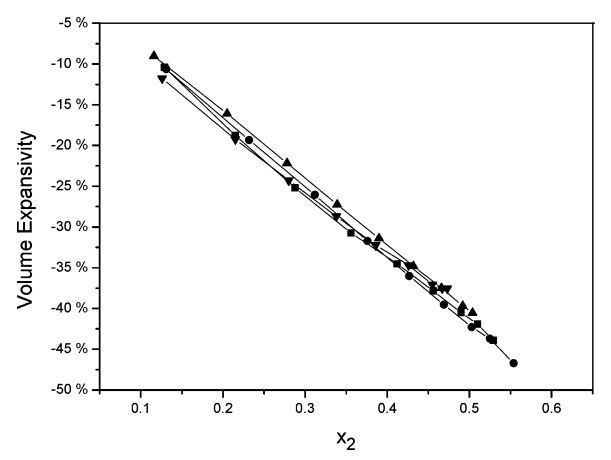


Figure 7. Liquid-phase volume expansivity, based on change in molar volume as defined by eq 2, of the system $CO_2(2) + [bmim][PF_6](1)$ with different water mass fractions at 40 °C: ■, 0.0067 %; ●, 0.15 %; ▲, 0.89 %: ▼, 1.6 %.

the same temperature and ambient pressure. The other is based on the change in molar volume:

$$\frac{\Delta V_{\rm m}}{V_{\rm m}} = \frac{\tilde{V}_{\rm L}(T, P, x_1) - \tilde{V}_2(T, P_0)}{\tilde{V}_2(T, P_0)} \tag{2}$$

where both \tilde{V}_L and \tilde{V}_2 are corresponding molar volume. Volume expansivity in Figure 6 was calculated with eq 1 and in Figure 7 with eq 2. It should be noticed that mole number of water must be taken into account for molar volume, at 40 °C, and ambient pressure, calculated from density data in Table 1.

The unusual phase behavior of CO₂ + IL systems may be explained by the unique structure of ionic liquids. The phase behavior of CO₂ + IL is very different from that of normal organic liquids + CO₂ systems. Although large amounts of CO₂ dissolve in ionic liquids at low pressure, no mixture critical point appears even at extremely high pressures (such as 310 MPa). 10 Volume of IL-rich phase barely increases even when large amounts of CO₂ dissolve in the liquid phase. Henry's law,²⁰ equation of state,14 and regular solution theory24,29 used in modeling at present are difficult to explain these unusual phenomena. But they are easy to understand with a view to the unique structure of IL. IL were composed of organic cations asymmetric in space and anions, which resulted in very low melting points. Also, the asymmetry of the cations and the strong Coulombic forces between the ions dominated the phase behavior of CO₂ + IL systems. The asymmetry of the cations inevitably led to large but finite interspaces between ions, which was the cause that CO₂ could dissolve in IL largely but finitely. The strong Coulombic forces between the ions resulted in the extremely low solubility of IL in CO2 and minor volume expansion of the liquid phase. Since the two phases can never become identical in composition and density even at extremely high pressures, a mixture critical point can never be reached. On the basis of this comprehension, a simple and effective model may be established to describe the phase behavior of CO2 and

Conclusions

The solubility of CO_2 in the IL [bmim][PF₆] and the liquidphase molar volume were determined for water mass fraction of [bmim][PF₆] ranging from 0.0067 % to 1.6 % and within temperature and pressure ranges of (40 to 60) °C and (1 to 25)

MPa. The deviation in solubility, at the same temperature and pressure, with different water mass fraction was not more than 15 %, and the average is 6.7 %. Solubility pressures were correlated with an average relative uncertainty of about 1 % by means of the extended Henry's law for all water contents investigated at relatively low pressures.

Literature Cited

- (1) Brennecke, J. F.; Maginn, E. J. Ionic liquids: innovative fluids for chemical processing. AIChE J. 2001, 47, 2384-2398.
- Welton, T. Room-temperature ionic liquids: solvents for synthesis and catalysis. *Chem. Rev.* **1999**, *99*, 2071–2083.
- Wasserscheid, P.; Keim, W. Ionic liquids-new "solutions" for transition metal catalysis. Angew. Chem., Intl. Ed. 2000, 39, 3773-
- (4) Seddon, K. R. Ionic liquids for clean technology. J. Chem. Technol. Biotechnol. 1997, 68, 351-356.
- (5) Olivier, H. Recent developments in the use of non-aqueous ionic liquids
- for two-phase catalysis. *J. Mol. Catal. A* **1999**, *146*, 285–289.

 (6) Huddleston, J. G.; Willauer, H. D.; Swatloski, R. P.; Visser, A. E.; Rogers, R. D. Room-temperature ionic liquids as novel media for 'clean' liquid-liquid extraction. Chem. Commun. 1998, 16, 1765-
- (7) Earle, M. J.; Seddon, K. R.; McCormac, P. B. The first high yield green route to a pharmaceutical in a room-temperature ionic liquid.
- *Green Chem.* **2000**, *2*, 261–262.
 (8) Blanchard, L. A.; Hancu, D.; Beckman, E. J.; Brennecke, J. F. Green processing using ionic liquids and CO₂. Nature (London) 1999, 399,
- (9) Blanchard, L. A.; Brennecke, J. F. Recovery of organic products from ionic liquids using supercritical carbon dioxide. Ind. Eng. Chem. Res. **2001**, 40, 287-292.
- (10) Blanchard, L. A.; Gu, Z.; Brennecke, J. F. High-pressure phase behavior of ionic liquid/CO₂ systems. *J. Phys. Chem. B* **2001**, *105*,
- (11) Wu, W.; Zhang, J.; Han, B.; Chen, J.; Liu, Z.; Jiang, T.; He, J.; Li, W. Solubility of room-temperature ionic liquid in supercritical CO₂ with and without organic compounds. Chem. Commun. 2003, 12,
- (12) Anthony, J. L.; Maginn, E. J.; Brennecke, J. F. Solubilities and thermodynamic properties of gases in the ionic liquid 1-N-butyl-3methylimidazolium hexafluorophosphate. J. Phys. Chem. B 2002, 106, 7315-7320.
- (13) Husson-Borg, P.; Majer, V.; Costa Gomes, M. F. Solubilities of oxygen and carbon dioxide in butyl methyl imidazolium tetrafluoroborate as a function of temperature and at pressures close to atmospheric pressure. *J. Chem. Eng. Data* **2003**, *48*, 480–485.

 (14) Shariati, A.; Peters, C. J. High-pressure phase behavior of systems with ionic liquids: measurements and modeling of the binary system
- fluoroform + 1-ethyl-3-methylimidazolium hexafluorophosphate. *J. Supercrit. Fluids* **2003**, *25*, 109–117.

 (15) Shariati, A.; Peters, C. J. High-pressure phase behavior of binary
- systems of carbon dioxide and certain ionic liquids. Proceedings of the 6th International Symposium on Supercritical Fluids; 2003; pp 687-691.

- (16) Shariati, A.; Peters, C. J. High-pressure phase behavior of systems with ionic liquids: II. The binary system carbon dioxide + 1-ethyl-3-methylimidazolium hexafluorophosphate. J. Supercrit. Fluids 2004, 29.43 - 48.
- (17) Shariati, A.; Peters, C. J. High-pressure phase behavior of systems with ionic liquids: Part III. The binary system carbon dioxide + 1-hexyl-3-methylimidazolium hexafluorophosphate. J. Supercrit. Fluids 2004, 30, 139-144.
- (18) Costantini, M.; Toussaint, V. A.; Shariati, A.; Peters, C. J.; Kikic, I. High-pressure phase behavior of systems with ionic liquids. 4. Binary system carbon dioxide + 1-hexyl-3-methylimidazolium tetrafluoroborate. J. Chem. Eng. Data 2005, 50, 52-55.
- (19) Kroon, M. C.; Shariati, A.; Costantini, M.; van Spronsen, J.; Witkamp, G.-J.; Sheldon, R. A.; Peters, C. J. High-pressure phase behavior of systems with ionic liquids. 5. The binary system carbon dioxide + 1-butyl-3-methylimidazolium tetrafluoroborate. J. Chem. Eng. Data **2005**, *50*, 173–176.
- (20) Kamps, A. P. S.; Tuma, D.; Xia, J.; Maurer, G. Solubility of CO2 in the ionic liquid [bmim][PF₆]. J. Chem. Eng. Data 2003, 48, 746-
- (21) Anthony, J. L.; Anderson, J. L.; Maginn, E. J.; Brennecke, J. F. Anion effects on gas solubility in ionic liquids. J. Phys. Chem. B 2005, 109,
- (22) Aki, S. N. V. K.; Mellein, B. R.; Saurer, E. M.; Brennecke, J. F. Highpressure phase behavior of carbon dioxide with imidazolium-based ionic liquids. J. Phys. Chem. B 2004, 108, 20355-20365.
- (23) Baltus, R. E.; Culbertson, B. H.; Dai, S.; Luo, H.; DePaoli, D. W. Low-pressure solubility of carbon dioxide in room-temperature ionic liquids measured with a quartz crystal microbalance. J. Phys. Chem. B 2004, 108, 721-727
- (24) Scovazzo, P.; Camper, D.; Kieft, J.; Poshusta, J.; Koval, C.; Noble, R. Regular solution theory and CO₂ gas solubility in room-temperature ionic liquids. *Ind. Eng. Chem. Res.* **2004**, *43*, 6855–6860.
- (25) Bonhote, P.; Dias, A.; Papageorgiou, N.; Kalyanasundaram, K.; Gratzel, M. Hydrophobic, highly conductive ambient-temperature molten salts. *Inorg. Chem.* **1996**, *35*, 1168–1178.
- (26) Dupont, J.; Consorti, C. S.; Suarez, P. A. Z.; de Souza, R. F. Preparation of 1-butyl-3-methyl imidazolium-based room-temperature ionic liquids. *Org. Synth.* **2002**, *79*, 236–241.
- (27) King, M. B.; Mubarak, A.; Kin, J. D.; Bott, T. R. The mutual solubilities of water with supercritical and liquid carbon dioxides. J. Supercrit. Fluids 1992, 5, 296-302.
- (28) Liu, Z. M.; Wu, W. Z.; Han, B. X.; Dong, Z. X.; Zhao, G. Y.; Wang, J. Q., Jiang, T.; Yang, G. Y. Study on the phase behaviors, viscosities, and thermodynamic properties of $CO_2/[C(4)mim][PF_6]/methanol$ system at elevated pressures. Chem.-Eur. J. 2003, 9, 3897-3903.
- (29) Camper D, Scovazzo P, Koval C, Noble R. Gas solubilities in room-temperature ionic liquids. *Ind. Eng. Chem. Res.* **2004**, *43*, 3049–3054.

Received for review July 1, 2005. Accepted January 23, 2006. Financial support from the National Natural Science Foundation of China (Grants 20276038 and 20490209) are gratefully acknowledged.

JE0502501



Studies on Properties of Interfacial Active Fractions from Crude and Their Effect on Stability of Crude Emulsions

Mingyuan Li, Jixiang Guo, Meiqin Lin, and Zhaoliang Wu

State Key Laboratory of Heavy Oil Processing and EOR Research Center, University of Petroleum Beijing, Beijing, China

The influence of indigenous interfacial active fractions from crude on the interfacial property between water and crude and its effect on stability of crude emulsions were studied. It is found that the carboxylic acids in the fractions of asphaltene from Gu Dong"1, Gu Dong"4 crude, the resin from Da Qing crude, and the fatty acid in the fractions of saturate from Da Qing crude are responsible for decreasing the interfacial tension between the crude oils and water. These acids have relatively smaller molecule mass, more branch chain, and more oxygen, but they are not able to stabilize emulsion formed by model oil and water. It is the acids with relatively larger molecule mass that are responsible for stabilizing the emulsions. For model oil and alkali solution system the salt or soap formed by fast reaction of the acid, ester with relatively smaller molecule mass, and alkali are responsible for decreasing the interfacial tension between crude oil and water. The salt or soap formed by slow reaction of the acid, ester with relatively larger molecule mass, and alkali are responsible for stabilizing crude oil emulsions.

Keywords Crude oil emulsions, interfacial active fraction, interfacial tension, emulsion stability

INTRODUCTION

Crude oil is a mixture of aliphatic, aromatic hydrocarbons and oxygen-, nitrogen-, and sulphur-containing compounds such as resin and asphaltene. There is no doubt that the interfacially active components come from resin and asphaltene of the crude oils. Asphaltene fraction from crude oils can be adsorbed at the interface between oil and water and form stable film to stabilize crude emulsions. Resin and asphaltene are polymeric, containing polyaromatic structures, and possess structural similarities. The asphaltenes contain large condensed aromatic rings compared to resins. The stability of water-in-crude-oil emulsions depends on the total structure of the molecular matrix of the interfacially active components, size, aromaticity, and types of carbonyl functionality, and other functional groups in the bulk play important role in the total stability of the emulsions.

Alkali reacts with the acidic components in crude oils to form interfacially active to components that accumulate at the oil-water interface and facilitates the formation of emulsion^[4] in alkaline-surfactant-polymer (ASP) flooding. The stability of this emulsion depends on the concentration of the reservoir-formed alkali-oil surfactant at the interface. This again depends on the concentration of the potential acidic components from crude oils that form interfacially active soap

components. [4] However, Da Qing crude oil contains very little asphaltenes (paraffinic crude oil) and has a lower acid number when sodium hydroxide used as the alkaline component the recovery of crude was enhanced and the oil recovered also contained stable water-in-crude-oil emulsion.

In order to study the formation of crude oil emulsions and the effect of alkali reactions with the interfacially active fractions from crude oil on the stability of emulsions, the saturate, aromatic, resin, and asphaltene fractions from a crude oil in Da Qing oil field and two Gu Dong crude oils from Sheng Li oil field in China were first separated. Then the acid number and molecular weight determinations of the fractions were made to evaluate the properties of the fractions. The correlations between the physical properties and molecular parameters such as molecular weight and functional groups were explored. Furthermore, the fractions were then used to prepare model oils with additive-free jet fuel. The interfacial tension and interfacial shear viscosity between the model oils and alkali solution and the stability of the emulsions formed with the model oils and alkali solution were determined.

EXPERIMENTAL SECTION

Separation of Crude Oil Fractions

The interfacially active fractions of saturate, aromatic, resin, and asphaltene used in these experiments were separated from

Address correspondence to Mingyuan Li, EOR Research Center, University of Petroleum Beijing, Beijing 102249, China. E-mail: myli@public3.bta.net.cn

678 M. LI ET AL.

Da Qing and Gu Dong crude oils. The separation of asphaltene fractions from the crude oil was carried out by pentane precipitation. A 100 g amount of crude oil was agitated with 3000 mL of pentane at room temperature for 30 min. The mixture was then left to stand for 15 days. The precipitated asphaltene fraction was filtered, washed with a small portion of pentane, and dried. The filtrate from the above was then poured on a column containing Al_2O_3 . The saturate fraction was extracted by 8000 mL petroleum ether, the aromatic fraction was extracted by 8000 mL benzene, the resin 1 fraction was extracted by 4000 mL benzene/ethanol (benzene/ethanol ratio: 1/1, v/v), and the resin 2 fraction was extracted by 4000 mL ethanol. The separation scheme is presented in Figure 1.

Molecular Weight and Content of Oxygen

The relative molecular weight of the fractions was measured by the vapor pressure osmometry (VPO) method using a molecular weight meter (Knauer, Germany). The oxygen of the fractions was determined by elementary analysis using a Vario EL (Elementar Analysen Systeme, Germany).

Model Emulsions and Measurement of Interfacial Properties

The water used in the experiments was double-distilled water or alkaline solution. The alkaline solution used for Gu Dong model oils is 1.2% Na₂CO₃ solution and for Da Qing model oils it is 1.2% NaOH solution. The alkaline solutions were prepared with double-distilled water. A jet fuel without

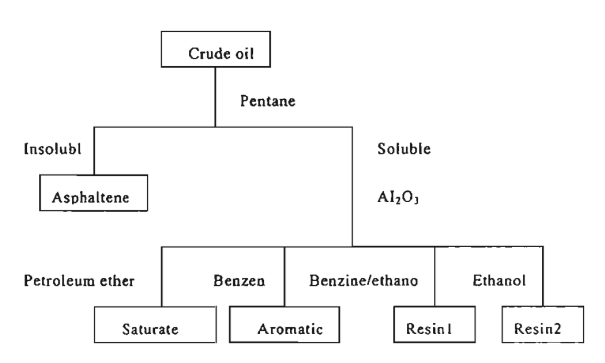


FIG. 1. Separation of crude oil fractions.

any additives from a refinery was used as the dispersion medium of the model oils. The jet fuel was purified by silica adsorption before the experiments were carried out. The composition of the model oils is shown in Table 1. The weight percentage of each fraction is selected to represent the weight percentage of the fraction (around 10%) in the crude oils (Table 2). This would allow us to compare the stability of emulsions formed between model oils containing the fractions and the chemical solutions. From Table 1 it can be seen that the crude model oil contains 10% of the crude oils in the jet oil and the saturate model oils contain 4.59%, 4.02%, and 6.43% saturate fractions from Gu Dong*1, Gu Dong*4, and Da Qing crude oils, respectively.

The model emulsions were prepared by mixing the model oils and alkaline solution (o/w ratio: 2/8, v/v) in a 50 mL cylinder. The emulsification was carried out by shaking the cylinder 50 times at 60°C. The emulsification was done twice every day, and the stability of the emulsions was determined visually by measuring the water separated from the emulsions at 60°C as a function of time. The emulsion stability experiments were carried out for 84 days. This would allow us to investigate the effect of reaction time of the alkali on the properties of the model emulsions.

Interfacial tension between the model oils and distilled water or the alkaline solution was measured by a spinning drop interfacial tension meter (JJ2000A, Shanghai, China) at 45°C. The interfacial shear viscosities were measured using an SVR·S Interfacial Viscoelastic Meter (Kyowa Kagaku Co. Ltd., Japan)^[2] at 25°C.

RESULTS AND DISCUSSION

Physical Properties of Crude Fractions

The composition of the crude oils is given in Table 2. The content of asphaltene fraction in Gu Dong #1 and Gu Dong #4 crude oils is 14.43% and 11.35% but it is only 0.09% in Da Qing crude oil. Da Qing crude contains more saturate fraction than Gu Dong crude oils. Because the resin 2 fraction was too little to do experiments with, resin 1 fraction was presented as the resin fraction in this article.

Table 3 shows that the saturate fraction from Da Qing crude oil contains the most oxygen $(0.375\,\mathrm{g}$ in $100\,\mathrm{g}$ crude oil), followed by the asphaltene fractions from Gu Dong #1 and

TABLE 1
Composition of model oil (wt%)

•	Crude oil	Saturate	Aromatic	Resin I	Asphaltene
Gu Dong #1	10.00	4.59	2.25	1.49	1.44
Gu Dong #4	10.00	4.02	2.19	1.49	1.14
Da Qing	10.00	6.43	1.52	1.41	0.01

TABLE 2 Composition of crude oil fractions

	wt%				
Fraction	Gu Dong #1	Gu Dong #4	Da Qing		
Saturate	47.08	46.54	68.09		
Aromatic	23.65	28.18	17.25		
Resin 1	14.73	13.81	14.47		
Resin 2	0.11	0.12	0.10		
Asphaltene	14.43	11.35	0.09		

TABLE 3
Oxygen in crude oil fractions

	Oxygen in 100 g crude oil/g				
Fraction	Gu Dong #1	Gu Dong #4	Da Qing		
Saturate	0.118	0.140	0.375		
Aromatic	0.170	0.211	0.086		
Resin 1	0.194	0.264	0.214		
Asphaltene	0.316	0.317	0.001		

Gu Dong $^{\#}4$ crude oils. The asphaltene fraction from Da Qing crude oil contains only 0.001 g oxygen in $100\,\mathrm{g}$ crude oil.

The molecular weight and acid number of the fractions are given in Tables 4 and 5. It is clear that the molecular weight of the fractions is in the order of saturate < aromatic < resin < asphaltene for the three crude oils and the molecular weight of the crude oils is close to their saturate fraction.

The values presented in Table 5 clearly show that the acid number of the fractions is in the order of saturate < aromatic < resin < asphaltene for Gu Dong crude oils. The order is the same as the order of molecular weight of the fractions. The acid number of the fractions from Da Qing crude oil is in the order of saturate < aromatic < asphaltene < resin. It seems that the resin fraction contains more acidic matter than the asphaltene fraction in Da Qing crude oil.

The above facts indicate that the asphaltene molecules are large and polyaromatic and contain the highest acidic oxygen components among the fractions for Gu Dong crude oils and

TABLE 5
Acid number of crude oils and their fractions

Fractions	Gu Dong #1	Gu Dong #4	Da Qing	
Saturate	2.397	3.014	0.4760	
Aromatic	5.386	5.242	1.039	
Resin	6.001	8.002	5.101	
Asphaltene	16.45	8.378	4.213	
Crude oil	3.640	3.217	0.5174	

the resin fraction from Da Qing crude oil contains the highest acidic oxygen components among the fractions from the crude oil.

INTERFACIAL TENSION

The interfacial tension between the model oils and aqueous phases is shown in Table 6. It shows that the interfacial tension between the model oils and alkaline solutions $(\gamma_{0/s})$ is lower than the interfacial tension between the same model oil and distilled water $(\gamma_{0/w})$. This indicates that all of the fractions from the crude oils reacted with the alkali to form intefacially active components and these components are more interfacially active than the indigenous interfacially active components in the crude oil. Therefore, the interfacial tension was decreased.

It is interesting to note that the interfacial tension between the asphaltene model oils and Na₂CO₃ solution is lower than that of the crude model oils and the alkaline solution for Gu Dong #1 and Gu Dong #4 crude oils, and the interfacial tension between asphaltene model oil and Na₂CO₃ solution for Gu Dong #1 crude oil is very low (0.056-0.0053 mNm⁻¹). It appears that the formation of interfacially active components is very significant in the reaction of the alkaline and asphaltene fraction. It is clear that the asphaltene fraction dominates the interfacial tension between crude model oil and the alkaline solution in comparing the interfacial tension between other fraction model oils and alkaline solution for Gu Dong crude oils. For Da Qing crude oil the resin fraction dominates the interfacial tension between crude model oil and NaOH solution. From Tables 3 and 5 it is clear that the asphaltene fraction of Gu Dong crude oils contains more oxygen and has higher acid number and the resin fraction of Da Qing crude oil contains more oxygen and has higher acid number than the other fractions. It seems

TABLE 4

MW of crude oils and their fractions

Crude oils	Saturate	Aromatic	Resin 1	Asphaltene	Crude oil
Gu Dong #1	434	601	1025	1499	433
Gu Dong #4	503	728	1117	1308	427
Da Qing	485	773	1396	2433	480

TABLE 6
Interfacial tension between model oils and aqueous phase (45°C)

		Model oil					
Crude oils		Saturate	Aromatic	Resin 1	Asphaltene	Crude oil	
Gu Dong #1	wt %	4.60	2.53	1.46	1.44	10.00	
	$\gamma_{\rm o/w}/{\rm mN\cdot m}^{-1}$	35.70	24.52	22.76	19.38	11.89	
	$\gamma_{o/s}/mN \cdot m^{-1}$	13.36	5.61	4.63	0.056	0.93	
	wt %	3.00	3.00	3.00	3.00	3.00	
	$\gamma_{o/w}/mN \cdot m^{-1}$	33.03	17.90	15.78	12.75	19.27	
	$\gamma_{o/s}/mN \cdot m^{-1}$	11.22	4.37	3.12	0.0053	0.762	
Gu Dong #4	wt%	4.02	2.19	1.38	1.14	10.00	
	$\gamma_{o/w}/mN \cdot m^{-1}$	33.55	18.85	18.36	16.90	17.21	
	$\gamma_{o/s}/mN \cdot m^{-1}$	9.12	7.11	4.30	0.86	1.71	
	wt%	3.00	3.00	3.00	3.00	3.00	
	$\gamma_{o/w}/mN \cdot m^{-1}$	30.07	14.42	13.33	7.03	21.48	
	$\gamma_{o/s}/mN \cdot m^{-1}$	10.45	5.32	2.62	0.43	1.35	
Da Qing	wt%	6.66	1.58	1.45	0.10	10.00	
	$\gamma_{o/w}/mN \cdot m^{-1}$	39.96	33.57	27.63	33.68	30.46	
	$\gamma_{\rm o/s}/{\rm mN\cdot m}^{-1}$	18.31	11.97	8.24	12.81	4.04	
	wt%	3.00	3.00	3.00	3.00	3.00	
	$\gamma_{o/w}/mN \cdot m^{-1}$	36.51	30.24	26.34	28.22	29.40	
	$\gamma_{o/s}/mN \cdot m^1$	14.68	10.30	2.64	4.07	2.86	

that the interfacially active components formed in the reaction of the alkali and the acidic oxygen components in asphaltene or resin fractions contribute to decreasing the interfacial tension.

INTERFACIAL SHEAR VISCOSITY

Figures 2-4 show that the interfacial shear viscosity between asphaltene or resin model oil and alkaline solution

is higher than that of the model oils and distilled water. It is clear that the interfacially active components formed in the reaction of the alkali and asphaltene or resin fraction are accumulated at the interface and the interfacial film has higher mechanical strength. [5]

Figures 5-7 show that the interfacial shear viscosity between asphaltene model oils and Na_2CO_3 or NaOH solution has the highest value among the model oils and the

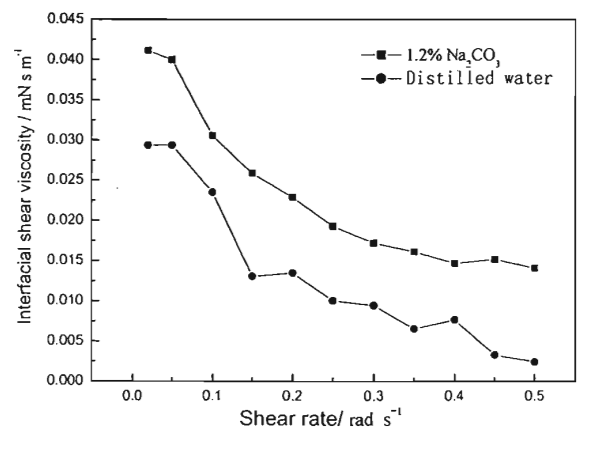


FIG. 2. Interfacial shear viscosity between 2% asphaltene model oil (Gu Dong*1) and distilled water/1.2% Na₂CO₃ solution, 25°C.

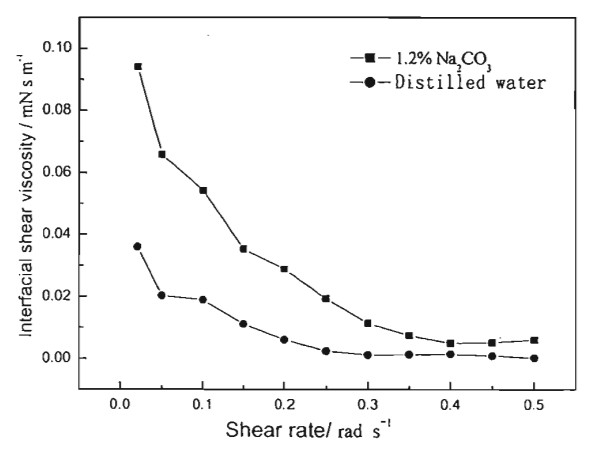


FIG. 3. Interfacial shear viscosity between 2% asphaltene model oil (Gu Dong[#]4) and distilled water/1.2% Na₂CO₃ solution, 25°C.

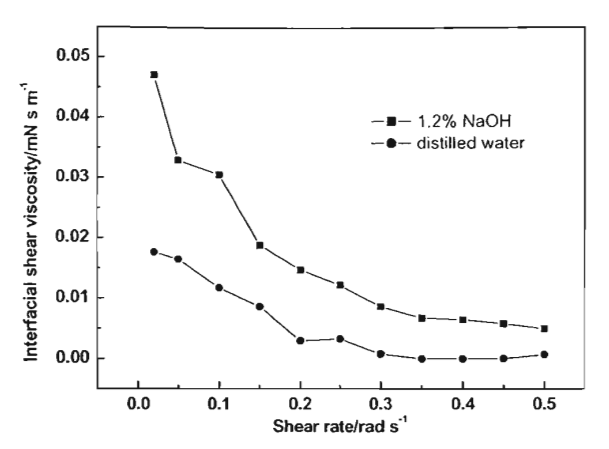


FIG. 4. Interfacial shear viscosity between 2% resin model oil (Da Qing) and distilled water/1.2% NaOH solution, 25° C.

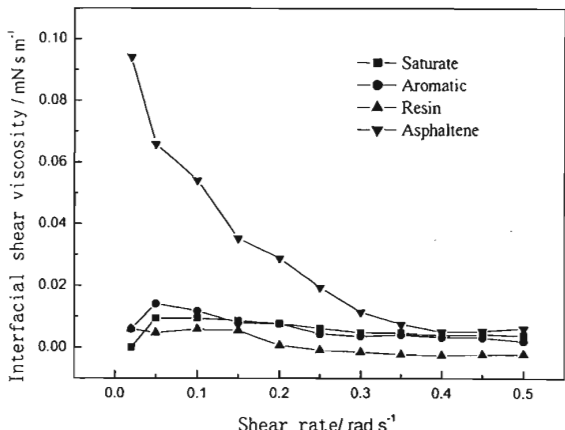


FIG. 6. Interfacial shear viscosity between model oil (Gu Dong[#]4) and 1.2% Na₂CO₃ solution, 25°C.

alkaline solutions measured. These indicate that the interfacial film of the interfacially active components formed in the reaction of asphaltene fractions and alkaline solutions has the highest mechanical strength and is able to enhance the stability of w/o emulsions. Because the asphaltene fraction has the largest molecular weight it is obvious that the interfacially active components formed in the reaction have larger molecules than those formed in the reaction of the alkali with other fractions. This proves that the interfacially active component has larger molecules and is able to form more stable interfacial film and emulsions. It should also be noted that the interfacial shear viscosity of the film decreases as the shear rate increases. This phenomenon shows that the film

was structured and the structure was broken down as the shear stress was increased.

Figures 8-10 show that the interfacial shear viscosity between the model oils prepared with deasphalted crude oil and alkaline solutions is lower than that of crude model oil and the alkaline solutions and the interfacial shear viscosity increases with the concentration of the crude oils in the jet fuel oil. This is a further indication that the asphaltene fraction contributes to the formation of interfacially active components and enhances the strength of the film.

All these experimental results proved that the interfacial film of the interfacially active components formed in the reaction of asphaltene fractions and alkaline solutions has the

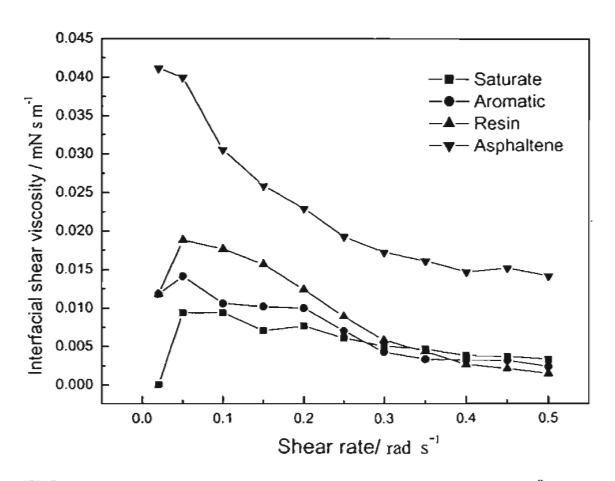


FIG. 5. Interfacial shear viscosity between model oil (Gu Dong*1) and 1.2% Na_2CO_3 solution, 25°C.

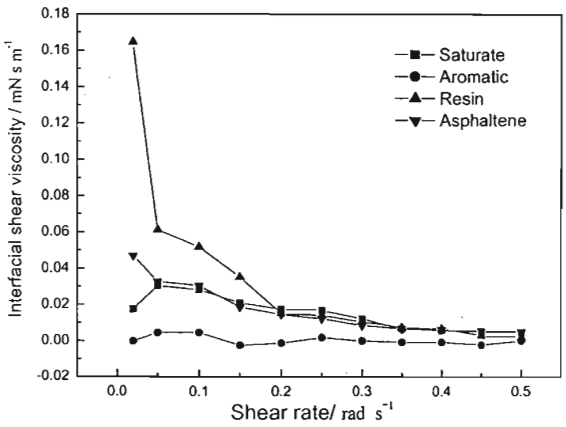


FIG. 7. Interfacial shear viscosity between model oil (Da Qing) and 1.2% NaOH solution, 25°C.

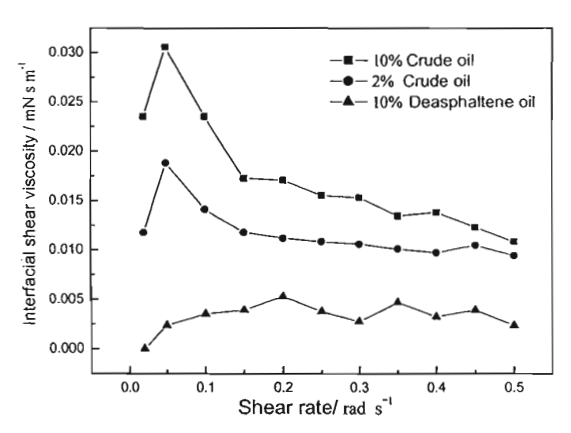


FIG. 8. Interfacial shear viscosity between crude model oil (Gu Dong*1) and 1.2% Na₂CO₁ water solution, 25°C.

highest mechanical strength and that the asphaltene fraction dominates the properties of the interfacial film when the alkaline solution was the aqueous phase.

STABILITY OF EMULSIONS

The stability of asphaltene model oil emulsions and crude model oil emulsions of Gu Dong*I crude oil are presented in Figures 11 and 12. When distilled water was the aqueous phase both asphaltene model oil and crude model oil were unable to form stable emulsions as the oils and the water reacted in 54 days. When 1.2% Na₂CO₃ solution was the aqueous phase there was no water separated from asphaltene model oil emulsions and crude model oil emulsions after a period of 7 and 3 days' reaction respectively of the oil and

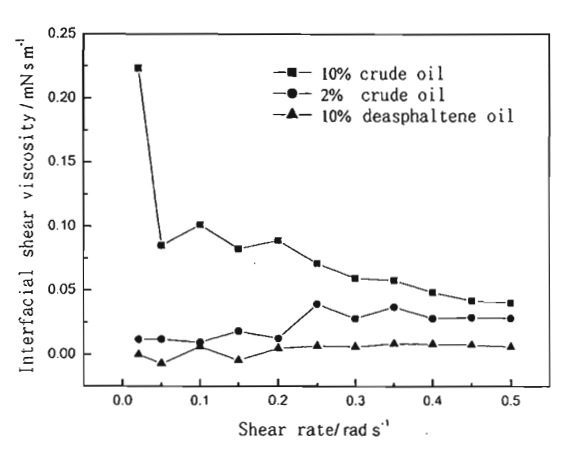


FIG. 9. Interfacial shear viscosity between crude model oil (Gu Dong*4) and 1.2% Na_2CO_3 water solution, 25°C.

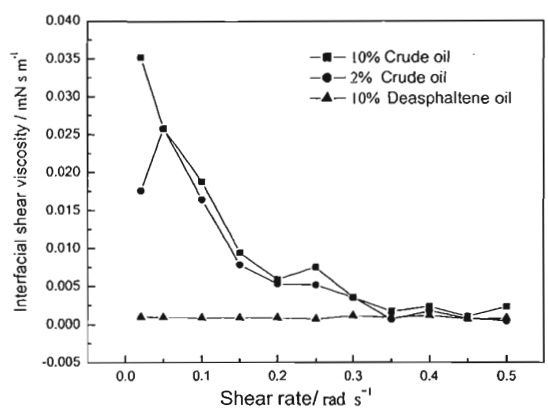


FIG. 10. Interfacial shear viscosity between crude model oil (Da Qing) and 1.2% NaOH water solution, 25° C.

water. In contrast, the saturate, aromatic, and resin model oils tested in the same manner were not able to form stable emulsions even after two months of reaction. It is clear that the asphaltene fraction is responsible for stabilizing Gu Dong #1 crude oil emulsions when Na₂CO₃ was used. This result is well supported by the measurement of interfacial shear viscosity of asphaltene model oil and the alkaline solution that we discussed above. This result also shows that the reaction of asphaltene and Na₂CO₃ may progress slowly until all of the possible acidic oxygen is replaced by sodium atoms.

Figures 13 and 14 show results similar to Figures 11 and 12. It is also the asphaltene fraction that dominates the stability of Gu Dong#4 crude oil emulsions in the same manner as Gu Dong#1 crude oil emulsions. The difference between Gu Dong#1 and #4 crude oils is that the asphaltene and crude model oil emulsions of Gu Dong#4 crude oil are more stable than those of Gu Dong#1 crude oil when distilled water was the aqueous phase.

Comparing the interfacial tension, interfacial shear viscosity, and physical properties of the fractions from Gu Dong crude oils the study shows clearly that the asphaltene fractions from Gu Dong crude oils have more polar, larger, and more acidic components than the other fractions. These characteristics can also be generalized to asphaltenes from other crude oils. The components in the asphaltene fraction react with $\rm Na_2CO_3$ solution and form soap-like interfacially active components that accumulate at the oil/water interface and form rigid film around water droplets. Therefore, the film is able to prevent the coalescence of the droplets. The result also reveals that the mechanical strength of the interfacial film can increase with the residence time of the sodium carbonate solution in the reservoir.

The emulsions of Da Qing crude oil have different characteristics than those of Gu Dong crude oils. Figures 15 and 16 show that saturate and resin fractions reacted with NaOH are

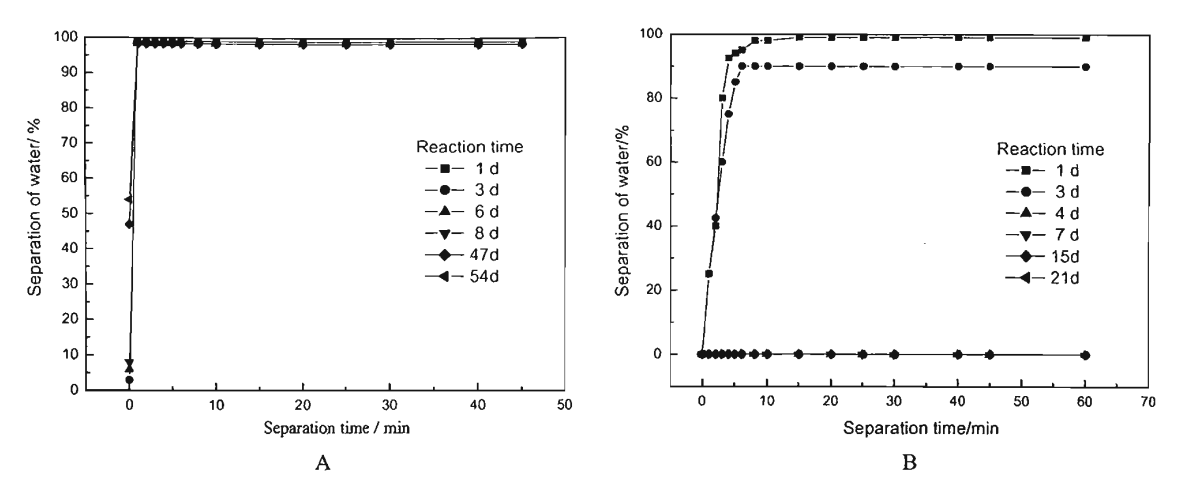


FIG. 11. Stability of the emulsion formed from asphaltene model oil (Gu Dong"1) and distilled water (A) and 1.2% Na₂CO₃ water solution (B), 60°C.

able to form more stable emulsions than the asphaltene fraction from Da Qing crude oil. Saturate and resin fractions contribute to stabilizing the crude oil emulsion after a period of reaction with NaOH. Like asphaltene model oil, the aromatic model oil tested in the same manner were not able to form stable emulsions after 84 days of reaction with NaOH.

INTERFACIAL ACTIVE FRACTIONS

Table 7 shows IR parameters of crude oils and their fractions. The band at $1380\,\mathrm{cm}^{-1}$ is $C\text{-CH}_3$ symmetric and at $1460\,\mathrm{cm}^{-1}$ is $C\text{-CH}_3$ and methylenic asymmetric, A_{1380}/A_{1460} is a measure indicating the degree of branch. The bond at $1600\,\mathrm{cm}^{-1}$ is conjugated C---C and aromatic

C=C, and $A_{1600}/A_{(1600+1460)}$ is a measure of the degree of aromaticity. Carbonyl stretching absorption appears in the range $1750-1650\,\mathrm{cm}^{-1}$, and $A_{(1750\sim1650)}/A_{(1600+1460)}$ is a measure of the content of carbonyl in the hydrocarbon. The band at $1100\,\mathrm{cm}^{-1}$ is ether -O- linkage, and $A_{1100}/A_{(1600+1460)}$ is a measure of the content of ether in the hydrocarbon. The band at $3200\,\mathrm{cm}^{-1}$ is OH stretching, and $A_{3200}/A_{(1600+1460)}$ is a measure of the content of acid, alcohol, and phenol in the hydrocarbon.

The data in Table 7 show that the asphaltene fractions from Gu Dong crude oils have a higher degree of branch and aromaticity and higher content of carbonyl, ether, acid, and acid number (Table 5) than other fractions. When asphaltene model oil reacted with Na₂CO₃ solution for a few days the

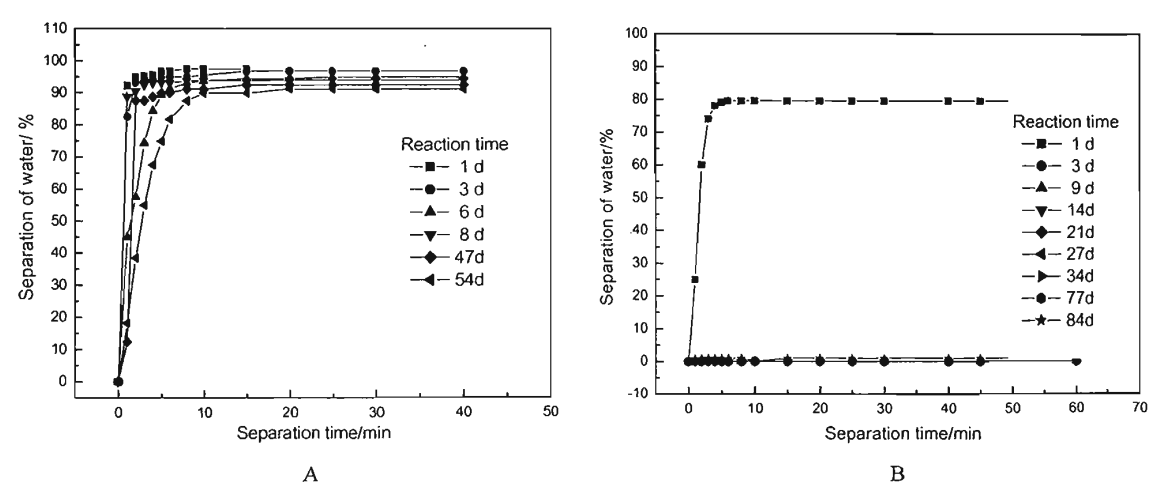


FIG. 12. Stability of the emulsion formed from crude model oil (Gu Dong"1) and distilled water (A) or 1.2% Na₂CO₃ water solution (B), 60°C.

684 M. LI ET AL.

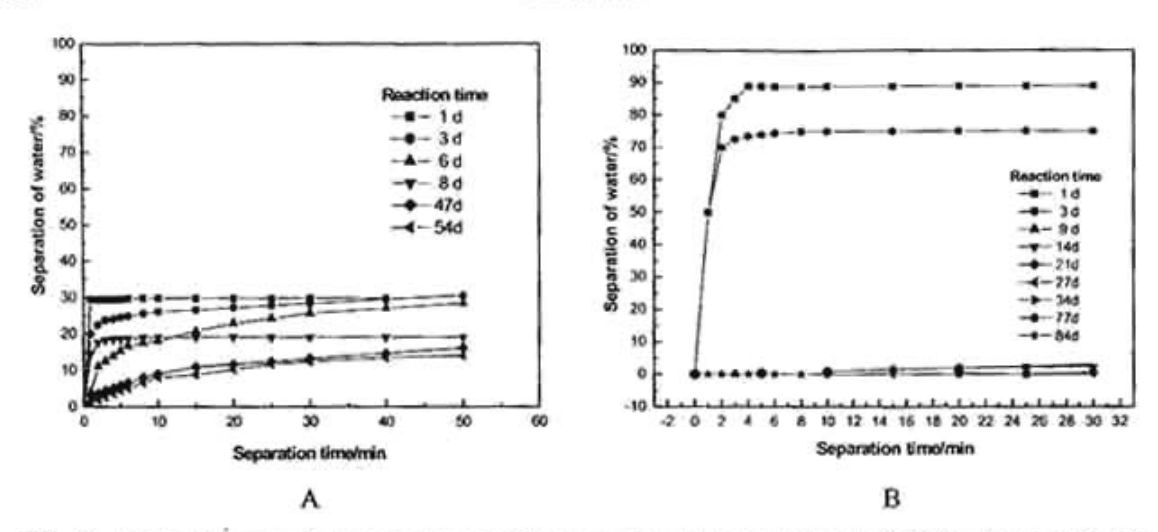


FIG. 13. Stability of the emulsion formed from asphaltene model oil (Gu Dong 4) and distilled water (A) and 1.2% Na₂CO₃ water solution (B), 60°C.

system could not form stable emulsion, but the interfacial tension between the model oil and the alkaline solution is very low (Table 6). These phenomena indicate that the carboxylic acids with relatively smaller molecular mass can react with Na₂CO₃ quickly and decrease the interfacial tension but cannot stabilize the emulsion. Only the substance formed by slow reaction of the acid, ester with relatively larger molecular mass, and alkali is responsible for stabilizing the emulsions.

Like the asphaltene fraction from Gu Dong crude oils it is easy to understand why the resin fraction from Da Qing crude oil reacted with NaOH can stabilize crude oil emulsion. The resin fraction has a higher degree of branch and aromaticity, higher content of carbonyl, ether, and acid (Table 7), and the highest acid number (Table 5) among the fractions from Da Qing crude oil, and the interfacial tension between resin model oil and NaOH solution has the lowest value of 2.64 mNm⁻¹ (Table 6). It is clear that the interfacially active components were formed by the acidic components in the resin fraction reacted with NaOH. However, what are the components in saturate fraction reacted with NaOH and how do they stabilize the emulsion? As a paraffinic crude oil Da Qing crude oil contains a large saturate fraction (68.09%, Table 2). The saturate fraction contains the highest oxygen of

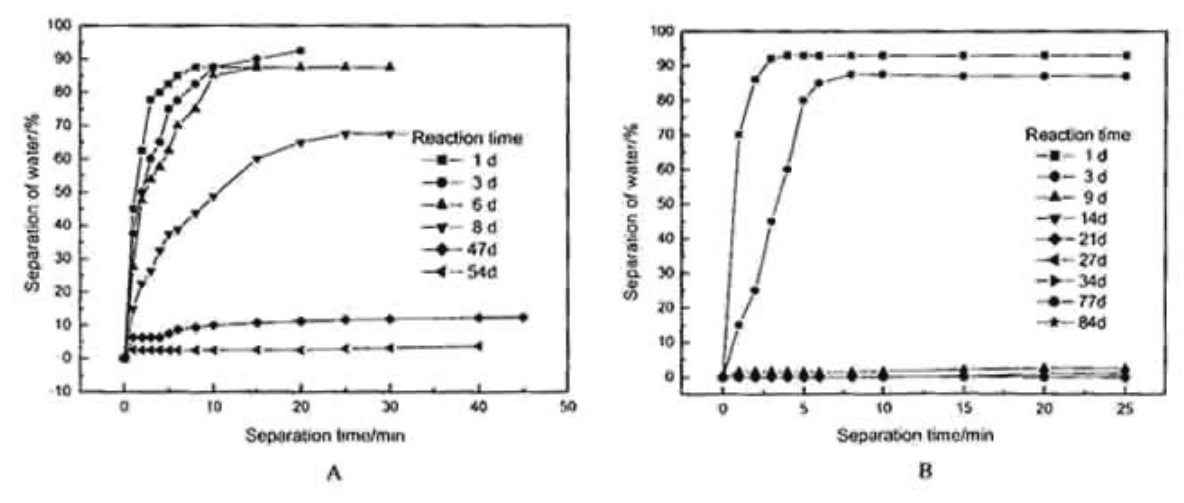


FIG. 14. Stability of the emulsion formed from crude model oil (Gu Dong*4) and distilled water (A) and 1.2% Na;CO; water solution (B), 60°C

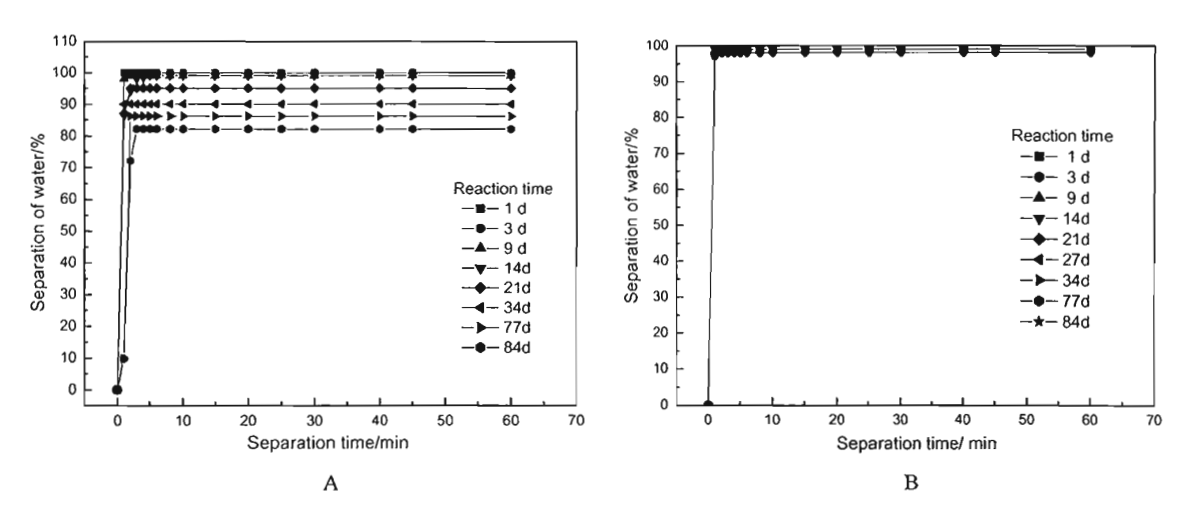


FIG. 15. Stability of the emulsion formed with saturate model oil (A) and asphaltene model oil (B) (Da Qing) and 1.2% NaOH water solution, 60°C.

0.375 g (Table 3) in 100 g crude oil and the lowest acid number of 0.476 (Table 5). The interfacial tension between saturate model oil of Da Qing crude oil and NaOH solution is the highest, 14.68–18.31 mNm⁻¹ (Table 6). It is obvious that it is not only the acidic components but also some other substances in the saturate fraction reacted with NaOH, and the components formed in the reaction are less interfacially active than the components formed in the reaction of resin fraction and NaOH.

To study the properties of the components formed in the reaction of saturate and NaOH, the interfacial tension, interfacial shear viscosity during the reaction process, and infrared spectra of saturate fraction and the components

formed were measured. The interfacial tension between saturate model oil and NaOH solution changing with reaction time is shown in Figure 17. The figure shows that interfacial tension decreased from the first day of the reaction. The interfacial tension decreased quickly in the first week and slowly during the following eight weeks.

The change of interfacial shear viscosity between the saturate model oil and NaOH solution during the first week is shown in Figure 18. An increase of the interfacial shear viscosity with reaction time confirms the formation of the interfacially active components again. Furthermore, the fact that the interfacial shear viscosity between the model oil and NaOH solution decreased with the increase of shear rate indicates the

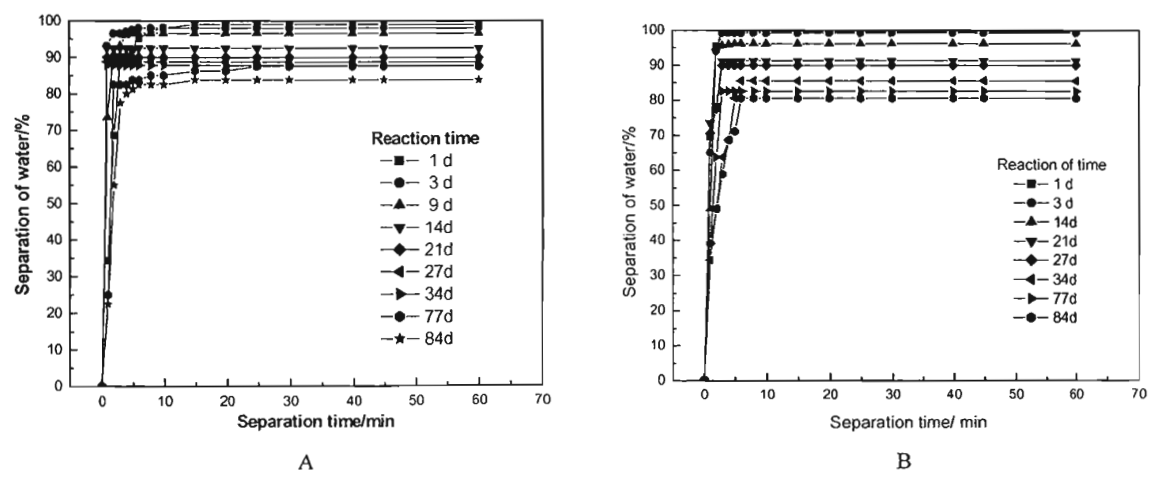


FIG. 16. Stability of the emulsion formed with resin model oil (A) and crude model oil (B) (Da Qing) and 1.2% NaOH water solution, 60°C.

TABLE 7 IR parameters of fractions and crude oils

Crude oils	Fractions	A1380/A1460	A1600/ A(1600 + 1460)	A(1750+1650)/ A(1600+1460)	A1100/ A(1600+1460)	A3200/ A(1600+1460)
Gu Dong*1	Saturate	0.463		0.037	0.031	_
	Aromatic	0.479	0.166	0.090	0.088	0.021
	Resin 1	0.696	0.355	0.385	0.201	0.204
	Asphaltene	0.769	0.356	0.435	0.171	0.254
	Crude oil	0.626	0.148	0.093	0.030	0.033
Gu Dong*4	Saturate	0.390	-	0.003	0.002	
	Aromatic	0.394	0.127	0.062	0.049	0.015
	Resin 1	0.546	0.265	0.264	0.095	0.150
	Asphaltene	0.676	0.303	0.421	0.213	0.232
	Crude oil	0.595	0.154	0.084	0.074	0.028
Da Qing	Saturate	0.369		0.052	0.0448	
10.0	Aromatic	0.386	0.162	0.199	0.067	0.024
	Resin 1	0.440	0.237	0.336	0.123	0.069
	Asphaltene	0.584	0.262	0.312	0.107	0.052
	Crude oil	0.510	0.108	0.071	0.020	0.019

interfacially active components form a network at the interface. This proves the interfacial film formed by the interfacially active components has some strength and is able to stabilize emulsions.

The IR spectroscopy in Figure 19(b) shows that the absorption at 1563 cm⁻¹ indicates the presence of COO⁻ groups in the component and the absorption at 1100 cm⁻¹ is due to the C-O stretching vibration of the carboxylic groups. This shows that there are sodium salts or soaps formed in the reaction of saturate fraction and NaOH. These salts or soaps may be formed by the reaction of NaOH with the acidic components and ester in the saturate fraction. Because the salts or soaps formed in the reaction have long hydrocarbon chains the salts or soaps are more oil soluble and less interfacially active than the components formed in the reaction of resin fraction and NaOH.

The study above shows that the ASP flooding process in the reservoir provides a long enough time to form interfacially active components, such as salt or soap, by the reaction of alkali with the acidic or nonacidic components in asphaltene, resin, and saturation fractions. These interfacially active molecules are responsible for providing stability for the water-in-crude-oil emulsion.

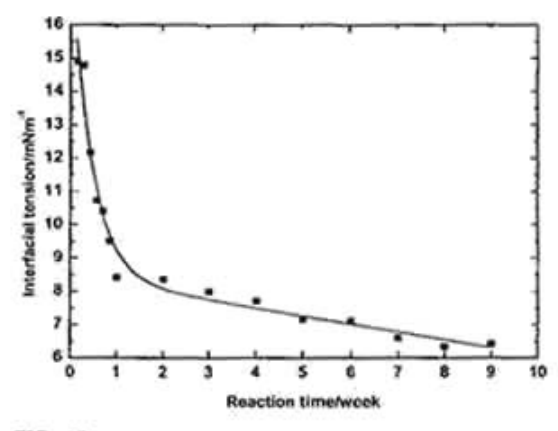


FIG. 17. Interfacial tension changing with reaction time (5.0% saturate model oil, 0.6% NaOH solution, 30°C).

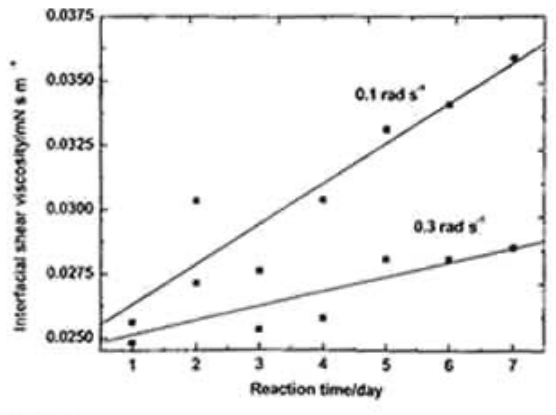
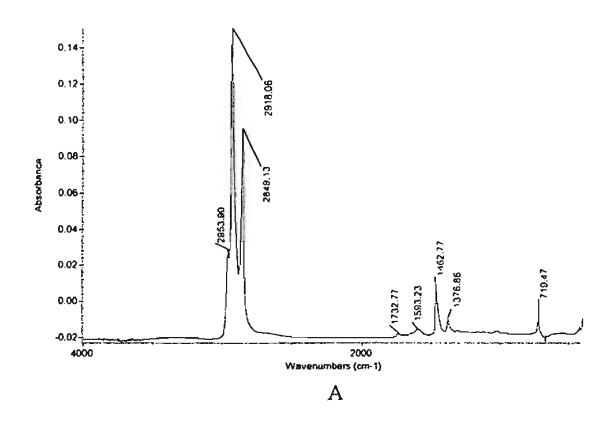


FIG: 18. Interfacial shear viscosity changing with reaction time (3.0% saturate model oil, 0.6% NsOH solution, 25°C).



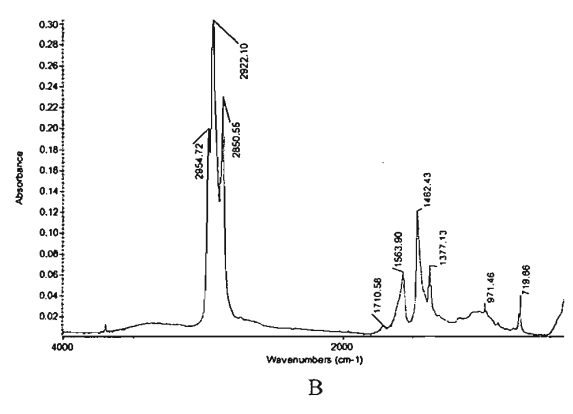


FIG. 19. IR spectroscopy of saturate fraction (A) and the interfacially active components (B) formed in the reaction of saturate and NaOH.

CONCLUSION

Based on this study it is found that the carboxylic acids in the fractions of asphaltene from Gu Dong#1, Gu Dong#4 crude, the resin from Da Qing crude, and the fatty acid in the fractions of saturate from Da Qing crude are responsible for decreasing the interfacial tension between the crude oils and water. These acids have relatively smaller molecular mass, more branch chains, and more oxygen, but they are not able to stabilize emulsions formed by model oil and water. It is the acids with relatively larger molecular mass that are responsible for stabilizing the emulsions. For model oil and alkali solution system the salt or soap formed by fast reaction of the acid, ester with relatively smaller molecular mass, and alkali is responsible for decreasing the interfacial tension between crude oil and water. The salt or soap formed by slow reaction of the acid, ester with relatively larger molecular mass, and alkali is responsible for stabilizing crude oil emulsions.

ACKNOWLEDGMENTS

National Key Research Development Program (G1999022505) and an International Cooperation Research Program (2002CB713906) are acknowledged for financial support and permission for publication of this article.

REFERENCES

- [1] Li, M., Xu, M., Ma, Y., Wu, Z., and Christy, A.A. (2002) Colloids. Surf., 197: 193-201.
- [2] Li, M., Xu, M., Ma, Y., Wu, Z., and Christy, A.A. (2002) Fuel, 81: 1847-1853.
- [3] Li, M., Christy, A.A., and Sjöblom, J. (1992) In Emulsions—A Fundamental and Practical Approach. Sjöblom, J. ed.; Kluwer Academic Publishers: Dordrecht, p. 157.
- [4] Li, M. (2002) In Basic Research for Enhancing Crude Oil | Recovery. Petroleum Industry Publisher.
- [5]\Li, M., Peng, B., Zheng, X., and Wu, Z. (2000) Interfacial rheology of crude oil emulsions. In *Encyclopedic Handbook of Emulsion Technology*. Marcel Dekker: New York, 515-523.



Available online at www.sciencedirect.com

journal of MEMBRANE SCIENCE

Journal of Membrane Science 280 (2006) 651-658

www.elsevier.com/locate/memsci

Pervaporation performance of crosslinked polyethylene glycol membranes for deep desulfurization of FCC gasoline

Ligang Lin, Gang Wang, Huimin Qu, Jinrong Yang, Yunfang Wang, Deqing Shi, Ying Kong*

State Key Laboratory of Heavy Oil Processing, China University of Petroleum (East China), Dongying 257061, PR China
Received 12 December 2005; received in revised form 21 February 2006; accepted 21 February 2006
Available online 29 March 2006

Abstract

An crosslinked polyethylene glycol (PEG) membrane was prepared for fluid catalytic cracking (FCC) gasoline desulfurization. Sulfur enrichment factor come to 4.75 and 3.51 for typical FCC gasoline feed with sulfur content of 238.28 and 1227.24 µg/g, respectively. Pervaporation performance of membranes kept stable within the long time run of 500 h, which indicated that crosslinked PEG membranes had the property of resisting pollution. Judging from chromatographic analysis, the membranes were more efficient for thiophene species. Effects of operation conditions including permeate pressure, feed temperature, feed flow rate and feed sulfur content level on the pervaporation performance were investigated. Permeation flux decreased with increasing permeate pressure while increased with the operating temperature increase. Sulfur enrichment factor increased firstly and decreased then when permeate pressure and temperature rose. The peak value occurred at 10.5 mm Hg and 358 K for model compounds feed (378 K for FCC gasoline feed). Arrhenius relationship existed between flux and operating temperature. Both sulfur enrichment factor and flux were shown to increase with increasing feed flow rate. Permeation flux increased while sulfur enrichment factor decreased as the feed sulfur content increased, but the influence of increasing sulfur content on pervaporation performance weakened when sulfur content come to 600 µg/g.

© 2006 Elsevier B.V. All rights reserved.

Keywords: Pervaporation; FCC gasoline; Deep desulfurization; PEG; Sulfur

1. Introduction

Environmental concerns have resulted in legislation which places limits on the sulfur content of gasoline. In the European Union, for instance, a maximum sulfur level of gasoline has been restricted to 50 ppm by the year of 2005. Sulfur in gasoline is a direct contributor of SO_X emissions [1,2]. FCC gasoline is major source of sulfur and contributes heavy amount of the gasoline pool, especially in China. National standard of China for sulfur content of gasoline is $800 \,\mu g/g$, which is far higher than developed countries. Technical development for deep desulfurization of FCC gasoline is urgent and attracting increasing attention.

A number of solutions have been suggested to reduce sulfur in gasoline, but none of them proven to be ideal. Since sulfur in the FCC feed is the prime contributor of sulfur level in

E-mail addresses: kongy@hdpu.edu.cn, yingkong@sohu.com (Y. Kong).

0376-7388/\$ – see front matter © 2006 Elsevier B.V. All rights reserved. doi:10.1016/j.memsci.2006.02.022

FCC gasoline, an obvious approach is hydrotreating the feed. While hydrotreating allows the sulfur content in gasoline to be reduced to any desired level, installing or adding the necessary hydrotreating capacity requires a substantial capital expenditure and increased operating costs. Further, alkene and cyclic alkane are susceptible to hydrogenation during hydrotreating. This leads to a significant loss in octane number since alkene and cyclic alkane mean higher octane number than paraffin.

Application of membrane technology in petrochemical field provides a newly efficient approach for the separation of organic mixture and has gained increasing attention of membrane and petrochemical field. Gasoline desulfurization by membrane process is newly emerged technology. It is an incorporate process of pervaporation and vapor permeation. The process involves contacting a gasoline feed with a membrane having sufficient flux and selectivity to separate a sulfur deficient retentate fraction from a sulfur enriched permeate fraction. Sulfur deficient retentate fractions are useful directly into the gasoline pool. Sulfur enriched permeate fractions need further treatment by conventional process. Membrane processing offers a number

^{*} Corresponding author. Tel.: +86 546 8391029/13706364264; fax: +86 546 8391971.

of potential advantages over conventional sulfur removal processes, including greater selectivity, lower operating costs, easily scaled operations, adaptability to changes in process streams and simple control schemes [3].

Little has been reported on the selective permeation of sulfur containing compounds using a membrane separation process. With regard to previous research, most of them were for patents or patents applications. These patents mainly involve in the following three companies: W.R.Grace, ExxonMobil Research and Engineering Company and Marathon Oil Company. Industrialization of this sulfur removal technology will produce enormous economic effect and provide an extraordinarily efficient approach for deep desulfurization of FCC gasoline.

Membrane is the core and key point of the membrane technology for deep desulfurization of FCC gasoline. This project was supported by Science and Technology Risk Innovation Fund of CNPC. In this study, crosslinked PEG membranes were developed for deep desulfurization of FCC gasoline. We will report the pervaporation and desulfurization performance of the membranes under various conditions.

2. Experimental

2.1. Materials

PEG (20000) was purchased from the Shanghai Reagent Factory. Gasoline feed with higher sulfur content level was obtained from Shenghua Refinery (China) and lower sulfur content level from Dushanzi Petrochemical Plant (China). Both the gasoline feed were after alkali cleaning process. Other chemicals used were of analytical reagent (A.R.) grade from Tianjin Chemical Reagent Factory and used without further purification.

2.2. Membrane preparation

The PEG polymer mixed with maleic anhydride as crosslinking agent and trimethylamine as catalyst dissolved in N-methyl pyrrolidone (NMP) to form a homogenous solution of 12 wt.% polymer at room temperature. Various crosslinking agent amount and crosslinking time were to control the density of crosslinking. Then, the solution, after filtration and degassing, was cast onto a glass plate using a casting knife. Then they were cast onto polyethersulfone UF membrane. The cast film was placed in an oven at 363 K for some time to crosslink and to evaporate the solvent, and then the membrane was dried at the room temperature in vacuum drying oven at least 24 h. All membrane samples were stored in dust-free and dry environment before used in the pervaporation experiments. The active layer has a thickness of about 20 μ m. Membranes involved in the paper are shown in Table 1.

2.3. Pervaporation apparatus

The schematic pervaporation apparatus is shown in Fig. 1. The permeation cell was made of stainless steel and the membrane was supported on a porous titanium disc with an effective membrane area of 20.45 cm². Pervaporation experiments were

Table 1
Some parameters of the membranes involved in the paper

Membrane no.	Amount of crosslinking agent (wt.%)	Amount of catalyst agent (wt.%)	Crosslinking time (min)
I	14.09	3.23	30
II	16.1	3.69	60

carried out by maintaining on one side of the membrane gasoline or model compounds feed at atmospheric pressure and on the other side (permeate) a reduced pressure of not more than 35 mm Hg. Feed flow was heated to constant temperature before entering the permeation cell by high-performance oven.

2.4. Analysis

The permeated vapor was collected in liquid nitrogen traps. About 2 h after starting the pervaporation process, the feed temperature was stable and a mass transfer equilibrium was deemed to have been established. The cold trap was exchanged every hour and the permeate was thawed and poured back into the feed tank to limit the loss of sulfur compounds from the feed. During the third hour, permeate was collected and samples from the feed tank were taken for analysis. Every data point in this manuscript was gained by considerable PV experiments using multiple pieces of membrane for every membrane preparation conditions until the experimental error meets the following statement

Each sample quality determination was based on three or four different weight analysis by electronic balance device with the precision accuracy of 0.001. The total flux was determined gravimetrically with an experimental error of 1-2%. The flux, J, at a steady state was obtained by

$$J = \frac{Q}{At} (\text{kg m}^{-2} \, \text{h}^{-1})$$

where, Q is the total amount permeated during the experimental time interval, t, at steady state and A is the effective membrane area. Flux or J used in the paper means total permeation flux if no special clarification.

The total sulfur content of feed and permeate was analyzed by Micro-Coulometric Analysis Instrument (Jiangsu, China). Each sulfur concentration determination was based on three or four

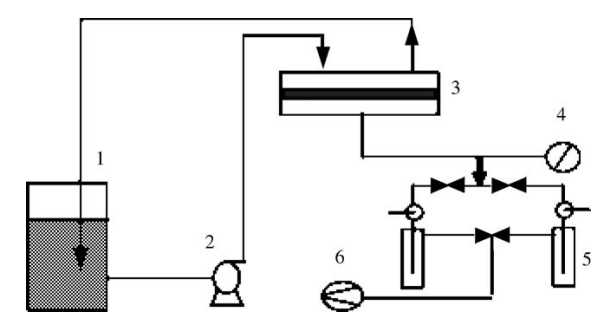


Fig. 1. Schematic diagram of experimental apparatus for pervaporation. 1, feed tank; 2, feed pump; 3, pervaporation cell; 4, pressure manometer; 5, cold trap; 6, vacuum pump.

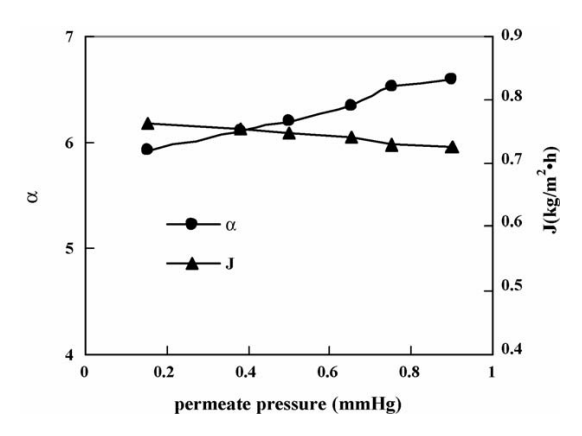


Fig. 2. The effect of permeate pressure (P) on J and α (P < 1 mm Hg).

different injections. The values of sulfur content varied by 1–3%. The sulfur enrichment factor, α , is defined as

$$\alpha = \frac{C_{\rm A}'}{C_{\rm A}}$$

where, $C_{\rm A}$ and $C_{\rm A}'$ are the total sulfur content of feed and permeate samples, respectively. Components analysis of feed and permeate samples was carried out by Varian 3800 gas chromatography (GC) equipped with a 3 m long column with pulsed flame photometric detector (PFPD). And enrichment factor for every component is defined as the ratio of peak area. Each sample analysis was based on three or four different injections. The values of components concentration varied by 2–5%.

3. Results and discussion

3.1. Effects of operating conditions on pervaporation performance

Membrane I was used for in the next pervaporation research if no special clarification. Feed flow rate was 1.2 L/h in the paper if no special clarification.

3.1.1. Effects of permeate pressure

Permeate pressure has great influence on pervaporation performance since it is an important driving force source for mass transfer and heat transfer [4]. If the desulfurization performance can fulfill under the higher permeate pressure, load of vacuum pump will decreased greatly at industrialization stage. Figs. 2 and 3 reveal the effect of permeate pressure on pervaporation performance at 373 K with 1464.1 μ g/g sulfur content level in the model compounds feed (thiophene and n-heptane).

From Fig. 2, under lower permeate pressure, flux decreased with increasing permeate pressure since there was a reduction of driving force for transport of components. Similar results were reported by a number of researches [5,6]. And the sulfur enrichment factor increased when permeate pressure increased. Reasons were similar to the next explanations of Fig. 3. However, the decrease of flux and increase of sulfur enrichment factor

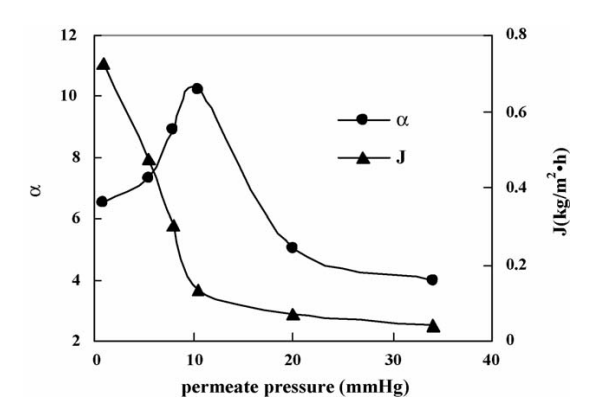


Fig. 3. The effect of permeate pressure (P) on J and α (P > 1 mm Hg).

was not large under rigorous vacuum state (permeate pressure, <1 mm Hg).

From Fig. 3, under higher permeate pressure, flux decreased with increasing permeate pressure for the same reason. However, sulfur enrichment factor was susceptible to the increase of permeate pressure, increased firstly and decreased then. At permeate pressure of 10.5 mm Hg, sulfur enrichment factor met its peak value. Table 2 shows that the decrease speed of flux of sulfur species was larger than that of hydrocarbon species, at 10.5 mm Hg particularly. Since the saturated vapor pressure or partial vapor pressures of n-heptane is lower than that of thiophene, an increase of permeate pressure slowed down evaporation of n-heptane relatively and caused a increase of sulfur enrichment factor. But with the continuous increase of permeate pressure, the difference of evaporation and permeation capacity weakened. Due to higher concentration at the feed side, heptane's permeation amount increased relatively and caused a decrease of sulfur enrichment factor.

3.1.2. Effects of feed temperature

The influence of feed temperature on pervaporation performance for model compounds feed is given in Fig. 4, at 1 mm Hg permeate pressure with 1464.1 μ g/g sulfur content level in the model compounds feed (thiophene and n-heptane). As expected, when temperature was increased, the total permeation flux increased, but sulfur enrichment factor increased firstly and decreased then. At 358 K, sulfur enrichment factor met its peak value.

Table 2
Comparison of permeation flux between sulfur and hydrocarbon components

Permeate pressure (mm Hg)	Flux of <i>n</i> -heptane J_1 (kg/m ² h)	Flux of thiophene J_2 (kg/m ² h)	$J_2 \times 100/J_1$
0.9	0.71	0.015	2.09
5.5	0.46	0.0109	2.36
8.0	0.29	0.00764	2.61
10.5	0.13	0.00458	3.54
20.0	0.068	0.00161	2.37
34.0	0.037	0.000841	2.26

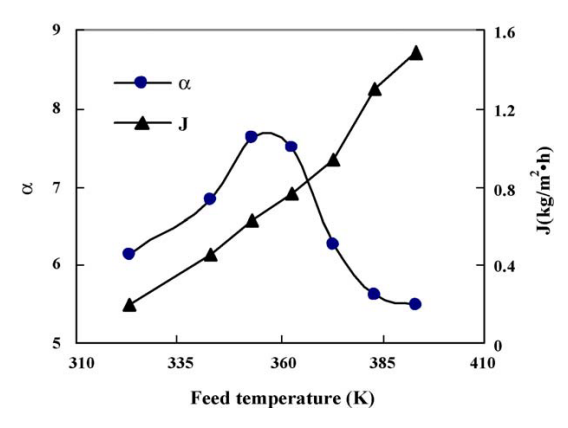


Fig. 4. The effect of feed temperature on J and α (model compounds feed).

Temperature affected the transport of components in the liquid feed and in the membrane. Both mass transfer coefficient of components in the liquid and sorption of components into the membrane increase with feed temperature [7,9]. In addition, the polymer chains were more flexible at higher temperature and caused larger available free volume of polymer matrix for diffusion. Increase of feed temperature enhanced the driving force source of mass transfer and the saturated vapor pressure of components at permeate side and availed components in permeating through the membrane. By all given reasons, flux increased with temperature. However, the continuous increase of feed temperature weakened the difference of solubility and diffusion velocity of sulfur and hydrocarbon species, and caused the decrease of sulfur enrichment factor.

Comparison of permeation flux of sulfur and hydrocarbon components availed the understanding of above results. From Fig. 5, increase velocity of flux for sulfur components was lager than that of hydrocarbon components at lower temperature for the stronger affinity between sulfur species and membrane, which caused increased sulfur enrichment factor. However, higher feed temperature weakened the influence of affinity. Considering the higher concentration of hydrocarbon components in the feed, lager increase velocity of flux for hydrocarbon components caused the decrease of sulfur enrichment factor.

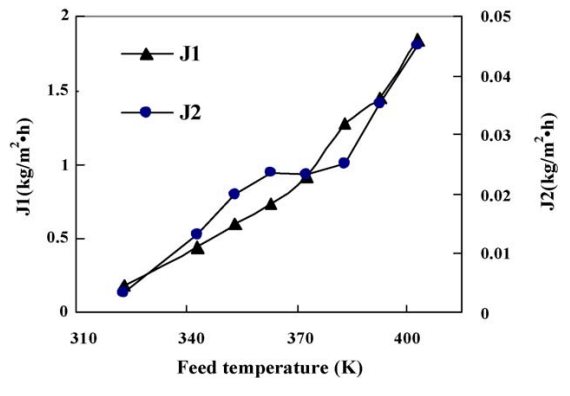


Fig. 5. The comparison of permeation flux of sulfur and hydrocarbon species $(J_1, \text{flux of hydrocarbon species}; J_2, \text{flux of sulfur species}).$

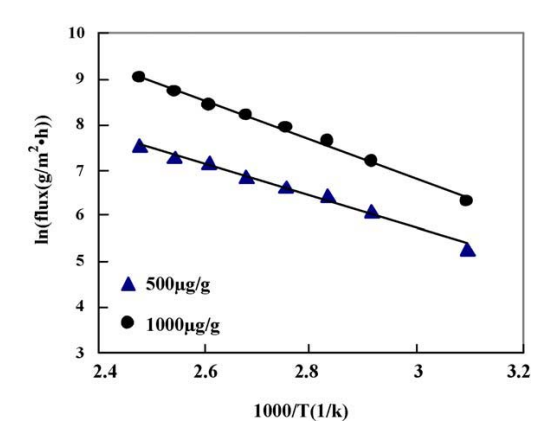


Fig. 6. Arrhenius relationship between heptane flux and temperature with various feed sulfur level.

The relationship between the permeation flux and operating temperature can normally be expressed by the Arrhenius-type formula: $J = A \exp(-E_p/RT)$, where A is the pre-exponential factor, E_p the activation energy of pervaporation, R the gas constant, and T is the absolute temperature [7–11]. Fig. 6 shows the relationship between logarithm of flux and reciprocal of absolute temperature for different feed. Sound linearity existed between the two parameters.

Fig. 7 revealed the influence of temperature on pervaporation performance for gasoline feed. The result was similar to that of Fig. 4 except that peak value occurred at 378 K. Since sulfur species in FCC gasoline mostly are methyl thiophene whose boiling point is higher than thiophene, higher temperature was needed to increase the driving force of permeation.

3.1.3. Effect of feed flow rate

Flux and sulfur enrichment factor both increased with the increase of feed flow rate as shown in Fig. 8, due to the decrease of concentration polarization and temperature polarization, at 373 K, 1 mm Hg permeate pressure and 1397.2 μ g/g sulfur content level in the model compounds feed (thiophene and n-heptane). In general, the concentration of sulfur compounds which were the more permeable components was lower on the membrane surface than that in the bulk phase. A reduction of

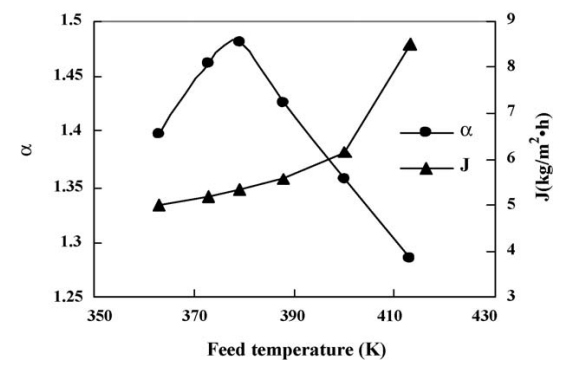


Fig. 7. The effect of feed temperature on J and α (FCC gasoline feed).

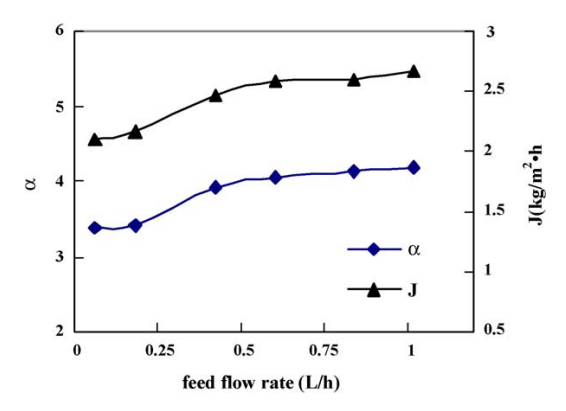


Fig. 8. The effect of feed flow rate on J and α .

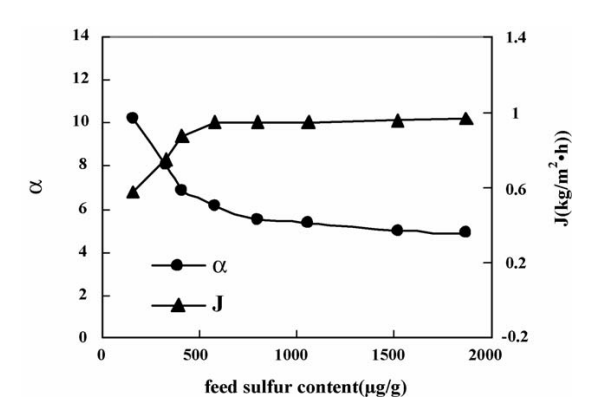


Fig. 9. The effect of feed sulfur level on J and α .

concentration polarization means that sulfur concentration near the membrane surface was close to that in the bulk. The increase of sulfur concentration on the membrane surface with the feed rate enhanced sulfur compounds sorption and swelling in the membrane such that the flux increased. A reduction of temperature polarization means that the temperature near the membrane surface was close to that in the bulk. Then due to the increase of the driving force for mass transfer, the sulfur enrichment factor increased. The above results and analysis indicated that the operation of pervaporation system at high flow rate was an advantage.

3.1.4. Effect of feed sulfur content level

Considering the various sulfur content level of worldwide refineries, Fig. 9 reveals the influence of feed sulfur content

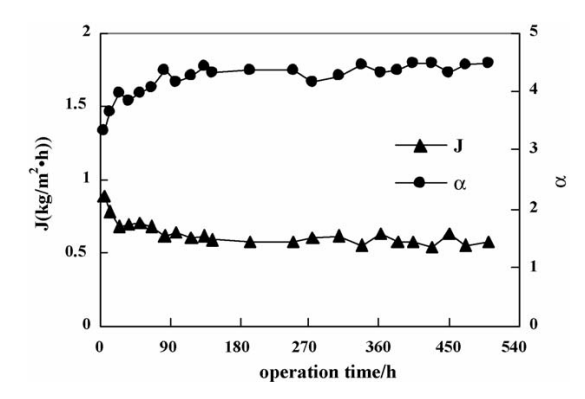


Fig. 10. The effect of long time operation on J and α .

level on pervaporation performance, at 373 K, 1 mm Hg permeate pressure with the model compounds feed (thiophene and n-heptane).

From Fig. 9, an increase of sulfur content in feed resulted in a sharp increase of total flux and a sharp decrease of sulfur enrichment factor. When the sulfur content in feed was increased, an extensive swelling of the membrane occurred due to the strong affinity of sulfur to the membrane. Consequently, total flux increased due to the enhanced activity of polymer chains and bonds. Hydrocarbon compounds are normally difficult to diffuse into the non-swollen membrane while they can diffuse easily through swollen membrane. Therefore, sorption selectivity toward sulfur decreased with increasing sulfur content in feed. However, the influence of increasing sulfur content on pervaporation performance weakened when sulfur content come to 600 µg/g. Since the occurrence of swelling balance in the membrane and the saturated sulfur concentration on the surface of the membrane, flux and sulfur enrichment factor changed little with the increasing sulfur content level of

3.1.5. Effect of long time operation

During the long time operation of 500 h, pervaporation performance was stable relatively except at the beginning time as shown in Fig. 10, which indicated that this kind of membrane had the property of resisting pollution. After some time of run, swelling balance of the membrane led to stable flux and sulfur enrichment factor. Experiments were conducted at 373 K feed temperature, 1 mm Hg permeate pressure and 1327.5 μ g/g sulfur content level in gasoline feed.

Table 3
Desulfurization performance for FCC gasoline of high sulfur content

Membrane no.	Feed type	Sufur content of feed (μg/g)	Sulfur enrichment factor α	Flux J (kg/m ² h)
I	1#	1227.24	2.10	2.33
	2#	565.61	4.83	0.64
	3#	1035.86	3.05	1.81
II	1#	1227.24	3.51	0.85

1#: FCC gasoline (full boiling range); 2#: FCC gasoline fraction (boiling range lower than 393 K); 3#: FCC gasoline fraction (boiling range lower than 433 K).

Table 4
Desulfurization performance for typical sulfur species in FCC gasoline

Peak no.	Sulfur speices	Feed gasoline		Permeate sampl	e	Enrichment factor
		Peak area	Percentage (%)	Peak area	Percentage (%)	
1	Methyl mercaptan	416509	2.46	175059	0.35	0.42
2	Ethyl mercaptan	98179	0.58	38246	0.08	0.39
3	Propyl mercaptan	225014	1.33	221751	0.44	0.99
4	Thiophene	1789782	10.59	2588070	5.12	1.45
5	C5 mercaptan	77275	0.46	145669	0.29	1.89
6	2-Methyl thiophene	2354961	13.93	5037115	9.96	2.14
7	3-Methyl thiophene	3424713	20.26	5961417	11.78	1.74
8	Sulfide	1565465	9.26	6181981	12.22	3.95
9	Dimethyl thiophene	4769199	28.22	22685067	44.84	4.76
10	Disulfide	113989	0.67	382899	0.76	3.36
11	Isopropyl thiophene	196579	1.16	1130438	2.23	5.75
12	Trimethyl thiophene	1613735	9.55	5741381	11.35	3.56
13	C4 thiophene	170028	1.01	226375	0.45	1.33

3.2. Desulfurization performance of crosslinked PEG membranes

3.2.1. Desulfurization performance for typical FCC gasoline of high sulfur content

For most of refineries in China, sulfur content level of FCC gasoline is high. Desulfurization performance is summarized in Table 3. From the performance of membrane I, high sulfur enrichment factor was obtained for FCC gasoline fraction of lower boiling range. Since the alkenes and aromatics with high boiling point swelled the membrane severely [12], flux increased and sulfur enrichment factor decreased for full boiling range gasoline.

Overall sulfur enrichment factor was 3.51 for membrane II and $25 \,\mu\text{g/g}$ low sulfur gasoline product was obtained when the permeate volume was 28% of the feed volume. GC experiments results for feed and permeate samples are shown in Table 4 with the corresponding chromatograms shown by Figs. 11 and 12.

From Table 4, principal sulfur species in FCC gasoline (Shenghua Refinery, China) are mercaptan, sulfide, disulfide and thiophene species, in which thiophene species contribute to 80% of total sulfur content. According to the enrichment factor in Table 4 and the comparison of chromatograph peaks between Figs. 11 and 12, removal effect for thiophene species from FCC gasoline was excellent.

3.2.2. Desulfurization performance for typical FCC gasoline of low sulfur content

It is necessary to investigate the desulfurization performance for low sulfur gasoline feed since the sulfur content level of

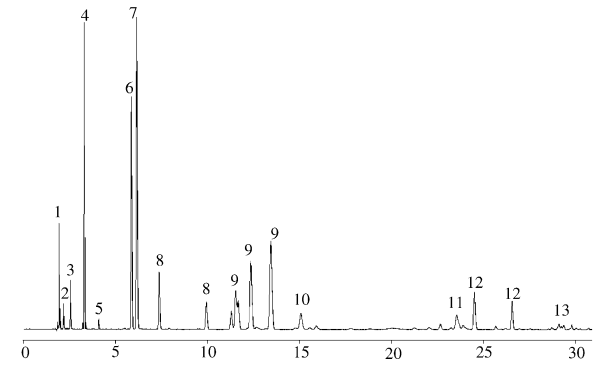


Fig. 11. Chromatogram for sulfur species distribution in feed FCC gasoline.

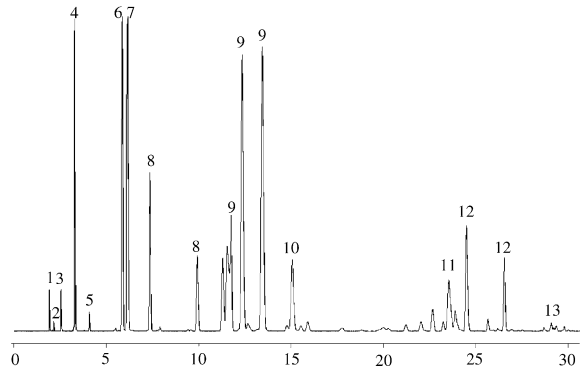


Fig. 12. Chromatogram for sulfur species distribution in permeate sample.

Table 5
Desulfurization performance for FCC gasoline of low sulfur content

Membrane no.	Feed no.	Sample source	Sufur content (µg/g)	Sulfur enrichment factor α	Flux J (kg/m ² h)
II	1#	Feed	238.28		
	2#	Permeate	779.45	3.27	0.98
	3#	Permeate	1132.84	4.75	0.93

Table 6
Desulfurization performance for typical sulfur species in FCC gasoline

Peak no.	Sulfur speices	Sample1#, peak area	Sample2#, peak area	Enrichment factor	Sample3#, peak area	Enrichment factor
1	Thiophene	1616398	3434111	2.12	3622975	2.24
2	2-Methyl thiophene	202394	1410902	6.97	2382634	11.77
3	3-Methyl thiophene	252387	1798030	7.12	2995981	11.87
4	Disulfide	98642	586631	5.95	924349	9.37
5	Dimethyl thiophene	419595	1051124	2.51	1046519	2.49
6	Isopropyl thiophene	58338	71062	1.22	42276	0.72
7	Methyl ethyl thiophene	13890	_	_	_	_
8	Trimethyl thiophene	142095	_	_	_	_

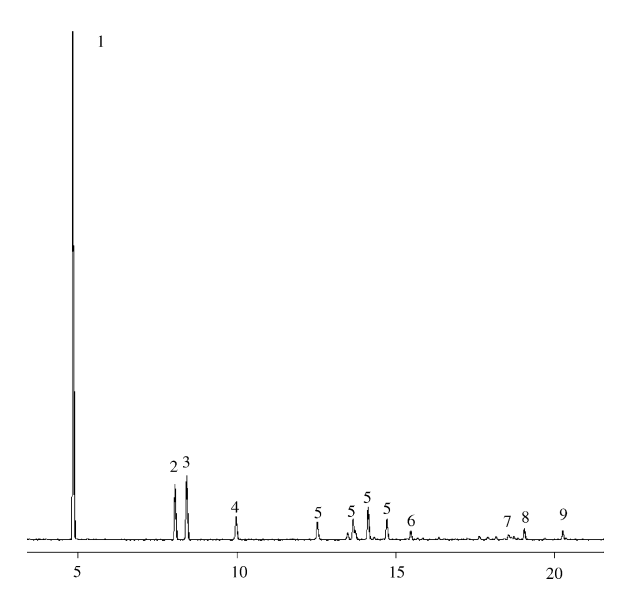


Fig. 13. Chromatogram for sulfur species distribution in gasoline feed.

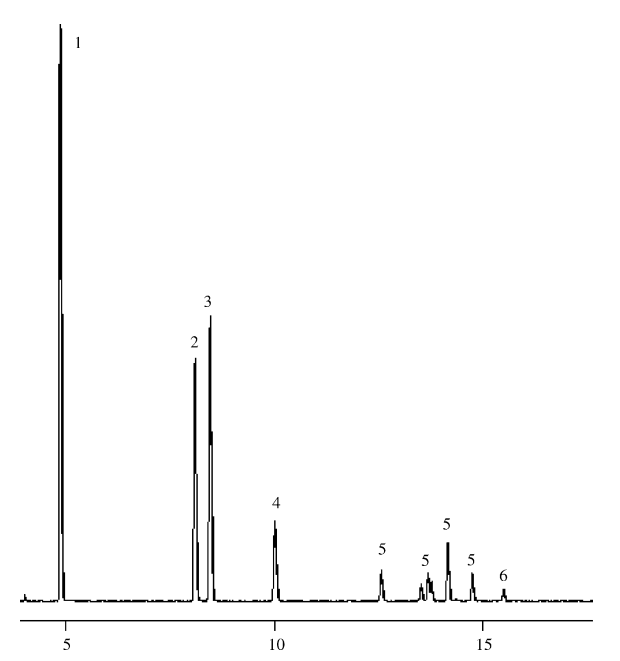


Fig. 14. Chromatogram for sulfur species distribution in permeate sample2#.

FCC gasoline was lower than 300 μ g/g in some refineries with a example of Dushanzi Petrochemical Plant (China). Desulfurization performance of membrane II for this kind of feed is summarized in Table 5.

Overall sulfur enrichment factor was 3.27 for sample 2# which was sampled at the unstable stage of the membrane. Permeate 3# was sampled after the membrane performance was stable and sulfur enrichment factor come to 4.75. Low sulfur gasoline product of $42 \mu g/g$ can be obtained when the permeate volume was 18% of the feed volume. GC experiments results for feed and permeate samples are shown in Table 6 with the corresponding chromatograms shown by Figs. 13–15.

From Table 6, principal sulfur species in this kind of FCC gasoline are thiophene species. Part of thiophene species with high boiling point did not permeate through the membrane under the experiment conditions. According to the enrichment factor in Table 6 and the comparison of chromatograph peaks between Figs. 13, 14 and 15, removal effect for thiophene species from FCC gasoline was excellent to PEG membrane. Enrichment factor of 2-methyl thiophene and 3-methyl thiophene were high especially.

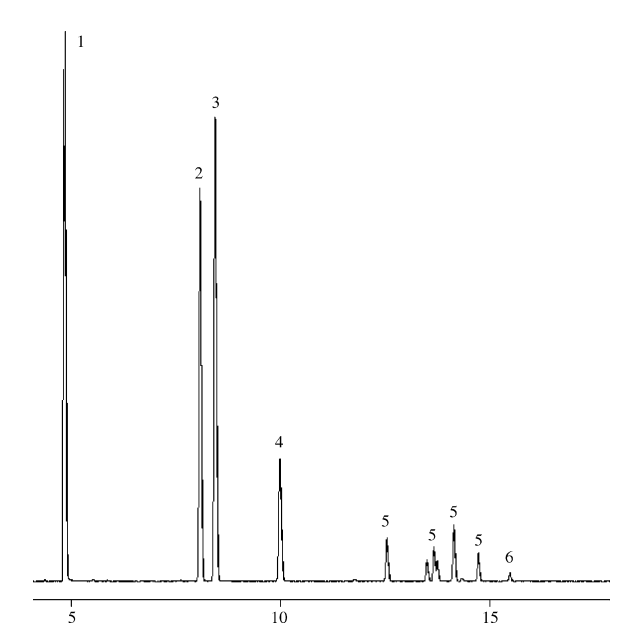


Fig. 15. Chromatogram for sulfur species distribution in permeate sample 3#.

4. Conclusions

FCC gasoline desulfurization can be conducted by pervaporation using a crosslinked PEG membrane. Permeation flux decreased with increasing permeate pressure while increased with the operating temperature increase. Sulfur enrichment factor increased firstly and decreased then when permeate pressure and temperature rose. The peak value occurred at 10.5 mm Hg and 358 K for model compounds feed (378 K for FCC gasoline feed). Arrhenius relationship existed between permeation flux and operating temperature. Both sulfur enrichment factor and permeation flux were shown to increase with increasing feed flow rate. Permeation flux increased while sulfur enrichment factor decreased as the feed sulfur content increased, but the influence of increasing sulfur content on pervaporation performance weakened when sulfur content come to 600 µg/g. As to the desulfurization performance, sulfur enrichment factor for high sulfur content FCC gasoline feed of different boiling range was from 2.10 to 3.51 by membranes with various membrane preparation parameters. Sulfur enrichment factor come to 4.75 for low sulfur content FCC gasoline feed of 238.28 μg/g. Membrane performance kept stable within the long time run of 500 h, which indicated that crosslinked PEG membranes had the property of resisting pollution. Judging from chromatographic analysis, the crosslinked PEG membranes were more efficient for thiophene species.

References

 Huan-zhang Chen, Advances in desulfurization of FCC gasoline, Sci. Technol. Chem. Ind. 12 (2004) 46–51.

- [2] Lloyd Steven White, Rlchard Franklin, Markus Lesemann, Membrane separation for sulfur reduction, US Patent 2002/0153284, 2002.
- [3] G. Krishnaiah, T. Cartwright, S-Brane Technology Brings Flexibility To Refiners' Clean Fuel Solutions, 2004 NPRA Annual Meeting, San Antonio, TX, 2004.
- [4] Jenny Olsson, Gun Trägårdh, Pervaporation of volatile organic compounds from water. I. Influence of permeate pressure on selectivity, J. Membr. Sci. 187 (2001) 23–37.
- [5] N. Rajagopalan, M. Cheryan, Pervaporation of grape juice aroma, J. Membr. Sci. 104 (1995) 243–250.
- [6] Y.M. Lee, S.Y. Nan, D.J. Woo, Pervaporation of ionically surface crosslinked chitosan composite membranes for water–alcohol mixtures, J. Membr. Sci. 133 (1997) 103–110.
- [7] R. Jiraratananon, A. Chanachai, R.Y.M. Huang, D. Uttapap, Pervaporation dehydration of ethanol-water mixtures with CS/HEC composite membranes. I. Effect of operating conditions, J. Membr. Sci. 195 (2002) 143–151.
- [8] Sang Yong Nam, Young Moo Lee, Pervaporation of ethylene glycol-water mixtures. I. Pervaporation permorance of surface crosslinked chitosan membranes, J. Membr. Sci. 153 (1999) 155–162.
- [9] P. Sampranpiboon, R. Jiraratananon, D. Uttapap, Pervaporation separation of ethyl butyrate and isopropanol with polyether block amide (PEBA) membranes, J. Membr. Sci. 173 (2000) 53–59.
- [10] Jie Yu, Chul Haeng Lee, Won Hi Hong, Performances of crosslinked asymmetric poly(vinyl alcohol) membranes for isopropanol dehydration by pervaporation, Chem. Eng. Process. 41 (2002) 693– 698.
- [11] M.Y. Kariduraganavar, A.A. Kittur, S.S. Kulkarni, K. Ramesh, Development of novel pervaporation membranes for the separation of water–isopropanol mixtures using sodium alginate and NaY zeolite, J. Membr. Sci. 238 (2004) 165–175.
- [12] S.H.A.N. Hong-hong, Distribution of sulfur in FCC gasoline and desulfurization with catalytic cracking, J. Chin. Univ. Petrol. 25 (2001) 78– 81.

The Semi-Ideal Solution Theory for Mixed Ionic Solutions at Solid-Liquid-Vapor Equilibrium

Yu-Feng Hu*

State Key Laboratory of Heavy Oil Processing and High-Pressure Fluid Phase Behavior & Property Research Laboratory, China University of Petroleum, Beijing 102200, China

Shuan-Shi Fan and De-Qing Liang

Laboratory of Gas Hydrates & High-Pressure Fluids, Guangzhou Institute of Energy Conversion, The Chinese Academy of Sciences, Guangzhou 510070, PR China

Received: August 1, 2005; In Final Form: January 14, 2006

The semi-ideal solution theory has been presented to describe the changes in thermodynamic properties accompanying the process of mixing the nonideal electrolyte solutions $M_i X_i - (NY)_{sat} - H_2 O$ (i = 1 and 2) at constant activities of NY and H_2O , including concentration, chemical potential, activities of all M_iX_i , Gibbs free energy, enthalpy, entropy, thermal properties, and volumetric properties. The theory states that, under the conditions of equal activities of NY and H₂O, the average hydration numbers characterizing the ionsolvent interactions have the same values in the mixture as in the subsystems and the process of mixing these nonideal electrolyte solutions is as simple as that of mixing the ideal solutions if the contributions from the ion-ion interactions to the solvent activity are assumed to be the same in the mixture as in its subsystems, which has been justified by the calculations of the Pitzer equation. Therefore, a series of novel linear equations are established for the thermodynamic properties accompanying the process of mixing these nonideal solutions as well as mixing the ideal solutions $M_iX_i-(NY)_{sat}-H_2O$ (i=1 and 2) of equal mole fractions of NY and H₂O. From these equations, the widely applied empirical Zdanovskii's rule is derived theoretically, and the important constant in the McKay-Perring equation under isopiestic equilibrium is determined theoretically, which has been substantiated by comparisons with the experimental results for 18 mixtures reported in the literature. Isopiestic measurements have been made for the systems BaCl₂-LaCl₃-H₂O, NaCl-BaCl₂-LaCl₃-H₂O, and NaCl-LaCl₃-BaCl₂·2H₂O_(sat)-H₂O at 298.15 K. The results are used to test the novel linear concentration relations, and the agreement is excellent. The novel predictive equation for the activity coefficient of M_iX_i in $M_1X_1-M_2X_2-(NY)_{sat}-H_2O$ has been compared with the calculations of the Pitzer equation, and the agreement is good.

1. Introduction

The Zdanovskii's rule was first discovered empirically by Zdanovskii for ternary unsaturated electrolyte solutions¹ and was derived for unsaturated nonelectrolyte solutions by Stokes and Robinson.^{2–5} Since then, it has been experimentally extended to unsaturated aqueous solutions of electrolytes and nonelectrolytes.^{6,7} The Zdanovskii's rule coupled with the McKay—Perring equation⁸ yields the simple equation for the activity coefficient of either solute in multicomponent unsaturated solutions.⁹ However, while the model parameter in the McKay—Perring equation was announced to be an arbitrary proportionality constant, in practice it was empirically set equal to the salt stoichiometric coefficient.^{9–12} Recently, this rule has received wide and growing attention^{9–15} and has been used to establish the novel predictive equations for the thermodynamic properties^{10,11} and viscosity¹² of multicomponent solutions.

Up to now, the Zdanovskii's rule has not been theoretically justified. Mikhailov derived the rule for very dilute electrolyte solutions where the Debye-Hückel theory applies. ¹⁶ However, extensive isopiestic results indicate that the rule is much more

widely applicable than can be theoretically justified by Mikhailov. 17,18 Rard also derived the rule by assuming that the osmotic coefficients of the binary and multicomponent solutions are equal under isopiestic equilibrium, 19 which is evidently quite reasonable for the solutions of 1:1 electrolytes. Therefore, in this study, a semi-ideal solution theory is proposed on the basis of the Debye-Hückel theory and the concept of the stepwise hydration equilibrium, from which the novel concentration relations for multicomponent saturated electrolyte solutions are established and the Zdanovskii's rule (for unsaturated solutions) is theoretically derived. The simple equation for the activity coefficient of each unsaturated solute in saturated solutions is also derived, from which the simplified McKay-Perring equation for unsaturated solutions is reproduced and its proportionality constant is theoretically determined. A new set of simple predictive equations are proposed for thermodynamic properties of saturated electrolyte solutions from those of their subsystems. The isopiestic measurements at 298.15 K have been made for the systems NaCl-BaCl2-LaCl3-H2O and NaCl-BaCl2. 2H₂O_(sat)-LaCl₃-H₂O. The results together with the calculations based on the Pitzer equation^{20,21} are used to test the proposed equations.

10.1021/jp0542672 CCC: \$33.50 © 2006 American Chemical Society Published on Web 03/07/2006

^{*} Corresponding author. E-mail: Huyf3581@sina.com. Fax: 86-10-69744849.

Semi-Ideal Solution Theory

2. The Semi-Ideal Solution Theory

Let electrolytes M_iX_i and NY represent the solute components present below their solubility limits and that present as saturated solutions, respectively. Let the superscript (io) denote the quantity in the ternary saturated subsystem M_iX_i -(NY)_{sat}-H₂O or in the binary unsaturated subsystem $M_iX_i-H_2O$. The other notations used in this paper are summarized in the Glossary. In this study, it is assumed that all electrolyte solutes are completely dissociated and produce v_{M_i} and v_N cations of charges (z_{M_i} and $z_{\rm N}$) and $(v_{\rm X_i}$ and $v_{\rm Y})$ anions of charges $(z_{\rm X_i}$ and $z_{\rm Y})$, respectively. Note that in this paper the cations and anions are denoted by $(M_i \text{ and } N) \text{ and } (X_i \text{ and } Y) \text{ instead of } (M_i^{z_{Mi}^+} \text{ and } N^{z_N^+}) \text{ and }$ $(X_i^{z_{Xi}}$ and Y^{z_Y}).21

2.1. Treatment of Ion-Ion and Ion-Solvent Interactions. In this study, the ion—ion interactions in the mixture M_1X_1 — M₂X₂-NY_(sat)-H₂O are treated with the Debye-Hückel theory, and the ion-solvent interactions are described by the stepwise hydration equilibrium.²⁻⁵ That is, the Gibbs energy of the above system is composed of two terms, namely, $G = G^{DH} + G^{Hy}$, where GDH is the Debye-Hückel contribution, and GHy describes the semi-ideal mixture of the resulting species based on the mole fraction x. Therefore, $\ln a = \ln a^{DH} + \ln a^{Hy}$, where $a^{\mathrm{Hy}} = x$. The stepwise hydration equilibrium can be symbolized by

$$NY(s) + H_2O = v_N N \cdot H_2O_{(1)} + v_Y Y(aq)$$
 (1)

and

$$U \cdot H_2 O_{(l-1)} + H_2 O \leftrightharpoons U \cdot H_2 O_{(l)}$$
 (2)

where U = N, Y, M_i, and X_i with i = 1 and 2, and l = 2, ..., n. If we assume that $a_{\text{U-H}_2\text{O}(l)}^{\text{DH}}/a_{\text{U-H}_2\text{O}(l-1)}^{\text{DH}} = 1$, then the equilibrium constants K_I^{U} for the hydration equilibrium denoted by eq 2 are given by

$$K_l^{\rm U} = \frac{x_{\rm U \cdot H_2O(l)}}{x_{\rm U \cdot H_2O(l-1)} a_{\rm H_2O}}$$
 (3)

It is clear that K_i^U and thereby the average hydration numbers, $\bar{h}_{\rm U-H_2O} = \sigma/\Sigma$ with $\sigma = \partial \Sigma/\partial \ln a_{\rm H_2O} = \sum_{l=1}^n l K_1^{\rm U} \dots K_l^{\rm U} a_{\rm H_2O}^l$ and $\Sigma = 1 + \sum_{l=1}^{n} K_1^{U} \dots K_l^{U} a_{H,O}^{l}$, depend only on water activity $Z = 1 + Z_{l=1} K_1 \dots K_l \ a_{H_2O}$, depend only on water activity a_{H_2O} . However, the equilibrium constant $K_1^N = x_{N \cdot H_2O_{(1)}} x_{Y_{(aq)}} / a_{H_2O}$ for the saturated solutes (equals $K'_0 = a_{NY_{(aq)}} / a_{NY_{(a)}} = a_{NY_{(aq)}}$ for $NY(s) \hookrightarrow NY(aq)$ times $K'_0 = x_{N \cdot H_2O_{(1)}} x_{Y_{(aq)}} / (a_{NY_{(aq)}} - a_{H_2O})$ for $NY(aq) + H_2O \hookrightarrow \nu_N N \cdot H_2O_{(1)} + \nu_Y Y(aq)$) is different from $K_1^M = x_{M_1 \cdot H_2O_{(1)}} / (x_{M_1 \cdot H_2O_{(0)}} a_{H_2O})$ for unsaturated solutes, and thus, $\bar{h}_{\rm N-H_2O}$ differs from $\bar{h}_{\rm M_1-H_2O}$ for a given water activity

2.2. Novel Linear Concentration Relations at Constant Activities of NY and H2O. The water activity for the semiideal mixture M_iX_i -(NY)_{sat}-H₂O (i = 1 and 2), $a_{H,O}^{(io)}$, is given

$$\ln a_{\rm H,O}^{(io)} = \ln a_{\rm H,O}^{(io),\rm DH} + \ln x_{\rm H,O}^{(io),\rm free}$$
 (4)

where the superscript free denotes the free quantity. $a_{\rm H,O}^{(io),\rm DH}$ and $x_{\rm H_2O}^{\rm (io),free}$ are the Debye-Hückel contribution to water and $n_{\rm H_2O}$ are the Debye-Huckel contribution to water activity and the mole fraction of the free solvent H₂O in the mixture. $x_{\rm H_2O}^{(i), \rm free} = n_{\rm H_2O}^{(io), \rm free}/n_{\rm total}^{(io)}$ with $n_{\rm H_2O}^{(io), \rm free} = n_{\rm H_2O}^{(io)} - \nu_{\rm N_i X_i-1}/n_{\rm N_i X_i-1}/n_{\rm H_2O}/n_{\rm N_i X_i-1}/n_{\rm N_i X_i$ salt stoichiometric coefficient, $\nu_{M_iX_i} = \nu_{M_i} + \nu_{X_i}$, and

 $\nu_{\rm M_iX_i} \bar{h}_{\rm M_iX_i-H_2O} = \nu_{\rm M_i} \bar{h}_{\rm M_i-H_2O} + \nu_{\rm X_i} \bar{h}_{\rm X_i-H_2O}. \ \nu_{\rm NY} \ {\rm and} \ \nu_{\rm NY} \bar{h}_{\rm NY-H_2O}$ are similarly defined.

Similarly, a_{H_2O} for the mixture $M_1X_1-M_2X_2-(NY)_{sat}-H_2O$ is given by

$$\ln a_{\rm H_2O} = \ln a_{\rm H_2O}^{\rm DH} + \ln \frac{n_{\rm H_2O}^{\rm free}}{n_{\rm total}}$$
 (5)

with $n_{\rm H_2O}^{\rm free}=n_{\rm H_2O}-\sum_{i=1}^2\nu_{\rm M_iX_i}\bar{h}_{\rm M_iX_i-H_2O}n_{\rm M_iX_i}-\nu_{\rm NY}\bar{h}_{\rm NY-H_2O-}n_{\rm NY}$ and $n_{\rm total}=n_{\rm H_2O}^{\rm free}+\sum_{i=1}^2\nu_{\rm M_iX_i}n_{\rm M_iX_i}+\nu_{\rm NY}n_{\rm NY}.$ Since $a_{\rm H_2O}=a_{\rm H_2O}^{\rm (io)}$, if we assume that $a_{\rm H_2O}^{\rm DH}=a_{\rm H_2O}^{\rm (io),DH}$, then combination of eqs 4 and 5 yields (see Supporting Information for the detailed derivation)

$$\frac{n_{\rm M_1X_1}}{n_{\rm M_1X_1}^{(1\,\rm o)}} n_{\rm H_2O}^{(1\,\rm o)} + \frac{n_{\rm M_2X_2}}{n_{\rm M_1X_2}^{(2\,\rm o)}} n_{\rm H_2O}^{(2\,\rm o)} = n_{\rm H_2O} \tag{6}$$

and

$$\frac{n_{\rm M_1X_1}}{n_{\rm M_1X_1}^{(1o)}} n_{\rm NY}^{(1o)} + \frac{n_{\rm M_2X_2}}{n_{\rm M_1X_1}^{(2o)}} n_{\rm NY}^{(2o)} = n_{\rm NY} \tag{7}$$

at constant activities of H₂O and NY and within the range 0 ≤ $[n_{M_iX}/n_{M_iX_i}^{(io)}] \le 1$. Equations 6 and 7 can be generalized to the mixtures $M_1X_1 - \cdots - M_nX_n - (N_1Y_1)_{sat} - \cdots - (N_{n'}Y_{n'})_{sat} - H_2O$ in terms of the concentrations of its subsystems $M_iX_i-(N_1Y_1)_{sat}$ ···-($N_{n'}Y_{n'}$)_{sat}- H_2O (i = 1, 2, ..., n) of equal activities of all N_1Y_1 , ..., $N_{n'}Y_{n'}$ and H_2O

$$\sum_{i=1}^{n} \frac{n_{\text{M}_{i}X_{i}}}{n_{\text{M}_{i}X_{i}}^{(io)}} n_{\text{H}_{2}\text{O}}^{(io)} = n_{\text{H}_{2}\text{O}}$$
 (8)

$$\sum_{i=1}^{n} \frac{n_{M,X_i}}{n_{M,X_i}^{(no)}} n_{N_jY_j}^{(io)} = n_{N_jY_j} \quad (j = 1, 2, ..., n')$$
(9)

where $0 \le [n_{M_iX}/n_{M_iX_i}^{(io)}] \le 1$, $a_{H_2O} = const$, and $a_{N_iY_j} = const$. That is

$$\sum_{i=1}^{n} \frac{m_{M,X_i}}{m_{M,X_i}^{(io)}} = 1 \tag{10}$$

$$\sum_{i=1}^{n} \frac{m_{M,X_i}}{m_{M,X_i}^{(no)}} m_{N_j Y_j}^{(io)} = m_{N_j Y_j} \quad (j = 1, 2, ..., n')$$
 (11)

It is clear that for the mixtures M₁X₁-M₂X₂-H₂O eq 10 reduces to the well-known Zdanovskii's rule

$$\frac{m'_{M_1X_1}}{m'^{(10)}_{M_1X_1}} + \frac{m'_{M_2X_2}}{m'^{(20)}_{M_2X_2}} = 1$$
 (12)

where $m_{M_iX_i}^{\prime tio}$ (i=1 and 2) are the molalities of M_iX_i in M_iX_i — H_2O (i=1 and 2) at the water activity of the mixed solution M₁X₁-M₂X₂-H₂O of given molalities $m'_{M,X}$. **2.3. New Simple Equations for the Thermodynamic**

Properties. The thermodynamic relations for the system M_iX_i

 $(NY)_{sat}-H_2O$ (i=1 and 2) at constant temperature and pressure can be expressed as

$$\nu_{M_i} n_{MX_i}^{(io)} d\mu_{M_i}^{(io)} + \nu_{X_i} n_{M_i X_i}^{(io)} d\mu_{X_i}^{(io)} + n_{H_2O}^{(io)} d\mu_{H_2O}^{(io)} = 0$$

$$(\mu_{H_1O}^{(io)} = const \text{ and } \mu_{NY}^{(io)} = const)$$
(13)

If we define the chemical potential $\mu_{M_iX_i}^{(io)}=(1/\nu_{M_iX_i})(\nu_{Mi}\mu_{M_i}^{(io)}+\nu_X\mu_{X_i}^{(io)})$, then eq 13 can be rewritten as

$$v_{\mathrm{M,X}} n_{\mathrm{M,X}}^{(\mathrm{io})} d \ln \mu_{\mathrm{M,X}}^{(\mathrm{io})} + n_{\mathrm{H,O}}^{(\mathrm{io})} d \ln \mu_{\mathrm{H,O}}^{(\mathrm{io})} = 0$$

$$(\mu_{\rm H,O}^{(io)} = const \text{ and } \mu_{\rm NY}^{(io)} = const) \tag{14}$$

That is

$$\left(\frac{\partial \mu_{{\rm M}_i {\rm X}_i}^{\rm (io)}}{\partial \mu_{{\rm H}_2 {\rm O}}^{\rm (io)}}\right)_{n_{\rm MIX}^{\rm (io)}} = -\left(\frac{n_{{\rm H}_2 {\rm O}}^{\rm (io)}}{\nu_{{\rm M}_i {\rm X}_i} n_{{\rm M}_i {\rm X}_i}^{\rm (io)}}\right)_{\mu_{{\rm H}_2 {\rm O}}^{\rm (io)}}$$

$$(\mu_{\text{H-O}}^{(io)} = const \text{ and } \mu_{\text{NY}}^{(io)} = const)$$
 (15)

In literature, a similar equation has been given for the system $J-H_2O$.²² For the system $M_1X_1-M_2X_2-(NY)_{sat}-H_2O$, we reach

$$\begin{pmatrix}
\frac{\partial \mu_{M_{i}X_{i}}}{\partial \mu_{H_{2}O}} \\
\frac{\partial \mu_{H_{2}O}}{\partial \mu_{H_{2}O}}
\end{pmatrix}_{n_{MIXI,}^{n_{M2X2}}} = \begin{pmatrix}
\frac{\partial n_{H_{2}O}}{\nu_{M_{i}X_{i}}\partial n_{M_{i}X_{i}}} \\
\frac{\partial \mu_{H_{2}O}}{\partial \mu_{H_{2}O,ami'Xi}} \neq M_{i}X_{i}
\end{pmatrix}$$

$$(\mu_{H_{2}O} = const \text{ and } \mu_{NY} = const) \tag{16}$$

with $i' \in (1, 2)$. Combination of eqs 8, 15, and 16 gives (see Supporting Information for the detailed derivation)

$$\mu_{M_{i}X_{i}} = \mu_{M_{i}X_{i}}^{(io)} + RT \ln \frac{\nu_{M_{i}X_{i}} x_{M_{i}X_{i}}}{\nu_{M_{i}X_{i}} x_{M_{i}X_{i}} + \nu_{M_{i}X_{i}} x_{M_{i}X_{i}}}$$
(17)

$$a_{M_{i}X_{i}} = \frac{\nu_{M_{i}X_{i}}x_{M_{i}X_{i}}}{\nu_{M_{i}X_{i}}x_{M_{i}X_{i}} + \nu_{M_{i}X_{i}}x_{M_{i}X_{i}}} a_{M_{i}X_{i}}^{(io)}$$
(18)

and

$$f_{M_{i}X_{i}} = \frac{\nu_{M_{i}X_{i}}x_{M_{i}X_{i}}^{(io)}}{\nu_{M_{i}X_{i}}x_{M_{i}X_{i}} + \nu_{M_{i}X_{i}}x_{M_{i}X_{i}}} f_{M_{i}X_{i}}^{(io)}$$
(19)

where i=1 and 2, $a_{\rm H_2O}=const$, and $a_{\rm NY}=const$. a and $f_{\rm M_iX_i}$ are the activity and the activity coefficient on the mole fraction scale. Equation 18 is equivalent to

$$a_{\mathrm{M_{i}X_{i}}} = \frac{\nu_{\mathrm{M_{i}X_{i}}} m_{\mathrm{M_{i}X_{i}}}}{\nu_{\mathrm{M_{i}X_{i}}} m_{\mathrm{M_{i}X_{i}}} + \nu_{\mathrm{M_{2}X_{2}}} m_{\mathrm{M_{2}X_{2}}}} a_{\mathrm{M_{i}X_{i}}}^{(io)} \quad (i = 1 \text{ and } 2)$$

$$(a_{\text{H,O}} = const \text{ and } a_{\text{NY}} = const)$$
 (20)

 $f_{\mathrm{M,X_i}}$ is related to its molal value $\gamma_{\mathrm{M,X_i}}$ by $f_{\mathrm{M,X_i}} = \gamma_{\mathrm{M,X_i}} [1 + M_{\mathrm{H_2O}} / 1000(\sum_{i=1}^2 m_{\mathrm{M,X_i}} + m_{\mathrm{NY}})]$, where M is the molar mass. Therefore, eq 19 can be rewritten as

$$\gamma_{M_{i}X_{i}} = \frac{\nu_{M_{i}X_{i}} m_{M_{i}X_{i}}^{(io)}}{\nu_{M_{i}X_{i}} m_{M_{i}X_{i}} + \nu_{M_{i}X_{i}} m_{M_{i}X_{i}}} \gamma_{M_{i}X_{i}}^{(io)} \quad (i = 1 \text{ and } 2)$$

$$(a_{\text{H,O}} = const \text{ and } a_{\text{NY}} = const)$$
 (21)

For the unsaturated solution $M_1X_1-M_2X_2-H_2O$, eq 21 reduces to the following well-known equation derived by Vdovenko and Ryazanov¹⁴

$$\gamma'_{M_{i}X_{i}} = \frac{\nu_{M_{i}X_{i}} m'^{(io)}_{M_{i}X_{i}}}{\nu_{M_{i}X_{1}} m'_{M_{i}X_{1}} + \nu_{M_{2}X_{2}} m'_{M_{2}X_{2}}} \gamma'^{(io)}_{M_{i}X_{i}} \quad (i = 1 \text{ and } 2)$$

$$(a_{H.O} = const) \tag{22}$$

where the superscript ' denotes the quantity of M_iX_i in unsaturated solutions $M_iX_i-H_2O$ (i=1 and 2) and $M_1X_1-M_2X_2-H_2O$.

Now, let $\Delta_{\rm mix}G^{(io)}$, $\Delta_{\rm mix}H^{(io)}$, $\Delta_{\rm mix}S^{(io)}$, and $\Delta_{\rm mix}V^{(io)}$ denote the changes in Gibbs free energy, enthalpy, entropy, and volume accompanying the process of preparing the subsystems $M_iX_i-(NY)_{\rm sat}-H_2O$ (i=1 and 2). Let $\Delta_{\rm mix}G$, $\Delta_{\rm mix}H$, $\Delta_{\rm mix}S$, and $\Delta_{\rm mix}V$ represent the corresponding properties accompanying preparation of the system $M_1X_1-M_2X_2-(NY)_{\rm sat}-H_2O$ having the same activities of NY and H_2O as those of the subsystems $M_iX_i-(NY)_{\rm sat}-H_2O$ (i=1 and 2). Then, combination of eqs 8 and 9 with eq 18 and the thermodynamic relations (remembering the fact that $a_{\rm H_2O}=a_{\rm H,O}^{(1o)}=a_{\rm H,O}^{(2o)}$ and $a_{\rm NY}=a_{\rm NY}^{(1o)}=a_{\rm NY}^{(2o)}$) gives

$$\Delta_{\text{mix}}G = \sum_{i=1}^{2} \frac{n_{\text{M}_{i}X_{i}}}{n_{\text{M}_{i}X_{i}}^{(io)}} \Delta_{\text{mix}}G^{(io)} + RT \sum_{i=1}^{2} \nu_{\text{M}_{i}X_{i}} n_{\text{M}_{i}X_{i}} \ln \frac{\nu_{\text{M}_{i}X_{i}} x_{\text{M}_{i}X_{i}}}{\nu_{\text{M}_{2}X_{2}} x_{\text{M}_{2}X_{2}} + \nu_{\text{M}_{1}X_{1}} x_{\text{M}_{1}X_{1}}}$$
(23)

$$\Delta_{\text{mix}}H = \frac{n_{\text{M}_1X_1}}{n_{\text{M}_1X_1}^{(1o)}} \Delta_{\text{mix}}H^{(1o)} + \frac{n_{\text{M}_2X_2}}{n_{\text{M}_2X_2}^{(2o)}} \Delta_{\text{mix}}H^{(2o)}$$
(24)

$$\Delta_{\text{mix}}V = \frac{n_{\text{M}_1X_1}}{n_{\text{M}_1X_1}^{(1o)}} \Delta_{\text{mix}}V^{(1o)} + \frac{n_{\text{M}_2X_2}}{n_{\text{M}_2X_2}^{(2o)}} \Delta_{\text{mix}}V^{(2o)}$$
(25)

$$\Delta_{\text{mix}} S = \sum_{i=1}^{2} \frac{n_{\text{M},X_{i}}}{n_{\text{M},X_{i}}^{(io)}} \Delta_{\text{mix}} S^{(io)} + R \sum_{i=1}^{2} \nu_{\text{M},X_{i}} n_{\text{M},X_{i}} \ln \frac{\nu_{\text{M},X_{i}} x_{\text{M},X_{i}}}{\nu_{\text{M},X_{i}} x_{\text{M},X_{i}} + \nu_{\text{M},X_{i}} x_{\text{M},X_{i}}}$$
(26)

$$C_{\rm P} = \frac{n_{\rm M_1X_1}}{n_{\rm M,X}^{(1o)}} C_{\rm P}^{(1o)} + \frac{n_{\rm M_2X_2}}{n_{\rm M,X}^{(2o)}} C_{\rm P}^{(2o)}$$
(27)

$$d = \frac{y_{M_1 X_1} + y_{M_2 X_2}}{\sum_{i=1}^{2} (y_{M_i X_i} / d^{(io)})}$$
(28)

with $y_{\text{M,X}_i} = (n_{\text{M,X}}/n_{\text{M,X}}^{(io)}) n_{\text{H,O}}^{(io)} M_{\text{H2O}} + n_{\text{M,X}_i} M_{\text{M_iX}_i} + (n_{\text{M_iX}_i}/n_{\text{M_iX}_i}^{(io)}) n_{\text{NY}}^{(io)} M_{\text{NY}}$, where C_{P} and $C_{\text{P}}^{(io)}$ are the specific heat capacities. d and $d^{(io)}$ denote the densities. Note that $n_{\text{M,X}_i}/n_{\text{M,X}_i}^{(io)}$ and n in eqs 23–28 can be replaced by $m_{\text{M,X}_i}/m_{\text{M,X}_i}^{(io)}$ and m, respectively, and that under this condition eqs 23–26 are the changes in the Gibbs

free energies, enthalpy, entropy, and volume of mixing per kilogram of solvent, respectively.

For the unsaturated solutions, eqs 23–28 reduce to the simple predictive equations for the Gibbs free energy, thermal properties, and volumetric properties of unsaturated solution M_1X_1 – M_2X_2 – H_2O from the properties of its subsystems M_iX_i – H_2O (i=1 and 2) of equal water activities, and the equations reproduced from eqs 27 and 28 have been shown to be in good agreement with the experimental results reported in the literature. 10,11

3. Comparisons with the Experimental Measurements and the Pitzer Equations

3.1. Justification of the Basic Assumption. According to the Pitzer equation, 20,21 the Debye-Hückel contribution to the osmotic coefficient $\phi_{\rm H,O}^{\rm DH}$ can be determined from

$$\phi_{\text{H}_2\text{O}}^{\text{DH}} = \frac{2}{\sum_{i} \nu_{\text{M},\text{X}_i} m_{\text{M},\text{X}_i} + \nu_{\text{NY}} m_{\text{NY}}} \frac{-A^{\phi} I^{3/2}}{1 + b I^{1/2}}$$
(29)

where I is the molal ionic strength (mol kg⁻¹), and A^{ϕ} is the molal Debye–Hückel coefficient (0.3915 at 298.15 K). b is a universal parameter with the value 1.2 kg^{1/2} mol^{-1/2}. Therefore, $a_{\rm H,O}^{\rm DH}$ can be calculated from eq 29 and

$$\ln a_{\rm H_2O}^{\rm DH} = - \, M_{\rm H_2O} \phi^{\rm DH} (\sum_i \nu_{\rm M_i X_i} m_{\rm M_i X_i} + \nu_{\rm NY} m_{\rm NY}) \eqno(30a)$$

The average deviation $\Delta_{\rm H_2O}^{(io),\rm DH}$ for the saturated solution $M_1X_1-M_2X_2-(NY)_{sat}-H_2O$ from the relation $a_{\rm H_2O}^{(io),\rm DH}/a_{\rm H_2O}^{\rm DH}=1$ is then defined as

$$\sum_{N} \left| \frac{a_{\rm H_2O}^{(io),\rm DH}}{a_{\rm H_2O}^{\rm DH}} - 1 \right|$$

$$\Delta_{\rm H_2O}^{(io),\rm DH} = 100 \times \frac{1}{N}$$
(30b)

where N is the number of experimental data points. The function $\Delta'_{\mathrm{H_2O}}^{(io),\mathrm{DH}}$ for the unsaturated solutions is similarly defined.

The calculated values of $a'_{\rm H_2O}^{\rm DH}$ (= $-M_{\rm H_2O}\phi'^{\rm DH}\Sigma_i \nu_{\rm M,X} m'_{\rm M,X}$) for 24 ternary unsaturated systems $M_1 X_1 - M_2 X_2 - H_2O$ at 298.15 K and those of $a'_{\rm H_2O}^{\prime (io), \rm DH}$ for their binary systems $M_i X_i - H_2O$ (i=1 and 2) of equal water activity are shown in Table S1 (Supporting Information). The values of $\Delta'_{\rm H_2O}^{\prime (io), \rm DH}$ are as follows: (1) $0.01\% \le \Delta'_{\rm H_2O}^{\prime (1o), \rm DH} \le 0.12\%$ and $0.02\% \le \Delta'_{\rm H_2O}^{\prime (2o), \rm DH} \le 0.12\%$ within the range $0.1 \le I \le 4.2$ mol kg⁻¹ for the (1:1 + 1:1) electrolyte mixtures, including NaCl-KCl-H₂O, NaCl-LiCl-H₂O, NaCl-NaClO₄-H₂O, and NaCl-NaNO₃-H₂O. (2) $0.09\% \le \Delta'_{\rm H_2O}^{\prime (1o), \rm DH} \le 0.84\%$ and $0.36\% \le \Delta'_{\rm H_2O}^{\prime (2o), \rm DH} \le 1.36\%$ within the range $0.22 \le I \le 4.92$ mol kg⁻¹ for the first 13 (1:1 + 1:2) electrolyte mixtures, including NaCl-CaCl₂-H₂O, NaCl-BaCl₂-H₂O, NaCl-MgCl₂-H₂O, NaCl-SrCl₂-H₂O, NaCl-BaCl₂-H₂O, NaCl-MgCl₂-H₂O, NaCl-SrCl₂-H₂O, HCl-BaCl₂-H₂O, HCl-CaCl₂-H₂O, HCl-CaCl₂-H₂O, HCl-MnCl₂-H₂O, HCl-SrCl₂-H₂O, HCl-MnCl₂-H₂O, HCl-BaBr₂-H₂O, HCl-SrCl₂-H₂O, HCl-MnCl₂-H₂O, HCl-BaBr₂-H₂O, HCl-SrCl₂-H₂O, and HBr-MgBr₂-H₂O. Note that the $\Delta'_{\rm H_2O}^{\rm (io), DH}$ values for these solutions are in general less than 0.60%. (3) $(2.96\% \le \Delta'_{\rm H_2O}^{\prime (1o), \rm DH} \le 4.08\%$, and $0.55\% \le \Delta'_{\rm H_2O}^{\prime (2o), \rm DH} \le 1.0\%$ within the range $0.70 \le I \le 7.6$ mol kg⁻¹) and $(6.43\% \le \Delta'_{\rm H_2O}^{\rm (1o), \rm DH} \le 13.78\%$ and $2.0\% \le \Delta'_{\rm H_2O}^{\rm (2o), DH} \le 3.25$ within the range $0.0 \le I \le 16.8$ mol kg⁻¹) for the ternary

systems KCl-CdCl₂-H₂O and KI-CdI₂-H₂O. (4) 0.13% \leq $\Delta'^{(10),DH}_{\rm H_2O}$ \leq 1.85% and 0.58% \leq $\Delta'^{(20),DH}_{\rm H_2O}$ \leq 1.76% within the range $0.22 \le I \le 7.8 \text{ mol kg}^{-1}$ for the (1:1+1:3), (1:1+1:4), and (1:2 + 1:3) electrolyte mixtures, including HCl-LaCl₃-H₂O, HCl-SmCl₃-H₂O, NaCl-LaCl₃-H₂O, HCl-ThCl₄-H₂O, and BaCl₂-LaCl₃-H₂O. The results for the examined (1:1 + 1:1) mixtures within the whole examined experimental range are in good agreement with the assumption (in derivation of eqs 6–12) that $a_{\rm H_2O}^{\rm (io),DH}/a_{\rm H_2}^{\rm DH}=1$, suggesting that these mixtures conform to eq 12 exactly, which is in accordance with the isopiestic measurements. For the first 13 (1:1 + 1:2) electrolyte mixtures, the values of $\Delta^{\rm (fo),DH}_{\rm H_2O}$ are in general less than 0.60%, implying that these systems also conform to eq 12 very well when recalling the fact that eq 12 is expressed in terms of molality but eq 30 in ionic strength. In fact, isopiestic measurements show that NaCl-MCl2-H2O and HCl-MCl2- H_2O with M = Ba, Ca, Mg, and Sr obey eq 12 exactly or at least quite well within the whole examined molality ranges. The values of $\Delta_{\rm H,O}^{\prime (\rm io),DH}$ for the examined (1:1 + 1:3), (1:1 + 1:4), and (1:2 + 1:3) mixtures are larger than those of the (1:1 + 1:1) and (1:1 + 1:2) electrolyte mixtures; however, these systems may still conform to eq 12 well, as supported by the isopiestic results for NaCl-LaCl₃-H₂O²³ and BaCl₂-LaCl₃-H₂O (see Table 1), which is attributed to, as mentioned above, the fact that eq 12 is expressed in terms of molality but eq 30 in ionic strength.

The results for the complex-forming systems KCl-CdCl₂— H_2O and KI-CdI₂— H_2O are noticeable. Their $\Delta'^{(10),DH}_{H_2O}$ is considerably larger than $\Delta'^{(20),DH}_{H_2O}$, and $\Delta'^{(10),DH}_{H_2O}$ and $\Delta'^{(20),DH}_{H_2O}$ increase rapidly with increasing molality, indicating that the deviations of these systems from eq 12 increase progressively as the concentration increases and the deviations from the Zdanovskii's linear plot are not symmetrical (the largest deviation does not appear at the point where $m'_{M_1X_1} = m'_{M_2X_2}$). All these are substantiated by the isopiestic results reported in the literature such as those for the system KI-CdI₂-H₂O at 298.15 K²⁴ illustrated in Figure 1. It is seen from Table S1 and Figure 1 that, while $|\Delta'^{(10),DH}_{H_2O}|^{(20),DH}_{H_2O}| > 1$, the deviations from the Zdanovskii plot correspondingly increase toward the regions where $m'_{M_1X_1} = m'_{M_2X_2} = 1$

regions where $m'_{M_1X_1}/m'_{M_2X_2} > 1$. **3.2. Test Whether** $k_{M_1X_1}$ **Must Be Set Equal to** $v_{M_1X_1}$ McKay and Perring⁸ derived an equation for the activity coefficient of either solute in ternary aqueous solution $M_1X_1-M_2X_2-H_2O$

$$\ln \gamma_{\rm M_1X_1}' = \ln \gamma_{\rm M_1X_1}'^{(10)} + \ln \frac{k_{\rm M_1X_1} m_{\rm M_1X_1}'^{(10)}}{m^*} + \frac{1}{M_{\rm H_2O}} \frac{k_{\rm M_1X_1}}{v_{\rm M_1X_1}} \int_0^{\ln a_{\rm H_2O}'} \left\{ -\frac{1}{m^{*2}} \left(\frac{\partial m^*}{\partial \ln r_{\rm M_2X_2}} \right)_{a_{\rm H_2O}} - \frac{1}{m^*} + k_{\rm M_1X_1} m_{\rm M_1X_1}'^{(10)} \right\} d \ln a_{\rm H_2O}'$$
 (31)

where $\gamma'_{M_1X_1}$ is the activity coefficient of solute M_1X_1 in the mixture, and $\gamma'^{(1o)}_{M_1X_1}$ is its value in $M_1X_1-H_2O$ at the water activity of the mixture. $k_{M_1X_1}$ is an arbitrary proportionality constant for solute M_1X_1 . m^* is equal to $(k_{M_1X_1}m'_{M_1X_1}+k_{M_2X_2}m'_{M_3X_2})$, and it may be, for example, the ionic strength if $k_{M_1X_1}$ and $k_{M_2X_2}$ are suitably chosen (here, we denote $k_{M_1X_1}$ and $k_{M_2X_2}$ under this condition by $k'_{M_1X_1}$ and $k'_{M_2X_2}$ for convenience). 8 The ratio $r_{M_2X_2}$ is equal to $k_{M_2X_2}m'_{M_2X_2}/m^*$. For the unsaturated solution $M_1X_1-M_2X_2-H_2O$ obeying eq 12, eq 31 reduces to

$$\gamma'_{M_1X_1} = \frac{k_{M_1X_1} m'_{M_1X_1}}{k_{M_1X_1} m'_{M_1X_1} + k_{M_1X_1} m'_{M_1X_2}} \gamma'_{M_1X_1}^{(1o)}$$
(32)

 $TABLE\ 1:\ Is opiestic\ Results\ for\ the\ Systems\ BaCl_2(M_2X_2)-LaCl_3(M_3X_3)-H_2O\ and\ NaCl(M_1X_1)-BaCl_2(M_2X_2)-LaCl_3(M_3X_3)-H_2O\ at\ 298.15\ K,\ Taking\ Aqueous\ NaCl\ as\ the\ Reference\ Solution^a$

$m'_{\mathrm{M_1X_1}}$	$m'_{\mathrm{M_2X_2}}$	$m'_{\mathrm{M_3X_3}}$	$\gamma'^{\text{L}}_{\text{M}_{1}\text{X}_{1}}^{b}$	$\gamma'^{P}_{M_1X_1}^{c}$	$\gamma'^{L}_{M_2X_2}$	$\gamma_{\mathrm{M_2X_2}}^{\prime\mathrm{P}}$	$\gamma_{M_3X_3}^{\prime L}$	$\gamma_{M_3X_3}^{\prime P}$
]	$BaCl_2(M_2X_2)-Lac$					
			$m_{\rm M_1X_1}^{(10)\prime} = 0.5058,$	$m_{\rm M.X.}^{(20)\prime} = 0.3650$	$m'_{\rm M,X}^{(30)} = 0.2815$	5		
	0.1020	0.2027	11	22	0.4080	0.4053	0.2665	0.2856
	0.1582	0.1594			0.4096	0.4071	0.2676	0.2872
	0.1987	0.1281			0.4110	0.4084	0.2685	0.2889
	0.2086	0.1207			0.4109	0.4088	0.2684	0.2894
			$m_{\rm M_1X_1}^{\prime (10)} = 0.8142,$	$m_{\rm M, X}^{\prime (20)} = 0.5769$	$m_{\rm M.Y}^{(30)} = 0.4286$	5		
	0.1264	0.3349	M ₁ A ₁	M ₂ A ₂	^M ₃ Ω ₃ 4008	0.3963	0.2611	0.2771
	0.3016	0.2043			0.4000	0.3970	0.2606	0.2780
	0.3682	0.1550			0.3995	0.3976	0.2608	0.2785
	0.4252	0.1126			0.3991	0.3980	0.2600	0.2788
			$m_{\rm M_1X_1}^{\prime(10)} = 1.1726,$	$m_{\rm MAX}^{(20)} = 0.8134$	$m_{\rm MNN}^{\prime(30)} = 0.5825$	5		
	0.1215	0.4956	1.0004	M ₂ A ₂	0.4126	0.4035	0.2707	0.2846
	0.2268	0.4198	0.9994		0.4104	0.4021	0.2693	0.2830
	0.4060	0.2912	0.9992		0.4062	0.4004	0.2665	0.2809
	0.5126	0.2158	1.0005		0.4035	0.3998	0.2648	0.2801
			$m'_{\rm M_1X_1}^{(10)} = 1.5068,$	$m'^{(20)} = 1.0243$	$m'^{(30)} = 0.7160$)		
	0.1508	0.6109	$m_{\rm M_1X_1} - 1.5000,$	$m_{M_2X_2} - 1.0245$	0.4271	0.4180	0.2842	0.2995
					0.4271			
	0.3467	0.4731				0.4142	0.2807	0.2946
	0.5520	0.3292			0.4161	0.4105	0.2769	0.2904
	0.7022	0.2260			0.4109	0.4087	0.2734	0.2881
	0.05.60	0.6465	$m'_{\rm M_1X_1}^{(10)} = 1.7950,$	$m'_{\rm M_2X_2}^{(20)} = 1.2013$	$5, m'_{M_3X_3}^{(30)} = 0.820$	1	0.2000	0.2125
	0.2562	0.6465			0.4417	0.4315	0.2990	0.3135
	0.5185	0.4655			0.4337	0.4251	0.2936	0.3056
	0.8002	0.2754			0.4231	0.4202	0.2864	0.2990
	0.9860	0.1462			0.4185	0.4171	0.2836	0.2952
			$m'^{(1o)}_{M_1X_1} = 2.1425,$	$m_{\rm M_2X_2}^{\prime (20)} = 1.4124$	$k, m'_{M_3X_3}^{(30)} = 0.946$	7		
	0.3167	0.7332			0.4637	0.4521	0.3220	0.3363
	0.5860	0.5552			0.4524	0.4450	0.3142	0.3270
	0.8255	0.3926			0.4458	0.4387	0.3096	0.3188
	1.0962	0.2134			0.4347	0.4334	0.3018	0.3116
			$m'_{\rm M_1X_1}^{(1o)} = 2.4569,$	$m_{\rm M_2X_2}^{\prime (20)} = 1.6001$	$m'_{\rm M,X}^{(30)} = 1.0505$	5		
	0.1991	0.9186	11	22	0.4931	0.4786	0.3487	0.3672
	0.6012	0.6548			0.4760	0.4652	0.3367	0.3496
	1.0025	0.3910			0.4609	0.4536	0.3262	0.3350
	1.3996	0.1307			0.4461	0.4451	0.3155	0.3228
		NaCl(M_1X_1)-BaCl ₂ (M_2X_1)	X ₂)-LaCl ₃ (M ₃ X ₃)- H_2O , $\Delta'_{average} d =$	= 0.09%		
			$m_{\rm M_1X_1}^{\prime (10)} = 0.7351,$					
0.1659	0.2864	0.0896	0.6316	0.6421	0.4064	0.4033	0.2644	0.2885
0.2864	0.1726	0.1100	0.6385	0.6489	0.4109	0.4056	0.2671	0.2948
0.2015	0.3015	0.0588	0.6336	0.6403	0.4077	0.4051	0.2656	0.2918
0.0988	0.3419	0.0837	0.6280	0.6391	0.4041	0.4020	0.2629	0.2858
0.0700	0.5417	0.0657					0.202)	0.2030
0.2743	0.5936	0.3285	$m'^{(10)}_{M_1X_1} = 1.8868,$ 0.6882	$m'_{M_2X_2}^{(60)} = 1.2544$ 0.7020	$k, m'_{M,X_3} = 0.856$ 0.4276	9 0.4230	0.2942	0.3085
0.4164	0.3778	0.4112	0.6942	0.7106	0.4315	0.4228	0.2967	0.3122
0.3155 0.6349	0.2498 0.3550	0.5436 0.3271	0.7056 0.6885	0.7296 0.6980	0.4385 0.4276	0.4271 0.4187	0.3016 0.2942	0.3157 0.3128
0.001)	0.5550	0.5271					0.27 12	0.5120
0.6456	0.8976	0.2526	$m'^{(10)}_{M_1X_1} = 2.6308,$ 0.7306	$m_{M_2X_2} = 1.7088$	$m_{M_3X_3} = 1.1082$ 0.4594	0.4571	0.3287	0.3471
0.4981	1.1120	0.1776	0.7350	0.7365	0.4551	0.4566	0.3256	0.3428
1.2603	0.5782	0.1776	0.7324	0.7303	0.4536	0.4515	0.3248	0.3428
0.6195	0.6131	0.4486	0.7608	0.7630	0.4706	0.4608	0.3370	0.3542

^a Results in mol/kg. ^b Calculated from eq 22. ^c Calculated from the Pitzer equation. ^d The average experimental deviation from eq 12, $\Delta'_{average} = 100 \times \sum_{N} |m'_{M_1X_1}/m'^{(10)}_{M_1X_1} + m'_{M_2X_2}/m'^{(20)}_{M_2X_2} + m'_{M_3X_3}/m'^{(30)}_{M_3X_3} - 1|/N$, where N is the number of experimental data points.

However, according to eq 21, the value of $\gamma'_{M_iX_i}$ for the unsaturated solution $M_1X_1-M_2X_2-H_2O$ obeying eq 12 is related to the $\gamma'^{(io)}_{M_iX_i}$ values of its subsystems $M_iX_i-H_2O$ (i=1 and 2) by eq 22, that is, $k_{M_iX_i}$ is not an arbitrary constant, and for eq 32 to hold, it is necessary that $k_{M_iX_i}=v_{M_iX_i}$ under isopiestic equilibrium. The 18 electrolyte solutions shown in Table 2 conform to eq 12 well, and thus, the activity coefficients of each solute in these systems are calculated from eq 22 and eq

32 with $k_{\mathrm{M,X_i}} = k_{\mathrm{M,X_i}}^I$ and then compared with the experimental results. ^{23,25–42} An inspection of the second and third columns of Table 2 reveals that eq 22 is in good agreement with the experimental results for all the systems being examined. Note that the present comparisons are limited to the cases where the Zdanovskii's rule works. However, eq 32 with $k_{\mathrm{M,X_i}} = k_{\mathrm{M,X_i}}^I$ shows significant deviations from the experimental results for all the examined systems except for the mixed solutions of 1:1

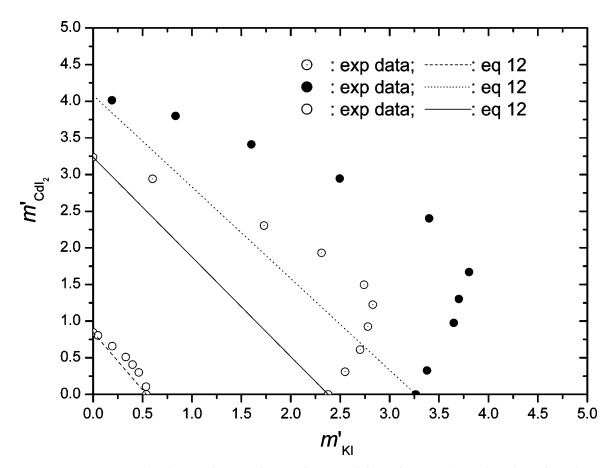


Figure 1. Deviations from the Zdanovskii's linear isopiestic plot for the system $KI-CdI_2-H_2O$ at 298.15 $K.^{24}$

TABLE 2: Values of the Δ'_{γ} Functions for the 18 Ternary Electrolyte Solutions at 298.15 K^a

$M_1X_1-M_2X_2-H_2O$	$\Delta'_{\gamma, M1X1}$	$\Delta'_{\gamma, ext{M2X2}}$	$\begin{array}{c}I_{\rm max}\\{\rm mol}\;{\rm kg}^{-1}\end{array}$	$k_{\mathrm{M_{1}X_{1}}}^{I}$	$k_{\mathrm{M_2X_2}}^I$
NaCl-KCl-H ₂ O ^{25 b}	0.0172	0.0172	4.2	1	1
NaCl-LiCl-H ₂ O ²⁶	0.0102	0.0102	3.0	1	1
NaCl-NaNO ₃ -H ₂ O ²⁷	0.0043	0.0043	3.0	1	1
NaCl-NaClO ₄ -H ₂ O ²⁷	0.0176	0.0176	3.2	1	1
NaCl-BaCl ₂ -H ₂ O ²⁷	0.0040	0.2296	5.0	1	3
NaCl-CaCl ₂ -H ₂ O ²⁷	0.0032	0.1260	1.2	1	3
NaCl-MgCl ₂ -H ₂ O ²⁷	0.0041	0.0868	5.2	1	3
NaCl-SrCl ₂ -H ₂ O ²⁷	0.0025	0.1969	3.0	1	3
HCl-BaCl ₂ -H ₂ O ²⁸	0.0134	0.2048	2.0	1	3
HCl-CaCl ₂ -H ₂ O ²⁹	0.0117	0.1866	4.8	1	3
HCl-CoCl ₂ -H ₂ O ³⁰	0.0022	0.1747	2.0	1	3
HCl-SrCl ₂ -H ₂ O ³¹	0.0050	0.2436	4.0	1	3
HCl-MnCl ₂ -H ₂ O ³²	0.0058	0.1585	2.5	1	3
HBr-CaBr ₂ -H ₂ O ³³	0.0069	0.2052	2.0	1	3
HBr-MgBr ₂ -H ₂ O ³⁴	0.0051	0.2326	2.5	1	3
HCl-LaCl ₃ -H ₂ O ³⁵	0.0165	0.2820	3.0	1	6
HCl-SmCl ₃ -H ₂ O ³⁶	0.0028	0.1932	2.5	1	6
HCl-ThCl ₄ -H ₂ O ³⁷	0.0042	0.1455	1.0	1	10

 $^a\Delta'_{\gamma,\mathrm{MIX1}}$ and $\Delta'_{\gamma,\mathrm{M2X2}}$ are the mean standard deviations of the predictions of eqs 22 and 32 with $k_{\mathrm{M,X_i}} = k_{\mathrm{M,X_i}}^J$ from the experimental results $(\Delta'_{\gamma,\mathrm{MiXi}} = \sum_N |\gamma'^{\mathrm{Pred}}_{\mathrm{M,X_i}} - \gamma'^{\mathrm{Exp}}_{\mathrm{M,X_i}}|/N$, where N is the experimental data points). b Reference.

electrolytes, of which $k_{M_iX_i} = \nu_{M_iX_i}$ (eq 32 is equal to eq 22). Therefore, the results from Table 2 substantiate that $k_{M_iX_i}$ is not an arbitrary constant and must be set equal to $\nu_{M_iX_i}$.

Table S2 (Supporting Information) shows $X_{M_1,N_2}^{(O),DH}$ and $a_{H_2,O}^{OB}$ for the system NaCl(M₁X₁)-BaCl₂-(M₂X₂)-LaCl₃(M₃X₃)-H₂O and its three binary subsystems at 298.15 K. The results are $\Delta_{H_2,O}^{(10),DH} = 1.5\%$, $\Delta_{H_2,O}^{(20),DH} = 0.24\%$, and $\Delta_{H_2,O}^{(30),DH} = 1.22\%$. These results along with those shown in Table S1 for BaCl₂(M₂X₂)-LaCl₃(M₃X₃)-H₂O suggest that both these systems may obey eq 12 well, which is supported by their isopiestic behavior at 298.15 K shown in Table 1. Because the systems NaCl(M₁X₁)-BaCl₂(M₂X₂)-H₂O and NaCl(M₁X₁)-LaCl₃(M₃X₃)-H₂O also obey eq 12 very well, ^{18,23} the activity coefficients of the solutes in these systems are calculated from eq 22. The Pitzer's parameters, Table 3, are determined from the resulting $\gamma_{M_2X_2}'$ and $\gamma_{M_3X_3}'$ in three ternary systems and then are used to give predictions for the activity coefficients of each solute in NaCl(M₁X₁)-BaCl₂(M₂X₂)-LaCl₃(M₃X₃)-H₂O at 298.15 K. The results are compared in Table 1 with those from eq 22, and the agreement is good. Note

TABLE 3: Pitzer Parameters Determined from the $\gamma'_{\mathrm{M,X_2}}$ in the Ternary Systems NaCl(M₁X₁)–BaCl₂(M₂X₂)–H₂O, ¹⁸ LaCl₃ (M₁X₁)–BaCl₂(M₂X₂)–H₂O, and NaCl(M₁X₁)–LaCl₃(M₂X₂)–H₂O²³ at 298.15 K

solute	β ⁽⁰⁾	$eta^{(1)}$	C^{ϕ}
NaCl	0.0519	0.3614	0.010
$BaCl_2$	0.2792	1.4387	0.0259
LaCl ₃	0.5889	5.600	0.0238
$ heta_{ ext{Na,Ba}} \ ext{(kg mol}^{-1}) \ 0.0076$	$ heta_{ m Na,La} \ ({ m kg\ mol^{-1}}) \ 0.3479$	$ heta_{ m Ba,La} \ ({ m kg\ mol^{-1}}) \ 0.02775$	
$\psi_{ ext{Na,Ba,Cl}} \ ext{(kg}^2 ext{ mol}^{-2} ext{)} \ 0.0187$	$\psi_{ ext{Na,La,Cl}} \ ext{(kg}^2 ext{ mol}^{-2}) \ -0.070$	$\psi_{ ext{Ba,La,Cl}} \ (ext{kg}^2 ext{ mol}^{-2}) \ -0.0185$	

that, while the tests of eq 12 reported in the literature are in general limited to (1:1+1:1), $^{39}(1:1+1:2)$, $^{18}(1:1+1:3)$, $^{23}(1:2+1:2)$, 40 and (2:2+1:2), 41 electrolyte mixtures, the present results show that the simple equation also holds for the mixtures of (1:2+1:3) and (1:1+1:2+1:3) electrolytes.

3.3. Test of Novel Linear Isopiestic Relations and the Novel Simple Equation for Activity Coefficient. The isopiestic behavior of the saturated solution $M_1X_1-M_2X_2-(NY)_{sat}-H_2O$ can be described by eqs 10 and 11. In this study, the experimental deviations from these equations are defined by $\Delta_0 = m_{M_1X_1}/m_{M_1X_1}^{(1o)} + m_{M_2X_2}/m_{M_2X_2}^{(2o)} - 1 \text{ and } \Delta_1 = (m_{M_1X_1}/m_{M_1X_1}^{(1o)})$ $m_{NY}^{(1o)} + (m_{M_2X_2}/m_{M_2X_2}^{(2o)})m_{NY}^{(2o)} - m_{NY} \text{ at constant activities of water and NY and within the range } 0 \leq [m_{M_1X_1}/m_{M_1X_1}^{(io)}] \leq 1.$

Tables 4 and S3 show the isopiestic results and the calculated values of $a_{H,O}^{DH}$ for the saturated system NaCl(M₁X₁)-LaCl₃- (M_2X_2) —BaCl₂·2H₂O_(sat)((NY)_{sat})—H₂O at 298.15 K and those of $a_{\rm H,O}^{(10),\rm DH}$ and $a_{\rm H,O}^{(20),\rm DH}$ for its subsystems, NaCl(M₁X₁)—BaCl₂·2H₂O_(sat)((NY)_{sat})—H₂O and LaCl₃ (M₂X₂)—BaCl₂·2H₂O_(sat)((NY)_{sat})—H₂O. The values of $\Delta_{\rm H_2O}^{(10),\rm DH}$ and $\Delta_{\rm H_2O}^{(20),\rm DH}$ are 1.30% and 0.00% and the requirement of $\Delta_{\rm H_2O}^{(10),\rm DH}$ and $\Delta_{\rm H_2O}^{(20),\rm DH}$ are 1.30% (AEN) and 0.92%, and the maximum values of $|\Delta_0|$ and $|\Delta_1^{Exp}|$ (Δ_1^{Exp}) = $(m_{\text{M}_1\text{X}_1}/m_{\text{M}_1\text{X}_1}^{(1\text{o})})m_{\text{NY}}^{(1\text{o})} + (m_{\text{M}_2\text{X}_2}/m_{\text{M}_3\text{X}_2}^{(2\text{o})})m_{\text{NY}}^{(2\text{o})} - m_{\text{NY}})$ are 0.0012 and 0.0042, respectively, where the superscript Exp indicates that the solubilities in the quaternary system are calculated from the new linear relation along with the $m_{NY}^{(io)}$ determined experimentally. The solubilities of NY in ternary and quaternary saturated solutions are also calculated from the Pitzer equation along with the Pitzer's parameters determined above. The results $(m_{\rm NY}^{(1{\rm o}),P},\,m_{\rm NY}^{(2{\rm o}),P},$ and $m_{\rm NY}^{P}$ shown in the fifth column of Table 4) agree well with the experimental data. The resulting solubilities $(m_{\text{NY}}^{(1\text{o}),\text{P}})$ and $m_{\text{NY}}^{(2\text{o}),\text{P}})$ are substituted into eq 11 to provide the solubilities $m_{\text{NY}}^{\text{L,P}}$ $(m_{\text{NY}}^{\text{L,P}} = (m_{\text{M_1X_1}}/m_{\text{M_1X_1}}^{(1\text{o})})m_{\text{NY}}^{(1\text{o}),\text{P}} + (m_{\text{M_2X_2}}/m_{\text{M_2X_2}}^{(2\text{o})})$ $m_{\rm NY}^{(20),\rm P}$) of NY in the quaternary saturated solutions, where the superscript L,P implies that the solubilities in the quaternary system are calculated from the new linear equation together with the $m_{\rm NY}^{(10),\rm P}$ and $m_{\rm NY}^{(20),\rm P}$ (in the subsystems) calculated from the Pitzer equation. The results $(m_{NY}^{L,P})$ are in good agreement with the predictions (m_{NY}^P) of the Pitzer equation, with $\Delta_1^{L,P}$ ($\Delta_1^{L,P} = (m_{M_1X_1}/m_{M_1X_1}^{(10)})m_{NY}^{(10)} + (m_{M_2X_2}/m_{M_2X_2}^{(20)})m_{NY}^{(20),P} - m_{NY}^P$) being less

The above comparisons show that eqs 10 and 11 are in good agreement with the experimental results. Therefore, $\gamma_{M_1X_1}^{(1o),P}$ and $\gamma_{M_2X_2}^{(2o),P}$ are calculated from the Pitzer equation and then substituted into eq 21 to yield $\gamma_{M_1X_1}^{L,P}$ and $\gamma_{M_2X_2}^{L,P}$, in NaCl(M₁X₁)—LaCl₃(M₂X₂)—BaCl₂·2H₂O_(sat)((NY)_{sat})—H₂O, where the superscript L,P indicates that the activity coefficient is calculated from the new simple equation along with the $\gamma_{M_1X_1}^{(1o),P}$ and $\gamma_{M_2X_2}^{(2o),P}$

TABLE 4: Isopiestic Results (mol/kg) for the Saturated Systems NaCl(M₁X₁)-LaCl₃(M₂X₂)-BaCl₂·2H₂O_(sal)- ((NY)_{sal})-H₂O at 298.15 K, Taking Aqueous NaCl as the Reference Solution

$m_{\mathrm{M_1X_1}}$	$m_{ m M_2X_2}$	$m_{ m NY}^{ m Exp}$	$m_{\mathrm{NY}}^{\mathrm{L,Exp}}$	$m_{\mathrm{NY}}^{\mathrm{P}}{}^{b}$	$m_{ m NY}^{ m L,P}{}^c$	$a_{ m H_2O}$
3.0736^{d}	0	0.7442^{d}		0.7464^{d}		0.8420
0	1.3920^{e}	0.3816^{e}		0.3850^{e}		
0.3146	1.2502	0.4162	0.4189	0.4203	0.4202	
0.7128	1.0682	0.4620	0.4656	0.4685	0.4671	
1.3660	0.7726	0.5406	0.5430	0.5458	0.5449	
2.0678	0.4560	0.6276	0.6255	0.6297	0.6288	
1.5065^{d}	0	1.2002^{d}		1.2025^{d}		0.8746
0	0.7186^{e}	0.9970^{e}		0.9925^{e}		
0.3182	0.5885	1.0691	1.0725	1.0744	1.0695	
0.6019	0.4485	1.1012	1.1031	1.1058	1.0990	
0.9107	0.2942	1.1336	1.1362	1.1380	1.1316	
1.2528	0.1210	1.1660	1.1621	1.1643	1.1602	
0.9476^{d}	0	1.4542^{d}		1.4631^{d}		0.8869
0	0.4980^{e}	1.2429^{e}		1.2499^{e}		
0.1509	0.4183	1.2788	1.2751	1.2824	1.2829	
0.2332	0.3752	1.2969	1.2942	1.3000	1.3017	
0.4481	0.2622	1.3426	1.3420	1.3461	1.3498	
0.6250	0.1693	1.3837	1.3811	1.3856	1.3896	
0.4480^{d}	0	1.6481^{d}		1.6485^{d}		0.8950
0	0.2623^{e}	1.5102^{e}		1.5146^{e}		
0.07282	0.2196	1.5362	1.5320	1.5378	1.5360	
0.1240	0.1896	1.5496	1.5478	1.5528	1.5512	
0.2196	0.1340	1.5825	1.5796	1.5805	1.5820	
0.3145	0.07806	1.6089	1.6065	1.6095	1.6078	

 a Calculated from eq 11 along with $m_{\rm NY}^{(io),\rm Exp}$ determined experimentally. b Calculated from the Pitzer equation. c Calculated from eq 11 together with $m_{\rm NY}^{(1o),\rm P}$ (the solubility of NY in M₁X₁-(NY)_{sat}-H₂O) and $m_{\rm NY}^{(2o),\rm P}$ (the solubility of NY in M₂X₂-(NY)_{sat}-H₂O) calculated from the Pitzer equation. d The values for $m_{\rm M,X_1}^{(1o)}$, $m_{\rm NY}^{(1o),\rm Exp}$, and $m_{\rm NY}^{(1o),\rm P}$, respectively. e The values for $m_{\rm M,X_1}^{(2o)}$, $m_{\rm NY}^{(2o),\rm Exp}$, and $m_{\rm NY}^{(2o),\rm P}$, respectively.

calculated from the Pitzer equation. The results are compared in Table 5 with the predictions of the Pitzer equation ($\gamma_{M_1X_1}^P$ and $\gamma_{M_2X_2}^P$), and the agreement is good. The above treatments do not include the cases where the examined rules are not accurate

4. Conclusions

The semi-ideal solution theory has been presented to describe the thermodynamic behavior of the multicomponent electrolyte solutions $M_1X_1 - \cdots - M_nX_n - (N_1Y_1)_{sat} - \cdots - (N_n'Y_{n'})_{sat} - H_2O$ at constant activities of all N_1Y_1 , ..., $N_{n'}Y_{n'}$, and H_2O . The theory proves that, under the condition of constant activities of all N₁Y₁, •••, $N_{n'}Y_{n'}$, and H_2O , the average hydration numbers characterizing the ion-solvent interactions have the same values in the mixture as in the subsystems, and it assumes that the contributions from the ion-ion interactions to the solvent activity are also the same in the mixture as in the subsystems if there exists no complex formation. Therefore, the process of mixing the nonideal electrolyte mixtures $M_iX_i-(N_1Y_1)_{sat}-\cdots-(N_{n'}Y_{n'})_{sat}-\cdots$ $H_2O(i = 1, 2, ..., n)$ at constant activities of all $N_1Y_1, \dots, N_{n'}Y_{n'}$ and H₂O is as simple as that of mixing the ideal mixtures M_iX_i- $(N_1Y_1)_{sat} - \cdots - (N_{n'}Y_{n'})_{sat} - H_2O \ (i = 1, 2, ..., n)$ of equal mole fractions of all N_1Y_1 , ..., $N_{n'}Y_{n'}$, and H_2O , so that the changes in thermodynamic properties accompanying the process of mixing the nonideal solutions obey the same linear iso-a relations as mixing the classical ideal solutions, including the linear concentration relations, the linear equations for changes in Gibbs free energy, enthalpy, entropy, thermal properties, and volumetric properties. From these linear iso-a relations, the well-known Zdanovskii's rule has been reproduced, and the

TABLE 5: Activity Coefficients in the Saturated Systems NaCl(M₁X₁)-LaCl₃(M₂X₂)-BaCl₂·2H₂O_(sat)((NY)_{sat})-H₂O at 298.15 K

$m_{ m M_1X_1}$	$m_{ m M_2X_2}$	$m_{ m NY}$				
mol kg ⁻¹	mol kg-1	mol kg-1	$\gamma_{M_1X_1}^{P}{}^a$	$\gamma_{\mathrm{M_{1}X_{1}}^{b}}^{\mathrm{L}}$	$\gamma_{\mathrm{M_2X_2}}^{\mathrm{P}}$	$\gamma_{\mathrm{M_2X_2}}^{\mathrm{L}}$
3.0736^{c}	0	0.7442^{c}	0.9031			
0	1.3920^{d}	0.3816^{d}			0.5796	
0.3146	1.2502	0.4162	0.9912	0.9742	0.5456	0.5665
0.7128	1.0682	0.4630	0.9936	0.9860	0.5582	0.5732
1.3660	0.7726	0.5406	0.9465	0.9536	0.5306	0.5542
2.0678	0.4560	0.6276	0.9196	0.9315	0.5377	0.5416
1.5065^{c}	0	1.2002^{c}	0.8192			
0	0.7186^{d}	0.9970^{d}			0.4171	
0.3182	0.5885	1.0700	0.8490	0.8255	0.4195	0.4012
0.6019	0.4485	1.1012	0.8434	0.8235	0.4118	0.4000
0.9107	0.2942	1.1336	0.8232	0.8234	0.4054	0.3996
1.2528	0.1210	1.1658	0.8028	0.8258	0.4008	0.4011
0.9476^{c}	0	1.4542^{c}	0.7786			
0	0.4980^{d}	1.2429^{d}			0.3860	
0.1509	0.4183	1.2788	0.7660	0.7476	0.3834	0.3892
0.2332	0.3752	1.2965	0.7665	0.7508	0.3821	0.3907
0.4481	0.2622	1.3426	0.7689	0.7590	0.3801	0.3950
0.6250	0.1693	1.3837	0.7721	0.7662	0.3796	0.3986
0.4480^{c}	0	1.6481^{c}	0.7572			
0	0.2623^{d}	1.5102^{d}			0.3585	
0.07282	0.2196	1.5362	0.6646	0.6626	0.3580	0.3632
0.1240	0.1896	1.5496	0.6768	0.6742	0.3574	0.3667
0.2196	0.1340	1.5825	0.7006	0.6958	0.3571	0.3696
0.3145	0.07806	1.6089	0.7242	0.7209	0.3565	0.3716

 a Calculated from the Pitzer equation. b Calculated from eq 21 with $\gamma_{\rm NY}^{(1o)}$ and $\gamma_{\rm NY}^{(2o)}$ calculated from the Pitzer equation. c The values for $m_{\rm M_1X_1}^{(1o)}$, and $m_{\rm NY}^{(1o)}$, respectively. d The values for $m_{\rm M_1X_1}^{(2o)}$ and $m_{\rm NY}^{(2o)}$, respectively.

value of the important parameter $k_{M_iX_i}$ in the McKay-Perring equation under isopiestic equilibrium has been theoretically determined.

The basic assumption made in the derivation of the novel linear isopiestic relations has proven to be exact or at least quite reasonable. As theoretically justified, the comparisons with the experimental results substantiate that k_{M,X_i} in the McKay Perring equation under isopiestic equilibrium must be set equal to $\nu_{M:X:}$. The novel linear relations have been shown to be in good agreement with the isopiestic measurements for the unsaturated systems BaCl2-LaCl3-H2O and NaCl-BaCl2-LaCl₃-H₂O and the saturated system NaCl-LaCl₃-BaCl₂· 2H₂O_(sat)-H₂O at 298.15 K. The new simple linear equation for $\gamma_{M_1X_1}$ and $\gamma_{M_2X_2}$ in $M_1X_1{-}M_2X_2{-}(NY)_{sat}{-}H_2O$ has been compared with the predictions of the Pitzer equation, and the agreement is good. Its reduced form for $\gamma'_{M_1X_1}$ and $\gamma'_{M_2X_2}$ in $M_1X_1-M_2X_2-H_2O$ and for $\gamma'_{M_1X_1}$, $\gamma'_{M_2X_2}$, and $\gamma'_{M_3X_3}$ in NaČl-BaCl₂-LaCl₃-H₂O has been shown to be in good agreement with the experimental results reported in the literature.

5. Experimental Section

All the examined chemicals are reagent grade and recrystal-lized twice from doubly distilled water. NaCl was dried under vacuum over $CaCl_2$ for 7 days at 423 K. $BaCl_2$ was dehydrated in an anhydrous HCl atmosphere rising from 298.15 to 573 K and treated by introducing purified argon gas at 573 K. The molalities of $LaCl_3$ stock solutions ware analyzed by EDTA and titration (of Cl^- with $AgNO_3$) methods.

The isopiestic apparatus and the sample cups used here are the same as those used in our previous studies.¹⁵ Preliminary experiments showed that equilibration could be achieved within 5 to 6 days. The real equilibration period for each run was then chosen as 9 days. At isopiestic equilibrium, the molality of each solute was determined by using the following procedure: (1)

Semi-Ideal Solution Theory

After weighing the equilibrium saturated samples, the liquid sample phase was withdrawn by a pipet fitted with a sintered-glass filter tip preheated slightly above 298.15 $\rm K^{42}$ and then was weighed and diluted. (2) All solutions were analyzed by 4–8 titrations of $\rm Cl^-$ with AgNO₃, with results agreeing to within $\pm 0.05\%$. (3) Calculation of the solute molalities was carried out by the following procedure.

Let w, w^{Eq} , and w_{total} denote the mass of initial unsaturated solution before equilibration, the mass of saturated equilibrium solution, and that of the saturated equilibrium solution withdrawn by the sintered-glass filter tip. Let n_{BaCl_2} and n_{M,X_i} (M_iX_i = NaCl and LaCl₃) represent the amount of BaCl₂ and unsaturated solute M_iX_i in a mass w of initial unsaturated solution, and $n_{\text{BaCl}_2}^{\text{S}}$ and $n_{\text{BaCl}_2}^{\text{Sd}}$ the amount of anhydrous solid BaCl₂ added to the sample cup before equilibration and that dissolved during equilibration. Then, the amount of Cl⁻, $n_{\text{total}}^{\text{Cl}^-}$, in a mass w_{total} of saturated solution can be expressed as

$$n_{\text{total}}^{\text{Cl}^-} = 2(n_{\text{BaCl}_2} + n_{\text{BaCl}_2}^{\text{Sd}}) w_{\text{total}} / w^{\text{Eq}}$$
 (33)

with

$$w^{\text{Eq}} = w + w_{\text{H},\text{O}}^{\text{Tr}} + M_{\text{BaCl}_2} n_{\text{BaCl}_2}^{\text{Sd}} - w_{\text{H},\text{O}}^{\text{Hy}}$$
 (34a)

$$w_{\rm H,O}^{\rm Hy} = 2M_{\rm H,O}(n_{\rm BaCl_2}^{\rm S} - n_{\rm BaCl_2}^{\rm Sd})$$
 (34b)

where $w_{\rm H_2O}^{\rm Tr}$ and $w_{\rm H_2O}^{\rm Hy}$ are the mass of water transported through the vapor phase during the equilibration and that needed to form the thermodynamically stable solid phase of BaCl₂· $2{\rm H_2O^{18}}$ at isopiestic equilibrium. $M_{\rm BaCl_2}$ is the molar mass of anhydrous barium chloride. Combining eqs 33 and 34, we obtain

$$n_{\text{BaCl}_2}^{\text{Sd}} = \frac{n_{\text{total}}^{\text{Cl}^-}(w + w_{\text{H}_2\text{O}}^{\text{Tr}} - 2M_{\text{H}_2\text{O}}n_{\text{BaCl}_2}^{\text{S}}) - 2w_{\text{total}}n_{\text{BaCl}_2}}{2w_{\text{total}} - n_{\text{total}}^{\text{Cl}^-}M_{\text{BaCl}_2} - 2M_{\text{H}_2\text{O}}n_{\text{total}}^{\text{Cl}^-}}$$
(35a)

The mass of water $(w_{\rm H_2O}^{\rm Eq})$ in a mass $w^{\rm Eq}$ of equilibrium solution is given by

$$w_{\text{H}_2\text{O}}^{\text{Eq}} = w_{\text{H}_2\text{O}} + w_{\text{H}_2\text{O}}^{\text{Tr}} - 2M_{\text{H}_2\text{O}}(n_{\text{BaCl}_2}^{\text{S}} - n_{\text{BaCl}_2}^{\text{S}})$$
 (35b)

where $w_{\rm H_2O}$ is the mass of water in a mass w of initial unsaturated solution. Because the molalities of M_iX_i and $BaCl_2$ of the initial unsaturated solutions are known, and the values of $w_{\rm H_2O}^{\rm Tr}$ and $n_{\rm total}^{\rm Cl^-}$ can be determined simply by weighing the samples at isopiestic equilibrium $(w_{\rm H_2O}^{\rm Tr}=w^{\rm Eq}-w)$ and by the titration measurements noted previously, the molality of each solute in NaCl–LaCl₃–BaCl₂·2H₂O_(sat)–H₂O can be determined by

$$m_{\text{M,X}_i} = \frac{n_{\text{M,X}_i}}{w_{\text{H,O}}^{\text{Eq}}} \quad (M_i X_i = \text{NaCl or LaCl}_3)$$
 (36a)

$$m_{\text{NY}} = \frac{n_{\text{BaCl}_2} + n_{\text{BaCl}_2}^{\text{Sd}}}{w_{\text{H-O}}^{\text{Eq}}} \quad (\text{NY} = \text{BaCl}_2 \cdot 2\text{H}_2\text{O}) \quad (36\text{b})$$

The results, the average between the duplicate cups for unsaturated solute and the mean of 4-8 replicate titration measurements for saturated solute in the duplicate cups, are reproducible to $\pm 0.05\%$ for the former and to $\pm 0.10\%$ for the latter

Acknowledgment. The authors thank the National Natural Science Foundation of China (20276037) and the 863 Program (2004AA616040) for financial support of the theoretical work. Valuable comments from the anonymous referees are also gratefully acknowledged.

Supporting Information Available: S1: Derivation of linear concentration relation. S2: Derivation of the simple equations. Also three tables of supporting data. This material is available free of charge via the Internet at http://pubs.acs.org.

Glossary

```
activity
              the molal Debye-Hückel coefficient
A^{\phi}
              the universal parameter in eq 29 with the value 1.2 kg1/2
b
                 mol^{-1/2}
C_{\rm P}
              specific heat capacity
d
              density
              the activity coefficient on the mole fraction scale
G^{\mathrm{DH}}
              the Gibbs energy resulted from the Debye-Hückel con-
G^{Hy}
              the Gibbs energy of the semi-ideal mixture of the resulting
                 species based on the mole fraction (x)
              average hydration number
              molal ionic strength (mol kg-1)
              the proportionality constant for solute MiXi in McKay-
k_{\text{M:X}}
                 Perring equation
K
              hydration equilibrium constant
              molality (mol kg-1)
m
              molar mass
M
              the electrolyte solute components present below their
M_iX_i
                 solubility limits
              mole number
              the amount of anhydrous solid BaCl2 dissolved during
                 equilibration
              the number of experimental data points
NY
              the electrolyte solute component present as saturated
                 solutions
R
              gas constant
              the mass of initial unsaturated solution before equilibration
w_{\rm H_2O}
              the mass of water in a mass w of initial unsaturated solution
              the mass of the saturated equilibrium solution withdrawn
                 by the sintered-glass-filter tip
w^{Eq}
              the mass of saturated equilibrium solution
              the mass of water needed to form the thermodynamically
                  stable solid phase of BaCl2 • 2H2O at isopiestic equilib-
W_{H_2O}^{Tr}
              the mass of water transported through the vapor phase
                 during equilibration
              mole fraction
              the changes in Gibbs free energy, enthalpy, entropy, and
(\Delta_{\min}G,
   \Delta_{\min}G^{(io)}),
                 volume accompanying the process of preparing the
                  system M<sub>1</sub>X<sub>1</sub>-M<sub>2</sub>X<sub>2</sub>-(NY)<sub>sat</sub>-H<sub>2</sub>O and its subsystems
   (\Delta_{mix}H,
   \Delta_{\rm mix}H^{(io)}),
                 M_iX_i-(NY)_{sat}-H_2O
   (\Delta_{mix}S,
   \Delta_{\text{mix}}S^{(io)}),
   (\Delta_{mix}V,
   \Delta_{\text{mix}} V^{(io)}
              the function defined by \Delta_0 = m_{\rm M_1X_1}/m_{\rm M_1X_1}^{(1{\rm o})} + m_{\rm M_2X_2}/m_{\rm M_2X_2}^{(2{\rm o})}
```

the function defined by $\Delta_1 = (m_{\rm M_1X_1}/m_{\rm M_1X_1}^{(1{\rm o})})m_{\rm NY}^{(1{\rm o})} + (m_{\rm M_2X_2}/m_{\rm M_2X_2}^{(2{\rm o})})m_{\rm NY}^{(2{\rm o})} - m_{\rm NY}$ the function defined by $\Delta_1^{\rm L,P} = (m_{\rm M_1X_1}/m_{\rm M_1X_1}^{(1{\rm o})})m_{\rm NY}^{(1{\rm o}),P} + (m_{\rm M_2X_2}/m_{\rm M_2X_2}^{(2{\rm o})})m_{\rm NY}^{(2{\rm o}),P} - m_{\rm NY}$

 $\Delta_{\rm H_2O}^{(io),\rm DH}$ the function defined by $\Delta_{\rm H,O}^{(io),\rm DH}=100\times \sum_{\rm M}(a_{\rm H_2O}^{(io),\rm DH}/$ $a_{\rm H_2O}^{\rm DH} - 1)/N$ charge Greek Symbols molal activity coefficient V φ osmotic coefficient ν salt stoichiometric coefficient chemical potential μ Subscripts average average property component indexes i, j, n, n'ideal solution mix property of mixing at constant temperature and pressure sat saturated solute(s) total total property

Superscripts

the quantity of M_iX_i in unsaturated solutions M_iX_i-H₂O (i = 1 and 2) and $M_1X_1-M_2X_2-\cdots-H_2O$

dilute infinite dilute behavior

DH the property resulted from the Debye-Hückel contribution

experimental property Exp.

free free quantity

Ну the property of the semi-ideal mixture of the resulting species based on the mole fraction (x)

ideal

L,P the property calculated using the linear relation $m_{NY}^{L,P}$ $(m_{\rm M_1X_1}/m_{\rm M_1X_1}^{(10)})m_{\rm NY}^{(10),P} + (m_{\rm M_2X_2}/m_{\rm M_2X_2}^{(20)})m_{\rm NY}^{(20),P}$

the properties of the components in the subsystems M_iX_i— (io) (NY)sat-H2O or MiXi-H2O

P the property calculated using the Pitzer equation

Pred predicted property

References and Notes

- (1) Zdanovskii, A. B. Tr. Solyanoi Lab., Vses. Inst. Galurgii, Akad. Nauk SSSR 1936, 6
 - (2) Stokes, R. H.; Robinson, R. A. J. Phys. Chem. 1966, 70, 2126.
 (3) Scatchard, G. J. Am. Chem. Soc. 1921, 43, 2387.
 (4) Scatchard, G. J. Am. Chem. Soc. 1921, 43, 2406.

 - (5) Stokes, R. H.; Robinson, R. A. J. Am. Chem. Soc. 1948, 70, 1870.
 (6) Robinson, R. A.; Stokes, R. H. J. Phys. Chem. 1962, 66, 506.

 - (7) Okubo, T.; Ise, N. J. Phys. Chem. 1970, 74, 4284.

- (8) McKay, H. A. C.; Perring, J. K. Trans. Faraday Soc. 1953, 49,
 - (9) Hu, Y. F. J. Chem. Soc., Faraday Trans. 1998, 94, 913.
 - (10) Hu, Y. F. Phys. Chem. Chem. Phys. 2000, 2, 2380.
- (11) Hu, Y. F. Bull. Chem. Soc. Jpn. 2001, 74, 47.
- (12) Hu, Y. F.; Lee, H. *Electrochim. Acta* 2003, 48, 1789.
 (13) Tang, I. N. *J. Geophys. Res.* 1997, 102, 1883.
- (14) Vdovenko, V. M.; Ryazanov, M. A. Sov. Radiochem. 1965, 7, 39.
- (15) (a) Hu, Y. F.; Wang, Z. C. J. Chem. Soc., Faraday Trans. 1998, 94, 3251. (b) Hu, Y. F. J. Phys. Chem. B 2003, 107, 13168.
 (16) Mikhailov, V. A. Russ. J. Phys. Chem. 1968, 42, 1414.
 (17) Rush, R. M.; Johnson, J. S. J. Phys. Chem. 1968, 72, 767.
- (18) Robinson, R. A.; Bower, V. E. J. Res. Natl. Bur. Stand., Sect. A: **1965**, *69A*, 19.
- (19) Rard, J. A. J. Chem. Thermodyn. 1989, 21, 539.
- (20) Pitzer, K. S. J. Phys. Chem. 1973, 77, 268.
 (21) Pitzer, K. S. In Activity Coefficients in Electrolyte Solutions, 2nd ed.; Pitzer, K. S., Ed.; CRC Press: Boca Raton, FL, 1991; p 75.
 - (22) Gokcen, N. A. J. Phys. Chem. 1960, 64, 401
- (23) Kingintsev, A. N.; Lukyanov, A. V. Russ. J. Phys. Chem. 1965, 39, 389.
- (24) Filippov, V. K.; Yakimov, M. A.; Makarevskii, V. M.; Luking, L. G. Russ. J. Inorg. Chem. 1971, 16, 1653.
 - (25) Huston, R.; Butler, J. N. Anal. Chem. 1969, 41, 1695
 - (26) Butler, J. N.; Huston, R.; Hsu, P. T. J. Phys. Chem. 1967, 71, 3294.
 (27) Lanier, R. D. J. Phys. Chem. 1965, 69, 3992.
- (28) Roy, R. N.; Rice, S. A.; Vogel, K. M.; Roy, L. N.; Millero, F. J. J. Phys. Chem. **1990**, *94*, 7706.
- (29) Roy, R. N.; Gibbons, J. J.; Owens, L. K. Bliss, G. A.; Hartley, J. J. J. Chem. Soc., Faraday Trans. I 1981, 78, 1405. (30) Khoo, K. H.; Lim, T. K.; Chan, C. Y. J. Chem. Soc., Faraday Trans.
- 1 **1978**, 74, 2037
- (31) Roy, R. N.; Gibbons, J. J.; Roy, L. M.; Farwell, G. D.; Smith, K.
- (32) Roy, R. N.; Gibbons, J. J.; Trower, J. K. J. Solution Chem. 1980, 9, 535
- (33) Khoo, K. H.; Lim, T. K.; Chan, C. Y. J. Chem. Soc., Faraday Trans. 1 **1979**, 75, 1067
- (34) Roy, R. N.; Lawson, M. L.; Nelson, E. J. Chem. Thermodyn. 1990, 22, 727
- (35) Roy, R. N.; Gibbons, J. J.; Peiper, J. C.; Pitzer, K. S. J. Phys. Chem. **1983**, 87, 2365
- (36) Roy, R. N.; Gibbons, J. J.; Peiper, J. C.; Pitzer, K. S. J. Phys. Chem. **1986**, 90, 3452
- (37) Roy, R. N.; Roy, L. N.; Gregory, D. R.; VanLanduyt, A. J.; Pierrot,
- D.; Millero, F. J. J. Solution Chem. 2000, 29, 1211. (38) Roy, R. N.; Vogel, K. M.; Good, C. E.; Davis, W. B.; Roy, L. N.;
- Johnson, D. A.; Felmy, A. R.; Pitzer, K. S. J. Phys. Chem. 1992, 96, 11065. (39) Covington, A. K.; Lilley, T. H.; Robinson, R. A. J. Phys. Chem.
- (40) Libus, Z.; Sadowska, T. J. Phys. Chem. 1970, 74, 3674
- (41) Wu, Y. C.; Rush, R. M.; Scatchard, G. J. Phys. Chem. 1968, 72, 4048.
- (42) Kelly, F. J.; Robinson, R. A.; Stokes, R. H. J. Phys. Chem. 1961, 65, 1958.

Synthesis and Structure Characterization of Chromium Oxide Prepared by Solid Thermal Decomposition Reaction

Li Li,†,‡ Zi F. Yan,*,† Gao Q. Lu,‡ and Zhong H. Zhu‡

State Key Laboratory for Heavy Oil Processing, Key Laboratory of Catalysis, CNPC, China University of Petroleum, Dongying 257061, China, and ARC Centre for Functional Nanomaterials, School of Engineering, University of Queensland, QLD 4072, Australia

Received: July 12, 2005; In Final Form: October 16, 2005

Mesoporous chromium oxide (Cr_2O_3) nanocrystals were first synthesized by the thermal decomposition reaction of $Cr(NO_3)_3 \cdot 9H_2O$ using citric acid monohydrate (CA) as the mesoporous template agent. The texture and chemistry of chromium oxide nanocrystals were characterized by N_2 adsorption—desorption isotherms, FTIR, X-ray diffraction (XRD), UV—vis, and thermoanalytical methods. It was shown that the hydrate water and CA are the crucial factors in influencing the formation of mesoporous Cr_2O_3 nanocrystals in the mixture system. The decomposition of CA results in the formation of a mesoporous structure with wormlike pores. The hydrate water of the mixture provides surface hydroxyls that act as binders, making the nanocrystals aggregate. The pore structures and phases of chromium oxide are affected by the ratio of precursor-to-CA, thermal temperature, and time.

Introduction

Ultrafine nanostructured chromium(III) oxide with high surface areas has attracted considerable interest because of a wide variety of applications such as in green pigments, coating materials for thermal protection and wear resistance, heterogeneous catalysts, solar energy collectors, and transparent colorants, etc.^{1–5} In catalysis, both chromium oxide and supported chromium have been used in many reactions such as polymerization,⁶ dehydrogenation,^{7–9} dehydrocyclization,^{10,11} and selective catalytic reduction of NO_x with ammonia.^{12–14} Various techniques have been developed to synthesize Cr₂O₃ nanoparticles such as precipitation,¹⁵ precipitation—gelation,^{16–18} solgel,^{19–21} mechanochemical reaction, and subsequent heat treatment,²² oxidation of chromium in oxygen,²³ and sonochemical methods.²⁴

Recently, it has been reported that chromium hydroxide gels were precipitated from Cr (NO₃)₃ solutions by the addition of hydrazine monohydrate. 25 Hexagonal crystallites of Cr₂O₃ were obtained at 380 °C to 405 °C, the space group being $R\bar{3}c$. Hou et al. prepared Cr₂O₃ nanoparticles with crystallite sizes of 17-25 nm by evaporation of a Cr(NO₃)₃ solution.²⁶ However, the most efficient method for providing a large surface area is homogeneous precipitation, that is, slow alkalinization of an aqueous Cr(NO₃)₃ solution by hydrolysis of dissolved urea. The samples obtained by this method are microporous materials with a surface area of 250-350 m²·g⁻¹, corresponding to a pore diameter of 0.6-2.0 nm. To prevent the collapse of the initial gel texture during the thermal treatment step, water was replaced by methanol, followed by supercritical release of the methanol at 305 °C. The produced mesoporous aerogels have high surface areas of about 503-785 m²·g⁻¹, which correspond to a pore diameter of 20 nm.²⁷ Therefore, several groups reported the direct synthesis of highly crystalline and monodisperse metal

Experimental Section

The mesoporous chromium oxide nanocrystals were synthesized using citric acid as a mesopore creating agent by the thermal decomposition of chromium nitrate salt in the autoclave at low temperature. $Cr(NO_3)_3 \cdot 9H_2O$ and citric acid monohydrate (CA) powders were milled separately and then mixed together. The mixture was transferred into an autoclave and heated from $100~^{\circ}C$ to $180~^{\circ}C$. The final products were washed with distilled water and dried at 373~K for 12~h.

Infrared spectra of the as-synthesized samples were recorded on a NEXus Fourier transform infrared (FTIR) spectrophotometer using KBr pellets containing 1% wt sample in KBr. Powder X-ray diffraction (XRD) measurement was carried out on a D/MAX-IIIA diffractometer (Japan) with Cu K α radiation generated at 40 kV, 40 mA at a speed of 0.01°/s, covering 2θ between 2° and 60°. Thermal gravimetric analysis (TGA) and

oxide nanocrystals via the thermal decomposition of organometallic precursors. $^{28-30}$ Hyeon et al. reported that $\gamma\text{-Fe}_2\mathrm{O}_3$ nanocrystals were synthesized by oxidation of the organometallic compound Fe(CO)₅ as the precursor with trimethylamine oxides as an oxidant.²⁸ Yin et al. prepared relatively monodisperse MnO nanocrystals using manganese acetate in a coordinating solvent composed of oleic acid and trioctylamine.²⁹ The quality of the nanocrystals produced by these nonaqueous solution methods is generally better than that of the nanocrystals synthesized in aqueous solutions.³⁰ However, to the best of our knowledge, the preparation of Cr₂O₃ nanocrystals by solid thermal decomposition of chromium salts at low temperatures has not been reported so far. Here, we report the synthesis of controlled Cr₂O₃ nanocrystals with mesostructure by the thermal decomposition reaction of chromium salt, which is an inexpensive process to obtain the mesoporous nanocrystals. Meanwhile, we investigated the thermal decomposition of the mixture and the relationship between the structure of the as-synthesized crystallites and the reaction conditions.

^{*} To whom correspondence should be addressed. E-mail: zfyancat@hdpu.edu.cn.

[†] University of Petroleum.

[‡] University of Queensland.

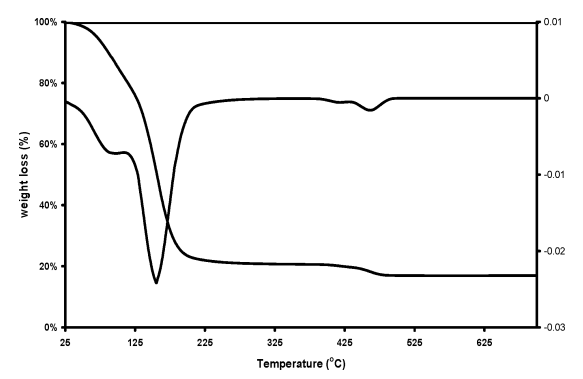


Figure 1. TGA-DTA plot of chromium nitrate.

differential thermalgravimetry (DTG) of the as-synthesized samples were performed at a heating rate of 10 K/min from room temperature to 700 °C in air flow by using a WCT-2 thermal analyzer (Beijing Optical Apparatus Co., China). The surface area, pore volume, and pore size distribution (PSD) of the samples were obtained by nitrogen adsorption—desorption isotherms. N₂ adsorption—desorption isotherms were recorded on a Micromeritics Tristar 2010 nitrogen absorber. The samples were degassed at 373 K for 24 h prior to analysis. The pore size is calculated from the desorption branches of isotherms based on the BJH and HK methods. Transmission electron microscopy (TEM) was conducted on a Philips CM200 microscope with an accelerating voltage 200 kV. The TEM sample was prepared by dipping ultrasonically dispersed Cr₂O₃ particles in ethanol on holey carbon grids. Scanning electron microscopy (SEM) examinations were performed on a JEOL 6300.

Results and Discussion

The TGA and DTG curves of chromium nitrate are shown in Figure 1. There are three different weight loss peaks at the temperature ranges 25-110, 110-217, and 408-490 °C. The first weight loss peak corresponds to the removal of water in the salt. The second is mainly attributed to the decomposition of Cr(NO₃)₃ to form Cr₂O₃. The weight loss is about 64%, which is close to the theoretical value. The third one may be ascribed to the removal of the oxygen lattice of Cr₂O₃ due to heating at high temperature. The decomposition reactions of Cr(NO₃)₃· 9H₂O are as follows³¹

$$Cr(NO_3)_3 \cdot 9H_2O \xrightarrow{30-60 \text{ °C}} Cr(NO_3)_3 \cdot (9-q)H_2O + qH_2O$$

$$Cr(NO_3)_3 \cdot (9-q)H_2O \xrightarrow{60-180 \text{ °C}} Cr_{1-x}^{3+}Cr_x^{m+}O_y(OH)_r(NO_3)_v + HNO_3 + NO + NO_2 + H_2O$$

$$Cr_{1-x}^{3+}Cr_x^{m+}O_y(OH)_r(NO_3)_v \xrightarrow{>120-150 \text{ °C}} Cr_2O_3 + NO + NO_2 + H_2O$$

It is implied that Cr₂O₃ nanocrystals can be obtained at 110-217 °C. So we choose the reaction temperatures at 110-180 °C to synthesize the Cr₂O₃ nanocrystals in this experiment.

Figure 2 shows the XRD patterns of the as-synthesized Cr₂O₃ nanocrystals at different temperatures with a 1:1 molar ratio of Cr(NO₃)₃•9H₂O-to-CA. The rhombohedra Cr₂O₃ nanocrystals (Figure 2) can be obtained above 130 °C with a precursor-to-CA molar ratio of 1:1. The unit cell parameters and atomic configuration for Cr₂O₃ samples are in good agreement with the known values of well-defined nanocrystals of α-Cr₂O₃,

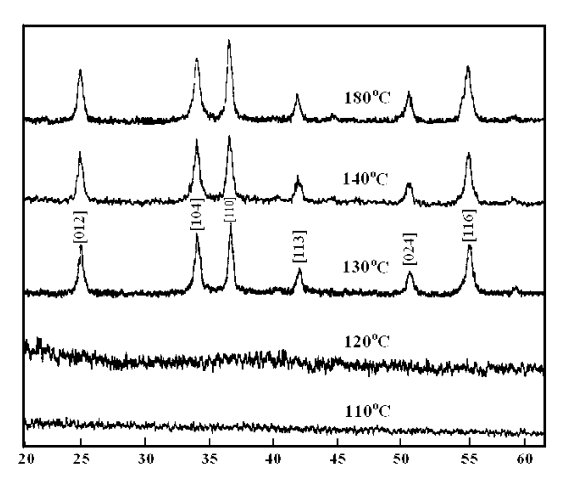


Figure 2. XRD patterns of chromium oxide obtained at different thermal decomposition temperatures for 24 h with the precursor-tocitric acid (CA) molar ratio of 1:1.

which belongs to the $R\bar{3}c$ space group with lattice parameters a = 4.958 Å and c = 13.594 Å.³² The crystallite sizes of Cr₂O₃ samples, calculated from the Debye-Scherrer equation, are about 10-15 nm, as also confirmed by the TEM image (Figure 3c). The SEM photographs (parts a and b of Figure 3) reveal the morphology of Cr₂O₃ nanocrystals. Each Cr₂O₃ particle consists of smaller lamellar grains.

The UV-vis spectrum of the Cr₂O₃ nanocrystals is shown in Figure 4. Two UV-vis peaks are observed in the vicinity of 445 (a) and 600 nm (b), corresponding to the $^4A_{2g} \rightarrow \,^4T_{1g}$ and ${}^{4}A_{2g} \rightarrow {}^{4}T_{2g}$ transitions in Cr₂O₃, respectively. The former is characteristic of the Cr³⁺ ions of six-coordinate geometry and the latter of octahedral symmetry.

Figure 5 shows FTIR spectra of the Cr₂O₃ nanocrystals. As seen in Figure 5, a broad band in the 3400-2500 cm⁻¹ region corresponds to stretching modes of surface OH groups. The band at 2010–2015 cm⁻¹ is ascribed to Cr=O vibration. The bands at $\sim 1700 \text{ cm}^{-1}$, $\sim 1680 \text{ cm}^{-1}$, and 1400 cm⁻¹ are attributed to hydroxyl groups associated with Cr3+ ions occurring in different environments. The 719 cm⁻¹ peak is ascribed to the A_{2u} model of Cr₂O₃. A single, strong band at ~590 cm⁻¹ corresponds to the characteristic vibrational mode of a symmetric CrO₆ octahedral of Cr₂O₃ in accordance with the UV-vis spectra analyses of six-coordinate Cr³⁺.

From the XRD, IR, and UV-vis data, we can conclude that the lattice of α-Cr₂O₃ nanocrystals is built on a hexagonal closepacked (hcp) array of oxygen. The octahedral and tetrahedral sites are located directly above one another in the hcp lattice. The octahedra share faces along a 3-fold axis and are distorted to trigonal antiprisms because of the Cr-Cr repulsion across the shared face. This crystal structure leads to a highly dense structure offering high polarizability, high refractive index, and intense color.33 The crystal lattice of the Cr₂O₃ sample synthesized is shown in the Figure 6. The character of the atomic structure and electronic configuration is important for the electronic, optical, and magnetic properties of Cr₂O₃.

Figures 7 and 8 show the nitrogen adsorption—desorption isotherms and pore size distribution of Cr₂O₃ nanocrystals obtained from the 1:1 ratio of Cr(NO₃)₃•9H₂O-to-CA at different thermal decomposition temperatures for 24 h and at 140 °C for different decomposition time. Nitrogen adsorption-desorption isotherms (Figures 7a and 8a) indicate that the isotherms of Cr₂O₃ nanocrystals are of type IV, according to the IUPAC

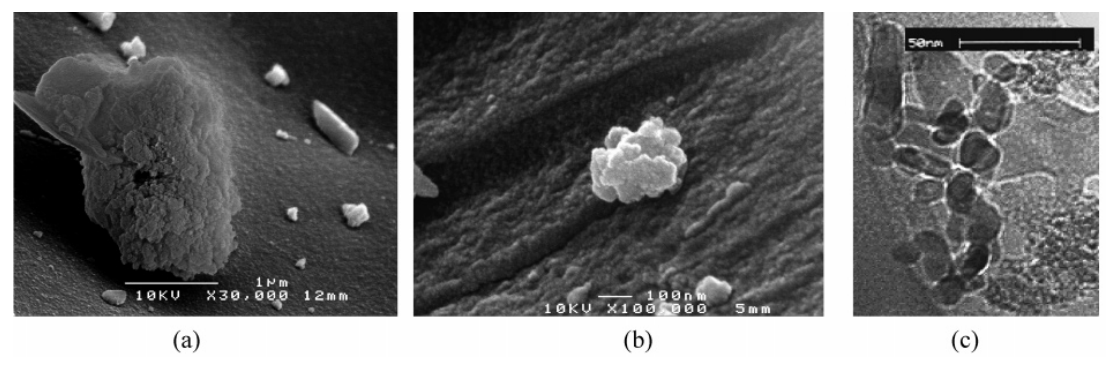


Figure 3. SEM photographs and TEM image of the γ -Cr₂O₃ nanocrystal. (a) SEM image (\times 30 000), (b) SEM image (\times 100 000), and (c) TEM image.

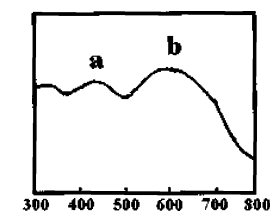


Figure 4. UV-vis spectrum of the Cr₂O₃ nanocrystal.

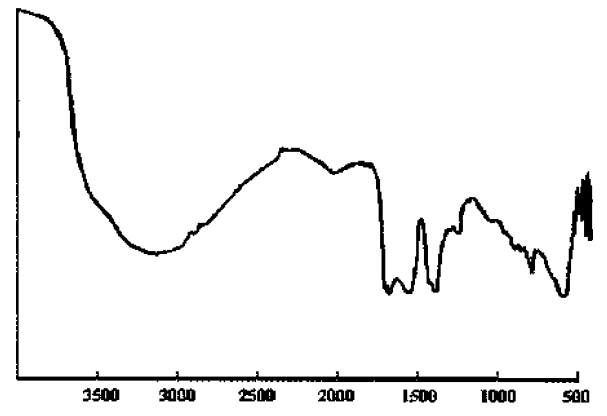


Figure 5. IR spectra of the Cr_2O_3 nanocrystal.

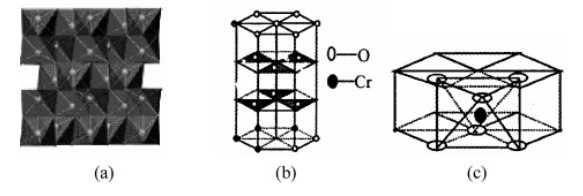


Figure 6. Crystal structure of the α -Cr₂O₃ nanocrystal.

classification, exhibiting the characteristic hysteresis loop of mesoporous materials. This means that the materials obtained by solid thermal decomposition have a mesoporous structure with a wormlike shape. The low-pressure portion of the isotherms is like I type isotherm, indicating the existence of micropores. Therefore, the Cr₂O₃ particles possess mesoporous and microporous dual structures, which are attributed to the removal of CA. Citric acid as an organic additive disperses fully in chromium nitrate. When the mixture is heated, the space occupied by CA remains as pores due to the decomposition of CA. The shape of the pores formed from CA is like vermiform. From Figures 7b and 8b, we can see that the mesopore of

chromia prepared with this method possesses bimodal distribution at about $3.5\ \mathrm{and}\ 7\ \mathrm{nm}.$

The above results show that nanocrystalline chromium oxide with the mesostructure can be synthesized by the solid decomposition reaction method. In the process, citric acid has an important effect on the mesopore formation of Cr_2O_3 . We prepared a Cr_2O_3 sample without CA using the same process and found that the resulting sample has no pores, which indicates that the presence of citric acid in the mixture is critical for the formation of the mesoporous structure. We will investigate the pore formation mechanism and structure of Cr_2O_3 obtained.

The shape, size, and pore structure of nanocrystals can be controlled by the precursor-to-CA ratio, thermal decomposition temperature, and thermal decomposition time. Figure 9 depicts the XRD patterns of Cr₂O₃ samples obtained in the different ratios of metal salt-to-citric acid at 140 °C. It can be seen that amorphous hydrous Cr₂O₃ particles (CrOOH) can be observed in the lower and higher ratios of chromic salt-to-citric acid (1: 3, 1:2, and 1:0.3). When the ratio of the precursor to CA was in the medium range such as 1:1 and 1:0.5, the Cr₂O₃ nanocrystals can be obtained. In the decomposition reaction of chromium nitrate in the autoclave, due to the existence of an organic additive, Cr³⁺ ions tended to form entangled cross-links with molten CA^{34,35} through hydrogen bonding. The excess of citric acid restrains the condensation of oxonitrates, resulting in the formation of CrOOH particles in the lower ratio of Cr-(NO₃)₃•9H₂O. With the increase in Cr(NO₃)₃•9H₂O content, the crystal growth proceeds and the crystals are formed. However, at a higher concentration of Cr(NO₃)₃·9H₂O, it causes the increase of nucleation to produce a mass of crystal nucleus, which tends to form amorphous Cr₂O₃ particles. We also found that when the reaction temperature was raised or reaction time was prolonged, the crystallite sizes increased accompanied by the broadening of the size distribution (Figures 7b and 8b). From Figure 2, it can be seen that mesoporous Cr₂O₃ crystallites increase with decomposition temperature, which is caused by the crystal growth. Tables 1 and 2 list the surface area, pore volume, and pore diameter of as-synthesized Cr2O3 obtained at different thermal decomposition temperatures for 24 h and at 140 °C for different thermal decomposition times, respectively. The surface area and pore volume of Cr₂O₃ samples increase with the rise of temperature and prolongation of time, which is caused by the full decomposition of CA during heating.

In addition, the hydrate water has a crucial effect on crystal growth of Cr_2O_3 from the nucleus clusters. It is found that the crystal nuclei of Cr_2O_3 are formed at a short reaction time from the XRD patterns (Figure 10). With the prolongation of reaction time, to find the low-energy configuration interface from

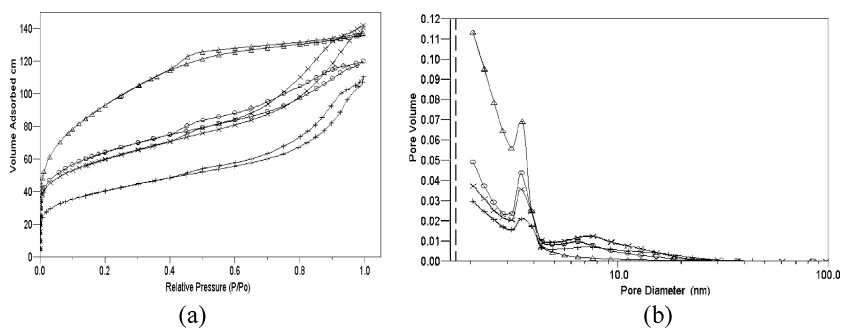


Figure 7. Nitrogen adsorption—desorption isotherms at 77 K and mesoporous size distributions for the Cr_2O_3 samples at different thermal decomposition temperatures when the ratio of $Cr(NO_3)_3 \cdot 9H_2O$ -to-CA is 1 (+, 130 °C; \bigcirc , 140 °C; \times , 160 °C; \triangle , 180 °C).

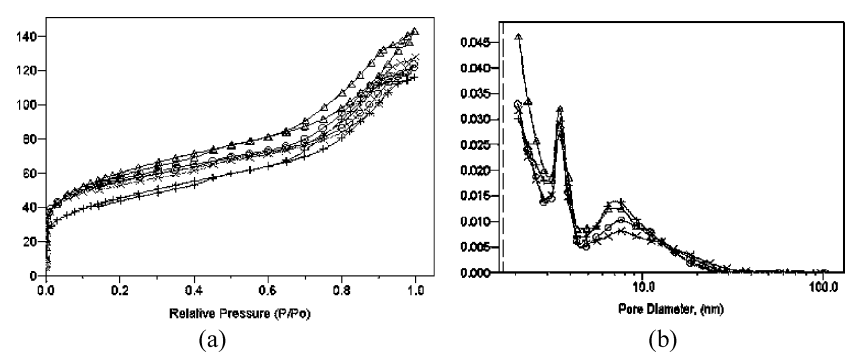


Figure 8. Nitrogen adsorption-desorption isotherms at 77 K and mesopore distributions for the Cr₂O₃ samples at 140 °C for different thermal decomposition times when the ratio of Cr(NO₃)₃·9H₂O-to-CA is 1 (+, 9 h; Ο, 12 h; ×, 36 h; Δ, 72 h).

TABLE 1: Surface Area, Pore Volume, and Diameter of As-Synthesized Cr_2O_3 at Different Temperatures with the $Cr(NO_3)_3 \cdot 9H_2O$ and CA Molar Ratio of 1:1

sample	$SA^a (m^2/g)$	SA MSb (m2/g)	$\begin{array}{c} SA \\ MI^c \\ (m^2/g) \end{array}$	PV^d (cm^3/g)	$rac{ ext{PV}}{ ext{MS}^e}$ $(ext{cm}^3/ ext{g})$	PV MI ^f (cm ³ /g)	PD ^g (nm)	PD MS ^h (nm)	PD MI ⁱ (nm)
Cr ₂ O ₃ -130	141.4	103.6	29.0	0.171	0.156	0.0135	4.83	6.04	0.64
Cr ₂ O ₃ -140	207.2	139.0	52.2	0.185	0.150	0.0657	3.34	4.31	0.70
Cr ₂ O ₃ -160	222.0	140.7	60.5	0.220	0.192	0.0628	4.24	5.46	0.60
Cr_2O_3-180	334.0	235.9	13.4	0.212	0.174	0.0843	2.54	2.95	0.71

^a BET surface area. ^b Surface area of mesopore. ^c Surface area of micropore. ^d Total pore volume. ^e Pore volume of mesopore. ^f Pore volume of micropore. g Average pore diameter. h Average pore diameter of mesopore. Average pore diameter of micropore.

TABLE 2: Surface Area, Pore Volume and Diameter of As-synthesized Cr₂O₃ at 140 °C for Different Crystallization Times When the Ratio of Cr(NO₃)₃ and CA is 1:1

sample	SA^a (m^2/g)	SA MS ^b (m ² /g)	SA MI ^c (m ² /g)	PV ^d (cm ³ /g)	PV MS ^e (cm ³ /g)	PV MI ^f (cm ³ /g)	PD ^g (nm)	PD MS ^h (nm)	PD MI ⁱ (nm)
Cr ₂ O ₃ -9 h	160.3	121.3	22.6	0.180	0.160	0.0102	4.48	5.54	0.61
Cr ₂ O ₃ -12 h	194.1	109.6	56.6	0.191	0.156	0.0273	3.94	5.70	0.62
Cr ₂ O ₃ -24 h	207.2	139.0	52.2	0.185	0.150	0.0657	3.34	4.31	0.70
Cr ₂ O ₃ -72 h	211.5	141.1	37.7	0.222	0.196	0.0172	4.19	5.57	0.63

^a BET surface area. ^b Surface area of mesopore. ^c Surface area of micropore. ^d Total pore volume. ^e Pore volume of mesopore. ^f Pore volume of micropore. g Average pore diameter. h Average pore diameter of mesopore. Average pore diameter of micropore.

nanocrystals and nanocrystal aggregates, the nuclei aggregation will further increase to form nanoparticles. The N₂ isotherms and pore distribution of Cr2O3 samples obtained at different thermal decomposition times are shown in Figure 8. It has been seen from Figure 8 and Table 2 that the pore structure and shape have no change but only the size distribution of the samples becomes broader, that is, the particle size of aggregates increases. In the solid thermal decomposition reaction herein, the hydrate water of the mixture provides surface hydroxyls that act as binders, making the nanocrystals aggregate. The aggregation process is slow in the solid reaction. It is easy and effective to control the particle size and distribution during the aggregation process by controlling the water present in the system. The larger the surface hydroxyl density, the larger the particles that form. Meanwhile, the addition of citric acid monohydrate hinders the continuous growth of grain through aggregation of the nanocrystals to form larger particles.

According to the above analyses, the thermal decomposition process of Cr(NO₃)₃·9H₂O through the addition of citric acid monohydrate as the mesoporous template agent results in Cr₂O₃ nanocrystals as the building blocks to form a mesoporous wormlike structure of nanoparticles. The formation mechanism of mesoporous Cr2O3 nanocrystals is proposed as follows, illustrated in Figure 11. After uniformly mixing with CA,

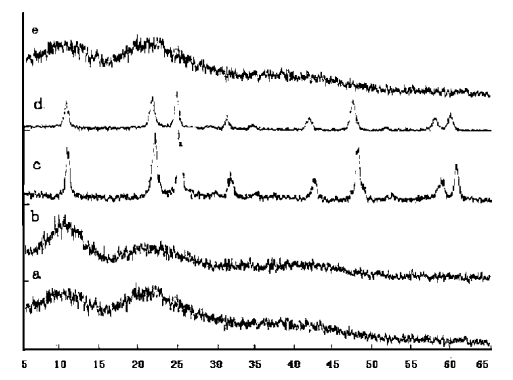


Figure 9. XRD patterns of the mesoporous Cr₂O₃ in the different ratios at 140 °C for 24 h: (a) 1:3, (b) 1:2, (c) 1:1, (d) 1:0.5, and (e) 1:0.3.

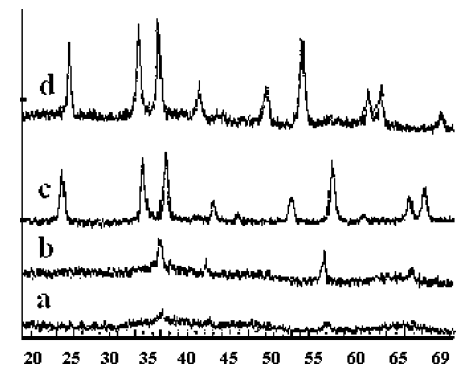


Figure 10. XRD patterns of the mesoporous Cr₂O₃ at 140 °C for different times in the 1:1 ratio of CA and Cr(NO₃)₃•9H₂O: (a) 12 h, (b) 18 h, (c) 24 h, and (d) 72 h.

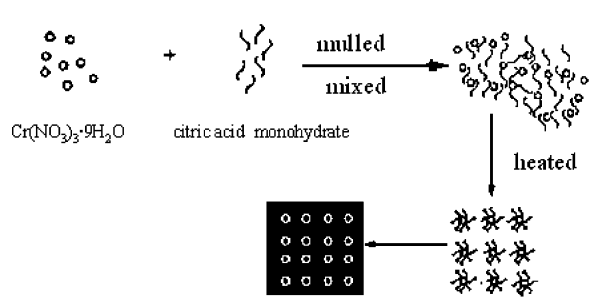


Figure 11. Schematic diagram of the possible mechanism for mesoporous Cr₂O₃ nanoparticles formation.

chromium precursors interact with the CA to form the CA-Cr(NO₃)₃·9H₂O composite through hydrogen bonding and electrostatic interaction. Thus, the CA-Cr(NO₃)₃ composite decomposes accompanied by the decomposition of the chromium salt and free CA during heating. Since the strength of hydrogen bonding between Cr3+ and oxonitrates of chromium and hydroxyl group in CA is not so strong as to restrict the condensation of chromium salt during heating, the Cr₂O₃ network can be formed despite the existence of CA. The introduction of organic additives effectively disperses inorganic species and inhibits the growth of particles. The space occupied with CA creates the disordered wormlike pore of chromium oxide after the thermal decomposition of CA. We also found that there is an optimum amount of critic acid as a dispersed template to stabilize the mesostructure and to achieve maximum porosity.

Conclusions

In summary, mesoporous α-Cr₂O₃ nanocrystals are prepared by a solid thermal decomposition of chromium nitrate with CA as the mesoporous template agent. The as-prepared particles are formed through the aggregation of the primary 3-4 nm nanocrystals and possess mesoporous structure. The XRD, N2 isotherms, and TEM results suggest that CA has an important effect on the mesopore formation of Cr2O3 nanocrystals and acts as a template. The size and pore structure can be tuned by the synthesis conditions, which is achieved by the amount of hydrate water and the addition of citric acid in the mixture system. The binder effect of surface hydroxyl groups is emphasized on the controlled aggregation of metal oxide nanocrystals because only the vicinity of particles can aggregate through surface hydroxyls to form Cr₂O₃ aggregates. The thermal decomposition of citric acid organic molecules makes the space occupied with CA as pores. In addition, such mesoporous Cr₂O₃ nanocrystals will have potential applications in heterogeneous catalysis and we will further investigate the relationships between crystal structure, surface morphology, and catalytic activity.

Acknowledgment. This work is supported by the Petroleum Limited Co. of China. We thank Mr. M. Yan for his assistance on the TEM analysis. Financial support from the Australian Research Council for the ARC Centre for Functional Nanomaterials is also gratefully acknowledged.

References and Notes

- (1) Marcus, M. A.; Flood, W.; Stiegerwald, M.; Zahurak, S. F.; Kortan, A. R. J. Phys. Chem. 1991, 95, 1572.
- (2) Boutonnet, M.; Andersson, C.; Larsson, R. Acta Chem. Scand. A **1980**, 34, 639.
 - (3) Osseo-Asare, K.; Arriagada, F. J. Colloids Surf. 1990, 50, 321.
- (4) Spanhel, L.; Haase, M.; Weller, H.; Henglein, A. J. Am. Chem. Soc. 1987, 109, 5649.
- (5) Abecassis-Wolfovich, M.; Rotter, H.; Landau, M. V.; Korin, E.; Erenburg, A. I.; Mogilyansky, D.; Gartstein, E. J. Non-Cryst. Solids 2003,
 - (6) McDaniel, M. P. Adv. Catal. 1985, 33, 48.
- (7) Derossi, S.; Ferraris, G.; Fremiotti, S.; Indovina, V.; Cimino, A. Appl. Catal., A 1993, 106, 125.
- (8) Derossi, S.; Ferraris, G.; Fremiotti, S.; Garrone, E.; Ghiotti, G.; Campa, M. C.; Indovina, V. *J. Catal.* **1994**, *148*, 36.

 (9) Cavani, F.; Koutyrev, M.; Trifiro, F.; Bartolini, A.; Ghisletti, D.; Iezzi, R.; Santucci, A.; DelPiero, G. *J. Catal.* **1996**, *158*, 236.
- (10) Sohn, J. R.; Ryu, S G.; Kim, H. W. J. Mol. Catal. Chem. 1998,
- 135.99
- (11) Praserthdam, P.; Phungphadung, J.; Tanakulrungsank, W. *Mater. Res. Innovations* **2003**, *7*, 118.
 - (12) Kobylinski, T. P.; Taylor, B. W. J. Catal. 1973, 31, 450.
- (13) Engweiler, J.; Nickl, J.; Baiker, A.; Kohler, K.; Schlapfer, C. W.; Vonzelewsky, A. *J. Catal.* **1994**, *145*, 141.
- (14) Curryhyde, H. E.; Musch, H.; Baiker, A. Appl. Catal. 1990, 65,
- (15) Grzybowska, B.; Sloczynski, J.; Grabowski, R.; Wcislo, K.; Kozlowska, A.; Stoch, J.; Zielinski, J. J. Catal. 1998, 178, 687.
 (16) Lazier, W. A.; Vaughen, J. V. J. Am. Chem. Soc. 1932, 54, 3080.
 (17) Burwell, R. L.; Taylor, H. S. J. Am. Chem. Soc. 1936, 58, 697.
- (18) Burwell, R. L.; Littlewood, A. B.; Cardew, M.; Pass, G.; Stoddart, C. T. H. *J. Am. Chem. Soc.* **1960**, *82*, 6272.
- (19) Burwell, R. L.; Taylor, K. C.; Haller, G. L. J. Phys. Chem. 1967, 71, 4580.
 - (20) Cross, N. E.; Leach, H. F. J. Catal. 1971, 21, 239.
- (21) Music, S.; Maljkovic, M.; Popovic, S.; Trojko, R. Croat. Chem. Acta 1999, 72, 789–791.
 - (22) Tsuzuki, T.; McCormick, P. G. Acta Mater. 2000, 48, 2795.
- (23) Mougin, J.; Le Bihan, T. Lucazeau, G. J. Phys. Chem. Solids 2001, 62, 553.
- (24) Arul Dhas, A.; Koltypin, Y.; Gedanken, A. Chem. Mater. 1997, 9, 3159.
- (25) Kawabata, A.; Yoshinaka, M.; Hirota, K.; Yamaguchi, Q. J. Am. Ceram. Soc. 1995, 78, 2271.

- (26) Hou, B.; Ji, X.; Xie, Y.; Li, J.; Shen, B.; Qian, Y. *Nanostruct. Mater.* 1995, 5, 599.
 (27) Carlson, E. J.; Armor, J. N.; Cunningham, W. J.; Smith, A. M. U.S. Patent 4828818, 1989.
- (28) Hyeon, T.; Lee, S. S.; Park, J.; Chang, Y.; Na, H. B. J. Am. Chem. Soc. 2001, 123, 12798.
 - (29) Yin, M.; O'Brien, S. J. Am. Chem. Soc. 2003, 125, 10180.
 - (30) Jana, N. R.; Chen, Y. F.; Peng, X. G. Chem. Mater. 2004, 16, 3931.
- (31) Malecki, A.; Gajerski, R.; Labus, S.; et al. *J. Therm. Anal. Calorim.*2000, 60, 17.
 (32) McMurdie, H. F.; Morris, M. C.; Evans, E. H.; Paretzkon, B.;
 Wong-Ng, W.; Zhang, Y.; Hubbard, C. R. *Powder Diffr.* 1987, 2, 45.
 (33) Vayssieres, L.; Manthiram, A. *J. Phys. Chem. B* 2003, 107, 2623.
 (34) Liu, G.; Jia, M. J.; Zhou, Z.; Zhang, W. X.; Wu, T. H.; Jiang, D.

- Z. Chem. Comm. 2004, 14, 1660. (35) Takahashi, R.; Sato, S.; Sodesawa, T.; Kawakita, M.; Ogura, M. J. Phys. Chem. B 2000, 104, 12184.

A new composite ionic liquid (IL) al-kylation process has been proven in a pilot plant and retrofitted into an existing 65,000-tonne/year H₂SO₄ alkylation unit in China. This article

Refining

discusses the new process, ionikylation, and presents results from the pilot plant

and retrofitted unit.

Process reactions take place at ambient temperatures and

moderate pressures. Alkylate from the ionikylation process compares favorably to alkylate from HF and H₂SO₄ units but without the safety and environmental concerns.

Alkylation

Isobutane alkylation is a common refinery process used to produce highquality gasoline (OGJ, Nov. 12, 1990, p. 79). The most desirable components in alkylate gasoline are trimethylpentanes (TMPs), which have research octane numbers (RONs) greater than 100.

Conventional alkylation processes use either H₂SO₄ or anhydrous HF acid as catalysts. This has significant safety and environmental concerns due to the handling of large quantities of spent H₂SO₄ or hazardous HF.

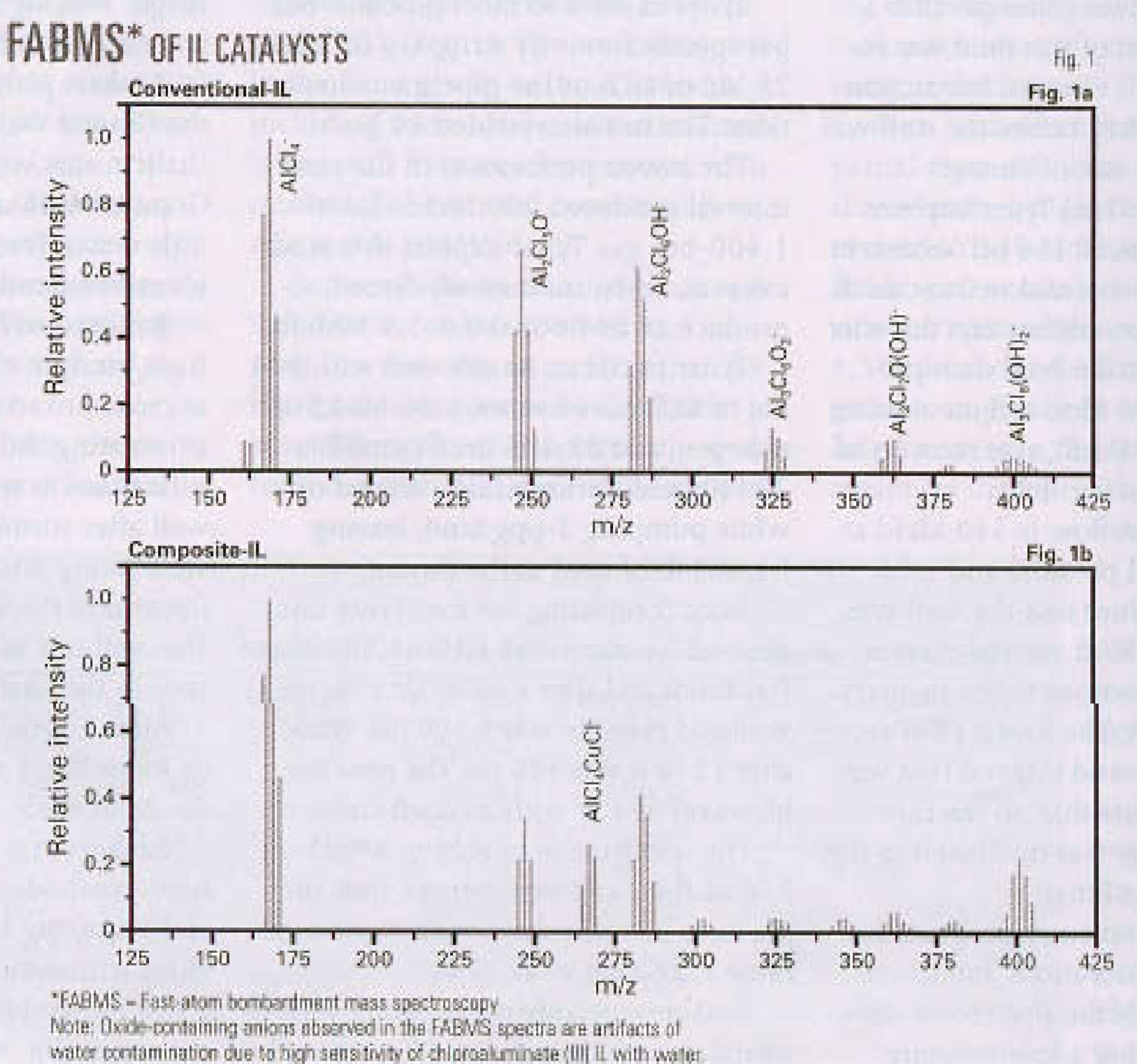
Solid acids have shown promise as less hazardous catalysts for alkylation¹ and have been subjected to extensive pilot scale testing.^{2 3} Solid-acid catalysts, however, deactivate rapidly, resulting in low product yield and loss of reaction selectivity.⁴

The rapid deactivation is due to a buildup of carbenium ions on active sites of the solid catalysts. Once this carbonaceous material is formed, it is difficult to remove from the narrow catalyst pores. Moreover, the cost of solid-acid catalysts is relatively high and there is no technically sound method for regenerating spent solid-acid catalysts.

lonic liquid alkylation process produces high-quality gasoline moderate pressures. Alk ionikylation process conto alkylate from HF and

Rui Zhang
Chunming Xu
China University of Petroleum
Beijing

Rongan Xia PetroChina Lanzhou Petrochemical Co. Lanzhou, China



Ionikylation

Ionikylation is an environmentally friendly and energy efficient isobutane alkylation process. The process uses a composite-IL as homogeneous catalyst for alkylation reactions at ambient temperatures and moderate pressures.

ILs are
ionic, salt-like
materials that
are liquid at
less than 100°
C.5 ILs have
been histori-

cally used as solvents and homogeneous catalysts due to their negligible vapor pressure, good solubility to a wide range of organic and inorganic compounds, and ability to be recycled for reuse.

Acidic chloroaluminate (III) IL has been used as a homogeneous catalyst for isobutane alkylation. Its use eliminates the diffusion limitation present with solid-acid catalyst systems, and alkylated gasoline is easily separated from the ionic liquid.⁸⁻¹⁰

TMP yield and selectivity, however, are low in systems with conventional-IL—with and without adjusting the IL's acidity by varying either the molar fraction of aluminum chloride (AlCl₃) of the IL or adding hydrochloric acid (HCl). ¹⁰⁻¹²

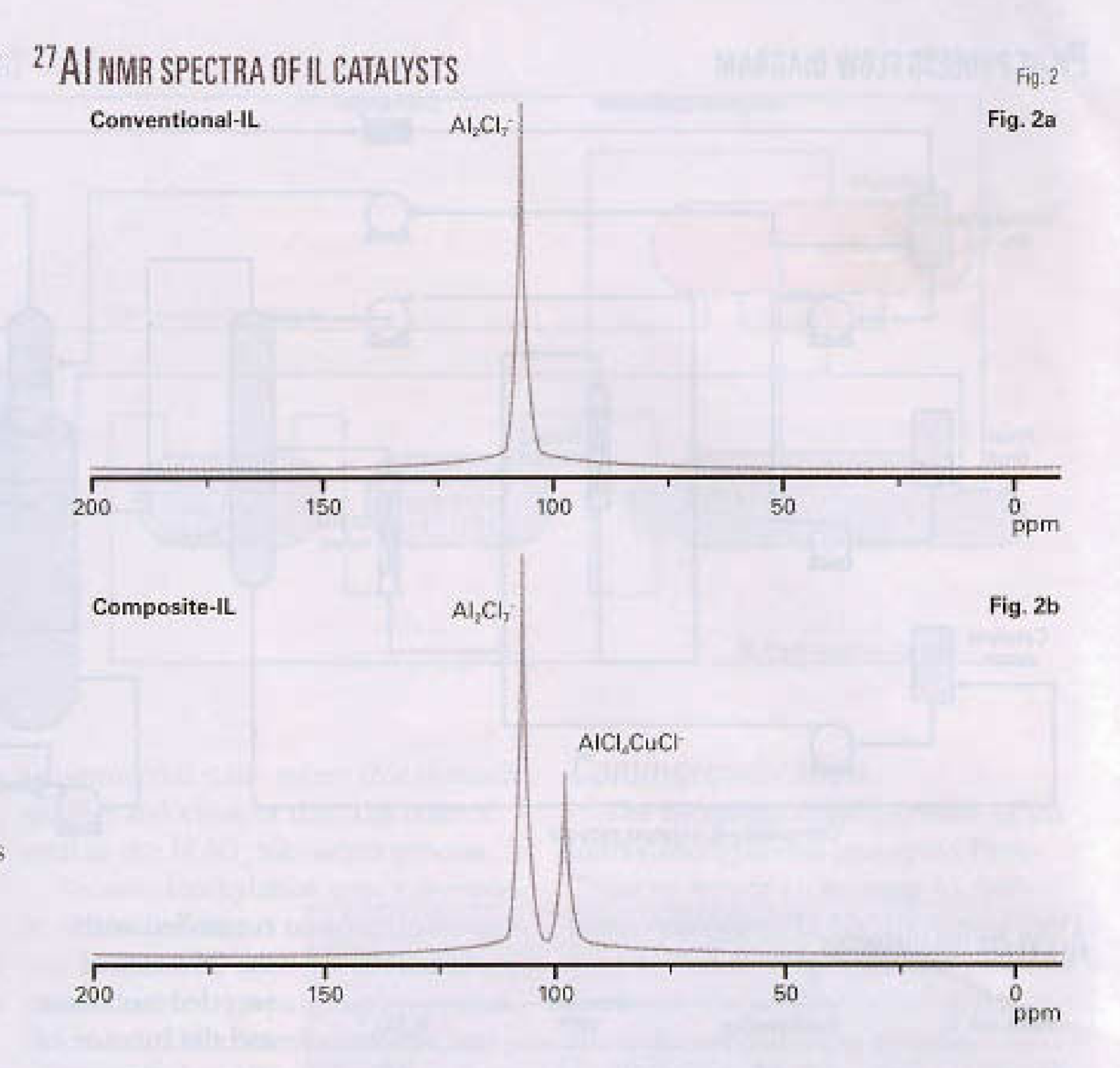
A study showed that adding aromatic hydrocarbons and metal chlorides to aluminum chloride-dialkyl ether complex enhanced TMP selectivity. It is theorized that adding aromatic hydrocarbons and metal chlorides enhances the acidity of catalyst for alkylation reactions and inhibits undesirable side reactions such as isomerization and cracking. [1]

In subsequent experiments, aromatic hydrocarbons and cuprous chloride (CuCl) were added to a conventional-IL, which showed high TMP yield and selectivity. 10 11 14 Adding CuCl to an aluminum chloride-dialkyl ether complex or conventional-IL, however, results in formation of a fine suspension that is difficult to separate and recycle in a continuous-flow system.

Composite-IL catalyst

A further development in the commercialization of IL-catalyzed isobutene alkylation is the development of a composite-IL catalyst. It is a liquid compound, which is synthesized with a conventional-IL catalyst and CuCl. 15 The composite-IL catalyst has anions in the form of ligands with two or more metallic centers.

Fast-atom bombardment mass spectrometry (Fig. 1) and ¹⁷Al nuclear magnetic resonance (NMR, Fig. 2) show



that a relatively high quantity of multicenter ligands of AlCl₄CuCl⁻ are formed in the composite-IL catalyst. By comparison, only a few AlCl₄CuCl⁻ ligands were detected in the IL-CuCl system when CuCl was added to a conventional-IL catalyst.¹⁶

Pilot plant

Extensive bench-scale laboratory tests were conducted to optimize the composite-IL catalyst's performance in alkylating isobutane. The ionikylation process was demonstrated in a continuous-flow pilot unit with 4-l./hr equivalent alkylate gasoline production for 60 days.

Fig. 3 shows the process flow diagram of the pilot unit. The pilot unit was constructed from carbon steel.

The composite-IL catalyst used in the pilot test unit was prepared commercially with industrial-grade chemicals. This was done to determine the effect of impurities on the composite-IL catalyst due to isobutane alkylation reac-

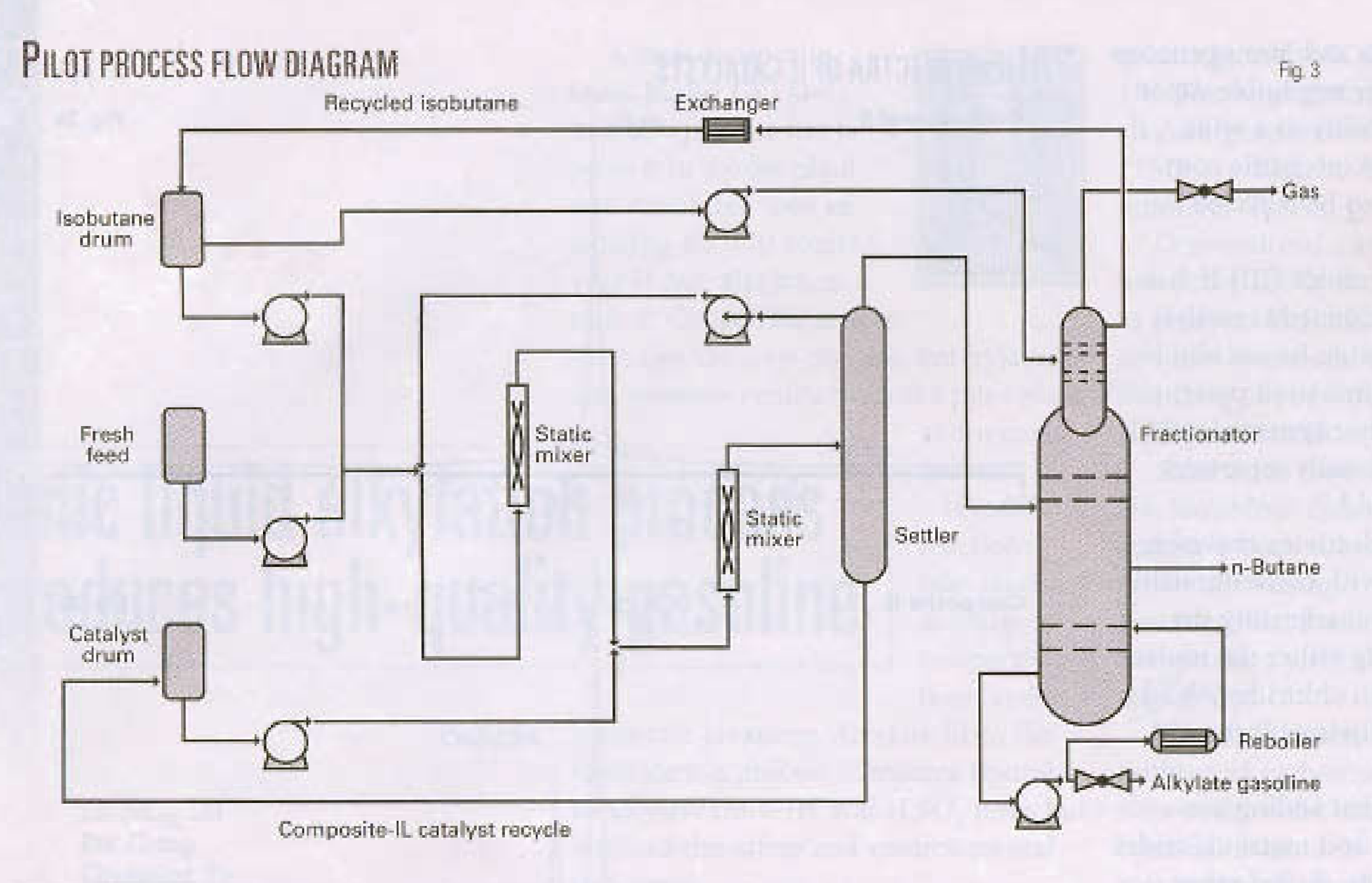
tions. The composite-IL catalyst was also subjected to an aging test by storing it in a tank for 8 months before the pilot test.

Fresh feed was a mixture of isobutane and a heavy C₄ fraction (primarily butene-2) in a 1:1 ratio. These streams were obtained from a commercial refinery. Fresh feed, recycled isobutane, and a mixture of excess isobutane and alkylate gasoline from the top of the settler were fed to the first static mixer.

The stream from the first static mixer was combined with the recycled composite-IL catalyst and fed to the second static mixer where the isobutane alkylation reactions occurred at 15° C. and 0.4 MPa.

Reaction products then flowed to a settler. The composite-IL catalyst, which is heavier than alkylate gasoline, was collected from the bottom of the settler and recycled and reused. A split stream of excess isobutane and alkylate gasoline at the top of the settler were recycled to the first static mixer. Remaining

PROCESSING



KYLATE COMPARI	0011		Table
Yield, wt %	lonikylation	Process —— HF*	H,SO,
C, C, C, C, C, C,	0.6	2.5 1.9	8.8
C.	1.0	1.9	4.9
C. H. WEITER	2.0	2.9	3.9
Ç,	95.6	90.1	80.7
37	0.8	2.6	5.7
Components	900 6	00.0	71.6
TMPs 2,2,3-TMP	89.6 0.1	80.9 1.6	2.3
2.2.4-TMP	51.6	49.7	31.1
2,3,3-TMP	18.1	10.8	19.8
2,3,4-TMP	19.8	18.8	18.4
DMHs	6.0	9.2	9.0
2,3-DMH	1.3		
2,4-DMH	1.3	HISHIRI TOTAL	11/19
2.5-DMH	1.3	en central 4° E	
3,4-DMH	0		-
TMP:DMH ratio	14.9	8.8	8.0
RON	100.1	97.3	97.6
MON	95.0	95.2	94.4

products from the top of settler were fed to a fractionation column.

Isobutane at the top of the fractionation column was cooled and recycled to the first static mixer. It maintained a relatively high isobutane-to-olefin (I:O) ratio and low reaction temperature. Product n-butane and alkylate gasoline were obtained from the middle and bottom of fractionation column, respectively.

The overall I:O ratio of reactants in the reactor was 500, which was controlled with
the flow rate of
recycled isobutane
and the mixture of
excess isobutane
and alkylate gasoline. The reaction
time was 10 min,
which depended
upon the residence
time in the second
static mixer and
sedimentation
time in settler.

The volumetric ratio of composite-IL catalyst to the stream from

the first static mixer was 1.2. This was done to maintain the composite-IL catalyst as a continuous liquid phase, which helped achieve high TMP selectivity.

Ionikylation performance

Olefin conversion was constantly more than 99% for the entire pilot test period.

Table 1 summarizes the product yield and properties of alkylate gasoline. The C_s yield in alkylate gasoline was higher than 95 wt % and the yield of

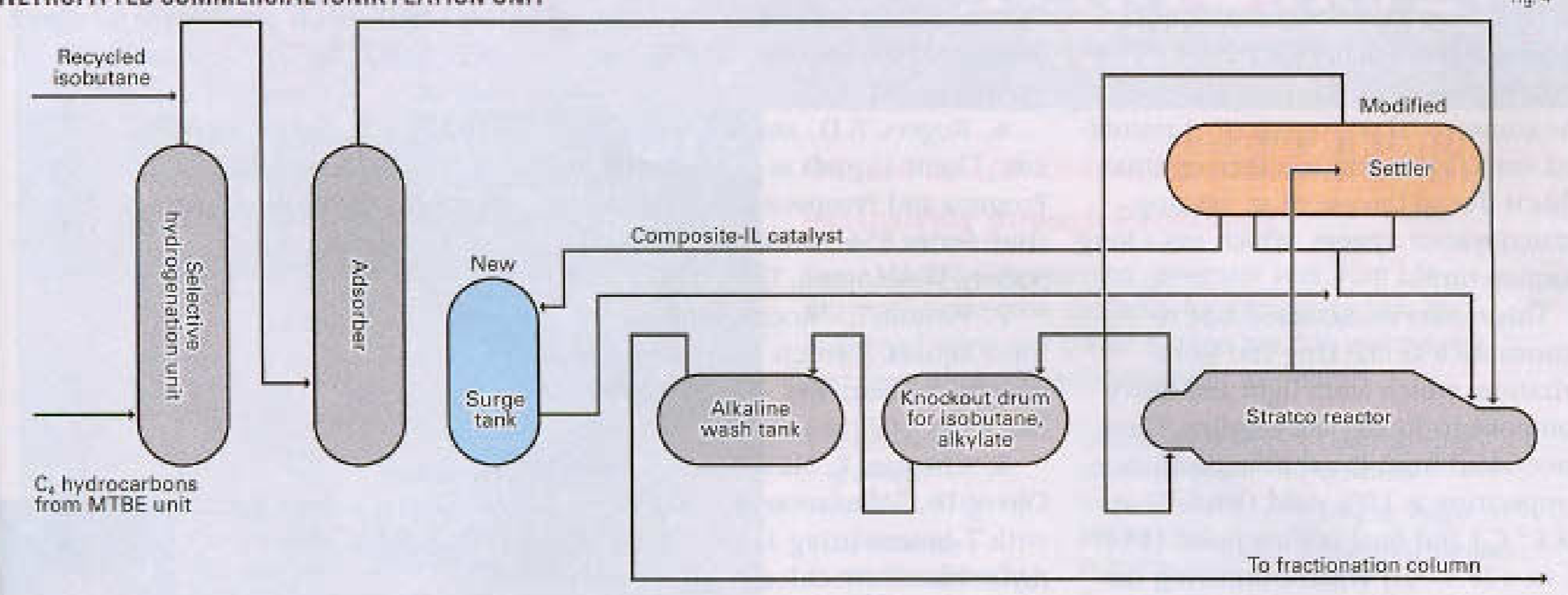
TMPs was 90%.

The ratio of TMPs to dimethylhexanes (DMHs) in alkylate gasoline is an important key criterion for comparing the performance of alkylation catalysts. Alkylate from the composite-IL catalyst had a high TMP:DMH ratio, indicating that a relatively small amount of undesirable side reactions such as isomerization and cracking occurred The high C, yield and TMP selectivity of composite-

IL catalyst are due to high concentration of AlCl_CuCl ligands.

Performance of the ionikylation process in the continuous pilot test was comparable to that of the bench-scale test. This shows that the commercial composite-IL catalyst performed in a similar manner as that developed in the laboratory, and its activity was stable.

The second secon		
		Test standard
Octane rating		
RON	100.1	GB/T 6478
MON	95.0	GB/T 503
Antiknock index	97.6	GB/T 547, GB/T 503
Distillation curve, *	C	GB/T 8536
10%	98.6	0.041.0000
50%	104.1	
90%	111.0	
Final boiling		
point	129.4	
Residual, vol %	1.8	
rvp, 1,000 Pa	25.5	GB/T 8017
Actual gum,	1 = 110.0	ADT COLO
mg/100 ml		GB/T 8019
Induction period,	>1,000	ASTM 0-526
Sulfur content.	- I MILL	HOTHY DEDZI
WI %	0.003	GB/T 17040
Doctor test	Pass	SH/T 0174
Copper corresion at 50° C.		
3 hr, grade	18	GB/T 5096
Aromatics, vol %	0.3	GB/T 11132
Alkenes, vol %	0	GB/T 11132



Neither the composite-IL catalyst nor its decomposed species was detected in alkylate gasoline, indicating good separation of composite-IL catalyst from alkylate gasoline and chemical stability of composite-IL catalyst. Metallurgical inspection of the pilot unit indicated that no detectable corrosion occurred in the process units during the 60-day continuous pilot test.

Also included in Table 1 are performance data of H₂SO₄ and HF catalyzed isobutane alkylation processes. ¹⁷ In general, the ionikylation process produces a higher-quality alkylate gasoline than either H₂SO₄ or HF alkylation processes.

Table 2 lists the detailed properties of alkylate gasoline produced by the ionikylation process. The quality of product from the ionikylation process exceeded the specifications for gasoline, such as higher RON and MON, lower rvp, and temperature at 50% and 90% distillation yield.

Benefits

Operating conditions in the ionikylation process are similar to those of commercial H₂SO₄ and HF alkylation processes. The reactor used in ionikylation, however, is a commercial static mixer that is much simpler and cheaper than the reactor used in the H,SO₄ alkylation process.

Because ionikylation uses a composite-IL catalyst that is noncorrosive, carbon steel can be used for the hardware such as reactors, piping, tanks, pumps, and valves. The control corrosion test of the composite-IL catalyst on carbon steel indicated that the corrosion rate was less than 0.001 mm/year.

Ionikylation can be easily retrofitted to an existing H₂SO₄ or HF alkylation unit.

Commercialization

The successful demonstration of the ionikylation process prompted Petro-China to retrofit an existing 65,000-tonne/year (tpy) H₂SO₄ alkylation unit (Fig. 4). A new surge tank was added to recycle the composite-IL catalyst and allow the spent catalyst to settle.

The internals of the settler were modified to enhance the separation of composite-IL catalyst from alkylate gasoline. The operating conditions in the selective hydrogenation unit were modified to meet the required concentration of 2-butene in the feed C₄ fraction for ionikylation.

Table 3 shows commercial performance data before and after the retrofit. The yield and RON of commercial ionikylation alkylate gasoline are 75 wt % (based on the amount of C₄ fraction from the MTBE unit upstream) and 98.8, respectively. This is higher than the yield and RON from H₂SO₄ alkylation (73 wt % yield and 95 RON) before the retrofit.

The retrofit also increased the process unit's capacity by 40%, to 248 tonnes/day (tpd) from 180 tpd. The economics of increased yield and RON of alkylate gasoline

ALKYLATE FROM COMMER	CIAL H2SO4 UNIT
----------------------	-----------------

		- Before retrofit H,SO, alkylation - Flow rate, Yield, tpd wt %		After retrofit Ionikylation - Flow rate, Yie tpd wt		
Feed Product	C, Light alkylate Heavy alkylate Gas Loss Total	180 125.9 10.8 41.7 1.4 180	70.0 6.0 23.2 0.8 100	248 186.1 8.2 53.7 248	75.0 3.3 21.7	
Octane rating RON MON Antiknock index		9	5.0 3.0 4.0	98. 93. 96.	1	
Distillation, "C. Initial boiling point 10% 50% 90% Final boiling point Actual gum, mg/100 ml Doctor test		7 10 10 13	5.0 7.0 11.5 8.5 2.0 0.9	45.5 81.5 101.0 108.0 154.0 1.6 Pass		
Copper co 3 hr, grad	rrosion at 50° C.,		1	S. S	1	

Dil & Gas Journal / Oct. 23, 2006

PROCESSING

from ionikylation are attractive, even though the cost of the composite-IL catalyst is more than H,SO,.

Compared with the pilot test results, the commercial performance of retrofitted ionikylation was less than optimal. This is due to the use of an existing Stratco reactor system, which has a long reaction time.

This results in increased side reactions such as cracking and isomerization, which form light and heavy components in alkylate gasoline. These are evident from the shift in distillation temperature at 10% yield (81.5° C. vs. 98.6° C.) and final boiling point (154° C. vs. 129.4° C.) when comparing the pilot results with those of the retrofitted unit.

We are currently conducting process optimization work to improve the commercial performance of ionikylation further by varying the size and type of static mixer and potentially replacing the Stratco reactor with a static mixer to minimize reaction time.

Acknowledgments

The National Natural Science Foundation of China provided strategic research grants and PetroChina provided financial support, feedstocks for the pilot test, and technical consultation for commercial implementation.

References

- 1. Corma, A., and Martinez, A., "Catalysts and processes for isoparaffin-olefin alkylation," Catal. Rev., Vol. 35 (1993), No. 4, pp. 483-570.
- Hommeltoft, S.I., Ekelund, O., and Zavilla, J., "Role of ester intermediates in isobutene alkylation and its consequence for the choice of catalyst system," Ind. Eng. Chem. Res., Vol. 36 (1997), No. 9, pp. 3491-97.
- Pryor, P.S., "Approaches to alkylation: a world review," Petroleum Technology Quarterly, Winter 2004, pp. 69-76.
- 4. Weitkamp, J., and Traa, Y., "Isobutane/butene Alkylation on Solid Catalysts," Catal. Today, Vol. 49 (1999), No. 2, pp. 193-99.

- Rogers, R.D., and Seddon, K.R.,
 "Ionic liquids: Solvents of the future?,"
 Science, 2003, Vol. 302 (2003), No. 5646, pp. 792-93.
- Rogers, R.D., and Seddon, K.R., eds., "Ionic Liquids as Green Solvents: Progress and Prospects," ACS Symposium Series 856, American Chemical Society, Washington, DC, 2003.
- 7. Welton, T., "Room-temperature ionic liquids. Solvents for synthesis and catalysis," Chem. Rev., Vol. 99 (1999), No. 8, pp. 2071-83.
- 8. Chauvin, Y., Hirschauer, A., and Oliver, H., "Alkylation of isobutane with 2-butene using 1-butyl-3-methylimidazolium chloride-aluminium chloride molten salts as catalysts," J. Mol. Catal., Vol. 92 (1994), No. 1, pp. 155-65.
- 9. Yoo, K., Namboodiri, V.V., Varma, R.S., and Smirniotis, P.G., "Ionic liquid-catalyzed alkylaton of isobutane with 2-butene," J. Catal., Vol. 222 (2004), No. 2, pp. 511-19.
- 10. Huang, C.P., Liu, Z.C., Xu, C.M., Chen, B.H., and Liu, Y.F., "Effects of additives on the properties of chloroaluminate ionic liquids catalyst for alkylation of isobutane and butene," Appl. Catal., A: General, 2004, No. 277, pp. 41-43.
- Olivier-Bourbigou, H., and Hugues, F., "Ionic Liquids in Synthesis," Wiley-VCH, Weinheim, Germany, 2003, pp. 258-81.
- 12. Smith, G.P., Dworkin, A.S., Pagni, M.R., and Zingg, S.P., "Brönsted superacidity of HCl in a liquid chloroaluminate, AlCl3-1-ethyl-3-methyl-1H-imidazolium chloride," J. Am. Chem. Soc., Vol. 111 (1989), No. 2, pp. 525-30.
- 13. Roebuck, A.K., and Evering, B.L., "Isobutane-olefin alkylation with inhibited aluminum chloride catalysts," Ind. Eng. Chem. Prod. Res. Dev., Vol. 9 (1970), No. 1, pp. 76-82.
- Chauvin, Y., Hirschauer, A., and Oliver, H., European Patent 0709356A1, 1996.
- 15. Liu, Z.C., Huang, C.P., and Xu, C.M., Chinese Patent 02149296.4, 2004.
 - 16. Liu, Z.C., Zhang, Y.H., Huang,

C.P., Gao, J.S., and Xu, C.M., "Effect of CuCl additive on catalytic performance of Et₃NHCl/AlCl₃ ionic liquid in C₄ alkylation," Chinese J. Catal., Vol. 25 (2004), No. 9, pp. 693-96.

Ma, B.W., ed., "Clean Fuel Production," China Petrochemical Press,
 2001, pp. 112.

The authors

Zhichang Liu is deputy director of the State Key Laboratory of Heavy Oil Processing, associate dean of the Faculty of Chemical Science and Engineering, and an associate professor at the China University of Petroleum, Beijing. He specializes in clean fuels and ionic liquids



processes. Liu holds a PhD in chemical engineering from Shanxi Institute of Coal Chemistry, Chinese Academy of Sciences.



Rui Zhang is PhD candidate at the China University of Petroleum. His area of study is isobutane alkylation using ionic liquids.

Chunming Xu is director of the State Key Laboratory of Heavy Oil Processing and vice-president of academics at China University of Petroleum. His research interests include petroleum processing, FCC kinetics of heavy oil, numerical simulation of FCC riser



reactor, heavy oil characterization, and ionic-liquid catalyzed alkylation. Xu holds a PhD from the China University of Petroleum.



Rongan Xia is vice-president of PetroChina Lanzhou Petrochemical Co. He has more than 20 years of operations and management experience. Xia holds an MBA from Dalian University of Technology and is currently a PhD candidate at the China University of

Petroleum.

Vol. 27 No. 10

Chinese Journal of Catalysis

文章编号: 0253-9837(2006)10-0868-07 研究论文: 868~874

含 HF 体系中 SAPO-11 分子筛的合成与表征

张胜振, 陈胜利, 董 鹏, 井秀娟, 姜 凯 (中国石油大学(北京) 重质油国家重点实验室, 北京 102249)

摘要:在含 HF 体系中合成了 SAPO-11 分子筛,并采用 X 射线衍射、扫描电镜、低温氮物理吸附、红外光谱和吸附氨的程序升温脱附等手段对其进行了表征.结果表明,相对于常规无 HF 合成体系,在 HF 体系中合成的 SAPO-11 分子筛样品结晶度提高,结晶速度加快,分子筛单晶增大,分子筛晶粒聚集体的粒径减小,比表面积降低,孔体积与平均孔径增大.合成体系中加入HF 后 SAPO-11 分子筛上 B 酸中心的总酸量和弱酸量降低,中强酸中心的比例有所提高,而 L 酸的酸量和酸强度无明显改变.

关键词: SAPO-11 分子筛; 氟化氢; 晶化; 酸性; 合成

中图分类号: O643 文献标识码: A

Synthesis and Characterization of SAPO-11 Molecular Sieve in the Presence of Fluoride Ions

ZHANG Shengzhen, CHEN Shengli*, DONG Peng, JING Xiujuan, JIANG Kai (State Key Laboratory of Heavy Oil Processing, China University of Petroleum, Beijing 102249, China)

Abstract: The silicoaluminophosphate SAPO-11 molecular sieve was synthesized by the hydrothermal crystallization method in the presence of fluoride ions and characterized by X-ray diffraction, scanning electron microscopy, N_2 adsorption, Fourier transform infrared reflectance spectroscopy, and temperature-programmed desorption of adsorbed NH3. The results showed that the addition of HF increased the crystallization rate of SAPO-11 and decreased the crystallization time considerably, and hence the relative crystallinity of SAPO-11 increased whereas the defects in the crystal lattice decreased. Prismatic crystal aggregates of $1\!\sim\!3~\mu m$ in length were obtained in the presence of HF during the preparation of SAPO-11, whereas spherical aggregates with diameters of $8\!\sim\!10~\mu m$ were synthesized without using HF. The SAPO-11 synthesized in the presence of HF possessed lower BET surface area, higher pore volume, and larger mean pore diameter and crystal size than that prepared without HF. The addition of HF into the synthesis system decreased the amount of surface acid sites and increased the acidic strength of B acid sites on SAPO-11, while the amount of L acid sites kept constant.

Key words: SAPO-11 molecular sieve; hydrogen fluoride; crystallization; acidity; synthesis

近年来,SAPO-11 分子筛以其独特的孔道结构及可调变的酸性,在正构烷烃的异构化反应中表现出较高的活性和选择性^[1~4]. 因而可以应用于烷烃的异构化反应来提高汽油的辛烷值,改善柴油和润滑油的低温性能,尤其是在润滑油馏分及中间馏分油的异构脱蜡反应中具有较好的应用前景^[5~7],引起了人们的极大兴趣. 此外,SAPO-11 还在 α-烯烃

的骨架异构化反应^[8,9]、间二甲苯异构化制备对二甲苯的反应^[10]以及合成气制备低碳烃^[11]的反应中表现出很高的择形作用.

SAPO-11 分子筛本身是一种亚稳态结构, Si⁴⁺, P⁵⁺和 Al³⁺均以四面体形式与氧配位形成基 本结构单元. 其非交叉的十元环主孔道是由四元环 和六元环构成的椭圆型一维直孔道,孔径为 0.39

收稿日期: 2006-02-28. **第一作者**: 张胜振, 男, 1976 年生, 博士研究生.

联系人: 陈胜利. Tel: (010) 89733396, (010) 89733783; Fax: (010) 69724721; E-mail: slchen @cup. edu. cn.

基金项目:中国石油天然气集团公司中青年创新基金(04 E7035)和中国石油天然气股份公司科技风险创新基金资助项目。

nm ×0.64 nm. SAPO-11 分子筛具有与 AIPO-11 相 同的三维骨架结构,为 AEL 构型. 通常采用水热法 合成 SAPO-11 分子筛,合成过程中原料的性质和配 比、成胶温度和方法、有机模板剂的类型和组成、晶 化时间和温度以及 pH 值等对产物的影响很大,合 成产物中经常含有 SAPO-5 及 SAPO-31 等杂晶.

研究表明,在沸石的合成过程中,氟离子的存在 不仅起重要的矿化作用,而且还有结构导向及模板 作用. 氟离子能够象有机模板剂一样进入材料的空 穴中并显著改善材料结构的稳定性[12]. 文献[13~ 171分别在含氟离子体系中合成了 SAPO-31 及 SAPO-34 分子筛,发现氟离子的加入可以提高分子 筛的结晶度并加快其晶化速率. Li 等[18]以二异丙 胺为模板剂,以 HF 为矿化剂,将 MgO 加入到合成 体系中制备了 MAPO-11 单晶,该单晶尺寸约是常 规法制备的 AIPO-11 晶粒尺寸的 8 倍,并且晶化时 间大大缩短,结晶度有所提高. 而氟离子的加入对 SAPO-11 的合成、结构及物化性质所产生的影响, 目前尚不很清楚.

本文在含 HF 体系中合成了 SAPO-11 分子筛, 并通过 X 射线衍射(XRD)、扫描电镜(SEM)、低温 氮物理吸附、红外光谱(FT-IR)和吸附氨的程序升 温脱附 (NH3-TPD) 等手段表征了催化剂,考察了 HF对 SAPO-11 分子筛的合成、结构及物化性质的 影响.

实验部分

1.1 SAPO-11 分子筛的制备

分别以拟薄水铝石粉($w(Al_2O_3) = 70\%$, 温州 双华集团)、酸性硅溶胶(w(SiO₂) = 25 %)和磷酸 $(w(H_3PO_4) = 85\%)$ 为铝源、硅源和磷源,以二正丙 胺(DPA, 化学纯)和二异丙胺(DIPA, 化学纯)的混 合物为模板剂. 按一定的摩尔比配料,在剧烈搅拌 将拟薄水铝石加入到磷酸溶液中,依次加入酸性硅 溶胶、模板剂混合成胶,然后加入一定量的 HF,搅 拌混合得到蜡状固体凝胶. 将反应物凝胶装入带有 聚四氟乙烯内衬的不锈钢晶化釜中,密封,在160~ 240 ℃自生压力下静态晶化 2~48 h. 晶化产物经 过滤、洗涤,于100 ℃干燥8~12 h即得分子筛原 粉. 非 HF 存在条件下 SAPO-11 分子筛采用相同方 法制备,只是制备过程中不加入 HF.

1.2 SAPO-11 分子筛的表征

采用 Shimadzu Lab XRD-6000 型 X 射线衍射仪

鉴定样品的晶相结构, Cu 靶, K_{α} 辐射源, 管电压 40 kV, 管电流 30 mA, 扫描范围 $2\theta = 5^{\circ} \sim 40^{\circ}$, 扫描 速率 2°/ min. 样品的相对结晶度定义为 XRD 谱中 $2\theta = 8.09^{\circ} \sim 23.15^{\circ}$ 间的所有特征衍射峰峰面积之 和与标准样品(本实验室合成的结晶度最高的 SAPO-11 分子筛) 的所有特征峰峰面积之和的比

采用日立 HITACHI S-4200 型扫描电子显微镜 观察样品的表面形貌,测试前样品采用物理法镀金.

采用 - 196 ℃下氮吸附-脱附方法在美国 Micromeritics 公司生产的 ASAP 2020 型多功能自动吸 附仪上对分子筛的比表面积和孔容进行测定. 利用 N_2 吸附曲线上相对压力 (p/p_0) 在 $0.05 \sim 0.30$ 间 的数据计算样品的比表面积 (A_{BET}) ,用BJH法测 定中孔孔体积(V_p)及平均孔径(d).

在 BIO-RAD FRS 3000 型 FT-IR 红外光谱仪 上测定 SAPO-11 吸附吡啶的红外光谱. 首先将样 品磨成细粉,压制成自撑片置于红外光谱仪的原位 池中密封,升温至350 C,保持2h,并保持真空度 $<1 \times 10^{-3}$ Pa,降温至室温测量 - OH 的红外谱图; 然后在室温下向原位池中通入吡啶蒸气,维持吸附 平衡 15 min 至吸附饱和,将体系分别升温至 200 和 350 C真空脱附(真空度 < 1 × 10 - 3 Pa), 再降温至 室温并测量红外谱图.

采用 NH₃-TPD 方法对催化剂的酸性进行表 征. 实验装置为 TP 5000 型多用吸附仪(天津先权 仪器有限公司),实验条件为: 称取 200 mg 催化剂 样品置于石英管中,以流量为 20 ml/ min 的氮气为 载气,样品首先在 500 °C下恒温 20 min 以脱除催化 剂表面吸附的杂质,然后冷却至100 ℃; 当基线平 稳后,通入NH,气至吸附饱和,继续通氮气吹扫一 段时间,以脱除样品表面物理吸附的氨,然后以10 C/min 的速率升温至 500 ℃进行 NH3 脱附,最后 在500 C下稳定30 min. 采用 TCD 检测器记录 NH3 的脱附信号,同时用稀盐酸溶液吸收脱附氨, 用滴定法测得催化剂样品上的总酸量.

2 结果与讨论

2.1 HF:P₂O₅比的影响

不同 SAPO-11 样品的 XRD 谱如图 1 所示. 两 种体系中合成的分子筛在 $2\theta = 8.1^{\circ}$, 9.4° , 13.1° , 15.6°, 20.3°, 21.0°和 22.1°~23.2°处均出现 SAPO-11 的特征峰[19], 没有其它杂质峰出现,说明 含 HF 体系中合成的分子筛样品具有较好的 AEL 晶相结构和较高的结晶度.在 HF 存在条件下合成的 SAPO-11 的特征衍射峰的半峰宽明显变窄,由 Scherrer 公式计算得出该样品的微晶晶粒尺寸为50.8 nm,大于无 HF 体系中合成的 SAPO-11 的微晶晶粒(46.9 nm).

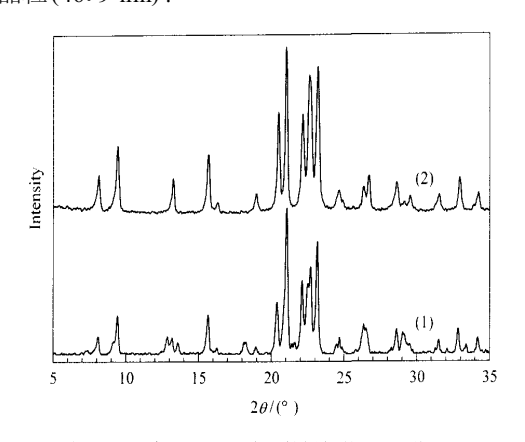


图 1 两种 SAPO 11 分子筛样品的 XRD 谱

Fig 1 XRD patterns of as synthesized SAPO-11 samples without (1) and with HF (2)

在本实验合成体系及晶化条件下,都可以得到 具有较高结晶度的 SAPO-11 分子筛纯相,且各样品 的 XRD 谱相同,样品中只有 SAPO-11 晶体,没有其 他杂晶. 在相同的晶化条件下, HF 的加入可以明 显地提高 SAPO-11 分子筛的相对结晶度; 并且在 190 ℃, 24 h 和反应混合物组成 1.0P₂O₅:1.0Al₂O₃ 0.4SiO₂:1.0(DPA + DIPA):28H₂O 不变的条件 下,当 HF:P2O5 由 0 增大到 0.8 时, SAPO-11 的相 对结晶度由 72.1%增大到 89.9%; 固定其它条件 不变,将晶化温度降至 175 ℃,含 HF 体系中得到 的 SAPO-11 分子筛样品的相对结晶度也比常规无 HF 体系中制备的样品的结晶度高. 这可能是由于 在含 HF 体系中氟离子的存在平衡了模板剂上的正 电荷,从而减少了分子筛晶体的缺陷,有利于形成高 质量的分子筛晶体;而体系中无氟离子时,模板剂 的正电荷大多由分子筛骨架缺陷造成的负电荷来平 衡.因此得到的分子筛往往缺陷较多.致使结晶度下 降 $^{[20]}$. 另外,体系中加入的 HF 与 DPA 和 DIPA 相 互作用,形成复合模板剂进入到微孔分子筛的骨架 中,在晶化过程中除起到矿化剂作用外,还对 SAPO-11 分子筛的形成起结构导向作用. 当 HF/ $P_2O_5 > 0.8$ 时,继续增加 HF 的量,样品的结晶度反 而减小.这是由于随着 HF 投料量的增加.体系的 pH值降低,体系凝固成蜡状凝胶的速度加快,使体系混合不均匀所致.

2.2 晶化温度的影响

常规水热法合成 SAPO-11 的过程中,晶化温度会影响水(溶剂) 在釜中的自生压力,改变分子筛晶体的成核与生长以及介稳态间的相变,从而影响分子筛的晶化过程及晶化产物的结晶度和晶相结构. 图 2 为 HF 存在条件下晶化温度对合成 SAPO-11 的影响. 在 160~230 ℃时,含 HF 合成体系中所得产物均为纯相的 SAPO-11,且随着晶化温度的提高,产物的相对结晶度增大. 这可能是由于升高晶化温度,不仅可以缩短晶体的陈化诱导期,还可以加快晶体的生长速率.

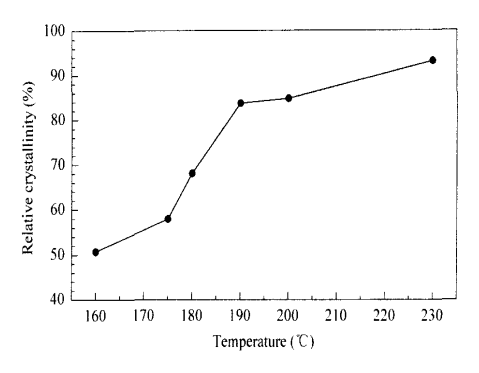


图 2 含 HF体系中晶化温度对合成 SAPO-11 分子筛的影响

Fig 2 Effect of crystallization temperature on synthesis of SAPO-11
(Crystallization conditions: 1.0P₂O₅:1.0Al₂O₃:

(Crystallization conditions: 1.0P₂O₅:1.0Al₂O₃: 0.4SiO₂:1.0(DPA + DIPA) 28 H₂O:1.0HF, 18 h. DPA — Dipropyl amine, DIPA — Diisopropyl amine.)

2.3 晶化时间的影响

据文献[21,22]报道,常规水热法合成 SAPO-11 分子筛时,在 4~6 h 后才能检测到 SAPO-11 晶体,20 h 后晶化完全.在 HF 存在和晶化温度为200 C的条件下,晶化时间对合成 SAPO-11 分子筛结晶过程的影响如图 3 和图 4 所示.在合成体系中加入 HF 后,初始凝胶的组成与不含氟化物的组成一样,仅包含块磷铝矿晶相及 AlPO₄ 方晶石相.当合成体系中有 HF 存在时,晶化时间为 2 h 时即可检测到 SAPO-11 晶相,且具有 82.2%的相对结晶度;而在原料组成相同的情况下用常规水热法合成,晶化 4 h 后尚无 SAPO-11 晶相产生(如图 3 (6)),直至 6 h 时才能检测到较弱的特征衍射峰,说明 HF 的加入能够明显缩短 SAPO-11 的诱导期,加速晶核的形成;含 HF 体系中晶化 8~16 h 时即

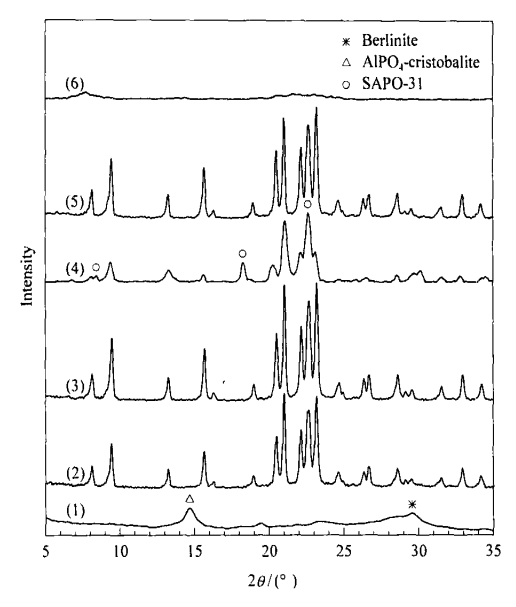


图 3 含 HF 体系中不同晶化时间时合成的 SAPO-11 分子筛的 XRD 谱

Fig 3 XRD patterns of SAPO-11 samples prepared in the presence of HF for 0 h (1) , 2 h (2) , 16 h (3) , 30 h (4) , and 48 h (5) , and SAPO-11 prepared without HF for 4 h (6) (Crystallization conditions: $1.0P_2O_3$ $1.9Al_2O_3$ $0.4SiO_2$: 1.0(DPA+DIPA) $28H_2O$ 1.0HF, 200 C.)

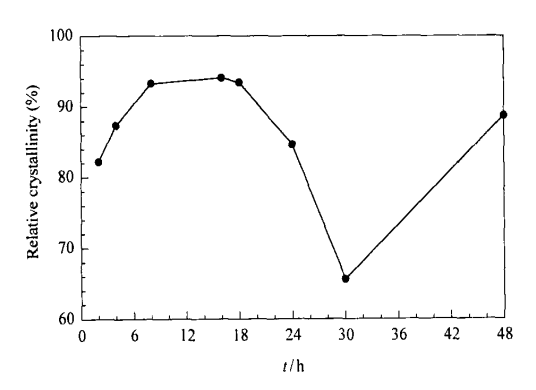


图 4 含 HF 体系中 SAPO-11 分子筛的晶化曲线

Fig 4 Crystallization curve of SAPO-11 synthesized in the presence of HF

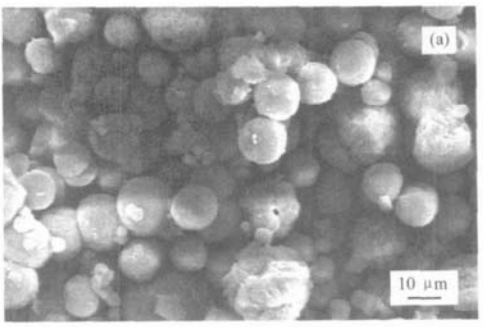
(Crystallization conditions: 1.0P₂O₅: 1.0Al₂O₃: 0.4SiO₂: 1.0(DPA + DIPA) 28H₂O: 1.0HF, 200 °C.)

可晶化完全,比常规法晶化时间大大缩短.继续延长晶化时间,发现 SAPO-11 分子筛在晶化过程中存在转晶现象,当晶化时间达 30 h 时,在 $2\theta = 8.5^\circ$, 19.3°和 22.6°处出现 SAPO-31 的特征衍射峰,表明有少量的 SAPO-31 分子筛生成.延长晶化时间至 48 h, SAPO-31 分子筛的特征峰消失,样品又完全转化为纯 SAPO-11 晶相.

SAPO-31 与 SAPO-11 的结构具有很大的相似 性,也是由六元环和四元环共同构成的具有一维圆 孔道的中孔硅铝磷分子筛,其孔径尺寸为 0.54 nm, 具有 ATO 型结构,合成过程中所用模板剂以 DPA 为主. 正是这种结构上的相似性,使得在 SAPO-11 的合成过程中常伴随 SAPO-31 或 SAPO-5 和 SAPO-41 等杂晶的出现. 文献[21,22]报道在常规 无氟体系中合成 SAPO-11 分子筛时也有类似的转 晶现象,作者认为晶化时间的诱导效应在这种变化 中起主要作用,也就是说一定时间内,体系中溶液相 和固体相组成的变化可能最终诱发分子筛晶体结构 的变化,但常规无氟合成的体系的转晶通常发生在 晶化 40 h 以后[22], 而本文含 HF 体系中的转晶发 生在 30 h 左右,这正是由于 HF 的存在使得晶化诱 导期较常规无氟合成体系大大缩短所致. 因此,在 含氟合成体系中, F 作为矿化剂与模板配合剂影 响着 SAPO-11 分子筛的晶化过程与晶化速度, F-的存在能够使晶核快速形成,使诱导期大大缩短.

2.4 SAPO-11 分子筛的表面形貌

不同体系中合成的 SAPO-11 分子筛的 SEM 照片如图 5 所示. 无氟体系中合成的 SAPO-11 分子



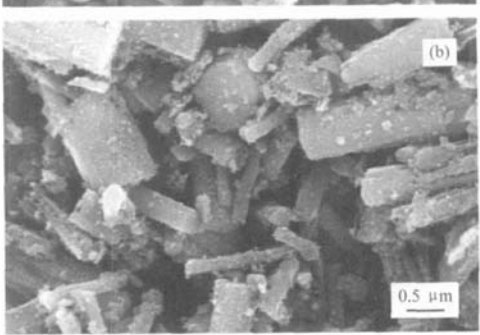


图 5 不同 SAPO-11 分子筛样品的 SEM 照片 Fig 5 SEM images of SAPO-11 samples synthesized without (a) and with HF (b) (Crystallization conditions: 1.0P₂O₅:1.0Al₂O₃:0.4SiO₂:

1.0(DPA + DIPA) 28H₂O 1.0HF, 190 °C, 24 h.)

筛微晶聚集成直径为 8~10 μm 的球形颗粒,而在含 HF 体系中制备的 SAPO-11 分子筛微晶聚集成长度为 1~3 μm 的细棒状颗粒.由此可知, HF 的加入有利于形成小颗粒的 SAPO-11 分子筛聚集体. HF 对于 SAPO-11 分子筛的颗粒大小及形貌特征的影响可能有两方面的原因:其一是 HF 可与铝源和硅源形成螯合物^[23],在成胶阶段可以消除 AlPO4 凝胶中的大晶核核心,在晶化阶段加大了晶核的形成速度和数量,从而分散了凝胶中物料的聚集,易于形成粒度较小的分子筛颗粒聚集体;其二是 HF 的加入使 AlPO4 初始凝胶凝固成蜡状固体,阻碍了晶核的聚集,改变了晶核的聚集方式,有利于形成小颗粒的分子筛.

2.5 SAPO-11 分子筛的孔结构性质

不同 SAPO-11 分子筛样品的孔结构性质如表 1 所示. 含 HF 体系中合成的 SAPO-11 分子筛样品的 比表面积为 175.8 m²/g, 小于无 HF 体系中合成的 SAPO-11 的比表面积(211.8 m²/g); 而含 HF 体系中合成的 SAPO-11 的孔体积及平均孔径却大于无 HF 体系中合成的 SAPO-11. 这说明在分子筛的合成过程中添加 HF,不仅可以提高分子筛的结晶度,而且有利于形成较大的 SAPO-11 分子筛单晶(XRD 谱图中特征峰变窄也证实了这一点),从而降低了 SAPO-11 分子筛聚集体颗粒的比表面积,形成了较大的孔体积和平均中孔孔径. Xu 等[24]详细研究了 F 对 CHA 型 SAPO-34 晶化的影响,发现当 F 存在时可以生成完美的较大单晶.

表 1 不同 SAPO-11 分子筛样品的孔结构性质

Table 1 Pore structure properties of different SAPO-11

samples			
HF :P2O5 molar ratio	$A_{BET}/(m^2/g)$	$V_{\rm p}/({\rm cm}^3/{\rm g})$	d∕ nm
0	211.8	0.186	3.5
1.0	175.8	0.257	5.8

Crystallization conditions: $1.0P_2O_5$: $1.0Al_2O_3$: $0.4SiO_2$: 1.0 (DPA + DIPA) $28H_2O$, 190 °C, 24 h.

2.6 SAPO-11 分子筛的表面酸性质

2.6.1 羟基红外光谱

SAPO-11 分子筛晶粒的外表面和结构缺陷处存在大量的具有弱酸性的 P-OH, Al-OH 和 Si-OH 等终端羟基. 在含 HF 体系中制备的 SAPO-11 分子筛样品羟基的红外光谱如图 6 所示. 样品在 3 741.9,3 674.4 和 3 630.3 cm⁻¹处出现三个羟基的吸收峰,其中 3 741.9 和 3 674.4 cm⁻¹处的吸收峰对应于 SAPO-11 分子筛晶粒外表面的 Si-OH 和

P-OH的伸缩振动, 3 630.3 cm⁻¹处的吸收峰归属于 Si-O(H)-Al,即质子酸中心^[25]; 无 HF 体系中合成的 SAPO-11 样品中 3 525.9 cm⁻¹处的吸收峰对应于 Al-OH 端羟基伸缩振动,而含 HF 体系中合成的 SAPO-11 样品在 3 525 cm⁻¹处未观察到明显的 Al-OH 端羟基峰,说明绝大部分 Al 处于分子筛的骨架四面体中,即 HF 的加入可以有效地避免非骨架铝的形成.

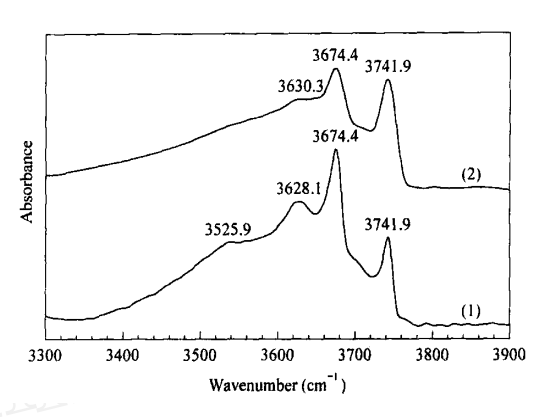


图 6 不同 SAPO-11 分子筛样品中羟基的红外光谱

Fig 6 IR spectra of hydroxyl groups in SAPO-11 samples synthesized without (1) and with HF (2) (Crystallization conditions: 1.0P₂O₅:1.0Al₂O₃:0.4SiO₂: 1.0(DPA+DIPA) 28H₂O:1.0HF, 190 °C, 24 h.)

2.6.2 吸附吡啶的红外光谱

图 7 为 HF 体系中合成的 SAPO-11 分子筛样 品在不同温度下吸附吡啶的红外光谱. 在 $1600 \sim 1400 \text{ cm}^{-1}$ 之间存在 3个吸附吡啶形成的 C- C 弯曲振动峰 其中 1541.1 和 1452.4cm -1 处的吸收

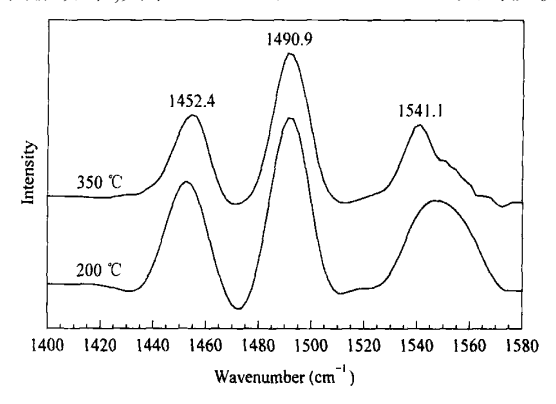


图 7 含 HF 体系中合成的 SAPO-11 分子筛样品 吸附吡啶的 IR 光谱

Fig 7 IR spectra of pyridine adsorbed on SAPO-11 samples synthesized in the presence of HF (Crystallization conditions: 1.0P₂O₅:1.0Al₂O₃:0.4SiO₂: 1.0(DPA+DIPA) 28H₂O:1.0HF, 190 C, 24 h.)

峰分别是由吡啶分子吸附在 B 酸位和 L 酸位上形成的;1 490.9 cm $^{-1}$ 处的最强峰是由吡啶吸附在 B 酸位和 L 酸位上共同形成的。B 酸量和 L 酸量由 Lambert-Beer 方程 $A=\varepsilon CL$ (A 是样品的 IR 谱的吸收率; ε 是相关校正系数,B 酸位上的 $\varepsilon_B=0.059+0.004A$,L 酸位上的 $\varepsilon_L=0.084+0.003A$;C 是酸量;L 为样品的特征参数) 计算,结果列于表 2. 以 350 C脱附后测得的吡啶吸附量为强酸量,以 200 C脱附后测得的吡啶吸附量作为总酸量,两者之差即为弱酸量。与常规无 HF 水热法合成的 SAPO-11 样品相比,含 HF 体系中合成的 SAPO-11 样品的弱 B 酸量降低,但强 B 酸量增加;两种 SAPO-11 样品上的 L 酸酸量的差别不大。说明在合成体系中加入HF 可以调变 B 酸酸量和酸强度,而对 L 酸的影响并不明显。

表 2 不同 SAPO 11 分子筛样品的 B酸和 L 酸酸量

Table 2 Amount of B and L acid sites in different SAPO-11 samples determined by IR bands of pyridine-adsorption

HF :P ₂ O ₅	B acid site (mmol/g)			d site	B/L ratio		
molar ratio	200 °C	350 °C	200 °C	350 °C	200 °C	350 C	
0	6.18	0.94	1.32	1.31	4.69	0.71	
1.0	1.81	1.72	1.41	1.27	1.28	1.35	

 $\label{eq:crystallization} \begin{array}{ll} Crystallization \ conditions\colon \ 1.\ 0P_2O_5\ \ \vdots 1.\ 0Al_2O_3\ \ \vdots 0.\ 4SiO_2\ \ \vdots 1.\ 0\\ (DPA+DIPA)\ \ 28\,H_2O\ ,\ 190\ \ \ C\ ,\ 24\ h. \end{array}$

2.6.3 NH-TPD 结果

表 3 为不同制备条件下得到的 SAPO-11 样品的 NH₃-TPD 结果. 130~190 C间 NH₃ 的脱附峰 I 和脱附峰 II 对应于 NH₃ 在 SAPO-11 分子筛骨架的弱酸中心上的脱附, 265~290 C间的脱附峰对应于 NH₃ 在 SAPO-11 分子筛骨架的中强酸中心上的脱附^[25]. 从表中可以看出,在相同晶化温度下,延长晶化时间,样品的酸量和酸强度逐渐增大,中强酸中心上 NH₃ 的脱附温度逐渐升高. 在相同晶化时间条件下,晶化温度越高样品的酸量和中强酸的比例增大. 这是由于提高晶化温度可以加快 SAPO-11 分子筛的晶化速率,促进 Si 进入分子筛的骨架之中

形成更多的酸中心. 与常规无 HF 水热法得到的分子筛(表 3 中样品 4)相比,在相同的制备条件下,含 HF 体系中制备的 SAPO-11 分子筛(表 3 中样品 2)的总酸和弱酸酸量降低,而中强酸量与弱酸量的比例却明显增大. 说明制备过程中 HF 的加入一方面降低了 SAPO-11 分子筛的酸量,另一方面却使弱酸中心变成中强酸中心,使得中强酸量与弱酸量的比例有较大幅度的提高. 这可能是由于氟离子的存在改变了分子筛样品中铝和硅的分布状态所致.

红外光谱和 NH3-TPD 结果说明在合成体系中 添加 HF 使 SAPO-11 分子筛的酸量(尤其弱酸中心 的量) 明显降低,而中强酸中心的比例却有较大幅度 的提高. 这可能是由于制备过程中氟离子的存在改 变了凝胶体系中 Si 的存在状态,从而影响了 Si 同晶 取代进入分子筛骨架的方式所致. SAPO-11 分子筛 与 AIPO4-11 具有相同的 AEL 拓扑结构,是由 Si 原 子同晶取代 AIPO4-11 骨架中的 P或(和) AI 原子后 形成的. 由于 $A1PO_4$ -11 分子筛的骨架是由 PO_4 ⁺ 和 AlO4 四面体交替组成的,因而骨架呈电中性,分子 筛样品不具有质子酸中心. Si 主要通过两种方式进 入 AlPO₄-11 分子筛的骨架^[26], SM2: 一个 Si 原子 取代 AIPO4-11 骨架中的一个 P 原子,产生一个质子 酸中心; SM3: 两个 Si 原子同时取代 AlPO4-11 骨 架中的一个 P 原子和一个 AI 原子. 当硅含量较低 时以 SM2 取代为主,产生 SAPO 区(Si(4Al), 如图 8中 Si^a); 当硅含量较高时同时发生 SM2 与 SM3 取代, SAPO-11 骨架中除了产生 SAPO 区外,还产 生纯硅区(Si(0Al),如图 8中的 Si^e)以及与 AIP 区 交界处的 Si(nAl)($n = 1 \sim 3$)区(如图 8 中的 Si^b, Si^c和 Si^d). SAPO-11 分子筛的酸性除了来源于 SAPO 区的 B 酸中心外,还来源于纯硅区与 PAI 区 交界处的 $Si(nAl)(n=1\sim3)$ 区,而且这种酸中心的 强度比 SAPO 区的 B 酸中心的酸强度高. 在无 HF 体系中,硅溶胶颗粒缓慢地转移到 SAPO-11 晶核周 围, Si 原子进入 AIPO4-11 骨架的速度较慢,取代方

表 3 不同 SAPO-11 分子筛样品的 NH₅-TPD 结果

Table 3 NH₃-TPD data of different SAPO-11 zeolite samples

	Crystallizati	rystallization condition Temperature of NH ₃ desorption peak (C) Acid amo					d amount (n	nmol/g)		
Sample	t/h	θ/ °C	I	II	III	I	II	\coprod	Total	II/ (I + II)
1	4	190	134.1	174.3	264.9	0.104	0.028	0.024	0.16	0.18
2	24	190	134.6	179.0	286.1	0.098	0.040	0.034	0.17	0.25
3	24	230	139.1	186.2	285.3	0.116	0.031	0.044	0.19	0.30
4 *	24	190	137.7	186.5	287.8	0.174	0.051	0.033	0.26	0.14

 $Crystallization\ conditions: 1.0P_2O_5\ 1.0Al_2O_3\ 0.4SiO_2\ 1.0(DPA+DIPA)\ 28\,H_2O\ 1.0HF. \quad \ ^*SAPO-11\ sample\ synthesized\ in\ the\ absence\ of\ HF.$

式以 SM2 为主,有利于形成较多的 SAPO 区,较少的纯硅区及与 PAI 区交界处的 Si(nAl)(n=1~3)区. 因此,无 HF 体系中合成的 SAPO-11 分子筛较含 HF 体系中制备的样品具有较多的弱 B 酸中心,且酸强度相对较弱;合成体系中加入 HF 后,HF 可以与硅溶胶形成 SiF 2_6 一整合物,加速了硅源的溶解,硅原子进入 AlPO 4 -11 骨架的速度较快,SM2 与SM3 两种取代方式同时发生,有利于形成较多的纯硅区及与 PAI 区交界处的 Si(nAl)(n=1~3)区,较少的 SAPO 区. 因而,HF 存在时合成的 SAPO-11的总酸量降低,而中强酸的比例有所提高.

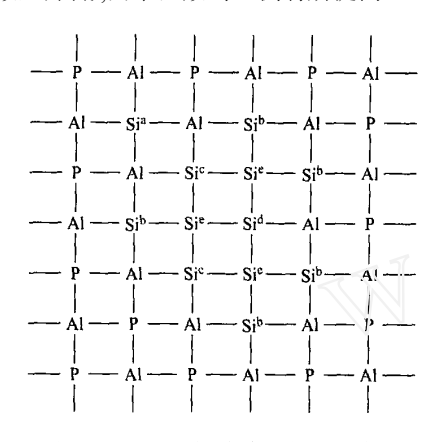


图 8 SAPO-11 分子筛中 Si 的化学环境 Fig 8 Chemical environment of Si in SAPO-11

3 结论

与常规无 HF 水热法合成的 SAPO-11 分子筛相比,在 HF 体系中合成的 SAPO-11 分子筛具有较高的结晶度, HF 在合成过程中不仅起到矿化剂和结构导向剂的作用,还能加速晶核的形成,缩短晶化诱导期,样品呈长度为 1~3 μm 的细棒状颗粒.含 HF 体系中合成的 SAPO-11 分子筛单晶增大,比表面积降低,孔体积和平均孔径增大.合成体系中加入 HF 后, SAPO-11 分子筛的总酸量和弱酸量降低,而强酸的比例提高.

参考文献

- Campelo J M, Lafont F, Marinas J M. J Catal, 1995,
 156(1): 11
- Campelo J M , Lafont F , Marinas J M. Zeolites , 1995 , 15
 (2): 97
- 3 Campelo J M , Lafont F , Marinas J M. J Chem Soc , Faraday Trans , 1995 , 91 (10) : 1551
- 4 Campelo J M, Lafont F, Marinas J M. Appl Catal A,

- 1997, 152(1): 53
- 5 Girgis M J , Tsao Y P. Ind Eng , Chem Res , 1996 , 35 (2): 386
- 6 Campelo J M, Lafont F, Marinas J M. Appl Catal A, 1998, 170(1): 139
- 7 Park K.C., Ihm S.K. Appl Catal A., 2000, 203(1): 201
- 8 Miller S J. US 6 281 404. 2001
- 9 Yang S M, Lin J Y, Guo D H, Liaw S G. Appl Catal A, 1999, 181(1): 113
- 10 Sinha A K, Seelan S. Appl Catal A, 2004, 207 (1-2): 245
- 11 Coughlin P K, Rabo J A. US 4 556 645. 1985
- 12 Kessler H. Microporous Mesoporous Mater, 1998, 22 (4-6): 517
- 13 Abbad B , Attou M , Kessler H. Microporous Mesoporous Mater , 1998 , 21(1-3): 13
- 14 刘红星, 谢在库, 张成芳, 陈庆龄. 催化学报(Liu H X, Xie Z K, Zhang Ch F, Chen Q L. *Chin J Catal*), 2003, **24**(4): 279
- 15 刘红星, 谢在库, 张成芳, 陈庆龄, 张玉贤. 催化学报 (Liu H X, Xie Z K, Zhang Ch F, Chen Q L, Zhang Y X. *Chin J Catal*), 2003, 24(11): 849
- 16 Vistad O B, Akporiaye D E, Taulelle F, Lillerud K P. Chem Mater, 2003, 15(8): 1639
- 17 Vistad O B, Akporiaye D E, Taulelle F, Lillerud K P. Chem Mater, 2003, 15(8): 1650
- 18 Li J J , Guo Y , Li G D , Chen J S , Li C J , Zou Y C. Microporous Mesoporous Mater , 2005 , 79 (1-3) : 79
- 19 Meriaudeau P, Tuan V A, Nghiem V T, Lai S Y, Hung L N, Naccache C. J Catal, 1997, 169(1): 55
- 20 徐如人, 庞文琴, 于吉红, 霍启升, 陈接胜. 分子筛与 多孔材料化学. 北京: 科学出版社(Xu R R, Pang W Q, Yu J H, Huo Q Sh, Chen J Sh. Chemistry — Zeolites and Porous Materials. Beijing: Sci Press), 2004. 238
- 21 汪哲明, 阎子峰. 燃料化学学报(Wang Zh M, Yan Z F. *J Fuel Chem Technol*), 2003, **31**(4): 360
- 22 Lopez C M, Machado F J, Goldwasser J, Mendez B, Rodriguez K. Zeolites, 1997, 19 (2-3): 133
- 23 祁晓岚, 刘希尧, 陈钢, 陈学艺, 李士杰, 林炳雄. 高等学校化学学报(Qi XL, Liu X Y, Chen G, Chen X Y, Li Sh J, Lin B X. *Chem J Chin Univ*), 2000, **21**(8): 1161
- 24 Xu Y, Maddox P J, Couves J W. J Chem Soc, Faraday Trans, 1990, 86(2): 425
- Meriaudeau P, Tuan V A, Lefebvre F, Nghiem V T, Lai S Y, Hung L N, Naccache C. Microporous Mesoporous Mater, 1998, 22(1-3): 435
- 26 Alfonzo M , Goldwasser M , Lopez C M , Machado F J , Matjushin M , Mendez B , Ramirez de Agudelo M M. J Mol Catal A , 1995 , 98 (1): 35

(Ed YHM)

文章编号: 0253-2409 (2006) 04-0427-07

大港减压渣油超临界萃取萃余残渣结构特征研究

张占纲1,2,郭绍辉1,赵锁奇1,牟 彤3

(1. 中国石油大学(北京)重质油国家重点实验室,北京 102249; 2 北京航空工程技术研究中心,北京 100076; 3. 中国石油天津石化分公司,天津 300271)

摘 要:通过超临界萃取方法对大港减压渣油进行深度窄馏分切割,利用钌离子催化氧化 (R LCO)对其抽余残渣进行选择性降解,对降解生成的混合物进行分离,其中非挥发性羧酸进行甲酯化处理,挥发性羧酸进行苯甲酰甲酯化,最后分别利用 GC-MS等方法进行定性定量分析。结果表明,大港减压渣油超临界萃取萃余残渣分子中含有大量与芳环相连的正构烷基侧链和桥接芳环的聚亚甲基链,芳环的缩合程度小于利用结构族组成等分析方法分析大港减压渣油沥青质得到的结果。大港减压渣油超临界萃取萃余残渣的共价结构信息可对该原料的加工和优化利用提供指导。

关键词:减压渣油;超临界萃取;钌离子催化氧化;结构特征

中图分类号: TE622 文献标识码: A

Structure features of the supercritical fluid extraction and fraction tailing of Dagang vacuum residue

ZHANG Zhan-gang^{1,2}, GUO Shao-hui¹, ZHAO Suo-qi¹, MU Tong³

- (1. State Key Laboratory of Heavy Oil Processing, China University of Petroleum, Beijing 102249, China;
 - 2 Beijing Aeronautical Technology Research Center, Beijing 100076, China;
 - 3. Tianjin Petrochemical Cooperation, Petrochina, Tianjin 300271, China)

Abstract: Dagang vacuum residue was cut into sixteen fractions with supercritical fluid extraction and fraction (SFEF) instrument. The tailing was degraded by ruthenium ions catalyzed oxidation (R ICO) reaction. From this reaction, homologous series of n-alkanoic acids, α , ω -di-n-alkanoic acids and benzenepolycarboxylic acids were detected and measured after esterification with diazomethane or phenacyl bromide. Wherein, n-alkanoic acids represented aromatic-attached n-alkyl side chains, α , ω -di-n-alkanoic acids presented the structure features of the polymethylene bridges between two aromaticunits, and those benzenepolycarboxylic acids indicated the major mode of aromatic condensations in the tailing. The products identified in this study show that the structure features of SFEF tailing, especially aromatic condensations mode, are not same as those results reported. Such information is very useful and important for the deep processing and optimize-use of Dagang vacuum residue. **Key words:** vacuum residue; SFEF; R ICO; structure

石油化学组成和结构一直是石油化工领域的重要研究内容之一,目前通用的方法可以分为两大类: 化学方法和物理方法。其中,化学方法又可以分为选择性降解^[1~5] (如钌离子催化氧化)和非选择性降解^[6~10] (如热裂解)。物理方法大多指的是仪器分析方法,如核磁共振 (NMR)、红外 (FT-R)、X射线近边结构吸收谱 (XANES)、X射线光电子谱 (XPS)、电子自旋共振 (ESR)等。

石油中重质组分的结构分为两类,一类是缔合结构,与分子极性和分子间相互作用力有关;另一类是共价结构,与分子的内部基团结构及其组成有关。

虽然通过现代仪器分析可以直接获取许多有价值的 结构信息,但大都是平均结构信息,如果需要获得石 油中的共价结构更详细的信息,还得依靠化学方法。

本研究利用超临界萃取 (SFEF)方法[11]对大港减压渣油进行了深度切割,通过钌离子催化氧化 (R ICO)反应对萃余残渣进行了选择性降解,将目前仪器无法直接分析的复杂大分子结构进行有选择的断裂,生成经过酯化处理后可以直接用 GCMS等仪器分析的有机羧酸。通过这些脂肪酸和苯多羧酸的分布对降解前残渣中的复杂大分子共价结构进行剖析,深入了解石油重质组分结构,最终为原料的加工

收稿日期: 2005-11-09; **修回日期**: 2006-03-17。

基金项目: 国家重点基础研究发展规划 (973计划, 2004CB217801)。

联系作者: 郭绍辉, Tel: 010-89733316, E-mail: shguo@cup. edu cn_°

作者简介: 张占纲 (1974-), 男, 河北蠡县人, 博士研究生, 主要从事石油化学和油料应用研究。Email: zzwsy@163. com。

路线和优化利用方案提供指导和帮助。

1 实验部分

1.1 样 品 大港减压渣油的性质见表 1,主要元 素组成见表 2。

表 1 大港减压渣油性质

Table 1 Property of Dagang vacuum residue

Property	Carbon	Density	V isco sity	Molecular
factor	residue w /%	$\rho / g \cdot cm^{-3}$	n /mPa⋅s	weight
Value	17. 02	0. 979 6	2 074	1 008

表 2 大港减压渣油的元素组成

Table 2 Elemental composition of Dagang vacuum residue

F1 .	w /	/%	H/C			w /10 ⁻⁶	5	A
Elements	C	Н	(mol ratio)	S	\circ N	16	Ni	V
Composition	85. 91	11. 43	1. 59	2 420. 73	6 052. 7	6	89. 30	1. 00

对大港减压渣油进行超临界萃取,将减压渣油 按质量分数约 5%切割成 16个窄馏分和 1个萃余 残渣,原理和流程见参考文献[12]。超临界萃取操 作条件如下:

分离压力: 4.5 MPa~12 MPa 萃取分馏柱温

度: 240 ℃-230 ℃-220 ℃

溶剂:正戊烷 溶剂流量: 100 mL/m in 原料: 1000 g 萃取时间: 450 m in 超临界萃取所得组分及其收率见表 3。

表 3 大港减压渣油超临界萃取组分切割收率

Table 3 Yield of different fractions by SFEF from Dagang vacuum residue

Fractions	1	2	3	4	5	6	7	8	9	10	11	12	13	14	15	16	Tailing
Pressure p /MPa	5. 73	6. 18	6. 39	6. 55	6. 73	6. 89	7. 09	7. 28	7. 52	7. 75	8 07	8 52	9. 10	9. 91	11. 10	12 00	
Yield w/%	4. 5	4. 9	5. 4	4. 8	4. 9	5. 1	5. 1	5. 1	5. 3	5. 1	5. 0	5. 1	4. 9	4. 9	4. 3	4. 3	24. 1
Accumulative totalw /%	4. 5	9. 4	14. 8	19. 6	24. 5	29. 6	34. 7	39. 8	45. 1	50. 2	55. 2	60. 3	65. 2	69. 9	74. 2	78. 5	102 6

1.2 化学降解 对大港减压渣油超临界萃取得到 的萃余残渣进行 R 100催化降解,采用朱军[13]使用 的反应装置,进行了局部改进,结果见图 1。

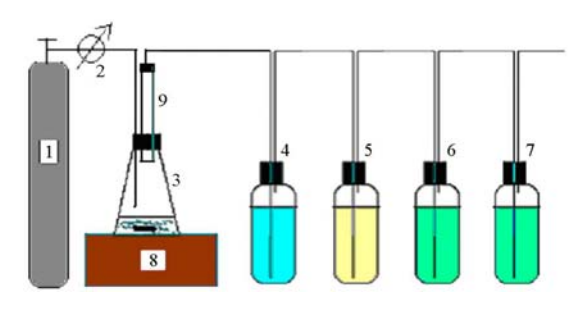


图 1 R ICO反应装置简图

Figure 1 Sketch of the instrument for R ICO reaction $1-N_2$; 2- rotameter, 3- R ICO reactor, 4- pyridine; $5 - H_2 SO_4$; $6,7 - Ba(OH)_2$; 8 - magnetic stirrer, 9—condenser

经研磨的大港减压渣油超临界萃取萃余残渣 200 mg RuCl₃ · 3H₂O 20 mg CCl₄ 20 mL CH₃CN 20 mL和 H₂O 30 mL加入到 200 mL锥形瓶,充分摇 匀后加入 6gNaD4。检查反应装置气密性后通氮 气,气流以气泡单个鼓出为宜。室温下剧烈搅拌反 应 24 h。反应过程中混合物的颜色由深逐渐变浅,

最终由黑色变为苍白色。

- 1.3 降解反应产物分离与处理 R ICO 反应最终产 物为混合物,可分为水相和有机相。样品中不同结 构单元在反应中的转化产物因极性、相对分子质量 不同,分布范围也不同。为了确保分析准确,需要对 反应产物进行分离和处理,生成的易挥发羧酸利用 苯甲酰甲基溴进行苯甲酰甲酯化;生成的非挥发性 组分利用重氮甲烷进行甲酯化,并对甲酯化的产物 进行一元酸酯和二元酸酯分离;反应生成的 002 利 用标准盐酸滴定。
- 1.4 分析检测 GC-MS分析采用 DSQ型色谱 质 谱联用仪。色谱柱为 HP-5MS 30 m ×0. 25 mm × 0. 25 μm。进样温度 290 C,接口温度 300 C,色谱 柱升温程序: 60 C恒温 5 min, 10 C/min 升至 260 ℃, 20 ℃/m in升至 300 ℃,恒温 10 m in。载气为 He气,分流比 30 1。质谱采用 EI电离方式,离子源 温度: 250 ℃,倍增器电压 1502 V,采用全扫描,最大 扫描数:500 amu。

红外分析采用 PE2000型中红外光谱分析仪, 应用了ATR附件。

2 结果与讨论

+8价氧化态的钌离子可以将芳香结构中没有

被取代的芳碳氧化成为 CO_2 ,有取代基的芳碳可以转化为羧基,而饱和结构中的碳原子不参与反应,因此芳香结构的烷基取代基在 R CO 中将转化为一元正构脂肪酸,连接芳环的聚亚甲基桥接链转化为 α , ω 二元正构脂肪酸,部分芳环因羧基的位阻影响无法进一步氧化,最终生成芳羧酸 $^{[14,15]}$ 。 这些羧酸因相对分子质量和极性的区别,在水相和有机相都有分布。

2.1 与芳环相连的正构烷烃取代基 REO中,芳环上连接取代基的碳原子转化为羧基,所以正构烷烃取代基最终将转化为正构脂肪酸。典型反应如:

其中 C₇₊的正构脂肪酸主要分布在有机相, C₆以下的主要分布在水相。这些正构脂肪酸不但证明了在样品中芳环上正构烷烃取代基的存在,还可以直接反映不同碳数取代基量的分布,只不过是取代基碳数要比正构脂肪酸碳数少一个。在对正构脂肪酸进行分析时必须注意的是,小于 C₁₄的羧酸因为挥发性或是在有机相和水相都有分布,造成在有机相的含量分析结果偏低。

有机相甲酯化后 GCMS分析结果见图 2。在质量色谱图中,一元正构脂肪酸甲酯的特征离子是 M clafferty重排峰,m /z 74结果见图 3。

在对有机相产物中的一元正构脂肪酸甲酯进行 归一化后,可以得到不同碳数一元正构脂肪酸的分 布,结果见图 4。

从图 3、图 4可以看出,大港减压渣油超临界萃取萃余残渣降解后生成一系列的一元正构脂肪酸,可以确定该样品分子结构中含有大量与芳环相连的正构烷基侧链,但烷基侧链的碳数分布与文献[2]、

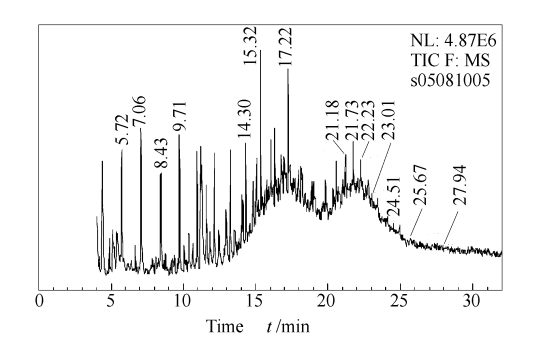


图 2 有机相羧酸甲酯化总离子流谱图
Figure 2 Total ion current mass (TIC) chromatograms of carboxylic acid methyl esters in the organic phase

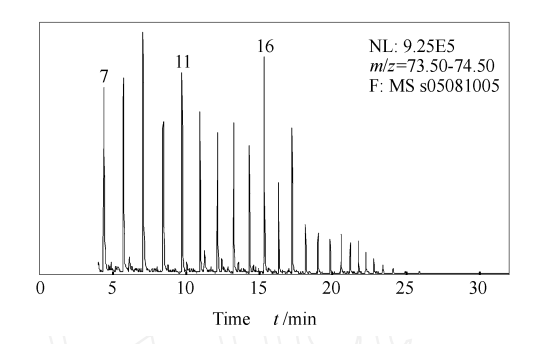


图 3 有机相甲酯化产物中一元正构脂肪酸甲酯质量 色谱图 (m/z=74) (标注数字为羧酸碳数)

Figure 3 Mass chromatograms of *n* -alkanoic acid methyl esters by R ICO from the organic phase (The numbers refer to the carbon numbers of the acids)

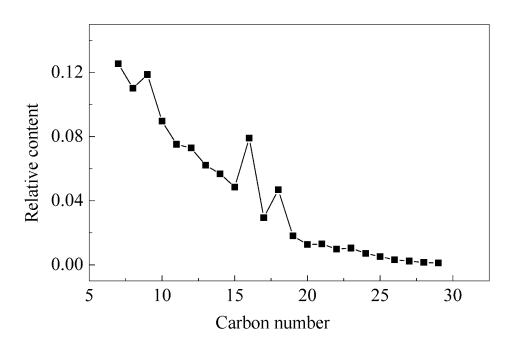


图 4 检测到有机相中一元正构脂肪羧酸甲酯归一化 得到的相对含量分布

Figure 4 The relative distribution of n -alkanoic acids by R ICO with the carbon number

[16]中的沥青质有区别。虽然整体上一元正构脂肪酸的量随着碳数增加呈下降趋势,但 C_{16} 、 C_{18} 明显上升,与 A lberta沥青质^[15]的特征相似,这可能是因为样品中存在 C_{16} 和 C_{18} 的羧酸或羧酸盐,或是因为沥青质中饱和羧酸的酯发生水解造成的^[16]。

图 3和图 4的分析结果还表明,羧酸的烷基链越长,羧酸量越小, C₃₀₊的羧酸就已经很难检测到了。因为 R CO反应中,饱和烷基链不参与反应,所以这就直接证明在大港减压渣油超临界萃取萃余残渣中与芳香结构连接的正构烷烃取代基也是以短链为主,长链取代基相对较少。另外,除了 a 甲酯外,在产物中还检测到了 a 乙酯、a 正丙酯、a 正丁酯以及一些带支链的异构羧酸甲酯,但量明显比正构羧酸甲酯少,这说明在原始样品中存在与其对应的结构单元。

对于挥发性大的羧酸,可以采用苯甲酰甲基溴进行酯化处理。图 5为萃余残渣 R IXO反应产物有机

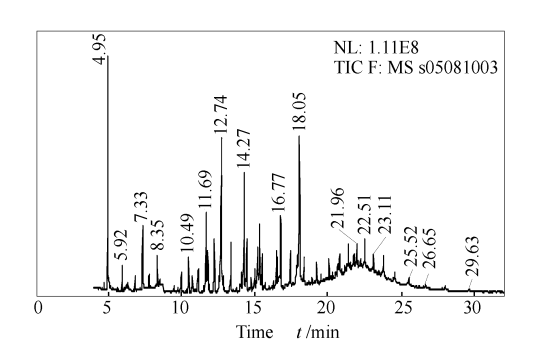


图 5 有机相羧酸苯甲酰甲酯化总离子流谱图 Figure 5 TIC mass chromatograms of carboxylic acid phenacyl ester from organic phase

相中挥发羧酸用苯甲酰甲基溴酯化后的总离子流图。 **2.2 芳环之间聚亚甲基桥接链分析** 桥接不同芳环的烷基链将在 R CO 中转化为二元羧酸 $^{[4]}$,如果这些烷基链是聚亚甲基链 ,转化的二元羧酸就是 α , ω 二元正构脂肪酸 。典型反应如

大港减压渣油超临界萃取萃余残渣的 R \mathbf{CO} 反应产物中也存在一定量的 α , ω 二元正构脂肪酸,其中 \mathbf{C}_8 以上 α , ω 二元正构脂肪酸主要分布在有机相, \mathbf{C}_6 、 \mathbf{C}_7 在水相和有机相都有分布, \mathbf{C}_4 、 \mathbf{C}_8 主要分布在水相中结果见图 6和图 7。由于联苯和二苯甲烷 R \mathbf{CO} 反应中氧化生成的乙二酸和丙二酸会继续被氧化,所以难以检测到,但可以通过苯多羧酸异构体的分析推测这些结构的存在与否,后文对此将继续讨论。

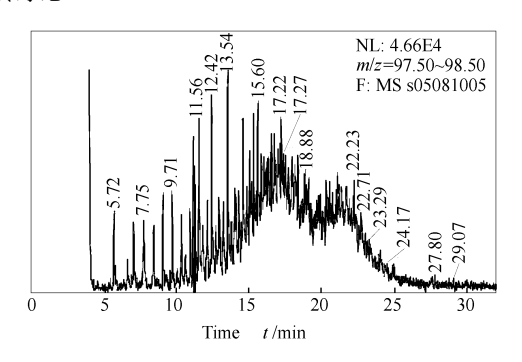


图 6 有机相羧酸甲酯化产物中 α, ω 二元脂肪酸 甲酯谱图 (m /z 98) (包括部分其他脂肪酸酯) Figure 6 TIC mass chroma togram s of α, ω -di-alkanoic

acid methyl esters from the organic phase (Some peaks should attribute to n-alkanoic acid)

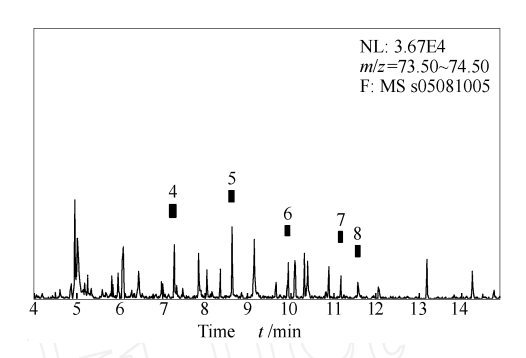


图 7 水相中 α,ω 二元正构脂肪酸甲酯的质量色 谱图 (标注数字为碳数)

Figure 7 Mass chromatograms of α , ω -di-alkanoic acid methyl esters from the aqueous phase

(The numbers refer to the carbon numbers of the acids)

除了直链亚甲基桥接链,还检测到带支链的桥接结构,但量明显小于直链桥接结构。聚亚甲基桥接链随着碳数的增加而减少,本研究中聚亚甲基桥接链最大碳数为 24。

2.3 苯多酸分析与芳香结构 R CO 反应产物中第三种重要的羧酸就是苯二~六元羧酸及苯多酸的一甲基衍生物。这些物质是样品中缩合芳核在氧化过程中因为连接羧基的位阻影响,致使最后一个芳环无法被钉离子进一步氧化,最终生成的一些苯多酸。三元以上的芳羧酸基本分布在水相,二元芳羧酸在有机相和水相都有分布。反应中生成芳羧酸的部分典型反应如下:

在 R ICO 反应中, 芳香结构, 特别是缩合程度较大的结构反应十分复杂, 受到取代基的影响非常大, 但可以通过分析产物中苯多羧酸结构与分布来探索分子中芳香结构缩合方式和程度。部分苯多酸的甲酯及其特征离子见表 4。

下面的结构:

表 4 RICO反应产物中可能存在的苯多酸的甲酯种类

Table 4 Benzenepolycarboxylic acid methyl esters may be detected in R ICO products

Benzenepolycarboxylic acid	Characteristic
methyl esters	ion, m/z
D in ethyl-o-phthalate	163
D in ethyl-p-phthalate	163
1, 2, 3-Benzenetriol, triacetate	221
1, 2, 4-Benzenetriol, triacetate	221
1, 2, 3, 4-Benzenetetracarboxylic acid, tetramethyl ester	279
1, 2, 3, 5-Benzenetetracarboxylic acid, tet-	279
ramethyl ester 1, 2, 4, 5-Benzenetetracarboxylic acid, tetramethyl ester	279

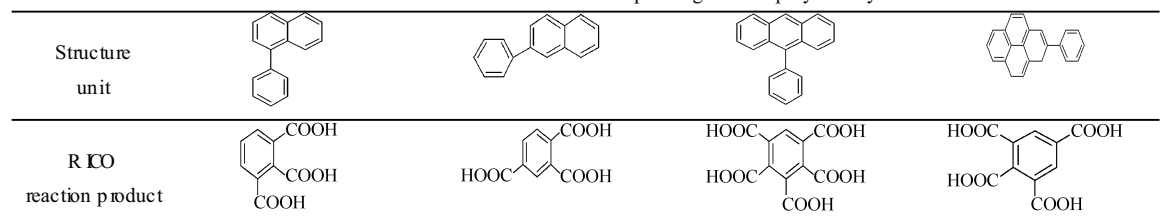
可以在 RICO 反应中转化邻苯二甲酸,后三种 结构除苯二甲酸外,还可以生成苯四酸。所以对于 表 5中的结构及其对应生成的苯多酸,可以分析联 苯结构存在与否。

但应注意的是 RICO 反应产物分析中苯二 ~五 元酸的量的分布并不代表样品中缩合芳香结构的量 的分布[16],从下列反应不难看出, 芳环上的取代对 产物生成倾向有着关键影响。

$$\begin{array}{c} R \quad RICO \\ \hline \\ COOH \\ \end{array} + R-COOH + CO_2 \\ \hline \\ R-COOH + 9CO_2 \\ \end{array}$$

表 5 部分共价结构单元及其对应的羧酸酸

Table 5 Some structure units and their corresponding benzenepolycarboxylic acids



另外,由于取代基对产物的影响,生成苯二~五酸的 几率也很小,以有两个烷基取代基的萘为例,下述十 个反应中只有一种情况能够生成苯二酸。

可见苯多酸的生成不但与结构有关,而且与取 代基数目和取代位置有着直接的关系。

以上对苯多酸的分布及含量对应关系讨论不包 括苯六酸,因为其结构特殊,不受取代基的影响,从 而可以确定样品中芳香结构的最低缩合程度以及量 的多少。如下列结构是可以转化为苯六酸的。

通过上述论理论分析可以确定,在大港减压渣 油超临界萃取萃余残渣的分子结构中, 芳环缩合程 度大于 7的芳核很少,前文提出高度缩合的 4环和 5环迫位缩合的芳香结构也很少。因此,基本可以 确定原来样品分子中以联苯和渺位缩合结构为主, 而且取代基丰富。

2.4 其他氧化产物分析 在 R ICO 中生成的除了 正构脂肪羧酸和苯多酸外,利用红外光谱还检测到 了一些含氧、氮、硫、磷等元素的官能团,其中特征最 明显就是羟基,见图 8和图 9。

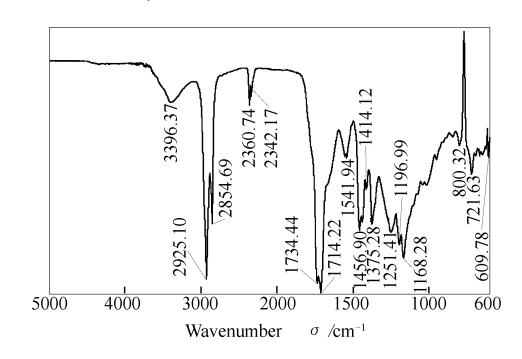


图 8 有机相甲酯化后的红外光谱

Figure 8 FTIR spectrum of the methylated organic phase of RICO

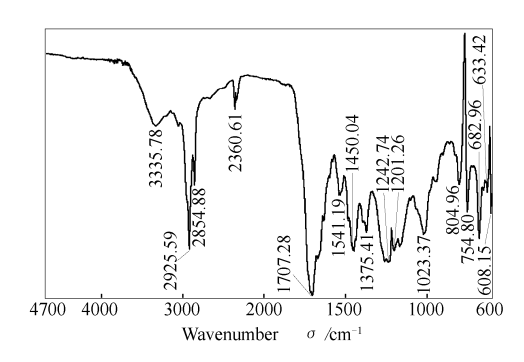


图 9 RICO水相甲酯化后的红外光谱

Figure 9 FTR spectrum of the methylated aqueous phase of R ICO

尤其是 $3\,450\,\,\mathrm{cm}^{-1}\sim 3\,225\,\,\mathrm{cm}^{-1}\sim 1\,470\,\,\mathrm{cm}^{-1}\sim 1\,410\,\,\mathrm{cm}^{-1}\sim 1\,370\,\,\mathrm{cm}^{-1}\sim 1\,325\,\,\mathrm{cm}^{-1}\sim 1\,205\,\,\mathrm{cm}^{-1}\sim 1\,150\,\,\mathrm{cm}^{-1}\sim 950\,\,\mathrm{cm}^{-1}\sim 890\,\,\mathrm{cm}^{-1}$ 处的红外吸收峰说明在水相和有机相的甲酯化产物中都存在叔醇。这可能与样品分子中的叔碳在 R ICO 中的反应有关,其可能历程如下:

由于空间位阻,叔醇的酯化比伯醇和仲醇困难的多,在这种条件根本无法完全进行。另外,在重质油分子结构中叔碳的含量较高,所以在大港减压渣油超临界萃取抽余残渣的 R CO 反应产物的 FT-R 谱图中可以明显观察到羟基的红外吸收峰。含有叔醇基团的物质的质谱中有极强的 m/z 59峰,从而可以进一步确定叔醇的存在。

检测到结构还有带支链的脂肪酸、环烷酸等物质。这些物质的量明显少于正构脂肪酸,但其与样品分子的共价结构也有着直接联系^[4,17]。如:

3 结 语

- (1) 大港減压渣油超临界萃取萃余残渣分子结构中芳香结构的取代基中以正构烷烃为主,最大碳数约为 30;随着碳数的增加,与芳环相连的正构烷基取代基数目呈递降趋势,但碳数为 16和 18的烷基侧链较多.不符合递降趋势:
- (2) 在残渣共价结构中存在链接不同芳环的聚亚甲基桥,最大碳数约为 24,这些亚甲基桥的数目 随着碳数增加呈递降趋势:
- (3) 结构中与芳环相连的正构烷基取代基和聚亚甲基桥的含量很丰富:
- (4) R CO水相检测到的苯多酸可以表明在大港减压渣油的超临界萃取萃余残渣中含有联苯结构,而且由于没有检测到苯六酸,说明在原始样品分子共价结构中稠环芳核的迫位缩合的芳环数一般界于 2~5,而且取代基丰富;超过 7个芳环的完整迫位缩合的结构单元较少:
- (5) 可以推测, 芳环以渺位缩合和联苯结构丰富。

参考文献:

- [1] WANG Z, L ANG W, QUE G Structural characterization of Gudao asphaltene by ruthenium ions catalyzed oxidation [J]. Petrol Sci Technol, 1997, 15(5-6): 559-577.
- [2] STRAUSZ O P, MOJELSKY TW, FARAJIF, LOWN EM. Additional structural details on athabasca asphaltene and their ramifications[J]. Energy Fuels, 1999, 13(2): 207-227.
- [3] 王子军, 梁文杰, 阙国和, 钱家麟. 钉离子催化氧化法研究大庆减压渣油组分的化学结构 [J]. 燃料化学学报, 1999, **27**(2): 102-109. (WANG Zi-jun, LANGWen-jie, QUE Guo-he, QAN Jia-lin. Investigation on chemical structure of fractions in Daqing vacuum residue by ruthenium ions catalyzed oxidation[J]. Journal of Fuel Chemistry and Technology, 1998, **27**(2): 102-109.)
- [4] PENG P, FU J, SHENG G, MORALES-IZQU IERDO A, LOWN E M, STRAUSZ O P. Ruthenium-ions-catalyzed oxidation of an immature asphaltene: Structural features and biomarker distribution [J]. Energy Fuels, 1999, 13(2): 266-277.
- [5] 王子军,阙国和,梁文杰,钱家麟,减压渣油中胶状沥青状物质的化学结构研究 [J]. 石油学报 (石油加工), 1999, 15(6): 39-46. (WANG Zi-jun, QUE Guo-he, L ANGWen-jie, Q AN Jia-lin Investigation on chemical structure of resins and pentane asphaltenes in vacuum residua [J]. Acta Petroleisinica (Petroleum Processing Section), 1999, 15(6): 39-46.)
- [6] 张龙力,杨国华,马魁菊,阙国和. 中东常压渣油热反应过程中沥青质的缔合性变化规律 [J]. 燃料化学学报,2004,32(2):171-174. (ZHANG Long-li, YANG Guo-hua, MA Kui-ju, QUE Guo-he Study on the conglomerating characteristics of middle east AR asphaltenes during the mal reaction [J]. Journal of Fuel Chemistry and Technology, 2004, 32(2):171-174.)
- [7] CALEMMA V, RAUSA R. Thermal decomposition behavior and structural characteristics of asphaltenes [J]. J Anal Appl Pyrolysis, 1997, 40-41:
- [8] del R D J C, MARTN F, GONZALEZ-V LA F J, VERDEJO T. Chemical structural investigation of asphaltenes and kerogens by pyrolysis-methylation [J]. Org Geochem, 1996, 23 (11-12): 1009-1022.

- [9] SCHLEPP L, ELIEM, ANDA IS P, ROMERO M A. Pyrolysis of asphalt in the presence and absence of water [J]. Fuel Process Technol, 2001, **74**(2): 107-123.
- [10] DOUDA J, LLANOSM E, ALVAREZR, FRANCO CL, de la FUENTE J A M. Pyrolysis applied to the study of a Maya asphaltene [J]. J Anal Appl Pyrolysis, 2004, 71(2): 601-612.
- [11] 周永昌,赵锁奇. 渣油超临界萃取馏分中硫化物的分离富集研究 [J]. 燃料化学学报, 2005, 33(3): 304-308. (ZHOU Yong-chang, ZHAO Suo-qi Study on sulfur distribution in supercritical fluid extraction fraction of residua [J]. Journal of Fuel Chemistry and Technology, 2005, 33(3): 304-308.)
- [12] 赵锁奇, 许志明, 胡云翔, 王仁安. 超临界流体萃取分馏仪石油重质油的深度精密分离技术 [J]. 石油仪器, 2001, 15(4): 12-15, 32 (ZHAO Suo-qi, XU Zhirming, HU Yun-xiang, WANG Ren-an The supercritical fluid extraction and fractionation instrument: A deep and precise separation method for heavy oil[J]. Petroleum Instrument, 2001, 15(4): 12-15, 32.)
- [13] 朱军. 石油沥青质化学组成与结构特征的研究 [D]. 北京:中国石油大学, 2002. (ZHU Jun Study on chemical composition and structural characteristics of petroleum asphaltenes [D]. Beijing China University Petroleum, 2002.)
- [14] DJERASSIC, ENGLE R R. Oxidations with ruthenium tetroxide [J]. J Am Chem Soc, 1953, 75 (15): 3838-3840.
- [15] MOJELSKY TW, KNASIAK TM, FRAKMEN Z, MCLNTYRE D D, LOWN EM, MONTCOMERY D S, STRAUSZO P. Structural features of Alberta oil sand bitumen and heavy oil asphaltenes [J]. Energy Fuels, 1992, 6(1): 83-96.
- [16] STRAUSZO P, MOJELSKY TW, LOWN EM, KOWALEW SKI I, BEHAR F. Structural features of Boscan and Duri asphaltenes [J]. Energy Fuels, 1999, 13(2): 228-247.
- [17] PENG P, MORALES-IZQU IERDO A, LOWN EM, STRAUSZO P. Chemical structure and biomarker content of Jinghan asphaltenes and kerogens[J]. Energy Fuels, 1999, 13(2): 248-265.

英国 Hiden Analytical Ltd.

小型在线气体分析质谱仪

IGA智能重量法吸附仪

催化剂表征系统

(催化微反应器 - 质谱仪)





·在线气体分析

·污染物研究

· CVD /MOCVD

· 环境气体分析

·催化剂研究 /反应动力学

·方便与热分析、GC等仪器连接

·定量数据输出:ppm, ppb, %

·反应速度快:120ms~500ms



·重量法直接测量样品的吸附量

·多种气体和蒸气吸附

·动态、静态多组分吸附

·物理吸附、化学吸附

利用探头尺寸表征孔径

·金属分散性测定

·吸附平衡及动力学

·比表面积、孔径分布

・储気研究



· TPD, TPO, TPR, TPRx

·金属表面区域

·动力学和热力学的测量

·活性表面区域

· 反应动力学

·催化剂筛选

·表面反应机理研究

·吸附 供吸附热

·在线连续的产物分析

其他仪器:各种四极杆质谱仪、等离子体表征分析仪、多路采样阀

Tel: 010-51661720, 68728590 E-mail: info@hiden cn http://www.hiden.cn

地址:北京市海淀区厂洼路 5号 东点写字楼 B座 8415 - 8416室,英国海德公司北京办事处 邮编: 100089



文章编号: 0254-0096(2006)02-0199-04

质子交换膜燃料电池专用碳纸的制备及性能测试

伟¹, 汪树军¹, 刘红研², 潘惠芳²

(1. 石油大学重质油国家重点实验室,北京 102249;2. 石油大学化工学院,北京 102249)

摘 要:采用湿法造纸技术制备质子交换膜燃料电池电极扩散层专用碳纸材料,考察了影响专用碳纸性能的主要 因素。研究结果表明:分散剂、粘合剂和纤维长度等对碳纸物性具有较大影响。以 3M 的 NaOH 处理碳纸的基体材 料,控制打浆度 20°SR,按比例加入自制功能性分散剂,在优化工艺系件下,制备的碳纸物性基本和日本东丽公司产 品(Toray 碳纸)物性相同。以自制的碳纸和 Toray 碳纸为电极扩散层基体材料组装成电池,放电性能测试表明,自 制碳纸是一种较为理想的燃料电池电极扩散层基体材料。

关键词:质子交换膜燃料室池:碳纸:电极扩散层

中图分类号: TMO11.4

文/献标识码: A

0 前 言

质子交换膜燃料电池作为一种理想的氢能发电 装置受到了人们的普遍关注,并成为氢能研究开发 的热点。质子交换膜燃料电池的放电性能不仅与电 极催化层的催化活性有关,而且与电极扩散层的结 构和性能等有直接的关系。电极扩散层的孔隙度、 厚度、体积电阻等都是影响电池放电性能十分重要 的理化参数[1~4]。目前用于质子交换膜燃料电池电 极扩散层的材料通常为碳纸,如日本东丽公司 Composite 事业部生产的 TGP-H 系列碳纸(Toray 碳纸)。 但进口的电极扩散层碳纸价格昂贵,因此开发具有 自主知识产权的碳纸材料具有十分重要的战略意义 和现实意义。

1 实验方法

1.1 专用碳纸基体材料的选择

选择市售典型的碳纤维(南通森友碳纤维有限 公司生产的沥青基碳纤维),分别用 3MNaOH、HNO,、 H,SO, H,PO, 浸渍 30min,蒸馏水洗至中性,用柱状 灯芯技术测不同溶液处理碳纤维的润湿性能。

1.2 电极扩散层专用碳纸材料的制备

准确称量一定量经处理的碳纤维,放入磨浆机 中磨浆,按比例量取自制分散剂溶液,与碳纤维浆液 充分混合,固定浆液浓度,采用常规湿法造纸技术,

收稿日期: 2004-05-10

基金项目: 国家重点基础研究项目(G2000026409)

在 ZOII-B 型纸样抄取器上抄片, 真空干燥, 后处理 得质子交换膜燃料电池专用碳纸。

1.3 质子交换膜燃料电池的组装和测试条件

以实验室制备的专用碳纸经聚四氟乙烯乳液 (PIFE 乳液)浸润、烘干、焙烧,制成电极扩散层。将 制备的电极扩散层与含有铂催化剂的催化层复压后 组装成质子交换膜燃料电池进行放电性能测试。其 中,电解质膜为美国 Dupont 公司生产的 Nafion-117 膜。电池运行测试条件为: H, 压强为 0.3MPa, 流量 为 6mL/min; O₂ 压强为 0.5MPa, 流量为 10mL/min; 电 池运行温度为 85℃;有效电极面积 3.14cm²。

1.4 性能测试

电阻测试:用自制的夹具,间距 20mm,用数字万 用表测其两点间电阻;

体积电阻率:用 ZC-36 型高阻仪、OJ23 直流电桥 测其体积电阻,再将体积电阻换算成体积电阻率;

孔隙度测试:使用9500 压汞仪测试专用碳纸的 孔隙率:

抗张强度: ZLL-30 纸张拉力实验机(四川宜宾造 纸厂):

润湿性能测试:根据毛细管渗透原理,液体渗入 粉末柱的高度与时间的关系,在稳定渗流条件下,应 符合 Washburn 方程:

$$h^2 = \frac{\varphi c r \cos \theta}{2 \, n} t$$

若为同一种液体,则 h² 与 t 符合线性关系。当 粉末堆积密度恒定时,直线斜率大小反映了接触角 θ 的大小。于是直线斜率越大,表明碳纤维粉与溶 剂间的润湿性能越好[5]。

实验结果与讨论

2.1 专用碳纸基体材料的制备

作为制备专用碳纸的基体材料-碳纤维,在水中 要有良好的润湿性能,才能均匀分散,制备的碳纸才 有较好的均匀性和较大的空隙率。为此我们选择 4 种溶液处理制备碳纸的基体材料-碳纤维,考察不同 处理溶液对碳纸性能的影响。结果见表 1。

表 1 处理溶液对碳级松削的影响

Table 1 Effects of the solutions used for treatment on the performance of carbon paper

h^2/m^2		时间	旬/8		
h /m	NaOH	H ₃ PO ₄	H ₂ SO ₄	HNO ₃	
1	50	105	145	265	
4	191	336	492	952	
9	428	782	1147	1856	
16	726	1336	1926	3682	
25	1112	2081	3008	5701	
料率	2.51		0.02		
$10^{-2} \text{m}^2 / \text{min}$	2.51	1.22	0.83	0.42	

由表1可知,4种不同酸碱溶液处理的碳纤维, 它们的润湿性能表现出明显的差异。其中以 3M NaOH 处理的碳纤维所作直线斜率最大,即润湿性能 最好,而 HNO, 处理的碳纤维润湿性能最差,这正好 和实验结果相一致。在实验中确实发现用 3M 的 NaOH、H₃PO₄、H₂SO₄和 HNO₃处理碳纤维,加入一定 量自制的功能性分散剂、打浆抄纸、以 NaOH 处理的 碳纤维制备的碳纸均匀性和空隙率较好。分析 4 种 不同溶液处理的基体材料制备的碳纸性能上造成的 差异,主要归因于4种溶液处理后的基体材料润湿 性能上的差别。润湿性能越好,碳纤维在浆液中的 分散性能好,纤维不至于在短时间内絮凝、沉积,制 备的碳纸的均匀性和空隙率越好。

2.2 粘合剂对专用碳纸性能的影响

根据制备碳纤维原料和碳化工艺条件的不同、 所制得的碳纤维具有不同的构造和表面化学性能。 通常碳纤维含有较多种类的表面官能团,如-OH、-COOH、内酯基、酸性和碱性官能团等,但由于数量 少,纤维表面的-OH、-H已基本被破坏,抄造过程中 很难形成氢键,同时由于碳纤维不易细纤维化,其自 身无结合能力,使纸面的交织性不好,成纸匀度差, 强度过低,所以一般都采用加入粘合剂。实验中,我 们控制打浆度为 15°SR,采用聚乙烯醇、聚丙烯酰胺 及水溶性酚醛树脂作为粘合剂抄纸,通过反复实验 得到如表 2 所示结果。

表 2 不同粘合剂对碳纸性质的影响

Table 2 Effects of different adhesives on the performance of carbon paper

	45
胶粘剂	抗张强度/kN·m ⁻¹
※乙烯 摩	
戏酒器西戏	
自制	0.104
改性淀粉	0.413
水溶性酚醛树脂	0.826

从表2可以看出,用一定分子量的的聚乙烯醇、 聚丙烯酰胺单独作为粘合剂抄纸,无论干强度还是 湿强度都很低,无法满足后处理的要求。选择水溶 性酚醛树脂做粘合剂,可以抄出成型的碳纸,抄出的 一次成型碳纸有一定的干强度,但在抄纸过程中产 生大量的泡沫,使纸的均匀性变差,而且水溶性酚醛 树脂不易保存,市售水溶性酚醛树脂的性能差别较 大,因此抄纸的重复性差,不适宜作为一次成型碳纸 的粘合剂。实验室自制的功能性粘合剂,在抄造的 过程中既起分散剂的作用,又起粘合剂的作用,抄造 的碳纸强度好,而且均匀性也好。

2.3 分散剂的选择

由于用于抄纸的碳纤维长度较大,普通碳纤维 又具有憎水性, 造成碳纤维在水中的润湿性差, 容易 沉淀、絮聚和结团,使成纸的均匀度不好。因此在抄 纸过程中必须加入合适的分散剂,以使碳纤维能均 匀地分散于水中。实验时,我们控制打浆度为 15° SR,选用聚丙烯酰胺、聚氧化乙烯及甘油和实验室自 制的分散剂抄纸,用自制的夹具测量一次成型碳纸 20个均匀分布点间电阻,求其平均值和相对标准偏 差,考察碳纸的均匀性,见表3。

由表 3 得知,不同分散剂对一次成型碳纸的均 匀性有较大的影响。4种不同分散剂制备的一次成 型碳纸虽然电阻平均值差别不是很大,但相对标准 偏差差别很大。其中,甘油作为分散剂制备的一次 成型碳纸相对标准偏差是自制的分散剂制备的一次 成型碳纸相对标准偏差的近5倍。比较4种分散剂 制备的一次成型碳纸的均匀性,以自制的分散剂制 备的碳纸均匀性最好,电阻平均值为 16.0Ω,相对标 准偏差为 1.16。偏差越小说明测量的电阻值的精密 度好,可以间接反应出碳纸的均匀性。制得的4种 一次成型碳纸性能有一定的差异主要是由于不同分 散剂能使浆液粘度有不同程度的提高,限制了纤维 在水中的运动自由度,使纤维不易相互接触,且不同 分散剂使纤维润湿性能的不同造成的。

表 3 不同分散剂对碳纸性质的影响

Table 3 Effects of different dispertant on the performance of carbon paper

分散剂	碳	纸的均匀度	
	平均值/(2	相对标准偏差/%	
聚丙烯酰胺	19.8	3.26	
聚氧化乙烯	20.6	4.93	
甘油	21.0	6.31	
自制	16.0	1.16	

2.4 打浆度对碳纸性能的影响

通常以纤维素为基体材料抄造的纸匀度、透气 性和强度等物性可通过控制打浆度实现。打浆可使 纤维分丝、帚化、润涨和短切。专用碳纸的制备与普 通造纸不同,打浆过程中不能使碳纤维分丝、帚化, 主要是将纤维切断,因而纤维长度成为影响碳纸性 能的重要因素。为了考察纤维长度对碳纸性能、特 别是均匀性、孔隙率的影响,我们通过控制打浆度来 控制纤维长度。打浆的程度对抄造出纸的性能的影 响见表 4。

表 4 打浆度对碳纸性能的影响

Table 4 Effects of beating degree on the performance of carbon paper

	碳纸的表观性质						
打浆度 ¯ /°SR	相对标准 偏差/%	电阻平均值 /Ω	抗张强度 /kN·m ⁻¹				
12	1.36	16.3	0.095				
17	0.73	15.2	0.123				
22	1.01	15.9	0.138				
27	1.56	16.7	0.034				

由表 4 我们可以看出:打浆度为 20°SR 左右时, 抄造出的纸的强度及均匀度都较好。当打浆度为 12°SR 或 27°SR 时,不仅制备的碳纸抗张强度差别很 明显,而且均匀度明显降低。由于较长的纤维容易 缠结,在加入粘合剂时,制备的碳纸有一定的强度:

当打浆程度过强时,由于将纤维打的过于细碎,过短 的纤维不易缠结,容易造成粘网等现象,使制备的纸 均匀性和强度都较差。因此,随着打浆程度的增强, 抄出纸的强度会由弱变强,又会由强变弱。

2.5 自制碳纸与 Toray 碳纸物性比较

按比例加入选择实验室自制功能性分散剂,控 制打浆度为 20°SR, 固定浆液浓度抄纸、后处理, 得到 质子交换膜燃料电池专用碳纸,测量自制碳纸和日 本东丽公司 TGP-H-90 碳纸体积电阻率等主要物性, 见表5。

及5 自制碳纸与 Torav 碳纸物性比较

Table 5 Comparison of performance between self-making carbon paper and Toray carbon paper

物性	单位	自制	TCP-H-90
厚度	mm	0.28	0.28
密度	g/cm ³	0.45	0.45
空隙率	%	74	77
体积电阻率面厚方向	Ω·cm	0.086	0.087

由表5可见,二者在主要物性上差别不大。自 制碳纸厚度、密度和空隙率等物性基本相同,体积电 阻率面厚方向稍好于日本东丽公司 TGP-H-90 碳纸, 价格却远低于日本东丽公司 TGP-H-90 碳纸。由此 可见自制碳纸是一种燃料电池电极扩散层的一种较 为理想的电极扩散层基体材料。

2.6 电极扩散层对燃料电池放电性能的影响

为了考察自制电极扩散层材料的性能,分别以 自制和日本东丽公司碳纸为基材制备电极扩散层, 并组装成燃料电池进行放电性能测试。两种不同扩 散层的燃料电池放电性能曲线对比情况见图 1。

由图 1 所示的燃料电池放电性能曲线对比结果 可看出:自制的电极扩散层碳纸材料和日本东丽公 司产品,它们的放电性能没有明显的差异。放电电 流较小时,两种碳纸制备的扩散层放电性能几乎相 同;在电流较大时,略有差异,但不很明显。结合表 5测出的自制电极扩散层碳纸在物性指标与 Toray 碳纸物性指标,可知决定碳纸性能的主要因素是碳 纸的空隙率和导电性、厚度等,表明两种基体材料作 为燃料电池电极扩散层基体材料性能相近,这从两 种不同扩散层组装的燃料电池放电性能曲线得到了 证实,也进一步证实自制的碳纸是制备燃料电池电 极扩散层的一种较为理想的电极扩散层基体材料。

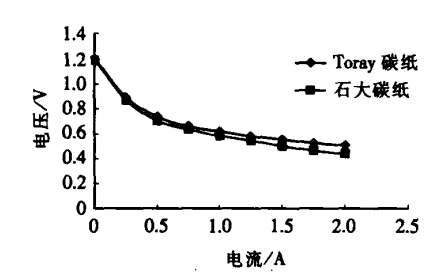


图 1 自制碳纸和 Toray 碳纸组装的 电池放电性能对比

Fig. 1 The comparison figure of homemade carbon paper discharge performance and toray carbon paper discharge performance

3 结 论

1)粘合剂的选择和制备是制备专用碳纸材料关键因素之一。本实验采用的实验室自制的粘合剂能满足碳纸后处理对强度的要求,而且均匀性较好;

2)分散剂和打浆度不仅对专用碳纸均匀性有较大影响,而且对碳纸的空隙率也有较大的影响。实验室自制的功能分散剂,不仅能对纤维起到分散作用,而且具有粘合作用。控制打浆度为 20°SR 左右,

以实验室合成的功能分散剂制备的碳纸空隙率达 74%:

3)自制的碳纸和 Toray 碳纸为基体材料制备电极扩散层,并组装成燃料电池进行放电性能测试,它们的放电性能没有明显的差异。因此可以认为自制的碳纸是制备燃料电池电极扩散层的一种较为理想的基体材料。

[参考文献]

- [1] Wilson M S, Gottesfeld S. Thin-film catalyst layers for polymer electrolyte fuel cell electrodes [J]. Journal of Applied Electrochemistry, 1992, 22: 1—7.
- [2] Araolini E, Passos R R, Ticianelli E A. Effects of the carbon power characteristics in the cathode gas diffusion layer on the performance of polymer electrolyte fuel cells [J]. Journal of Power Sources, 2002, 109(2): 477—482.
- [3] 汪树军,刘红研,赵永丰. 氢能发电技术的研究(Ⅳ) [J].太阳能学报,2001,22(4):390—394.
- [4] 汪树军,张 伟,刘红研,等.燃料电池电极扩散层碳 纸材料的制备新方法[P]. CN02104470.8.
- [5] 袁 伟. 钴改性磁粉的表面活性剂处理[J]. 北京化工_。 大学学报,1995,22(1): 67-70.

PREPARATION AND PERFORMANCE TEST OF SPECIAL CARBON PAPER MATERIALS FOR PROTON EXCHANGE MEMBRANE OF FUEL CELL

ZhangWei¹, Wang Shujun¹, Liu Hongyan², Pan Huifang²
(1. State Key Laboratory of Heavy Oil Processing, University of Petroleum, Beijing 102249, China;
2. Faculty of Chemical Engineering, University of Petroleum, Beijing 102249, China)

Abstract; Special carbon paper materials for proton exchange membrane fuel cells were prepared by wet papermaking technique. The effects affecting the performance of special carbon paper were investigated. It was shown that dispersant, bond and length of fiber have great effects on the characteristics of carbon paper. Under the optimized technical conditions, the raw materials of carbon paper were processed by 3M NaOH solution. The beating degree of the pulp is 20°. Homemade functional dispersant is added in appropriate proportion. The properties of carbon paper were close to or better than that of Toray carbon paper. The discharge performance of cells, assembled by the raw materials of electrode diffusion layer with homemade carbon paper and Toray carbon paper, were determined. It was found that homemade carbon paper is the perfect raw material of electrode diffusion layer in the electrode diffusion layer of fuel cells.

Keywords: proton exchange membrane fuel cell; carbon paper; electrode diffusion layer 联系人 E-mail: wsjw@bjpeu.edu.cn

二硫代钨酸铵晶体的合成、表征与热分解机理的研究

安高军 柳云骐* 柴永明 周同娜 刘晨光 (中国石油大学,重质油国家重点实验室,CNPC 催化重点实验室,东营 257061)

摘要:本工作用偏钨酸铵和硫化铵为原料,在水溶液中合成二硫代钨酸铵晶体[(NH₄)₂WO₂S₂]。用紫外-可见光谱(UV-Vis)的方法研究了二硫代钨酸铵晶体的形成机理。采用元素分析、X 射线衍射(XRD)、傅里叶变换红外光谱(FTIR)、激光拉曼光谱(LRS)等对化合物进行了表征。结果表明采用该方法制备出的二硫代钨酸铵晶体,晶型良好。热重-差热分析(TG-DTA)、原位 X 射线衍射(in situ XRD)和 FTIR 等结果表明二硫代钨酸铵晶体在氢气气氛下的热分解主要发生在 160~450 ℃之间,分两步进行,首先分解为{WOS}}、随后转化为二硫化钨。

关键词:二硫代钨酸铵; 偏钨酸铵; 原位 XRD; 热分解机理 中图分类号: 0614.61⁺³ 文献标识码: A 文章编号: 1001-4861(2006)10-1813-06

Synthesis, Characterization and Thermal Decomposition Mechanism of Ammonium Tungsten Oxide Sulfide Crystal

AN Gao-Jun LIU Yun-Qi* CHAI Yong-Ming ZHOU Tong-Na LIU Chen-Guang

(State Key Laboratory of Heavy Oil Processing, Key Laboratory of Catalysis, CNPC,

China University of Petroleum, Dongying, Shandong 257061)

Abstract: Ammonium tungsten oxide sulfide $[(NH_4)_2WO_2S_2]$ crystal was synthesized in aqueous solution using ammonium metatungstate (AMT) and ammonium sulfide as raw materials. The formation mechanism of $(NH_4)_2WO_2S_2$ was studied by Ultraviolet-visible (UV-Vis) spectroscopy. The as-synthesized compound was characterized by Elemental analysis, X-ray power diffraction (XRD), Fourier transform infrared (FTIR) and Laser Raman spectroscopy (LRS). The results show that the as-synthesized $(NH_4)_2WO_2S_2$ is with good crystallinity. In addition, thermogravimetric analysis (TG), differential thermal analysis (DTA), in situ XRD and FTIR results reveal that $(NH_4)_2WO_2S_2$ undergoes thermal decomposition in the range of $160\sim450~$ °C in hydrogen by two steps, where $(NH_4)_2WO_2S_2$ is converted to $\{WOS_2\}$ firstly between 160~°C and 300~°C and then transformed to WS_2 eventually.

Key words: ammonium tungsten oxide sulfide; ammonium metatungstate; in situ XRD; thermal decomposition mechanism

0 引 言

过渡金属硫属化物由于具有令人感兴趣的结构 化学、不平常的电学性能和丰富的插入化学而使它 们成为化学、固体物理及材料化学的研究热点^[1]。另 一方面,由于这类化合物在生物体系方面的潜在应 用而日益受到人们的重视^[23],目前国内外已对作为 固氮酶活性中心的钼 (钨) 铁硫原子簇化合物的合成、结构及性质做了大量研究的。此外,硫代金属铵盐还是油品加氢脱硫和加氢脱氮过程中常用的催化剂前驱体[5-7]。二硫代钨酸铵是一类重要的硫代金属铵盐,其热分解后可以得到氧化钨的硫化中间产物{WOS2},对研究氧化钨催化剂预硫化过程的相转变具有重要意义。目前此类化合物的合成方法主要是

收稿日期:2006-05-23。收修改稿日期:2006-07-28。

国家重点基础研究发展规划(973 计划)(No.2004CB217807)和中国石油重点基础研究项目(No.04A50502)。

^{*}通讯联系人。E-mail:liuyq@mail.hdpu.edu.cn

第一作者:安高军,男,26岁,博士研究生;研究方向:催化反应工程。

· 1814 ·

将钨酸溶于碱液后,于冰浴环境中,在液体表面快速 通入 H_2S 反应,冷却、结晶 10 。这种方法的缺点是操作 条件苛刻,不易控制;合成过程中需要使用剧毒、易挥发的 H_2S 气体作硫化剂,不仅对操作人员造成危害,而且还易污染环境。

为了寻找一种反应条件温和、操作简便、安全、对环境无污染的合成方法,在本工作采用硫化铵作硫化剂,在缓和的条件下合成二硫代钨酸铵晶体。采用元素分析、XRD、FTIR、LRS等方法对所合成的化合物进行表征,同时利用 TG-DTA、in situ XRD 和FTIR 等方法对二硫代钨酸铵晶体在氢气气氛下的热分解机理进行了研究。

1 实验部分

1.1 合成方法

称取 5 g 偏钨酸铵(A.R.,上海化学试剂公司),加入 5 mL 去离子水,搅拌溶解;接着加入 15 mL 浓 氮水,于 60 ℃搅拌反应 20 min(此时反应体系的 pH 值约为 9);然后加入 35 mL 硫化铵溶液(A.R.,上海振兴化工二厂),于 60 ℃搅拌反应 30 min,停止反应,真空抽滤,去掉反应过程中出现的少量蓝色沉淀,然后将滤液于 0 ℃静置 24 h,得到黄色晶体,真空抽滤,去离子水和无水乙醇分别洗涤三遍,晾干即得最终的二硫代钨酸铵晶体,产率约为 45%。

1.2 仪器及表征

二硫代钨酸铵晶体的 XRD 分析采用荷兰 Panalytical 公司产的 X' Pert Pro MPD 型原位 X 射线衍射仪。测定条件为:辐射源为 Cu $K\alpha(\lambda=0.154\ 06\ nm)$,管压 45 kV,管流 40 mA,扫描速度 5°·min-1,发散狭缝 1°,接收狭缝 0.3 mm,检测器为闪烁计数器。在对二硫代钨酸铵晶体进行氢气气氛下的原位 XRD 分析时,先在室温下(25 °C)通氢气将整个系统吹扫 20 min,接着以 40 °C·min-1 的速度从室温分段升至 600 °C,在达到预定段的扫描温度后稳定 15 min 再进行扫描,扫描完成后立即进入下一段升温程序。扫描段的温度分别为 25 °C、150 °C、200 °C、300 °C、400 °C、600 °C,当系统冷至室温后(25 °C)再对 600 °C分解的样品进行一次扫描。

二硫代钨酸铵合成产物的元素分析(N、H、O)采用 Varil EL-3 型元素分析仪进行; 硫含量测定采用 SLFA-800 型 X 射线荧光硫分析仪进行; FTIR 分析 采用美国 Thermo Nicolet 公司 NEXUS 型傅里叶变换红外光谱仪,采用 KBr 压片,扫描范围:400~4000

cm⁻¹;UV-Vis 光谱分析则在 Varian Cary50 型紫外可见分光光度计上进行,扫描范围:200~600 nm,扫描速率:600 nm·min⁻¹;TG-DTA 分析采用北京分析仪器厂的 WCT-2 型微机热重-差热天平,测试时可以控制 3 种不同的气氛,测试温度范围:室温至 1 400 $^{\circ}$ C,升温速度:10 $^{\circ}$ C·min⁻¹;LRS 光谱分析则采用法国 J.Y.公司的 LabRam-010 激光拉曼光谱仪,He/Ne激光光源,激发功率为 15 mW,扫描范围 100~4 000 cm⁻¹,积分时间为 20 s,扫描次数为 3 次;管式炉分解时,先通氢气将系统吹扫 20 min,然后升至预定温度,稳定 15 min,随后快速冷至室温,分解温度分别为 150 $^{\circ}$ C、250 $^{\circ}$ C、350 $^{\circ}$ C、450 $^{\circ}$ C。

2 结果与讨论

2.1 合成过程的 UV-Vis 光谱分析

实验发现,反应时间和溶液的 pH 值对产物的生成有明显的影响,要得到目标产物二硫代钨酸铵,控制反应时间是关键。为了探索合成过程与产物生成的关系,我们采用加入碱液提高溶液 pH 值的方法,控制适当的反应时间,利用 UV-Vis 光谱的方法对整个合成过程中间产物的存在形式进行了监测。典型的反应过程为:5 g 偏钨酸铵溶于5 mL 去离子水中,澄清后加入15 mL 氨水,开始加热搅拌(温度保持在60 $^{\circ}$ C),同时每隔5 min 取样一次,分别记录不同反应时间产物的 UV-Vis 光谱,结果如图1 所示。图中曲线 e 为钨酸与氨水反应后的溶液(即(NH4)2WO4 溶液)的 UV-Vis 光谱图。

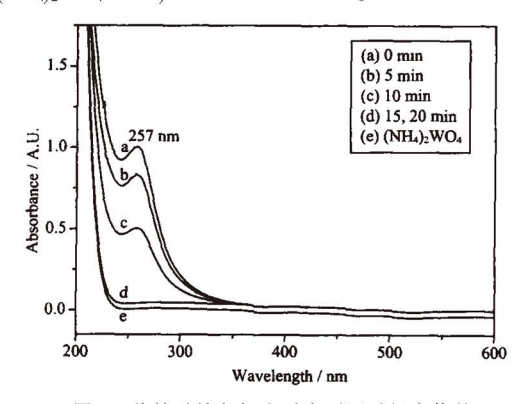


图 1 偏钨酸铵与氨水反应不同时间产物的 UV-Vis 谱图

Fig.1 UV-Vis spectra of ammonium metatungstate hydrolysis products at different time

从图 1 可以看出,反应初期在 257 nm 处均出现偏钨酸铵的特征吸收峰,只是吸收峰的强度随反

应时间的延长而逐渐减弱,15 min 后该吸收峰则完全消失,并且与曲线 e 完全一致,表明 15 min 后偏钨酸铵已水解转化为正钨酸铵。而若水解时间超过30 min,则合成产物中会混有少量白色的仲钨酸铵晶体;水解时间超过2 h,则得不到二硫代钨酸铵晶体,而几乎全部是仲钨酸铵晶体。这可以从不同形式钨酸根相互转化的关系图(图 2)得到解释,在碱性体系中偏钨酸根离子可以转化为正钨酸根离子,但是增加反应时间正钨酸根离子会进一步转化为仲钨酸根离子。因此在本工作条件下水解时间控制在20 min 为宜,以保证溶液中钨主要以正钨酸根离子的形式存在。

图 3 为上述反应溶液与硫化铵反应制备(NH₄)₂ WO₂S₂ 过程中不同反应时间中间产物的 UV-Vis 光谱图。从图 3 可以看出 5 min 时即在 272、335 nm 处出现(NH₄)₂WO₂S₂ 的二取代的特征吸收峰⁶, 10 min, 15 min, 20 min, 25 min, 30 min 均为二取代的吸收峰,但从 35 min 开始在 386 nm 处出现三取代的迹象,40 min 后三取代的趋势逐渐变得明显,386 nm 处的吸收峰随反应时间的延长而逐渐增强,因此在本实验条件下取代反应的时间控制在 30 min 为宜。根据 UV-Vis 的分析结果可以得出反应过程的示意图,如图 4 所示。

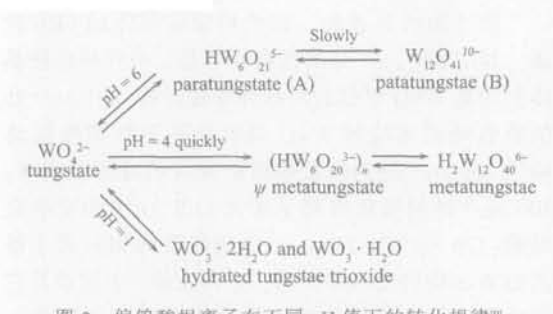


图 2 偏钨酸根离子在不同 pH 值下的转化规律^[9]

Fig.2 Relationships between WO_4^{2-} polymerization and pH values

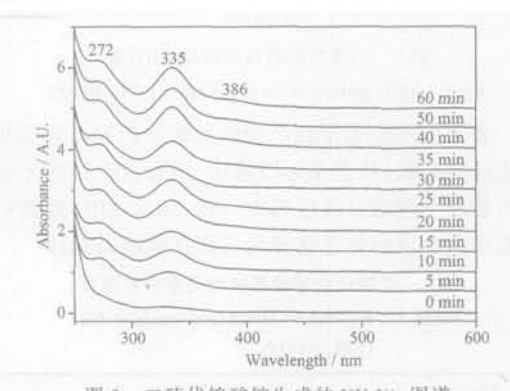


图 3 二硫代钨酸铵生成的 UV-Vis 图谱 2.3 UV-Vis spectra for the formation of (NH₂)₂WO₂S₂

WOS.3



Fig.4 Process of replacement of S²- for WO₄²

根据前面的分析,整个反应过程可以表述如下: (1) $(NH_4)_6H_2W_{12}O_{40} \cdot 5H_2O + 18NH_3 \cdot H_2O \rightarrow$

 $12(NH_4)_2WO_4 + 15H_2O$

(2) $(NH_4)_2WO_4 + (NH_4)_2S + H_2O \rightarrow$

 $(NH_4)_2WO_3S + 2NH_3 \cdot H_2O$

(3) $(NH_4)_2WO_3S + (NH_4)_2S + H_2O \rightarrow$

 $(NH_4)_2WO_2S_2 + 2NH_3 \cdot H_2O$

(4) $(NH_4)_2WO_2S_2 + (NH_4)_2S + H_2O \rightarrow$

 $(NH_4)_2WOS_3 + 2NH_3 \cdot H_2O$

据此,可以认为由于偏钨酸根离子在不同 pH 值下是以不同形式存在,而要制备二硫代钨酸铵晶 体的关键是先将偏钨酸根离子转变为正钨酸根离 子;在正钨酸根离子与硫化铵反应过程中,要适当控制反应时间,过长的反应时间不利于二取代产物的生成。另外,从上面的反应可以看出生成二硫代钨酸铵的反应是一个放出氨气的过程,因此在反应的后期及时将氨气释放出反应体系有利于反应向正方向移动,并且有利于产物的结晶和产率的提高。

2.2 XRD 表征

图 5 为所合成的二硫代钨酸铵晶体的 XRD 图。 从图 5 可以看出,合成产物具有良好的结晶度,图中 衍射峰的位置与 JCPDS 标准卡片(No.01-071-0759) 中二硫代钨酸铵特征衍射峰的位置完全一致,无任 何杂质的衍射峰,表明所合成的产物为单斜晶系的 二硫代钨酸铵晶体,且晶型良好。

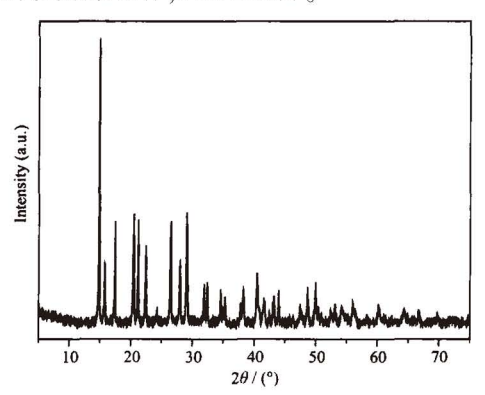


图 5 二硫代钨酸铵晶体的 XRD 图 Fig.5 XRD pattern of as-synthesized (NH₄)₂WO₂S₂

表 1 为所合成得到产物的元素分析实测数据和理论计算数据,从表 1 可以看出,所合成产物的元素分析数据与理论计算值基本一致。结合 XRD 数据可以看出所合成的化合物确为二硫代钨酸铵晶体。

表 1 二硫代钨酸铵晶体的元素分析结果 Table 1 Results of elemental analysis for (NH₄)₂WO₂S₂

Element	N	H	\mathbf{W}	O	S
Calcd. / %	8.86	2.54	58.20	10.12	20.28
Found / %	8.94	2.68	57.93	10.25	20.20

2.3 FTIR 光谱分析

图 6 为二硫代钨酸铵和四硫代钨酸铵晶体的 FTIR 光谱图。从图 6 可以看出,与四硫代钨酸铵相比,二硫代钨酸铵光谱中振动峰的数目要明显多于四硫代钨酸铵。其中最显著的差别就是在二硫代钨酸铵光谱的 863 cm⁻¹ 和 806 cm⁻¹ 处出现两个很强的

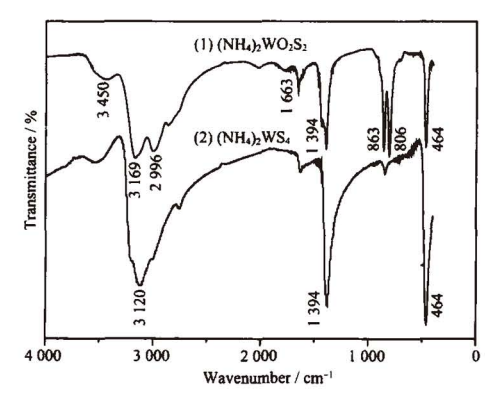


图 6 二硫代钨酸铵和四硫代钨酸铵的 FTIR 谱图 Fig.6 FTIR spectra of as-synthesized (NH₄)₂WO₂S₂ (1) and (NH₄)₂WS₄ (2)

振动峰,这是由二硫代钨酸铵晶体中 W-O 键振动引起的¹⁸,表明所合成晶体中含有氧元素;在 464 cm⁻¹ 处出现一个强吸收峰,这是 S²-在 W⁶⁺为核心的周围配位形成的 W-S 键的特征吸收峰;3 450 cm⁻¹ 处的吸收峰可归属为 O-H 键的伸缩振动峰,这可能是由于所合成晶体吸附空气中微量的水而引起的;3 169 cm⁻¹ 和 2996 cm⁻¹ 处的振动峰归属于 NH_4 +中 N-H+的伸缩振动峰;1 663 cm⁻¹ 和 1 394 cm⁻¹ 处的振动峰则归属于 NH_4 +中 N-H 的变形振动峰^{10]}。除此之外其他杂质峰极少,表明所合成的产物应该就是(NH_4) $_2$ WO₂S₂ 晶体。

2.4 LRS 光谱分析

图 7 为所合成的二硫代钨酸铵晶体的 LRS 光谱。其中 846 cm⁻¹ 处的强吸收峰是二硫代钨酸铵晶体中端基 W=O 双键的对称伸缩振动峰;801 cm⁻¹ 处的吸收峰则是端基 W=O 双键的不对称伸缩振动峰"1,468 cm⁻¹ 处的吸收峰则是 W-S 的特征吸收峰;309 cm⁻¹ 处的吸收峰则是桥式 O-W-O 键的变形振动峰;275 cm⁻¹ 与 235 cm⁻¹ 处的吸收峰则归属于桥式 O-W-S 键的变形振动峰。这与文献^[12]中按照其它方法合成的二硫代钨酸铵晶体的 LRS 报道结果一致。

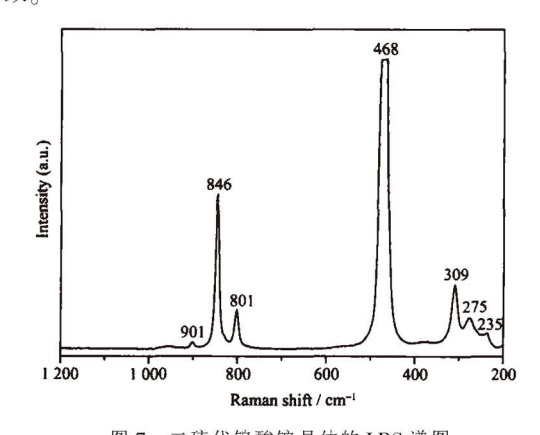


图 7 二硫代钨酸铵晶体的 LRS 谱图 Fig.7 LRS spectrum of as-synthesized (NH₄)₂WO S_2

2.5 TG-DTA 分析

图 8 为二硫代钨酸铵晶体在氢气气氛中热分解的 TG-DTA 结果。从图 8 可以看出,二硫代钨酸铵在氢气气氛下的热分解主要分两个阶段进行。第一阶段的分解主要发生在 160~300 ℃之间,失重率为15.90%。据此推断第一阶段的分解过程为:

 $(NH_4)_2WO_2S_2 \rightarrow \{WOS_2\} + H_2O + 2NH_3 \uparrow (1)$ 反应(1)的理论失重率为 16.47%, 与实际失重率

基本吻合,表明推断的分解方程式是正确的。这一阶段是一个吸热过程,在 227 ℃处出现一个明显的吸热峰。在 300 ℃后又立即发生第二阶段的分解,这与二硫代钨酸铵在氮气气氛的分解过程有明显的不同^[12]。氮气气氛下二硫代钨酸铵在第一阶段分解结束后会稳定一段时间再发生第二阶段的分解,而在氢气气氛下则不存在这一稳定期,这可能是由于氢气的存在更有利于{ WOS_2 }的还原,使{ WOS_2 }在更低的温度下即可被进一步还原。第二阶段的分解主要发生在 300~450 ℃之间,失重率为 5.27%。据此推断第二阶段的分解过程为:

$$\{WOS_2\} \rightarrow WS_2 + H_2O$$
 (2)

反应(2)的理论失重率为 5.06%,与实际失重率基本吻合,表明推断的分解方程式是正确的。这一阶段是一个轻微放热的过程,且放热峰的范围较宽,这可能是由于无定形的 $\{WOS_2\}$ 转变为晶态的 WS_2 是一个能量降低的过程,所生成的 WS_2 在氢气存在的情况下,晶格排列并聚集,逐渐趋于规整所造成。从 TG 曲线还可以看出,随着分解温度的进一步提高,在 700 C以后仍有少量的失重,这可能是由于 WS_2 在高温下被氢气进一步还原又失去部分的硫所造成。此外,在 100~130 C之间出现少量失重,这可能是由于二硫代钨酸铵晶体中微量吸附水的失去所造成(从前面 FTIR 结果亦可看出所合成的晶体中可能吸附空气中微量的水)。

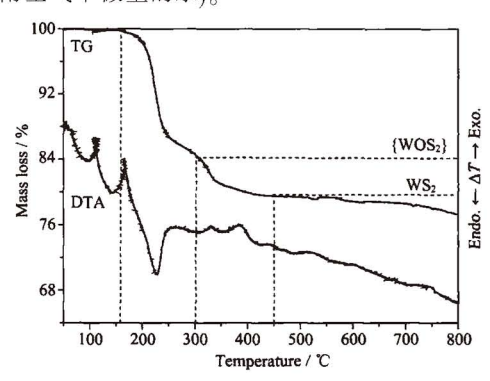


图 8 二硫代钨酸铵在氢气气氛中热分解的 TG-DTA 图

Fig. 8 TG-DTA curves for the decomposition of as-synthesized $(NH_4)_2WO_2S_2$ under hydrogen atmosphere

2.6 二硫代钨酸铵热分解的原位 XRD 研究

二硫代钨酸铵晶体在氢气气氛下热分解的原位 XRD结果如图9所示。从图9可以看出,二硫代钨 酸铵在氢气气氛 150 ℃分解 15 min 后晶型基本上没有发生变化,其 XRD 图与 25 ℃时基本相同,只是某些衍射峰的强度略有下降,说明二硫代钨酸铵在 150 ℃时基本上未发生分解。这一结果与前面 TG-DTA 的分析结果一致,因为 TG-DTA 的分析结果表明二硫代钨酸铵在氢气气氛下的热分解是从 160 ℃ 才开始进行。

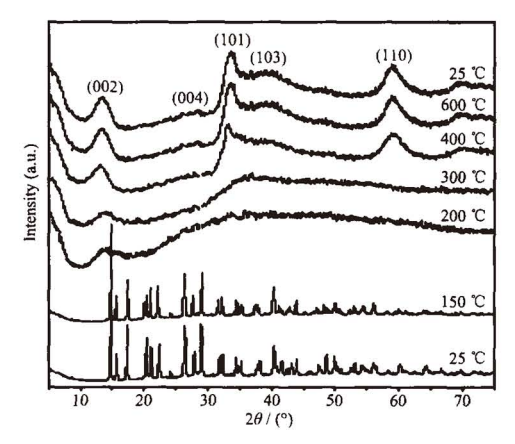


图 9 二硫代钨酸铵在氢气气氛下的原位 XRD 图 Fig.9 XRD patterns of *in situ* decomposition products of (NH₄)₂WO₂S₂ in hydrogen

而在氢气气氛 200 ℃分解 15 min 后,二硫代钨 酸铵的特征衍射峰完全消失,其 XRD 图中几乎无明 显的衍射峰出现, 说明此时二硫代钨酸铵已分解转 化为无定形的钨硫氧化合物(WOS₃),这一结果也与 TG-DTA的分析结果一致。300 ℃分解后产物基本上 仍为无定形的. 只是在 $2\theta=35.0$ °左右的位置略凸出 一个峰,表明此时分解产物基本上仍为{WOS₃},但可 能已有少量的二硫化钨微晶生成。这与 TG-DTA 的 分析结果一致, 因为 TG-DTA 的结果表明 300 ℃是 二硫代钨酸铵晶体发生相转变的关键点, 其从 300 ℃开始由{WOS₂}转化为二硫化钨。而在 400 ℃分解 15 min 后, 二硫化钨的晶型已比较明显, 其{002}、 {101}、{110}等晶面的衍射峰均已出现。随着分解温 度的进一步升高,二硫化钨的特征衍射峰愈加明显, {002}、{004}、{101}、{103}、{110}等晶面的衍射峰(对 应 d 值分别为 6.46、3.13、2.65、2.27、1.56)逐渐增强, 峰面宽度变窄。说明随着分解温度的升高,二硫化钨 的晶型逐渐完整、二硫代钨酸铵最终完全转化为六 方晶系的 2H-WS₂ (特征衍射峰的 d 值分别为 6.18、 3.09、2.67、2.27、1.58)。此外,从图 9 还可以看出冷却 后产物的 XRD 图与 600 ℃分解产物的 XRD 图完全 一致,说明分解产物在冷却的过程中晶相结构保持 不变。

2.7 二硫代钨酸铵热分解的 FTIR 研究

本小节我们将二硫代钨酸铵在管式炉氢气气氛下不同温度的分解产物分别做红外光谱,从而为二硫代钨酸铵在氢气气氛下热分解机理的研究提供进一步的依据。图 10 为二硫代钨酸铵在氢气气氛下不同温度分解产物的 FTIR 谱图。

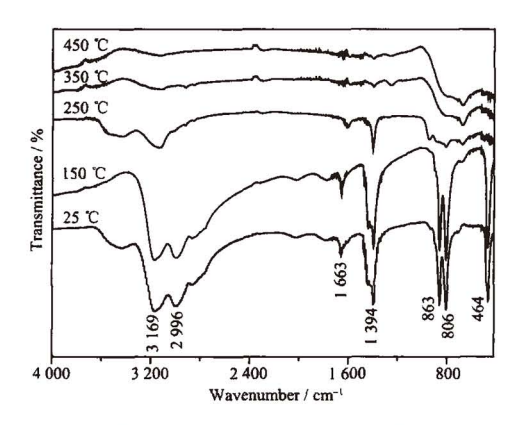


图 10 二硫代钨酸铵在氢气气氛不同温度分解产物 的 FTIR 谱图

Fig.10 FTIR spectra of decomposition products of (NH₄)₂WO₂S₂ under different temperatures in hydrogen

从图 10 可以看出,二硫代钨酸铵在 150 ℃分解 后产物的 FTIR 谱图与 25 ℃时的谱图相比几乎没 有发生变化,说明此时二硫代钨酸铵并没有发生分 解,这与前面的分析结果一致。而 250 ℃分解产物的 谱图与 25 ℃时相比则发生明显的变化, 其中 NH4+ 中 N-H+的伸缩振动峰(3 169 cm-1 和 2 996 cm-1)和 N-H的变形振动峰(1663 cm-1和1394 cm-1)均明显减 弱或消失,但并没有完全消失,这可能是由于分解时 间较短,产物中仍残留有少量的 N-H 结构。此外 W-O 键的吸收峰(863 cm⁻¹ 和 806 cm⁻¹)亦明显减弱,但 在 806 cm-1 处仍存在一个弱的吸收峰,说明此时产 物中仍含有 W-O 结构,这与前面的分析结果也是基 本一致。另外值得注意的一点是,二硫代钨酸铵在 250 ℃分解后原来结构中 W-S 的特征吸收峰(464 cm⁻¹)完全消失,这可能是由于在 250 ℃分解后原来 以 W⁶⁺为核心的四面体结构遭到破坏, 从而导致原 来以 W⁶⁺为核心配位形成的 W-S 键的特征吸收峰消 失。二硫代钨酸铵在 350 ℃、450 ℃分解后,原有结 构中 N-H 键和 W-O 键的吸收峰均完全消失,表明 此时已转化为二硫化钨,这也与前面的分析结果一 致

3 结 论

- (1) 本工作以偏钨酸铵和硫化铵为原料在水溶液中合成出二硫代钨酸铵晶体,与以硫化氢为硫化剂的合成方法相比,该制备方法简单有效、易于操作。XRD、元素分析、FTIR和 LRS表征结果均表明合成产物为二硫代钨酸铵晶体,且晶型良好。
- (2) 合成过程的 UV-Vis 结果表明,二硫代钨酸 铵晶体的形成是按照偏钨酸铵先转化为正钨酸铵,再被硫化铵取代的机理进行;控制适当的反应时间 有利于二硫代钨酸铵的生成。
- (3) TG-DTA、 $in\ situ\ XRD$ 和 FTIR 的表征结果表明,二硫代钨酸铵在氢气气氛下的热分解过程分两个阶段进行,第一阶段发生在 160~300 ℃,二硫代钨酸铵转化为钨硫氧化合物 $\{WOS_2\}$;第二阶段则发生在 300~450 ℃,钨硫氧化合物转化为二硫化钨。

参考文献:

- [1] DONG Yan-Zhi (董言治), JIA Cui-Ying (贾翠英), AN Yong-Lin (安永林), et al. Wuji Cailiao Xuebao(J. Inorg. Mater.), **2002,17**(3):605~608
- [2] Cramer S P, Hodgson K O, Gillum W O, et al. J. Am. Chem. Soc., 1978.100(11):3398~3407
- [3] Cramer S P, Gillum W O, Hodgson K O, et al. J. Am. Chem. Soc., 1978,100(12):3814~3819
- [4] WEI Chang-Ping (魏长平), LI Hai-Dong (李海东), WU Guang-Feng (吴广峰). Jilin Gongxueyuan Xuebao(J. Jilin Insti. Te-chnol.), 1994,15(3):56~59
- [5] Alvarez L, Espino J, Ornelas C, et al. J. Mol. Catal., 2004,210 (1~2):105~117
- [6] Alonso G, Berhault G, Aguilar A, et al. J. Catal., 2002,208 (2):359~369
- [7] Nava H, Ornelas C, Aguilar A, et al. J. Catal., 2003,86(4):257 ~265
- [8] McDonald J W, Friesen G D, Rosenhein L D, et al. Inorg. Chimica Acta, 1983,72:205~210
- [9] LIU Jiu-Qing, XU Zhen-Liang, ZHOU Kang-Gen. J. Memb. Sci., 2004,240(1~2):1~9
- [10]KE Yi-Kan (柯以侃), DONG Hui-Ru (董慧茹). Analytical Chemistry Handbook, Vol.2(分析化学手册(第三分册),第二版). Beijing: Chemical Industry Press, 1998.
- [11]Horsley J A, Wachs I E, Brown J M, et al. J. Phys. Chem., 1987,91(15):4014~4020
- [12]van der Vlies A J, Kishan G, Niemantsverdriet J W, et al. J. Phys. Chem. B, 2002,106(13):3449~3457

[Article] www.whxb.pku.edu.cn

颗粒模板法制备大孔 Al₂O₃ 材料

王晓冬 董 鹏* 陈胜利

(中国石油大学重质油国家重点实验室,北京 102249)

摘要 采用颗粒模板法制备了大孔氧化铝(Al₂O₃)材料. 扫描电子显微镜(SEM)结果显示, 大孔 Al₂O₃ 结构中的大孔呈"囊泡状"且孔道的贯通性较差. Zeta 电位测量表明, 共沉积条件下聚苯乙烯(PS)和 Al₂O₃ 两种胶体颗粒带有相反的电荷, 在静电引力作用下先发生了吸附, 再沉积在一起. 吸附在 PS 微球表面的 Al₂O₃ 纳米颗粒形成的吸附层是导致大孔呈"囊泡状"和孔道不贯通的主要原因. 采用聚二烯丙基二甲基氯化铵(PD)溶液对 PS 胶体微球带电性质进行了改性, PS 微球的 Zeta 电位由-44.36 mV 变成了+37.41 mV, 进而消除了沉积过程中二元颗粒间的吸附现象. 扫描电子显微镜显示, 大孔样品中"囊泡状"大孔消失, 同时孔道贯通性得到改善.

关键词: 大孔 Al₂O₃ 材料, 模板法, PS 微球, 铝溶胶, 电性改性 中图分类号: O647

Preparation of Macroporous Al₂O₃ by Template Method

WANG, Xiao-Dong DONG, Peng* CHEN, Sheng-Li (State Key Laboratory of Heavy Oil Processing, China University of Petroleum, Beijing 102249, P. R. China)

Abstract Macroporous material of Al_2O_3 was prepared through mixing a Al_2O_3 sol with polystyrene (PS) particles as templates, drying the suspension, and finally calcining it to remove the templates. The measurement obtained from the scanning electron microscopy (SEM) showed that the formed macroporous materials had a vesicle-like structure and most of the voids left by the templates were isolated from each other. The Zeta-potential value indicated that the PS spheres carried negative charges, whereas the alumina particles carried positive charges. During the preparation of macroporous Al_2O_3 , the Al_2O_3 colloidal particles were adsorbed on the surface of the PS particles, and the PS with the shell of Al_2O_3 particles played the role of templates, resulting in the formation of vesicle-like structures. To avoid the formation of the vesicle-like structure materials, the PS was switched from a negative charge to a positive charge through surface modification with PD (poly(diallyl-dimethyl ammonium chloride)), so that PS spheres carried the same kind of charge as the Al_2O_3 colloidal particles. The SEM images showed that the macroporous material of Al_2O_3 prepared using the modified PS spheres as templates, was free from the vesicle-like structure and voids left by the templates were connected through some windows.

Keywords: Macroporous material of Al₂O₃, Template method, Polystyrene spheres, Alumina sol, Electric property modification

近年来, 大孔(≥ 50 nm)金属氧化物材料的研究 引起了人们广泛的兴趣, 因为它在过滤分离材料、催 化剂载体、色谱载体、细胞固定载体等研究领域有着 广泛的应用前景. 大孔金属氧化物材料的研究为解

决重油催化领域中重油分子在催化剂孔道内扩散阻力过大,因而阻碍产物液体收率提高以及影响选择性的改善等问题提供了机会^[1]. Al₂O₃ 作为一种良好的吸附剂、分离材料和催化剂载体材料,在工业上有

Received: January 16, 2006; Revised: March 16, 2006. *Correspondent, E-mail: p.dong@china.com; Tel: +8610-89733783; Fax: +8610-69724721. 国家重点基础研究发展规划(973)项目(2004CB217808)和国家自然科学基金(20376046)资助

©Editorial office of Acta Physico-Chimica Sinica

着广泛的应用^[2-5]. 将Al₂O₃制成大孔材料对于重油乃 至渣油转化催化剂的研制将具有十分重要意义.

颗粒模板技术为实现较为理想化的大孔 Al₂O₃ 材料孔结构创造了可能的所谓颗粒模板技术是将接 近于单分散的胶体颗粒实现最紧密排列, 当模板体 积分数为 74%时, 每一个颗粒可与 12 个颗粒相邻 (配位数 12), 并将这种紧密排列的颗粒作为模板在 颗粒间隙中填充所需要的材料, 然后将模板去除, 余 下的便是一个刚好与模板相反且非常开放的大孔结 构. 虽然文献已有报道使用颗粒模板技术制备大孔 材料,但这项技术尚不成熟. 当前主要用于制作三维 光子晶体的研究[7-8], 也有尝试用分子筛作为孔壁材 料的研究[9-10]. 相关研究多局限于选用不同的材料来 制备大孔结构, 而对大孔材料中孔道的贯通性关注 较少[11-14]. 本课题组曾研究用PS微球与Al₂O₃颗粒共同 沉积的方法来制备大孔 Al₂O₃ 载体[15-16], 并通过对制 成催化剂的活性表征证实了这类大孔结构在重油转 化中的有效性[17] 但是在共沉积过程中, 二元颗粒的 体积配比可能成为决定大孔材料孔结构和孔道贯通 性的一个重要因素. 当 PS 模板的体积比例低于 74%时, 因模板颗粒处于非密堆积状态容易使其彼 此不接触,从而导致大孔孔道不贯通. 因此,如何确 保大孔材料中孔道的贯通性就成为颗粒模板法制备 大孔材料亟待解决的新问题.

孔道贯通性是由悬浮液中二元颗粒的分布状态 决定的, 其分布状态又是由 PS 模板颗粒间的相互 作用和 PS 模板颗粒与 Al₂O₃ 颗粒间的相互作用决 定的. 本研究仅就后者进行了研究, 并改善了大孔 Al₂O₃ 材料的孔道贯通性.

1 实验部分

1.1 PS 微球的制备

1.2 Al₂O₃ 溶胶的制备

室温下,将 10 g 的硝酸铝溶解于 15 mL 去离子水中. 搅拌的同时向硝酸铝溶液中缓慢滴加质量分

数为 3.5%的稀氨水, 至生成氢氧化铝凝胶时停止滴加. 氢氧化铝凝胶经过3次"洗涤/离心"处理, 除去凝胶中的NO₃和NH;等杂离子. 按照n(H+)/n(Al²+)=0.18 计算所需浓硝酸(胶溶剂)的量^[19], 然后将浓硝酸直接加入到氢氧化铝凝胶中, 强烈搅拌 10 min, 放置在120 ℃烘箱内加热至淡蓝色, 就制得了 Al₂O₃ 溶胶.

1.3 大孔结构 Al₂O₃ 的制备

将按照一定的纯颗粒体积比例(V_{PS} $V_{Al_2O_2}$)换算的 PS 悬浮液和 Al_2O_3 溶胶混合, 搅拌 1 min, 超声 10 min, 放置在鼓风干燥箱内加热. 烘箱温度设定在 100 °C, 通常经过 4~5 h 二元颗粒组装完成, 得到 PS 与 Al_2O_3 颗粒的共混物. 600 °C煅烧共混物除去 PS 模板, 得到大孔结构 Al_2O_3 .

1.4 PS 胶体颗粒的改性

PS 胶体颗粒改性使用的是聚二烯丙基二甲基氯化铵(PD, Aldrich产品, 相对分子质量M_w=2.0×0°~3.5×0°), 它是一种聚阳离子溶液^[20]. 取PS微球悬浮液 (质量分数约为10%)10 mL于离心管中, 加入 5 mL的PD 溶液(质量分数为1%), 搅拌1 min, 超声6 min, 静置 30 min, 使吸附充分. 再通过 2 次"离心/去掉上清液/在二次蒸馏水中分散"的循环处理, 除去未吸附的 PD 溶液.

1.5 PS和Al₂O₃胶体颗粒的粒度与Zeta电位测量

将样品经稀释, 超声分散后, 用英国 Malvern 公司生产的 Zetasizer ZS 型激光粒度仪对胶体颗粒的粒度及 Zeta 电位进行测量. 测量温度 $25 \, ^{\circ}$ C, 记数速率 $3.10 \times 10^5 \, \mathrm{s}^{-1}$.

1.6 SEM对大孔Al₂O₃材料的显微孔结构进行观测 采用日立 S-4200 型电子扫描显微镜对大孔 Al₂O₃ 结构进行表面、断面和底面的扫描观测. 施加电压: 15 kV.

2 结果和讨论

2.1 PS 微球与 Al₂O₃ 颗粒的粒度测量

图 1 显示了 1# PS 微球和 Al₂O₃ 颗粒的粒度及其分布. PS 微球平均粒径为 252 nm, 多分散指数 (PDI)为0.018, 表明PS微球的单分散性较好, PDI反映颗粒粒径均一的程度, 其值介于 0 到 1 之间. 数值越小,表示颗粒的单分散性越好, 粒径分布越窄^[21]. Al₂O₃ 溶胶中 Al₂O₃ 颗粒的粒径为44 nm, PDI 为 0.370,表明颗粒的粒度较小,分布较宽.

2.2 未改性 PS 微球作为模板制备大孔 Al₂O₃ 材料 图 2 为未改性的 1#PS 微球与 Al₂O₃ 颗粒共沉

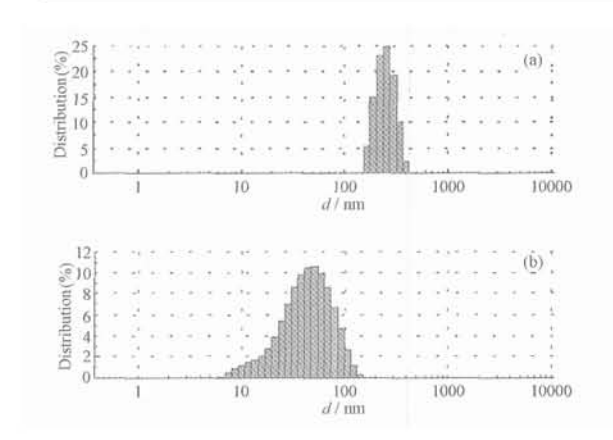


图1 PS 徽球与 Al₂O₃ 颗粒的粒度分布图

Fig.1 Size distributions of 1#PS spheres and alumina particles

(a) PS spheres, (b) alumina particles

积,再煅烧得到的大孔Al₂O₃材料的SEM照片. 图2(a),图 2(b)分别是大孔 Al₂O₃结构表面和断面的形貌像.质量分数分别为 10%的 1#PS 微球悬浮液和 46%的 Al₂O₃ 溶胶混合,悬浮液的量依照 PS 微球与 Al₂O₃ 颗粒的体积比 74 26 的比例配制. 一元亚微米PS微球进行自组织时通常会形成面心立方(fcc)形式的排列,按照 fcc 形式排列的组装体中模板颗粒所占体积为 74%,颗粒间孔隙占 26%^[23]. 对于二元颗粒共沉积,只有 PS 模板颗粒能够彼此接触,被去除后形成的孔道才能彼此贯通. 因此上述比例的选择是希望

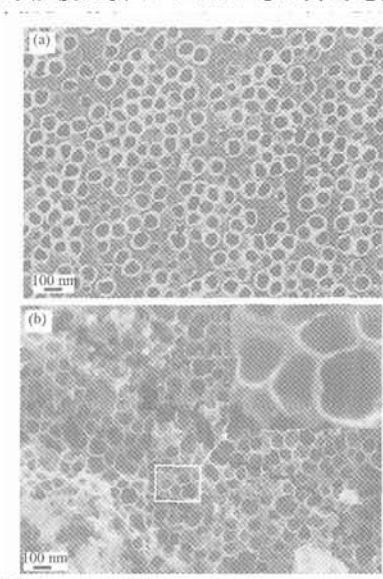


图 2 大孔 Al₂O₃结构的 SEM 照片

Fig. 2 SEM images of macroporous Al₂O₃
(a) and (b) are the surface and the cross section of the sample, respectively.

PS 模板颗粒呈 fcc 密堆积, 占据 74%体积比例的同时, 间隙被26%的Al₂O₃颗粒所填充, 最终在大孔结构中出现贯通的孔道网络. 从图2(a)、图2(b)中可以看出, 大孔并没有呈fcc有序排列, 基本是无序状态. 同时, 无论是样品的表面还是断面都可以清楚地发现"囊泡状"的大孔, 而且孔道的贯通性较差, 如图2(b)中放大图所示.

图 3 是用粒径 288 nm 的 2# PS 微球与 29 nm 的氧化硅(SiO₂)颗粒采用相同的方法、相同体积比 $(V_{PS} \ V_{SiO_2} = 74 \ 26)$ 制备的大孔 SiO_2 结构 SEM 照片. 其中图 3(a)、图 3(b)分别为样品的表面和断面的形貌像. 从图 3(a)中可以看出,样品中没有出现"囊泡状"的大孔,而且孔道的贯通性比较好,如图 3(a)中放大图所示. 从样品的断面图同样可以看出孔道的贯通性较好,也不存在"囊泡状"的大孔,如图 3(b)所示.

经过对比分析后发现, 两种材料的大孔结构之间之所以存在如此显著的差异, 究其原因可能与二元颗粒悬浮液中两种无机氧化物纳米颗粒和 PS 微球之间的静电作用力有关. 为此, 分别测量了共沉积条件下(pH=5.5)PS 微球、Al₂O₃ 颗粒、SiO₂ 颗粒以及与铝溶胶混合再离心分离出的 PS 微球粒径和 Zeta 电位.

2.3 胶体颗粒 Zeta 电位测量

表 1 显示了不同胶体颗粒在 pH=5.5 的水悬浮液中粒径及 Zeta 电位值. 从表 1 中可以发现, 在共

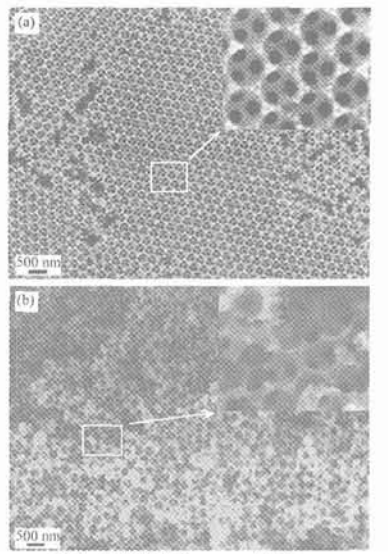


图 3 SiO₂ 三维大孔结构的 SEM 照片

Fig.3 SEM images of macrop orous SiO₂

(a) and (b) are the surface and the cross section of the sample, respectively.

表 1 pH 5.5 的水悬浮液中胶体颗粒的粒径和 Zeta 电位 Table 1 Diameter and the Zeta potential of different colloidal particles in water suspension (pH=5.5)

Sample	Diameter(nm)	Zeta potential(mV)
1# PS sphere	252	- 44.36
2# PS sphere	288	-45.56
Al ₂ O ₃ particle	44	+22.25
SiO₂ particle	29	- 52.04
1#PS sphere adsorbing Al ₂ O ₃ particles	332	+54.91°, +37.86°°

* and ** indicate Zeta-potential of PS sphere adsorbing Al₂O₃ particles after one and two centrifugal treatments, respectively.

沉积的实验条件下 PS 微球与 SiO₂ 颗粒均带有负电. 由于静电力的排斥作用两种颗粒之间保持着独立的分散状态, 不存在颗粒间的吸附现象. 这可能就是大孔 SiO₂ 结构没有"囊泡状"大孔, 且孔道贯通性比较好的主要原因. 而 PS 微球与 Al₂O₃ 颗粒所带电的电性相反, 两种颗粒悬浮液混合后, 由于静电力的吸引作用首先发生了颗粒间的吸附, 然后再进行组装. 形成的吸附层可能就是大孔材料中"囊泡状"大孔形成的主要原因, 同时也是样品内大孔间不贯通的原因所在.

为验证以上分析, 进一步对与 Al_2O_3 溶胶混合后 PS 微球的粒径和 Zeta 电位进行了测量. 为了测量 的准确性, 实验中将混合均匀的 PS 微球和 Al_2O_3 颗粒二元颗粒悬浮液先静置 30 min, 然后进行了离心分离(离心机转速 $10000 \, r \cdot min^{-1}$). 其目的在于消除悬浮液中未被吸附的 Al_2O_3 颗粒对测量 PS 微球 Zeta 电位的影响. 由于纳米 Al_2O_3 颗粒的粒度较小, 未被吸附的 Al_2O_3 颗粒的粒度较小, 未被吸附的 Al_2O_3 颗粒不会随亚微米 PS 颗粒一起离心沉降, 而是留在上层清液中被除去. 连续"离心/去离子水分散"两次, 并对每次离心分离出来的 PS 微球分别进行了 Zeta 电位测量.

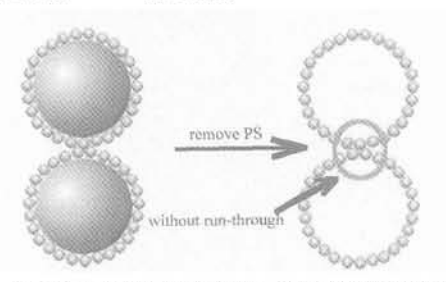


图 4 PS 徽球表面的吸附层导致三维大孔结构内孔道不贯 通的示意图

Fig. 4 Sketch of the adsorption layer on the surface of PS spheres leads to the voids of macroporous materials with out run-through

表 1 显示了吸附了 Al_2O_3 颗粒的 1# PS 微球的粒径和 Zeta 电位值. 从表 1 数据可以看出, 吸附了 Al_2O_3 颗粒的 PS 微球粒径由 252 nm 增加到 332 nm, 增加了80 nm, 几乎为 Al_2O_3 颗粒粒径的2倍. 同时, 1# PS微球的Zeta电位由- 44.36 mV变成了+54.91 mV. 通过以上数据可以认为, 带正电的 PS 微球与带负电的 Al_2O_3 颗粒之间确实发生了吸附. 另外发现, 多次"离心/分散"处理会使 PS 微球的电位有所降低. 这可能与处理过程中会有部分 Al_2O_3 颗粒从PS 微球表面脱落有关.

分析认为, 大孔 Al_2O_3 结构中的"囊泡状"大孔 是由 PS 微球表面的 Al_2O_3 颗粒吸附层形成的. 而吸 附层的存在使得在 PS 微球煅烧被除去之后, 大孔 之间变得不能贯通, 可用图 4 示意表示.

2.4 电性质改性后的 PS 微球作为模板制备大孔 Al₂O₃ 材料

为了消除PS微球与Al₂O₃颗粒间的吸附作用,进而实现大孔Al₂O₃结构内孔道的贯通,对PS微球的带电性质进行改性. PS 微球的改性使用的是聚二烯丙基二甲基氯化铵(PD),它是一种聚阳离子溶液. 改性后用激光粒度仪测量Zeta电位的变化. Zeta电位测量结果表明,经过改性后1#PS微球的Zeta电位由原来

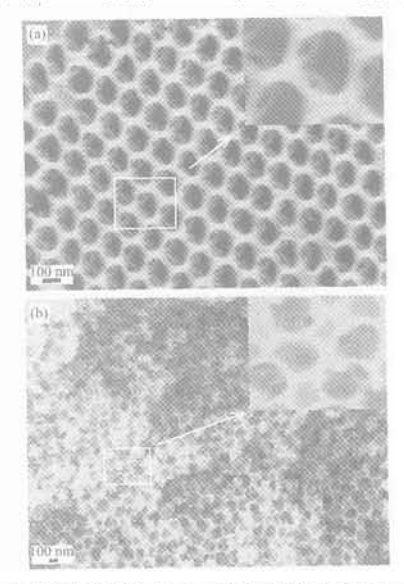


图 5 改性后 PS 微球与 Al₂O₃ 颗粒共沉积制得的 Al₂O₃ 三 维大孔结构的 SEM 照片

Fig.5 SEM images of macroporous Al₂O₃ prepared by co-deposition of modified PS spheres and Al₂O₃ particles

(a) and (b) are the surface and the cross section of the sample, respectively. 的-44.36mV变成了+37.41mV, 改性的效果比较明显.

图 5 为用 PD 改性后的 1# PS 微球与 Al₂O₃ 颗粒共沉积, 最终得到的大孔 Al₂O₃ 结构的 SEM 照片. 其中图 5(a)为样品的表面形貌像, 图 5(b)为样品的断面形貌像. 从图 5(a)样品的表面可以看出, 图 2 中的"囊泡状"大孔消失了, 大孔的形貌得到改善. 出现面心立方 fcc 形式的有序孔结构, 孔道贯通性良好, 如图 5(a)中的放大图所示. 从图 5(b)样品的断面可以看出, 孔道的贯通性也明显改善, 孔径变得较为均匀, 基本不存在"囊泡状"的大孔, 其形貌基本可以与大孔 SiO₂ 结构相当. 大孔之间通过"小窗口"相互连接, 如图 5(b)中放大图所示.

上述实验结果说明,通过先对 PS 微球进行带电性质的改性,然后再与 Al₂O₃ 颗粒进行共沉积的方法,可以消除 PS 微球与 Al₂O₃ 颗粒两种胶体颗粒之间由静电引力而发生的吸附现象. 吸附现象的消除,不仅使得大孔 Al₂O₃ 结构的"囊泡状"大孔消失,大孔孔径变得均匀,而且可以显著地改善孔道的贯通性. 这对于采用颗粒模板技术来制备大孔 Al₂O₃ 催化材料具有重要的应用意义.

3 结 论

在用颗粒模板法制备Al₂O₃大孔材料过程中, PS 微球、Al₂O₃ 颗粒和吸附了 Al₂O₃ 颗粒的 PS 微球的 粒径及 Zeta 电位测量说明, 共沉积条件下 PS 微球与 Al₂O₃ 颗粒所带电的电性相反. PS 微球悬浮液与 Al₂O₃ 溶胶混合后, 由于静电力的吸引作用发生了颗粒间的吸附现象, 在 PS 微球的表面形成了 Al₂O₃ 颗粒吸附层. 吸附层的存在使得最终制得的大孔 Al₂O₃ 结构中出现"囊泡状"的大孔, 并且大孔之间贯通性较差. 使用 PD 改性 PS 微球后, PS 微球 Zeta 电位由负变成正. 采用改性后的 PS 微球与 Al₂O₃ 颗粒进行共沉积, 最终制得的大孔 Al₂O₃ 结构的形貌得到改善, "囊泡状"大孔消失, 孔道贯通性较好.

References

- 1 Dong, P. Progress in Natural Science, 2000, 10: 575
- 2 Ma, Z. F.; Jin, Y. L.; Liu, Y. M.; Yao, H. Q. J. Chem. Eng. Chin. Univ., 1994, 8: 288 [马正飞, 金叶玲, 刘艳梅, 姚虎卿. 高等学校化学工程学报(Gaodeng Xuexiao Huaxue Gongcheng Xuebao), 1994, 8: 288]
- 3 Lin, L.; Lin, W.; Wang, P.; Zhu, Y. X.; Zhao, B. Y.; Xie, Y. C. Acta Phys. -Chim. Sin., 2004, 20 (10): 1179 [林 莉, 林 伟, 王 培, 朱月香, 赵璧英, 谢有畅. 物理化学学报(Wuli Huaxue Xuebao), 2004, 20(10): 1179]

- 4 Chen, L. B.; Guo, S. H.; Song, L. Q.; Zhao, Z. X.; Zhang, Z. G. J. Fuel Chem. Techn., 2004, 32 (6): 684 [陈立波, 郭绍辉, 宋兰琪, 赵志翔, 张占纲. 燃料化学学报(Ranliao Huaxue Xuebao), 2004, 32(6): 684]
- 5 Li, S. L.; Chen, G. W.; Jiao, F. J.; Li, H. Q. Chin. J. Catal., 2004, 25(12): 979 [李淑莲, 陈光文, 焦风军, 李恒强. 催化学报 (Cuihua Xuebao), 2004, 25(12): 979]
- 6 Avelino, C.; Maria, J.; Diaz, C. Nature, 2002, 418: 514
- 7 Vlasov, Y. A. Nature, 2001, 414: 289
- 8 Cao, J. M.; Chang, X.; Zheng, M. B.; Huang, H. B.; Ji, H. M.; Liu, J. S.; Ke, X. F. Acta Phys. -Chim. Sin., 2005, 21(5): 560 [曹洁明, 常 欣, 郑明波, 黄海宾, 季红梅, 刘劲松, 柯行飞. 物理化学学报 (Wuli Huaxue Xuebao), 2005, 21(5): 560]
- 9 Huang, L. M.; Wang, Z. B.; Sun, J. Y.; Miao, L.; Li, Q. Z.; Yan, Y. S.; Zhao, D. Y. J. Am. Chem. Soc., 2000, 122: 3530
- 10 Blanford, C. F.; Yan, H.; Schroden, R. C.; Al-Daous, M.; Stein, A. Adv. Mater., 2001, 13(6): 401
- 11 Wang, Y. J.; Tang, Y.; Wang, X. D.; Yang, W. L.; Ni, Z.; Hua, W. M.; Yue, Y. H.; Gao, Z. Chem. J. Chin. Univ., 2000, 21:1013
 [王亚军, 唐 颐, 王星东, 杨武利, 倪 铮, 华伟明, 乐英红, 高 滋. 高等学校化学学报(Gaodeng Xuexiao Huaxue Xuebao), 2000, 21:1013]
- 12 Zhu, G. S.; Qiu, S. L.; Gao, F. F.; Li, D. S.; Li, Y. F.; Wang, R. W.; Gao, B.; Li, B. S.; Guo, Y. H.; Xu, R. R.; Liu, Z.; Terasaki, O. J. Mater. Chem., 2001, 11: 1687
- Liu, L. X.; Dong, P.; Yi, G. Y.; Cheng, B. Y. Chemistry, 2005, 9:
 674 [刘丽霞, 董 鵬, 仪桂云, 程丙英. 化学通报(Huaxue Tongbao), 2005, 9: 674]
- 14 Wang, Y. J.; Tang, Y.; Ni, Z.; Hua, W. M.; Yang, W. L.; Wang, X. D.; Tao, W. C.; Gao, Z. Chem. Lett., 2000, 5: 510
- 15 Dong, P.; Chen, S. L.; Wang, D. J. Macro-porous hydrogenation catalysts and its preparation. CN patent, 200510089821. 2005 [董 鹏, 陈胜利, 王大军. 大孔加氢催化剂及其制备方法. 中国发明专利, 200510089821. 2005]
- 16 Chen, S. L.; Dong, P.; Qi, Y. P.; Xu, K. Q. Preparation of macroporous catalytic cracking catalyst for heavy Oil. CN patent, 200510082624. 2005 [陈胜利, 董 鹏, 祁彦平, 徐克琪. 重油加工大孔催化裂化催化剂合成方法. 中国发明专利, 200510082624. 2005]
- 17 Qi, Y. P.; Dong, P.; Chen, S. L; Shen, B. J. Primary study on macro porous FCC catalysts prepared using the nano polystyrene particles as template. Abstract of Papers of the Acs 229 130- Fuel Part 1, 2005; U871
- 18 Reese, C. E.; Guerrero, C. D.; Weissman, J. M.; Lee, K.; Asher, S. A. J. Colloid Interface Sci., 2000, 232 (1): 76
- 19 Wang, B. Y.; Huang, C. Z.; Ai, X. Journal of Ceramics, 1998, 19 (4): 209 [王宝友, 黄传真, 艾 兴. 陶瓷学报(Taoci Xuebao), 1998, 19(4): 209]
- 20 He, C. Y.; Liang, Z. P.; Wang, C. Y.; Liu, X. X.; Tong, Z. Chem. J. Chin. Univ., 2005, 26: 88 [何成毅, 梁振鹏, 王朝阳, 刘新星, 章 真. 高等学校化学学报(Gaodeng Xuexiao Huaxue Xuebao), 2005, 26: 88]
- 21 Wong, S.; Kitaev, V.; Ozin, G. A. J. Am. Chem. Soc., 2003, 125: 15589
- 22 Im, S. H.; Lim, Y. T.; Suh, D. J. Adv. Mater., 2002, 14: 1367

文章编号:1673-5005(2006)06-0107-05

纤维液膜萃取分离器的流动、传质规律研究

范怡平1, 尤明扬1, 鄂承林1, 李涛子2, 卢春喜1, 顾春来2, 时铭显1

(1.中国石油大学 重质油加工国家重点实验室, 北京 102249; 2.北京欣博通创新能源技术开发有限公司, 北京 100083)

摘要:在一直径为70 mm,高为2630 mm的有机玻璃纤维液膜萃取分离器冷态实验装置上考察了操作参数及结构参数对其传质性能和流动特征的影响。通过考察体积传质系数,确定了纤维液膜萃取分离器的最佳填充密度和最佳流量比。建立了流动模型,提出了以无量纲准则数雷诺数为设计纤维液膜萃取分离器的准则。实验结果表明,其最佳填充密度为2.8%~3%,最佳操作流量比为5。

关键词:纤维液膜;萃取分离器;流动;传质;填充密度;流量比;雷诺数;设计

中图分类号: TH 213.5 文献标识码:A

Flow and mass-transfer laws in a fiber film extractor

FAN Yi-ping¹, YOU Ming-yang¹, E Cheng-lin¹, LI Tao-zi², LU Chun-xi¹, GU Chun-lai², SHI Ming-xian¹

- (1. State Key Laboratory of Heavy Oil Processing in China University of Petroleum, Beijing 102249, China;
 - 2. New Baron Innovative Energy Technology Development INC, Beijing 100083, China)

Abstract: The performances of the fiber film extractor were investigated using a cold plexiglass pipe of 70 mm in diameter and 2630 mm in height. The influences of the operating and structural parameters on the flow and mass transfer characteristics of the fiber film extractor were revealed. By analyzing the volume mass transfer coefficient, the optimal operating flow-ratio and packed density were obtained. A flow model was built. Moreover, based on the theoretical analysis, Renault number was proposed as the design principle dimensionless number for fiber film extractor design purpose. The experimental results indicate that the optimal operating flow-ratio for a fiber film extractor is 5 while the best packed density is 2.8% %.

Key words: fiber film; extractor; flow; mass transfer; packed density; flow ratio; Renault number; design

在炼油、化工工业中,不互溶液-液两相的萃取工艺非常普遍。为了实现高效萃取,一般将两相液流破碎为小液滴以增加接触面积、强化传质。但当传质过程完成后,两相乳化、夹带现象较为严重,很难实现清洁分离。纤维液膜萃取分离器是一种新型的高效传质设备,由一个装填有大量纤维丝的立罐及分离沉降罐组成。原料液和萃取剂都从萃取器顶部流入立罐,两相在纤维之间形成顺向流动的液膜。其中一相在纤维表面形成很薄的液膜,由于两相的流速不同,二者间的曳力将液膜拉得极薄,提供了极大的传质面积。在传质过程中,两相界面始终保持,无弥散现象。当完成传质之后密度较大的一相沿着

纤维直接流到分离沉降罐底,而密度较轻的一相则浮在上面。两相得以迅速地分离,避免了乳化和夹带现象的出现。纤维液膜萃取分离器最早是由美国Merichem公司开发的。但该技术被外商独家垄断,相关专利中一些关键参数并没有给出[1-11],学术刊物更是很少涉及,更多的是用户对萃取器使用效果的介绍[12-19]。蔡卫滨等[20]虽曾对纤维液膜萃取分离器的传质特性进行了研究,但实验中采用的设备尺度偏小,使其结论的适用性受到了限制。为了跟踪这项先进的萃取技术,笔者对纤维液膜萃取分离器内流动、传质的机理及过程进行研究,为实现该技术的国产化提供理论依据。

收稿日期:2006 - 09 - 18

基金项目:中国石油化工股份有限公司基础理论研究资助项目(X504016)

作者简介:范怡平(1972-),男(汉族),河南洛阳人,讲师,博士,从事化工过程装备与控制的教学及多相流技术的研究工作。

实验装置及测试

1.1 测试参数的选取

重点考察不同纤维丝填充密度、不同两相体积 流量比对纤维液膜萃取分离器传质性能的影响。此 处填充密度定义为:在传质空间中所有纤维丝截面 积的总和与萃取器截面积之比。本文中纤维丝的填 充密度为 1.893 %~3.769 %, 而两相体积流量比则 为 2~7。

纤维液膜萃取分离器 的传质特性通过考察传质 体系体积总传质系数来确 定。

取图 1 所示高度为 dh 的微分单元分析萃取器内传 $Q_{\mathbf{x}},\mathbf{x}+\mathbf{dx}$ 质过程。根据其内部两相实 际流动特点,采用平推流模 型。设原料液相、萃取剂相 的体积流量分别为 $o_{\rm w}$ 和 Q_0 ,两相的进、出口浓度分

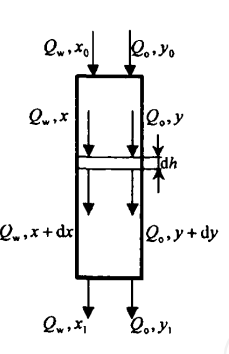


图 1 传质微分单元

别为 x_0 , v_0 和 x_1 , v_1 , 平衡浓度曲线为 $x^* = f(v)$, 则 以浓度差为推动力的体积总传质系数表达式为

$$K_{\rm L} \ a = \frac{K_{\rm x} a}{C} = -\frac{Q_{\rm w}}{HA} \int_{x_0}^{x_{\rm f}} \frac{\mathrm{d} \ x}{x - f \left(\frac{Q_{\rm w} (x_0 - x)}{Q_{\rm o}} + y_0 \right)} \ . \ (1)$$

式中, $K_{L}a$ 为以 ΔC 为推动力的体积总传质系数, 1/s; $K_x a$ 为以 Δx 为推动力的体积总传质系数, kmol/(m³·s); C为浓度, kmol/m³; H为纤维丝的高 度, \mathbf{m} : A 为两相接触传质总面积, \mathbf{m}^2 : x, v 分别为原 料液和萃取剂中溶质的摩尔分率。

1.2 传质体系的确定

综合考虑了萃取两相介质的理化性质、腐蚀性、 安全性以及实验成本等多方面的因素,确定以煤油-苯甲酸水溶液为考察对象。根据相似相溶的原则,苯 甲酸在水中的溶解度小于其在煤油中的溶解度,当 苯甲酸的水溶液与煤油发生接触时,苯甲酸将越过 油水的界面进入到煤油中。测量苯甲酸水溶液在萃 取分离器进出口处的浓度变化,并根据式(1) 计算 传质系数。实验中苯甲酸浓度用 0.0025 mol/L 氢氧 化钠溶液来滴定。

1.3 实验装置

实验装置及流程如图 2 所示。启动计量泵 B.可 将煤油从萃取剂罐中输送到纤维液膜萃取分离器的 顶部,并沿着纤维表面顺重力流动形成极薄的液膜。 待浸润纤维丝一段时间后,开启计量泵 A 将苯甲酸 水溶液从原料液罐中抽出并输送至萃取器顶部,两 相沿着纤维丝同向顺重力流动,发生接触并进行传 质。当传质过程完成之后,两相一同流入到分离沉降 罐中,由于存在着明显的密度差,二者将自动分层实 现分离。萃取剂煤油经过处理后可以重复使用,引入 到萃取剂再生罐中进行下一步的处理。

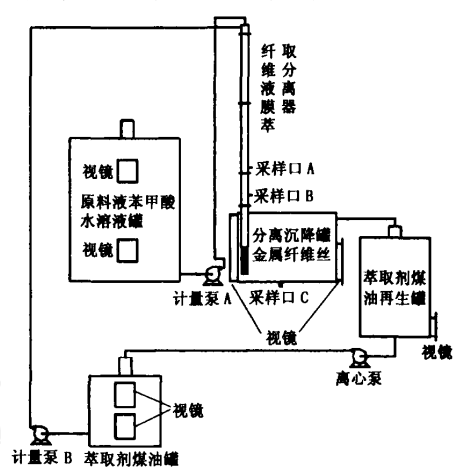


图 2 实验装置流程图

纤维液膜萃取分离器采用高 2650 mm、内径 70 mm 的有机玻璃管。分离沉降罐为一长 1 200 mm、内 径 850 mm 的卧式罐。为了考察传质体系的流动特 性,在各个罐体上安装了一系列有机玻璃视镜。

实验结果及其分析

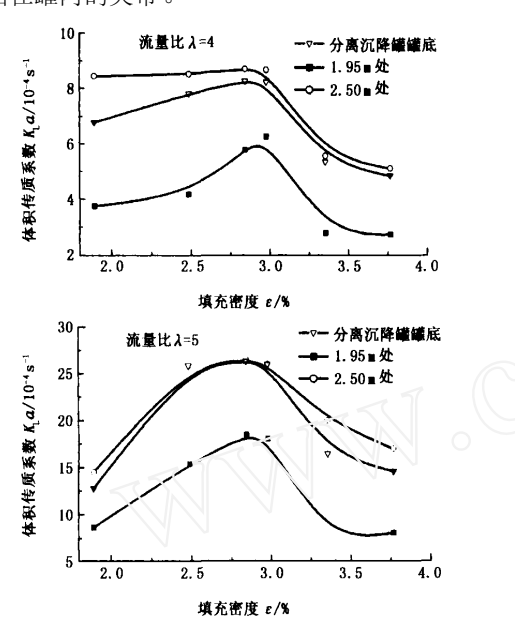
2.1 纤维液膜萃取分离器最佳填充密度的确定

图 3 中给出了体积流量比为 4 和 5 条件下传质 系数随纤维丝填充密度的变化规律。由图可见.虽然 两相流量比不同,但是变化规律却是相同的,即随着 填充密度的增加,传质系数先是增加,而后又逐渐下 降。说明在纤维液膜萃取分离器的操作中存在着一 个最佳填充密度,其值在2.8%~3%。

当 1.893 $\leq \varepsilon$ ≤2.8 ~ 3 时,传质系数随填充密 度增加而增加,因为填充密度的增大,萃取器中传质 表面积也迅速增加,传质效率得到提高。但是如果纤 维丝填充密度过大,则两相流道面积减小,两相流速 均增加,二者在接触器中停留时间减小,因而传质系 数下降。

由图 3 可见,距两相入口 1.95 m 处的传质系数 与距入口 2.5 m 以及分离沉降罐罐底处相比,其数 值明显较低,这一点说明文献[20]中关于萃取器长 度对传质系数影响不大的假设并不十分准确。

与入口 2.5 m 处的传质系数相比,分离沉降罐 罐底处的传质系数略小。笔者认为,这是由于两相存 在着一定程度的夹带,在进入到分离沉降罐之后,二 者并没有迅速分离,而是继续发生传质。在分离沉降 罐中,煤油中的苯甲酸接近饱和,因而致使一部分溶 质由萃取剂中又重新回到了原料液相中。可见,在实 际生产中分离沉降罐中应设置聚结器等部件以消除 两相在罐内的夹带。



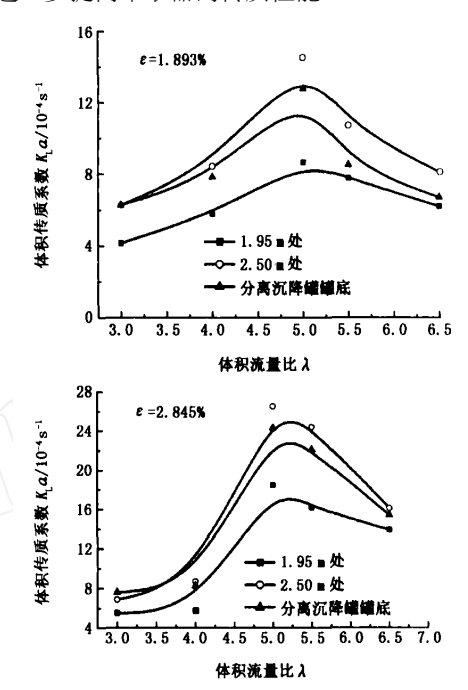
体积传质系数随纤维丝填充密度的变化

2.2 纤维液膜萃取分离器最佳操作流量比的确定

图 4 中给出了两种填充密度条件下传质系数随 两相流量比的变化情况。由图可见,在流量比λ为2 ~ 5 时,随着流量比的增加,传质系数逐渐增大。但 随着流量比继续增大, 当λ>5时, 传质系数则有所 降低。这说明纤维液膜萃取分离器存在着一个最佳 操作流量比,其值约为5。

传质系数随着流量比的增大而增大,主要原因 在于接触两相之间的速度差增大,加速了溶质(在这 里是苯甲酸) 在两相间的动量交换速度, 因而传质 速率也随之增大。但是如果流量比过大,则一方面原 料液过量,另一方面由于流量比过大可能导致夹带 加剧,影响传质效果。

分析图 3,4 可见,在萃取分离器顶端两相入口 至其近75%长度的空间范围内,尚有进一步改善结 构、强化传质的必要。主要表现在距两相入口 1.95 m 处的体积传质系数明显小于 2.5 m 处。说明在目 前的萃取器结构中,有相当一部分传质高度没有得 到充分利用。这主要是由于在萃取器上部纤维丝的 固定方式还不尽完善,致使入口附近纤维丝的排布 难以做到十分均匀。笔者认为,可通过优化纤维丝固 定形式或在该区域内设置两相液体再分布部件的方 式进一步提高萃取器的传质性能。



体积传质系数随两相流量比的变化

分离器设计的无量纲准则数

纤维液膜萃取分离器设计的关键是确定结构参 数、操作参数与传质系数之间的关系.即找到某一个 无量纲参数作为设计、放大的准则。通过对式(1)中 各项进行分析,可以初步推断传质系数与操作参数、 结构参数的关系。

通过量纲分析可以得知, $Q_{\mathbf{w}} C / A$ 表示的是原 料液的流量强度, 因此该项应与原料液相的密度 $\rho_{\rm w}$ 、流速 $u_{\rm w}$ 以及接触器的直径密切相关。a 的物理 意义为单位体积填料所能提供的两相接触面积,该 参数显然与设备中纤维丝的填充密度以及沿纤维丝 流动两相接触的传质面积存在着密切联系。x-反映了传质推动力的大小, 该参数应当不仅与接触两相的理化性质有关,还应

与粘度密切相关,因为粘度本身就反映了在流体中 分子扩散的剧烈程度。如果流体的粘度太高,溶质在 其中的扩散将变得非常困难。因此,该项应当是流体 粘度及其化学性质的综合反映。

由此可以初步确定, 雷诺数应当是较为合适的 设计准则无量纲参数。

3.1 纤维液膜萃取分离器雷诺数的计算

3.1.1 纤维液膜萃取分离器雷诺数的表达式

纤维膜萃取分离内的两相分布如图 5 所示。设 萃取器内任意相邻两根纤维丝之间的距离相同,则 填充密度可表达为

$$\varepsilon = \frac{\pi R_0^2}{2\sqrt{3} R_2^2}.$$
 (2)

式中, R_0 为纤维丝的半径, m; R_2 为沿任一根纤维表 面原料液流通截面半径。

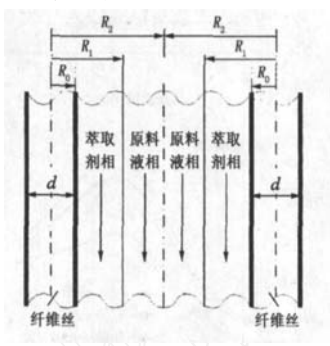


图 5 纤维液膜萃取分离器 两相流道示意图

设两相流道中原料液相与萃取剂相的速度比为 α,则原料液相雷诺数 Rew 可表示为

$$Re_{w} = \rho_{w} \lambda Q_{o} / \left[\mu_{w} \left(0.231D + \frac{0.372D^{2}}{R_{0}} + \frac{1.361\sqrt{\varepsilon}D}{R_{0}} \right) \left(0.906 + \varepsilon \frac{\lambda}{\alpha} \right) / \left(\varepsilon + \varepsilon \frac{\lambda}{\alpha} \right) + \frac{0.393\varepsilon D^{2}}{R_{0}} \sqrt{0.906 + \varepsilon \frac{\lambda}{\alpha}} / \left(\varepsilon + \varepsilon \frac{\lambda}{\alpha} \right) \right].$$
(3)

式中.D 为纤维液膜萃取分离器的直径.m: uw 为原 料液的动力粘性系数, $Pa \cdot s$; ρ_w 为原料液的密度, kg/m^3 o

3.1.2 萃取两相流动模型的建立及雷诺数的计算 根据实验观察,两相在纤维液膜萃取分离器内 的流动为平推流。

假设条件 : (1) 流动是定常的, 即 $\frac{\partial}{\partial t} = 0$; (2) 沿 着任意一根纤维丝的周向流场是轴对称的,即有 $\frac{\partial}{\partial t}$ =0; (3) $u_r = u_\theta = 0$, $r = R_0 \exists j$, $u_0 = 0$; $r = R_1 \exists j$, $u_{\rm o} = u_{\rm w}$, $\mu_{\rm o} = \frac{{\rm d}\,u_{\rm o}}{{\rm d}\,r} = \mu_{\rm w} \frac{{\rm d}\,u_{\rm w}}{{\rm d}\,r}$; $r = R_2$ H, $\frac{{\rm d}\,u_{\rm w}}{{\rm d}\,r} = 0$. 在此条件下,N-S 方程可以简化为

$$\frac{\mathrm{d}p}{\partial z} - \rho_{\mathrm{o}}g = \frac{\mu_{\mathrm{o}}}{r} \frac{\mathrm{d}}{\mathrm{d}r} \left(r \frac{\mathrm{d}u_{\mathrm{o}}}{\mathrm{d}r} \right), \quad R_{\mathrm{0}} \leqslant r \leqslant R_{\mathrm{1}};$$

$$\frac{\mathrm{d}p}{\partial z} - \rho_{\mathrm{w}}g = \frac{\mu_{\mathrm{w}}}{r} \frac{\mathrm{d}}{\mathrm{d}r} \left(r \frac{\mathrm{d}u_{\mathrm{w}}}{\mathrm{d}r} \right), \quad R_{\mathrm{1}} \leqslant r \leqslant R_{\mathrm{2}}.$$
(4)

式中,t为时间,s;r,z分别为沿任一根纤维丝的柱 坐标径向、轴向位置,m; θ 为沿任一根纤维丝柱坐标 周向位置; p 为压力, Pa; R1 为沿任一根纤维表面两 相接触界面半径, m; uo, uw 分别为萃取剂和原料液 流动速度, \mathbf{m}/\mathbf{s} ; $\mu_{\mathbf{o}}$ 和 $\mu_{\mathbf{w}}$ 分别为萃取剂和原料液的 动力粘度, $Pa \cdot s$; ρ_o 和 ρ_w 分别为萃取剂和原料液的 密度,kg/m³。

求解可得

$$\frac{8 \mu_{0} Q_{w}}{n\pi} = \left[\frac{8 \mu_{0} Q_{o}}{n\pi} + (\rho_{w} - \rho_{o}) gX_{2}}{X_{1} + X_{2}} \right] X_{2} + \left(\frac{8 \mu_{0} Q_{o}}{n\pi} - (\rho_{w} - \rho_{o}) gX_{1}}{X_{1} + X_{2}} \right] X_{3}.$$

$$\downarrow + \psi$$
(5)

 $X_1 = (R_1^4 - R_0^4) + 4 R_1^4 \ln \frac{R_0}{R_1} + 2 (R_1^2 - R_0^2)^2$

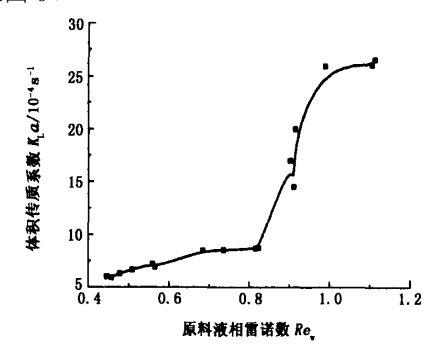
$$X_2 \, = 4 \, (\, R_1^2 \, - \, R_0^2) \, \, R_1^2 {\rm ln} \frac{R_0}{R_1} \, + 2 \, (\, R_1^2 \, - \, R_0^2) \, \, (\, R_2^2 \, - \, R_1^2) \, \, ,$$

$$X_{3} = \frac{\mu_{0}}{\mu_{w}} (R_{2}^{4} - R_{1}^{4}) + 2(R_{2}^{2} - R_{1}^{2})^{2} \times \left[\frac{\mu_{0}}{\mu_{w}} + 2\ln\frac{R_{0}}{R_{1}} \right] + 4 \frac{\mu_{0}}{\mu_{w}} R_{2}^{4} \ln\frac{R_{1}}{R_{2}}.$$

式中,n 为萃取分离器中纤维丝的数量。式(5) 与式 (3) 联立,即可求得原料液相雷诺数。

3.2 雷诺数准则的验证

原料液相雷诺数与其体积总传质系数之间的关 系见图 6。



纤维液膜萃取分离器雷诺数 与传质系数的关系

可见纤维液膜萃取分离器内体积传质系数随雷 诺数增加而递增。因此,在设计过程中将雷诺数作为 无量纲参量与传质系数进行关联是较为合理的。进行设计时,首先由进口两相表观速度确定设备的直径 D,再选择合适的 ε 与 λ 组合,使雷诺数的值最大。

4 结 论

(1) 纤维液膜萃取分离器最佳流量比为 5, 最佳 填充密度应控制在 2.8%~3%。

(2) 优化纤维丝固定方式或在萃取分离器两相 入口至其近 75%的长度内设置两相液体再分布部 件能够进一步改善设备的传质性能。将雷诺数作为 纤维液膜萃取分离器设计准则是合理的。

谨以此文献给烛炬五十载、桃李满天下的恩师 时铭显院士!

参考文献:

- [1] CLONTS, KENYON E. Liquid-liquid mass transfer apparatus: US, 3977829[P]. 1976-06-12.
- [2] PAN, SAMUEL C. Liquid-liquid extraction apparatus including fibrous strand packing: US, 3989466 [P]. 1976-11-02.
- [3] VERACHTERT. Countercurrent liquid-liquid contacting apparatus: US, 4491565[P]. 1985-06-01.
- [4] MAPLE, RALPHE, REDD, et al. Process for regenerating an alkaline stream containing mercaptan compounds: US, 4666089[P]. 1987-02-11.
- [5] SUAREZ, FELIPEJ. Process for treating an effluent alkaline stream having sulfur-containing and phenolic compounds: US, 5997731[P]. 1999-11-07.
- [6] MAPLE, RALPH E, SUAREZ, et al. Treatment of sour hydrocarbon distillate: US, 4675100[P]. 1987-06-23.
- [7] MAPLE, RALPH E, SUAREZ, et al. Treatment of sour hydrocarbon distillate: US, 4746494[P]. 1988 05-24.
- [8] LANGFORD, VIRGIL. Process for treating hydrocarbons containing mercaptans: US, 4875997[P]. 1989-10-24.
- [9] LEE, BINH N, WAL THER. Treatment of sour hydrocarbon distillate with continuous recausticization: US, 5961819[P]. 1999-10-05.
- [10] KIM KWANGWOOK, LEE, et al. Highly packed fiber bundle contactor and static liquid liquid contacting method using same: US, 5904849[P]. 1999-05-08.
- [11] CLONTS, KEN YON E. Mass transfer apparatus: US, 3992156[P]. 1976-12-03.
- [12] 胡尧良. 油品脱硫精制的纤维膜接触器技术及应用 [J]. 炼油 ,1999 ,25(1) :20-24. HU Yao-liang. Application of fiber-film contractor in oil

- desulfurize unit[J]. Oil Refining, 1999,25(1):20-24.
- [13] 杨秀峰. 纤维膜接触器在汽油碱洗中的应用[J]. 炼油设计,1998,28(6):25-30.
 - YANG Xiurfeng. Application of fiber-film contactor in gasoline caustic washing [J]. Petroleum Refinery Engineering, 1998, 28(6):25-30.
- [14] 胡尧良. 轻质油品脱硫精制乳化难题的技术突破[J]. 炼油设计,1999,29(5):47-53.
 - HU Yao liang. A breakthrough in dealing with emulsification problem in light oil treatment application of fibre film contactor technology[J]. Petroleum Refinery Engineering, 1999, 29(5):47-53.
- [15] 王立新. 喷气燃料的纤维膜精制工艺[J]. 炼油设计, 2001, 31(7):29-31.
 - WANG Li-xin. Jet fuel refining by fiber-film contactors [J]. Petroleum Refinery Engineering ,2001 ,31 (7):29-31.
- [16] 黄祖娟. 纤维膜接触器在脱硫装置中的应用[J]. 金陵 科技,2003,10(1):32-34.
 - HUANG Zurjuan. Application of fiber-film contractor in desulfurize Unit [J]. Jinling Science and Technology, 2003,10(1):32-34.
- [17] 刘振宁,王宏,李永安.纤维膜脱硫技术在 RFCC 汽油 脱臭单元的应用[J]. 石油炼制与化工,2002,33(5): 5-9
 - L IU Zherrning, WANG Hong, L I Yong an. Application of fiber film desulfurization technology for resid FCC naphtha sweetening [J]. Petroleum Processing and Petrochemicals, 2002, 33(5):5-9.
- [18] 严卫. 纤维膜技术在催化汽油精制的应用[J]. 南炼科技,2002,9(1):22-27.
 - YAN Wei. Application of fiber film technology to catalyst gasoline refinement [J]. Nanjing Petro Science and Technology, 2002, 9(1):22-27.
- [19] 胡荣海,刘振宁,胡尧良.纤维膜技术在催化汽油精制的应用[J]. 南炼科技,2002,9(2):14-19.
 - HU Rong hai , L IU Zherrning , HU Yao-liang. Application of fiber-film contactor in gasoline caustic washing [J]. Nanjing Petro Science and Technology , 2002 , 9 (2) :14-19.
- [20] 蔡卫滨,王玉军,朱慎林. 纤维膜萃取器的传质特性 [J]. 清华大学学报:自然科学版,2003,43(6):738-741.
 - CAI Wei-bin, WANG Yu-jun, ZHU Sher-lin. Mass transfer characteristics of fiber membrane extraction module[J]. Journal of Tsinghua University(Science and Technology) ,2003 ,43(6):738-741.

(编辑 沈玉英)